Proceedings of the Fifteenth International Symposium on Space Terahertz Technology

Gopal Narayanan, Editor
University of Massachusetts,
Amherst, MA

April 27-29, 2004
Hotel Northampton
Northampton, Massachusetts

SOFIA

HERSCHEL

SAFIR

ALMA

AST/RO

PREFACE

On behalf of the Organizing Committee, I wish to thank all of the authors and the presenters who have done a wonderful job of making this Symposium successful and productive. The 15th International Symposium on Space Terahertz Technology was organized by the University of Massachusetts, Amherst, and was co-sponsored by the IEEE Microwave Theory and Techniques (MTT) Society, and by the Electromagnetics Division of the National Institute of Standards and Technology (NIST).

Forty-four abstracts were accepted for oral presentation, and twenty-eight papers were accepted for poster presentations. We also had three invited talks at the beginning of each day. The breakdown of the accepted abstracts in terms of the broad technology category is as follows:

Hot Electron Bolometers	15
SIS Technology	11
LO Sources	8
Direct Detectors	11
Terahertz Systems	13
Optics and Related Technologies	14

All of the accepted papers that have been submitted on time have been included in the proceedings. Only a handful of papers were not submitted and they have been replaced with the accepted abstracts. Online proceedings of the conference are also available at **http://www.stt2004.org**.

I would like to take this opportunity to thank people who helped in the organization of this symposium. Pamela Poissant and Denise Parent in the Department of Astronomy at UMass helped tremendously in the administrative aspects of the symposium. Barbara Keyworth, Dept. of Astronomy helped arrange the reception. Karen Werner provided invaluable help, especially in the compilation of the submitted abstracts, and in computer support for the conference. Financial support from NIST and Millitech, Inc. are gratefully acknowledged. Special thanks go to our technical review committee listed below for helping to review all the submitted abstracts. I also want to thank our dedicated team of staff member and graduate student volunteers who were on hand to make the event a success.

Gopal Narayanan
(UMass, Amherst)

Please note the dates and location for the 16th International Symposium on Space Terahertz Technology to be held in 2005:
May 2-4, 2005
Chalmers University of Technology, Göteborg, Sweden. (http://www.mc2.chalmers.se/conferences/ISSTT)
Organizers: Jan Stake, Harald Merkel, Victor Belitsky, and Erik Kollberg.

15th International Symposium on Space Terahertz Technology

Invited Talks

1. Session 1: HEB Mixers 1

Session Chairs: Dr. Sigfrid Yngvesson, UMass and Dr. Erik Kollberg, Chalmers

5. Session 5: Direct Detectors 2
Session Chair: Dr. S. Harvey Moseley, NASA GSFC

6. Session 6: HEB Mixers 2
Session Chair: Dr. Eyal Gerecht, NIST

7. Session 7: Poster Session

Session 8: Sources 2
Session Chair: Dr. Neal Erickson, University of Massachusetts, Amherst

Session 9: Systems
Session Chair: Dr. Grant Wilson, University of Massachusetts, Amherst

Session 11: Optics And Related
Session Chair: Dr. Anthony Kerr, National Radio Astronomy Observatory

James Webb Space Telescope, SAFIR, SPECS, and the future of Space Astronomy

John C. Mather[1], Dan Lester[2], and Harold Yorke[3]
[1]Code 685, NASA's Goddard Space Flight Center
Greenbelt, MD 20771
301-286-8720, john.c.mather@nasa.gov
[2]Astronomy Department, University of Texas, Austin, TX 78712-0259
[3]M/S 169-529A, Jet Propulsion Laboratory, Pasadena, CA 91109

The James Webb Space Telescope (JWST) is the first in a possible series of deployable infrared to millimeter wave space telescopes. The design process for JWST has already produced ultra-light mirrors, deployment methods, and cooling approaches that could lead to much larger and more capable equipment in the future. We will describe the progress on JWST in the context of its history and illustrate some new concepts for future missions that spring from it. These include the SAFIR (Single Aperture Far Infrared) telescope and the SPECS (Submillimeter Probe of the Evolution of Cosmic Structure). The JWST will operate at the Sun-Earth Lagrange point L2, where radiative cooling lowers the telescope and instrument temperatures to about 35 K. It will have an 18-segment beryllium primary mirror with a 25 m^2 area fitting inside a 6.6 m circumscribed circle, and will provide spectroscopy and imaging over the wavelength range from 0.6 to 28 μm. It is planned for launch in 2011 on an Ariane 5 rocket. The project is a partnership of NASA, ESA, and CSA, and the prime contractor is Northrop Grumman. See http://www.jwst.nasa.gov for more details on JWST.

Missions to follow JWST will be able to draw on a greatly expanded technological base. Other uses ranging from Earth sciences to surveillance demand large space telescopes and interferometric systems, and the infrastructure for remote assembly and astronaut servicing will continue to improve as the Space Station is completed and experience is gained.

The SAFIR (http://safir.jpl.nasa.gov/, http://safir.gsfc.nasa.gov/) and SPECS (http://space.gsfc.nasa.gov/astro/specs/) missions have been approved by NASA for Vision Mission studies. SAFIR was mentioned prominently in the 2000 NRC Decadal Report on Astronomy as "the recommended next step in exploring the cosmos at far-infrared wavelengths." The report furthermore states that SAFIR could "form the basis for developing a far-infrared interferometer in the succeeding decade." We will summarize both of these concepts and the unique science capabilities enabled by these missions as well as outline how they might further develop as other projects come on line, scientific priorities evolve, and technological capabilities expand.

Title: Development status of Herschel-Heterodyne Instrument for the Far-Infrared (HIFI)

Authors:
1. Nick Whyborn, SRON, POBox 800, 9700 AV Groningen, the Netherlands
2. Thijs de Graauw, SRON, Groningen, the Netherlands;
3. Emmanuel Caux, CESR, Toulouse, France
4. Tom Phillips, Caltech, Pasadena, USA
5. Juergen Stutzki, KOSMA, Koln, Germany

Abstract:

The Heterodyne Instrument for the Far-Infrared is a single-pixel, high-resolution (>300.000), spectrometer for ESA's Herschel Space Observatory.
The instrument is designed to provide a wide and continuous frequency coverage with velocity resolved resolution and high sensitivity. This will allow detailed investigations of a wide variety of astronomical sources, ranging from solar system objects, star formation regions to nuclei of galaxies. The frequency bands cover many emission and absorption lines of molecules, like water, and atomic and ionic lines, like CII and NII.

The instrument comprises 5 frequency bands covering 480-150 GHz with SIS mixers and a sixth dual band for the 1410-1910 GHz range with Hot Electron Bolometer Mixers.
The LO subsystem consists of a Ka-band synthesiser followed by 14 chains of frequency multipliers, 2 for each frequency band. Each frequency band has two mixers operating on orthogonal polarisations. All mixers are designed to have noise performance close to the quantum noise limit. One frequency band is operated at a time. Modular design of the Focal Plane Unit, with a common optical path for all the mixer bands, and of the Local Oscillator Unit with a common LO Source Unit for all the LO chains, make the instrument very compact.

A pair of Auto-Correlators and a pair of Acousto-optic spectrometers process the two IF signals from the dual-polarisation front-end and provide instantaneous frequency coverage of 4 GHz with a set of resolutions (140 KHz to 1 MHz) better than < 0.1 Km/s.

We will present instrument design, qualification status and an update of expected performances based upon instrument level tests of the Development Model together with a summary of the specific HIFI science goals.

The Submillimeter Array – Antennas and Receivers

Raymond Blundell
rblundell@cfa.harvard.edu
Harvard-Smithsonian Center for Astrophysics
60 Garden Street, Cambridge, MA 02138

Abstract

The Submillimeter Array (SMA) was conceived at the Smithsonian Astrophysical Observatory in 1984 as a six element interferometer to operate in the major atmospheric windows from about 200 to 900 GHz. In 1996, the Academica Sinica Institute of Astronomy and Astrophysics of Taiwan joined the project and agreed to provide additional hardware to expand the interferometer to eight elements. All eight antennas are now operating at the observatory site on Mauna Kea, and astronomical observations have been made in the 230, 345, and 650 GHz bands.

The SMA antennas have a diameter of 6 m, a surface accuracy of better than 25 μm rms, and can be reconfigured to provide spatial resolutions down to about 0.5" at 200 GHz and, eventually, 0.1" at 850 GHz. Coupling to the receiver package within each antenna is achieved via a beam waveguide, in a bent Nasmyth configuration, comprised of a flat tertiary mirror and two ellipsoidal mirrors that form a secondary pupil used for receiver calibration. An additional fixed mirror and a rotating wire grid polarizer are then used for receiver selection. Each antenna houses a single cryostat, with an integrated cryocooler capable of cooling up to eight receivers to 4 K. In the current configuration only three receiver bands are available: 175 – 255 GHz, 250 – 350 GHz, and 600 – 720 GHz, and simultaneous operation of the 650 GHz receiver with either of the lower frequency receivers is possible. Eventually dual polarization will be available from 325 – 350 GHz, and dual frequency operation will be possible, pairing either of the lower frequency receivers with any of the high frequency units: 325 – 425 GHz, 425 – 510 GHz, 600 – 720 GHz, and 800 – 900 GHz.

Each receiver currently uses a single superconductor-insulator-superconductor junction as the mixing element, and has first stage intermediate frequency amplification at 4 K with an instantaneous bandwidth of 2.5 GHz, centered at 5 GHz. The mixers are of a fixed-tuned waveguide design, are inherently broad band, typically 80 – 100 GHz, and provide for relatively low receiver noise, typically 5 – 10 hν/k for the low frequency bands, and 10 – 15 hν/k for the 650 GHz receivers. Local oscillator power to each receiver is provided by a mechanically tunable Gunn oscillator followed by the appropriate diode frequency multiplier or multiplier combination.

Introduction

It has long been recognized that the wavelength range 0.3 to 1.3 mm observable with ground-based telescopes offers unique opportunities in the study of cool (10 – 100 K) dust and gas clouds in the Milky Way and other galaxies. By the mid 1980's the California Institute of Technology 10 m diameter telescope (the Caltech Submillimeter Observatory), and the James Clerk Maxwell Telescope (JCMT), a 15 m diameter instrument of the United Kingdom, the Netherlands, and Canada were under construction specifically for observations in the submillimeter. The 10 m diameter Submillimeter Telescope, a collaborative effort between the University of Arizona and the Max Planck Institut für Radioastronomie, was also under construction on Mount Graham in Arizona. In addition, the 15 m diameter Swedish European Submillimetre Telescope (SEST), designed predominantly to access the southern sky at millimeter wavelengths, was also under construction at the European Southern Observatory facility of La Silla which borders the southern extremity of the Atacama Desert in northern Chile. At their shortest wavelengths these instruments had an angular resolution of approximately 6" – 15".

Also during the mid 1980's, the pioneering millimeter wavelength interferometers at Hat Creek (University of California, Berkeley) and at Owens Valley (California Institute of Technology) offered spatial resolutions of somewhat less than 5". Two other interferometers, at the Plateau de Bure in the French Alps and at Nobeyama were being developed by the Institut de Radio Astronomie Millimétrique and by the

National Astronomical Observatory of Japan, respectively. Both of these instruments were designed to offer higher spatial resolution ~ 1". Furthermore, having demonstrated high resolution imaging through interferometry at millimeter wavelengths, and with the anticipated success of the CSO and JCMT, a natural step forward was to propose to design and construct a submillimeter interferometer. Such an instrument could be used to provide additional high resolution information about, for example, the solar system, star formation, astrochemistry, the structure of galaxies, and the energetics of quasars and active galactic nuclei.

In 1984, following a request by the Director of the Harvard-Smithsonian Center for Astrophysics, Dr. Irwin I. Shapiro, the Submillimeter Telescope Committee, headed by Dr. James M. Moran, proposed the design and construction of a Submillimeter Wavelength Telescope Array [1]. They envisioned an array of six 6 m diameter antennas, situated at a dry high altitude site, configured to offer sub arc-second resolution in the wavelength range 0.3 to 1.3 mm. The committee also recognized that the investment in receiver technology would be both substantial and crucial to the ultimate performance of the array, and recommended that the development of a receiver laboratory be given the highest priority. Start-up funding was received in 1989 to set up such a lab, and SAO's Major Scientific Instrumentation fund, set up in 1992, has been used to fund the design and construction of the array. Finally, in 1996, the Academica Sinica Institute of Astronomy and Astrophysics of Taiwan joined the SMA project and agreed to provide an additional two antennas and associated hardware to enable eight element operation.

From experience at existing millimeter and submillimeter telescope sites it was evident that a high altitude plateau of reasonable extent (>500 m) would be required to site the SMA. Furthermore, in order to keep construction costs at a reasonable level, a mainland site with existing infrastructure, such as access, electricity supply, local industry, etc. would be preferable. In 1984, Mount Graham was believed to be the best of the candidate mainland sites; Jelm Mountain in Wyoming was quickly eliminated due to its high latitude; and the Aquarius Plateau in Utah, Chalk Mountain in Colorado, and the White Mountain in California were also identified as worthy of further study. Outside the continental US, the South Pole was known to offer an extraordinarily dry environment, but was eliminated due primarily to extreme logistical problems, and the summit of Mauna Kea in Hawaii was believed to be a good candidate site. Subsequently, a number of large-area high-altitude locations in northern Chile were also identified as candidate sites [2]. Finally, based primarily on available site-testing data and local infrastructure, and the proximity of the CSO and the JCMT, Mauna Kea was selected as the site for the SMA in 1992.

Having selected Mauna Kea as the SMA site, it was immediately obvious that, unlike existing millimeter wavelength interferometers, which make use of rail (Nobeyama, Owens Valley, Plateau de Bure) or paved road (Hat Creek) for array reconfiguration, the SMA antennas would have to be moved over more difficult terrain. Any reconfiguring of the array to change angular resolution consequently excluded the use of protective radomes, so that the SMA antennas would be unprotected from the environment. This, coupled with the fact that abrasive volcanic particles are often blown about the summit and severe icing conditions can occur in periods of high wind, effectively ruled out the use of aluminized carbon fiber panels for the antenna reflector surface. Finally, also in 1992, after a letting number of design study contracts to industry, SAO became prime contractor for the design and construction of the SMA antennas.

Antennas

In order to proceed with the SMA antenna design, the Mauna Kea specific environmental conditions, set out in Table 1, were developed [3]. Referring to the table, we should note that the nominal operating environment was specified to exceed the 90th percentile conditions, so observing under the so-called 'worst case' conditions would be unusual. While the general specifications for the SMA antennas are given with reference to Table 2 below, a number of other factors not listed as specifications were deemed critical. For example, the desire to reconfigure the array in a day implied moving a single antenna to a new location over unpaved road with up to 15% grade in 1 hour. Also, the requirement to maintain a physically stable environment with respect to gravity, for the cryogenically cooled receivers, effectively ruled out secondary focus operation. In other words, antenna designs of only the Nasmyth or Coudé configuration were considered.

In addition to the general specifications laid out in Table 2, there was also a requirement that the antenna remain sufficiently stable to enable blind operation, i.e. without pointing checks, under the nominal operating environment for periods of at least 1 hour. For the average operating environment in which

thermal effects are only half the nominal, and for wind speeds < 10 ms^{-1}, this implied a pointing accuracy of better than 2" rms. A phase stability requirement, and a minimum observing interval of 20 minutes

Nominal operating environment	
Wind	14 ms^{-1} average, 20 ms^{-1} peak
Air temperature	-15 to +25 C with 10 C diurnal fluctuations
Worst case operating environment (including antenna transport)	
Wind	25 ms^{-1} average
Air temperature	-20 to +30 C day and night operations
Survival environment	
Wind	60 ms^{-1} average
Rain	0.1 mhr^{-1} for 1 hour
Snow	0.5 m
Ice	10 mm on flat surfaces, 75mm on tubular structures

Table 1: Environmental considerations for antennas placed on Mauna Kea.

between calibrations, resulted in the additional requirement that the antenna cabin housing the receivers and other sensitive electronic equipment be temperature controlled to ±1 C. Other specifications, such as antenna leveling and the repeatability of antenna placement after transport were not defined at that time. However, the azimuth axis verticality was specified to be better than 15".

Antenna configuration	Alt – Az
Operating range	Azimuth ±270°
	Elevation 5 – 90°
Sun exclusion zone	None
Intersection of axes	< 0.10 mm
Non-perpendicularity of axes	< 10"
Azimuth bearing run-out	< 30 μm axial and radial
Non repeatable run-out	< 2 μm both axes
Azimuth bearing wobble	< 3"
Non repeatable wobble	< 0.2"
Slew rate	> 4°s^{-1} azimuth, > 2°s^{-1} elevation
Tracking accuracy	1.3" rms per axis
Tracking resolution	0.3" rms per axis
Absolute pointing accuracy	2.8" rms per axis
Antenna cabin (receiver enclosure)	2.6 m x 2.6 m x 2 m high
Nominal reflector diameter	6 m
Antenna surface	Aluminum panels
Antenna efficiency	> 50% at 350 μm
Secondary mirror translation	X and Y ±7 mm (50 μm resolution)
	50 mm travel in Z (2 μm resolution)
Non-chopping position	Centered to ±3" to give ±0.3" on sky
Chopping amplitude	±24' to yield ±2.5' on sky
Chopping rate	DC to 10 Hz

Table 2: General specifications for the SMA antenna.

Following the specifications laid out in Table 2, the SMA mechanical engineering staff developed an antenna design based on a bent Nasmyth configuration. Referring to Figure 1 (Left), the design of the antenna pedestal was driven primarily by the stiffness required to maintain pointing and phase accuracy for the expected wind loads, and a detailed thermal analysis determined that an all steel structure could maintain the required performance as long as it is properly isolated from the external environment. To this end, the bulk of the structure is housed inside the receiver cabin which is temperature controlled to ±1 C, and the base, below the azimuth bearing, is thermally insulated from its surroundings.

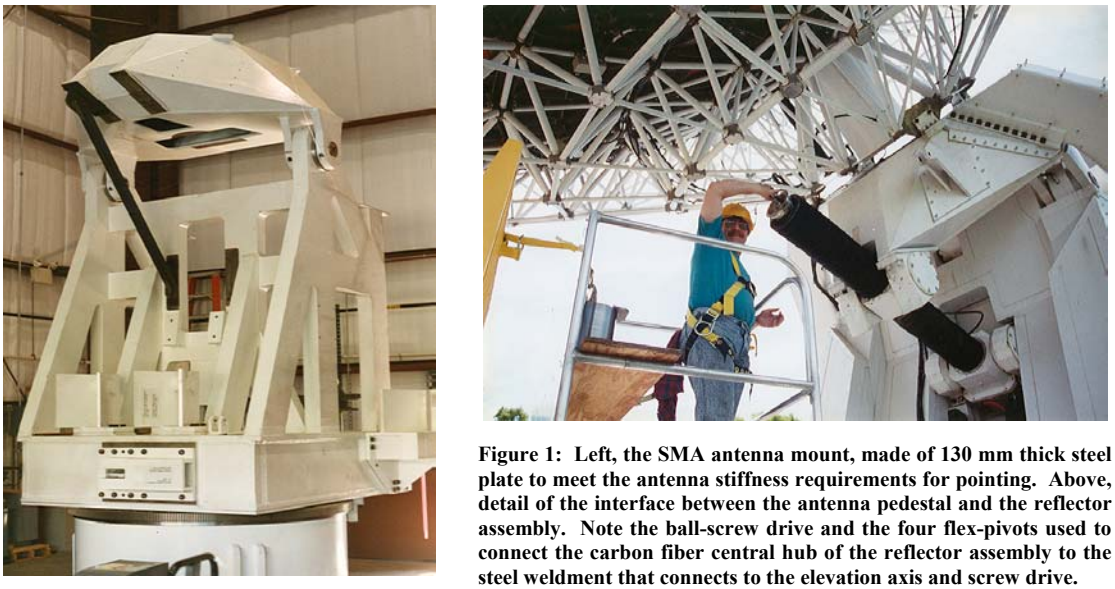

Figure 1: Left, the SMA antenna mount, made of 130 mm thick steel plate to meet the antenna stiffness requirements for pointing. Above, detail of the interface between the antenna pedestal and the reflector assembly. Note the ball-screw drive and the four flex-pivots used to connect the carbon fiber central hub of the reflector assembly to the steel weldment that connects to the elevation axis and screw drive.

Having eliminated the use of aluminum coated carbon fiber reflector panels, despite their inherently better temperature stability and light weight, the SMA antenna reflector assembly was designed to incorporate machined aluminum panels. Furthermore, as thermal considerations excluded the use of panels no larger than 1 m in extent, a 4-ring structure was chosen with 12 panels in the innermost ring and 24 in rings 2, 3, and 4. The panels are supported above the steel nodes of a back-up structure made up of a truss-work of carbon fiber tubes. Apart from the inner ring of panels which each has 3 support points, a redundant four point panel support scheme was chosen. In this way, individual panels can be deformed in-situ to correct for any large scale manufacturing defects. Finally, a quadrupod, made from carbon fiber in order to meet focus and pointing stability requirements, was included to support the chopping secondary mirror assembly.

Referring to Table 3, in which cross polarization effects and other minor losses have been neglected, we split the signal losses due to an imperfect antenna into two main categories. The first depends strongly on

Focus errors	0.92
Ohmic losses	0.99
Phase errors	0.89
Pointing errors	0.87
Pointing jitter	0.97
Surface errors	0.84
Sum of antenna dependent errors	0.57
Blockage	0.93
Alignment errors	0.95
Illumination	0.87
Sum of other ‘fixed’ errors	0.77
Total	0.44

Table 3: Efficiency error budget for the SMA antennas, designed to the general specifications given in Table 1, under the nominal operating environment.

the particular type of antenna design chosen and the second, apart from the blockage component, should be considered fixed and unrelated to the particular choice of antenna design. In other words, in order to meet the overall antenna efficiency specification of better than 50% at 350 μm wavelength, the sum of the antenna dependent efficiencies should exceed 0.65. Given that the sum of the projected antenna efficiencies, 0.57, is discrepant, it is useful to examine the sources of the largest errors: focus, phase, pointing, and Ruze, in more detail. While it may be possible to correct for some focus errors, such as deflections due to gravity or global ambient temperature changes, deflections due to wind loads and temperature gradients present more of a problem. These errors were calculated, for the nominal operating wind load of 14 ms^{-1} and worst case thermal gradients, via structural and thermal models, and were transformed to an error in separation along the antenna bore-sight between the focus of the secondary mirror and the focus of the best-fit deflected parabola of the primary. The efficiency due to focus errors [4] at a wavelength of 350 μm was then calculated using

$$\eta_f = \exp\text{-}6.5(\varepsilon_f)^2$$

where the focus error, ε_f, is expressed in millimeters [3]. Path length errors, or phase errors, are somewhat related to focus errors, and are especially relevant to interferometer operation in which the difference in variation of path length between the astronomical source and the receiver in each antenna results in a de-correlation of the interferometer signal and a consequent loss of gain. Fortunately, changes in path lengths that affect all antennas equally and simultaneously do not produce a resultant error, and almost all of the path length errors are therefore due to variations in the local environmental conditions at each antenna. The efficiency due to path length errors was calculated, assuming that three of the six antennas have path length errors while the path length to the other antennas remains constant [5], using

$$\eta_{pl} = \exp\text{-}650(\varepsilon_{pl})^2$$

where the path length error, ε_{pl}, is expressed in millimeters [3]. For single dish operation path length errors would not be an issue, $\eta_{pl} = 1$, so the projected antenna efficiency at 350 μm would be 50%. Pointing errors are defined as the combination of the residual error of the antenna pointing model and quasi-static errors resulting from a steady wind and thermal distortions of the antenna mount and reflector assembly. Short-term pointing fluctuations due to wind gusts and servo errors fall under the category of pointing jitter. The efficiency resulting from pointing errors [5] was calculated using

$$\eta_p = \exp\text{-}0.017(\varepsilon_p)^2$$

where the pointing error, ε_p, is expressed in arc-seconds [3]. Finally, we consider the loss in efficiency due to phase front errors arising from an imperfect reflector surface. Referring to Table 4 we note that, largely as a result of improved thermal performance, the use of carbon fiber reflector panels would reduce the sum of the panel errors to about 8 μm rss and result in a reflector efficiency of 87%. However, the SMA baseline antenna design excluded the use of carbon fiber panels on the grounds of durability given the harsh environment of Mauna Kea, and the projected reflector efficiency is somewhat higher.

We should also note that, under average operating conditions in which thermal effects are only half the nominal, and for wind speeds < 10 ms^{-1}, this design should result in an antenna efficiency greater than 50%

Panel accuracy (manufacturing)	5 μm rms
Panel setting errors	5 μm rms
Other panel errors (mainly thermal)	7 μm rms
Sum of panel errors	10 μm rss
Backup structure (BUS)	Carbon fiber with steel nodes
BUS errors (mainly thermal + gravity)	6 μm rss
Sum of reflector errors	12 μm rss
Reflector efficiency (surface errors)	84%

Table 4: Antenna surface error budget for the nominal operating environment.

at a wavelength of 350 μm. Furthermore, since it is extremely unlikely that the worst case thermal conditions will occur in winds approaching the nominal 14 ms^{-1}, it is likely that this design will provide an overall antenna efficiency greater than 50% at a wavelength of 350 μm under the nominal operating conditions.

The requirement to have a relatively large receiver enclosure that was fixed in elevation resulted in the use of the ball-screw arrangement for the antenna elevation drive. In azimuth, a more standard drive system, consisting of two motors driven in opposition against a spur gear cut directly on the azimuth bearing of the antenna, was selected. In both cases high torque, 1,100 Nm, brushless servo motors were chosen, in part to fulfill the desire for fast antenna position switching. In order to provide the required controlled antenna motion and to easily accommodate the variability of the elevation gear ratio a digital servo control drive system was implemented. In simple terms, the antenna servo control consists of three nested feedback loops. The innermost, the motor commutation loop, consists of the brushless servo motor, position resolver, and servo amplifier, and includes a hardware safety function to limit the maximum velocity the motor can attain. The second feedback loop is the velocity loop in which a tachometer is used to provide the servo control board (SCB), designed and programmed by receiver lab staff, with a direct feedback of the motor's speed. The outermost loop, the position loop, incorporates a 23 bit high resolution encoder and issues the SCB with a velocity command, based on the desired position, via the real-time antenna control computer (LynxOS) which communicates with a central computer in the SMA control building. New velocity requests are computed and transmitted to the SCB at 100 Hz, but the effective position loop bandwidth is about 5 Hz in both axes. The elevation velocity loop uses PID gains, while the azimuth velocity loop uses only PI terms. Finally, a Palm Pilot can be used to control the antenna via the SCB for maintenance and system diagnostics.

The quality of the servo control system as a whole is best assessed through the tracking and slewing performance of the antennas measured at the observatory site on Mauna Kea. Under calm conditions we typically achieve sidereal-rate tracking errors of ~ 0.3" rms on both axes on all six SAO built antennas. To demonstrate performance we plot the response of antenna 4 tracking and switching between a source and calibrator in strong winds in Figure 2. The tracking specification of < 1.3" rms is clearly met for both axes, suggesting that losses in antenna efficiency as a result of antenna drive or tracking errors are likely to be small. However, the data presented are based on antenna encoder readings and do not include errors in absolute pointing, or errors due to misplacement of the chopping secondary mirror. Errors in the absolute pointing of the antenna are removed with the help of an optical guide-scope and a multi-parameter mount model in the usual way and residual pointing errors of 2" rms are typical for the SMA antennas. In addition to an optical pointing model, models of the radio pointing of each SMA antenna are made on a regular basis and radio to optical offsets are incorporated into each antenna pointing model. Referring to Figure 2, we note that the slew rate specifications of $4°s^{-1}$ in azimuth and $2°s^{-1}$ elevation have been met, and a duty cycle of better than 50% is achieved for on-source times as short as 10 s. However, with a source acquisition time of ~ 3 s in azimuth, the observing efficiency degrades significantly for shorter timescales.

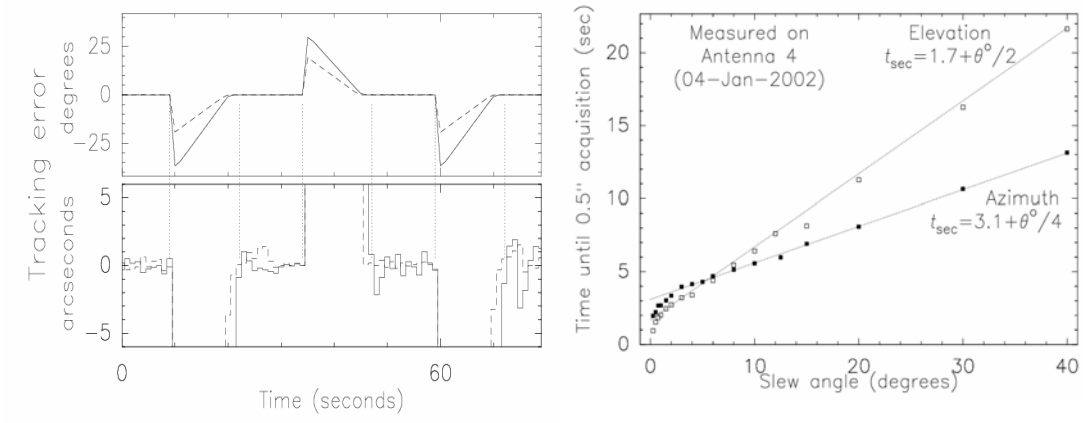

Figure 2: Left, demonstration of the tracking and slewing performance of the SMA antennas in high winds. During the time the antenna is either 'on-source' or tracking a calibrator, the specification of < 1.3" rms is easily met. Right, fast switching of the antennas is ultimately limited by the source acquisition time of 3 s in azimuth.

During assembly, each SMA reflector surface was first set to ~ 60 μm rms using a mechanical swing template equipped with capacitive sensors. The surface of the first of the SMA reflectors was improved using a near-field holographic technique employing a transmitter at 94 GHz and two purpose-built room-temperature Schottky diode mixer receivers. One of these, the reference receiver, was mounted behind the secondary mirror, the other was mounted on the elevation axis and was coupled to the SMA antenna via a flat tertiary mirror. As soon as two SMA antennas, equipped with working low-noise SIS receivers designed for astronomical use, became available the holographic technique was extended to 232.4 GHz, and surface adjustments are now based on measurements that include the complete set of receiver and antenna optics. Simply put, the complex beam pattern of the antenna under test is measured using on-the-fly mapping with a second antenna in the array providing the phase reference. The resultant beam pattern is Fourier-transformed to produce amplitude and phase distributions on the aperture of the antenna under test. This aperture phase is then corrected for systematic errors due to the fact that the measurements are made in the near-field, leaving behind phase errors attributable to surface deviations from a best-fit paraboloid. This gives a surface error map from which a list of individual panel adjustments can be derived. Figure 3 shows a plot of the surface of antenna 4 as originally set using the swing template, and a plot of the surface after three rounds of surface adjustments based on holographic data taken at 232.4 GHz. All of the SMA antennas have now been set to better than 25 μm rms using this technique. At the present time only one antenna has been set to better than the specification of 12 μm rms, and verification of performance at different elevations has yet to be demonstrated through celestial holography.

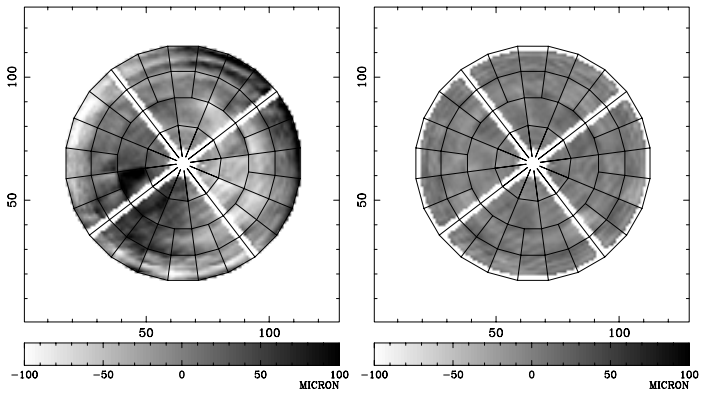

Figure 3: The SMA antenna reflectors are typically set to 60 μm rms using the mechanical swing template. A near-field holographic technique, using a phase-locked transmitter at 232.4 GHz, is then used to progressively improve the surface. Two to four iterations are usually required to reach the design specification of 12 μm rms.

The preliminary design for the SMA beam waveguide to relay the signal beam from the subreflector to the receivers excluded the use of curved mirrors primarily for ease of optical alignment and freedom from mirror-induced cross-polarization [3]. However, the all flat design introduced problems relating to frequency dependence and beam truncation. For example, a large tertiary mirror > 500 mm in extent would have been required in order to keep truncation losses at an acceptable level. In order to avoid these problems two ellipsoidal mirrors, mirrors M4 and M5, were introduced in the horizontal plane of a bent Nasmyth configuration after the tertiary mirror, and an additional flat mirror, M6, was introduced to direct the signal beam downwards and into the receiver package. Coupled with a lens in front of each mixer, mirrors M5 and M4 are used to produce a frequency independent image of the feed horn aperture at the subreflector. Furthermore, referring to Figure 4 (left), a compact image of the feed is produced between these mirrors providing a good location for receiver gain calibration and for insertion of the quarter wave plates required for polarization measurements.

Besides providing efficient coupling to the receivers, the antenna must also provide a phase stable environment for the entire signal path within the antenna receiver cabin including the beam waveguide, receiver optics, reference frequency distribution, and intermediate frequency transmission. For example, a 1 C temperature change in a 2 m long optical train, supported by a structure made predominantly from steel, would result in a 1 radian phase change at the highest operating frequency of the SMA. For this

reason, and to ensure adequate thermal stability of the antenna mount, a temperature stability requirement of ±1 C was therefore imposed on the receiver enclosure. In order to achieve this stability we developed an air handler; basically a blower and two dampers that mix inside and outside air in the proper proportions to obtain the desired temperature. One damper controls the flow of cool outside air into the receiver cabin, the other controls the amount of warm air, heated by passing through the electronics rack, reentering the cabin. In the event that the electronics rack does not dissipate enough heat to maintain the desired temperature, a heater located in the ductwork can be energized. This system can maintain the cabin air temperature to ±0.5 C for indefinite periods under a variety of atmospheric conditions. Furthermore, unlike commercial air conditioners no refrigerant material is required. A slight overpressure is maintained inside the cabin to keep dusty air out, outside air entering the cabin via the air handler is filtered and free of dust, and waste heat from the electronics rack is put to good use.

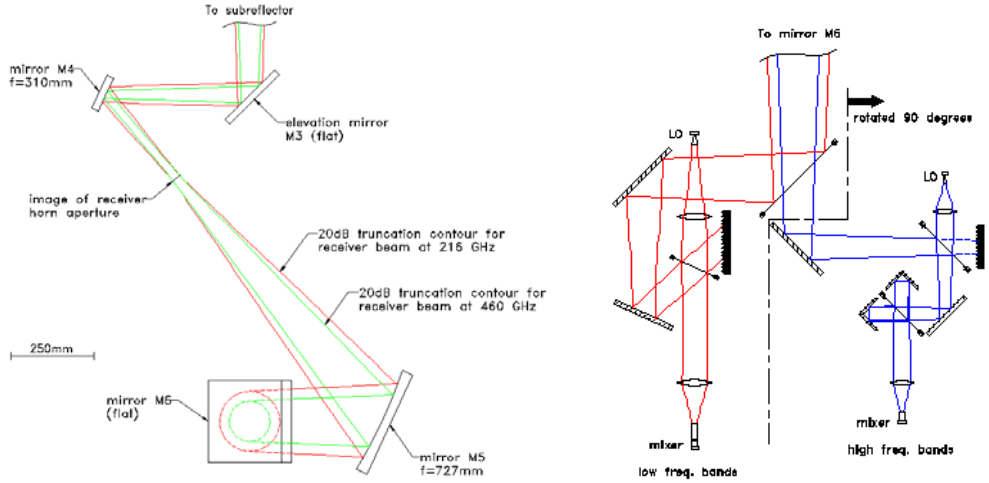

Figure 4: Left, two ellipsoidal mirrors are used in a bent Nasmyth configuration to provide a convenient location for receiver gain calibration and wave plates used for polarization measurements. Right, schematic of the optical arrangement used to couple multiple receivers to the SMA antenna. By a simple rotation of either the central mirror or wire grid assembly, any one of the four high frequency receivers can be used with either of the low frequency receivers, and dual polarization is possible in the frequency range 325 – 350 GHz.

Receivers

Even though sensitivity, beam size, and angular resolution estimates for the array had been presented for 230, 345, 460, 690, and 850 GHz operation, as originally proposed [1] the SMA was to be equipped with heterodyne receivers operating in only three frequency bands. However, by 1994, it was clear that more receivers would be required to meet both scientific and technical requirements [4]. Referring to Table 5, the lowest frequency of operation was set by the need to be able to operate reliably and make useful astronomical observations in periods of average weather conditions, and for calibration and testing of the

Receiver	Frequency (GHz)	1984 Noise (K)	1992 Noise (K)
230	175 – 255	300	60
345	250 – 350	900	150
400	325 – 425		
460	425 – 510	2000	200
650	600 – 720	5000	
850	800 – 900	8000	750

Table 5: The current SMA receiver plan calls for single pixel receivers to operate throughout the bulk of the major atmospheric windows from about 200 to 900 GHz. The first column gives the receiver designation, the second gives the sky frequency coverage, and the third and fourth columns respectively give the best measured SSB receiver noise at the time the SMA was proposed [1], and the projected SSB receiver noise performance figures from the SMA design study of 1992 [3].

instrument. The highest frequency was set by the need to have reasonable atmospheric transmission during periods of good weather. The intermediate receiver bands were set primarily to ensure frequency coverage throughout the major atmospheric windows, and a dual polarization capability was included in order to permit efficient polarization measurements of the dust continuum in the frequency range of maximum sensitivity of the array, 330 – 350 GHz. Finally, in order to provide accurate phase calibration during the highest frequency observations, dual frequency operation, in which a low frequency receiver is paired with a high frequency receiver, was required.

Due to the large number of receivers the coupling optics were kept as simple as possible and the optical scheme, shown in Figure 4 (right), was developed to couple to the multiple receivers housed in a single cryostat. Referring to the figure, the lowest frequency receivers are coupled to M6 via the rotating wire grid assembly and local oscillator (LO) injection is achieved via a simple mesh coupler. As LO power is abundant at these frequencies, signal losses are kept below 1%. In contrast, the polarization of the high frequency receivers is orthogonal to the lowest frequency units, and the selection of the high frequency receivers is achieved via a rotation of the central mirror assembly. Since available LO power for the highest-frequency bands is more limited, LO power is coupled to the mixer using a Martin-Puplett interferometer. It is worth noting that because of the relatively wide IF bandwidth to IF center frequency of the SMA, 2 GHz centered at 5 GHz, the performance of the mesh coupler is actually superior to that of the Martin-Puplett when sufficient LO power is available.

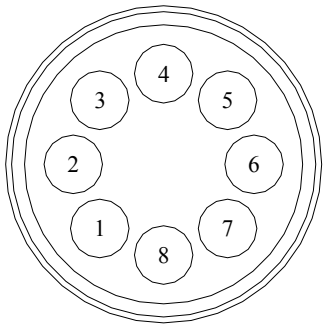

Port number	Frequency (GHz)	Polarization
1	650	↗
2	850	↗
3	230	↖
4	Spare	
5	400	↗
6	460	↗
7	345	↖
8	Spare	

Figure 5: Top view of the SMA cryostat, showing the relative position and polarization of the various receivers.

Referring to Figure 5, the receivers in ports 3 and 7, the 230 and 345 GHz units, have radial polarization and are coupled to M6 by reflection off the rotating central wire grid assembly. The receivers in ports 1 and 5, the 650 and 400 GHz units, also have radial polarization, which is orthogonal to that of the 230 and 345 GHz units, and are coupled to M6 by reflection off the central rotating mirror assembly immediately beneath the wire grid assembly. Receivers to cover the 850 and 460 GHz bands will eventually be installed into ports 2 and 6, will couple to the antenna by reflection off the central rotating mirror assembly, and will have the same polarization as the 650 and 400 GHz receivers so that they can be used with either of the lowest frequency receivers.

The desire to operate with both low frequency and high frequency receivers simultaneously, either for phase calibration or for scientific purposes, imposes stringent requirements on receiver alignment. Referring to Table 2, the pointing requirement for efficient antenna operation was set at 2.8" rms per axis at 850 GHz. If we assume that, under dual frequency operation, each antenna is pointed with the aid of a pointing model, derived for the high frequency receiver in use, the low and high frequency receivers must be co-aligned to within about 6" in order to maintain a similar pointing loss for both receivers. With this in mind, implementation of the optical coupling of each mixer to the antenna via M6 relies heavily on a robust design concept, accurate machining, and sound metrology. After fabrication and careful alignment of each set of receiver optics, a near-field vector scanning technique, pioneered at SAO [6], is used to determine beam parameters from which minor mirror adjustments can be made to co-align each receiver. Ideally, the near-field scan should be made at either an image of the telescope focus (where pointing relates to lateral offset), or an image of the telescope pupil (where pointing relates to wave-front tilt.) In the SMA optics design a lateral offset of the beam results in a pointing offset of about 2" per mm in the plane of the image of the telescope focus, located about half way between the cryostat vacuum windows and M6.

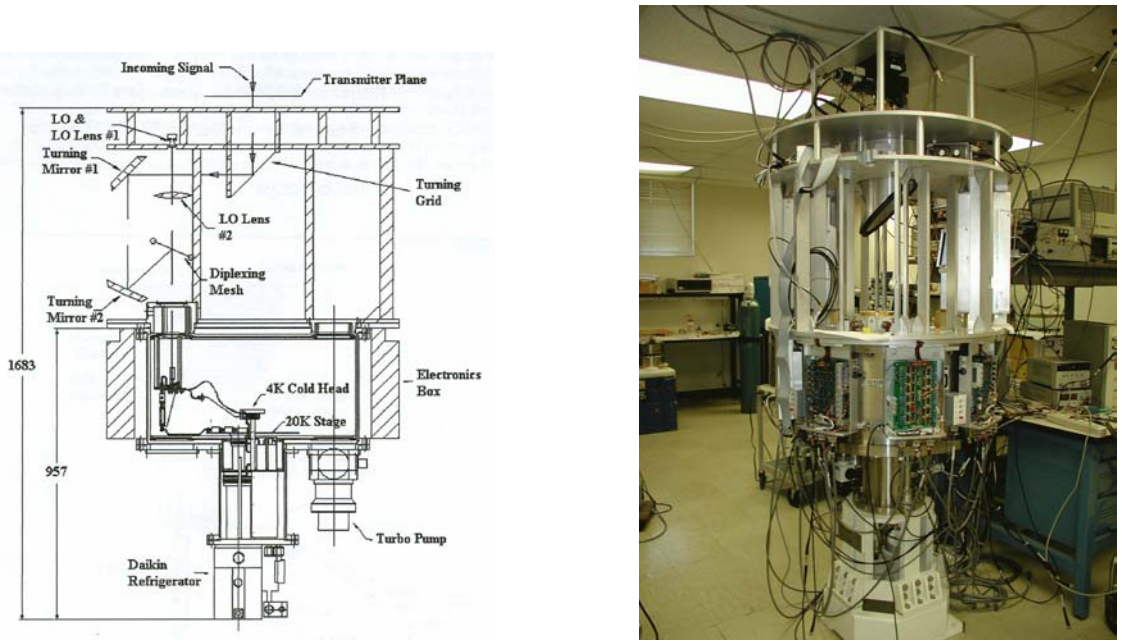

Figure 6: Left, schematic of the SMA receiver system showing the optics, receiver insert, and cryostat assemblies. Right, photograph of a complete SMA receiver system showing the cryostat surrounded by the receiver control electronics, the optics cage supporting the various sets of receiver coupling optics, and the central wire grid assembly used to select between the lower frequency receivers. The near-field scanning unit is also visible in place of M6 at the center and above the complete receiver system.

Unfortunately, due to mechanical constraints, near field scans cannot be made at this image of the telescope focus. Instead, scans are made in a plane just beneath M6. Nevertheless, fitting the data measured on a 71x71 grid with a 1 mm spacing generally results in co-alignment of the receiver beams to within 5" on the sky after a few iterations.

Since dual frequency operation of the SMA is possible, the relative pointing between the high and low frequency receivers can be measured simultaneously by making azimuth and elevation scans across a planet and monitoring the receiver outputs using a synchronous detection scheme. In Figure 7 we present azimuth and elevation scans obtained using this method to demonstrate the relative pointing of the three receivers installed in antenna 1. The largest offset between receivers, ~ 6", occurs between the 230 GHz and 650 GHz units in antennas 1 and 4. More typically we achieve pointing offsets of order 3" – 4" and

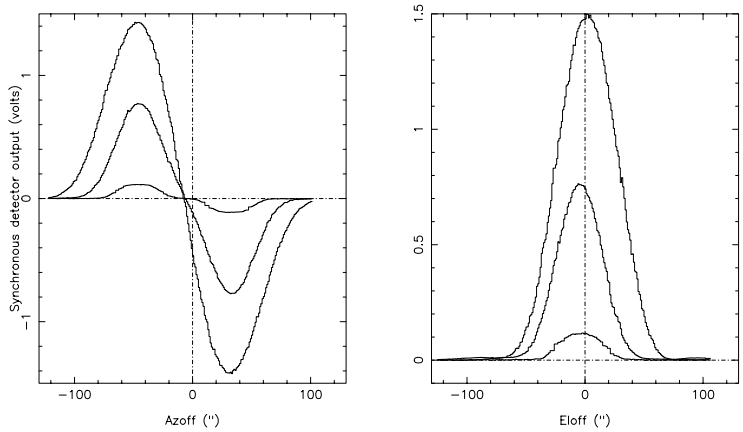

Figure 7: Continuum detector output scans in azimuth and elevation across Jupiter showing the relative alignment of the beam positions on the sky of the 3 receivers: 230 GHz (top), 345 GHz (middle), and 650 GHz (bottom) installed in antenna 1.

efficient simultaneous dual frequency operation is possible. In practice, since the majority of the radio pointing data is obtained using the 230 GHz receivers, we generally use the 230 GHz radio pointing model with the corresponding feed offset when observing with the 650 or 345 GHz receivers. In order to proceed with dual polarization measurements we have designed and implemented a switching scheme incorporating rotating quarter wave plates for operation at 342 GHz using a single receiver in each antenna. Eventually dual polarization will be possible in the frequency range 325 – 350 GHz using the orthogonally polarized 345 and 400 GHz receivers. In this case, assuming co-alignment similar to that of the existing receivers, a pointing intermediate between the two receivers would be used, and cross polarized contamination between receivers would be kept to a minimum via the central wire grid beneath M6.

Referring once more to Figure 6, left panel, we can identify 3 major systems: the optics, the receiver insert, and cryostat infrastructure. The optical components are used to steer the signal and LO, which is housed on a shelf below M6 but above the individual sets of receiver optics, to a given receiver either by reflection off a rotating wire grid polarizer or a rotating mirror assembly, each of which has 4 positions. The signal then enters the cryostat through a vacuum window in the receiver insert, and passes through some infrared blocking filters, through a lens cooled to ~ 70 K, and into the mixer via a corrugated feed. Output from the mixer, at 4 – 6 GHz, is then coupled to a low noise cryogenic amplifier via an isolator equipped with an integrated bias tee. At this point, the signal passes to the infrastructure components of the cryostat: a 4-way FET switch and band-pass filter, and is further amplified to -30 dBm before exiting the cryostat.

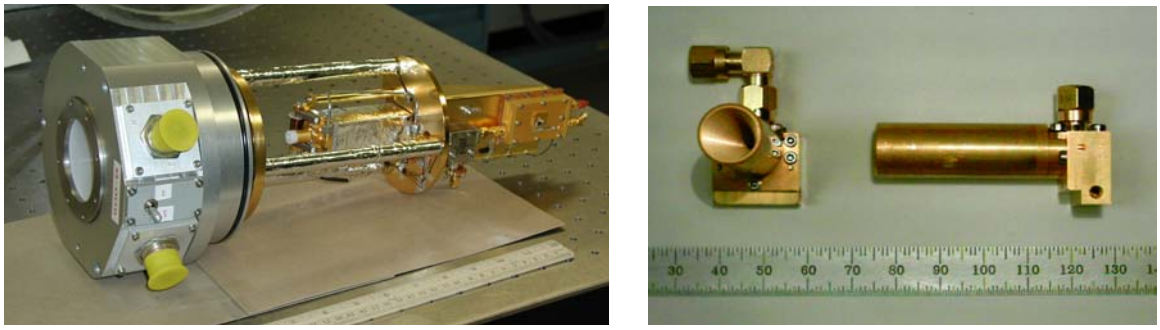

Figure 8: Left, photograph of a 650 GHz receiver insert showing, from left to right, the vacuum window, electrical connectors, radial o-ring seal, interface to 70 K radiation shield, mixer feed with Teflon dust cover, magnetic field coil, isolator and 4 – 6 GHz IF preamplifier. Right, photograph of a 345 GHz SIS mixer block.

In Figure 8 we show a 650 GHz receiver insert in detail, the vacuum window, mixer block with corrugated feed, isolator, and IF amplifier are clearly visible. The vacuum window is made of Teflon, half a wavelength thick, and the lens, also made of Teflon, is cooled via a link to the cryostat radiation shield at 70 K. The mixer block and associated IF amplifier are cooled via individual copper heat straps connected to the 3rd stage of a Daikin CG-308SCPR cryo-cooler, which has a cooling capacity in excess of 2 W at 4 K, 2 W at 15 K, and 25 W at 70 K. In the SMA antennas, the cryo-cooler is operated with its displacer aligned vertically and the cold-surface uppermost. In this orientation the 3rd stage temperature remains stable to within ± 5 mK on some units, although ± 50 mK is more typical. Such large temperature changes induce mixer gain fluctuations which result in receiver output fluctuations of up to 1%. Using a gain stabilization technique developed for the SMA [7] these fluctuations can be reduced to < 0.1% and the receivers can be made sufficiently stable to permit continuum monitoring of the atmosphere for phase correction techniques to be tested.

For simplicity we consider receiver noise to be made up of three major components: that arising due to losses in the receiver optics, mixer noise, and multiplied IF noise. Generally speaking, losses in the receiver optics can be kept small through the use of reflective optics, and IF amplifiers with a noise level of < 1 K/GHz can be purchased, so the majority of receiver design effort is often placed on mixer design. In the case of the SMA a complete set of receiver specifications was never developed. Instead, a goal to provide double side-band receivers to cover the frequency bands specified in Table 5 with the projected noise figures was set. To this end, we have developed a series of single-ended, fixed-tuned waveguide SIS mixers for the 230, 345, and 650 GHz frequency bands [8,9,10], and a number of laboratory measurements have been made at other frequencies [11]. In all cases, the mixer block is a fixed-tuned, half-height

waveguide unit similar to that shown in Figure 8 (right). Referring to the figure, an SIS junction with the required tuning circuit is deposited on a crystalline quartz substrate, which in turn is simply sandwiched between a corrugated feed horn and a copper back-piece containing a waveguide section, machined to the appropriate depth. IF output from the mixer is via an SMA connector mounted on top of the block. This type of mixer mount is extremely simple yet provides a fixed impedance of ~ 25 Ω to the SIS mixer chip over a large input bandwidth.

A sample of receiver noise measurements is given in Figure 9. Referring to the figure, the on-telescope performance appears to be about a factor of 2 worse than that measured in the lab, so it is worth noting the major differences between the measurements. Lab measurements are generally made using a liquid helium test cryostat with the appropriate thickness Teflon vacuum window. This cryostat is equipped with an IF amplifier chain that has a noise temperature of 4 K, measured over a 1 GHz bandwidth, centered at 5 GHz. For the 230 and 345 GHz receiver measurements the lens in front of the mixer feed is mounted on the 4.2 K cold-plate and the infra-red filtering blocking filters are attached to the 77 K radiation shield. In the case

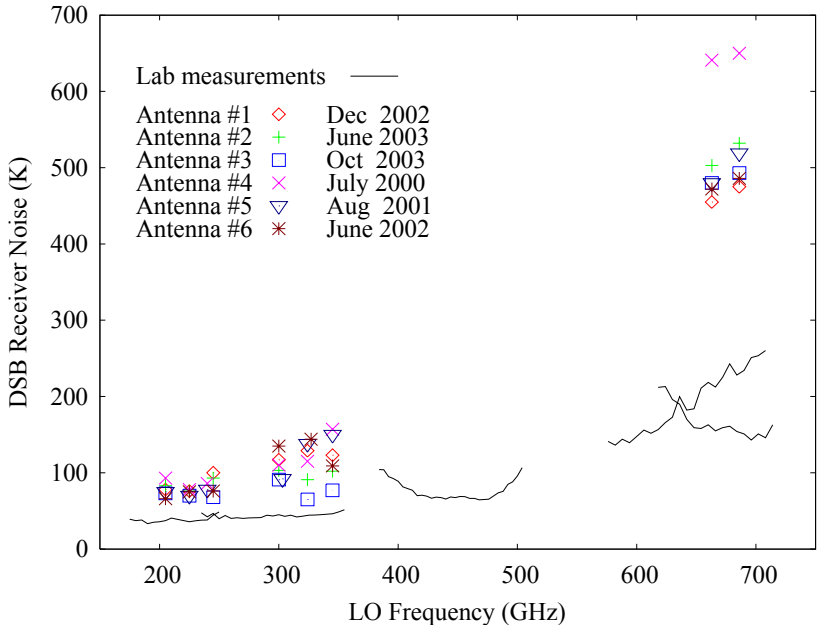

Figure 9: The measured lab performance of receivers developed for the SMA and the on-telescope performance of all 18 SAO built SMA receivers is plotted as a function of frequency. The discrepancies between lab and on-telescope performance are understood and improvements to receivers deployed the on the SMA antennas will be made as time permits.

of the 650 GHz measurements, the signal is coupled to the mixer via reflecting optics, and LO power is injected via a low-loss beam splitter. Receiver noise measurements on the telescopes are made using room temperature and liquid nitrogen cooled loads placed at the image of the mixer feed aperture between M4 and M5, and consequently include noise arising from losses in the optics above the cryostat (see right panels of Figures 4 an 6). At all frequencies, the lenses in front of the mixers are cooled via a connection to the 70 K radiation shield, and are significantly warmer than in the lab test cryostat, and LO power is coupled to the 650 GHz receivers using Martin Puplett diplexers. Finally, all receiver noise measurements are made using IF amplifier chains that have a noise temperature of typically 10 – 12 K averaged over the full 2.5 GHz IF bandwidth. At the present time we are developing a receiver design for the 325 – 425 GHz frequency range to provide increased sensitivity and to enable more efficient dual polarization measurements to proceed. Developments to improve on-telescope performance of existing receivers will occur as time permits.

Finally, in Figure 10 we show a picture of the current status of the array, astronomical observations are proceeding in the 230, 345, and 650 GHz bands, and will shortly be open for general observing.

Figure 10: All 8 antennas of the SMA observing during the SMA dedication, November 22nd 2004.

References

[1] J. M. Moran, M. S. Elvis, G. G. Fazio, P. T. P. Ho, P. C. Myers, M. J. Reid, and S. P. Willner, "A Submillimeter-Wavelength Telescope Array: Scientific, Technical, and Strategic Issues," SAO, 1984.
[2] P. Raffin and A. Kusunoki, "Searching for Submillimeter Sites in Chile," SMA Technical Memo #59, 1992.
[3] C. R. Masson, E. E. Bloemhof, R. Blundell. W. R. Bruckman, P. T. P. Ho, E. R. Keto, M. W. Levine, P. Raffin, M. J. Reid, and M. G. Wolfire, "Design Study for the Submillimeter Interferometer Array of the Smithsonian Astrophysical Observatory," SAO, 1992.
[4] R. Padman "Design Considerations for SMA Antenna Optics," SMA Technical Memo # 21, 1990.
[5] C. R. Masson, "Effect of Pointing Errors on the SMA," SMA Technical Memo # 45, 1991.
[6] C.-Y. E. Tong, D.V. Meledin, D.P. Marrone, S.N. Paine, H. Gibson, and R. Blundell, "Near field vector beam measurements at 1 THz," *IEEE Microwave & Wireless Components Lett*., vol 13(6), pp. 235-237, 2003.
[7] J. Battat, R. Blundell, T. R. Hunter, R. Kimberk, P. S. Leiker, and C.-Y. E. Tong, "Gain Stabilization of a Submillimeter SIS Heterodyne Receiver." To appear in: *IEEE Transactions on Microwave Theory and Techniques, 2004.*
[8] R. Blundell, C.-Y. E. Tong, D. C. Papa, R. L. Leombruno, X. Zhang, S. N. Paine, J. A. Stern, H. G. LeDuc, and B. Bumble, "A Wideband Fixed-Tuned SIS Receiver for 200 GHz Operation," *IEEE Transactions on Microwave Theory and Techniques,* vol. 43(4), pp. 933-937, 1995.
[9] C. – Y. E. Tong, R. Blundell, S. N. Paine, D. C. Papa, J. Kawamura, X Zhang, J. A. Stern, and H. G. LeDuc, "Design and Characterization of a 250-350 GHz Fixed-Tuned Superconductor-Insulator-Superconductor Receiver," *IEEE Transactions on Microwave Theory and Techniques,* vol. 44(9), pp. 1548-1556, 1996.
[10] C.-Y. E. Tong, R. Blundell, K. G. Megerian, J. A. Stern, and H. G. LeDuc, "Quantum-limited Mixingn in a Transformer-coupled SIS Resonator for the 600 GHz Frequency Band," *Thirteenth International Symposium on Space Terahertz Technology*, pp. 23-32, 2002.
[11] R. Blundell, C.-Y. E. Tong, D. C. Papa, J. W. Barrett, J. Kawamura, R. L. Leombruno, S. Paine, X. Zhang, J. A. Stern, H. G. LeDuc, and B. Bumble, "A Fixed Tuned SIS Receiver for the 450 GHz Frequency Band," *Sixth International Symposium on Space Terahertz Technology*, pp. 123-133, 1995.

Optimization of HEB mixer for the Herschel Space Observatory.

S. Cherednichenko[1], P. Khosropanah, T.Berg, H. Merkel, E. Kollberg

Department of Microtechnology and Nanoscience, Chalmers University of Technology, Gothenburg, S-412 96, Sweden

[1] serguei.cherednichenko@mc2.chalmers.se

V.Drakinskiy, B. Voronov, G. Gol'tsman

Department of Physics, Moscow State Pedagogical University, Moscow, 119435, Russia

A mixer development for the HIFI instrument of the Herschel Space Observatory has come to the final stage. In our paper and conference presentation we will describe the most important details of the Band 6 Low and High Mixer Unit design. Special attention will be given to the optimization of the hot- electron bolometer mixer chip, which is based on 3.5nm NbN superconducting film on silicon. As the HEB's local oscillator power requirements depend on the bolometer size, we have compared mixer noise temperature for different bolometer width- to- length ratio. A trade- off between mixer performance and local oscillator power requirements results in the mixer units equipped with optimized mixer chips, providing the largest coverage of the Band6 RF band with the lowest possible receiver noise. A short account of the beam pattern measurements of Band6 mixers will be given as well.

Hot Electron Bolometer mixers with improved interfaces: Sensitivity, LO power and Stability

J.J.A.Baselmans[1], M.Hajenius[1,2], J.R. Gao[1,2], A. Baryshev[1], J. Kooi[-3], T.M. Klapwijk[2], P.A.J. de Korte[1], B. Voronov[-4], and G. Gol'tsman[-4]

[1]*Space Research Organisation of the Netherlands (SRON), Sorbonnelaan 2, 3584 CA Utrecht, The Netherlands*
[2]*Faculty of Applied Sciences, Delft University of Technology, Lorentzweg 1, 2628 CJ Delft, The Netherlands.*
[-3] California Institute of Technology, MS 320-47 Pasadena, California 91125, USA
[4]*Moscow State Pedagogical University, Moscow 119435, Russia*

Abstract – We study twin slot antenna coupled NbN hot electron bolometer mixers with an improved contact structure and a small volume, ranging from 1 μm × 0.1 μm to 2 × 0.3 μm. We obtain a DSB receiver noise temperature of 900 K at 1.6 THz and 940 K at 1.9 THz. To explore the practical usability of such small HEB mixers we evaluate the LO power requirement, the sensitivity and the stability. We find that the LO power requirement of the smallest mixers is reduced to about 240 nW at the Si lens of the mixer. This value is larger than expected from the isothermal technique and the known losses in the lens by a factor of 3-3.5. The stability of these receivers is characterized using a measurement of the Allan Variance. We find an Allan time of 0.5 sec. in an 80 MHz bandwidth. A small increase in stability can be reached by using a higher bias at the expense of a significant amount of sensitivity. The stability is sufficient for spectroscopic applications in a 1 MHz bandwidth at a 1 Hz chopping frequency.

1: Introduction

The development of new space based [1] and airborne [2,3] telescopes will create new opportunities for sub-mm astronomy, as ground-based observatories suffer from limited atmospheric transmission in this spectral range. In the past years the main focus in the Thz frequency range has been on Lattice Cooled Hot Electron Bolometer mixers (HEBm) [4,5]. These devices have benefited strongly from large advancements in NbN thin film technology and nowadays yield double sideband receiver noise temperatures of around 10 hf/k at Thz frequencies. However, other parts of the device structure, especially the contact interface between the NbN bolometer and the contact structure, have been ignored in the device optimization process until very recently [6-9]. In this study we have demonstrated that the contact structure plays a crucial role in the mixer performance. We illustrate this using Fig.1. In the left panel we show the cross sectional drawing of a conventional NbN based hot electron bolometer mixer. In the fabrication process of these mixers the NbN film is generally exposed to ambient atmosphere for a prolonged period prior to the deposition of the contact pads and the antenna structures [10-12]. No cleaning process whatsoever is performed. Hence there is a contact resistance between the NbN film and the contact pad. We have found

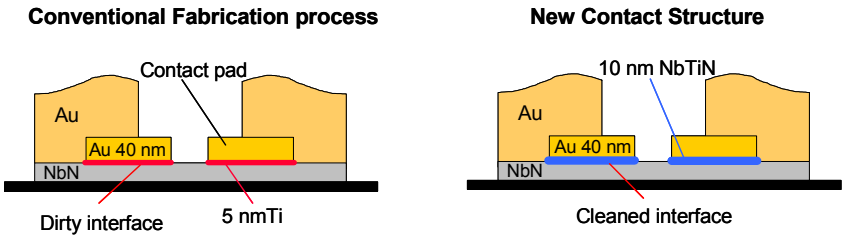

Fig. 1: Cross sectional drawing of 2 HEB mixers with different contact structures. In the left panel we show a conventional HEB mixer. In the right panel we show the novel contact structure. In this case. The NbN film is cleaned using an in-situ Argon etch prior to the deposition of the contact pad.

that a novel contact structure, as indicated in the right panel of Fig.1, results in a negligible contact resistance, a doubling in sensitivity and in bandwidth compared to conventional devices fabricated on the same wafer during the same process run [13]. The only difference with a conventional NbN HEBm is that the NbN film surface is cleaned *in-situ* prior to the contact pad deposition, which consists of 10 nm NbTiN and 40 nm Au. The NbTiN is added to prevent the critical temperature of the contact pad to be reduced due to the stronger superconducting proximity effect. The latter is a result of an increased transparency between the NbN and the contact pad, caused by the Argon etch. For details we refer to Refs. [6-9]. We obtain, for large volume (4 x 0.4 μm) HEB mixer with a spiral antenna $T_{N,DSB}$=950 K at 2.5 Thz and $T_{N,DSB}$=750 K at 1.89 Thz, uncorrected for optics losses, together with a gain bandwidth of 6 Ghz at the optimal operating point.

Despite the good performance of these devices, the present design is not optimized for use in a real receiver system for the following reasons:
1: The antenna used is a log spiral antenna. Spiral antennas have a large bandwidth and a circular polarization. This is useful for a laboratory setup, but less suitable for actual applications in a telescope.
2: The large device volume implies that a rather high Local Oscillator power is needed to be able to pump the mixer that becomes a difficult issue if a solid state LO source is used.

To overcome these problems we have designed and fabricated small volume (0.1x1 μm and larger) HEBm's coupled to twin slot antenna mixer using a model described in Ref. [14]. The center frequency of the twin slot design is 1.6 Thz or 1.8 Thz. In contrast to spiral antennas, twin-slot antennas are polarization sensitive and have an acceptable beam pattern. The small device volume reduces the LO power needs. To evaluate the performance of these HEB mixers we study three essential practical issues of these receivers:
a: The receiver noise temperature, evaluated using the standard Y factor method [15].
b: The Local Oscillator power requirement. This is evaluated using the so called isothermal method as well as a measurement of the real pumping level using a calibrated LO source
c: The stability of the mixers, evaluated by means of a measurement of the Allan Variance.

2: Mixer Fabrication

We start with a 3.5 nm NbN film, obtained from MSPU, Moscow, on a high purity Si wafer. The critical temperature of the film is 9.3-9.7 K. As a first step we define the contact pads using a standard PMMA double layer positive e-beam resist, e-beam lithography and a wet development. Subsequently, we use an in-situ 15 sec Argon etch, prior to the sputter deposition of the contact pad, consisting of 10 nm NbTiN and 40 nm Au. In the next step we deposit the antenna and ground plane structure using thermal evaporation of 5 nm Ti, 150 nm Au and 10 nm Ti. The bottom layer of Ti is used as an adhesion layer, the cap layer of Ti is used as a protection of the gold during the following step, which consists of the reactive ion etching of the NbN using CF_4 / O_2 to define the HEB bridge width. A Scanning Electron Micrograph of a finished device is given in Fig. 2.

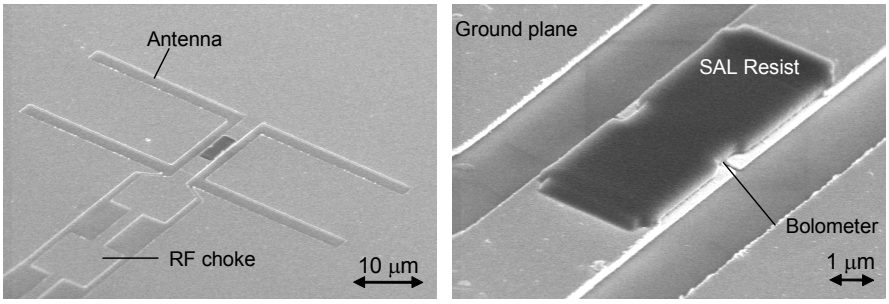

Fig. 2: Scanning Electron Micrograph of a NbN hot electron bolometer coupled with a twin slot antenna. The device shown has a planar dimension of 0.3 x 2μm.

3. Sensitivity

The sensitivity of the twin slot coupled hot electron bolometers is evaluated by means of the standard Y factor measurement technique [15]. We use a quasi-optical setup in which the HEBm chip is glued to the back of an elliptical Si lens. We use a 295 K hot load and a 77 K liquid nitrogen cold load as signal sources. The distance from the hot/cold load to the vacuum window is 30 cm. For the optimum bias point we also use a direct hot/cold load consisting of 295 K and 77 K Eccosorb® at 15 cm from the cryostat window. The optics in the signal path consist of the 3.5 μm mylar beam splitter, a 0.9 mm HDPE vacuum window, one Zytex G 104 heat filter and the Si lens. We have been using both a coated and an uncoated Si lens in the measurements. The total loss in the optics between the Hot/Cold load and the HEB mixer is -4.2 dB for a direct hot/cold load close to the cryostat window using an uncoated Si lens [16]. The IF signal from the HEB mixer passes through a Bias T (which is also used for the DC biasing) to a 1-2 GHz circulator and a 1-2 Ghz Berkshire LNA with 2 K noise temperature. Further amplification is done at room temperature using a Mitec® 0.1-12 Ghz amplifier. The signal is detected in an 80 MHz bandwidth around 1.35 Ghz using a HP power meter. The double sideband receiver noise temperature, $T_{N,DSB}$ is calculated from the measured Y factor using the Callan and Welton equations [15]. The LO used is a FIR laser pumped by a CO_2 laser. We use the 1.63 and 1.89 Thz CH_2F_2 laser lines to evaluate the HEB mixers designed for 1.6 Thz and 1.8 Thz respectively.

Two typical results of such measurements are shown in Fig. 3. In the left panel we show a mid-size HEB (0.3 x 2 μm) mixer with a 1.8 Thz antenna, evaluated at 1.89 THz. The lines corresponds to the unpumped and optimally pumped IV curves, the dots give the uncorrected values of $T_{N,DSB}$ at the optimally pumped curve. Using a coated lens and a direct Hot/Cold load 15 cm from the cryostat we obtain $T_{N,DSB}$=900 K. The LO power is evaluated using the isothermal technique (see Section 4). The right panel shows the result for a small (0.15 x 1 μm) mixer using an uncoated Si lens. This results in a receiver noise temperature of $T_{N,DSB}$ = 1100 K at 1.6 THz. This corresponds to 950 K if we would have used an anti-reflection coated lens [16]. Note that in the smallest devices we also observe a direct detection effect, which is found to reduce the heterodyne sensitivity. This effect is at least of the same order as the small remaining volume dependence of the noise temperature.

These results show that we have successfully transferred the new contact structure technology from large spiral antenna coupled devices to much smaller twin slot antenna coupled HEBm's. A great advantage of this technology, despite the noise performance, is the good reproducibility of mixer performance. This is

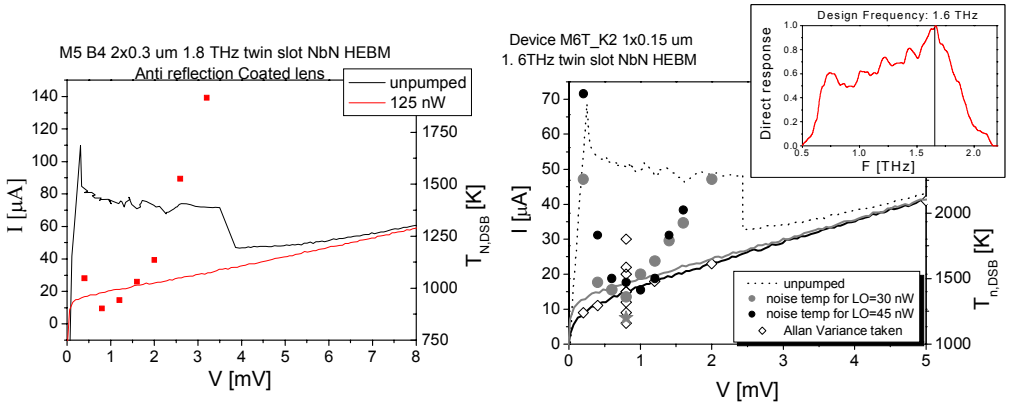

Fig. 3: Noise performance of 2 HEB mixers with twin slot antenna's. To the left we give the result of a 2 x 0.3 μm HEB, identical to the one shown in Fig. 3 with an antenna design optimized for 1.8 Thz The lines give the pumped and unpumped IV curve, the dots $T_{N,DSB}$ evaluated at 1.89 THz using an uncoated lens and a manual Hot/Cold load 15 cm from the cryostat window. The right panel shows $T_{N,DSB}$ and the pumped/unpumped IV curves for a 0.15 x 1 μm HEB with a 1.6 Thz twin slot antenna design, evaluated at 1.63 THz. The dots give $T_{N,DSB}$ obtained using a mirror hot/cold load 30 cm from the cryostat window. The star gives $T_{N,DSB}$ using a manual hot-cold load at 13 cm from the window.. The inset shows the direct response, obtained using a Fourier Spectroscopy measurement. The diamonds are the points at which the Allan Variance is measured (Section 4).

illustrated in Table I where we give the results of similar measurements on a set of devices from 4 different batches; all fabricated in different fabrication runs. It is obvious that the receiver noise temperatures differ only by about 15% between all devices. Given the fact that the mixer volume, and with that the LO power requirements, differ largely between different mixers this is surprising. Past results [10,11,12,18] always have shown a rather strong dependence of the receiver noise temperature on mixer volume that is hardly present in our data. A possible explanation is the new contact pad structure used for these devices. The noise dependence on the HEB volume has been attributed in the past to the presence of a contact resistance [12], which is absent in our devices [6-9].

Table I: $T_{N,DSB}$ *for several twin slot coupled HEB mixers with different volumes. The device ID is indicated as "batch-device", showing that results from 4 batches (M5,M6,M8,M9) are given. The receiver noise temperature is evaluated at 1.63 Thz fore the 1.6 Thz antenna and 1.89 Thz for the 1.8 Thz antenna. The real LO power given in the leftmost columns differs strongly from a measurement of the LO power need using the isothermal technique.*

Device ID	Twin Slot center frequency [THz]	Planer Dimension [μm x μm]	Measurement Frequency [Thz]	$T_{N,DSB}$ with coated lens [K]	LO power at mixer (isothermal/ technique) [nW]
M6-11K	1.8	1x0.15	1.89	940*	30
M6-2K	1.6	1x0.15	1.62	960*	30, ~240nW at mixer lens $#
M6-3K	1.6	1x0.15	1.62	900*	45
M9-C3	1.6	1x0.2	1.62	880*	75
M8-H1	1.8	1x0.15	1.89	1000*	65
M5-4B	1.8	2 x 0.3	1.89	900	125, 700nW at mixer lens#
M6-3D	1.6	1.5x0.25	1.62	860*	170
M6-5A	1.6	2x0.3	1.62	800*	330

# See section 4. This value is measured using a calibrated LO source.
$ obtained for a slightly overpumped IV that yields 45 nW according to the isothermal technique.
* Obtained from a measurement using an uncoated lens.

4: LO power requirement

The Local Oscillator power requirement is a crucial issue for the practical use of a Thz receiver. For real (space based) applications the output power of solid state LO sources in the THz frequency range is limited to the order of a few μW. Optics losses and antenna coupling limitations reduce the LO power available for the mixer itself to less than 1 μW. In the past the LO power needed to pump a HEB mixer has always been evaluated using the isothermal technique. Referring to Fig. 3 and table I we see that, according to the isothermal technique, all the devices need less than 330 nW of LO power. This is a sufficiently low value for virtual all applications. However, for a real application it is essential to verify whether the isothermal technique is correct.

To address this issue, we have tried to pump two different HEB mixers using a JPL solid state LO source operating at 1.524 Thz. Schematically the experimental setup is shown in Fig. 4. As a source we use a phase locked Gunn oscillator as input for a x16 JPL multiplier. This ensures low phase noise in the multiplied output signal.. According to JPL measurements, the LO output power at 1.524 THz is ~ 7 μW.

In the first experiment we use a 0.4 x 4 μm HEB mixer coupled with a spiral antenna. The device is glued to the back of an uncoated Si mixer lens. The absorbed LO power for the optimal pumping level is 750 nW, determined by the isotheral method. Surprisingly, with 7 μW of output power from the LO, the strongest pumping of the device we can reach is this optimal pumping level. Partly, this difference might be attributed to optics losses. Between the LO and the surface of the mixer lens there is 2 dB loss, due to

Teflon the lens, [-1 dB], window [-0.7 dB] and heat filter [-0.3 dB]. Hence at the mixer lens (denoted by "1" in Fig. 4) we have 4.4 μW of power available. The power available at the input of the antenna in the HEB mixer is about 2.3 dB less than the power available at the front of the Si lens, due to lens reflection, lens absorption and antenna coupling efficiency. Hence at the mixer we estimate to have 2.5 μW of LO power available. The isothermal technique, which is an estimate of the LO power absorbed in the bridge, gives hence a factor of 3.5 (or 5.4 dB) smaller than the actual power available at the mixer.

Two other experiments using similar LO systems and two different bolometers give similar results: For device M5 B4, presented already in the left panel of Fig, 3 we find, at an LO output power of 1.1 μW at 1.524 Thz (using the same JPL LO source), a power at the mixer lens ("1" in Fig. 4) of 700 nW, and 400 nW at the HEB itself ("2" in Fig. 4). The isothermal technique gives in this case 125 nW, hence there is a factor 3.3 between the real LO power need and the isothermal technique. For device M6 K2 (presented in the right panel of Fig. 3) we perform an identical experiment using a phased locked Gunn oscillator with a x6 multiplier chain at 673 GHz. The antenna response at this frequency is reduced by a factor 2 when compared to the center frequency of 1.6 Thz. This is shown at the insert of Fig.3. We measure the LO power need for an IV curve that requires 45 nW according to the isothermal technique, corresponding to an slightly overpumped operation, because at the optimal operating point 30 nW is required according to the isothermal technique (see Fig.3). We find a real LO power available at the mixer lens of 240 nW and 140 nW at the mixer, a factor 3.1 with the isothermal technique. The factor of 2 due to the reduced antenna response is included in the LO power quoted [19]. At the optimal pumping we estimate therefore that roughly 2/3 of 240 nW is needed, i.e. 160 nW.

From these three measurements we can conclude that the smallest volume HEB mixers need about 0.16 μW of LO power. Hence they are suitable for Space based applications or remote systems. It is also clear that the isothermal technique gives a large underestimate of the real LO power needed to pump the mixer. At the mixer level the difference is a factor 3-3.5. If the isothermal technique is used to estimate the LO power at the mixer lens needed to pump the mixers the difference is a factor of 5-5.5. Moreover the difference between the real LO power needs and isothermal technique seems to be roughly constant, contrasting findings by other groups presented in these proceedings [18]. Again, this might be related to the better reproducibility of the contact structure in our HEB mixers.

5: Stability

Until now, most HEB mixer development has focused on the area of improving device sensitivity, increasing IF bandwidth and gaining a better theoretical understanding of the device workings. However, before a phonon cooled HEB mixer can be integrated into a receiver system in a telescope suitable for astronomical observations, it is important to have an understanding of the fundamental stability limitations of the mixer. This is particularly important because telescope system noise temperatures are likely to be high. This in turn makes efficient integration of the noise of utmost importance. If the noise in the receiver system is completely uncorrelated, the noise integrates down with the square root of time, according to the radiometer equation [20]:

$$\sigma(t)=\langle x(t)\rangle\cdot(Bw\cdot\tau)^{-1/2} \qquad (1)$$

with σ the signal variance, $\langle x(t)\rangle$ the time average of the signal, Bw the signal bandwidth and τ the integration time. However, in practice the noise from a receiver such as a HEB or SIS mixer appears to be a combination of three terms: 1/f electronic noise, low frequency drift and uncorrelated (white) noise. Hence there is an optimum integration time, known as the "Allan" time (T_A), after which observing efficiency is lost. Experimentally a measurement of the "Allan Variance", defined as $\sigma_A(t)^2 = ½\ \sigma(t)^2$ is a powerful tool to discriminate between the various noise terms in a real receiver. From a mathematical

analysis it can be shown that for a noise spectrum that contains drift noise, 1/f noise and white noise that the Allan variance is given by

$$\sigma_A^2(t)=at^{\beta} + b/t + c \qquad (2)$$

For short integration times, the second term in the above Equation dominates and the Allan variance decreases as $t^{-1/2}$, as expected from the radiometer equation (1). For longer integration times, the drift will dominate as shown by the term at^{β}. In that case, the variance starts to increase with a slope β which is experimentally found to be between 1 and 2. On certain occasions, it is observed that the variance plateaus at some constant level. This is attributed to the constant factor and is representative of flicker or 1/f noise in the electronics. Plotting σ_A (t) on a log-log plot demonstrates the usefulness of this approach in analyzing the radiometer noise statistics. For reference Eq.1 has been drawn in Fig. 5. This represents the uncorrelated (white) noise part of the spectrum. The minimum in the plot gives the "Allan" time (T_A), the crossover from white noise to 1/f or drift noise. For the sake of optimum integration efficiency, one is advised to keep the integration time well below the system's Allan" time.

We present in Fig. 5 a measurement of the Allan Variance of device M6 K2. The noise performance and antenna response of this device has been discussed in Section 3 (see Fig.3), the LO power need of this device has been discussed in Section 4. The setup used to measure the Allan Variance is essentially the same as the one used to measure the LO power for this device. We use a phase locked Gunn oscillator, and x6 multiplier chain with a total output power of 70 μW at a frequency of 673 GHz as the LO. We have measured the double sideband receiver noise temperature at 673 Ghz with the exact same setup to be 1100 K, indicating that the mixer still has a reasonable sensitivity at the frequency in which the Allan variance is taken. The IF signal from the HEB passes through a thermally anchored Bias T, a 1-2 Ghz isolator and a 1-2 GHz Berkshire low noise amplifier (based on a GaAs HEMT), all thermally anchored to the 4.2 K plate of a Infrared liquid He Dewar. The signal is further amplified at room temperature using a commercial Miteq amplifier, filtered around 1.4 Ghz in an 80 MHz bandwidth and is attenuated by a tunable attenuator to keep the power at the input of the power meter constant. The amplified signal is measured at 200 Hz using an Agilent E4418 B power meter. A computer program is used to calculate $\sigma_A/\langle x(t)\rangle$ from this data.

In Fig. 5 we plot, in the right panel, the normalized Allan Variance $\sigma_A/\langle x(t)\rangle$ for several bias points along the optimally pumped IV curve (see Fig. 3) and, in the left panel at the optimum DC Voltage Bias for different pumping levels. At the optimal Bias point, V=0.8 mV, we obtain an Allan time of roughly 0.5 sec in the 80 MHz bandwidth. As sown in the figure, the Allan time increases slowly with increasing DC bias.

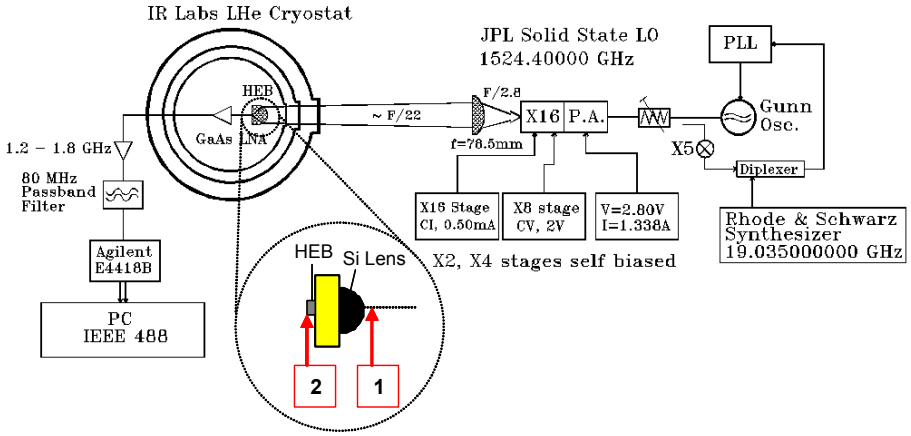

Fig. 4: Measurement setup to measure the real LO power need of a HEB mixer. The inset shows the two relevant points where the LO power is evaluated: "2" refers to the position of the HEB mixer itself, within the antenna. This is the point of reference when the LO power can be estimated using the isothermal technique. "1" refers to the front of the mixer lens, usually the reference point for the integration of a complete receiver system.σ

Saturating the device with either DC power or RF power yields an Allan variance that integrates down exactly along the radiometer equation. Hence it is clear that we are not limited by electrical noise sources in the system. However, noise in the LO source cannot be excluded directly. But given the fact that we use a phase locked LO system and given the observed clear bias dependence of the variance we believe that there is no direct indication of excess noise in the LO system. This finding is furthermore confirmed by the fact that another measurement of the Allan Variance on another device using another LO system essentially gives the same stability [21]. From the data presented in this paper and in ref [21] we can conclude that the present day HEB mixers cannot be used for on the fly mapping or continuum observations. However, for spectroscopic observations in a 1 Mhz bandwidth or smaller the stability is sufficient. This is because we have a relation $T_A \sim BW^{\alpha}$, with $1/2<\alpha<1$ [20]. Hence, at 1 MHz bandwidth the Allan time is to be expected to be of the order of 5 – 50 sec, allowing a chopping frequency of about 1 Hz.

6: Conclusions

Past results on large volume HEB mixers (0.4x4 μm) coupled with spiral antennas have indicated that a novel contact structure improves the sensitivity and bandwidth of HEB mixers. We have used this contact structure to fabricate smaller volume HEB mixers coupled with twin slot antennas. We observe a double sideband receiver noise temperature of 900 and 950 K at 1.63 Thz and 1.89 Thz respectively. The measurements on a large set of devices made in several different batches indicate a good reproducibility of the performance. They also show negligible dependence of the receiver noise temperature on the device volume. The real local oscillator power required to pump the HEBm's, evaluated at the level of the mixer itself, is found to be about 3-3.5 larger than estimated using the isothermal technique. This difference increases to a factor of 5-5.5 when the LO power is evaluated in front of the mixer lens. We find that the LO power of ~0.2 μW is required at the mixer lens to optimally pump the smallest HEB mixers. . The stability of the HEB mixers has been evaluated using a measurement of the Allan. The Allan time is found to be 0.5 sec. in an 80 MHz bandwidth. For real spectroscopic applications in a 1 Mhz bandwidth the stability is sufficient for integration times up to about 1 sec.

Acknowledgements

We wish to thank Jon Kawamura , S Cherednichenko, and T. Berg their helps and stimulating discussion during measurements at Chalmers University. We wish to thank John Pearson for making the JPL LO source available for our experiments. Furthermore we wish to thank Willem Jan Vreeling for all lab assistance.

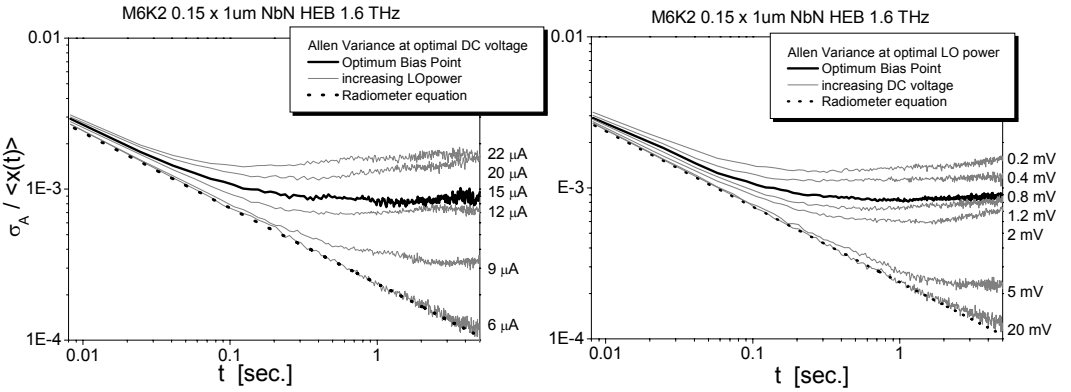

Fig. 5: Right: Normalized Allen Variance along the optimally pumped IV curve of the small HEB mixer (M6 K2, 0.15 x 2 μm) also discussed in Fig. 4. The numbers to the right indicate the DC voltage bias. Left: As a function of bias current at the optimal DC voltage V=0.8 mV. The bias current is indicated. Right: As a function of DC voltage along the optimally pumped IV curve. The dotted line represents the radiometer equation, Eq. 1, and the fat black line the optimal operating point.

References

[1]: Herschel home Page at ESA: http://astro.estec.esa.nl/SA-general/Projects/First/first.html

[2]: SOFIA Home page: http://sofia.arc.nasa.gov

[3]: TELIS home page: http://telis.af.op.dlr.de/

[4]: E.M. Gershenzon, G.N. Gol'tsman, I.G. Gogidze, A.I. Eliantev, B.S. Karasik and A.D. Semenov, "Millimeter and submillimeter range mixer based on electron heating of superconducting films in the resistive state", *Sov. Phys. Supercondcutivity* **3**, 1582, 1990.

[5]: D.E. Prober, "Superconducting terahertz mixer using a transition-edge microbolometer", *Appl. Phys. Lett.* **62**, 2119, 1993.

[6]: M.Hajenius, J.J.A. Baselmans, J.R. Gao, T.M. Klapwijk, P.A.J. de Korte, B. Voronov, G. Gol'tsman, "Improved NbN Phonon Cooled Hot Electron Bolometer Mixers" *14th Int. Symp. On Space Terahertz Technology, 22-24 April 2003, Tucson, Arizona, USA* (2003).

[7]: M. Hajenius, J.J.A. Baselmans, J.R. Gao, T.M.Klapwijk, P.A.J. de Korte, B. Voronov and G. Gol'tsman "Low noise NbN superconducting hot electron bolometer mixers at 1.9 and 2.5 THz" *Supercond. Sci. Technol. **17** (2004) S224–S228*

[8]: J.J.A. Baselmans, J M.Hajenius, R. Gao, T.M. Klapwijk, P.A.J. de Korte, B. Voronov, G. Gol'tsman, "Noise performance of NbN Hot Electron Bolometer mixers at 2.5 THz and its dependence on the contact resistance.*"14th Int. Symp. On Space Terahertz Technology, 22-24 April 2003, Tucson, Arizona, USA* (2003)

[9]: J.J.A. Baselmans, J M.Hajenius, R. Gao, T.M. Klapwijk, P.A.J. de Korte, B. Voronov, G. Gol'tsman. "Doubling of sensitivity and bandwidth in phonon cooled hot electron bolometer mixers" *Appl. Phys. Lett.* **84**, 1958 (2004).

[10]: S. Cherednichenko, P. Khosropanah, E. Kollberg, M. kroug, H. Merkel, "terahertz superconducting hot-electron bolometer mixers" *Physica C* 372-376, 407-415 (2002).

[11]: A. D. Semenov, H.-W. Hübers, J. Schubert, G. N. Gol'tsman, A. I. Elantiev, B. M. Voronov, E. M. Gershenzon, "Design and Performance of the Lattice-Cooled Hot-Electron Terahertz Mixer", *J. Appl. Phys.* **88**, 6758-6767, 2000.

[12]: M. Kroug. Ph.D thesis, Chalmers University of Technology, Goteborg,,Sweden, (2001).

[13]: Note that the factor of two decrease in noise temperature is only valid for the devices fabricated in this single process run. The best noise performance of a HEB mixer at 2.5 Thz with a conventional contact structure is $T_{N,DSB}$=1400 K [Ref. 9], roughly 1.5 times higher than the value reported here.

[14]: W.F.M., Ganzevles, L.R. Swart, J.R. Gao, PA.J. de Korte, and T.M. Klapwijk, "Direct response of twin-slot antenna-coupled hot-electron bolometer mixers designed for 2.5 THz radiation detection" *Appl. Phys. Lett.*, **76**, 3304(2000).

[15]: A. R. Kerr, " Suggestions for Revised Definitions of Noise Quantities, Including Quantum Effects". *IEEE Trans. Microwave Theory Tech*. **47-3**, 325 (1999).

[16]: The optics losses are identical at 1.63 and 1.89 Thz. Using a coated lens reduces the loss with 1 dB, using a mirror hot cold load in stead of a direct hand held Hot/Cold increases the loss with ~0.3 dB due to the longer air path.

[17]: This value is obtained using a 1 dB correction for the presence of an anti reflection coating on the lens.

[18]: S. Cherednichenko1, P. Khosropanah, T.Berg, H. Merkel, E. Kollberg, V.Drakinskiy, B. Voronov, G. Gol'tsman, "*Optimization of HEB mixer for the Herschel Space Observatory*" These proceedings (2004)

[19]: In this experiment we have 70 μw of LO power at the LO output. The LO is coupled reflectively through a 12.5 μm Mylar beam splitter (5.4% calculated reflection, -12.7 dB loss), the optics are a HDPE lens (-0.2 dB), cryostat window (-0.45 dB), heat filter (-0.2 dB) and a wire grid (-8.5 dB). This gives a total loss oof 21.6 dB. Hence we have 480 nW LO power available at the mixer lens. Including a factor 0.5 from the relative antenna response at 673 Ghz we arrive at the 240 nW quoted.

[20]: J.W. Kooi, G. Chattopadhyay, M. Thielman, T.G. Phillips, and R. Schieder, "Noise Stability of SIS Receivers*", Int J. IR and MM Waves*,, Vol. 21, No. 5, May, (2000).

Stability Measurements of a NbN HEB Receiver at THz Frequencies

T. Berg, S. Cherednichenko, V. Drakinskiy, H. Merkel, E. Kollberg

Department of Microtechnology and Nanoscience, Chalmers University of Technology

J.W. Kooi

California Institute of Technology

Abstract

To improve the signal to noise ratio, the operation of a receiver for radio astronomy applications requires an integration of the received signal over a certain time. When the integration time is too short, the effective observation time suffers from unavoidable black-out periods. Simultaneously an increase of the integration time is limited by the system stability, which consists of the stability of the mixer itself, the local oscillator (LO), the bias network and the read-out electronics. Using three LO-sources: a far infrared laser (FIR), a backward wave oscillator (BWO) and a multiplication chain, we have measured noise and gain stability of NbN hot electron bolometer (HEB) mixers of different sizes. As a stability measure we used the Allan variance time. We found that small HEB mixers are more unstable due to stronger noise-to-LO power dependence. For each HEB mixer size, we present data over stability and receiver noise temperature and discuss the trade off between system stability and noise.

Introduction

Due to the atmosphere's low transmission of radiation at terahertz frequencies, the receivers used to observe this radiation are usually placed on high and dry places or sent out in space. To use the observation instruments on these very remote places is expensive. It is therefore important that time is optimized to suit the wanted observation method (e.g. beam-, frequency-, position switching, etc), as discussed by Schieder and Kramer [1].

Radio astronomical receivers generally detect very weak signals deeply embedded in noise. To extract the signal of interest, synchronous detection is often used, i.e. the receiver is switched between on and off signal. However, since it takes a certain time to make this switch high chopping frequency will interrupt the integration time with many black-out periods. On the other hand low chopping frequency will give long observation time. However, the integration time is limited by the stability of the receiver.

If the noise is uncorrelated (white), it will, through integration, reduce independently of the chopping rate according to the radiometer equation:

$$\sigma = \frac{\langle x(t) \rangle}{\sqrt{B\tau}}$$

where σ is the standard deviation of the signal fluctuations, $<x(t)>$ is the signal mean, B is the bandwidth and τ is the integration time. In addition to white noise there is also drift and 1/f-noise in a real astronomical heterodyne receiver. Longer integration time does not necessarily give better signal-to-noise ratio since the noise is not uncorrelated. A method to determine the optimum integration time for a system is to measure and plot the Allan variance.

During the last ten years the phonon-cooled hot electron bolometer (HEB) has shown promising low noise properties for spectroscopic detection in the terahertz frequency regime [2]. Large efforts have been made to minimize noise, maximize the IF bandwidth and to achieve a theoretical understanding of the HEB. However, before the HEB detector can be fully integrated into a receiver, the stability of the device must be thoroughly investigated. In this paper we investigate stability of HEB receiver with regards to the bolometer size, type of local oscillator and IF chain.

The Allan Variance

To obtain the Allan plot used to determine the Allan time, we record the output power of a HEB receiver chain. We call the data points p_n n=1,…N, where N is 10^3-10^4. These values are grouped in *M* groups of *K* data points and averaged within the groups

$$X_i(K) = \frac{1}{K}\sum_{n=1}^{K} p_{(iK+n)} \qquad i = 0,...M \qquad M = N/K - 1$$

The Allan variance is then calculated using

$$\sigma_A^2(K) = \frac{1}{2M}\sum_{i=1}^{M}\left(X_{i+1}(K) - X_i(K)\right)^2$$

The variance is plotted as a function of the integration time $\tau = Kt$, where t is the time between the data points [3].

There are three main contributions to be aware of in the Allan plot [4]. The first is the white noise. It follows the radiometer equation and has a slope equal to -1. It is the left part in the Allan plot, see fig. 1. The second contribution is the 1/f-noise which has a slope equal to zero and will therefore not be reduced by longer integration. The last contribution is low frequency drift noise. This has slope ≥1 and is usually found for longer integration time in the Allan plot. Thus longer integration time will only give less efficient observations and not lower noise level if drift noise is present. These three contributions can be summarized as

$$\sigma_A^2(T) = \frac{a}{T} + b + cT^{\alpha}$$

Where *a*, *b* and *c* are appropriate constants. The Allan time (T_A) is defined as the integration time where the Allan plot deviates from the radiometer equation. Integration longer than the Allan time is not efficient and might reduce signal to noise ratio.

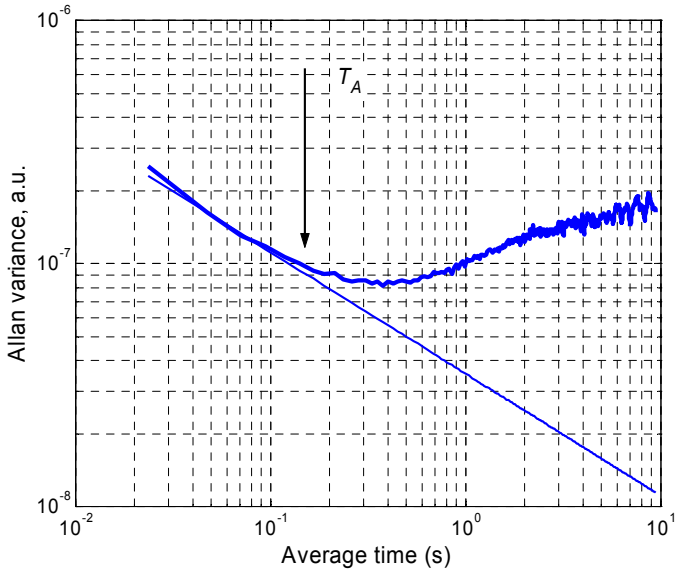

Figure 1 A Allan variance plot. The straight line shows the radiometer equation. The leftmost slope shows how white noise is integrated down, the middle part is the 1/f-noise and the right slope comes from slow drift phenomena.

Measurements

HEB mixers with bolometer size of 4x0.4 μm^2, 2x0.2 μm^2 and 1x0.15 μm^2 have been used. They are made of 3.5 nm thick NbN films. The films are processed with e-beam lithography as described in [5].

Three types of local oscillators were used: a FIR gas laser, a solid state source or a Backwards Wave Oscillator (BWO). The former is a ring gas laser pumped with a CO_2 laser. CH_2F_2 gas provided 1.63 THz and 0.69 THz lines. The solid state source is a chain consisting of three power amplifiers and four diode doublers. The chain is pumped with a 95 GHz Gunn diode oscillator to obtain an output signal of 5-10 μW at 1.5 THz. As an alternative to the Gunn oscillator, a 15.8 GHz synthesizer with x6 multiplier was also used with the output power of 5 mW. The solid state source is a Band 6 Low LO prototype for the Herschel Space Observatory. The BWO radiates at approximately 600 GHz.

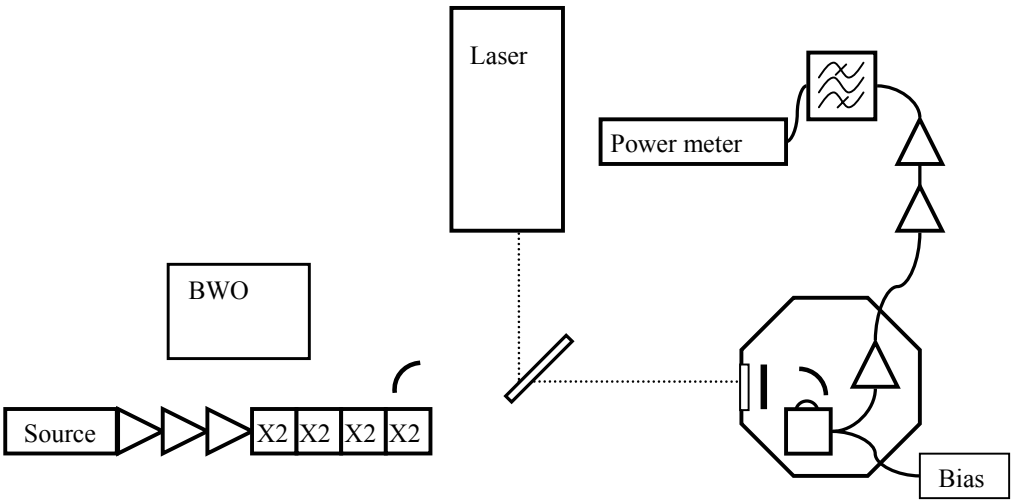

Figure 2 The setup: LO source, beam splitter (only used with the laser), cryostat with the mixer unit and LNA, room temperature IF chain with two Miteq amplifiers, a 30 MHz YIG filter and the power meter.

To measure the noise temperature of the receiver, the Y factor method is used. The cold load is an absorber in a bath of liquid nitrogen placed approximately 50 cm from the mixer. The radiation is transmitted via a mirror and chopped with the hot load, i.e. a chopper covered with Eccosorb at 295 K. During measurements with the FIR laser the LO signal is coupled into the mixer via a beam splitter made of thin polyethylene. An elliptical mirror and a parabolic mirror were used to match the beams of the LO and the mixer. Verification of the noise temperature of the HEB receiver was done with the FIR laser, as well as with the BWO. The noise temperature results are uncorrected.

The bolometer is integrated with a double slot antenna optimized for 1.6 THz. The HEB chip is glued on a 5 mm elliptical lens mounted in a HIFI band 6 prototype mixer unit. It is connected to a 2-4 GHz InP (Chalmers) LNA without an isolator in between. The cryostat is cooled with LHe.

The signal from the mixer is further amplified at room temperature with two 0.1-12 GHz Miteq amplifiers and filtered with a YIG-filter. The bandwidth of the filter is 30 MHz and it is tuned to 2 GHz. A HP power meter E4419B with an E4412A power head is used as IF detector. The detected signal is sampled with 40 Hz with the help of GPIB and Labview.

Stability Budget

The resulting Allan time that we measure represent the overall receiver stability. It is important to try to identify the part of the receiver that limits the stability. In general, one should pay attention to disturbances like thermal drifts of

the amplifiers and microwave detector, instruments warming up etc. Some of the details in the setup are analyzed further below.

When it comes to the stability of the HEB mixer itself, the mixer bias and LO power plays an important role. The IF output power as a function of current for changing LO power level is plotted in fig. 4a. They are obtained by following a vertical cross-section of the iv-curves (fig. 3). If the mixer is in the operation point it will react on all small changes in LO power amplitude, due to that the curves which are close to optimum operation point (0.7 mV and 1 mV) are steeper than the curves taken at higher bias (5 mV). The stability of the bias point also affects the output noise stability. How big this effect will be is determined by the steepness of the output power vs. bias voltage curve (fig. 4b).

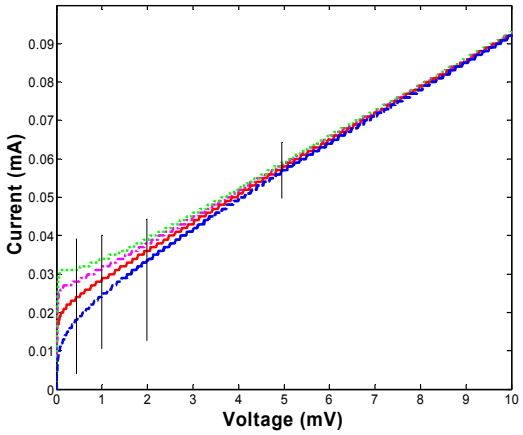

Figure 3 A set of iv-curves, increasing LO power from dotted green curve to dashed blue.

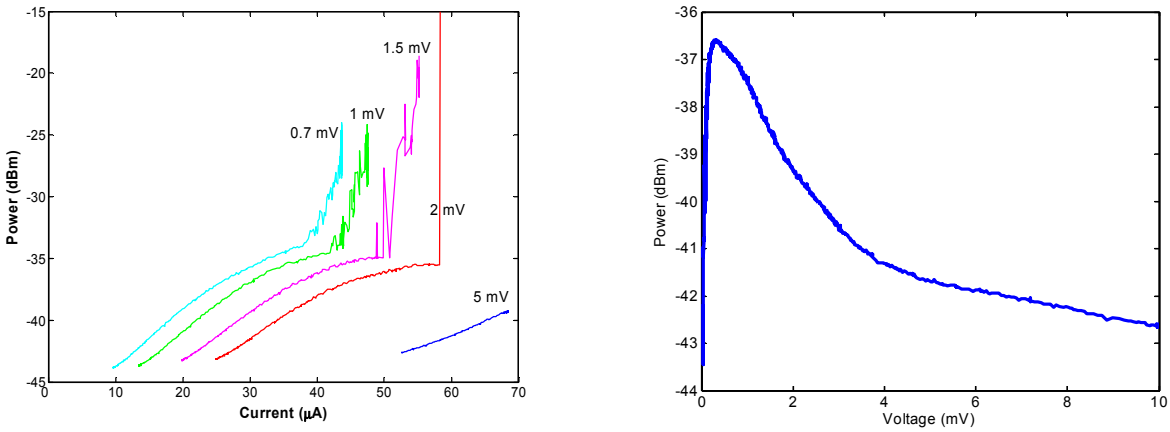

(a) *(b)*

Figure 4 (a): Output IF power as a function of the HEB current for changing LO pumping levels. The curves are obtained along the vertical black lines (constant bias voltage) in fig.3. (b): Output IF power as a function of bias voltage.

Another device in the setup which will affect the stability result is the LNA. The output noise from the mixer is 5-10 dB above the IF-chain noise, therefore gain fluctuations from the amplifier will immediately be detected (fig. 5). The noise from the IF-chain can be investigated with the mixer at a high bias point when the HEB basically acts as a resistor. The influence from the LO and mixer bias is according to fig. 4 minimized. The problem is that the

amplifier characteristics changes when the input impedance is changed. A LNA which is unconditionally stable with a resistor on the input can be unstable and oscillate when another impedance is present at the input.

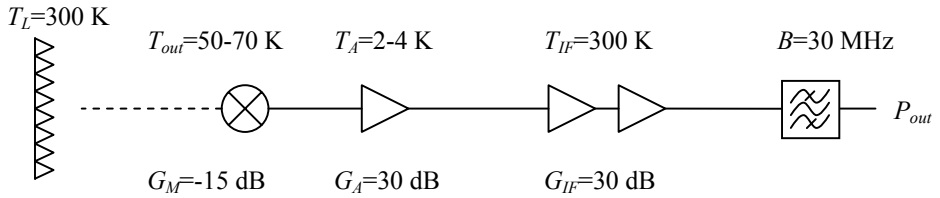

Figure 5 Noise budget

The total output power is

$$P_{out} = k_B B(2 \cdot T_L \cdot G_M \cdot G_A \cdot G_{IF} + T_{out} \cdot G_A \cdot G_{IF} + T_A \cdot G_{IF} + T_{IF})$$

Another factor which influences the amplifier is the bias source and at which bias point it is used. How sensitive the amplifier is depends on the design, type of transistor etc. Further investigations of the amplifier alone need to be done.

As a reference case in the Allan measurements we used the mixer biased to the resistive state. It is also possible to use the superconducting state. The difference is that the mixer does not produce any noise in the superconducting state and it will reflect the signal that comes from the input of the LNA. The risk of standing waves and oscillations in the amplifier is bigger.

Variations in LO power can come from both mechanical and electrical instabilities in the source. The former can for instance come from vacuum pumps or water cooling systems. In the FIR laser the resonating length is determined by grids moved by motors and pietzo crystals. Any instability in the position of the grid will be translated to fluctuations in the LO power. In the case of a solid state multiplier LO electrical oscillations can come from the biasing of the multiplier elements (i.e. diods), the power amplifiers or from the Gunn diode.

The optical path goes through room temperature air before it enters the cryostat. Possible fluctuations and effects from standing waves in the air are investigated by J.W. Kooi [6].

Results

Below the results follow as Allan plots categorized after which LO source that is used to pump the mixer. Noise temperatures are also indicated. The results are summarized in a table at the end.

Measurements with the FIR laser at 1.63 THz.

The time where the measured curve deviates from the radiometer equation line (T_A) is 2.5 s for the 4x0.4 μm^2 sized device. Noise temperature at optimum bias point (curve 2 in fig. 6) is 750 K. The mixer is in superconducting state as a reference case. The blue curve (1) is obtained with the mixer at higher bias voltage than optimum. For the 2x0.1 μm^2 device is the light blue curve (4) in fig. 7 measured in the optimum operation point (1 mV, 35 μA). The noise temperature is then 1250 K and the Allan time 0.2 s. For more (green curve (5), 30 μA) respectively less (pink curve (2), 45 μA) pumped device changes the stability, the Allan time for curve 2 and 5 is 0.1 s and 0.5 s, respectively. However, the noise temperature is 1500 K for both cases. The third device that we measured with the laser at 1.63 THz has the size 1x0.15 μm^2. The resulting Allan time is plotted in fig. 8. The LO power level is constant; the measurements are done at different points along one iv-curve. The stability at optimum operation point (between the purple (1) and the pink curve (2)) is 0.1 s. The lowest noise temperature measured for this device is 1550 K.

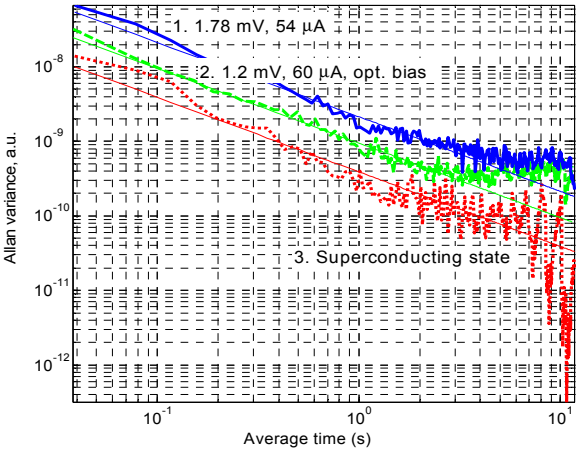

Figure 6 4x0.4 µm², FIR laser at 1.63 THz. Green curve (2) is optimum.

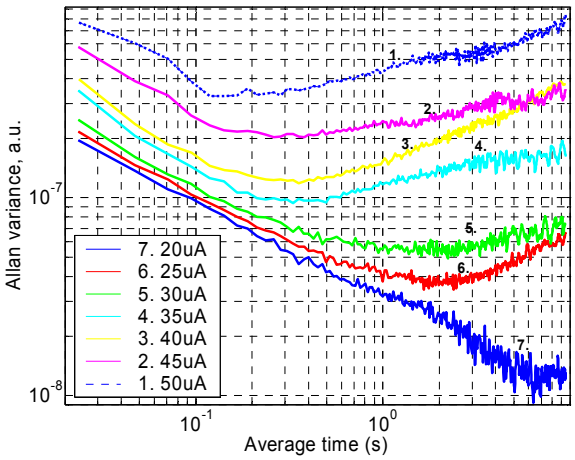

Figure 7 2x0.1 µm² device, FIR laser at 1.63 THz. Bias voltage is 1 mV, LO power level varied. Llight blue (4) curve is measured in optimum bias point..

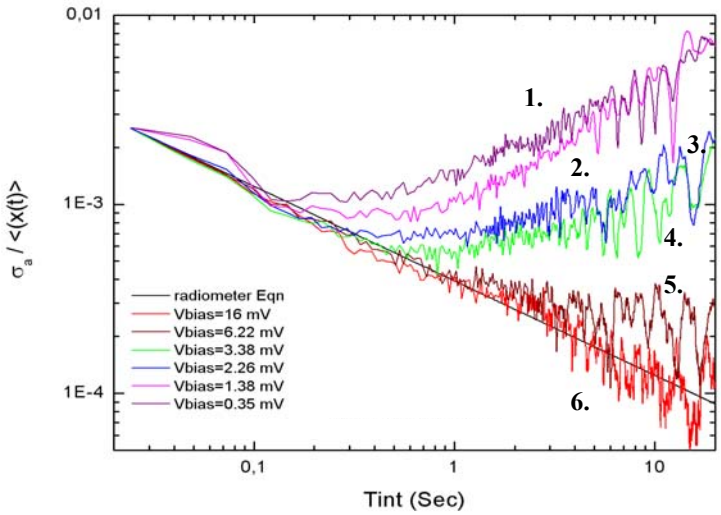

Figure 8 1x0.15 µm² device measured with FIR laser at 1.63 THz.

Measurements with the solid state LO at 1.5 THz.

It was only enough power to pump a small device (1x0.15 µm²) with the solid state LO. It is the same device as was measured with the laser in fig. 8. The curves in fig. 9 are obtained in the same way as in fig. 8, with constant LO power level and different bias voltages. The Allan time for the optimum point (pink curve (2) with bias 0.6 mV) is 0.2 s. The noise temperature is 1550 K. The effect of varying the pump level with the device in optimum voltage bias point was also investigated. The results for three pump levels are shown in fig. 10. The red curve (4) is the reference case with the mixer in resistive state. The best Allan time is the same as in fig. 9, 0.2 s for the optimum curve (green curve (2)).

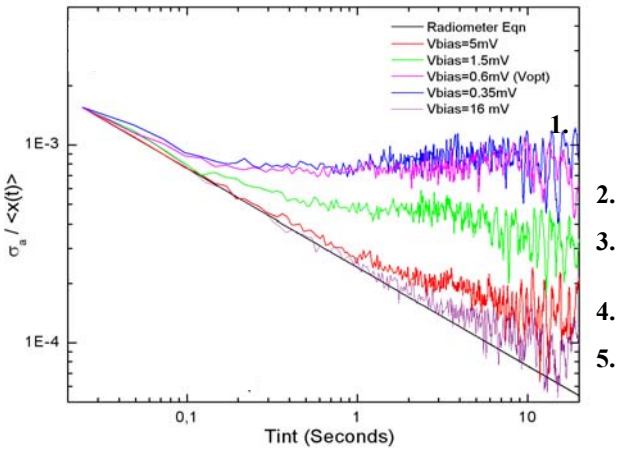

Figure 9 1x0.15 µm device measured with the solid state LO at optimum power level with varied bias voltage.

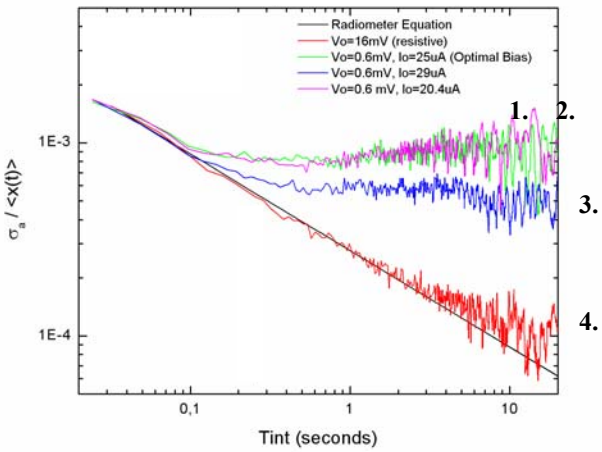

Figure 10 A 1x0.15 µm device measured with solid state LO. The LO pump level is varied.

Measurements with the BWO at 0.6 THz.

The middle sized (2x0.1 μm^2) device was also measured with a BWO at 0.6 THz. The resulting Allan time is 0.4 s (fig. 11). The antenna of this device is designed for 1.6 THz. However, a Y-factor of 0.2-0.3 dB was measured at 0.6 THz. During the measurements with the BWO we discovered that the bias of the LNA influenced the Allan time. This was not the case during the first measurements with the laser and the solid state LO. The measurements are done in the optimum bias point of the device for three settings of the LNA bias.

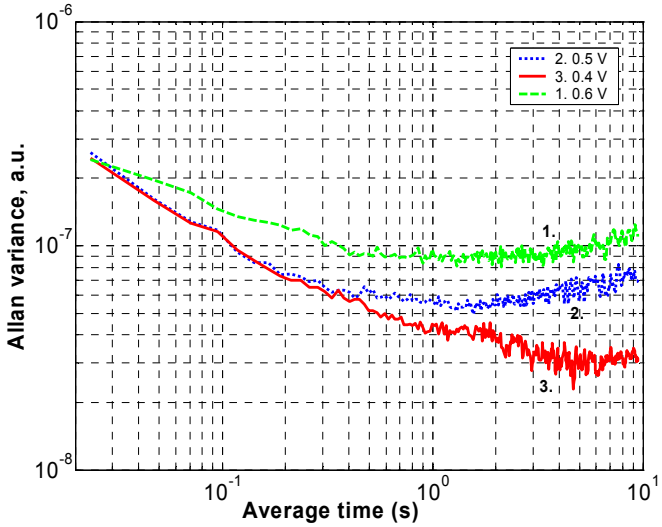

Figure 11 2x0.1µm2 device. BWO at 600 GHz, varying LNA bias

Measurements with the FIR laser at 0.69 THz.

To verify whether the improved result with the BWO was due to the LO itself or an effect of the lower frequency, we repeated the measurement with the laser tuned to 0.69 THz. The Allan time with the laser is 0.5 s with the best setting of the LNA (fig. 12).

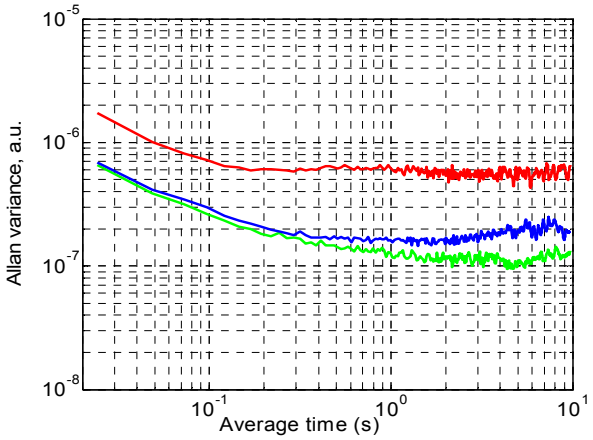

Figure 12 The bias to the LNA is varied. Measured with laser at 0.69 THz, device size is 2x0.1 μm².

Table 1 Allan time results summarized

Device size	FIR 1.63 THz	Solid state 1.5 THz	BWO 0.6 THz	FIR 0.69 THz	T_r
1x0.15 μm²	0.1 s	0.2 s			1550 K
2x0.1 μm²	0.2 s		0.5 s	0.4 s	1250 K
4x0.4 μm²	2.5 s				750 K

Conclusions

To measure stability of HEBs has shown to be a challenging task. It is difficult to draw clear conclusions from the results but a few tendencies can be commented. The size of the HEB plays a role; a larger device is more stable. A larger device also has better noise properties, but the drawback is that it needs more LO power to be pumped to the optimum point. A higher bias voltage and more LO power also gives more stability, as expected. When it comes to the different types of LO source it looks like the drift behaviour can be stronger with the laser. Compare for instance fig. 8 and 9. Otherwise it looks like the 1/f-part of the noise is limiting the stability of the overall receiver. The BWO gives a longer Allan time than both the laser and the solid state LO, this effect comes partly from the fact that the LO frequency is lower. One area that we will investigate further is the role of the amplifier.

References

[1] Optimization of heterodyne observations using Allan variance measurements. R.Schieder, C. Kramer. Astronomy and Astrophysics, v. 373, p. 746-756, 2001

[2] 1.6 THz heterodyne receiver for the far infrared space telescope. S. Cherednichenko, M, Kroug, H. Merkel, P. Khosropanah, A. Adam, E. Kollberg, D. Loudkov, G. Goltsman, B. Voronov, H. Richter, H.-W Huebers. Physica C 372-376, 427-431, 2002.

[3] Characterization and Measurement of System Stability. R. Schieder, G. Rau, B. Vowinkel, SPIE Vol. 598 Instrumentation for Submillimeter Spectroscopy, 1985

[4] Noise stability of SIS receivers. J.W. Kooi; G. Chattopadhyay; M. Thielman; T.G. Phillips; R. Schieder. International Journal of Infrared and Millimeter Waves, v 21, n 5, May, 2000, p 689-716

[5] Geometry dependence of the performance of NbN heterodyne hot electron bolometer superconducting mixers. P. Khosropanah, S. Cherednichenko, H. Merkel, S. Svechnikov, V. Drakinskiy, E. Kollber, G. Goltsman, Proc. EUCAS 2003.

[6] Regarding Atmospheric and Mechanical Stability Requirements of (LO-pumped) Mixers. J.W. Kooi, R. Schieder. Proc. Fifteenth International Symposium of Space Terahertz Technology, 2004

Development of NbN Terahertz HEB Mixers Coupled Through Slot–Ring Antennas*

Eyal Gerecht[1], Dazhen Gu[1], Xin Zhao[2], John Nicholson[2], Fernando Rodriguez-Morales[2], and Sigfrid Yngvesson[2]

[1]National Institute of Standards and Technology
Boulder, CO 80305

[2]Department of Electrical and Computer Engineering, University of Massachusetts
Amherst, MA 01003

ABSTRACT - In order to improve the power coupling to phonon-cooled hot electron bolometer (PHEB) devices, we are experimenting with a different type of antenna. The development of focal plane arrays (FPAs) with HEB devices requires a new approach for local oscillator (LO) injection. The goal of the project is to eliminate the need for a beam splitter or diplexer and to couple both the LO beam and the signal beam directly to the antenna. This direct coupling can be done by fixing the polarizations of the LO and signal beams to be orthogonal to each other. The slot-ring antenna has been used successfully at millimeter-wave frequencies, up to 94 GHz, integrated with Schottky barrier diodes. It can be easily coupled to a dielectric lens since it has a roughly symmetric radiation pattern. Slot-ring antennas are well suited for use with terahertz PHEBs.

We have designed, fabricated, and tested the first generation of slot-ring antenna coupled HEB mixers. The slot-ring antenna frequency is centered at 1.6 THz. A coplanar waveguide (CPW) stub filter, which presents an open circuit at the slot-ring, is used. The CPW requires air bridges (well-known in monolithic microwave integrated circuit (MMIC) technology at lower frequencies) in order to ensure that only the main CPW mode can propagate. Although slot-ring antennas have been used successfully at much lower frequencies, they present a challenge at terahertz frequencies. Nevertheless, a preliminary result of noise temperature of 2000 K at 1.6 THz represents the suitability of the slot-ring antenna in future FPAs based on HEB devices.

I. INTRODUCTION

Hot electron bolometric (HEB) mixer receivers for terahertz frequencies have been under development for the last 10 years. A few instruments based on HEB technology have been deployed primarily for astrophysical application [1]. Heterodyne detection is the most sensitive spectroscopic technique over a broad frequency range. In astronomical applications, observations of spectral lines

---

have played a major role in expanding our understanding of the interstellar medium and planetary atmospheres. In order to achieve the required sensitivity for astronomical, remote-sensing, and plasma-diagnostics applications, we need to develop receivers operating at sensitivities near the quantum noise limit, and focal plane arrays (FPAs) with multiple mixer elements. HEB mixers, which use nonlinear heating effects in superconductors near their transition temperature, have become an excellent candidate for applications requiring low noise temperatures at frequencies from 1 THz to 12 THz. In order to develop focal plane arrays with tens or hundreds of HEB devices, a new type of array architecture is needed.

Figure 1 illustrates a conceptual design for an FPA with multiple HEB devices. One of the main barriers for the development of terahertz imagers is the availability of LO sources with sufficient power and high tunability. Despite the low power requirement of a single HEB mixer (on the order of

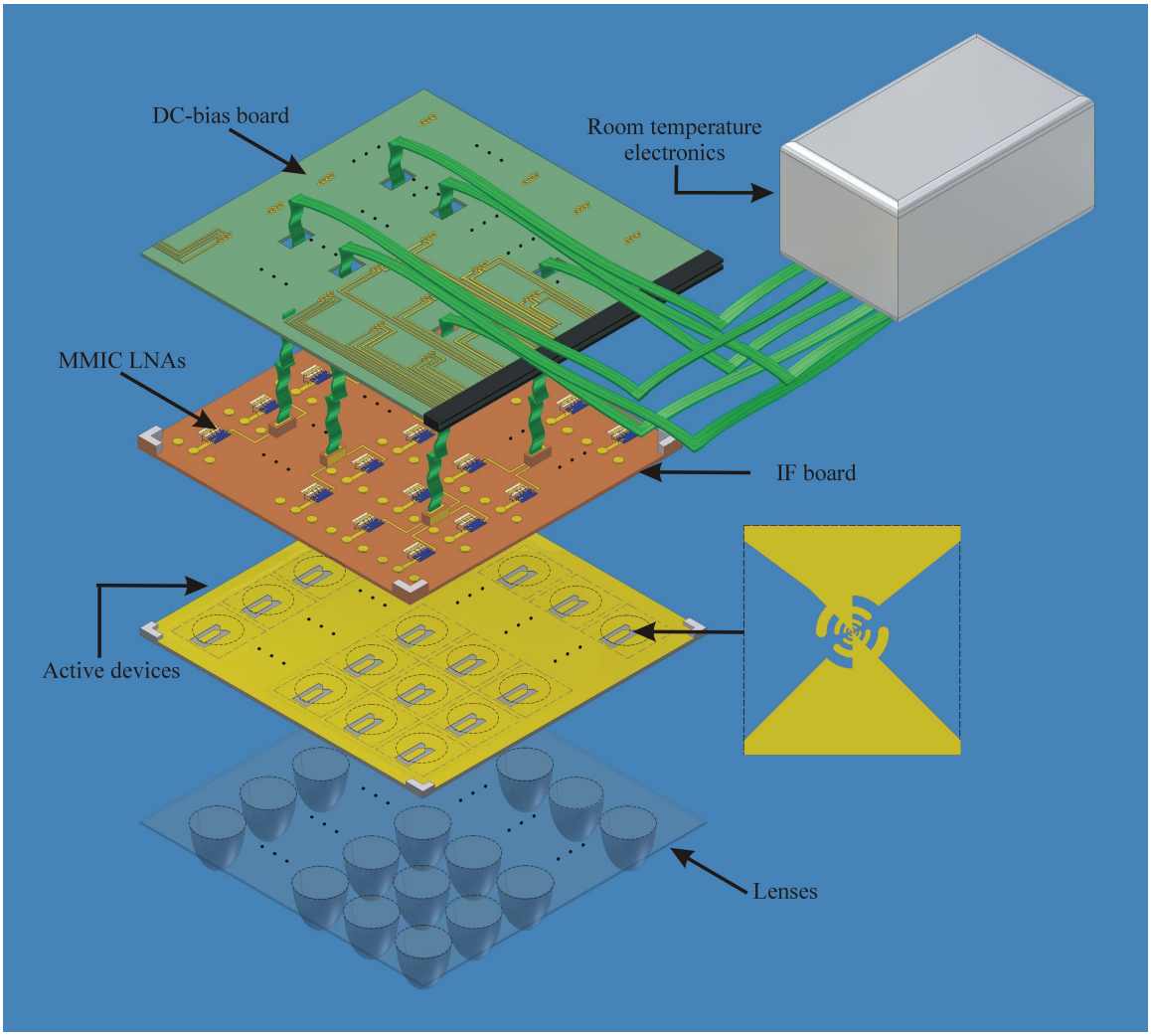

Figure 1: A proposed configuration for a terahertz heterodyne focal plane array with HEB devices.

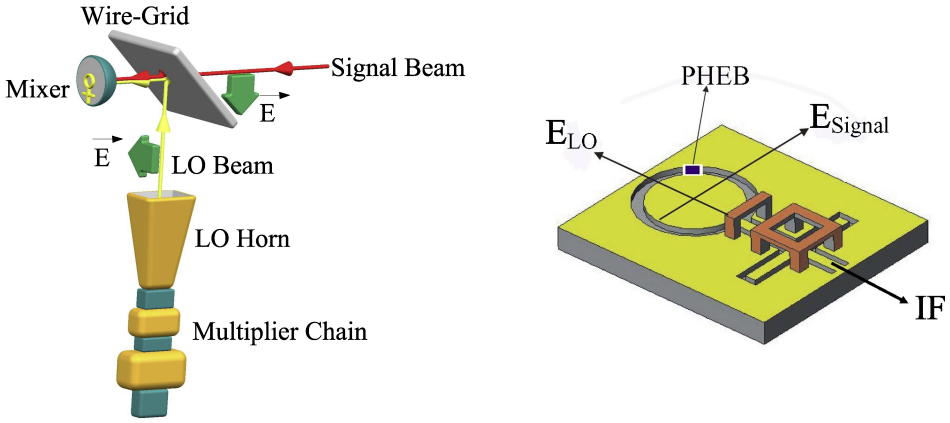

Figure 2: LO injection scheme using a slot-ring antenna and HEB mixer.

a few hundreds of nanowatts) only far-infrared (FIR) laser sources have sufficient LO power for an FPA. FIR gas lasers are not tunable and are very costly. The LO power is injected into the HEB device through a diplexer or a beam splitter so only a small portion (1-6%) of the LO power is utilized. Antenna designs used so far with HEB devices dictate that the polarizations of the LO and signal beams are parallel. By introducing slot-ring antennas, the polarizations of the LO and signal beams can be orthogonal to each other, thus allowing us to replace the beam splitter with a simple wire grid for LO injection, as shown in Figure 2. This method of injection was demonstrated to work well for a slot-ring antenna loaded with two Schottky-barrier diodes in the 45 degree positions [2], at 9 GHz and 35 GHz. Since the wire grid has almost no loss, both the signal and the LO will be coupled very efficiently. In the HEB mixer case, only one device can be used since the HEB devices are non-reciprocal. This paper describes the development of slot-ring antennas for HEB mixers at terahertz frequencies.

II. ANTENNA DESIGN

Slot-ring antennas were developed for use in millimeter wave frequencies with Schottky -barrier diode receivers and other active devices [2,3,4]. This type of antenna is well suited for quasi-optical design configuration where the antenna and mixer are placed on the planar side of a dielectric lens. This configuration yields a symmetric radiation pattern. Most of the energy radiates into the dielectric half-space. Slot-ring antennas can be used with single or dual polarizations. This antenna/lens configuration is compact and of low cost compared to other antenna designs and thus suitable for array configuration. The slot resonance is set by the circumference of the ring where the radius, a, corresponds to one wavelength ($_g$) in the dielectric half space. A more careful design of a slot-ring antenna calls for the circumference of the ring to be 1.08 $_g$. The width of the slot, 2w, is set by scaling from lower frequency (10, 35, 94 GHz) designs. A ratio of w/a=0.025 results in an antenna

resistance of 105 [3]. The intermediate frequency (IF) signal is then extracted through a CPW with two parallel quarter-wavelength open stubs placed a quarter wavelength away from the slot-ring. The purpose of the open stub filter is to introduce an open circuit at the slot-ring port, preventing any leakage of the signal or LO radiations into the IF port. The small dimensions of the open stubs make them preferable to other types of filters, which require a much larger footprint. In order to ensure that only the main CPW mode propagates, air bridges are placed on the filter. The HEB mixer device can be positioned in the orthogonal direction with respect to the CPW port to allow both the signal and LO beams, with the same polarization, to couple into the device. By altering the position of the HEB device to 135 degrees away from the CPW port, as in Figure 2, the polarizations of the signal and LO beams can be modified such that they are orthogonal to each other, as described above. The resulting efficient LO and signal injection represent the main incentive for choosing the slot-ring antenna design. Slot-ring antennas are well suited for use with terahertz PHEBs.

In order to study the coupling of the slot-ring structures at terahertz frequencies, we first designed a slot-ring antenna with a resonance frequency centered at 1.56 THz and a mixer placed at 90 degrees away from the CPW filter. The loading of the device on the slot-ring broadens the response of the antenna and produces a small shift in the resonance frequency. The design produced a slot-ring with a radius of 13.5 m and a width of 2 m (w/a=0.074). The width was determined by fabrication restrictions. The w/a ratio is larger than the one analyzed previously, so the design was simulated (see Figure 3) to determine the antenna impedance. At the design frequency of 1.56 THz, the antenna resistance was simulated using HFSS and found to be about 90 . The theory presented in [3] yields about 110 Both these values are close to what is required to match a typical HEB device (200).

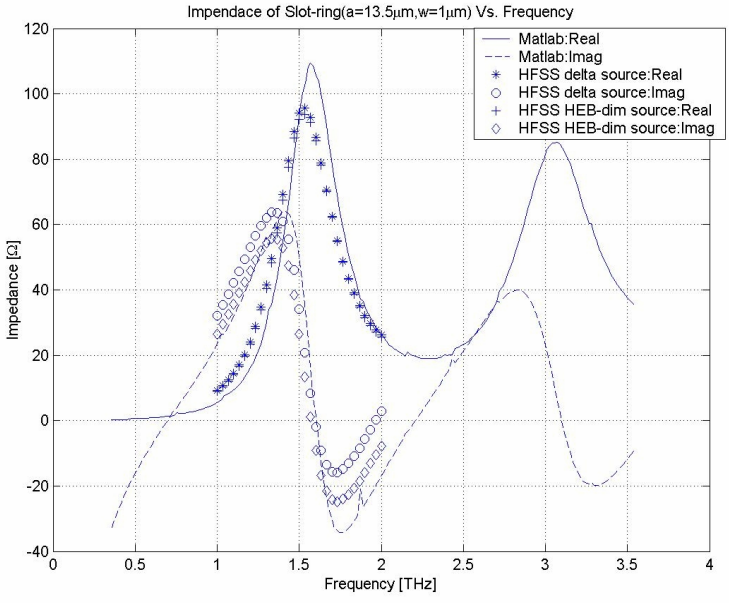

Figure 3: Slot-ring antenna impedance simulations using both MATLAB and HFSS.

Future development will study the coupling dependencies of slot-ring antennas with lower w/a ratios centered at terahertz frequencies. Edge effects altered the dimensions of the CPW filter stub compared with the nominal quarter-wavelength value, and our use of the SONNET simulator determined the stub length to be 2 m at a distance of 19 m away from the slot-ring. The HEB device is 0.4 m long and 4 m wide. The CPW requires air bridges (well-known in MMIC technology at lower frequencies) in order to ensure that only the main CPW mode can propagate. Due to the small dimensions of the structure air bridges were not introduced at this stage. With the HEB mixer device at 90 degrees away from the CPW port, and the LO and signal polarizations in the direction of the device, there is no field at the CPW port and the air bridges can be omitted.

III. DEVICE FABRICATION

PHEB devices were fabricated on 3.5 nm thick NbN film, which was deposited on silicon substrate by DC magnetron sputtering. The active area of the device was 4 μm wide by 0.4 μm long located in the center of the slot.

Figure 4 illustrates the main steps of the fabrication process. Due to the limitations of standard contact UV lithography, we have developed a process using an advanced stepper lithographic instru-

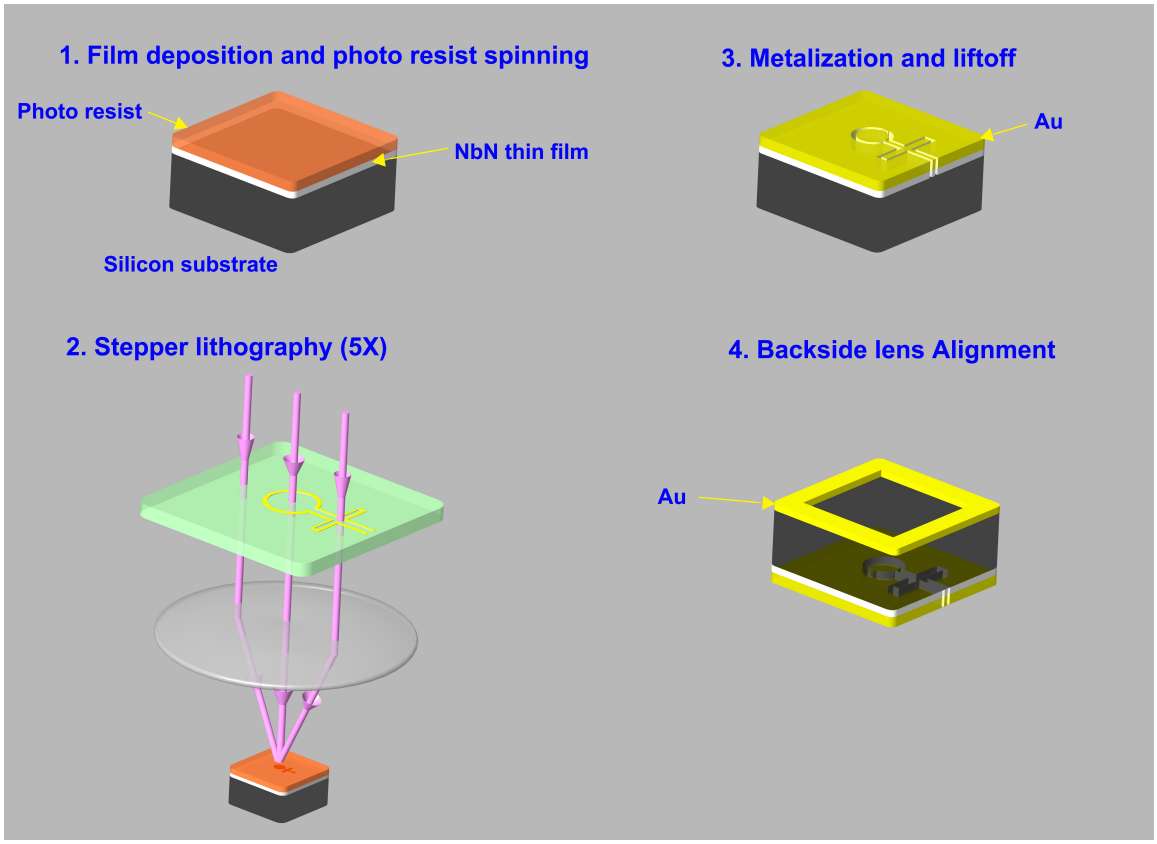

Figure 4: HEB device fabrication steps.

ment. This technique utilizes a very short wavelength UV light to reduce diffraction and thus achieve higher resolution. Furthermore, the stepper instrument uses lenses of high numerical aperture to project the exposure light, and consequently achieve a reduction by a factor of five of the image size on the wafer. The stepper lithographic technique is well suited for fabrication of multi-pixel arrays as opposed to electron-beam writing. We have also introduced a bi-level lift-off process that improves the success on this critical submicrometer lift-off step. In addition to the standard photo resist layer, a polymer lift-off resist (LOR) layer was spun first. At a specific pre-bake temperature, the LOR layer yields a 10 nm/sec undercut rate. After the metallization and lift-off steps, a strip of photo resist was patterned on the wafer to protect the device region from the reactive ion etch (RIE) step. Next, the excess NbN film was etched away by RIE.

The last step consists of a backside alignment window for lens positioning. This step was performed by use of a standard contact aligner and an infrared camera. Then, an elliptical silicon lens was affixed to the backside of the substrate with purified bee's wax. A photograph of the slot-ring antenna and PHEB device is shown in Figure 5.

IV. EXPERIMENTAL SETUP

The lens/substrate assembly was inserted into a mixer block [1], also serves as a bias tee. The mixer block is attached to a copper post, which is thermally anchored at its other end to the liquid helium reservoir of a commercial dewar. A heater controls the temperature of the mixer block. A cooled HEMT MMIC amplifier with a gain of 30 dB is used inside the dewar. This IF amplifier has a pass band from 0.5 GHz to 10 GHz and a noise temperature varying from 5 K to 10 K. The receiver noise temperature was measured with a CO_2 laser pumped far-infrared (FIR) gas laser as the LO source. Thin polyester film beam splitters with a thickness of 6 m acted as a diplexer between the LO and a chopped hot/cold noise source. The LO radiation was focused by an off-axis paraboloid mirror.

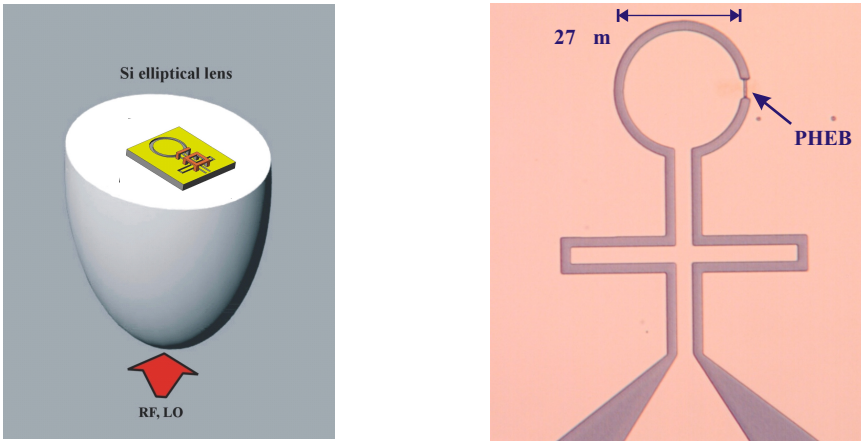

Figure 5: (left) an illustration of a quasi-optical configuration for the slot-ring antenna design; (right) a photograph of the antenna/ device structure.

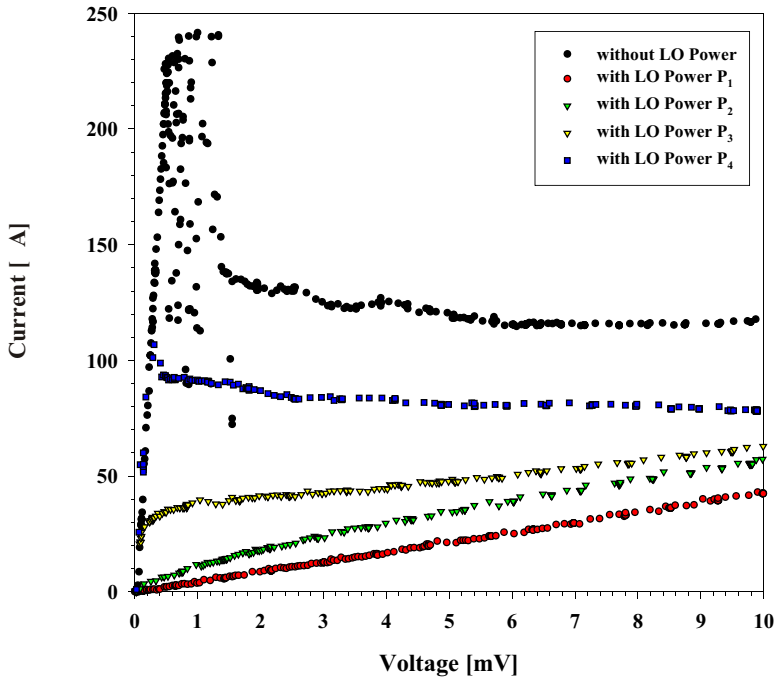

Figure 6: Measured I-V curves for the HEB device and the slot-ring antenna with no LO power and with decreasing levels of LO power (P_1>P_2>P_3>P_4).

V. RESULTS AND FUTURE DEVELOPMENT

The room temperature and the 20 K resistance values of one of our first PHEB devices are R_{300}=160 and R_{20}=270 , respectively. Total coupling efficiency of the structure is 14 dB, partly due to the mismatch between the device resistance (270 and the antenna resistance (90). The measured I-V characteristics suggests good HEB performance (see Figure 6). The optimum operating point for the noise temperature measurement is 0.5 mV and 55 A. The best uncorrected double-sideband noise temperature was 2000 K at 1.63 THz. There was no significant degradation of noise temperature at 1.4 THz confirming the wideband response expected for the slot-ring antenna. This preliminary result demonstrates the feasability of slot-ring antennas in future FPA with many PHEB devices.

The next step in the development of a dual polarization slot-ring antenna at terahertz frequencies is the design for the air-bridge structure. The small dimensions of the antenna makes this task difficult. Our approach is to fabricate the structure illustrated in Figure 7 using the deep reactive ion etching (DRIE) technique on a separate silicon substrate. A window is used on the back side of the slot-ring antenna to ensure 97 % of the power couples to the antenna. Special alignment marks are designed for assembly with the device substrate. This technique is well-suited for future development of multi-pixel arrays.

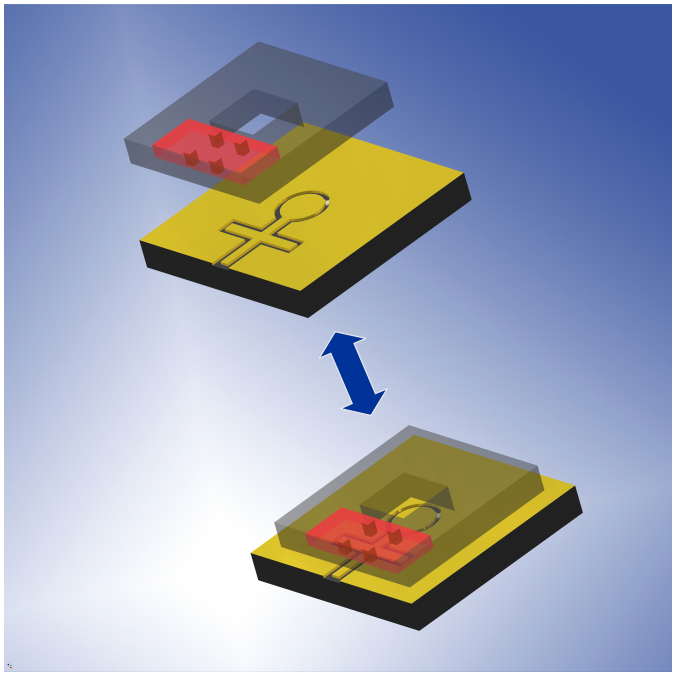

Figure 7: Concept for an integrated air-bridge/antenna design.

ACKNOWLEDGMENTS

This work was supported by NASA through grant NRA-00-01-SARA-012 to NIST and UMass/Amherst, and contract NAS1-01058 to UMass/Amherst.

REFERENCES

1. E. Gerecht, S.Yngvesson, J. Nicholson, Y. Zhuang, F. Rodriguez Morales, X. Zhao, D. Gu, R. Zannoni, M. Coulombe, J. Dickinson, T. Goyette, W. Gorveatt, J. Waldman, P. Khosropanah, C. Groppi, A. Hedden, D. Golish, C.Walker, J.Kooi, R. Chamberlin, A. Stark, C. Martin, R. Stupak, N. Tothill and A. Lane, "Deployment of *TREND* – A Low Noise Receiver User Instrument at 1.25 THz to1.5 THz for AST/RO at the South Pole". 14th Intern. Symp. Space THz Technology, Tucson, Az, Apr. 2003.
2. S.K. Masarweh, T.N. Sherer, K.S. Yngvesson, R.L. Gingras, C. Drubin, A.G. Cardiasmenos, and J. Wolverton (1994). "Modeling of a Monolithic Slot Ring Quasi-Optical Mixer, *IEEE Trans. Microw. Theory Techniques*, MTT-42, 1602.
3. S. Raman and G. M. Rebeiz, "An Annular Slot Antenna on a Dielectric Half-Space," IEEE Trans. Antennas Propagat. Vol. 42, pp. 967-974, July 1994.
4. Tong and R. Blundell, "Single- and Dual-Polarized Millimeter-Wave Slot-Ring Antennas," IEEE Trans. Antennas Propagat. Vol. 44, pp. 1438-1444, Nov. 1996.

Phonon-cooled hot electron bolometers on freestanding 2µm Si_3N_4 membranes for THz applications

Pedro Muñoz, Sven Bedorf, Michael Brandt, Thomas Tils, Martina Wiedner, Martin Brüll, Netty Honingh, Karl Jacobs

KOSMA, *I. Physikalisches Institut, Universität zu Köln, Zülpicher Str. 77, 50937 Köln, Germany*

ABSTRACT

KOSMA is working on the development of a heterodyne receiver channel (1.7 to 1.9 THz) for the GREAT instrument on SOFIA. We report on recent progress in fabricating and characterizing prototype mixers at 800 GHz on 2µm thick SiN membranes. The HEB is fabricated from a 5-6 nm thin NbTiN film with T_c= 8 K which was sputtered on a 20 nm thick AlN buffer layer at 400° C substrate temperature. An individual membrane device is then "flip-chip" bonded to a separately fabricated silicon frame. The frame assembly is mounted into the waveguide mixer such that the membrane is suspended in a substrate channel crossing the waveguide. All device fabrication including the thin NbTiN films is done at KOSMA. Heterodyne measurements with receiver noise temperatures of 1000 K at 1 GHz IF and 4.2 K bath temperature at first go are very promising for phonon-cooled HEBs on thin membranes as THz mixers.

1. INTRODUCTION

At KOSMA, we develop waveguide HEB mixers for SOFIA at 1.9 THz and APEX at 1.4 THz. Fabrication of mixer blocks at 1.9 THz with waveguide dimensions of 130 µm * 60 µm is complicated, but not impossible. The device substrate thickness must be thin enough to inhibit wave propagation in the substrate channel instead of coupling into the waveguide probes. At 1.9 THz, a substrate thickness less than 15 µm is the upper limit for a dielectric constant of 3.8 (crystalline quartz). Grinding and polishing crystalline quartz down to 25 µm has been realised elewhere [Loudkov]. Unfortunately quartz is very brittle at this thickness and it seems that the polishing and subsequent handling limits are around 20 µm. We have therefore concentrated on the development of a fabrication process on 2 µm thin Si_3N_4 layers. A successful attempt to fabricate devices on 3 µm thin Si-layers has been presented at the conference [Bass].

2. PHONON COOLED HOT ELECTRON BOLOMETER FABRICATION

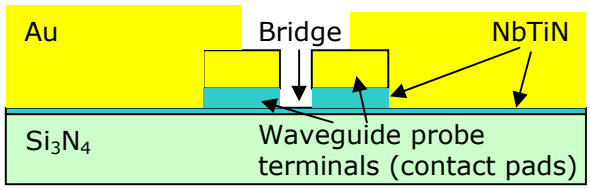

Fig. 1 simplified cross section of our HEB device

Phonon cooled NbTiN-HEBs on Si_3N_4 membranes were fabricated at KOSMA with exception of the Si_3N_4 layer, which was fabricated at Berkeley Microfabrication Lab. The 5-6 nm ultrathin NbTiN film was deposited by DC reactive magnetron sputtering at a substrate temperature of 400 °C on a 20 nm AlN buffer layer. Next the contact pads were patterned using a 210 nm single-layer PMMA mask with E-Beam lithography and liftoff. Before sputtering the 50 nm Au-contact pads, we applied an O_2 and Ar in-situ sputter clean and deposited a 20nm thick NbTiN layer [Baselmans]. The distance between the Au-contact pads determines the length of the HEB bridge. The RF-Filter structures are then patterned with UV lithography and liftoff. A bilayer of 80 nm low-stress Nb and 300nm Au are sputtered for the RF-filters. The last step of the device fabrication ist the patterning of the bolometer bridge itself with E-beam lithography and liftoff of an 30nm Al etch mask. A RIE etch process with NF_3 defines the width of the bridge.

3. Si_3N_4 Membranes

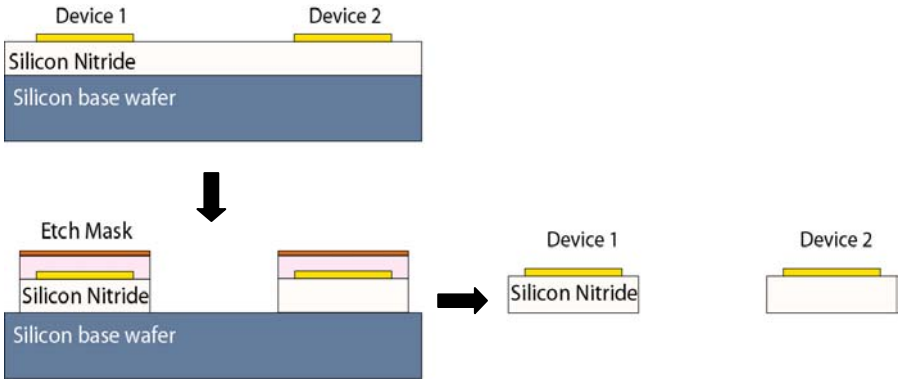

Fig. 2 Schematic description of the patterning and exposure of the Si_3N_4 membranes

The first step in fabricating the free-standing membranes is to define the boundaries of each device by patterning the Si_3N_4 layer in a grid as shown in picture 2, using a bilayer UV-Resist/Cu mask for increased etch resistance for the 2µm Si_3N_4 etch. After NF_3 RIE etch the devices are still connected, but the Si_3N_4 is removed between the individual devices. Before removing the etch mask, 500nm Au is sputtered onto the exposed Si surface, which helps to protect the devices during the wet etching step described below. After liftoff, we dice the devices to isolate them electrically in order to perform DC-characterization. After device characterization the wafer pieces are glued face down with w-wax. on a glass carrier wafer. The back side of the Si-wafer is polished to 80 µm thickness. This step eases the consequent wet etching with a solution of HNO_3 and HF dissolved in acetic acid. This is a standard isotropic Si-etching recipe and takes around two minutes to completely dissolve the Si on the back side of the membranes. As the acid solution is very abrasive, it is important to protect the devices well enough. Gold between the membranes has shown to be a resistant etch-stopper. The gold between the devices is now wet etched with an iodine based solution. Finally, the comb-like membrane structures with 14-33 devices are freed from the w-wax. Due to residual film stress, the membranes are slightly convex. As it turns out, this does not pose a mounting problem. More details on fabrication can be consulted in [Brandt].

4. Si-Frames

On one batch we produce a maximum of about 200 devices, which can be quite identical if so designed, assuming a realistic production yield of 80%. This rather large number of devices per batch is only possible because the frames to which the membranes are mountd in the mixer block are fabricated separately, so they do not occupy space on the membrane wafer. This also prevents device damage during frame fabrication.

The Si frames are fabricated from of a Si wafer with a top layer of Si_3N_4. 300nm gold films are patterned as bond contact pads for the membrane devices on opposite sides of the frames. The Si_3N_4 layer is patterned to frames similar to the device membranes. The Si_3N_4 is used as a mask for the Si wet etch in TMAH at 90 °C. The etch is stopped at the required depth and the wafer is polished from the backside precisely to the desired frame thickness.

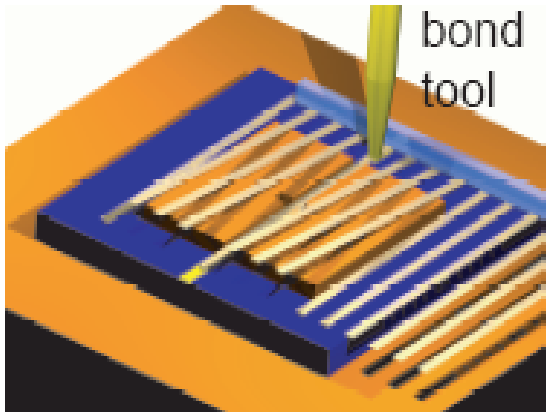

Fig. 3 Schematic description of bonding individual HEB device into the mixer block.

5. Mounting into The Mixer Block

The Cu mixer blocks including the waveguide and substrate channel are made at KOSMA. The Si-frame is glued with w-wax into a pocket surrounding the waveguide area. The comb-like membrane structure is placed on the mixer block. The membrane structure is shifted until the selected device falls into the substrate channel with the metallization facing down. A bond tool is used to attach the membrane device to the frame contact pads. An ultrasonic pulse on the back side of the membrane (now facing the bond tool) bonds the metallized side of the membrane to the gold contact pad of the Si frame (see fig. 3). The individual device can be easily broken off and the remaining devices of the comb structure are untouched. Details can be looked up in [Brandt]

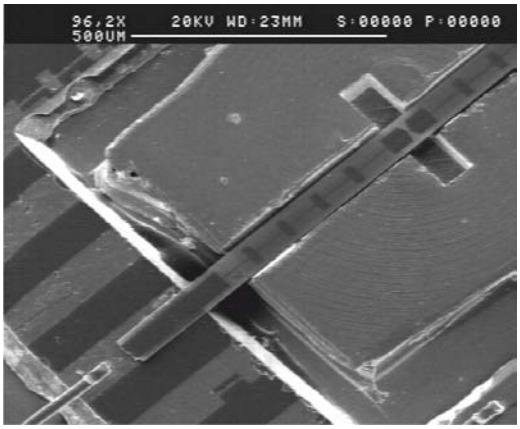

Fig 4. SEM-Picture of suspended membrane into the waveguide

6. DC-Measurements

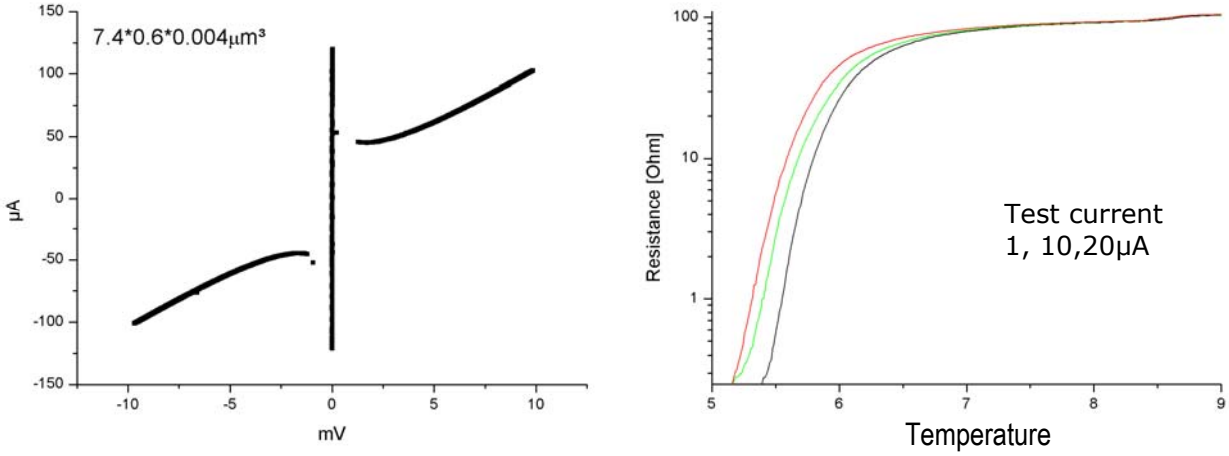

Fig. 5 Left: IV-Curve of the measured device. Right: RT-curve with three different test currents(20, 10 and 1µA, left to right)

In Fig. 5 an I-V characteristic of the selected HEB device is shown at 4.2 THz. This curve was measured during the initial DC tests of the device, using a dipstick setup. The nominal device dimensions are LxWxH=0.6x7.4x0.006 µm³. The critical current of 125µA implies that the critical current density of this device is 282 kA/cm². The normal state resistance is 70 Ω. The device dc parameters (resistance and critical current) scale very well with the geometry of the device. This fact points to the spatial uniformity of the film and the reproducibility of the fabrication process. The bridge becomes superconducting at a critical temperature of about 6 K.

7. RF-MEASUREMENTS

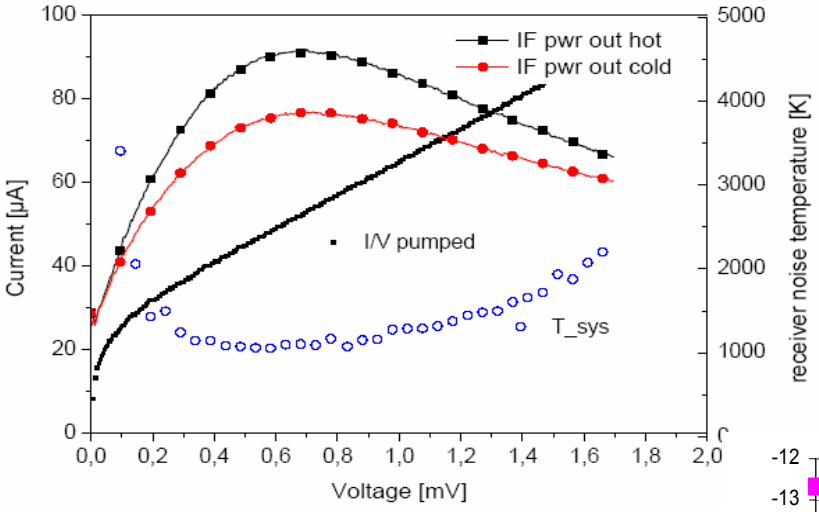

Fig. 6 Pumped IV curve (solid line). Hot and cold output (dots + line). Receiver temperature (dots).

measured with a solid state LO (Gunn diode with 2x and 3x multipliers) with an optimal output power of 40 µW. The Y-factor was measured by inserting a liquid nitrogen cooled absorber by hand into the path of the beam using a 35µm Mylar beam splitter (5% LO power reflection). The LO had to be manually detuned from optimal performance in order not to overpump the HEB.

To determine the noise bandwidth a tuneable band pass filter (Bandwidth 50MHz) was used to measure the noise temperature at different IFs. At fig. 7 this results are shown. The noise of the IF chain was previously determined in the same experiment through heating the HEB and using it as a Johnson noise source. Independently the IF chain was also calibrated using a SIS junction as a shot noise source. Both calibrations were in good agreement. The IF chain accounts for 6-10K over the IF-bandwidth. We measured a minimum receiver noise temperature 1000K at 0.4 mV voltage bias. At 1.0 GHz IF the calculated mixer gain is –13dB, whereas at 1.3-1.4 GHz IF it is –16db. Measurements of similar devices on bulk Si (measured using a quasioptical design at 800GHz) and devices from other groups using still thinner NbTiN HEB bridge films (4nm) [Loudkov] do not show significantly higher bandwidths. This points out the fact that the bandwidth, which is expected to increase reciprocally with the film thickness, may be limited by other factors, such as the escape time of the phonons into the substrate, which is in this case given by the phonon transparency and coupling of the NbTiN and AlN layers.

Prior to characterizing HEB mixer performance the RF spectral response has been checked using a Bruker IFS66v/s Fourier-transform spectrometer. The center frequency (800GHz) and bandwidths (=20%) in general agreed with that expected for our computer simulations. The HEB was used as a direct detector for the spectral response measurements. In order to increase the HEB voltage responsivity, the device was operated at 9K.

The receiver noise temperature was

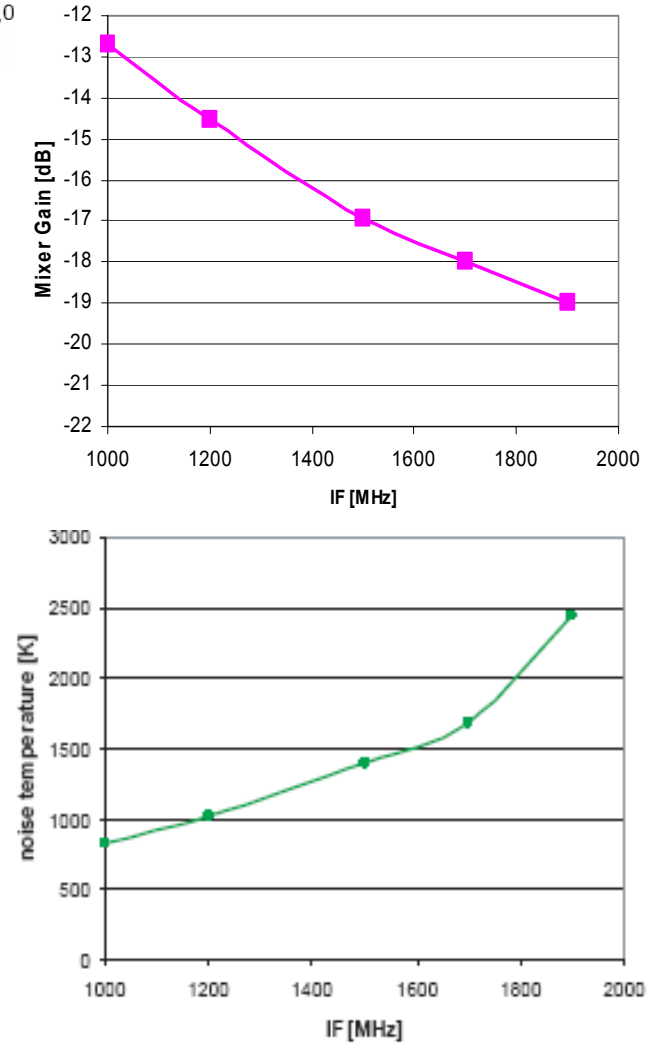

Fig. 7 Calculated mixer gain (upper diagramm) and measured noise temperature (lower diagramm) over the IF.

8. Astronomical Observations and Allan Variance

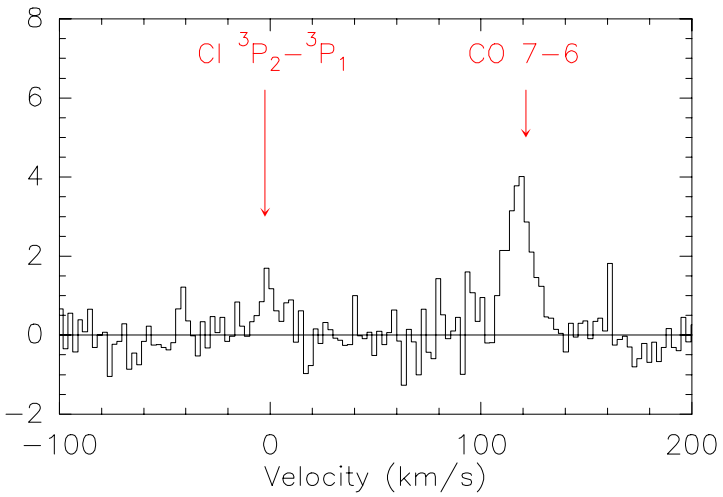

Fig. 8 Observation of DR21 with HEB mixer. The CO 7-6 line (right) lays in the lower band.

Spectrometers (AOS) with a resolution of 1MHz and over a band width of 735 MHz. From the data a spectral Allan variance similar to the one described in [Schieder] was calculated, resulting in a minimum time of around 7 sec, see Fig. 9. The SIS mixers in the same set-up are slightly more stable with a minimum time around 10s. The spectral Allan variance is sensitive to variations in the spectral response of the device over time and thus is a significant quantity for spectral line observations. It is a different quantity than the total power Allan variance which traces gain variations averaged over the whole band.

We also performed the first astronomical observations with a HEB in a closed cycle system, as far as we know. The atmospheric tau was between 1 and 2. We successfully detected DR21 (Fig. 8) in the CO 7-6 rotational transition. There is also a hint of the C0 3P2-3P1 (809 GHz) line, which was in the other (upper) side band.

We mounted the HEB mixer discussed above in the SubMillimeter Array Receiver for Two frequencies (SMART) [Graf] at the Koeln Observatory for SubMillimeter Astronomy (KOSMA) on the Gornergrat in Switzerland. SMART is a dual frequency array receiver currently containing four 490 GHz SIS mixers and three 810 GHz SIS mixers and the 800 GHz HEB. The mixers are pumped by two Local Oscillator at 490 and 810 GHz respectively and cooled by a Gifford-McMahon closed cycle refrigerator. Unfortunately, a low quality diagonal feed horn had to be used to direct the signal to the HEB as the Potter horn was needed for further laboratory measurements. This is the main reason that the noise temperature of the HEB at the telescope was 4000K.

With this set-up Allan variance measurements were performed looking at a liquid nitrogen load and using the read out of the Acousto-optical

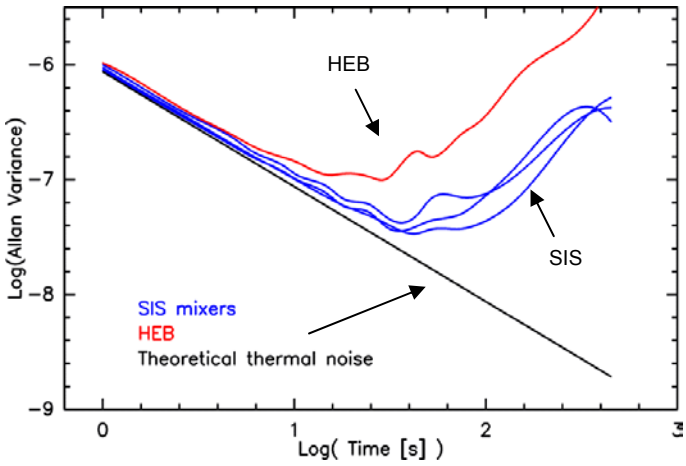

Fig. 9 Spectral allan variance of the HEB and SIS versus the theoretical thermal noise (straight line)

9. Conclusions and Outlook

We have demonstrated receiver noise temperature of 1000K at 800GHz for a NbTiN HEB waveguide mixer on suspended 3μm Si_3N_4 membrane. The measured IF noise bandwidth was 1.3 GHz. We did not observe a limitation of the IF bandwidth caused by the use of Si_3N_4 membranes instead of bulk substrate materials. The device was also used for astronomical observations at the KOSMA telescope at Gornergrat, Switzerland, showing sufficient stability operated in a closed cycle refrigerator. At KOSMA we are optimizing the NbTiN film characteristics as well as device fabrication in order to improve the IF bandwidth and reduce noise temperature, moving up to 1.2, 1.4 and 1.9 THz RF frequencies.

Acknowledgment

This work is supported by Deutsche Forschungsgemeinschaft SFB 494

References

[Loudkov] Loudkov D, Tong E, Blundell R, Megerian K, Stern J. "Characterization of NbTiN Hot Electron Bolometer Mixers" Fifteenth International Symposium on Space THz Technology, Northampton, MA, April 2004

[Baselmans] Baselmans JJA, Hajenius M, Gao JR, Klapwijk TM, de Korte PAJ, Voronov B, Gol'tsman G, "Doubling of sensitivity and bandwidth in phonon cooled hot electron bolometer mixers", APL 84 (11): 1958 (2004)

[Brandt] Brandt M. "Superconducting hot electron bolometers on silicon nitride membranes for terahertz waveguide mixers" PhD Universität zu Köln, 2004

[Schieder] Schieder R, Kramer C "Optimization of heterodyne observations using Allan variance measurements" *Astronomy & Astrophysics* 373 (2): 746-756 JUL 2001

[Bass] R.B. Bass, A.W. Lichtenberger, R.M. Weikle, S.-K. Pan, E. Bryerton, C.K. Walker, "Ultra-Thin Silicon Chips for Submillimeter-Wave Applications," Fifteenth International Symposium on Space THz Technology, Northampton, MA, April 2004

[Graf] U. U. Graf , S. Heyminck, E. A. Michael, S. Stanko, C. E. Honingh, K. Jacobs, R. T. Schieder, J. Stutzki, B. Vowinkel, "SMART: the KOSMA submillimeter array receiver for two frequencies", Millimeter and Submillimeter Detectors for Astronomy, Proc. SPIE, 4855-41: 322-329, (2002)

The Role of Quantum Noise in Terahertz Receivers

Sigfrid Yngvesson
Department of Electrical and Computer Engineering, University of Massachusetts, Amherst MA 01003, USA

Erik Kollberg
Department of Microelectronics and Nano Science, Chalmers University of Technolgy, SE-41296 Gothenburg, Sweden

Abstract: We have revised and considerably extended our paper on quantum noise at the 13th ISSTT. In the present paper we first review general quantum mechanical limits on the sensitivity of heterodyne receivers. We introduce the ideal broad band mixer (IBBM), which has a receiver noise temperature of zero Kelvin. Based on the hot-spot model of a real HEB mixer, we model it as an IBBM in series with a passive resistance. An expression for the HEB receiver noise temperature, including optical input loss is then derived. We find that the predicted DSB receiver noise temperature agrees well with three sets of measured data. The result suggests that quantum noise and classical HEB noise contribute about equally at low terahertz frequencies while at higher terahertz frequencies quantum noise dominates.

1. INTRODUCTION

Hot Electron Bolometer (HEB) heterodyne detectors for the THz frequency range use devices fabricated from thin films of low temperature superconductors, such as NbN. They have recently given rise to a radical re-evaluation of our ideas of this frequency range, which has traditionally been regarded as one in which no very sensitive heterodyne detectors exist. The sensitivity of HEB heterodyne detectors ('mixers') has become so good, i.e. the receiver noise temperature has become so low, in fact, that it is worthwhile to discuss if Quantum Noise will influence the receiver noise temperature of THz HEB receivers. Our theoretical analysis in this paper indicates that at frequencies of about 2 THz quantum noise is equal to the "classical" HEB noise, while at higher THz frequencies, quantum noise represents a dominant fraction of the total noise of HEB mixer receivers. We present a detailed analysis of quantum noise in HEB receivers. The analysis represents a substantial extension and revision of our first, preliminary paper on this subject given at the 13th ISSTT [1]. We introduce the **I**deal **B**road **B**and **M**ixer (IBBM), which shows no other noise than quantum noise (QN). Our basic assumption in the analysis is that the IBBM model applies to an IDEAL HEB heterodyne detector. We then continue to use the IBBM concept to discuss a more realistic HEB "hotspot" model, and derive an expression for the expected receiver noise temperature of HEB mixer receivers as a function of frequency. Finally, we show that available experimental data of receiver noise temperature at frequencies up to 5.3 THz can be fitted to this expression with good agreement. A considerably expanded and more detailed version of this paper will be submitted to a journal shortly [2].

2. QUANTUM NOISE AND THE IDEAL BROADBAND MIXER

It is important to emphasize that "Quantum Noise" is a concept, which fundamentally expresses the limit in our ability to perform a measurement of an electromagnetic field, imposed by the quantum mechanical nature of this field. Callen and Welton [3] showed in their generalization of the Nyquist theorem that fluctuations (noise) are intimately connected to the process of power dissipation. They calculated the average energy density of an electromagnetic field, in equilibrium with an environment at a temperature, T_0. They obtained two terms, one of which yields the Planck blackbody radiation formula. This term, when applied to a single mode transmission line case, produces the familiar Nyquist noise expression. The second term yields an energy of $hf/2$, which represents the vacuum (zero-point) fluctuations of the field. Formally we might find the power emitted due to the second term into a single mode transmission line in the same way as done by Nyquist. The total power radiated into a single mode in a band B at frequency f then becomes:

$$P_{CW}(T_0) = \frac{hfB}{\exp\left(\frac{hf}{kT_0}\right)-1} + \frac{hfB}{2} = P_{Planck}(T_0) + \frac{hfB}{2} \qquad (1)$$

The first term in this expression is the single-mode form of the Planck law. The thermal "Planck" noise power term rapidly goes to zero for frequencies higher than kT/h, and when this happens, the second term in Eq. (1) begins to dominate.

How are we to interpret the second term in (1)? It cannot represent exchangeable power, since it is impossible to extract power from the vacuum fluctuations. However, if we imagine an electromagnetic field with a power given by (1) at the input of a heterodyne detector with large photon number gain, it can be shown that *the minimum noise fluctuations at the output* of an ideal such detector can be regarded as having been produced by the second term in (1), which we will call the "quantum noise" term [4-9]. A general heterodyne detector generates an output at a very low frequency (the "IF") by down-converting radiation near the local oscillator. Using quantum mechanics Marcuse [4], and later Haus [6], rigorously analyzed such a detector (an ideal photo-detector mixer), with no frequency dependence of its properties close to the local oscillator frequency. In microwave terminology we would call this a "*broadband mixer*", or '*BBM*', i.e. a mixer with equal response in both sidebands. We will initially use this photo-detector model to discuss heterodyne detectors and later show that it applies to ideal HEB mixers. Haus chose a balanced mixer, which has the advantage that the fluctuations in LO power cancel to first order at the IF output. The noise temperature of a balanced mixer should be the same as that of a single ended mixer if the mixer devices are equivalent.

The result of Haus' analysis is that the fluctuations in the IF output with no external signal present is equivalent to a signal power corresponding to an expectation value for the photon number $\langle n_s \rangle$ per observation time, of one photon. Since the observation time τ is the inverse of the bandwidth, B, of the system then $P_s \cdot \tau = \langle n_s \rangle hf = hf$, and the equivalent noise power becomes hfB. This defines the minimum noise power one can have, the quantum noise. We thus have the following important conclusion:

The minimum output noise of an IBBM SYSTEM corresponds to an input noise power of *hfB* (2)

Based on Eq. (1) we see that the sum of the minimum input noise powers for the signal and the image which we can ascribe to the input source is also hfB. Since the vacuum input fluctuations already explain the output fluctuations, *there is no extra contribution required from the IBBM itself to satisfy the minimum system noise level. A second important conclusion is then*

The noise power added by an IBBM is ZERO (3)

The detailed analysis in Haus shows that the output fluctuations arise due to the properties of the commutator of the signal and image field operators, respectively. As Haus notes, "one may interpret this result as fluctuations induced by the signal (and image) zero-point fluctuations in the charge (or current) generated by the local oscillator photons."

In the ideal model for an HEB mixer, the IF current can be given a completely equivalent expression [9] to that for the photodetector case: $I_{IF} \propto \sqrt{P_s P_{LO}}$. Formally, the two types of mixers produce output currents which are equivalent functions of the input photon fluxes, and we can thus directly apply the results of the analysis in Haus to an (ideal) HEB mixer:

The noise power added by an Ideal Broadband HEB mixer is ZERO (4)

The same minimum noise output power as in Eq. (2) was also derived for a general linear amplifier by Caves [5] and many others. Wengler and Woody [7] showed that an optimum double sideband (DSB) SIS mixer operates in a manner similar to an ideal photodetector, and approaches the same minimum output noise power. SIS mixers require additional quantum considerations of the quantized charge in the device [9], which turn out in the ideal case to result in zero added noise, as in the photo-detector mixer case discussed above. Reference [8] stated the same conclusion as in (2), (3) and (4); that reference built on earlier papers analyzing quantum noise primarily in SIS mixers. Reference [7] concludes *that the only remaining noise source in an ideal SIS mixer is the process of "photon absorption"*. This reference added to previous analyses of SIS mixers a fully quantized model of the external circuit to which the mixer input was connected. The above references thus are unanimous in reaching the same conclusion as the one we stated in Eqs. (2), (3) and (4). We see that the limiting *total* noise power is the same for *any* coherent, phase-insensitive, receiver, whether an amplifier or a mixer, as expected on general quantum-mechanical grounds.

An ideal broadband receiver will consist of an IBBM with large photon number conversion gain, an IF amplifier, and a power detector, as shown in Figure 1. Due to the relatively low IF frequency (a few GHz), a THz mixer will always have a large photon number gain. Also, noise directly emitted at the IF (see below for details) should show

negligible quantum effects due to the low IF frequency. Apart from quantum noise, a real mixer may show other (classical) noise sources, $T_{CL,MIX}^{out}$. Also, the IF amplifier has a noise temperature, T_{IF}. We will disregard these classical noise sources for the moment, and discuss them later. This is done since we are first trying to identify the absolute minimum value which is allowed by quantum mechanics for the noise temperature. We further want to define the *system noise temperature* and the *receiver noise temperature* of the circuit in Figure 1. In doing so we use the convention that noise temperature is proportional to noise power [8], through

$$P_n = kT_nB \tag{5}$$

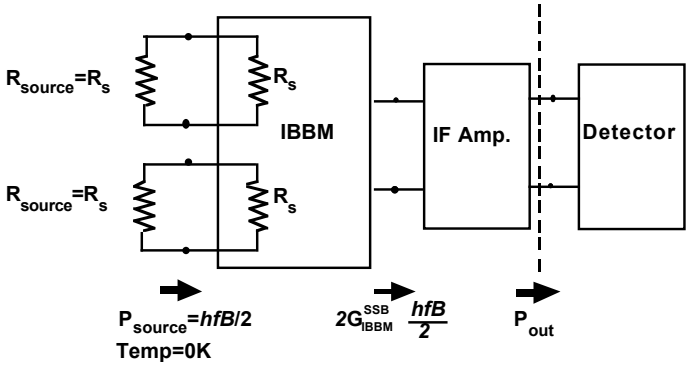

Figure 1. An IBBM receiver.

The system noise temperature is derived from (5) based on the noise power output of the entire system, including both the receiver and the input sources. If we can neglect all other noise sources except the quantum noise, we find from Fig.1 that

$$T_{sys,SSB} = \frac{hf}{k} \tag{6}$$

This is the quantum-limit for the *system* noise temperature of a broadband mixer receiver when performing narrow-band measurements (within a single sideband) [8]. If we instead perform broadband (continuum) measurements, the desired signal will be twice as large, and the ideal system noise temperature will be

$$T_{sys,DSB} = \frac{hf}{2k} \tag{7}$$

When calculating the *receiver* noise temperature, we will follow the usual convention [8] and subtract the noise power of the input source(s) from the total system noise output. For the ideal receiver in Fig. 1, we have (for both types of measurements)

$$T_{rec,DSB} = 0 \tag{8}$$

The results (6), (7) and (8) agree with those given in a recent paper by Kerr, Feldman and Pan [8]. These authors discussed a similar diagram as Fig. 1, and several others like it.

3. MEASUREMENTS OF THE NOISE TEMPERATURE OF HETERODYNE DETECTORS, INCLUDING QUANTUM NOISE

A standard Y-factor measurement involves measuring the ratio of the output powers obtained from the receiver when two input loads at different temperatures T_{hot} and T_{cold} are inserted at its input. As proposed by Kerr et al.[8], we use the CW expression (1) in the Y-factor expression to find the noise temperature.

$$T_{Rec,DSB} = \frac{T_{CW}^{Hot} - Y \cdot T_{CW}^{Cold}}{Y - 1} \tag{9}$$

Using Eq. (9) as written gives the total noise power *added* by the receiver, including QN, correctly. To find the system noise temperature for DSB measurements, we add $hf/2k$ plus any thermal input noise temperature in the particular system configuration:

$$T_{sys,DSB} = T_{\mathrm{Re}c,DSB} + \frac{hf}{2k} + T_{Planck}(in) \tag{10}$$

4. MODEL FOR THE BROADBAND HEB RECEIVER

In what follows in this paper, we will make use of both the Callen-Welton expression, and the concept of an IBBM, in order to estimate the minimum noise temperature of a broadband HEB receiver. The HEB device basically acts as an absorber of the radiation (LO plus signal plus image), and has no shot noise. As explained earlier, we will assume that an ideal, matched, broadband HEB receiver will approach the noise performance of the ideal heterodyne detector, i.e. its noise output, referred to its input, will be given by Eq. (2), and the limit for its receiver noise temperature is zero K, as stated in Eq. (8).

Any HEB mixer also necessarily produces noise output due to the fact that the HEB is a resistive device with finite heat capacity and finite temperature. There are two "classical" noise sources to take into account because of this: (1) Thermal fluctuation noise (T_{FL}) and (2) Johnson noise (T_J). The total is :

$$T^{out}_{CL,MIX} = T_{FL} + T_J \tag{11}$$

We use the subscript 'CL' ('classical') for this noise contribution. The typical magnitudes are T_{FL}≈50-100 K, and T_J≈T_c, which is about 10 K for NbN. We also need to include the noise temperature of the IF amplifier, T_{IF}, typically about 5 K or less. Assuming now that the circuit properties of the upper and lower sidebands are identical (which they are if $f_{IF} << f_{LO}$) and that we add signals at the upper and lower sideband respectively, we have a situation as indicated in Fig. 2: This figure summarizes the noise power flow for an ideal HEB mixer receiver, and the concepts we have introduced so far. We have also introduced input RF losses, which will turn out to be very important for the receiver and system quantum noise; these losses are actually the most important topic of this paper and will be discussed in detail next.

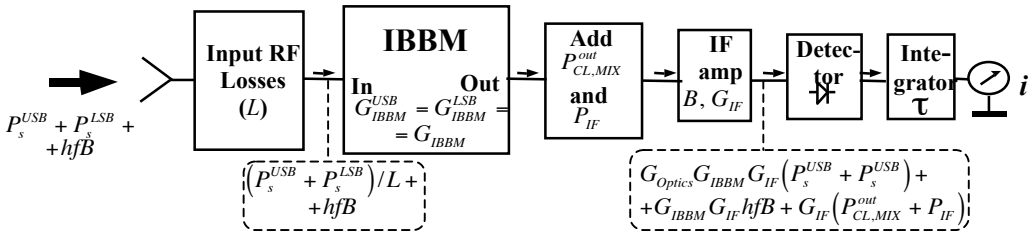

Fig. 2 Noise power flow in the HEB mixer receiver. The noise powers can all be translated into noise temperatures by using Eq. (5).

5. NONIDEAL HEB DEVICE: INFLUENCE OF "SERIES RESISTANCE"

It is obvious that the traditional model for the HEB mixer, where the device is assumed to be a dimension-less temperature dependent resistance, is a simplification of reality. It has recently been emphasized that it is important to take the contact resistance into account [13,14,15], and this will add a non-active series resistance. Even more important are the consequences of the hot-spot model [16], which suggests that the device at DC and IF frequencies is essentially a normal conductor in a central "hot spot" region and superconducting near the contacts. It turns out that the sensitivity to radiation absorption along the bolometer bridge is strongest near the boundary between the hot-spot and the superconducting regions. In a forthcoming paper [2] we will present a more detailed discussion of the influence of these effects on the QN, while in this paper we discuss a simple model which takes into account the contact resistances and the division of the bolometer into active and passive regions.

In the simplified model, we assume that the bolometer at THz frequencies is composed of two resistors in series, R_A (active resistance) and R_p (passive resistance). Recent modeling work [16] indicates that R_A may be of the order of 30 % of the full bolometer normal resistance, $R_B = R_A + R_p$. We assume that

(1) R_A represents the actual mixer, modeled as an IBBM, which also provides a "classical" IF noise output as given by (11),

(2) R_p is modeled as a passive resistor in series with R_A. We use the Callen-Welton expression to calculate the THz noise generated in R_p.

(3) The ratio $R_B/R_A = \beta$.

We insert an ideal circulator (Fig. 3) into our HEB model in order to take into account the fact that the active part, R_A, is also radiating Callen-Welton noise into the input circuit (from port 2). The circulator emphasizes that R_A is the

IBBM input impedance and nothing else. We assume that the IBBM has zero receiver noise temperature, and acts as a resistive load to the circuit to the left. In Fig. 3 we indicate that at the output of the HEB mixer to the IF circuit we must also include the "classical" HEB noise according to Eq. (11), i.e.:

$$P_{IF,out} = 2P_{in}G_{IBBM} + kT_{CL,MIX}^{out}B \qquad (12)$$

Note that G_{IBBM} is the conversion gain from R_A to the output port of the mixer device, see Fig. 3, and not the total mixer gain. We next calculate the noise power entering the IBBM in *one sideband*, and then refer it to the source. We get after some calculations [2]:

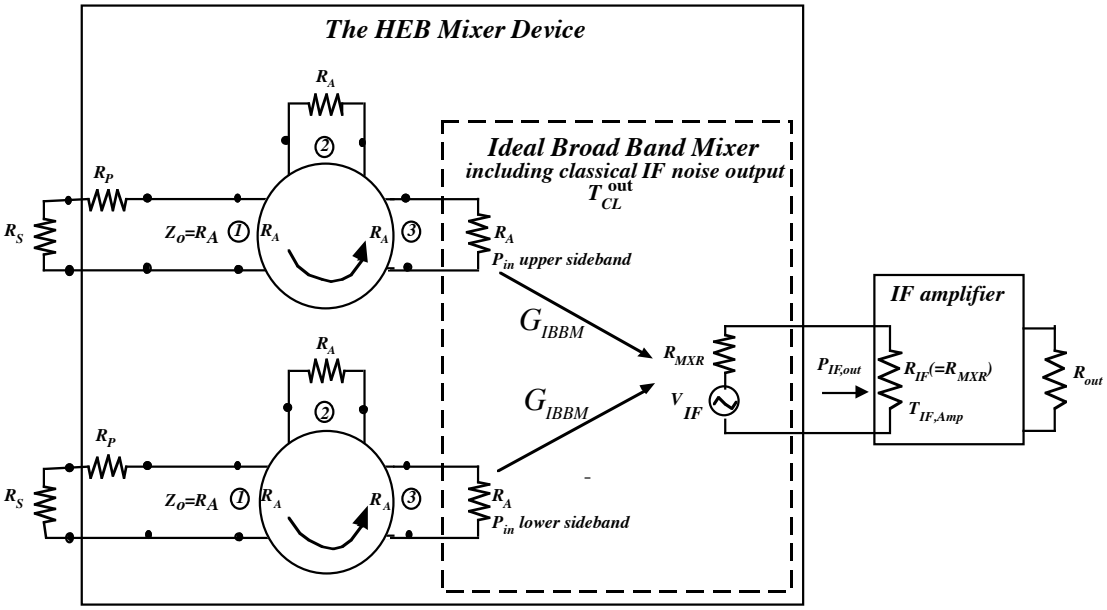

Figure 3. Model for the broadband HEB mixer only; optics not included.

$$P_{Source} = P_{Planck}(R_s) + \frac{R_p}{R_s}P_{Planck}(R_p) + \frac{\left(R_s + R_p - R_A\right)^2}{4R_sR_A}\cdot P_{Planck}(R_A) + \frac{hfB}{2}\frac{\left(R_s + R_B\right)^2}{4R_sR_B}\frac{R_B}{R_A} \qquad (13)$$

The first three different contributions in this expression are Planck noise related to respectively R_s, R_p, and R_A, while the last term is the quantum noise contribution. Notice that the $hfB/2$ is multiplied by a term always larger than one. Also notice that R_p is part of the reasons for the existence of input losses (compare Fig.2).

Incidentally, non-ideal photodetectors are often characterized by using a quantum efficiency, η [4]. Wengler and Woody also discuss the SIS mixer by introducing a quantum efficiency [7,17]. This is similar to our case; however, the increased insertion loss in the HEB is resistive, and then the CW expression should be used to calculate the modified noise properties.

6. RECEIVER AND SYSTEM NOISE TEMPERATURE FORMULAS FOR HEB THz MIXERS, INCLUDING OPTICAL INPUT LOSS

To analyze the noise due to ordinary attenuation in the optics we first consider the situation described in Fig 4. The optics part is represented by a two-port matched in both ends to R_s. The "characteristic impedance" of the optics is assumed equal to R_s, i.e. there are no reflections anywhere. The optical circuit introduces an attenuation L_{optics} and has a physical temperature of T_{optics}. If T_s=T_{optics} the noise power transmitted to the load (P_{CW}^{Load}) must be identical to the noise power $P_{CW}(R_s)$ from the source. Next consider $T_S \neq T_{optics}$. Then the noise contribution to P_{CW}^{Load} from the source is $P_{CW}(R_s)\cdot 1/L_{optics}$ whereas the contribution from the lossy two-port must be $P_{cw}^{optics}(T_{optics})\cdot\left(1-1/L_{optics}\right)$. Through similar calculations as performed above, we can now find the equivalent DSB receiver noise temperature for the case when both sidebands are matched. In order to facilitate comparison with experimental results it is

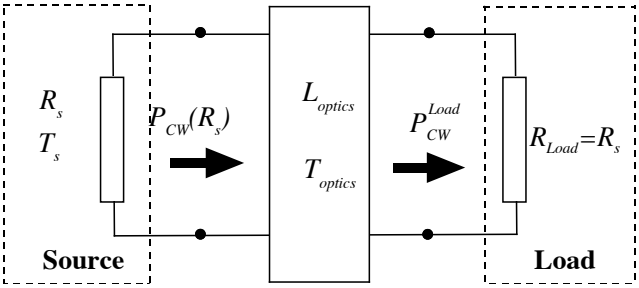

Fig. 4. A model for analyzing the equivalent noise from the quasi optical input circuit. Notice that both P_{CW}^{Load} and $P_{CW}(R_s)$ obviously include the same equivalent noise power due to the vacuum fluctuations, $hfB/2$.

convenient to break L_{optics} up into contributions from components at room temperature, L_{300}, and at liquid helium temperature, L_4, respectively. We can then neglect Planck noise at 4 K, and finally obtain:

$$T_{RX}^{DSB} = (L_{300} - 1)\frac{P_{Planck}(300K)}{kB} + \frac{hf}{2k}[L_{300}L_4 \cdot \beta - 1] + \frac{L_{300}L_4}{2G_{MXR}}(T_{CL,MIX}^{out} + T_{IF,Amp}) \qquad (14)$$

7. COMPARISON WITH EXPERIMENTAL RECEIVER NOISE TEMPERATURE DATA

In comparing experimental receiver noise temperature data with our predictions we will use Eq. (14), which assumes that the bolometer is matched to the source, and that the sidebands have equal conversion loss. There is only one set of data which extends far into the THz frequency range, up to 5.3 THz, that of the DLR/MSPU collaboration ("DLR"), [18]. A recent paper at the 15th ISSTT gives two points, at 2.5 THz and at 3.8 THz, respectively ("MSPU"), [19]. All other data sets have as their highest frequency 2.5 THz, and we will use measurements performed by the Chalmers University group ("CTH"), [20], which presently represent the best measured values at these frequencies[1]. In order to compare these data with Eq. (14) we also need to know the optical losses, and these are available in the DLR and CTH references. For the MSPU data we use the same optical losses as for DLR. We found simple polynomial fits to the optical loss as a function of frequency, and used these in the calculations to be described below. We extrapolated the optical losses to 10 THz based on these functions, beyond the highest frequency measured.

Equation (14) has three terms: (TERM 1): The optical input loss (Planck) term. These losses are assumed to be at 300 K; TERM 1 is generally small.; (TERM 2): The QN term; (TERM 3): The Classical HEB mixer and IF amplifier noise terms.

TERM 3 can be estimated from measurements at the lowest THz frequencies (1 to 1.5 THz), for which TERM 2 can initially be neglected as a first step in an iterative process. By calibrating the mixer output noise power compared with the case when the device is superconducting it is then possible to calculate $T_{CL,MIX}^{out}$, and $G_{MXR}^{tot} = G_{IBBM}/\beta$. The values of these two parameters also determine $T_{R,DSB}$. The IF amplifier noise temperature and the optical losses are measured or estimated separately. This general type of method is described in greater detail in [20]. Note that the classical HEB parameters are assumed to NOT depend on the frequency in the present paper. We can now determine a value of β which provides a best fit of $T_{R,DSB}$ calculated from Eq. (14) over the entire measured frequency range, by iteration. Figure 5a shows fits of the three sets of data mentioned above, obtained in this way. A straight line is also drawn for $T_{RX,DSB} = 10 \times hf/k$.

A reasonable fit can be found. In particular, the steep frequency dependence of the DLR data at the highest frequencies is modeled well by our expression. We interpret the different noise temperatures obtained at the lower frequencies as being due to less efficient HEB operation because of such effects as contact resistance and a large value for R_p outside the hotspot, which are expressed by the parameter β (compare the discussion in Sec. 5 above).

To get further insight into the results in Figure 5a, we plot the three terms in Eq. (14) separately in Figure 5b. We use the CTH data. **Note that even for the lowest THz frequencies (already employed in ground-based HEB**

[1] Recent data from the Delft/ESRON group are about equal to those obtained by CUT, but we do not have optical loss data available for these.

receiver systems, and soon to be employed in the first HEB mixers in a space instrument, Herschel) the QN term and the classical HEB noise term are of comparable size! As the frequency increases further, the QN term is predicted to rapidly become completely dominant. The curve for the classical HEB noise term also shows a weak frequency dependence due to the optical losses which depend on frequency. The input Planck noise (TERM 1) is very small in comparison with both TERM 2 and TERM 3. Similar plots are obtained for the two other sets of data. It is also of interest to note that if our extrapolation to higher frequencies of the best receiver noise temperatures up to 2.5 THz, obtained so far, is correct, then **it may be possible to obtain DSB receiver noise temperatures of 10×*hf/k* (straight line in Figure 5b) or better, at least up to 6 THz, and with future improvements of the devices and the optical coupling up to 10 THz.** Our analysis also gives an indication that improvements in device performance over the entire frequency range can be obtained by finding ways of decreasing the value of β for the devices.

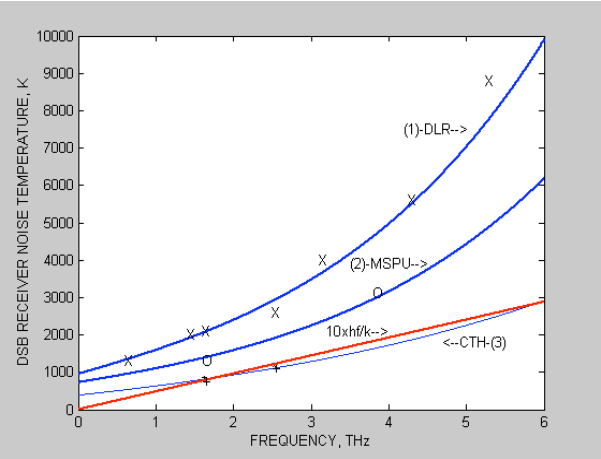

(a)

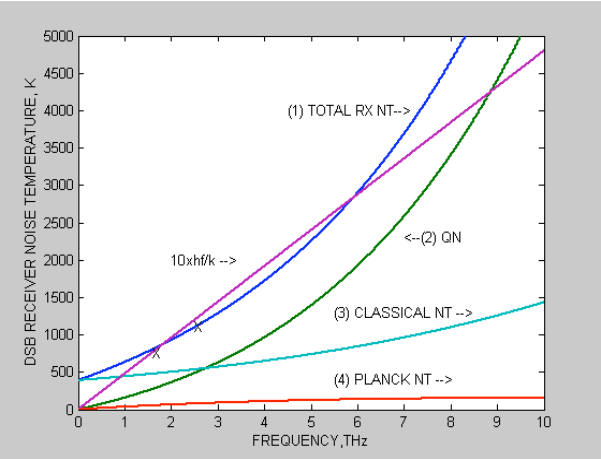

(b)

Figure 5(a). Fits of Eq. (14) to measured DSB receiver noise temperature data versus LO frequency from three sources (the values used for β are given after the symbols used for the plots): (1) DLR [18] (x) (β=10); (2) MSPU [19] (o) (β=6); and (3) CTH [20] (+) (β=4). The straight line represents $T_{RX,DSB}=10\times hf/k$.

Figure 5(b). Extrapolation of estimates of the three terms in Eq. (14) for the CTH data. The curves are (1) total receiver noise temperature; (2) the QN term; (3) the classical HEB and IF amplifier term; and (4) the Planck term of the optical input losses. The straight line again represents $10\times hf/k$.

10. CONCLUSION AND DISCUSSION

In this paper we derived an expression for the noise temperature of a "real" HEB receiver. This expression has two main terms, the QN term and the "classical" HEB noise term. The ratio of these two terms goes from about one at 2.5 THz to about five at 10 THz, as the quantum noise "takes over". By adjusting a single parameter, β, we can fit measured receiver noise temperatures as a function of frequency to this expression with good agreement. Since β represents resistive division between active and passive parts of the bolometer, high conversion loss at the lower THz frequencies is correlated with a more rapid increase of the receiver noise temperature at the highest THz frequency range. The values we obtain for β from our fitting procedure agree well with those derived from the latest hot spot model simulations. Although β is not determined with great accuracy (perhaps 20 %) the fact that a single value for β suffices to describe the behavior over a wide frequency range for at least two sets of measured data suggests that our model captures the basic features of the noise temperature variation with device quality and frequency. **Given this, one can be hopeful that HEB receivers in the reasonably near future can be developed up to 10 THz that will have receiver noise temperatures of 10×*hf/k* or better**. Such receivers, particularly in the form of focal plane arrays, are required for planned NASA projects in this frequency range such as SAFIR. Clearly, a much larger set of measured data is required to more definitely confirm or disprove the validity of the fundamental picture of HEB operation over a wide frequency range that we present. It appears possible to separate through more extensive measurements the two main terms in our noise temperature expression, and we plan to pursue such measurements and present the results in a future paper.

11. ACKNOWLEDGEMENT

We would like to acknowledge Harald Merkel for fruitful discussions and kindly supplying us with theoretical results. We would also like to acknowledge Antony Kerr and Jonas Zmuidzinas for discussions concerning the understanding of quantum noise. One of us (SY) would like to acknowledge support from NASA contract NAS1-01058 with the NASA Langley Research Center. EK would like to thank the Swedish National Board for Space Science and The Adlerbertska Research Foundation for support.

12 REFERENCES

[1] E. Kollberg, S. Yngvesson, "Quantum Noise Contribution to the Receiver Noise Temperature of HEB THz Heterodyne Receivers," 13th Intern. Symp. Space THz Technol, Cambridge, MA, 2002, pp. 73-74.

[2] E. Kollberg, S. Yngvesson, "Quantum Noise in HEB THz Heterodyne Receivers," to be submitted for publication.

[3] H. B. Callen and T. A. Welton, "Irreversibility and Generalized Noise", Phys. Rev. vol. **83**, no. 1, pp. 34-40, July 1951.

[4] D. Marcuse, "Engineering Quantum Electrodynamics", Harcourt, Brace and Worlds (1970; 2nd Edition 1980).

[5] C. M. Caves, "Quantum Limits on Noise in Linear Amplifiers", Phys. Rev. D, vol. **26**, No. 8, pp. 1817-1839, October 1982.

[6] H. A. Haus, "Electromagnetic Noise and Quantum Optical Measurements", Springer-Verlag, Berlin-New York, 2000.

[7] M.J. Wengler and D.P. Woody, "Quantum Noise in Heterodyne Detection," IEEE J. Qu.Electronics, vol. **QE-23**, 613-622,1987.

[8] A.R. Kerr, M. J. Feldman, and S. –K. Pan, "Receiver Noise Temperature, the Quantum Noise Limit, and the Role of the Zero-Point Fluctuations," in Proc. 8th Internat. Symp. Space Terahertz Technology, March 25-27, 1997, pp. 101-111. Available: URL: http://colobus.aoc.nrao.edu/memos as MMA Memo 161.

[9] J. R. Tucker and M. J. Feldman, Quantum Detection at Millimeter Wavelengths," Rev. Modern Physics, vol. **57**, no. 4, pp. 1055-1153, Oct. 1985.

[10] Harald Merkel, private communication.

[11] H. Ekström, B. Karasik, E. Kollberg, S. Yngvesson, "Conversion Gain and Noise of Niobium Superconducting Hot-Electron Mixers," IEEE Transactions on Microwave Theory and Techniques, vol. 43, pp. 938-947, 1995.

[12] A. I. Harris, "Coherent and Incoherent Detection at Submillimeter and Far-Infrared Wavelengths," Coherent Detection at Millimeter Wavelengths and Their Applications," (pp.7-73), Eds. P. Encreanz et al, Nova Science Publishers (Les Houches Series), NY, 1991.

[13] M. Kroug et al., "HEB Quasioptical Heterdyne Receiver for THz Frequencies," 12th International Symposium on Space THz Technology, San Diego, CA, pp. 244-252, 2001.

[14] P. Khosropanah et al., "Geometry Dependence of the Performance of NbN Heterodyne Hot Electron Bolometer Superconducting Mixers", Proceedings of EUCAS, Naples, 2003

[15] J. Baselmans et al., "NbN Phonon Hot Electron Bolometer Mixers with Improved Interfaces: Noise Temperature and LO Power Requirement," 15th International Symposium on Space Terahertz Technology, Northampton, MA, 2004

[15] H. Merkel et al., "NbTiN and NbN Hot Electron Bolometer – A Comparison," Proceedings of the 14th International Symposium on Terahertz Technology (to be published), 2003.

[16] D. Woody, and M. Wengler, "Experimental Verification of the Photodiode Theory of SIS Mixers," IEEE Transactions on Applied Superconductivity, vol 3, no 1, pp. 2230-2233, 1993.

[18] A.D. Semenov et al., "Design and Performance of the Lattice Cooled Hot-Electron Terahertz Mixer," J.Appl.Phys. vol. **88**, p.6758, 2000.

[19] Yu. B. Vachtomin et al, 15th International Symposium on Space Terahertz Technology, Northampton, MA, 2004.

[20] S. Cherednichenko, et al., "1.6 THz Heterodyne Receiver for the Far Infrared Space Telescope", Physica C, Superconductivity and its Applications, 372-376: pp. 427-431, 2002.

The ALMA Band 6 (211-275 GHz) Sideband-Separating SIS Mixer-Preamplifier

A. R. Kerr [1], S.-K. Pan [1], E. F. Lauria [1], A. W. Lichtenberger [2], J. Zhang [2]
M. W. Pospieszalski [1], N. Horner [1], G. A. Ediss [1], J. E. Effland [1], R. L. Groves [1]

[1] National Radio Astronomy Observatory
Charlottesville, VA 22903

[2] The University of Virginia
Charlottesville, VA 22904

ABSTRACT

The ALMA Band 6 (211-275 GHz) receivers use sideband-separating SIS mixer-preamplifiers with dual 4-12 GHz IF outputs. The sideband-separating mixers are of the phasing type, with the LO driving two component mixers in-phase and the RF signal connected to the mixers through a quadrature hybrid. The IF outputs of the mixers are amplified, then combined in a quadrature hybrid which separates the upper and lower sideband signals. The RF circuit components are all in a single split waveguide block — quadrature hybrid, LO power divider, LO couplers, cold image termination, and the two mixer chips. To achieve the wide IF bandwidth, a low-parasitic mixer is used and the preamps are bolted directly to the mixer block.

INTRODUCTION

The Atacama Large Millimeter Array* will have 64 antennas and will cover 35-960 GHz in ten bands using dual-polarized heterodyne receivers. In Band 6 (211-275 GHz), sideband-separating SIS mixers with dual 4-12 GHz IF outputs are used. Sideband separation (or rejection) in the front end is desirable for spectral line observations to reduce the contribution of atmospheric noise in the image sideband to the overall system noise. There are three ways to suppress the image response of a broadband mixer receiver: (i) A filter can be inserted in front of the mixer to terminate the mixer reactively at the image frequency. This is difficult in widely tunable receivers. (ii) A tunable four-port diplexer with a cold image termination can be used. This can be done quasioptically, *e.g.*, using a Martin-Puplett interferometer, but has limited IF fractional bandwith, requires mechanical tuning, and is cumbersome at millimeter wavelengths. (iii) A sideband-separating mixer can be used, and this is the approach used in the present work. Different approaches to sideband separation are described in [1]. At the 1998 ISSTT, we described a single-chip Band 6 sideband-separating mixer [2], and in 2000 proposed a waveguide version of a similar circuit but with balanced mixers [3]. Other waveguide based sideband-separating SIS mixers have been described by Claude *et al.* [4], Belitsky *et al.* [5], and Chin *et al.* [6]. The configuration used in the present work is shown schematically in Fig. 1. Of particular importance in Fig. 1 is the resistor R_{IM} on the fourth port of the RF quadrature hybrid. From the symmetry of the circuit, it is clear that this resistor is the image source for the sideband-separating mixer; USB thermal noise from this resistor is downconverted to the LSB IF output port, while LSB thermal noise appears at the USB IF output.

MIXER CIRCUIT DESIGN

Although a single-chip design with all the RF components on the same substrate may seem attractive, the large size of the chip compared with that of a simple elemental mixer results in a relatively small number of mixers per wafer. As ALMA requires well over 100 mixers for each band, we explored the feasibility of machining the RF components as waveguide circuits in a single E-plane split metal block which also contains two elemental mixer chips. The most difficult component to fabricate with acceptable gain and phase imbalance is the waveguide quadrature hybrid, but this

* The Atacama Large Millimeter Array (ALMA) is an international astronomy facility. ALMA is an equal partnership between Europe and North America, in cooperation with the Republic of Chile, and is funded in North America by the U.S. National Science Foundation (NSF) in cooperation with the National Research Council of Canada (NRC), and in Europe by the European Southern Observatory (ESO) and Spain. ALMA construction and operations are led on behalf of North America by the National Radio Astronomy Observatory (NRAO), which is managed by Associated Universities, Inc. (AUI), and on behalf of Europe by ESO.

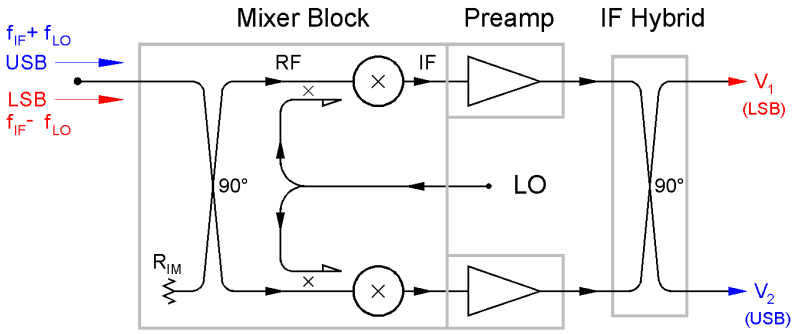

Fig. 1. Sideband-separating mixer configuration used for Band 6.

is possible using a branch-line coupler machined with a small (0.004" diameter) end-mill[1] with long (0.020") working depth. The quadrature hybrid is similar to those described in [7]. The LO power splitter is a matched E-plane T-junction [8]. Cross-guide and broad-wall hole-coupled waveguide directional couplers, commonly used for LO injection, are not suitable for E-plane split block circuits. Instead, the LO couplers use multiple broad-wall coupling probes [9] [10]; the coupling can be changed from 22 dB to 18 dB by using six probes instead of four. The waveguide loads on the LO couplers and the RF hybrid must be compact but well matched at the 4 K operating temperature; their design is described in [11]. Geometrical constraints imposed by the preamplifiers and the magnetic circuit make it desirable for the signal and LO input waveguides to enter the mixer perpendicular to the plane of the split between the halves of the block. This requires a well matched H-plane bend, as described in [8]. Bias to the elemental mixers is provided through the IF preamplifiers as in [12], which eliminates the need for a separate bias connector on the mixer block and also allows the preamps to be mounted closer to the mixer chips. Figure 2 shows one half of the mixer block. Figure 3 shows a front view of the assembled mixer-preamp with the lids removed, and Fig. 4 shows a rear view of the assembly. The magnetic pole pieces, visible in Fig. 3, are made of annealed Consumet magnet iron after the design described in [13] and [14].

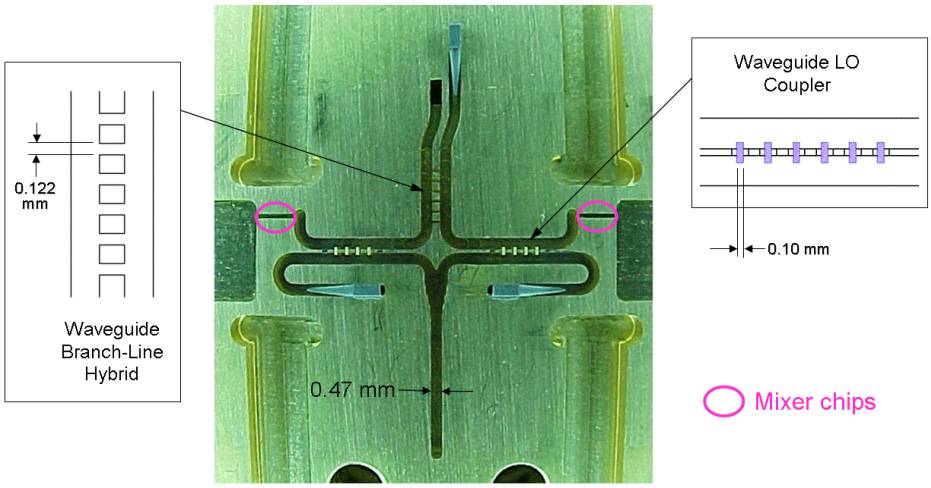

Fig. 2. One half of the mixer block. At the top are the cold image termination [11] and the signal input waveguide which enters from below the page via an H-plane bend [8]. The signal is split by the branch-line hybrid and passes to the mixer chips via the LO couplers [9]. The LO power enters the lower waveguide from above the page via an H-plane bend, is divided by the matched T-junction [8] and is coupled to the mixers through the LO couplers.

[1] Cutting Edge Technologies/Richards Micro-Tool, Inc., 250 Nicks Road, Plymouth, MA 02360.

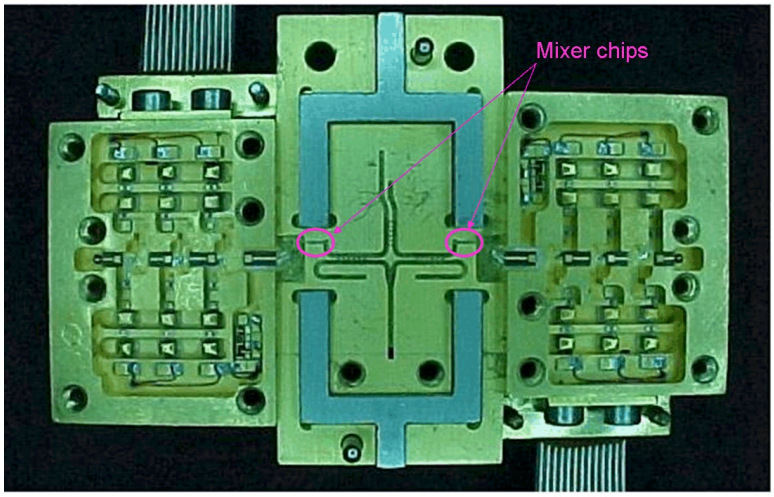

Fig. 3. Mixer-preamp assembly with the mixer and preamp lids removed. The Y-shaped magnetic pole pieces are visible in the upper and lower parts of the mixer block. The IF/DC connection between the mixer chips and the preamplifiers is by a (series) bond wire and (shunt) chip capacitor.

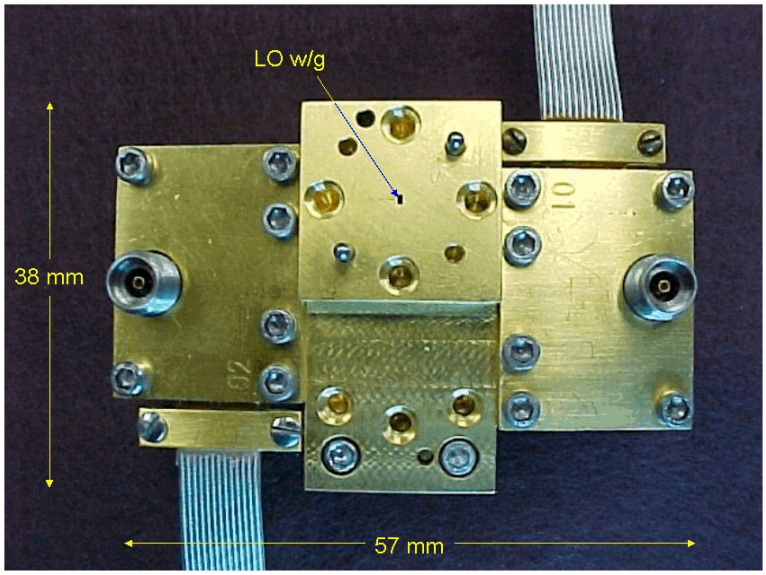

Fig. 4. Mixer-preamp assembly showing the LO input waveguide and the type-K IF connectors.

SIS MIXER DESIGN

The elemental SIS mixers, shown in Fig. 5, are based on our earlier broadband wide-IF design [15]. The main differences are the use of a quasi-lumped element tuning circuit in place of the quarter-wave short-circuit stubs in [15] and a shorter RF choke to reduce parasitic capacitance and inductance in the IF circuit. The mixers are fabricated on fused quartz substrates using the UVA Nb/Al-AlO_x/Nb process [16], [17]. The upper frame of Fig. 5 shows the whole mixer chip with the waveguide coupling probe on the left and a length of suspended stripline leading to a broadband transition to capacitively-loaded coplanar waveguide (CLCPW) [1]. The Nb ground plane has gold contact pads (top and bottom in the upper frame) which contact shoulders in the mixer block. The middle frame in Fig. 5 shows the end of the CLCPW (at the left) connected to a short microstrip line and a short section of CPW. The microstrip and CPW form a shunt-C/series-L impedance transformer. Between the CPW and the series array of four SIS junctions, a pair of

resonators (at the top and bottom of the middle frame) are connected in parallel via short microstrip lines. The resonators each consist of a short short-circuit microstrip stub in parallel with a short open-circuit microstrip stub and closely approximate a parallel LC circuit. The short microstrip lines between the resonators and the main signal path have negligible effect on the circuit. Details of the four-junction array are shown in the lower frame. To the right of the junctions is a section of microstrip, forming a capacitor to ground, followed on the right by a high impedance RF choke circuit consisting of a quarter-wave high impedance CPW and a microstrip capacitor. At the right end of the substrate is the IF/DC bonding pad. The circuit minimizes parasitic inductance and capacitance in the IF circuit in two ways [15]: (i) IF currents are kept out of most of the RF circuit by the low impedance paths through the ground vias at the ends of the inductors in the RF resonators, and (ii) the short, high impedance RF choke has low capacitance as seen at IF.

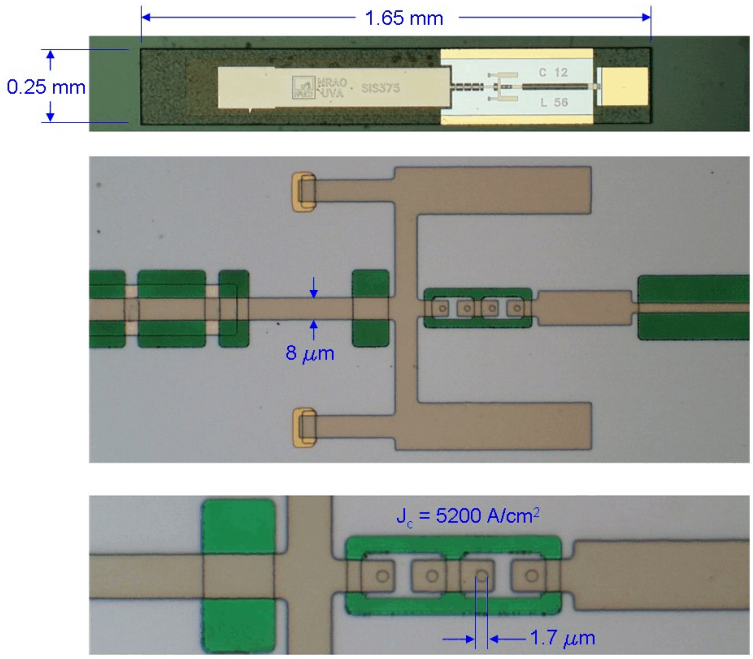

Fig. 5. The SIS mixer substrate.

MIXER-PREAMP MEASUREMENTS

There are two ways to define the image rejection (or sideband ratio) of a sideband-separating receiver. These are illustrated in Fig. 6. In spectral line radio astronomy measurements, the signal of interest is normally in one sideband, so it is desirable to suppress atmospheric noise entering the receiver in the image band. The image rejection R_b, defined in Fig. 6(b), is therefore the relevant quantity. To measure R_b accurately using an RF signal generator would require an accurate knowledge of the relative signal levels entering the receiver when the generator was tuned to the upper and

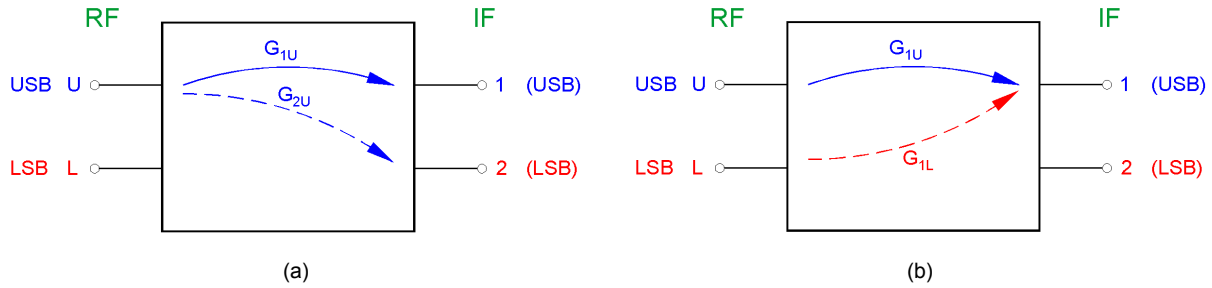

Fig. 6. Two definitions of image rejection. (a) Image rejection $R_a = G_{1U}/G_{2U}$. (b) Image rejection $R_b = G_{1U}/G_{1L}$. In the context of radio astronomy, (b) is the appropriate definition.

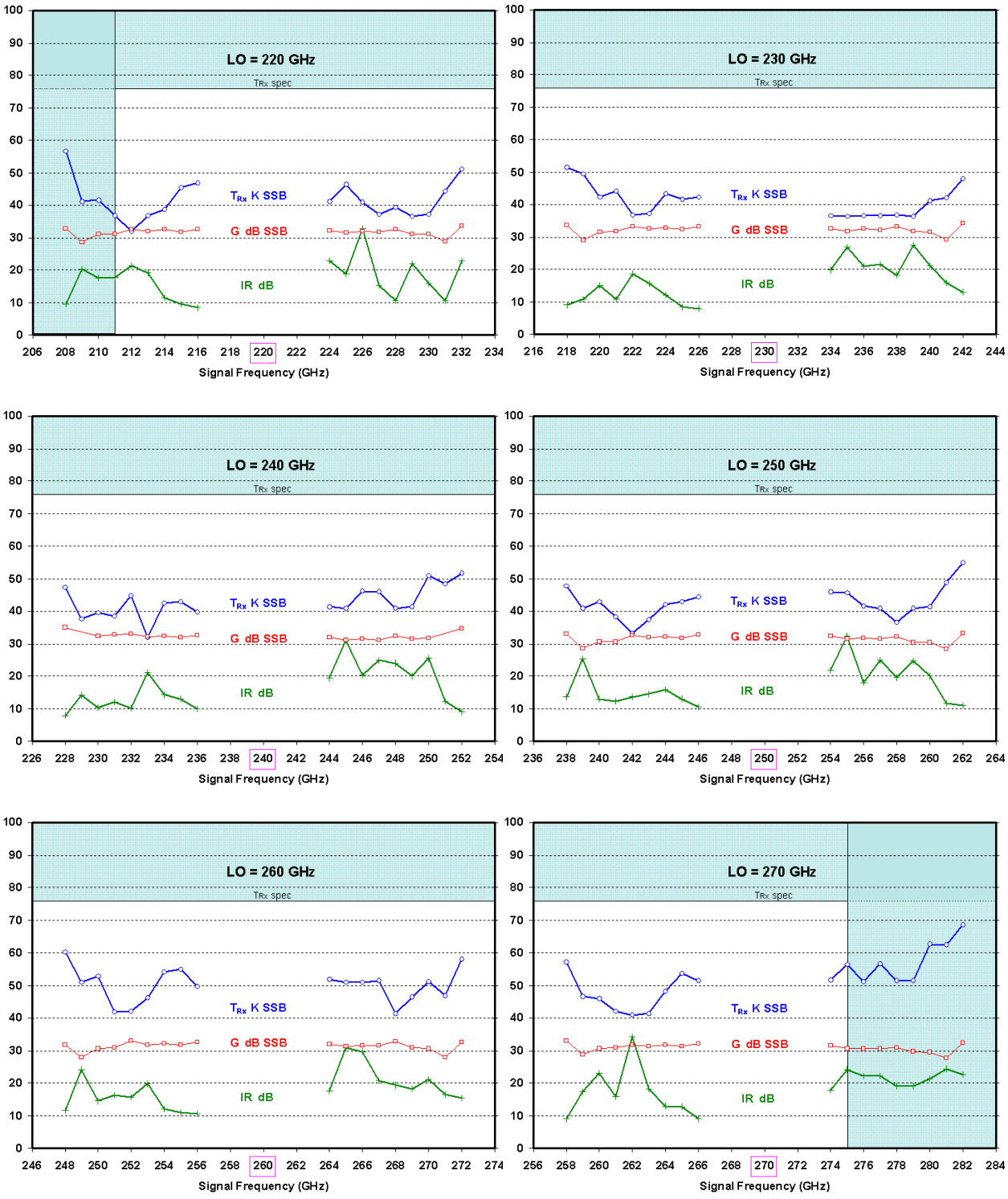

Fig. 7. Measured SSB noise temperature, gain, and image rejection for the complete sideband-separating receiver with the mixer-preamp at 4.2 K. Each frame is for the LO frequency indicated. The upper and lower sideband data are shown as functions of signal frequency over the range corresponding to the 4-12 GHz IF band.

lower sidebands. Relative signal levels are difficult to measure within ± 3 dB at millimeter wavelengths, especially with the high IF (4-12 GHz) for which upper and lower sideband signals can be as much as 24 GHz apart. The need to know the relative signal levels is avoided if additional measurements are made with two well matched spectrally flat noise sources with different noise temperatures — *e.g.*, the hot and cold loads used for measuring the receiver noise temperature. This is described in ALMA Memo 357 [18].

Using the standard procedure for measuring the noise temperature of a millimeter-wave receiver, hot (room temperature) and cold (liquid nitrogen) loads are placed in front of the receiver. This gives the receiver gain and noise temperature at each IF output, uncorrected for image rejection. The quantity $M_{DSB} = (P_{hot} - P_{cold})_{IF\ port\ 1} / (P_{hot} - P_{cold})_{IF\ port\ 2}$ is calculated. Then, a small CW test signal is applied at corresponding upper and lower sideband frequencies $f_{LO} + f_{IF}$ and $f_{LO} - f_{IF}$. The change in IF output powers at IF ports 1 and 2, ΔP_1^{USB}, ΔP_2^{USB}, ΔP_1^{LSB}, and ΔP_2^{LSB}, when the source is switched on is measured. For the CW source in the upper sideband, the quantity $M_U = \Delta P_1^{USB} / \Delta P_2^{USB}$ is calculated, and for the CW source in the lower sideband the quantity $M_L = \Delta P_1^{LSB} / \Delta P_2^{LSB}$ is calculated. The relative CW source powers in the upper and lower sidebands need not be known. The image rejection at each output is then given by [18]

$$R_1 = M_U \cdot \frac{M_L M_{DSB} - 1}{M_U - M_{DSB}} \qquad \text{and} \qquad R_2 = M_L \cdot \frac{M_U - M_{DSB}}{M_L M_{DSB} - 1} \ .$$

The measured noise temperatures and gains are then corrected for the image rejection to give the true single sideband quantities. Figure 7 shows the measured SSB noise temperature, gain, and image rejection for the complete receiver. Each frame is for the LO frequency indicated, and the upper and lower sideband data are shown as functions of signal frequency over the range corresponding to the 4-12 GHz IF band.

DISCUSSION

The SSB receiver noise temperatures were < 50 K (< 4.5hf/k) over most of the band and < 60 K across the whole of Band 6 (211-275 GHz). The image rejection was > 10 dB except at a few isolated frequencies where it was as low as 9 dB — sufficient to give effective suppression of unwanted atmospheric noise in the image band. The mixer-preamp gain was 32 ± 3 dB, and at any given LO frequency the gain variation was ± 2 dB across the 4-12 GHz IF band. All gains and noise temperatures are for the complete receiver and are referred to the receiver input outside the vacuum window. The measurements were made with the mixer-preamp heated to a physical temperature of 4.2 K as required for ALMA testing (the temperature at the cold stage with the heater off was 3.5 K).

ACKNOWLEDGMENTS

The authors thank the following NRAO employees for their essential contributions to this work: F. Johnson, A. Marshall, G. Morris, G. Petencin, and V. Summers.

REFERENCES

[1] A. R. Kerr and S.-K. Pan, "Design of Planar Image-Separating and Balanced SIS Mixers," *Proc. Seventh Int'l. Symp. on Space Terahertz Tech.*, pp. 207-219, 12-14 March 1996. (ALMA Memo 151 at http://www.alma.nrao.edu/memos/.)

[2] A. R. Kerr, S.-K. Pan, and H. G. LeDuc, "An Integrated Sideband Separating SIS Mixer for 200-280 GHz," *Proc. Ninth Int'l. Symp. on Space Terahertz Tech.*, pp. 215-221, 17-19 March 1998. (ALMA Memo 206 at http://www.mma.nrao.edu/memos/.)

[3] S. M. X. Claude, C. T. Cunningham, A. R. Kerr and S.-K. Pan, "Design of a Sideband-Separating Balanced SIS Mixer Based on Waveguide Hybrids," ALMA Memo No. 316, 16 Aug 2000, at http://www.alma.nrao.edu/memos/.

[4] S. M. X. Claude, "Sideband-Separating SIS Mixer for ALMA Band 7 — 275-370 GHz," *Proc. 14th Int'l. Symp. on Space Terahertz Tech.*, 22-24 April 2003.

[5] V. Vassilev, V. Belitsky, C. Risacher, I. Lapkin, A. Pavolotsky and E. Sundin, "A Sideband Separating Mixer for 85–115 GHz," to appear in *IEEE Microwave and Wireless Components Letters*, June 2004.

[6] C. C. Chin, D. Derdall, J. Sebesta, F. Jiang, P. Dindo, G. Rodrigues, D. Bond, S.-K. Pan, A. R. Kerr, E. Lauria, M. Pospieszalski, J. Zhang, T. Cecil, and A. W. Lichtenberger, "A Low Noise 100 GHz Sideband-Separating Receiver," *Int. J. Infrared and Millimeter Waves*, vol. 25, no. 4, pp. 569-600, Apr. 2004.

[7] S. Srikanth and A. R. Kerr, "Waveguide Quadrature Hybrids for ALMA Receivers," ALMA Memo 343, 11 Jan. 2001, http://www.alma.nrao.edu/memos/.

[8] A. R. Kerr, "Elements for E-Plane Split-Block Waveguide Circuits," ALMA Memo 381, 1 July 2001, http://www.alma.nrao.edu/memos/.

[9] A. R. Kerr and N. Horner, "A Split-Block Waveguide Directional Coupler," ALMA Memo 432, 26 Aug. 2002, http://www.alma.nrao.edu/memos/.

[10] A. R. Kerr, N. Horner, and V. Summers, "Fabrication of Small Metal Parts by Electroforming Through a Photomask," NRAO Electronics Div. Tech. Note No. 194, 21 Jan. 2003, http://www.gb.nrao.edu/electronics/edtn/.

[11] A. R. Kerr, H. Moseley, E. Wollack, W. Grammer, G. Reiland, R. Henry, K. P. Stewart, "MF-112 and MF-116: Compact Waveguide Loads and FTS Measurements at Room Temperature and 5 K," ALMA Memo 494, May 2004, http://www.alma.nrao.edu/memos/.

[12] E. F. Lauria, A. R. Kerr, M. W. Pospieszalski, S.-K. Pan, J. E. Effland, and A. W. Lichtenberger, "A 200-300 GHz SIS Mixer- Preamplifier with 8 GHz IF Bandwidth," *2001 IEEE International Microwave Symposium Digest*, pp. 1645-1648, May 2001. (ALMA Memo 378, http://www.alma.nrao.edu/memos/.)

[13] G. A. Ediss and K. Crady, "Measurements of Materials for SIS Mixer Magnetic Circuits," ALMA Memo 438, 14 Nov. 2002, http://www.alma.nrao.edu/memos/.

[14] G. A. Ediss, "Calculations of Magnetic Circuits for SIS Mixers," National Radio Astronomy Observatory, Electronics Division Technical Note No. 190, January 23, 2002, http://www.gb.nrao.edu/electronics/edtn/.

[15] A. R. Kerr, S.-K. Pan, A. W. Lichtenberger and H. H. Huang, "A Tunerless SIS Mixer for 200–280 GHz with Low Output Capacitance and Inductance," *Proceedings of the Ninth International Symposium on Space Terahertz Technology*, pp. 195-203, 17-19 March 1998. (ALMA Memo 205, http://www.alma.nrao.edu/memos/.)

[16] W. Clark, J. Z. Zhang and A. W. Lichtenberger, "Ti Quadlevel Resist Process for the Fabrication of Nb SIS Junctions," *IEEE Trans. Appl. Superconductivity*, vol. 13, pp. 115-118, 2003.

[17] R. B. Bass, L. T. Lichtenberger, and A. W. Lichtenberger, "Effects of Substrate Preparation on the Stress of Nb Thin Films," *IEEE Trans. Appl. Superconductivity*, vol. 13, pp. 3298-3300, 2003.

[18] A. R. Kerr, S.-K. Pan and J. E. Effland, "Sideband Calibration of Millimeter-Wave Receivers," ALMA Memo #357, 27 March 2001, http://www.alma.nrao.edu/memos/.

A Fixed-Tuned SIS Mixer with Ultra-Wide-Band IF and Quantum-Limited Sensitivity for ALMA Band 3 (84-116 GHz) Receivers

S.-K. Pan[1], A. R. Kerr[1], M. W. Pospieszalski[1], E. F. Lauria[1], W. K. Crady[1], N. Horner, Jr.[1], S. Srikanth[1], E. Bryerton[1], K. Saini[1], S. M. X. Claude[2], C. C. Chin[2], P. Dindo[2], G. Rodrigues[2], D. Derdall[2] J. Z. Zhang[3] and A. W. Lichtenberger[3]

[1]National Radio Astronomy Observatory*, Charlottesville, VA 22903
[2]Herzberg Institute of Astrophysics, National Research Council of Canada
[3]Department of Electrical Engineering, University of Virginia, Charlottesville, VA 22904

Abstract - This paper describes an 84-116 GHz Nb/Al-oxide/Nb SIS mixer with multi-octave IF bandwidth and quantum-limited sensitivity. The mixer can be integrated with a three-stage 4-12 GHz HFET preamplifier or fitted with a coaxial connector for operation with an external isolator and IF amplifier. An 84-116 GHz receiver using the mixer with an integrated 4-12 GHz HFET preamplifier has a double sideband noise temperature of 16-20 K (3 to 4 $h\nu/k_B$) over most of the IF band. Analysis of the mixer-preamp using Tucker's theory shows good agreement with measurements. The mixer is easy to build and is being used as a building block for the Band 3 sideband-separating receivers for the Atacama Large Millimeter Array (ALMA)**. With minor modifications, this mixer design can be scaled to other ALMA bands.

I INTRODUCTION

Fixed-tuned SIS heterodyne receivers have been successfully used for radio astronomy in the millimeter and submillimeter-wave bands. These receivers offer near quantum-limited sensitivity but in most cases have an IF bandwidth of only 1 to 2 GHz. Recently, SIS receivers with wider IF bandwidths have been built by integrating an IF preamplifier with the SIS mixer [1,2] or by using a wideband cryogenic isolator and IF amplifier [3]. The mixer-isolator-amplifier scheme may give less variation of receiver noise temperature across the IF band, but the loss of the isolator increases the effective IF noise temperature, and the thermal noise from the internal termination of the isolator is reflected at the output of the mixer and increases the overall receiver noise. In addition, the achievable IF bandwidth of the receiver is limited by the bandwidth of the cryogenic isolator. On the other hand, direct connection of the mixer and preamplifier requires a more detailed knowledge of the mixer and preamplifier in order to design the coupling network. Recent reports [1,2] have demonstrated that this approach is practical for higher frequency mixers (above 200 GHz). It is more difficult to design wide IF bandwidth integrated mixer-preamplifiers for lower frequencies. This is because the IF circuit parasitic capacitance and inductance are, in general, larger in the lower frequency mixer. Also, as pointed out in [4], when the intermediate frequency is a significant fraction of the LO frequency (*i.e.*, low frequency mixers with high IF), quantization of the IF becomes significant and the conversion loss, sideband ratio, noise temperature, and output impedance of the mixer all become IF dependent.

---

*The National Radio Astronomy Observatory is a facility of the National Science Foundation operated under cooperative agreement by Associated Universities, Inc.

**The Atacama Large Millimeter Array (ALMA) is an international astronomy facility. ALMA is an equal partnership between Europe and North America, in cooperation with the Republic of Chile, and is funded in North America by the U.S. National Science Foundation (NSF) in cooperation with the National Research Council of Canada (NRC), and in Europe by the European Southern Observatory (ESO) and Spain. ALMA construction and operations are led on behalf of North America by the National Radio Astronomy Observatory (NRAO), which is managed by Associated Universities, Inc. (AUI), and on behalf of Europe by ESO.

In this paper, we describe the design of an 84-116 GHz Nb/Al-oxide/Nb SIS mixer with multi-octave IF bandwidth and quantum-limited sensitivity. The mixer can either be connected to the IF amplifier through a cold (4.2 K) isolator or integrated directly with an IF preamplifier. Mixer simulations are carried out using a quasi five-frequency approximation [5] to Tucker's theory, and includes the excess shot noise due to Multiple Andreev Reflections (MAR) [6]. Experimental data agree well with simulated results. The mixer is being used as a building block for the ALMA Band 3 receiver cartridges.

II MIXER DESIGN

To fulfill the ALMA science requirements and take full advantage of the exceptionally good site conditions, the Band 3 mixer must meet the following specifications:

(i) RF band at least 86-116 GHz; 84-116 GHz if possible.
(ii) Intermediate frequency: 4-12 GHz.
(iii) Double-sideband (DSB) noise temperature < 17 K, or single-sideband (SSB) noise temperature < 34 K, across 80% of the RF band.
(iv) High saturation power. The large signal gain compression caused by the exchange of RF load temperatures of 77 and 300 K must be less than 5 %.
(vi) A moderately well-matched RF input is desirable to avoid excessive baseline ripples due to vertex reflections from the subreflector.

The SIS mixer design procedure is as follows: A 4-junction series array is chosen to ensure that the mixer has sufficient dynamic range for solar observations [7]. A series array of junctions also allows the use of larger junctions, which gives greater uniformity and improved yield. To achieve wide bandwidth, a value of $\omega R_N C_J \sim 3$ (at 100 GHz) is chosen; this requires a critical current density $J_C = 2{,}500$ A/cm^2. A junction diameter of 2.2 μm is chosen, for which the array normal resistance is 70 ohms and the optimum source impedance is 35 ohms at 100 GHz [8]. Table I gives the junction and circuit parameters for this mixer when using the UVA niobium trilayer process.

Table 1. ALMA Band 3 Device Parameters for UVA Niobium Trilayer Process

J_C	2,500 A/cm^2
Junction size (diameter)	2.2 μm
Normal resistance of the array	70 Ω
Cs	65 fF/μm^2
SiO dielectric constant	4.2
I2 (SiO)	2,850 Å
M3	4,000 Å
Pd/Au	300 Å

The mixer circuit layout is similar to that described in [9], and minimizes the IF circuit parasitic capacitance and inductance. The junction capacitance is tuned out by a series CPW inductor to achieve an RF bandwidth approaching the fundamental limit for broadband matching to a capacitive device [10]. The complete mixer circuit, shown in Figs. 1 and 2, occupies a 4.3 x 0.6 x 0.2 mm quartz substrate. The waveguide is coupled to a 50-ohm suspended substrate stripline which makes a transition to a 50-ohm capacitively-loaded coplanar waveguide (CLCPW). Short sections of microstrip and CPW just to the left of the broadbanding stubs form a parallel-C — series-L impedance transformer. The CPW inductor immediately to the left of the junctions tunes out the junction capacitance. The RF circuit is completed by a capacitor to ground in parallel with the low impedance RF choke.

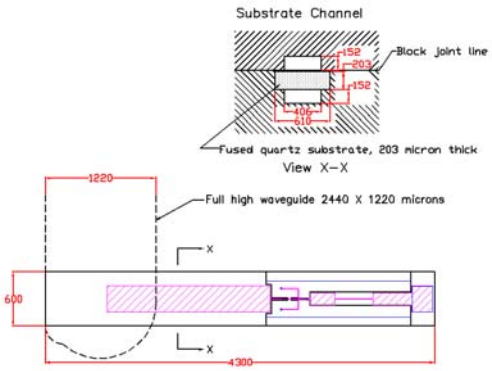

Fig. 1. Diagram of the mixer substrate. At the left is the waveguide probe. All dimensions are in microns.

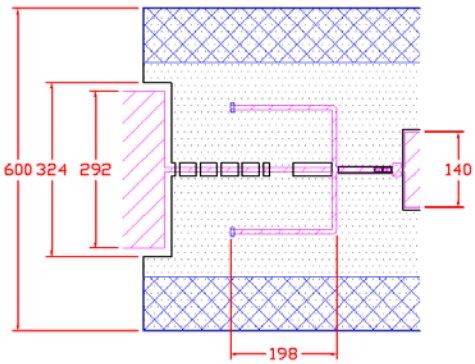

Fig. 2. Details of the RF matching circuit. From left to right: suspended microstrip to CPW transition, CLCPW, microstrip and CPW C-L transformer, the pair of microstrip short-circuit stubs, CPW inductor, four-junction series array, grounding capacitor, and RF choke.

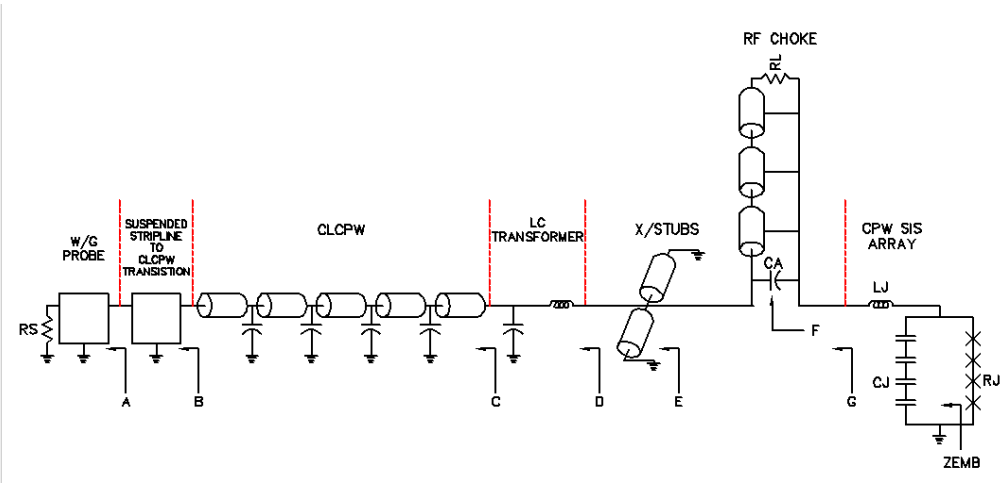

Fig. 3. Schematic circuit of the mixer. (The RF impedance transformation through the circuit is shown, section by section, in Fig. 4.)

The RF circuit of the mixer transforms the input waveguide impedance to the optimum embedding impedance for the array of junctions over the 84 to 116 GHz RF band. The waveguide to suspended stripline transducer was designed using QuickWave [11] FDTD EM simulator as described in [12]. The mixer tuning circuit and RF choke were designed and optimized using Sonnet *em* [13] and MMICAD v. 2 [14]. The RF impedance at successive stages of the circuit is shown on 50-ohm Smith charts in Figs. 4(A)-(G) — the letters A-G correspond to the labeled planes in Fig. 3. Figure 5 shows the embedding impedance seen by the SIS array (including the junction capacitance) on a Smith chart normalized to the 35-ohm optimum source impedance. Since the embedding impedance falls within the $|\rho| = 0.4$ circle over the entire 84-116 GHz band, good broadband mixer performance is expected [10].

Following [9] the mixer circuit is designed to exclude IF signals from most of the RF circuit, thereby reducing the parasitic capacitance and inductance in the IF circuit. One end of the SIS array is connected to DC/IF-ground through the CPW tuning inductor and the pair of short-circuit microstrip stubs, thus isolating the IF signals from the rest of the RF circuit. Figure 6 shows the simulated output impedance of the mixer at the output bonding pad on the mixer substrate for a LO frequency of 100 GHz. With an IF load impedance of 50 ohms, a 4-12 GHz IF band is practical with this design.

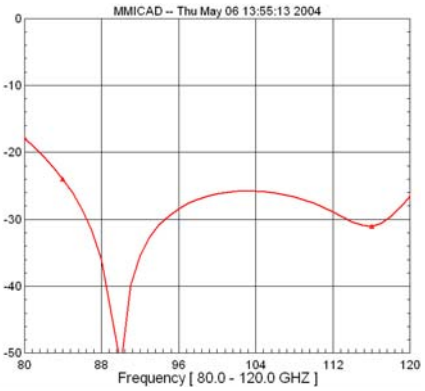

(A)

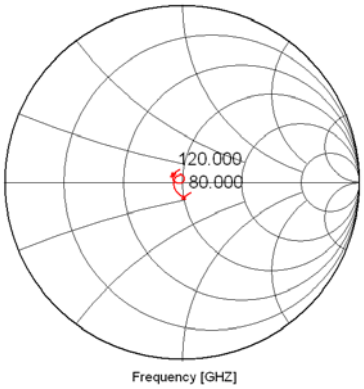

(B)

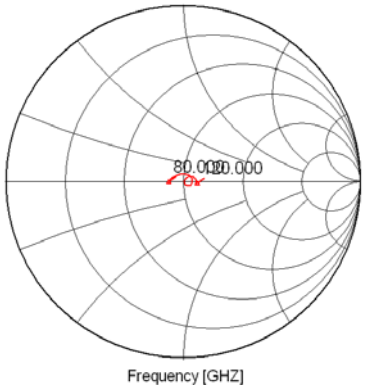

(C)

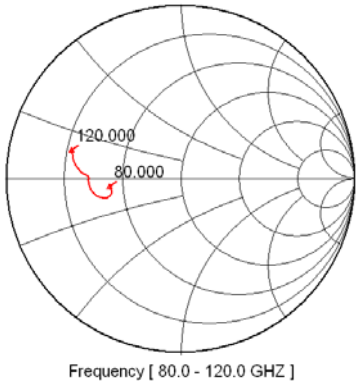

(D)

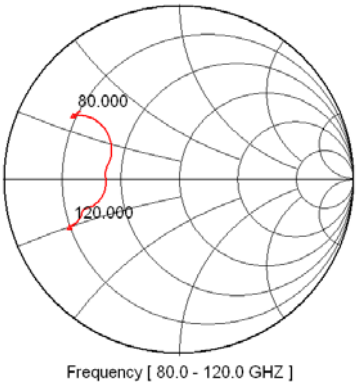

(E)

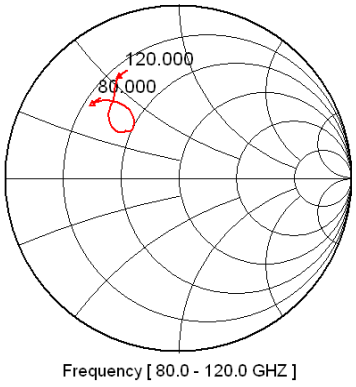

(G)

Fig. 4. RF impedance transformation through matching circuit as seen at each of the labeled planes in Fig. 5: (A) Quickwave simulation of |S11| dB of the waveguide probe. (B) Impedance of the waveguide probe and the suspended microstrip to CPW transition. (C) Including the CLCPW line. (D) Including the LC impedance transformer. (E) Including the two stubs. (G) Including the RF choke. All charts in this figure are normalized to 50 ohms.

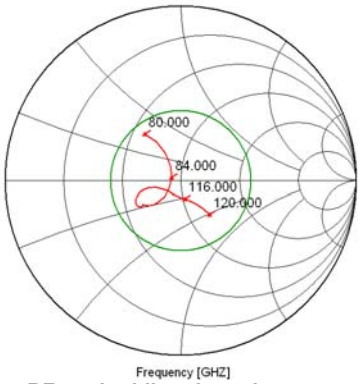

Fig. 5. The RF embedding impedance seen by the 4-junction array. The junction capacitance and the array inductance are taken as part of the embedding circuit. The Smith chart is normalized to 35 ohms, the optimum source impedance. The circle is at |ρ| = 0.4.

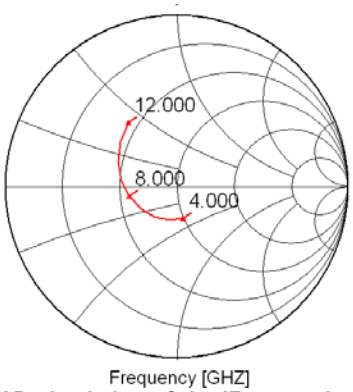

Fig. 6. MMICAD simulation of the IF output impedance of the SIS mixer, measured at the bonding pad on the mixer substrate, at an LO frequency of 100 GHz. Normalized to 50 ohms.

III FABRICATION

The Band 3 mixers were fabricated in the University of Virginia Microfabrication Laboratory [15] on 30–mm diameter amorphous quartz wafers. The system used to deposit the low-stress Nb/Al-oxide/Nb trilayer + Cr/Au films for these devices has been described in [16,17]. For our system, the critical current density is related to the oxygen exposure dose by J_C (kA/cm^2) = 20.5 x E^{-4} (T-sec), and for the present mixers an oxygen exposure dose E = 192 Torr-sec was used. The Nb film stress for these mixers is less than 1 x 10^9 dyne/cm^2. The junctions are fabricated using a modification of our quad-level resist process [18] whereby a fifth layer is added to the resist stack. A thin (10-nm) Nb layer added between the polyimide and Ti layers results in the production of less debris by preventing interaction between the Ti and polyimide layers. The junction insulation is by a gold overlayer process [9,19] which eliminates the need for physical cleaning of the junction counter electrode before depositing the Nb wiring layer. Sublimated SiOx films were used for both dielectric layers; the dielectric constant of these films was measured to be 4.2. All film thicknesses were within 7% of the design values.

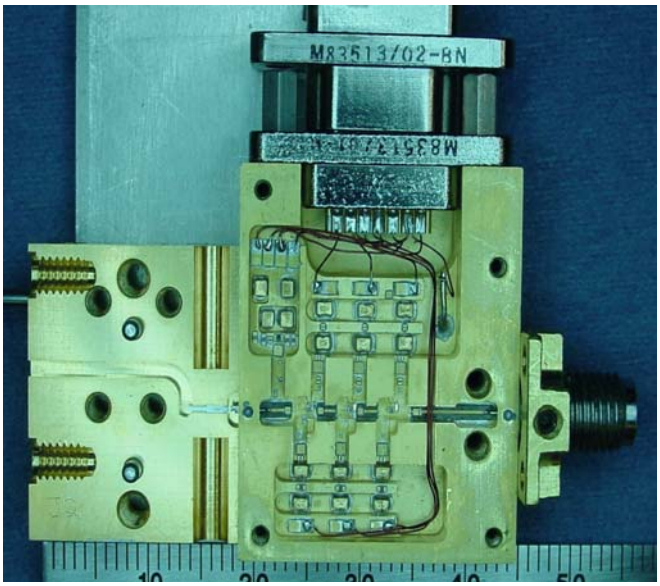

Fig. 7. The integrated mixer-preamplifier assembly with the top half of the mixer and the amplifier cover removed. The mixer is the left module and the 4-12 GHz preamplifier is on the right. The bias-T for the mixer is in the upper left corner of the preamplifier.

The quartz mixer substrate is mounted in an E-plane split waveguide block. The ground connections between substrate and block are made by two gold crush wires, 0.025-mm diameter, on the shoulders of the substrate channel, which are compressed when the block halves are assembled. The mixer block is designed so that it can either accommodate a 2.9-mm connector or be connected directly to an IF preamplifier by a wire bond to the input of the preamplifier. Figure 7 shows a photograph of the integrated mixer-preamplifier assembly with the top half of the mixer block and the amplifier lid removed. The 3-13 GHz, three-stage InP HFET cryogenic low-noise preamplifier was designed according to the general guidelines presented in [20], with the mixer bias circuit inside the preamplifier housing as in [2] to minimize the distance between the mixer and preamplifier. The mixer is connected to the preamplifier by a bond wire 0.001" diameter x 0.020" long. With a 50-ohm source, the preamplifier has a noise temperature of ~ 4.5 K with 35 dB gain over 4-12 GHz when operated at 4.2 K. The power dissipation of the amplifier is 7.7 mW at 4.2 K.

IV EXPERIMENTAL RESULTS

The integrated Band 3 mixer-preamplifier was tested in a liquid helium cooled dewar. Figure 8 shows a block diagram of the receiver and test setup. The incoming RF signal enters the dewar through a plastic film vacuum window supported by polystyrene foam [21], and an expanded PTFE infrared filter [22] attached to the 77 K radiation shield, and is coupled to the mixer by a pyramidal horn at 4.2 K. LO power is injected through a 23 dB branch-line directional coupler, also at 4.2 K. Josephson currents in the junctions were not suppressed by an applied magnetic field during the measurements; this is not necessary for ~ 100 GHz SIS mixer operation.

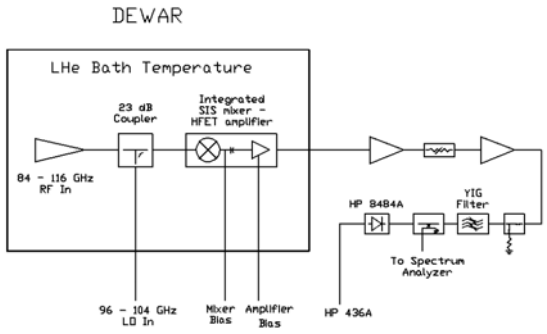

Fig. 8. Block diagram of the receiver and test setup.

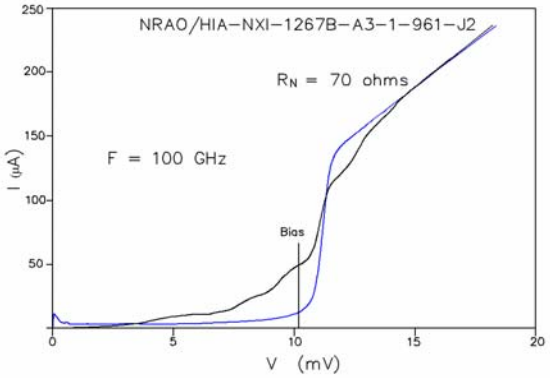

Fig. 9. I(V) curves for the mixer at 4.2 K without LO power (blue) and with LO power (black). The bias voltage is indicated by the vertical line.

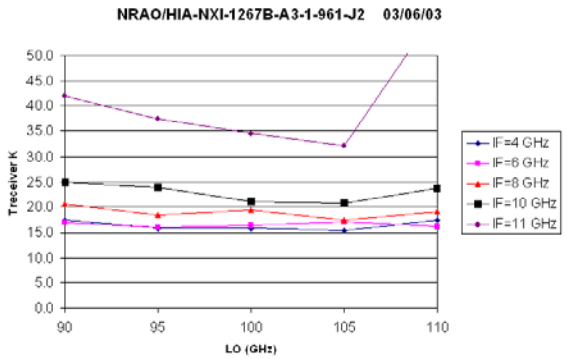

Fig. 10. Double-sideband noise temperature of the receiver, measured outside the receiver dewar, as a function of LO frequency, with intermediate frequency as parameter.

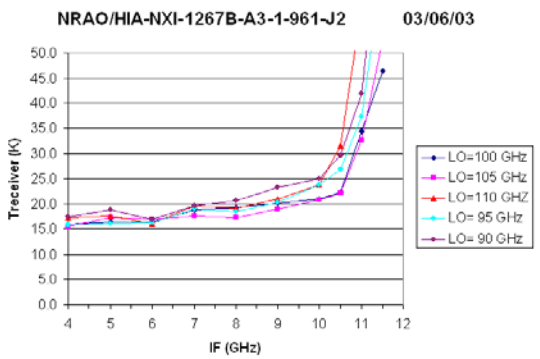

Fig. 11. Double-sideband noise temperature of the receiver, measured outside the receiver dewar, as a function of intermediate frequency, with LO frequency as parameter.

The I(V) curve of the mixer at 4.2 K, with and without 100 GHz LO power applied, is shown in Fig. 9. Figure 10 shows the double sideband (DSB) noise temperature of the receiver, measured in front of the vacuum window of the dewar, as a function of LO frequency, with intermediate frequency as parameter. Figure 11 also shows the DSB noise temperature of the receiver, but as a function of intermediate frequency, with LO frequency as parameter. The noise rise at high IF (~ 10.5 GHz) is partly caused by the non-optimum mixer-amplifier coupling circuit and partly by the amplifier gain roll-off.

V SIMULATION

Extensive simulations were carried out in designing the mixer. The mixer performance was calculated at an LO frequency of 100 GHz using the quasi five-frequency approximation [5] to Tucker's quantum mixer theory, with non-zero IF [4] and includes the excess Multiple Andreev Reflection (MAR) shot noise [6]. In order to compare the simulated results with the measurements, the measured I(V) curve, shown in Fig. 10, was used in the simulation, and the upper and lower sidebands were terminated in the simulated RF embedding impedance shown in Fig. 5. It is further assumed in the mixer simulation that (i) the second harmonic sidebands are terminated by the junction capacitance alone, (ii) the IF load impedance is 50 ohms, and (iii) the pumping parameter $\alpha = 1.2$. The complete receiver performance is calculated assuming an amplifier noise temperature of 4.5 K and an RF input loss of ~0.05 dB, with an added input noise of 3 K. The LO noise contribution injected through the 23 dB LO coupler is estimated to be 1.5 K in each sideband. Figure 12 shows the simulated and measured DSB receiver noise temperatures as functions of the intermediate frequency with the LO at 100 GHz.

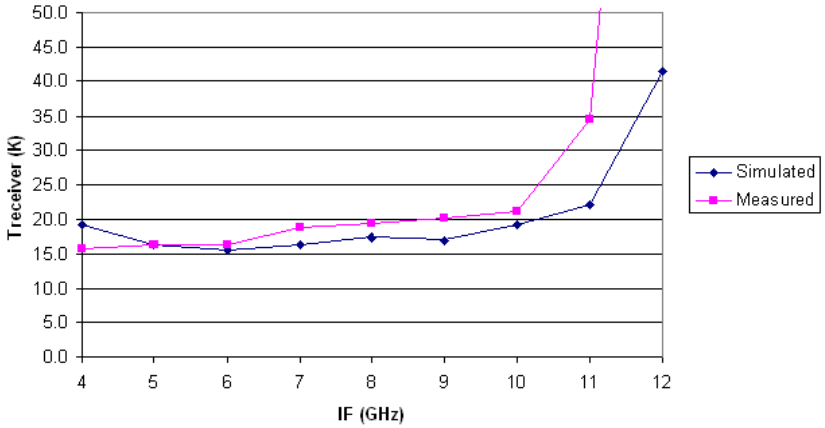

Fig. 12. Simulated (blue) and measured (magenta) DSB receiver noise temperatures, as a function of intermediate frequency, at an LO frequency of 100 GHz.

VI CONCLUSION

An 84-116 GHz SIS mixer with a multi-octave IF bandwidth has been successfully developed without design iterations. The mixer can either be connected to the amplifier and IF isolator via a 2.9-mm connector or integrated directly with an IF preamplifier. With the integrated preamplifier, the DSB receiver noise temperature measured outside the Dewar was 16-20 K (3-4 $h\nu/k_B$) over the 84-116 GHz RF band, for most of the 4-12 GHz IF band. The receiver measurements agree well with the simulated results predicted by Tucker's theory using the actual array I(V) curve and the embedding impedances obtained by simulation during the mixer design. The success of this mixer is due to the quality of the SIS junctions and accurate modeling, which includes careful SIS device modeling and electromagnetic analysis of the passive matching structures.

The mixer is easy to build and is being used as a building block in the ALMA Band 3 sideband-separating receivers [23]. With minor modification, this mixer design can be scaled to other ALMA bands.

ACKNOWLEDGMENTS

The authors thank J. Webber of NRAO and C. Cunningham and K. Yeung of HIA for their support of this work. Special thanks goes to R. Harris, F. Johnson, W. Lakatosh, M. Lambeth and A. Marshall of NRAO for their expert fabrication and assembly of the mixer, preamplifier, and test system.

REFERENCES

[1] S. Padin, D. P. Woody, J. A. Stern, H. G. LeDuc, R. Blundell, C.-E. E. Tong and M. Pospieszalski, "An Integrated SIS Mixer and HEMT IF Amplifier," *IEEE Trans, Microwave Theory Tech,* vol. MTT-44, no. 6, pp. 987-990, June 1996.

[2] E. F. Lauria, A. R. Kerr, M. W. Pospieszalski, S.-K. Pan, J. E. Effland and A. W. Lichtenberger, "A 200-300 GHz SIS Mixer-Preamplifier with 8 GHz IF Bandwidth," *IEEE International Microwave Symposium Digest,* pp. 1645-1648, June 2001.

[3] A. Baryshev, E. Lauria, R. Hesper, T. Zijlstra and W. Wild, "Fixed-Tuned Waveguide 0.6 THz SIS Mixer with Wide Band IF," *Proceedings of the Thirteenth International Symposium on Space Terahertz Technology*, pp. 1-4, March 2002.

[4] S.-K. Pan and A. R. Kerr, "SIS Mixer Analysis with Non-Zero Intermediate Frequencies," *Proceedings of the Seventh International Symposium on Space Terahertz Technology*, pp. 195-206, March 1996.

[5] A. R. Kerr, S.-K. Pan, and S. Withington, "Embedding Impedance Approximations in the Analysis of SIS Mixers," *IEEE Trans. Microwave Theory Tech.*, vol. 41, no. 4, pp. 590-594, April 1993.

[6] P. Dieleman, H. G. Bukkems and T. M. Klapwijk, "Observation of Andreev Reflection Enhanced Shot Noise," *Phys. Rev. Lett.*, 79, pp. 3486-3489, (1997).

[7] A. R. Kerr, "Saturation by Noise and CW Signals in SIS Mixers," *Proc. of the Thirteenth International Symp. on Space Terahertz Tech.*, Harvard University, pp. 11-22, 26-28 March 2002, see ALMA Memo 401 at http://www.alma.nrao.edu/memos/.

[8] Q. Ke and M. J. Feldman, "Optimum Source Conductance for High Frequency Superconducting Quasi-Particle Receivers," *IEEE Trans. Microwave Theory Tech.*, vol. MTT-41, no. 4, pp. 600-604, April 1993.

[9] A. R. Kerr, S.-K. Pan, A. W. Lichtenberger and H. H. Huang, "A Tunerless SIS Mixer for 200-280 GHz With Low Output Capacitance and Inductance," *Proc. of the Ninth International Symp. on Space Terahertz Tech.*, pp. 195-203, 17-19 March 1998. See ALMA Memo 205 at http://www.alma.nrao.edu/memos/html-memos/alma205/memo205.pdf.

[10] A. R. Kerr, "Some Fundamental and Practical Limits on Broadband Matching to Capacitive Device and the Implications for SIS Mixer Design," *IEEE Trans. Microwave Theory Tech.*, vol. MTT-43, no. 1, pp. 2-13, Jan. 1995.

[11] QuickWave FDTD EM simulator, QWED s.c., Zwyciezców 34/2, 03-938 Wasrszawa, Poland.

[12] A. R. Kerr, "Elements for E-Plane Split-Block Waveguide Circuits," ALMA Memo 381 at http://www.alma.nrao.edu/memos/.

[13] Sonnet Software, Inc., Liverpool, NY 13090.

[14] MMICAD v. 2 is a microwave integrated circuit analysis and optimization program, and is a product of Optotek, Ltd.

[15] http://www.ece.virginia.edu/UVML/index.html.

[16] R. B. Bass, L. T. Lichtenberger, and A. W. Lichtenberger, "Effects of Substrate Preparation on the Stress of Nb Thin Films," *IEEE Transactions on Applied Superconductivity*, vol. 13, pp. 3298-3300, 2003.

[17] W. W. Clark, IV, J. M. Beatrice, and A. W. Lichtenberger, "Effects of Geometry and Hardware on the Stress of Nb Thin Films," *IEEE Transactions on Applied Superconductivity*, vol. 7, pp. 3824-3827, 2001.

[18] W. Clark, J. Z. Zhang and A. W. Lichtenberger, "Ti Quadlevel Resist Process for the Fabrication of Nb SIS Junctions," *IEEE Transactions on Applied Superconductivity*, vol. 13, pp. 115-118, 2003.

[19] H. G. LeDuc, B. Bumble, S. R. Cypher, A. J. Judas, and J. A. Stern, "Submicron Area Nb/AlO_x/Nb Tunnel Junctions for Submm Mixer Applications," *Third International Symposium on Space Terahertz Technology*, 1992.

[20] M. W. Pospieszalski and E. J. Wollack, "Ultra-Low-Noise InP Field-Effect Transistor Amplifiers for Radio Astronomy Receivers," *Proc. GaAs 2000 Conference*, Paris, France, pp. 5-8, October 2-3, 2000.

[21] A. R. Kerr, N. J. Bailey, D. E. Boyd and N. Horner, "A Study of Materials for Broadband Millimeter-Wave Quasi-Optical Vacuum Window," NRAO Electronics Division Internal Report No. 292, Aug. 1992. See ALMA Memo 090 at http://www.alma.nrao.edu/memos/.

[22] Gore RA-7957 expanded PTFE.

[23] C. C. Chin, D. Derdall, J. Sebesta, F. Jiang, P. Dindo, G. Rodrigues, D. Bond, S.-K. Pan, A. R. Kerr, E. Lauria, M. Pospieszalski, J. Zhang, T. Cecil and A. Lichtenberger, "A Low Noise 100 GHz Sideband-Separating Receiver," *Int. J. Infrared and Millimeter Waves*, vol. 25, no. 4, p. 569, April, 2004.

Low noise 1.2 THz SIS mixer for Herschel radio observatory

A. Karpov[a], D. Miller[a], F. Rice[a], J. A. Stern[b], B. Bumble[b], H. G. LeDuc[b], J. Zmuidzinas[a]
[a] California Institute of Technology, Pasadena, CA 91125, USA
[b] MDL, Jet Propulsion Laboratory, Pasadena, CA 91109, USA

ABSTRACT

We present a low noise SIS mixer developed for the 1.2 THz band of the heterodyne spectrometer of the Herschel Space Observatory. With the launch of the Herschel SO in 2007, this device will be among the first SIS mixers flown in space. This SIS mixer has a quasi-optical design, with a double slot planar antenna and an extended spherical lens made of pure Si. The SIS junctions are Nb/AlN/NbTiN with a critical current density of about 30 KA/cm2 and with the junction area of a quarter of a micron square. Our mixer circuit uses two SIS junctions biased in parallel. To improve the simultaneous suppression of the Josephson current in each of them, we use diamond-shaped junctions. A low loss Nb/Au micro-strip transmission line is used for the first time in the mixer circuit well above the gap frequency of Nb. The minimum uncorrected Double Sideband receiver noise is 550 K (Y=1.34). The minimum receiver noise corrected for the local oscillator beam splitter and for the cryostat window is 340 K, about 6 hν/k, the lowest value achieved thus far in the THz frequencies range.

Keywords: Low noise receiver, NbTiN, Niobium, SIS receiver, THz detector.

1. INTRODUCTION

In the last decade, SIS heterodyne receivers using Nb/AlOx/Nb junctions and superconducting Nb circuits have become the best practical solution for the ground-based radio astronomy at mm and submm wavelengths [1]. The lowest noise achieved in the submm band is only three times above the quantum limit [2]. This type of ultra low noise receiver is needed to cover the upper part of the atmosphere transparency band accessible to ground-based radio astronomy facilities. One upper frequency limit of SIS receivers is determined by the gap frequency of Nb (f_{Nb}=0.65-0.7 THz); above this frequency the Nb will have losses like a normal metal. Another frequency limit for Nb devices is near 1.7 f_{Nb} =1.0 THz-1.1 THz; above this frequency the bias voltage region where reverse quantum assisted tunneling does not occur is shrinking rapidly, and this bias region is non-existent at $2f_{Nb}$.

The SIS mixers may be also useful at the frequencies over 1 THz for sensitive receivers for ground-based, airborne and space observatories. This motivates research on alternative materials to provide low loss THz circuits as well as new types of SIS junctions with higher gap voltages. Recent progress in thin film NbTiN technology [3] has demonstrated low loss circuits above 0.6-0.7 THz and improved the performance of the SIS mixers with Nb/AlOx/Nb junctions up to 1 THz [4, 5]. Another approach uses a low loss normal metal circuit to build a low noise 1.05 THz SIS mixer [6, 7]. The development of the Nb/AlN/NbTiN SIS junctions along with NbTiN circuits [3] allows a substantial improvement of the SIS mixer operation up to 900 GHz, with the minimum noise within a factor of ten of the quantum limit [8]. The gap voltage of the existing Nb/AlN/NbTiN junctions is about 3.5 mV [3], potentially allowing the extension of SIS mixer operation above 1.4 THz. The goal of our work is to extend the low noise performance of the SIS receivers into the THz band using the NbTiN and Nb technology.

2. APPROACH

Our approach to build a low noise 1.1-1.25 THz SIS mixer uses a Nb/AlN/NbTiN tunnel junction with a high critical current density and a low loss tuning circuit made of normal metal and Nb thin films in a quasi-optical mixer design. In contrast to previous work we do not use a NbTiN ground plane in the mixer circuit, but an epitaxial Nb film. The gap frequency of Nb is about 700 GHz, and at the frequency of 1.2 THz it behaves as a normal metal. The use of Nb ground plane at a frequency well above the gap frequency of Nb is suitable for two different reasons. First, this approach simplifies the integration of the Nb/AlN/NbTiN junction in the mixer circuit. When a normal metal or NbTiN are used in the ground plane of the mixer circuit, a Nb base electrode of the junction must be deposited on

the top of the ground plane film. The etching through the additional layers in the junction structure makes the production process more difficult, and reduces the yield. Our approach improves the reproducibility of the mixers and the junction production yield.

The second reason is related to the possibility of low RF loss in the epitaxial Nb film. The resistivity of the Nb film in our device is 0.28 μOhm cm at 10 K. This is about 20 times improvement, compared with polycrystaline Nb films usually used in the SIS mixers. The 0.28 μOhm cm resistivity is close to the best achieved with the normal metals films made of gold, silver, or aluminum. The estimated loss at 1.2 THz in the circuit using the epitaxial Nb is only 10% larger, compared with estimation for the circuit using an ideal NbTiN film, still super conducting at this frequency. Another advantage of our design is the absence of the quasi-particle trapping, possible when a Nb electrode is embedded in a higher gap superconductor as NbTiN in a circuit with NbTiN ground plane.

3. SIS JUNCTION

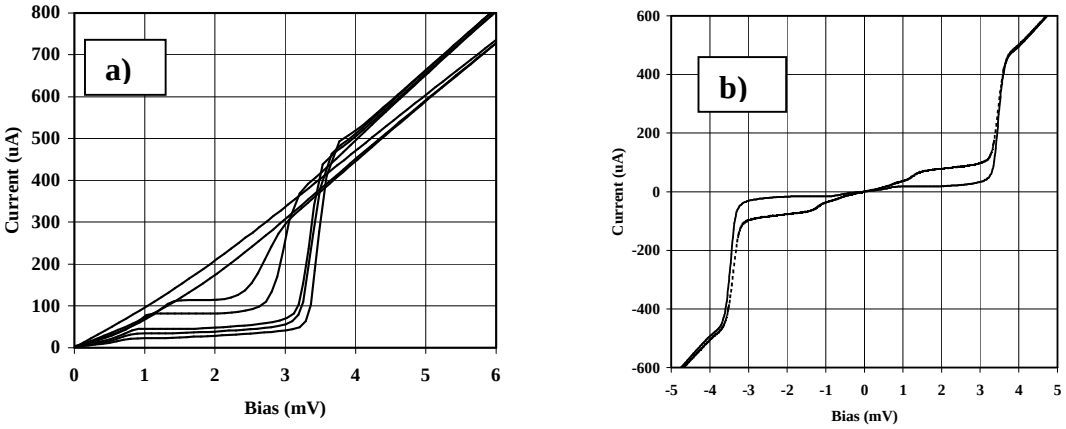

.

Fig. 1. a) Current-Voltage characteristic of the Nb/AlN/NbTiN junction measured at the different temperatures 12 K – 2.5 K. Below the critical temperature of the Nb base electrode (9.2 K), the junction type changes from SIN to SIS. One can see evolution of the sum gap voltage up to 3.5 mV. At 2.5 K the critical Josephson current density is about 30 KA/cm^2
b) A CVC of a Nb/AlN/NbTiN junction with and without 1.13 THz LO signal. We can see a sharp quantum step feature when the LO power is applied. The quantum step width is reduced due to the mutual cancellation of the steps from the positive and negative branches of CVC.

We use Nb/AlN/NbTiN SIS junctions with critical Josephson current densities around 30 kA/cm^2 [3]. This junction is composed of two different superconductors with different critical temperatures. The bottom electrode is made of Nb with critical temperature T_C=9.2 K and the top electrode – of NbTiN. The critical temperature of NbTiN film is around T_C=15 K, however, the layer immediately on top of the barrier is reduced to 13 or 14 K The composition of the junction is well readable over the temperature dependence of the junction current – voltage characteristic (CVC) in Fig. 1 a. The CVC are measured at the temperature 12 – 2.5 K. These temperatures are below T_C=15.6 K of NbTiN and allows to observe the transition over the T_C of Nb. The Josephson current is suppressed with a magnetic field. The upper curve is measured at 12 K, and looks like a typical CVC of an SIN junction. Here the NbTiN top electrode of the junction is already super conducting, and the bottom electrode of Nb is still in a normal state. At the temperature below 9 K a small knee structure starts to form around the NbTiN gap voltage. With the decrease of the temperature to 2.5 K, the differential gap voltage decreases down to 0.7 mV and the junction sum gap voltage rises to 3.5 mV. We can deduce the gap voltage of Nb Δ_{Nb}/e=1.4 mV and the Δ_{NbTiN}/e=2.1 mV. The sum gap voltage of the junction is slightly lower then expected 4-4.4 mV, apparently due to a reduced gap voltage in NbTiN electrode in a vicinity of the AlN barrier. At the temperature of 2.5 K, used in our experiments, this junction has a sub-gap to normal state resistance ratio of about R_{SG}/R_N=12. In other samples we observed a ratio R_{SG}/R_N=30.

The quantum assisted tunneling in a Nb/AlN/NbTiN SIS junction is demonstrated in Fig. 1 b. A sharp quantum step appears at the junction CVC when the local oscillator (LO) radiation is applied at 1.13 THz. The quantum step width

is reduced from hν/e=4.8 mV to hν/e-4Δ/e=2 mV, due to the mutual cancellation of the two quantum steps, at the positive and the negatives branches of CVC.

For a stable operation of an SIS mixer, the Josephson currents have to be suppressed applying a magnetic field B. The full suppression of the Josephson DC current is more difficult in a mixer with two junctions, as the optimum B may differ in the two junctions. Our mixer design has a pair of SIS junctions with a relatively small area of only 0.25 μm^2, and minor non-uniformities make it difficult to simultaneously suppress the critical current in both junctions. For the ease of the Josephson current suppression, we use diamond-like shaped SIS junctions, who have a broad minimum in the DC Josephson current versus magnetic field. Doing so we are less sensitive to non-uniformities between the two SIS junctions in the couple. The DC Josephson current is well suppressed by the magnetic field (fig. 2), down to below 1% at the magnet current of 2 mA. The final result for the operation of the SIS receiver is denoted in Fig. 2 b), where the SIS receiver IF power (upper line) is plotted versus the current in the electrical magnet. There is a clear and broad minimum in the IF power at 5 mA and it is nearly constant when the magnet current is above 10 mA

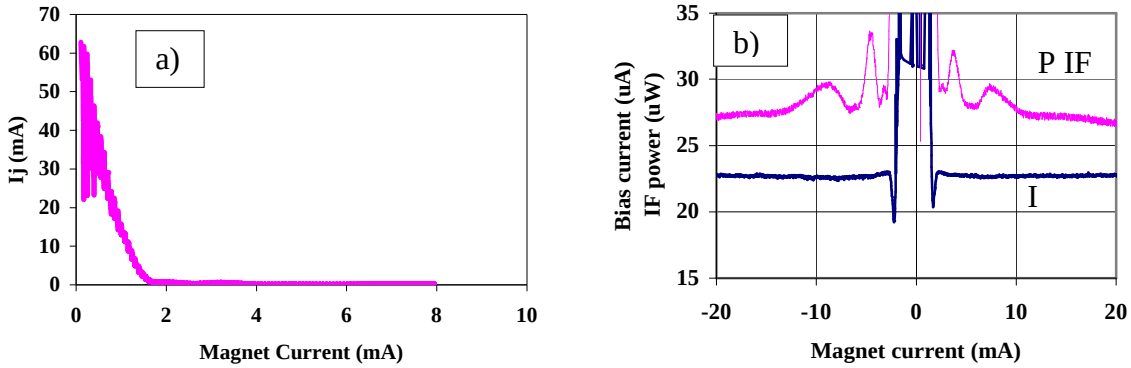

Fig. 2. a) The DC Josephson current of a mixer with a couple of a diamond-shaped SIS junctions reaches the 1% level at about 2 mA magnet current. b) The SIS receiver IF power (upper line) and SIS junction bias current versus magnet current. The 1.13 THz LO power is applied. The IF power is nearly constant when the magnet current is above 10 mA.

Fig. 3 a) The mixer housing contains the mixer optics, IF / DC board and connectors. b) On the final integration of the mixer a magnet and a mixer cover are attached to the mixer housing.

4. SIS MIXER DESIGN

In this work we are using a quasi-optical SIS mixer design, similar to one described in [6]. The SIS junction with a double slot planar antenna is mounted at the silicon extended spherical lens. The SUPERMIX program [9] was used for the circuit design and optimization. We expect about 1.5 dB Ohmic loss in the mixer circuit in the 1.1 THz – 1.25 THz range when using an epitaxial Nb ground plane, a gold wiring layer and SiO insulating layer.

The mixer is built using a modular approach to separate the operations with the parts made with a standard technology and with expensive custom developed parts, such as the SIS junctions. The mixer housing structure is outlined in the left part of the Fig. 3. It is build of the main frame, of the IF / DC bias board, of the Si lens, and of the DC and IF connectors. The mixer main frame is made of the 7075-aluminum alloy and provides the mechanical and thermal interfaces of the SIS mixer. It serves for the precise positioning of the mixer optics. The SIS mixer chip is attached at the center of the back side of the Si lens with an UV solidified glue. The lens is clamped between the retaining ring (front part) and the IF board. The wire bonding is used to connect the mixer chip to the IF board. At the second step of integration we attach the magnet and the mixer cover (Fig 3, b). The mixer total mass is below 75 gr., as required for the use in the space observatory. The final view of the mixer is in the Fig. 4.

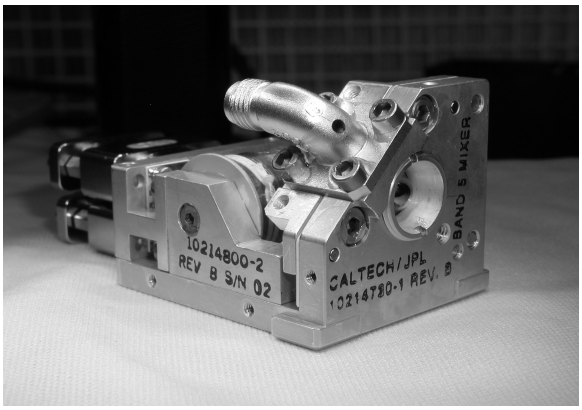

Fig. 4 The assembled 1.2 THz SIS mixer without cover.

We are using the SIS junctions with a relatively low cross sections to reduce the LO power. To suppress the Josephson current this type of junctions requires a magnetic field of the order of B=300-800 G. The electrical magnet serves to suppress the Josephson currents in the SIS junctions. Because there are mass, power and current constraints imposed by the Herschel spacecraft conditions, we needed to use many turns of fine magnet wire. The flight magnet uses 2 kilometers of fine Nb-Ti wire with a diameter of about 25 microns. The magnet provides the magnetic field close to 95% of the theoretical maximum.

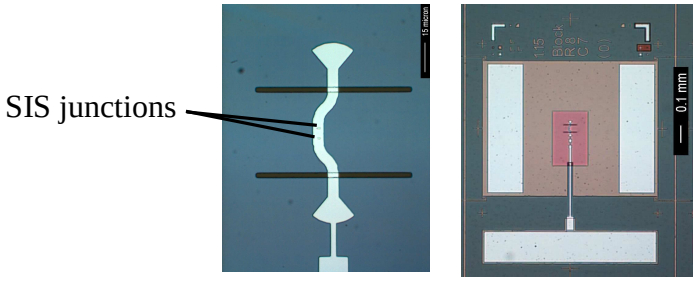

Fig. 5. The SIS mixer chip layout. At the left - the details of the mixer circuit. The two SIS junctions are coupled to a double slot antenna in a circuit with anti parallel excitation.

The mixer chip layout is presented in Fig. 5. In the left part of the Fig. 5 we give the details of the mixer circuit design. The mixer double slot antenna is etched in the epitaxial Nb ground plane. The gold matching circuit (white color in the Fig. 5) covers two SIS junctions 0.24 μm^2 each.

5. EXPERIMENT

The SIS mixer was tested in an Infrared Laboratory HL-3 cryostat. The cryostat vacuum window is in Mylar 12 μm thick. An infrared filter made of Zitex is located at the 77 K stage of the cryostat. The local oscillator power is coupled to the mixer beam using a Mylar beam splitter 5 or 12 micron thick. The intermediate frequency range is 4 GHz – 8 GHz and the IF amplifier noise is about 3 K. The physical temperature at the mixer block was about 2.5 K.

An example of the SIS receiver operation at LO frequency of 1.13 THz is in the Fig. 6. There is a set of the pumped and unpumped SIS mixer current-voltage characteristics and the receiver IF power data. The IF power is measured in the full 4-8 GHz band. The SIS receiver Y factor has a maximum of 1.34. The minimum uncorrected DSB receiver noise is 550 K The receiver noise corrected for the beam splitter and for the cryostat window is close to 340 K, or 6 hν/k.. The loss in a 12.5 μm beam splitter is 16% and the loss in the cryostat window 12%. In the entire 1.1-1.25 THz range the corrected receiver noise is below 600 K (Fig. 7). The receiver operation was stable and reproducible.

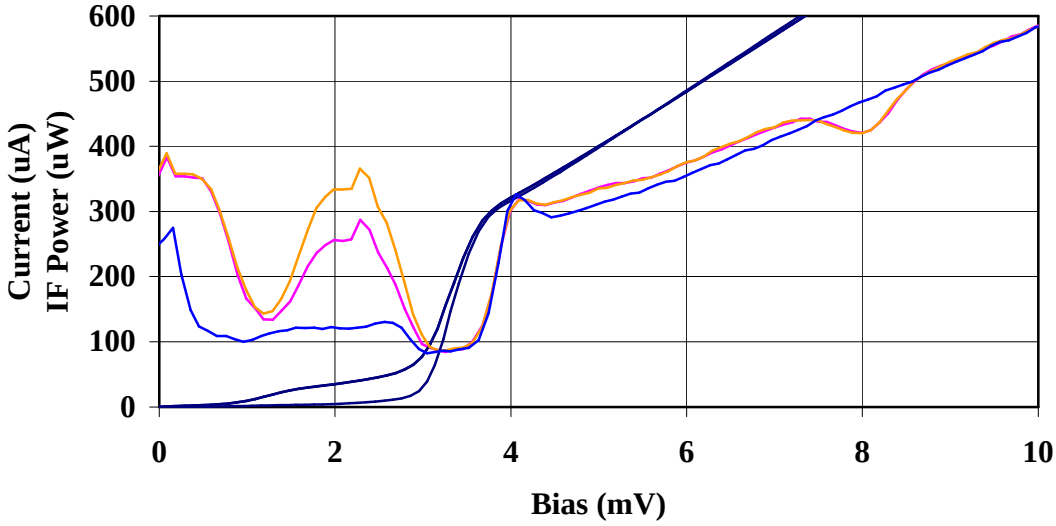

Fig. 6. Receiver operation at 1.13 THz. The receiver IF power is plotted versus bias for the receiver without LO power, with LO power and a 80 K load, and 294 K load (from lower to upper curves). The minimum in IF power at 1.1 mV corresponds to the end of the quantum step from the negative branch of the CVC. The maximum Y factor is 1.34, or 550 K uncorrected receiver noise temperature

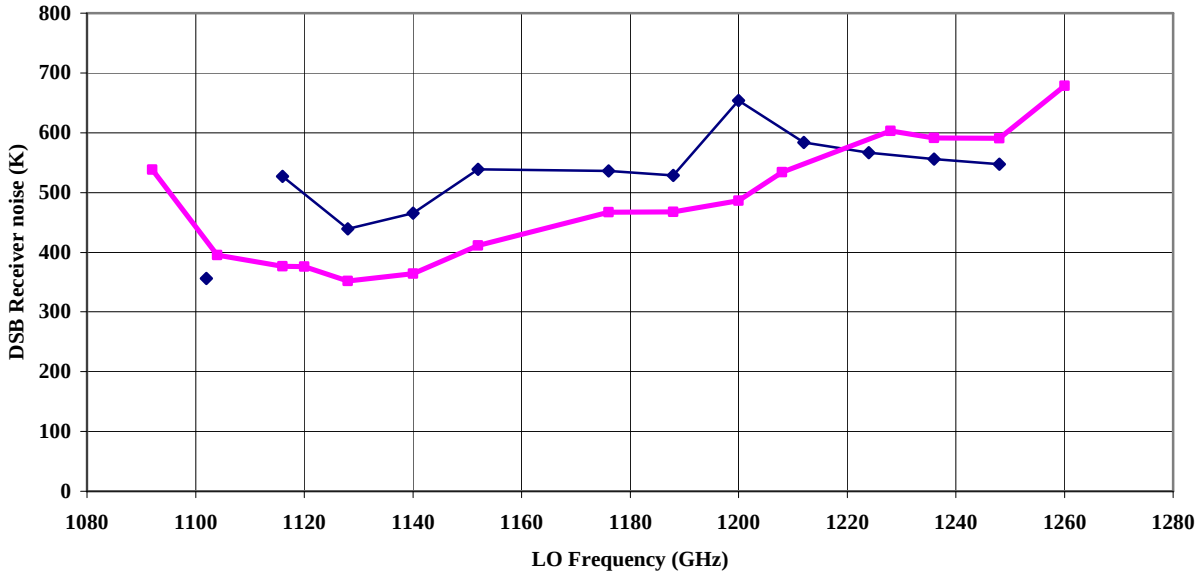

Fig. 7 Performance of the receiver with the two different SIS mixers. The receiver noise is corrected for the beam splitter and for the cryostat window loss. The corrected receiver noise is below 600 K in entire 1.1 – 1.25 THz band. The minimum corrected receiver noise is 340 K, about 6 hν/k.

The mixer beam pattern has been measured using the heterodyne detection of a hot black body (a heater) of a small size. The signal was modulated with a chopper and detected with a lock-in amplifier. The E and H plane measured data are presented in Fig. 8. The measured beam is symmetrical. At the –11 dB level the beam f/d ratio is about 4.

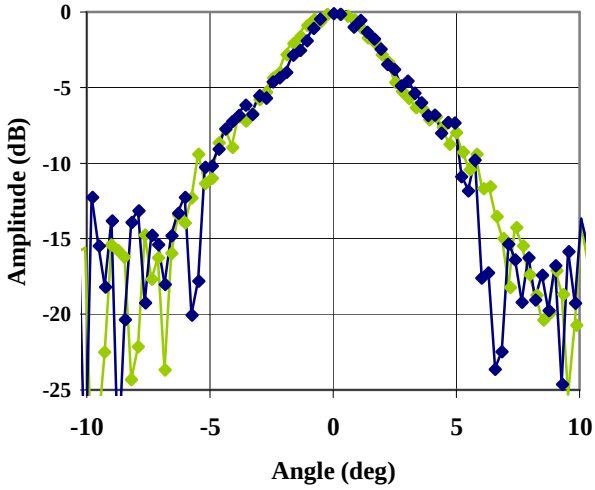

Fig. 8. The beam pattern of the SIS mixer measured at 1.13 THz.

VI. CONCLUSION

We described a low noise SIS mixer developed for the 1.1 – 1.25 THz band of the heterodyne spectrometer of the Herschel Space Observatory. The SIS mixer has a quasi-optical design, with a double slot planar antenna and an extended spherical lens made of pure Si. The SIS junctions are Nb/AlN/NbTiN with the critical current density of 30 KA/cm2 and with junction areas of a quarter of a micron square. The junction areas are diamond shaped to improve the simultaneous suppression of the Josephson current in the two SIS junctions. Another new element of our design is a low loss epi-Nb/Au micro-strip line realized at a frequency well above the gap frequency of Nb. The minimum uncorrected Double Sideband receiver noise is 550 K (Y=1.34). The minimum receiver noise corrected for the local oscillator beam splitter and for the cryostat window is 340 K, about 6 hv/k, the lowest value achieved thus far in the THz frequencies range.

REFERENCES

1. J. E. Carlstrom, J. Zmuidzinas, "Millimeter and submillimeter techniques", in "*Review of radio science 1993 - 1995*", ed. W. R. Stone, Oxford, The Oxford University Press, 1996.
2. A. Karpov, J. Blondel, M. Voss, K. H. Gundlach, "A three photon noise SIS heterodyne receiver at submillimeter wavelength", *IEEE Trans. on Applied Superconductivity*, Vol. 9, No. 2, pp. 4456-4459, 1999
3. B. Bumble, H. G. LeDuc, J. A. Stern, and K. G. Megerian "Fabrication of Nb/Al-Nx/NbTiN Junctions for SIS mixer applications *IEEE Trans. on Applied Superconductivity*, Vol. 11, No. 1, pp. 76-79, 2001.
4. J. W. Kooi, J. A. Stern, G. Chattopady, B. Bumble, and J. Zmuidzinas, "Low-loss NbTiN films for THz mixer tuning circuits", *Int. J. IR and MM Waves*, vol. 19, pp. 373-383, 1998.
5. B. D. Jackson, N. N. Iosad, G. de Lange, A. M. Baryshev, W. M. Laauwen, J.-R. Gao, and T. M. Klapwijk, "NbTiN/SiO_2/Al tuning circuits for low noise 1 THz SIS mixers", *IEEE Trans. on Applied Superconductivity*, Vol. 11, N. 1, pp. 653-656, March 2001.
6. M. Bin, M. G. Gadis, J. Zmuidzinas, T. G. Phillips, and H. G. Leduc, "Low-noise 1 THz niobium superconducting tunnel junction mixer with a normal metal tuning circuit", *Appl. Physics Letters*, vol. 68, pp.1714-1716, 1996.
7. H. van de Stadt *et al.*, "A 1 THz Nb SIS heterodyne mixer with normal metal tuning structure", in *Proc. of the 6th Int. Symp. on Space THz Tech.*, CIT, Pasadena, CA, March 21-23, pp. 66-77, 1995.
8. J. Kawamura, J. Chen, D. Miller, J. Kooi, and J. Zmuidzinas, "Low noise submillimeter wave NbTiN superconducting tunnel junction mixers", *Appl. Physics Letters*, vol. 75, pp. 4013-4015, 1999.
9. J. Ward, F. Rice, G. Chattopadhyay, J. Zmuidzinas, "Supermix", in *Proc. of the 10th Int. Symp. on Space THz Tech.*, March 16-18, pp. 268-280, 1999.

Development of the HIFI band 3 and 4 mixer units

G. de Lange[*a] ,B.D. Jackson[a], M. Eggens[a], H. Golstein[a], M. Jochemsen[a], W.M. Laauwen[a], L. de Jong[a], S. Kikken[a], C. Pieters[a], H. Smit[a], D. Van Nguyen[a], M. Kroug[b], T. Zijlstra[b], T.M. Klapwijk[b]
[a] SRON National Institute for Space Research Postbus 800, 9700 AV Groningen, the Netherlands
[b] Department of Nanoscience, Faculty of Applied Science, Delft University of Technology.
Lorentzweg 1, 2628 CJ Delft, the Netherlands

ABSTRACT

We describe the current status of the HIFI mixer units for Band 3 and Band 4. The mixer units cover the 800-960 GHz and 960-1120 GHz frequency range and have a 4-8 GHz IF frequency band. The major requirements and the design strategy are described. Functional tests of the magnet, the de-flux heater, IF-circuit, and the corrugated horn were performed. Details of the design of the mixer units and the performance status are presented. The DSB receiver noise performance ranges from 210 K at 850 GHz to 430 K at 1075 GHz.

1. INTRODUCTION

The Herschel Space Observatory (launch date 2007) will fly two cameras/medium resolution spectrometers (PACS and SPIRE) and the heterodyne instrument HIFI[1,2,3]. An international consortium led by the PI institute, SRON, is building HIFI[4]. Within HIFI, 7 frequency bands cover the spectral range from 480-1250 GHz (SIS mixers) and 1.41-1.91 THz (HEB mixers). During observations a single frequency band will be operational. SRON is also responsible for the development of the mixer units for band 3 (800-960 GHz) and 4 (960-1120 GHz)[5]. Each of these bands contains two tunerless waveguide mixers to measure both signal polarizations simultaneously. The mixer units are mounted on a 2 K platform in a mixer console that thermally isolates the mixer units from the Focal Plane Unit (10 K ambient temperature). Within the Focal Plane Unit, each of the SIS mixer units is connected to a 4-8 GHz IF chain consisting of two isolators (one at 2K and one at 10 K) a low noise first stage IF amplifier close to the mixer unit, and a common second stage IF box. The second stage IF box provides further amplification, signal equalization, and finally power combining of the 10 separate SIS IF channels into two coax lines that run between the cold and warm (outside the dewar) IF back-end. In the back-end a Wide Band Spectrometer and a High Resolution Spectrometer are available for IF spectral analysis. During observations, the instrument will run in an autonomous mode. Optimal settings of the mixer units (bias voltage, magnet current, LO power) therefore have to be available from look-up tables or simple optimization routines.
The mixer unit development program is currently in the Qualification/Flight Model phase. Extensive environmental testing will prove the flight worthiness of the units. In this paper we present the mixer unit requirements, the current status of the mechanical layout of the mixer unit, the design strategy, the experimental results of its functional behavior, and the performance status.

2. REQUIREMENTS

A summary of the design drivers for the mixer units is given in Table 1. The two main requirements for the instrument are reliability and sensitivity. Note that the challenging goal sensitivities of the mixer units given in Table 1 are the sensitivities of the mixer unit only, without noise contributions from the optics and IF. Constraints on mass, envelope, magnet current, and heater current are mainly determined by the need to minimize the dissipation and heat load on the 2 K and 10 K level. The choice of materials and procedures in the assembly of the unit is driven by the environmental conditions of the instrument during shelf-life (several years), bake-out (80 degrees for 72 hrs), thermal cycling (approximately 25 times), launch (vibration levels, 20 G rms in qualification) and in-orbit operation (>3 years). To allow the use of a magnet current look-up table it is necessary to be able to remove trapped flux from the SIS device and superconducting electrodes. A de-flux heater that can warm up the superconducting layers above their critical temperatures (in Band 3 and 4 this is about 16 K) is therefore implemented.

The potential high levels of electromagnetic fields within the instrument (specified as 2 mV/m in 3-9 GHz range, 2 V/m outside this range) require that the mixer units have proper shielding for EMI, especially in the 4-8 GHz IF range. Protective circuitry to avoid ESD damage during handling and operation is also required.

3. MAIN FEATURES

T_{mix} DSB	Band 3		Band 4	
Frequency	*800 GHz*	*960 GHz*	*960GHz*	*1120 GHz*
Baseline	119 K	158 K	158 K	190 K
Goal	99 K	129 K	129 K	151 K

Sensitivities, excluding contributions from IF chain and optics losses

- Withstand shelf life, bake-out, launch and in-orbit operation (9 years)
- Mass < 75 grams
- Envelope 32x32x45 mm
- IF range 4-8 GHz, ripple < 2dB/1 GHz
- De-flux heater operating at current < 20 mA
- Magnet current < 10 mA for second minimum in the Fraunhofer pattern
- Beam quality
- Optical alignment tolerances (goal): x,y: 42 μm, tilt 0.2°
- ESD protection, EMC shielding
- Bias circuit isolation > 30 dB in IF range

Table 1 Summary of the main requirements of the HIFI band 3 and 4 mixer units

The current design of the mixer unit is shown in Figs. 1, 2, 3, and 5.
The unit consists of four sub-units:
The horn bracket. This bracket holds the horn, the low frequency filtering and ESD circuit board, and the bias connectors (type: Cannon MDM 3401 9 pins). Also on the horn bracket are the mechanical reference planes that define the position of the bracket on the mixer console. The alumina ESD/EMC filtering board is held in place with two aluminum springs to allow for thermal expansion and contraction.
The IF-box. This box houses the magnet, the IF circuit board, an auxiliary PCB, and the IF output connector (Radiall female bulkhead). The alumina IF circuit board is clamped with 2 titanium springs into the housing (Fig. 2).
The device mount. The SIS device and the heater are mounted in the device mount. Attached to the device mount is a leaf spring that is used for alignment purposes (Fig. 3).
The pressure unit. This unit holds a pressure plate that is pushed forward against the device mount. Releasing a stack of washer springs inside the pressure unit applies a controlled pressure to the waveguide/device mount interface (Fig. 3).

The mixer units for band 3 and 4 are identical, except for the dimensions of the waveguide, horn, and horn bracket. The assembly flow is such that all sub-units can be pre-assembled and the SIS-device is inserted only at the final stage of the assembly. In case of a failure or device upgrade, the mixer unit can be re-used without major disassembly or cleaning steps. This allows for a late stage device selection program (as long as the overall HIFI schedule permits) and the possibility to insert the best device available at the time of the delivery for further integration.

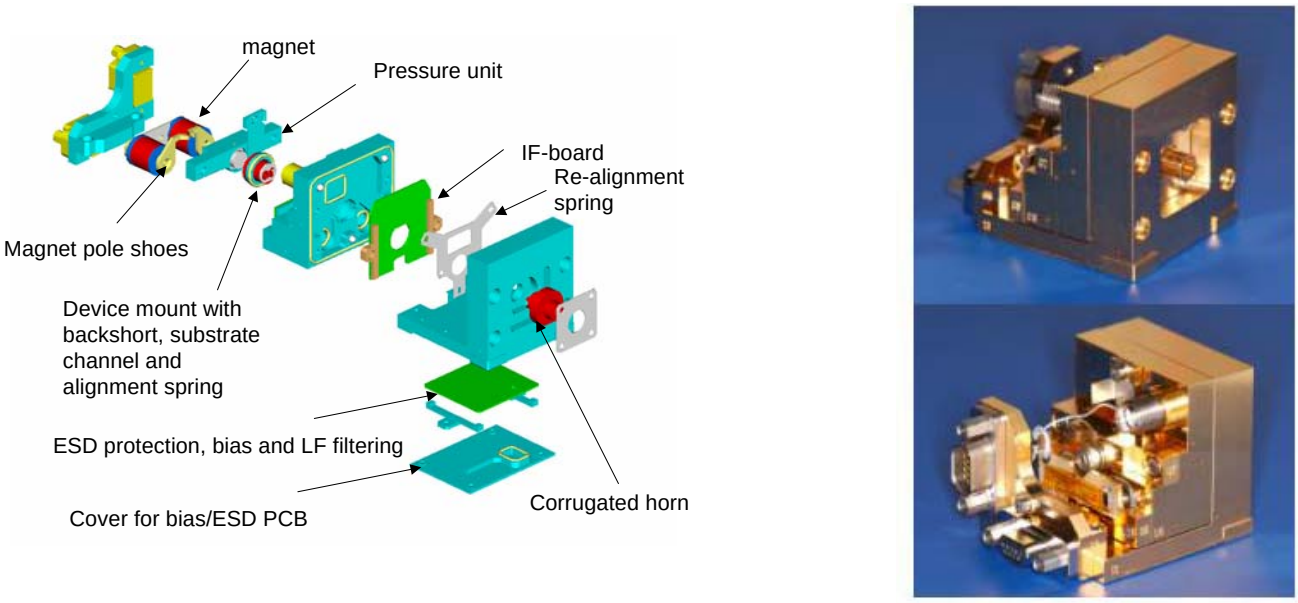

Figure 1 Left: Exploded view of the mixer block. Right: Front and backside view of an assembled mixer unit

4. DESIGN STRATEGY

Based on the specifications given above, the following design strategy was used to come to a final design:

4.1 Optical Alignment

The correct optical alignment of the mixer unit is of major importance for the assembly and operation of HIFI. All optical elements within HIFI, except for the mixer units, are aligned with visible light and therefore are positioned with high accuracy. An incorrect location of the quasi-optical beam of the mixer unit therefore is a potential source of misalignment, especially since there is no means for an in-situ adjustment of the mixer unit alignment (e.g. with moveable mirrors). The alignment can be adjusted with shimming, but it is practically undoable to correct the final instrument cryogenic alignment in this way (7 channels, 14 mixer units). For the waveguide mixers the mechanical position of the corrugated horn envelope is used to determine the position of the quasi-optical beam. It is assumed and actually experimentally shown, that a correct location of the corrugated horn corresponds to a correct location of the quasi-optical beam. Since the alignment is so critical, the design of the band 3 and 4 units is such that after initial mounting of the horn, and verification of its position (with a profiler), it is not necessary to remove the horn from the bracket again in subsequent device mounting assembly steps. The horn and bracket are manufactured with a tight tolerance and measurements with a profiler show that the horn position is indeed within the specifications stated above.

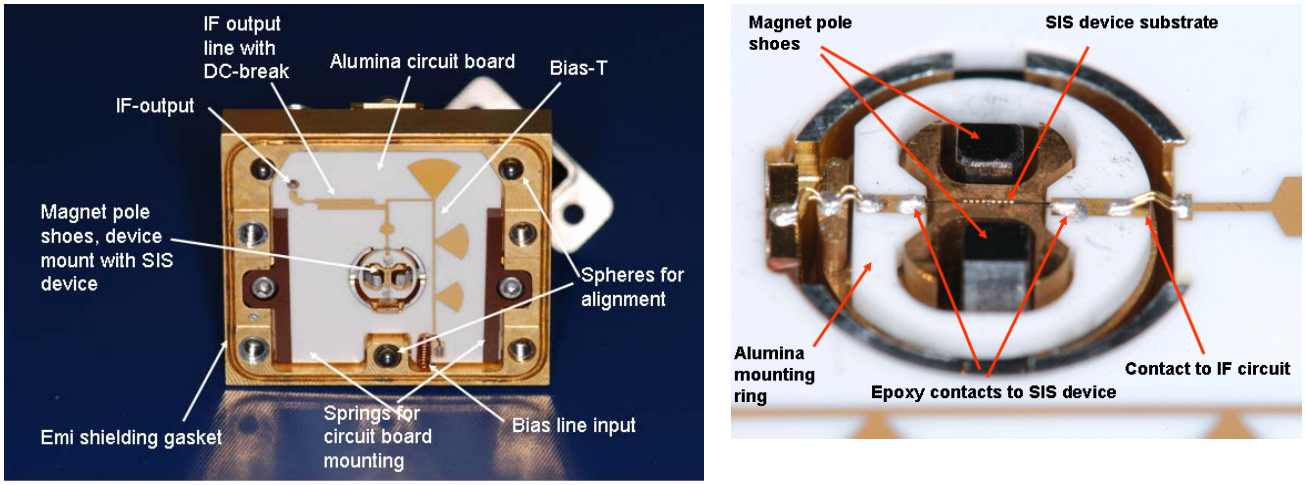

Figure 2 Details of the 'IF-box' of the mixer unit (left) and the device mounting and contacting (right)

4.2 IF and bias circuitry

The IF and bias circuit are fabricated on two alumina substrates. Alumina is chosen because of the compatibility with ceramic components and the heritage from previous cryogenic space missions (ISO-mission). The IF-circuit board is mounted parallel to the SIS device (see Fig. 2), to facilitate electrical contacting and to have a short distance between the device and the IF-circuit (impedance matching). In the initial design of the IF and bias-T board, ceramic capacitors were used for DC-blocking and filtering. In the final design both the bias-T and DC-blocking in the IF output line are implemented with planar circuitry. The planar circuit design improves both the reliability of the board (no components or electrical contacts that can fail) and the manufacturing (no need for electrical contacts).

4.3 Electrical contacts

Important issues for the possible procedures to make electrical contacts (soldering, wire-bonding, conductive epoxy) are the cleanliness, reliability, the thermal compatibility with the part to be mounted (or with parts already mounted) and the reliability against repeated thermal cycling. For example, many conductive epoxies require curing temperatures of 150 °C for several hours, but this temperature would degenerate the SIS device characteristics and also the insulating layer of the superconducting wires of the magnet. Conductive epoxy with a low temperature curing schedule (like Epotek H20 E) is very attractive for SIS device mounting, because it can be used for both the mechanical mounting and the electrical contacting. Furthermore it requires no cleaning step after application (soldering would require removal of excess flux) and it applies no force on the ultra-thin (40 µm) device substrate. Conductive epoxy is also used for some of the other final electrical contacting steps, (e.g. device to IF-circuit, IF-circuit to IF output connector). Connectors, auxiliary circuitry (magnet, heater) and the components on the DC-bias board are all soldered. Flexible connections are used at those electrical contacts that are subject to thermal stress (see Figs. 2 and 5). For example the SMA IF output pin is not mounted directly to the IF-board, but via two gold wires.

4.4 Device mounting

In our laboratory mixer designs at lower frequencies, SIS devices are mounted into the device mount substrate channel with (super-)glue, and electrical contact is made via silver paint or wire bonding on the device substrate. Direct bonding of 17 µm wires to the 40 µm contact pads on the thin (25-35 µm) substrates turned out to be a major cause of failure in the assembly procedure of the HIFI mixer units. We therefore developed an alternative mounting method in which the electrical contact to the device is made via silver epoxy (Epotek H20E). The device is mounted with the silver epoxy on a gold patterned alumina carrier. The carrier is then mounted with Scotchweld 2216 to the device mount (Fig. 3). A potential problem of this mounting method is breakage of the substrate, if it would touch the substrate channel bottom. It actually turns out to be advantageous to make use of a suspended substrate design in which the substrate is suspended about 15 µm above the channel bottom. Both Epotek H20 and Scotchweld 2216 have a flight record. Multiple gold wires are used for the electrical contact from the contact pads on the carrier to IF-board circuitry (see Fig 2).

During the test phase we make use of silver paint for the electrical contacting of the device. After noise performance testing the device is easily removed from the device mount and restored. This gives us the opportunity to characterize the device performance in a test unit and use the flight model mixer units only for the final assembly.

Figure 3 Left: Alumina device mounting ring with a SIS device mounted with two dots of silver epoxy.
Middle: device mount with alignment spring attached. The heater is mounted in the backside of the device mount.
Right: The pressure unit that pushes the device mount against the horn. The bullet-like part is pushed forward with an (internal) stack of spring washers.

5 PERFORMANCE

5.1 Corrugated horn

The mixer unit uses a corrugated horn antenna, tapering down to a reduced height waveguide of 300x75 μm (Band 3) or 240x60 μm (Band 4). The horn design is equal for all bands (except for a scaling factor). For the band 3 horn (with a center frequency of 880 GHz) the aperture radius is 1.6 mm and the horn slant length is 9.8 mm. At 880 GHz the far field divergence angle is 8.46 degrees and the waist size is 0.729 mm. Band 3 and 4 horns are fabricated at RPG and Thomas Keating. Results of amplitude measurements on an RPG horn at 890 GHz and a Thomas Keating Horn at 1030 GHz are shown in Fig. 4. The experiments show that both manufacturers can fabricate horns with a well predicted and symmetric beam pattern at these high frequencies.

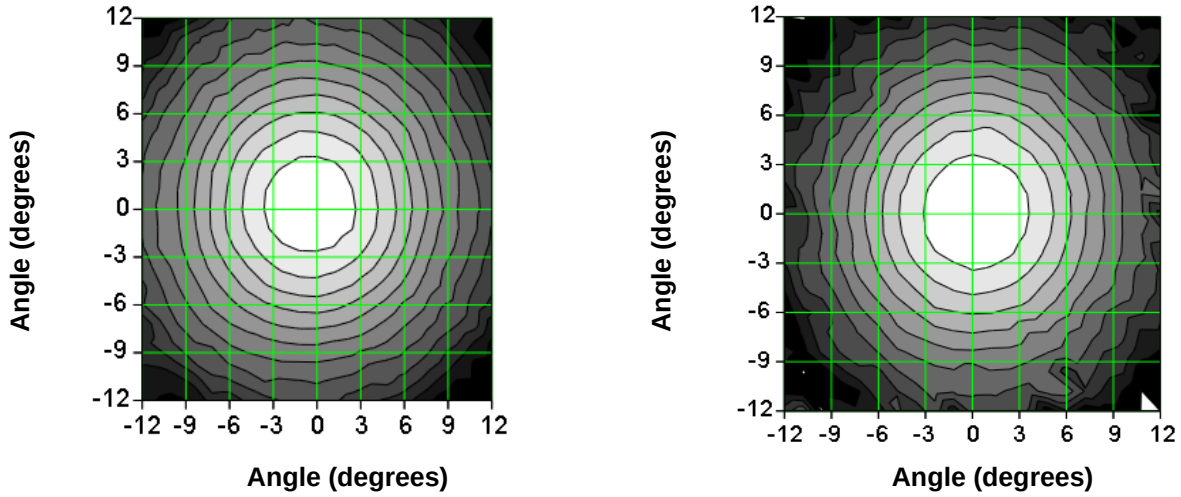

Figure 4 Measured far field beam patterns for a RPG horn at 893 GHz (left) and a Thomas Keating horn at 1030 GHz (right). Contours are at 2 dB spacing.

5.2 IF circuit

The mixer units have an internal 4-8 GHz bias-T and an IF output circuit with a DC-break. The IF-box with the device mount and the 625 μm thick alumina board with IF circuitry are shown in Fig. 2. The IF circuit contains a bias-T with three radial stubs and an IF-output coupling line with a planar 4-8 GHz band-pass filter. The co-planar 4-8 GHz band-pass filter provides the DC-break. It is based on the work of Zhu et al.[6] and was developed at SRON with help of HFSS simulations by J. Kooi. The advantage of this filter in comparison with a traditional DC-blocking capacitor is the reliability (no components to be mounted) and the low loss. Results of noise measurements within the IF band are shown in Fig. 5. The figure shows results from mixer units in the development phase, and the final result as it will be in the Flight Model mixer units. It was found that a proper ground return path of the IF signals was far more critical than originally anticipated. For reasons of cleanliness, flexibility and ease of assembly, the IF board is mounted with spring clamps in the housing. EMI gaskets underneath the board are used to achieve a proper ground contact between the housing and the board (Fig. 5). Traditionally one would use epoxy or a conductive sticky film for proper grounding of the IF board in its housing, but in the event of a failure this would make re-use of the mixer unit impossible. The most critical part of the ground return path is at the interface between the moveable device mount and the IF-box housing. Because of the in-situ alignment of the device mount, there has to be a gap between the IF-housing and the device mount, but at the same time this gap has to provide a proper ground in the 4-8 GHz frequency range and sufficient EMI shielding. A ring with two EMI gaskets is used to provide both the mechanical flexibility and the electrical continuity. After several experimental iterations it was found that the compression of the EMI gaskets was insufficient to provide a proper ground return path, especially in the 7-8 GHz range. Adjustment of the gasket compression solved the problem.

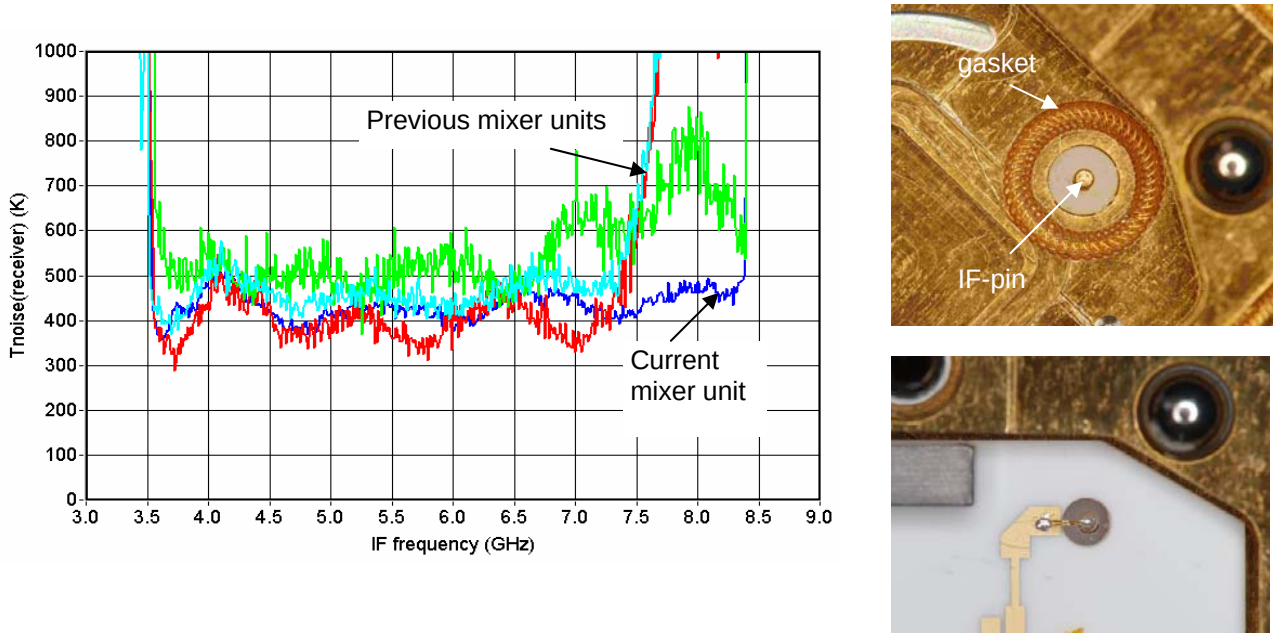

Figure 5. Left: Noise temperature within the 4-8 GHz IF band, of various mixer unit models. The increase in noise temperature in the 7-8 GHz range with the early models is due to an increase in resistance of EMI gaskets at these frequencies. Upper right: One of the EMI gaskets used for grounding the of the IF board to the metal housing. The picture is a top view of the IF-output connector pin. Lower right: top view of the IF output connector after mounting of the IF-board.

5.3 Sensitivity status

The heterodyne elements in the mixer units are $Nb/Al_2O_3/Nb$ SIS twin junctions with Al and NbTiN top and bottom electrodes, respectively. The devices are fabricated at DIMES[7,8]. For band 4 we use NbTiN films grown at the Jet Propulsion Laboratory by J. Stern. Some typical receiver DSB Noise Temperatures versus RF frequency of band 3 and 4 mixer units are shown in Fig. 6. The figure shows noise measurements performed at 2 K with a thin 14 μm thick Mylar beam splitter. The noise temperature is measured with the full 4-8 GHz IF-band. The overall receiver noise temperature

ranges from 240 to 450 K DSB. The receiver noise temperature in HIFI will be considerable lower (approximately 100-150 K) than our laboratory receiver, since HIFI will operate with a 15 K cooled diplexer and without vacuum windows or heat filters in the signal path. Data at the lower end of band 3 and the upper end of band 4 are missing because of lack of LO-power. The direct detection response of the mixer units is shown in Fig. 7. The centre frequency and bandwidth of the units corresponds well with the band 3 and 4 requirements.

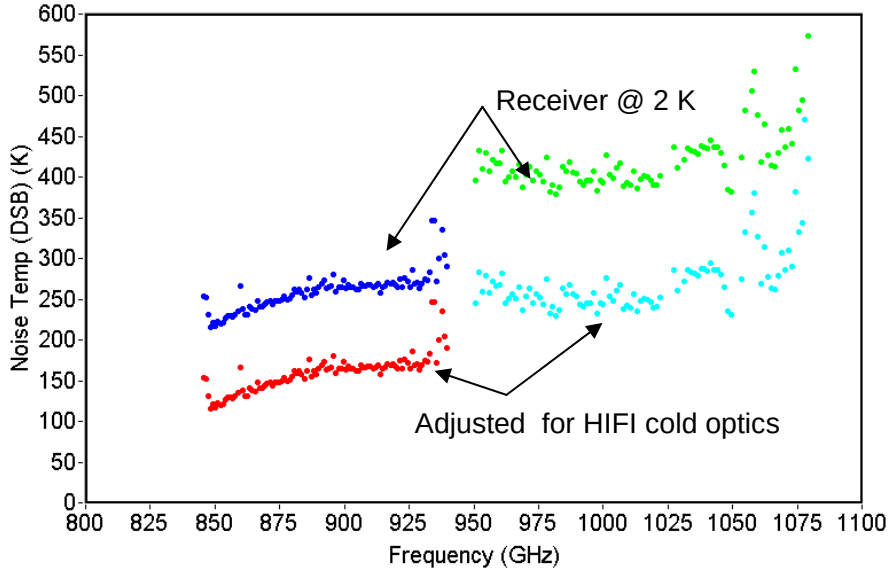

Figure 6 DSB receiver noise temperatures of band 3 and band 4 mixer units, measured with a 14 μm beam splitter (85 % transmission, 300 K ambient temperature) and at 2 K He bath temperature. Also shown are the corrected noise temperatures as expected in the HIFI environment. The noise contribution of the HIFI optics will be very low because of the high transmission of the Martin-Pupplet diplexer and the low ambient temperature (15 K) of the optics.

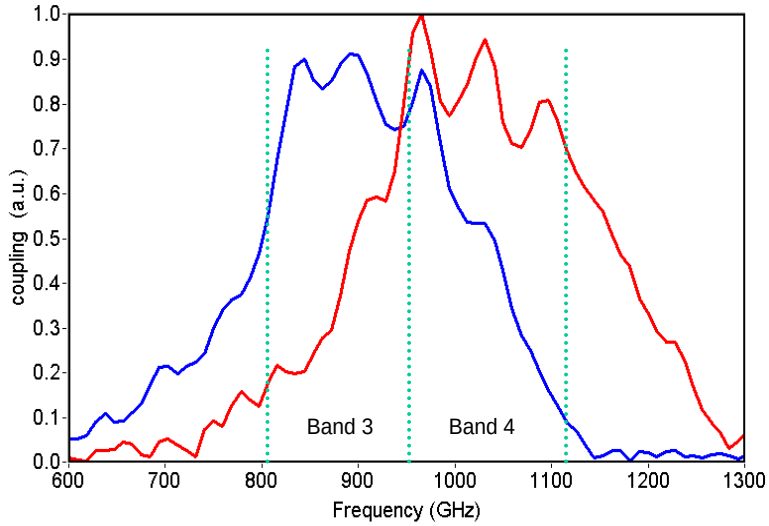

Figure 7 Fourier Transform Spectrometer measurements of the band 3 and 4 mixer units shown in Fig. 6. Note that 70 GHz ripple in the measurement is due to an artifact in the FTS set-up.

6 SUMMARY

We have presented the status (in July 2004) of the band 3 and 4 mixer units for HIFI. The mixer unit is complying with the mechanical, electrical and optical interface requirements. The mixer magnet, the de-flux heater, and the novel IF circuit board are operating as required. Measurements on the beam quality of the corrugated horns, the RF sensitivities and the mixer unit bandwidth are very promising.

ACKNOWLEDGEMENT

We would like to thank Jeff Stern from JPL for providing the NbTiN films of the band 4 mixer unit and Wim Kooi from Caltech for the detailed simulation and discussions on the IF and RF design.

REFERENCES

* gert@sron.rug.nl; phone (31) 50-3634051

1. T. de Graauw, F. P. Helmich, "Herschel-HIFI: The Heterodyne Instrument for the Far-Infrared", in *The Promise of the Herschel Space Observatory*, edited by G. L. Pilbratt et al., ESA SP-460, pp. 45-51, 2001.
2. B. D. Jackson, K. J. Wildeman, N. D. Whyborn on behalf of the HIFI Focal Plane Consortium, "The HIFI Focal Plane Unit", *Proc. 13th International Symposium on Space Terahertz Technology*, pp. 339-348, 26-28 March 2002, Harvard University, Cambridge, Massachusetts, USA.
3. Web site at *: http://spdext.estec.esa.nl/home/herschel/*
4. Web site at: *http://www.sron.nl/divisions/lea/hifi/*
5. G. de Lange , B.D. Jackson, M. Eggens, H. Golstein, W.M. Laauwen, L. de Jong, S. Kikken, C. Pieters H. Smit, D. Van Nguyen,, "Development of the HIFI band 3 and 4 mixer units", *Proc. 13th International Symposium on Space Terahertz Technology*, pp. 359-368, 26-28 March 2002, Harvard University, Cambridge, Massachusetts, USA.
6. L. Zhu, H. Bu, K. Wu, "Aperture compensation technique for innovative design of ultra-braodband microstrip bandpass filter ", *IEEE Inter. Microwave Symp. MTT-S*, 2000, Boston, pp 315-318.
7. B.D. Jackson, G. de Lange, W.M. Laauwen, L. de Jong, T. Zijlstra, N.N. Iosad, and T.M. Klapwijk, "THz SIS mixer development for HIFI", *Proc. 13th International Symposium on Space Terahertz Technology*, pp. 561-570, 26-28 March 2002, Harvard University, Cambridge, Massachusetts, USA.
8. B.D. Jackson, A.M. Baryshev, G. de Lange, S.V. Shitov, J.-R. Gao, N.N. Iosad, and T.M. Klapwijk, "Low-noise 1 THz superconductor-insulator-superconductor mixer incorporating a NbTiN/SiO_2/Al tuning circuit", *Appl. Phys. Lett.*, vol. 79, no. 3, pp. 436-438, 16 July 2001.

Waveguide-type all-NbN SIS mixers on MgO substrates

Masanori Takeda[1], Yoshinori Uzawa[1], Akira Kawakami[1], Zhen Wang[1], and Takashi Noguchi[2]
[1]Kansai Advanced Research Center, National Institute of Information and Communications Technology
[2]Nobeyama Radio Observatory, National Astronomical Observatory of Japan
E-mail: takeda@po.nict.go.jp

Abstract

We present the first experimental results on waveguide-type all-NbN SIS receivers fabricated on MgO substrates designed in a frequency range from 780 to 960 GHz. The receiver has a resonant distributed SIS junction one wavelength long at 870 GHz as the tuning circuit and a diagonal feed horn. The mixer chip was fabricated with accuracies of less than 10 μm in width and +/- 5 μm in thickness by optimizing the cutting and polishing conditions for MgO substrates and was successfully mounted in a waveguide-mixer block. Using a conventional Y-factor method for receiver-noise measurement, a minimum DSB receiver-noise temperature of 700 K was obtained at an LO frequency of 770 GHz. The contribution to noise made by the input system was dominant in receiver noise and the input-noise temperature was more than 300 K over the measured band.

1. Introduction

The Atacama Large Millimeter Array (ALMA) requires superconductor-insulator-superconductor (SIS) receivers with ultra-low noise performance [1]. ALMA receivers cover a frequency range from 30 to 960 GHz, which is divided into ten bands. The highest (band 10) is in a frequency range from 787 to 960 GHz. Although Nb-based SIS receivers have achieved excellent performance below a gap frequency of 700 GHz [2, 3], it is well known that receiver-noise temperature rapidly degrades above the gap frequency. The major loss component is in Nb microstrips. Therefore, band-10 receivers require their microstrips to be fabricated using high-gap materials such as NbN and NbTiN. Additionally, there is a real need for SIS receivers to involve waveguide coupling techniques in the ALMA.

Single-crystal NbN films fabricated on MgO substrates have a high superconducting critical temperature of 16.5 K, which corresponds to a gap frequency of about 1.4 THz. Also, the tunnel junctions are able to be fabricated using MgO or AlN tunnel barriers [4, 5]. This indicates that NbN-based SIS receivers offer the possibility of low-noise operation to at least 1.4 THz. Actually, good mixing properties have been obtained in SIS receivers with quasi-optical coupling techniques [6, 7]. Following these encouraging results, we have developed waveguide-type all-NbN SIS mixers fabricated on MgO substrates for the band-10 ALMA.

However, the waveguide-mixer chip must be reduced in size because MgO has a relatively large dielectric constant ($\varepsilon \sim 9.6$), and it is extremely difficult to cut and polish the MgO substrate compared to its quartz and silicon counterparts because MgO has strong cleavage properties. Therefore, some technical solutions are needed for the waveguide mixer. These are to reduce the cutting-edge chipping that occurs in cutting the MgO substrate, control the substrate thickness in polishing and chip handling, and mount the extremely small mixer chip into the mixer block. In this paper, we describe the design of the waveguide mixer, the method used to fabricate the mixer chip, and the experimental results of receiver-noise measurements.

2. Mixer design

2.1 Waveguide mixer

The design of the waveguide input circuit including the RF choke was done using Ansoft's High Frequency Structure Simulator (HFSS version 9), which has a finite-element method incorporated [8]. The dielectric constant of the MgO substrate was assumed to be 9.6. The center frequency was set to 870 GHz, which is the center frequency for band-10 ALMA. The schematic layout for the waveguide input circuit is in Fig. 1. The aperture of the substrate channel is 0.074 x 0.074 mm and the mixer chip is 1-mm long, 0.064-mm wide, and 0.025-mm thick. We chose a half reduced-height waveguide with dimensions of 0.265 x 0.065 mm as the input waveguide and the length

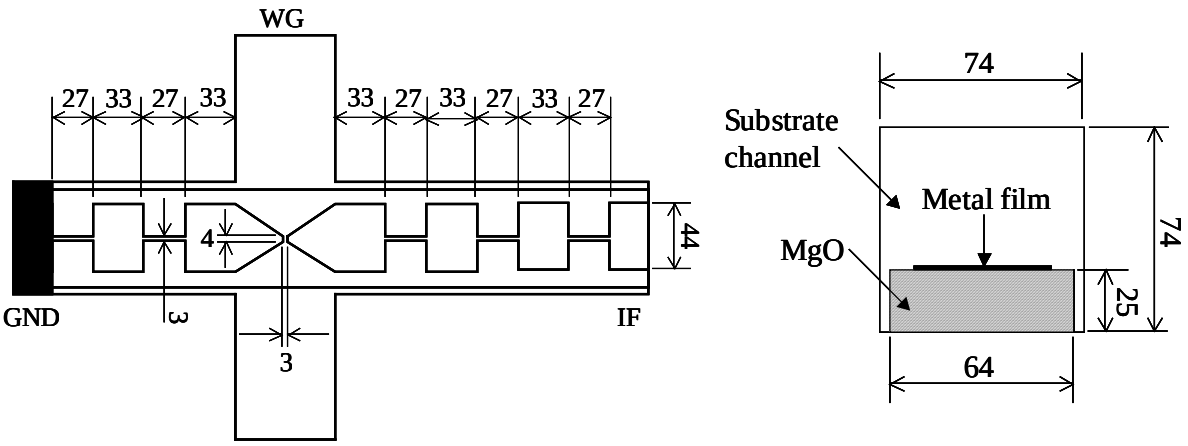

Fig. 1 Schematic layout of waveguide input circuit with MgO substrate. All dimensions are in μm. Mixer chip is 1-mm long, 0.064-mm wide, and 0.025-mm thick.

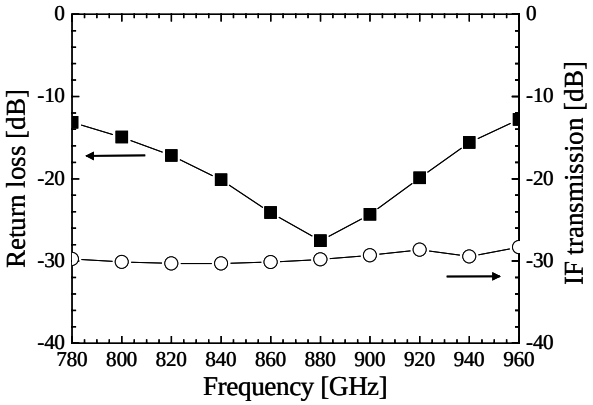

(a)

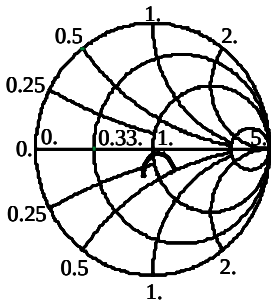

(b)

Fig. 2 (a) Return-loss characteristic at feed point and IF transmission characteristics to IF port. (b) Impedance Smith chart at feed point normalized to 60 Ω.

of the backshort cavity was 0.021 mm. We determined the optimum backshort position so that the calculated return losses were minimized in the frequency range of interest. The feed point was set to the center of the bow-tie probe.

Figure 2(a) plots the return-loss characteristic of the RF signal at the feed point and the transmission characteristics to the IF port. The return loss was less than -10 dB in a frequency range from 780 to 960 GHz. The transmission of the RF signal to the IF port is less than -28 dB and the RF signal was not considered to have leaked to the IF port The impedance Smith chart at the feed point normalized to 60 Ω is in Fig. 2(b). The feed point impedance was set to 60 Ω from this Smith chart.

To evaluate the tolerances of variations in width and thickness, we calculated the dependence of return-loss characteristics on variations. Figure 3(a) plots the return loss at a substrate width of 0.054 mm and 3(b) plots the return losses at thicknesses of 0.02 and 0.03 mm. We can see from these figures that a variation of a few microns changes the characteristics dramatically. Therefore, the mixer chip must be fabricated within accuracies of 10 μm in cutting and +/- 5 μm in polishing the MgO substrate.

We choose a diagonal horn with an aperture of 2.5 x 2.5 mm as the feed horn. A diagonal horn is easy to machine and has good beam efficiency in the E- and H-planes [9].

2.2 Tuning circuit

In general, the reactance of an SIS mixer due to its large geometrical capacitance must be removed by adding an appropriate tuning circuit to efficiently feed the signal to the junction. Distributed mixing using nonlinear SIS

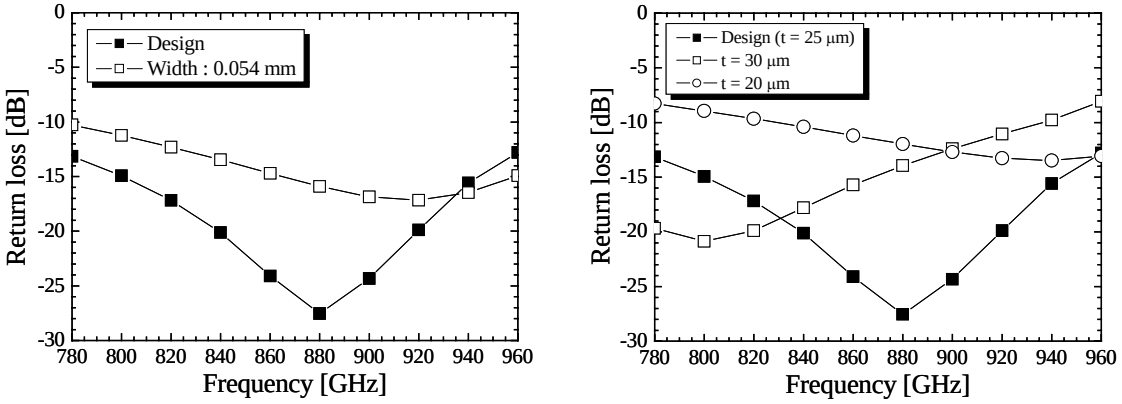

Fig. 3 Variations in return-loss characteristics due to dimensional change in substrate: (a) return-loss characteristics at widths of 0.064 mm (design) and 0.054 mm. (b) return-loss characteristics at thicknesses of 0.025 mm (design), 0.03 mm, and 0.02 mm.

transmission lines have demonstrated low noise and good tunability at submillimeter wavelengths [10-12]. We adopted a resonant distributed SIS mixer as the tuning circuit. The resonant distributed SIS junction consisted of an NbN/MgO/NbN tunnel junction and an NbN/MgO/NbN microstrip as we can see from Fig. 4(a). A 0.6-μm-wide SIS junction with a symmetrical counter-electrode overhang of 1 μm on either side was assumed. The critical current density of the junction was set to 20 kA/cm^2. Also, the junction specific capacitance was assumed to be 145 fF/μm^2 and the I_cR_n product was assumed to be 3.8 mV. The input impedance of the resonant distributed SIS junction at 870 GHz is plotted as a function of its length in Fig. 4(b). We found that an open long SIS junction becomes a resonator when its length equals integer multiples of $\lambda_g/2$. We chose a full-wave resonant distributed SIS junction with a junction length of 7 μm taking the tuning bandwidth and moderate input impedance into consideration. The input impedance of the junction was matched the feed point through a $\lambda_g/4$-microstrip transformer.

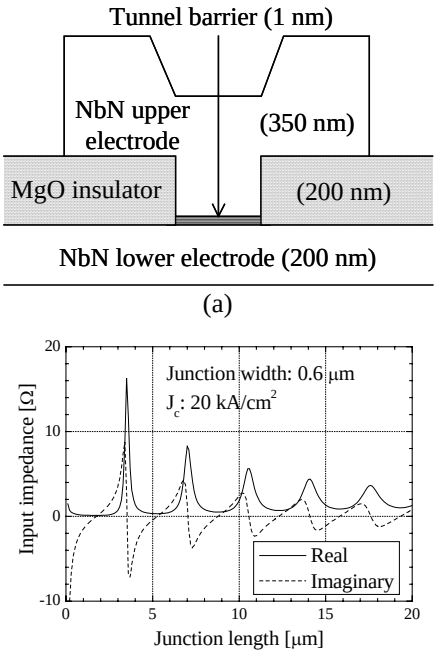

Fig. 4 (a) Schematic layout of distributed NbN SIS junction. (b) Input impedance of distributed junction as a function of junction length at 870 GHz for 0.6-μm-wide junction with symmetrical counter-electrode overhang of 1 μm on either side.

3. Mixer fabrication

The epitaxial NbN/MgO/NbN trilayers that formed the tunnel junctions were deposited *in situ* on single-crystal (100) MgO substrates 15-mm square and 0.3 mm in thickness at ambient temperature. The base and counter NbN electrodes of the tunnel junctions were deposited by reactive dc-magnetron sputtering. The MgO tunnel barrier was deposited by rf sputtering. The base and counter NbN were each 200 nm thick. The critical current density was controlled by the thickness of the MgO barrier. The bow-tie waveguide probe was formed with conventional photolithography and reactive etching (RIE). Then an SIS-junction mesa was formed using photolithography and RIE. After a 200-nm-thick MgO film was deposited by rf- and dc-magnetron sputtering to electrically insulate the base electrode and contact-wiring layer, the photoresist was lifted off. Finally, a 350-nm-thick NbN film was deposited and the wiring layer and transformer were defined by photolithography and RIE.

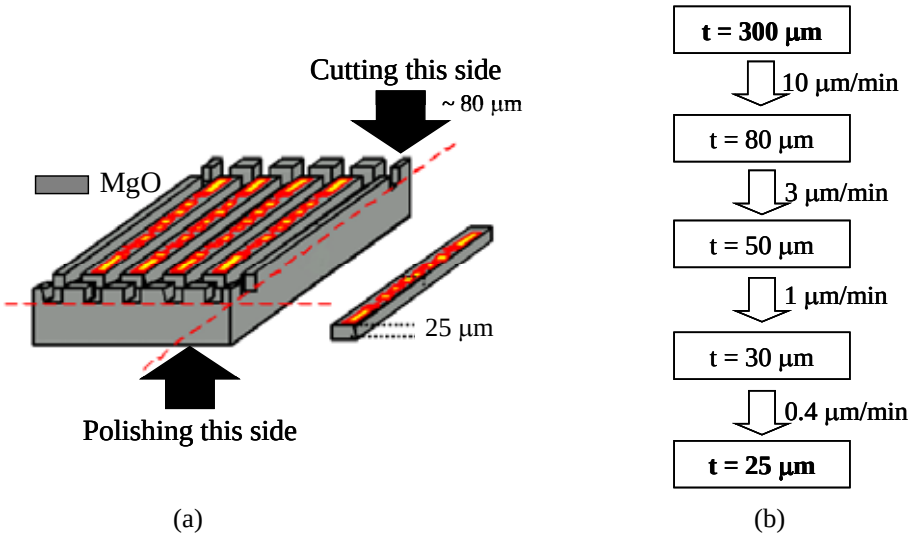

(a) (b)

Fig.5 (a) Fabrication of mixer chip. MgO substrate is first cut to depth of 80 μm from surface, and then its backside is polished down to thickness of 25 μm. (b) Polishing process for MgO substrate. Polishing rate is changed by replacing diamond lapping film.

After the fabrication process was completed, the MgO substrate was first cut to a depth of 80 μm from the surface with a (DISCO) dicing machine (Fig. 5(a)). In general, the tip of the blade is rounded. Therefore, we cut more deeply than the design thickness using a narrow blade with a thickness of 25 μm (NBC-Z1050) so that the shape of blade did not appear in the cutting plane. In dicing, the MgO had larger cutting-edge chipping than either quartz or silicon. Although the amount of chipping in quartz and silicon substrates is several microns, it is more than several tens of microns in MgO substrate if cutting is done under the same conditions. Chipping is a serious problem in defining the width of the mixer chip with sufficient accuracy. By optimizing dicing conditions and doing appropriate pre-cutting, we were able to reduce the chipping to around 3 μm using an NBC-Z1050 blade.

The cut substrate was glued upside down on a dedicated plate and its backside was then polished down to a design thickness of 25 μm using a lapping machine. The polishing was started with a diamond lapping film that had rough grain. We then lowered the polishing rate by replacing the lapping film with one that had finer grain and by reducing the speed the stage rotated at. Finally, polishing could be done with sufficient accuracy at a rate of 0.4 μm/min. We confirmed that the final thickness was accurate within 5 μm with both a micrometer and an optical microscope. The process of polishing is outlined in Fig. 5(b).

The fabricated mixer chip was mounted into the waveguide mixer block. However, the pressure bonding with indium metal was very difficult because the substrate was very thin. We first bonded the mixer chip with an adhesive (crystal bond 509) that was acetone soluble. Then, both ends of the mixer chip were directly connected to a 50-Ω microstrip and the mixer block with 18-μm-diameter aluminum wires to extract the IF output and to supply the DC bias. The bend in the substrate becomes much more pronounced as the substrate gets thinner, and could lead to breakage during mounting. In fact, we observed a large bend in our mixer chip. However, the substrate seldom broke

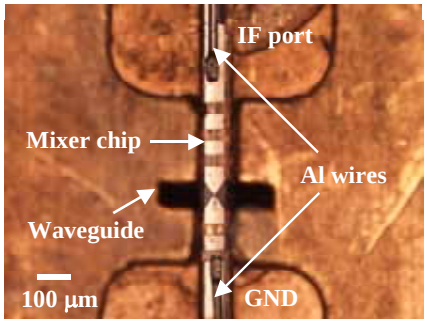

Fig. 6 Optical micrograph of mixer chip installed into substrate channel in waveguide mixer block.

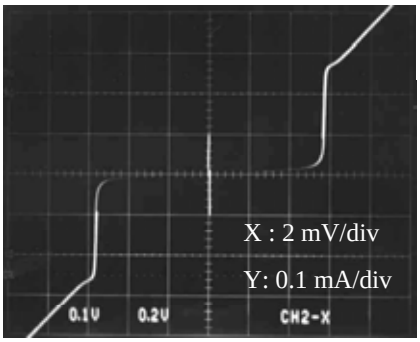

Fig. 7 Current-voltage characteristic of epitaxial NbN SIS mixer at 4.2 K. The horizontal scale is 2 mV per division, and the vertical scale is 0.1 mA per division.

when mounting with this method. Figure 6 is an optical micrograph of the mixer chip installed into a slot on the inside of the mixer block. The dc I-V characteristics of the mounted mixer chip are plotted in Fig. 7. The cutting and polishing processes did not affect the I-V characteristics, as far as the gap voltage, the leakage current, and the normal-state resistance were concerned. Additionally, the characteristics did not change for some heat cycles between room temperature and 4.2 K. However, the critical current density of the fabricated mixer was about 2.6 kA/cm^2, which is considerably less than the design value. An extremely small sub-gap leakage current and strong nonlinearity were observed in the I-V characteristics, where the ratio of sub-gap resistance at 4.0 mV to normal-state resistance was around 18 at 4.2 K.

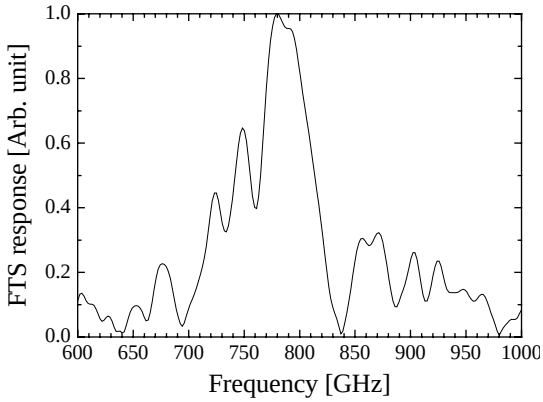

Fig. 8 FTS response of mixer as a function of frequency.

4. Receiver-noise measurements

The receiver response as a function of frequency was measured with a Fourier transform spectrometer (FTS) using the fabricated mixer as a direct detector prior to estimating the receiver-noise temperature. The FTS consisted of a Martin-Puplett interferometer using wire grids as polarizers and an Hg arc lamp as a broadband radiation source. The mixer was cooled by liquid He in a cryostat and was placed in front of the Teflon window of the FTS. The FTS response was directly related to the input coupling efficiency of the RF signal to the mixer. It is well known that the shape of FTS response as a function of frequency is strongly correlated to the receiver-noise temperature as a function of frequency and that minimum receiver-noise temperature can be obtained at a frequency where a maximum peak is observed for FTS response. The FTS response of the mixer is plotted in Fig. 8. We can see from the FTS data that the 3-dB bandwidth ranges from 760 to 810 GHz and low-noise temperature can be obtained in that frequency range. The best noise temperature can be expected at a frequency of around 780 GHz. Although the designed center frequency was 870 GHz, the measured center frequency shifted lower. This was because the dimensions of the fabricated junction were different from that designed. This is especially as fabrication error in the counter-electrode overhang severely affects center frequency, and a smaller overhang contributes to a lower center frequency. Additionally, the ratio of the spectrum of interest to its sideband was very small, i.e., the S/N ratio was very poor. This will create large input losses including the matching loss between the feed point and the junction in measuring the receiver-noise temperature.

The noise temperature of the receiver was estimated with the conventional Y-factor method using blackbody radiation on 295- and 77-K loads as the RF signal source. The RF signal was quasi-optically coupled to the LO signal from a backward-wave oscillator (BWO) through a 9-μm-thick Mylar film used as a beam splitter and this was guided to the mixer block cooled to 4.2 K through a 0.5-mm-thick Teflon vacuum window and a diagonal feed horn. A permanent magnet was attached to the sidewall of the mixer block to suppress the Josephson current. The IF output signal was first amplified with a high electron-mobility transistor (HEMT) amplifier with a bandwidth of 500 MHz centered at 1.5 GHz through an isolator at 4.2 K, and then amplified with a room-temperature post-amplifier. The IF signal was finally fed to a power meter. No corrections were made for the losses in front of the receiver.

Figure 9 plots the IF-output-power characteristics to hot and cold loads, along with the dc I-V characteristics with and without LO power at the 770 GHz of the receiver as a function of bias voltage. When LO power was applied, photon-assisted tunneling steps could clearly be observed. In terms of I-V characteristics, the lowered gap voltage compared with that in Fig. 7 is due to the strong magnetic

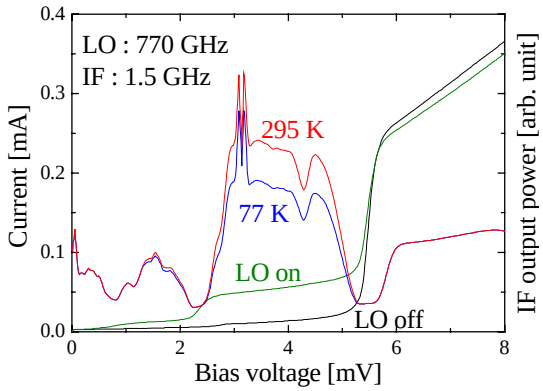

Fig. 9 Measured dc current-voltage characteristics of mixer with and without LO at 770 GHz. Also shown is receiver IF output power as a function of bias voltage for hot (295 K) and cold (77 K) loads.

field. A maximum Y-factor of 1.28 was obtained at a bias voltage of 4 mV, and this provides a double sideband (DSB) receiver-noise temperature of 700 K. Shot-noise calibration [13] yielded IF system noise of about 5 K and mixer conversion loss of about 12 dB, including losses in the optics and beam splitter. The poor input coupling efficiency was considered to be the cause of the large conversion loss.

Figure 10 plots the receiver-noise temperature as a function of LO frequency. The narrow bandwidth is due to the low critical-current density of the fabricated junction. The receiver-noise temperature was very large over the measured band. To find the cause of the large noise temperature, we compared it with that obtained with an SIS mixer using quasi-optical coupling. The quasi-optical SIS mixer consisted of a 3-mm-radius MgO hyperhemispherical lens with a 50-μm-thick Kapton-JP antireflection cap and a single-crystal twin-slot antenna. A resonant distributed SIS junction was also adopted in the quasi-optical mixer as the tuning circuit. The dimensions of the junction and λ_g/4-microstrip transformer in the quasi-optical mixer were the same as those for the waveguide mixer. Since the quasi-optical and waveguide mixer were arranged on the same photomask, both had the same critical-current density of 2.6 kA/cm^2. The receiver-noise temperature in the quasi-optical mixer is also plotted in Fig. 10. It was less than 400 K (DSB) in a frequency range from 762 to 810 GHz and a minimum noise temperature of 278 K, which is about seven times larger than the quantum limited noise, obtained at an LO frequency of 788 GHz. The receiver noise in the waveguide mixer was more than twice that in the quasi-optical mixer. From this, we considered that the large receiver noise in the waveguide mixer was due to losses originating between the horn and feed point, rather than matching loss between the feed point and junction. Actually, the input-noise temperature was more than 300 K in the measured band. The waveguide losses due to a roughness of the inside wall of the waveguide and RF leakage due to undesirable higher RF-signal modes in the substrate channel were considerable factors. If the higher RF-signal modes in the substrate channel are the main cause, the receiver noise can be reduced by making the substrate thinner and redesigning the waveguide input circuit.

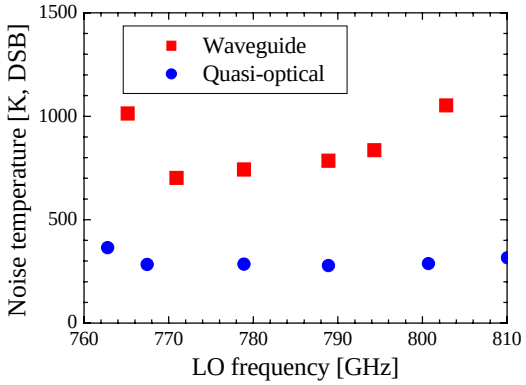

Fig. 10 Receiver-noise temperatures of waveguide and quasi-optical mixers as a function of frequency.

5. Summary

We are developing waveguide-type all-NbN SIS mixers on MgO substrates for the band-10 ALMA. The mixer chip we designed was able to be fabricated within an accuracy of 6 μm in width and 5 μm in thickness by optimizing the dicing and polishing conditions. The dicing and polishing processes did not affect the dc I-V characteristic of the fabricated mixer. Additionally, the characteristics did not change during some heat cycles between room temperature and 4.2 K. The micro mixer-chip was able to be successfully installed into a substrate channel in a waveguide mixer block and the receiver performance was estimated with FTS and heterodyne measurements. The minimum noise temperature of the receiver was 700 K (DSB) at an LO frequency of 770 GHz. The large input losses, especially in the waveguide input circuit, were the cause of the poor receiver performance. We believe that receiver performance can be improved by redesigning the waveguide input circuit.

References

[1] http://www.alma.nrao.edu/

[2] J. W. Kooi, M. Chan, B. Bumble, H. G. LeDuc, P. Schaffer, and T. G. Phillips, "230 and 492 GHz low noise SIS waveguide receivers employing tuned Nb/AlOx/Nb tunnel junctions", *Int. J. Infrared Millim. Waves*, Vol. 16, No. 12, pp. 2049-2068, 1995.

[3] C. E. Tong, R. Blundell, S. Paine, D. C. Papa, J. Kawamura, X. Zhang, J. A. Stern, and H. G. LeDuc, "Design and characterization of a 250-350 GHz fixed-tuned superconductor-insulator-superconductor receiver", *IEEE Trans. Microwave Theory Tech.*, Vol. 44, No. 9, pp. 1548-1556, 1996.

[4] Z. Wang, A. Kawakami, Y. Uzawa, and B. Komiyama, "NbN/AlN/NbN tunnel junctions fabricated at ambient substrate temperature", *IEEE Trans. Appl. Supercond.*, Vol. 5, No. 2, pp. 2322-2325, 1995.

[5] A. Kawakami, Z. Wang, and S. Miki, "Fabrication and characterization of epitaxial NbN/MgO/NbN Josephson tunnel junctions", *J. Appl. Phys.*, Vol. 90, No. 9, pp. 4796-4799, 2001.

[6] Y. Uzawa, M. Takeda, A. Kawakami, and Z. Wang, "A tuning circuit with two half-wave distributed junctions for all-NbN SIS mixers", *Int. J. Infrared Millim. Waves*, Vol. 24, No. 10, pp. 1749-1757, 2003.
[7] A. Kawakami, Y. Uzawa, and Z. Wang, "Development of epitaxial NbN/MgO/NbN-superconductor-insulator-superconductor mixers for operations over the Nb gap frequency", *Appl. Phys. Lett.*, Vol. 83, No. 19, pp. 3954-3956, 2003.
[8] *High Frequency Structure Simulator*, Ansoft Co., Four Station Square Suite 200, Pittsburgh, PA 15219, USA.
[9] S. Withington and J. A. Murphy, "Analysis of diagonal horns through Gaussian-Hermite modes", *IEEE Trans. Antennas Propagat.*, Vol. 40, No. 2, pp. 198-206, 1992.
[10] V. Yu. Belitsky and E. L. Kollberg, "Superconductor-insulator-superconductor tunnel strip line: Features and applications", *J. Appl. Phys.*, Vol. 80, pp. 4741-4748, 1996.
[11] T. Matsunaga, C. E. Tong, R. Blundell, and T. Noguchi, "A 600-700 GHz resonant distributed junction for a fixed-tuned waveguide receiver", *IEICE Trans. Electron.*, Vol. E85-C, pp. 738-741, 2002.
[12] Y. Uzawa, A. Kawakami, S. Miki, and Z. Wang, "Performance of all-NbN quasi-optical SIS mixers for the terahertz band", *IEEE Trans. Appl. Supercond.*, Vol. 11, No. 1, pp. 183-186, 2001.
[13] D. P. Woody, R. E. Miller, and M. J. Wengler, "85-115-GHz receivers for radio astronomy", *IEEE Trans. Microwave Theory Tech.*, Vol. 33, pp. 90-95, 1985.

Acknowledgments

We would like to thank Dr. C. E. Tong of the Harvard-Smithsonian Center for Astrophysics for his invaluable comments. We also wish to thank Dr. S. Saito of the National Institute of Information and Communications Technology for his technical assistance in testing the FTS measurements. This work was supported in part by the ALMA Joint Research Fund by the National Astronomical Observatory of Japan.

15th International Symposium on Space Terahertz Technology

Arrays of Bolometers for Far-Infrared and Submillimeter Astronomy

D.T. Chuss, [1] C.A. Allen, [1] S. Babu, [1] D.J. Benford, [1] J.L. Dotson, [2] C.D. Dowell, [3] M. Jhabvala, [1] D.A. Harper, [4] S. Harvey Moseley, [1] R.F. Silverberg, [1] J.G. Staguhn, [1] G. Voellmer, [1] E.J. Wollack, [1]

ABSTRACT

We describe 12 x 32 arrays of semiconducting cryogenic bolometers designed for use in far-infrared and submillimeter cameras. These 12 x 32 arrays are constructed from 1 x 32 monolithic pop-up detectors developed at NASA Goddard Space Flight Center. The pop-up technology allows the construction of large arrays with high filling factors that provide efficient use of space in the focal planes of far-infrared and submillimeter astronomical instruments. This directly leads to a significant decrease in integration time. The prototype array is currently operating in the second generation Submillimeter High Angular Resolution Camera (SHARC II), a facility instrument in use at the Caltech Submillimeter Observatory (CSO). The elements of this array employ a bismuth absorber coating and quarter wave backshort to optimize the bolometer absorption for a passbands centered at 350 and 450 microns. A second array is to be installed in the High-resolution Airborne Widebandwidth Camera (HAWC), a far-infrared imaging camera for the Stratospheric Observatory for Infrared Astronomy (SOFIA). This array has been completed and is now awaiting integration into the HAWC test cryostat. HAWC is scheduled for commissioning in 2005. The HAWC array employs titanium-gold absorbers and is optimized for uniform absorption from 40 to 300 microns to accommodate all four of its far-infrared passbands. We describe the details of the HAWC array construction including the mechanical design and electrical characterization of the constituent linear arrays.

1. Introduction

In recent years, improvements in direct detection technology used in far-infrared and submillimeter astronomy have allowed astronomers to fill focal planes of telescope with larger and larger arrays of detectors that efficiently couple to astronomical radiation. Such technologies have allowed for increased observing efficiency and therefore a decrease in integration times.

The Pop-up Detector (PUD) technology developed at NASA Goddard Space Flight Center (Moseley et al. 2000) exhibits marked advantages over previous bolometer architectures. Because the electrical leads are folded out of the focal plane, it is possible to achieve filling factors close to 95%. Also, depending on the bandwidth specifications, it is possible to implement absorber strategies that achieve quantum efficiencies of close to 100% over a finite bandwidth. Finally, the architecture enables large format two-dimensional arrays to be constructed through the stacking of individual 1×32 monolithic linear arrays.

To date, two 12×32 arrays have been built using this technique. The first is currently operating in the SHARC II camera at the Caltech Submillimeter Observatory (CSO; Dowell et al., 2002). The second has recently been delivered to the University of Chicago for integration into HAWC(Harper et al. 2000), a facility imaging photometer for SOFIA (the Stratospheric Observatory for Infrared Astronomy). In section 2, we describe the two instruments. In section 3, we review pop-up technology. We discuss the constrasting absorber strategies of the two arrays in section 4. The details of the HAWC array construction are given in section 5. Finally, the current status of each detector is given in section 6.

[1]NASA Goddard Space Flight Center

[2]NASA Ames Research Center

[3]JPL/Caltech

[4]University of Chicago, Yerkes Observatory

2. SHARC II and HAWC

Interstellar dust at temperatures from 20 to 200 K is abundant both in our own Galaxy as well as in external Galaxies. Dust at such temperatures radiates strongly in the submillimeter and far-infrared. Specific astronomical objects that can be studied using high resolution telescopes operating at these wavelengths include galactic star formation regions, galaxy mergers, and bright ultraluminous infrared galaxies at z$\sim$1.

Because of the presence of water vapor, the atmosphere is opaque in the far-infrared and submillimeter. This fact makes ground-based astronomy at these wavelengths difficult. In the submillimeter, atmospheric "windows" at 350 and 450 μm are available during good weather at a few selective high-altitude locations, but from 40 through 300 μm, the only way to do astronomy is to place a telescope above most of the atmospheric water vapor. The Stratospheric Observatory for Infrared Astronomy (SOFIA) is NASA's next generation airborne observatory designed to provide a platform to study this wavelength regime. Offering a larger primary mirror than contemporary satellites operating at comparable wavelengths, SOFIA will achieve angular resolution in the far-infrared that will allow the most detailed maps of far-infrared sources to date.

As the facility imaging camera, HAWC will provide high resolution mapping and photometric capability to SOFIA. It will have four passbands from 40 μm through 300 μm and therefore will be able to measure spectral energy distributions (SEDs) of sources at high resolutions. This will directly lead to temperature profiles. The four HAWC passbands are given in Table 1 along with their bandwidths and angular resolutions.

The prototype array for the HAWC development effort, SHARC II (Submillimeter High Angular Resolution Camera), is currently operating at the CSO. Its primary observations are done in the 350 and 450 μm atmospheric windows; however, it is also capable of undertaking observations at 850 μm. The large aperature (10 m) of the CSO provides an angular resolution of 9$''$at 350 μm. Scientifically, observations with SHARC II will serve to complement HAWC observations by providing long wavelength data at a comparable angular resolution.

The SHARC II and HAWC angular resolutions as a function of their passbands are shown and compared with other contemporary far-infrared and submillimeter instruments in Figure 1.

Two-dimensional arrays of bolometers are constructed from constituent 1$\times$32 linear arrays (Voellmer et al. 2002). Each linear array consists of thirty-two 1 mm square bolometer membranes that are fabricated from a single piece of silicon. The bolometer membranes are ion-implanted over their full area with phosphorus and boron. Silicon straps on either side of each bolometer membrane provide mechanical support from the pixels to the frame. Aluminum traces run down both straps to provide thermal and electrical connections to the frame. Figure 2 shows a schematic of a section of a 1$\times$32 linear array before it is folded.

The individual linear arrays are deposited with an appropriate absorber coating, and then the frames are folded back and glued to the sides of a ceramic busbar. The stress of the fold is absorbed by the torsion bars on either side of the bolometer membrane (see Fig. 2). In this way, the area to either side of the bolometer membranes is unobstructed and thus free to accommodate adjacent rows of PUDs.

Table 1. HAWC Passbands

$\lambda(\mu$m)	$\Delta\lambda/\lambda$	Angular resolution($''$)
53	0.1	6
88	0.1	9
155	0.15	15
215	0.2	21

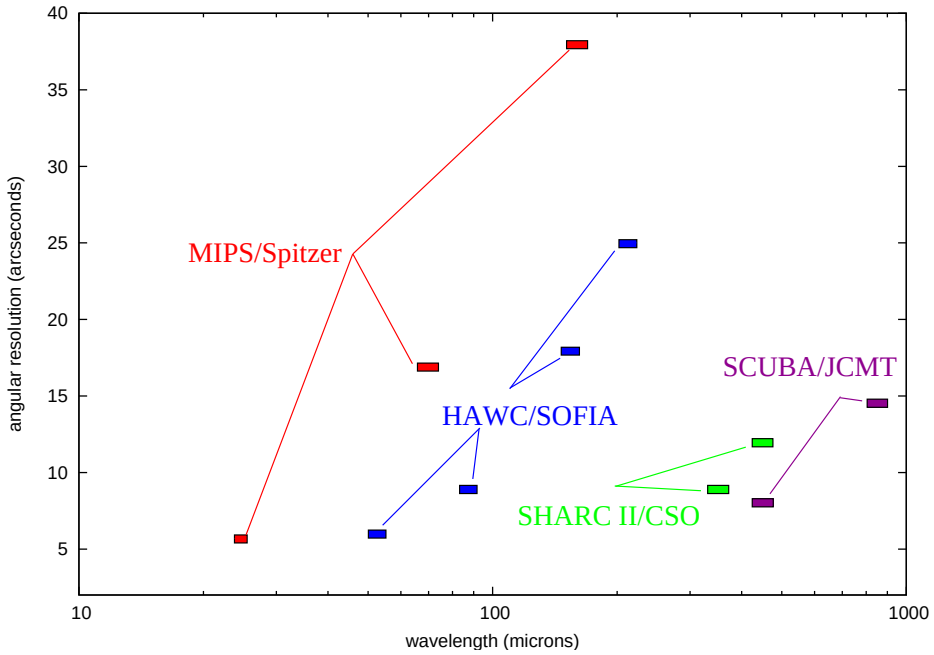

Fig. 1.— The angular resolutions and wavlength coverages of SHARC II and HAWC are compared with other contemporary far-infrared and submillimeter imagers.

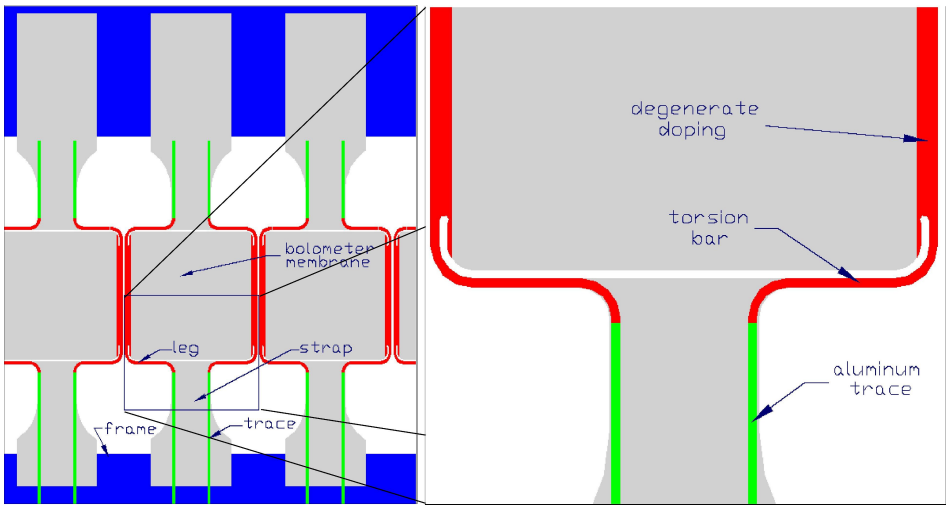

Fig. 2.— A schematic of a section of the unfolded 1×32 linear array is shown. (Dowell et al. 2002) The blowup on the right shows the details of the torsion bar that allows the straps to be folded out of the image plane.

3. Absorber Strategies

The absorber strategies for the two arrays differ. For SHARC II, the spectral proximity of the two atmospheric windows at 350 and 450 μm allows for the efficient implementation of a resonant absorber that works well across both bands. Thus, the absorbing strategy of SHARC II consists of a 400 $\Omega/\Box$ coating of bismuth absorber on the bolometer membrane accompanied by a quarter wave backshort located 100 μm behind the pixels. This configuration allows for >95% transmission across both SHARC II bands. The transmission line model and a schematic representation of this strategy are shown in the left side of Figure 3. Note the backshort is formed by the gold coated surface of the ceramic busbar. In practice, the absorption is dependent on the precision of backshort placement and surface impedance of the absorbing film on the bolometer.

In contrast, the passbands for HAWC, chosen for spectral properties of the atmosphere at 41,000 feet, span a much larger region of the spectrum. Because of the difficulties in matching these windows with a resonant backshort, the HAWC absorber strategy was chosen to maximize the bandwidth of the absorber. As shown in the right hand side of Figure 3, the bolometer membrane is coated with an optimal surface impedance of 157 $\Omega/\Box$. Because bismuth has an unacceptable reactance over parts of the HAWC passband, the absorbing layer is a thin film metal alloy of titanium-gold. The gold-plated busbar is painted with an epoxy infused with carbon lamp black and 40 μm glass beads to form a cold absorber. This leads to a predicted 50% absorption that is flat across all four passbands. How close the actual absorption is to this prediction will depend on the values of the surface impedances of the Ti-Au films and the efficiency of the busbar absorber.

The titanium-gold absorbers have been found to be unstable when stored at room temperatures for periods of a year or longer. The instability manifests itself in a slow rise of the surface impedance. Thus, in order to maintain the quality of the array over the useful lifetime of HAWC, the array will be stored below -40°C when not in use. Such cold storage has been found to halt the aging process.

4. HAWC Array Construction

The fundamental unit in the construction of the two dimensional HAWC array is the folded, absorber-coated linear array. Many such PUD linear arrays are fabricated. They then undergo a series of electrical and optical tests at cryogenic temperatures that define the criteria for downselecting the candidates to the 12 rows that make up the 384 pixel HAWC array. The rows are tested, two at a time, in a He-3 cooled test dewar. The procedures for the row testing are similar to those that were performed for SHARC II (Freund et al. 2002).

The time constants of the bolometers on each row are tested. This is done by applying a small square wave signal on top of the bias voltage. The responses of the detectors over many cycles of this signal are co-added, and a fit is done to the resulting data to determine the bolometer's time constant. For the HAWC detector, the time constants for each detector must be below 10 ms. Figure 4A shows a typical time constant data set with an exponential fit to the data.

Load curves are taken at three temperatures: 250 mK, 300 mK, and 450 mK. The current-voltage response of the detectors are found by changing the bias voltage and measuring the DC voltage across the bolometer. A sample load curve is shown in Figure 4B. The load curves provide a check to the electrical viability of each detector in a row. The electrothermal properties of the bolometers are modeled by the equations

$$R = R_o \exp \sqrt{T_o/T},\ G = G_o(T/1K)^{\beta}.$$

These equations describe the resistance(R) and the thermal conductance(G) of a bolometer as functions of temperature. The determination of R_o, T_o, G_o, and β allow for optimal placement of the bolometers in the final two-dimensional configuration. In the HAWC cryostat, each adjacent pair of bolometers shares a bias voltage. Thus, by placing electrically similar rows next to one another, the six independent bias lines can be adjusted to maximize the sensitivity of the array. An electrical and thermal summary of the 12 rows of the HAWC detector is given in Table 2.

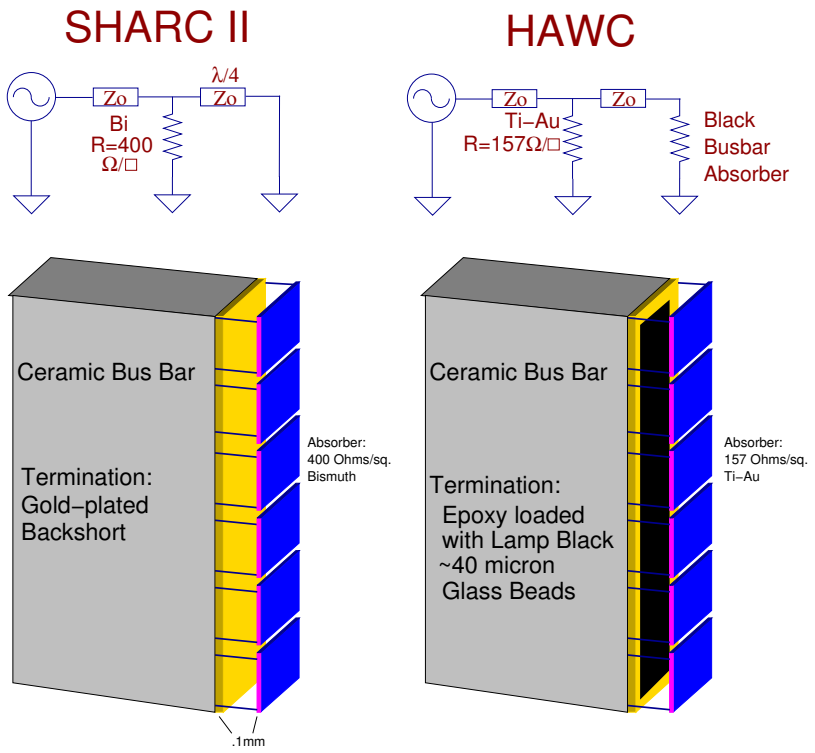

Fig. 3.— Contrasting absorber strategies for SHARC II and HAWC are shown below their respective transmission line representations. For HAWC, the absorption scheme is such as to allow for 50% absorption over the entire 40-300 μm HAWC band. The SHARC II strategy is optimized for ∼95% absorption over the 350 and 450 μm bands.

Table 2. HAWC Electrical and Thermal Properties

Row	$R_o(\Omega)$ †	T_o(K) †	G_o(nW/K) †	β†	$R_{\rm surface}(\Omega/\Box)$‡	τ(ms) †
1	803±342	29.5±3.1	2.95±0.61	1.93±0.16	115	6.67±0.74
2	456±31	34.3±1.7	3.73±0.15	2.06±0.06	125	6.94±1.50
3	619±175	30.0±1.2	3.93±1.95	1.98±0.31	128	9.13±2.13
4	952±158	27.7±2.4	1.48±0.41	1.93±0.03	118	8.13±1.30
5	907±152	29.0±6.4	1.88±0.62	1.66±0.31	110	5.52±1.35
6	1285±211	27.0±2.0	1.30±0.25	1.34±0.05	96	5.14±0.95
7	640±194	33.5±3.2	1.85±0.21	1.86±0.11	116	6.94±1.35
8	800±199	34.5±2.6	1.94±0.53	1.70±0.07	123	8.64±0.88
9	720±122	37.9±2.0	2.15±0.30	1.61±0.06	120	5.14±0.58
10	842±537	36.8±3.3	2.15±0.30	1.78±0.12	123	5.52±1.25
11	475±195	43.1±3.5	2.15±0.30	1.80±0.08	127	8.05±1.39
12	576±258	39.3±2.3	2.15±0.30	2.01±0.15	126	5.78±1.61

†Values are the mean values of the working pixels across each row. The error bars are calculated from the standard deviation of the same pixels.

‡The surface resistances are values obtained from witness samples immediately after the absorber deposition.

Noise tests are done on each row in order to check for rows that have excess noise. The rows are placed in the test dewar in the dark. The power spectrum of the data taken then gives the noise spectrum. Typically, baseline noise levels were found to be 20-40 nV $Hz^{-1/2}$. Given typical responsivities of 3-4$\times 10^8$ V/W, this translates to detector NEPs of 7-13$\times 10^{-17}$ W $Hz^{-1/2}$. The atmospheric NEP is expected to be 2.3-6.6$\times 10^{-16}$ W $Hz^{-1/2}$(Harper et al. 2000). Thus, it can be seen that these detectors will indeed provide background limited performance. A typical noise spectrum is shown in Figure 4C. The bumps that occur at various frequencies are due to external noise and microphonic sources present in the laboratory environment.

Radiation tests were also done on the HAWC arrays. These were done by pulsing an unfocused, uncalibrated thermal source (Beeman et al. 2002) behind a 350 μm filter. This source verified that submillimeter radiation couples to the bolometers. In addition, it provided an additional check on the consistency of the absorber coatings from PUD to PUD.

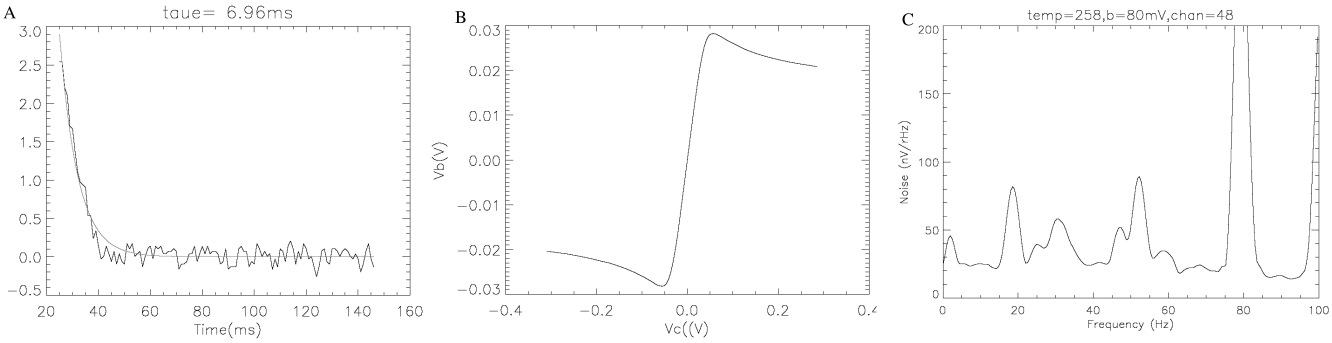

Fig. 4.— (A) Coadded time constant data are shown (jagged line) along with the best fit exponential decay (smooth line). (B) A typical load curve is given. The horizontal axis is proportional to the bias current, and the vertical axis is the voltage across the bolometer. (C) Noise results for a typical HAWC bolometer are shown.

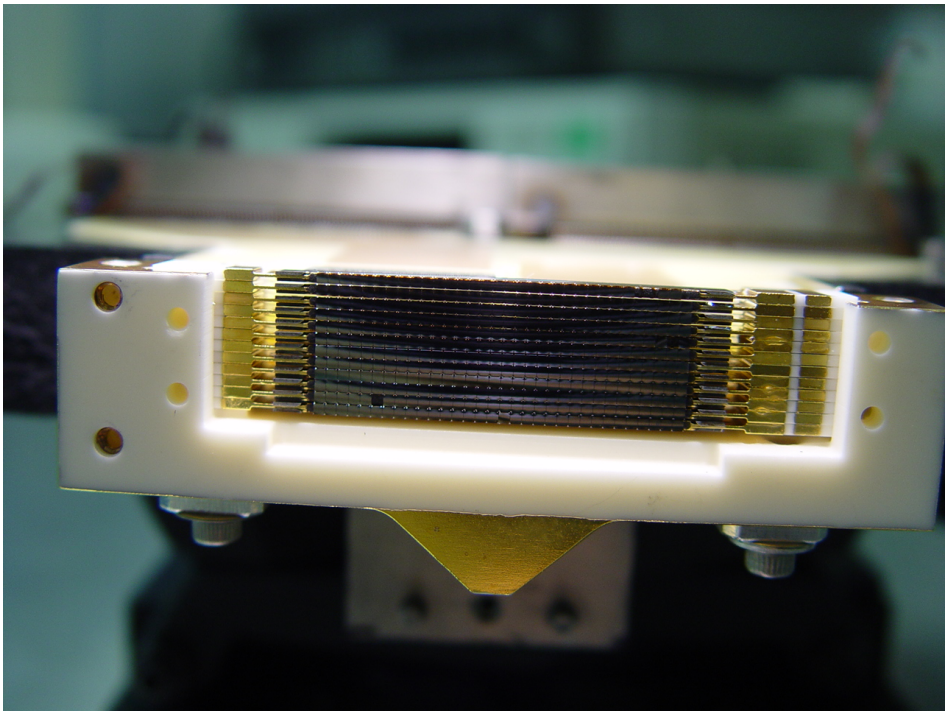

Fig. 5.— The completed HAWC array is shown.

There are two additional selection criteria that were considered. The first is that there is a 10% limit on the

number of bad pixels. Therefore, any rows containing more than 3 bad pixels were downgraded. Also, because of the concern over the absorber aging issue, rows having lower surface impedances were given higher rankings than those with higher surface impedances.

5. Current Status

The SHARC II array is currently operating at the CSO. For an example of the imaging capabilities of this instrument, see Houde et al. (2004). The HAWC array has been completed and is awaiting its integrated testing phase. A photograph of the completed HAWC array is shown in Figure 5. First light is expected for HAWC in 2005.

REFERENCES

Beeman, J., Collins, P., Hargrave, P., Pisano, G., & Haller, E. 2002, in Far-IR, Submm and mm Detector Technology Workshop, Proc. NASA Laboratory Astrophysics Workshop

Dowell, C. D., Allen, C., Babu, S., Freund, M., Gardner, M., Groseth, J., Jhabvala, M., Kovacs, A., Lis, D., Moseley, S., Phillips, T., Silverberg, R., Voellmer, G., & Yoshida, H. 2002, in Proc. SPIE, Vol. 4855, Millimeter and Submillimeter Detectors for Astronomy, ed. T. Phillips & J. Zmuidzinas, 73

Freund, M., Silverberg, R., Ponce, V., Allen, C., Sappington, C., Moseley, S., Harper, D., Loewenstein, R., & Dowell, C. 2002, in Proc. SPIE, Vol. 4855, Millimeter and Submillimeter Detectors for Astronomy, ed. T. Phillips & J. Zmuidzinas

Harper, D., Allen, C., Amato, M., Ames, T., Bartels, A., Casey, S., Derro, R., Evans, R., Gatley, I., Heimsath, S., Hermida, A., Jhabvala, M., Kastner, J. H., Loewenstein, R., Moseley, S., Pernic, R., Rennick, T., Rhody, H., Sanford, D., Shafer, R., Shirron, R., Voellmer, G., Wang, S., & Wirth, J. 2000, in Proc. SPIE, Vol. 4014, Airborne Telescope Systems, ed. R. Melugin & H. Roesner, 43–53

Houde, M., Dowell, C., Hildebrand, R., Dotson, J., Vaillancourt, J., Phillips, T., Peng, R., & Bastien, P. 2004, ApJ, 604, 717

Moseley, S., Dowell, C., Allen, C., & Phillips, T. 2000, in ASP Conference Series, Vol. 217, Imaging at Radio through Submillimeter Wavelengths, ed. J. Mangum & S. Radford, 140–149

Voellmer, G., Allen, C., Amato, M., Bartels, A., Benford, D., Derro, R., Dowell, C., Harper, D., Moseley, S., Shirron, P., Smith, W., & Staguhn, J. 2002, in Proc. SPIE, Vol. 4855, Millimeter and Submillimeter Detectors for Astronomy, ed. T. Phillips & J. Zmuidzinas

A 90 GHz Bolometer Camera Detector System for the Green Bank Telescope

Dominic J. Benford[1], Mark J. Devlin[2], Simon R. Dicker[2], Christine A. Allen[1], Troy J. Ames[1], Ernest D. Buchanan[1,3], Tina C. Chen[1,4], James A. Chervenak[1], Joshua B. Forgione[1], Kent D. Irwin[5], Jeff Klein[2], Brian S. Mason[6], S. Harvey Moseley[1], Roger D. Norrod[6], Philip R. Jewell[6], Johannes G. Staguhn[1,3], Mark P. Supanich[2], Edward J. Wollack[1]

1 – NASA / Goddard Space Flight Center, Greenbelt, MD 20771 USA

2 – University of Pennsylvania, Philadelphia, PA 19104 USA

3 – SSAI, Lanham, MD 20706 USA 4 – GS&T, Greenbelt, MD 20770 USA

5 – NIST / Boulder, Boulder, CO 80305 USA 6 – NRAO, Green Bank, WV 24944 USA

Abstract

We describe a close-packed, two-dimensional imaging detector system for operation at 90GHz (3.3mm) for the 100m Green Bank Telescope (GBT). This system will provide high sensitivity (~500μJy in 1s) rapid imaging (15'x15' to 250μJy in 1 hr) at the world's largest steerable aperture. The heart of this camera is an 8x8 close-packed, Nyquist-sampled array of superconducting transition edge sensor (TES) bolometers. We have designed and are producing a functional superconducting bolometer array system using a monolithic planar architecture and high-speed multiplexed readout electronics. With an NEP of ~$2\cdot10^{-17}$ W/√Hz, the TES bolometers will provide fast, linear, sensitive response for high performance imaging. The detectors are read out by an 8x8 time domain SQUID multiplexer. A digital/analog electronics system has been designed to enable read out by SQUID multiplexers. First light for this instrument on the GBT is expected within a year.

Introduction

The Green Bank Telescope (GBT; Prestage & Maddalena 2003) is an off-axis Gregorian telescope with a 100 m diameter unobstructed beam, providing a clear view of the sky from Green Bank, West Virginia (Figures 1 & 2). Designed to operate at frequencies between 290MHz and 115GHz, its surface can be actively controlled to provide an RMS surface error of around 0.21mm (although this control system is still under development). Factoring in the beam efficiency at 90GHz, the effective aperture of the GBT is around 2500m^2, with a 90GHz beamwidth of 8.4″.

We have undertaken to build a camera for the GBT for operation at its highest frequency of operation (90GHz, or 3.3mm). This camera will feature a close-packed detector array of 8×8 pixels, covering a field of view of 32″×32″. The camera will be optimized to obtain rapid, high-fidelity images of the sky with unprecedented sensitivity. Its mapping speed will be faster than that of previous telescopes, achieving a better sensitivity and a better angular resolution. The instrument team is led by Mark Devlin at the University of Pennsylvania, where construction of the instrument is taking place, including responsibility for the cryogenics and optics. The detectors and portions of the

Figures 1 & 2. Views of the Green Bank Telescope from above and below; the primary mirror is 100 m across.

readout electronics are provided by NASA/GSFC, while SQUID components and other readout electronics are provided by NIST/Boulder, and software is developed by the NASA/GSFC and NRAO/Green Bank.

Scientific Justification

At a wavelength of 3.3mm the dominant astrophysical sources of emission are thermal continuum emission from dust, the cosmic microwave background, and nonthermal emission.

One of the key science projects for a 90GHz camera of such high sensitivity and angular resolution will be to conduct a deep survey of distant galaxies. At cosmological distances, the dust emission in the submillimeter will be redshifted towards millimeter wavelengths. This observed 90GHz flux is thus emitted at higher frequencies, and so the steeply rising spectrum of such emission means that galaxies do not become substantially fainter as they are seen at greater distances. This "negative K correction" implies that a deep survey at 90GHz would find galaxies at all redshifts equally well (Blain et al. 1999), as shown in Figure 3. As a result, the number of sources detected at 90GHz can be very large… tens of thousands per square degree (Figure 4). An example of what such a survey would look like is shown in Figure 5. This simulation shows the high detection capability of this camera.

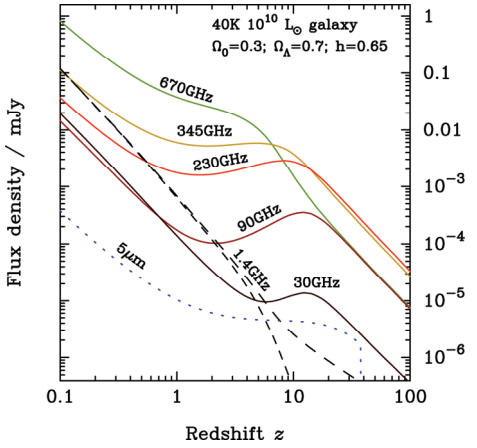

Figure 3. Redshifted flux densities (Blain et al. 2002).

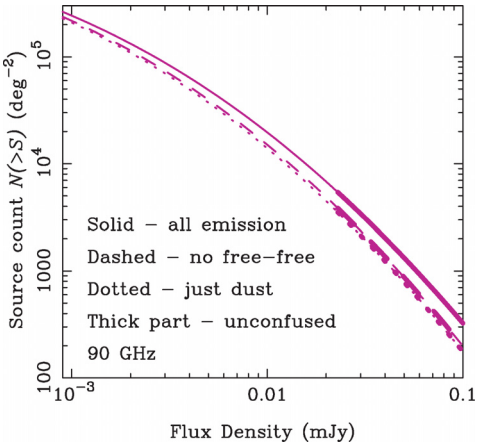

Figure 4. Galaxy counts at 90GHz (Blain 2004).

The power of a 100m telescope with an imaging array will produce a potent mapper of the Sunyaev-Zeldovich effect. For example, the Nobeyama 45m telescope operating at 21GHz can map to 500μJy in 34 hours with an 80″ beam (similar to cluster angular size); the GBT operating at 90GHz will map at 8″ resolution to 50μJy in 15 minutes. In addition to cosmological studies, nearby star and planet formation regions will be opened up for study by the GBT with its 90GHz camera. It can see the very faint emission from cold dust around protostars with unprecedented sensitivity and angular resolution.

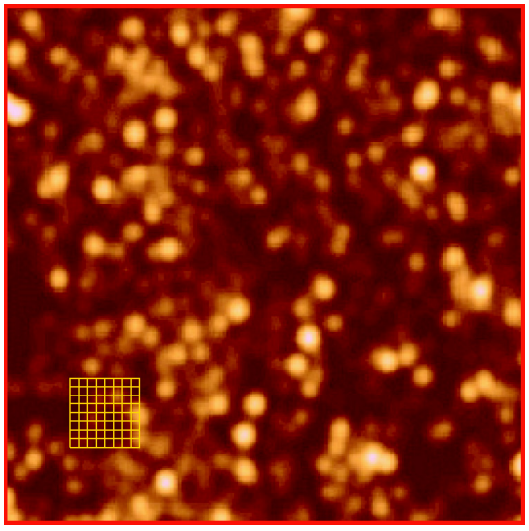

Figure 5. Simulated image of the sky showing the distribution of galaxies seen by the GBT at 90GHz.

Instrument Description

We are building the Penn Array Receiver (PAR), the first-generation 90GHz camera for the GBT. The detector system for the PAR is a superconducting transition edge sensor (TES) bolometer array and readout electronics providing 64 pixels in a close-packed 8×8 format. Compact on-axis reimaging optics provide a 32″×32″ image on the sky and an operating wavelength of 3.3mm, where the diffraction-limited beamwidth is 8″. The detectors are read out by a super-conducting quantum interference device (SQUID) amplifier produced at NIST/Boulder and high performance electronics developed at NASA/GSFC and NIST/Boulder. The

software for controlling the PAR and for reducing the data is being produced by a combination of U.Penn, NASA/GSFC, and NRAO/GB efforts, based on the Instrument Remote Control architecture (Ames 2004).

Cryogenics

The PAR requires a cryogen-free cooling system to provide refrigeration of the optics to ~3K and the detectors to ~300mK, while inducing a minimum of vibration and operating in non-vertical orientations. The requirements on the PAR cryogenic system are several:

- The system must provide cooling of the optics to ≤3K without the use of liquid helium. Estimated load at 3K is <100mW with an intermediate cooling of <4W at 40K.
- 15μW of cooling at temperatures below 290 mK: This must be maintained at angles of at least 57° from the vertical (corresponding to observations 20° above the horizon).
- When the receiver is not in use it may be tipped by up to 72° in any direction. After this it must be ready to use within 90 min of being returned upright.
- A minimum hold time at <290mK of 24 h (to allow deep observations), with a goal of 68 h (to allow for flexible scheduling of the telescope) is required.
- The receiver must be easily operated remotely by members of the astronomical community who are not familiar with cryogenics.
- So as not to affect the bolometers, low mechanical vibration and moderate temperature stability are needed.

Due to the remote operation requirement, expendable liquid cryogens were ruled out. A cryostat has been designed using two multi-stage closed-cycle coolers providing several stages of cooling between 300 K and 300 mK. This cryostat is shown at right in Figure 6.

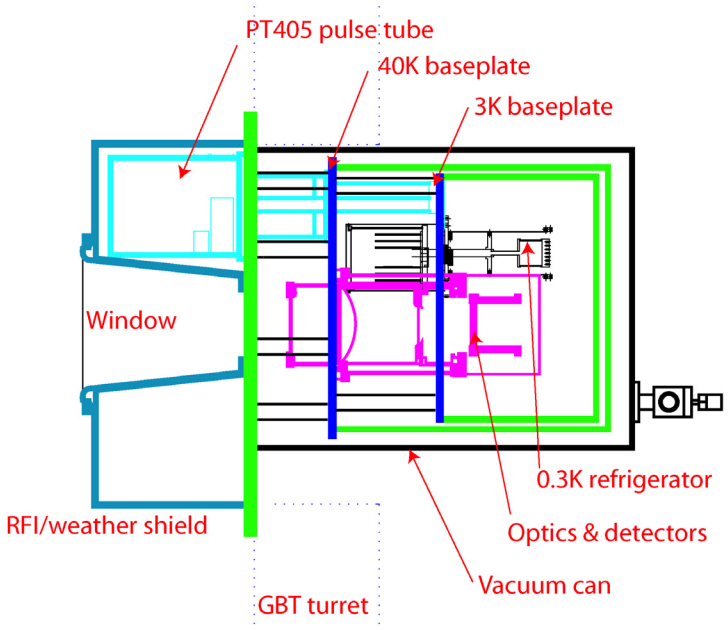

Figure 6. Side view of cryostat design; light enters from left.

The 300 K→3 K cooling is realized by means of a commercially available pulse tube cooler (Cryomech Inc.). This cooler can provide a cooling power of 150 mW at 3 K and 5 W at 40 K. It has no moving parts at the cold end, and so is a low-vibration mechanical cooler option. Its mean time between servicing of 20 kH is well suited to operation at the remote instrument chamber of the GBT. Under expected parasitic loading, the temperatures of the two stages will be around 40.5 K and 2.7 K. The only difficulty with this cooler is that it is orientation-dependent: the cooling power at fixed temperature can drop by a factor of two when tilted to 30° off of vertical. Tipping the system to 57° from the vertical resulted in the first stage warming up to 70 K in 2 h. The second stage was relatively unaffected, showing only a rapid warming to 3.4 K before becoming stable. Tests of the cooler indicated that the temperature of the first stage under constant load changes dramatically but transiently when the cold head is tilted. For tilts of Δ~40°, a transient of around 2 K occurs with a settling time of perhaps half an hour; similar transients of ~6 K occur for larger (Δ~80°) tilts.

Closed cycled cooling to 250 mK

We use the two-stage pulse tube cryocooler to cool the condenser of a ^{4}He sorption refrigerator, which is in turn used to cool the condenser of a ^{3}He sorption refrigerator (Figure 7; Devlin et al. 2004). This system has nominal temperatures of 40.5 K (pulse tube first stage), 2.7 K (pulse tube second stage), 0.7 K (^{4}He refrigerator) and 0.250 K (^{3}He refrigerator—unloaded). With a load of 15 μW the ^{3}He refrigerator runs at 270 mK and has a hold time of 72.7 h. This temperature was stable to 0.09 mK on timescales from 1 s to 10 min. After initial cooling, long-term drifts dropped below 0.2 mK/h, and the refrigerator RMS temperature noise is 90 μK at a timescale of one minute.

The cycling of the refrigerators is computer controlled, occurring on demand or autonomously when the ^{3}He refrigerator runs out. Typically it takes 4.5 h from the start of a cycle to when the ^{3}He refrigerator is stable below 290 mK. The cycling time is dominated by the limited cooling power of the pulse tube. Cycling has been shown to be effective at tilts up to at least 45° from the vertical.

The pulse tube is designed to operate vertically, whereas the sorption coolers are designed to be relatively orientation-insensitive. When tilted to 57° off of vertical the ^{3}He stage is unaffected, while the ^{4}He stage warms up by 10mK. On tilting the system to 72° the second stage of the pulse tube warms to 20 K in an hour and the charcoal pumps stop working, but the system then recovers within 40 min of being returned to vertical. With this last test we were able to conclude that the cryogenic system would meet all the above requirements on the GBT.

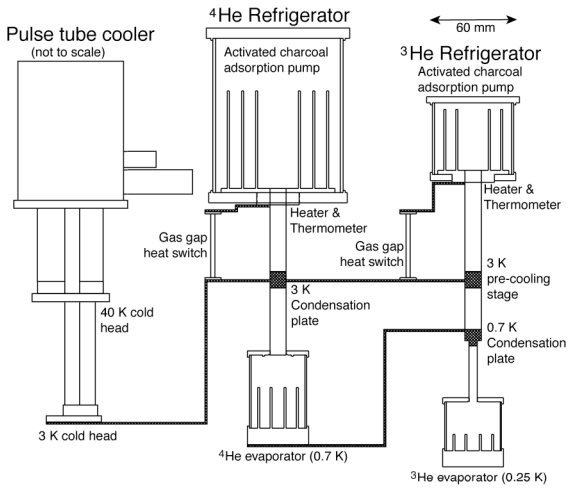

Figure 7. Diagram illustrating the thermal connections of the ^{4}He/^{3}He refrigerator.

Optics

Previous feedhorn-coupled bolometer arrays such as SCUBA (Holland et al. 1999) have had beams spaced by two resolution elements ($2f\lambda$) on the sky. Due to $1/f$ noise, missing data must be filled in as quickly as possible using complex scan strategies. This is often accomplished using the secondary or tertiary optics of a telescope to chop the beams on the sky. While this does reduce the influence of slow drifts on the final map, the fidelity of the image is compromised by the fact the chopping is an inherently differential technique. In the case of a large map of isolated sources, the result is an accurate map, but with additional noise arising from the differenced measurement. In the case of extended sources, the map is often inaccurate as well. The SHARC II instrument on the Caltech Submillimeter Observatory (Staguhn et al. 2003) has recently yielded excellent imaging quality without the use of a chopped measurement, by means of redundant sampling.

There is no easy fast way to chop the GBT. By using a fully sampled array with pixels spaced by $0.5f\lambda$ on the sky, maps can be made in a single scan and no fast chopping is needed. To get beams this close, feedhorns cannot be used above our array. We also note that 90 GHz feedhorns are expensive and difficult to manufacture. Reimaging with mirrors requires large volumes and a difficult alignment process. Lenses are compact and yield good off-axis image quality, and so are a good choice. However, they require good anti-reflective coatings and careful design to reduce ghosting.

Instead, illumination of the detectors is controlled using two aspheric silicon lenses with a cold Lyot stop between them (Figure 8). The bandpass is defined using reflecting capacitive mesh filters from U. Cardiff. The Lyot stop controls stray light and, along with filter 3, it limits the amount of power incident on each detector. Everything inside the Lyot stop is cooled to either 2.7 or 0.270 K. Power landing on the detectors comes from two main directions; through the Lyot stop (which is a sum of emission from the telescope, the atmosphere and the astronomical signal) and the 2.7 K structure around the Lyot stop (which is reduced to acceptable levels by bandpass filter 3). When all sources of power are considered, the telescope's optics (warm and cold) will contribute 0.7 pW per detector. The atmosphere should contribute 0.5–2.8 pW (depending on atmospheric opacity and telescope elevation) to give a total of 1.2–3.5 pW. Given the low intrinsic noise from the detectors, the receiver noise should be limited by the atmosphere to 1.2×10^{-17} W/√Hz, corresponding to a sensitivity on astronomical sources of 500–730 μJy·√s/detector.

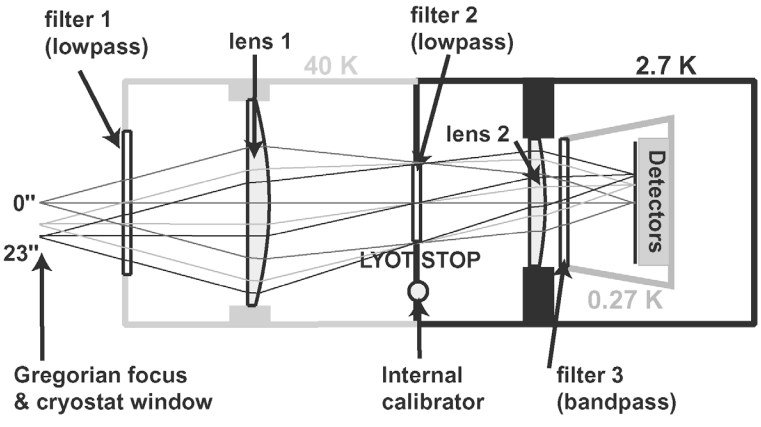

Figure 8. Optical design of the PAR.

Detector Array

The detector array format is chosen to be an 8×8 pixel array with a pitch of 3.3mm (chosen to be the wavelength). The power from the atmosphere sets the saturation power of the detectors to 12pW. The operating temperature will be around 450mK, which then limits the detector NEP to $2 \cdot 10^{-17}$ W/√Hz. The detectors are planar silicon membrane bolometers, each with a superconducting transition edge sensor (TES) of a Mo/Au bilayer (Benford et al. 1999).

From the ground, the atmosphere is the only important source of background power on the bolometers. Figure 9 shows the expected atmospheric emissivity (Grossman 1989) for the site of the GBT at left; this can be converted into an atmospheric photon noise equivalent power (NEP), as shown at right. The PAR detectors will need to achieve a phonon and Johnson noise sum of $<4 \cdot 10^{-17}$ W/√Hz in order to be background-limited, and must be able to absorb up to ~8pW in order to avoid saturation (a conservative value, since the actual power will be known only after engineering observations). This puts a stiff requirement on the dynamic range of the bolometers: the ratio of maximum power detected to the minimum power detectable in unity bandwidth is over 10^5.

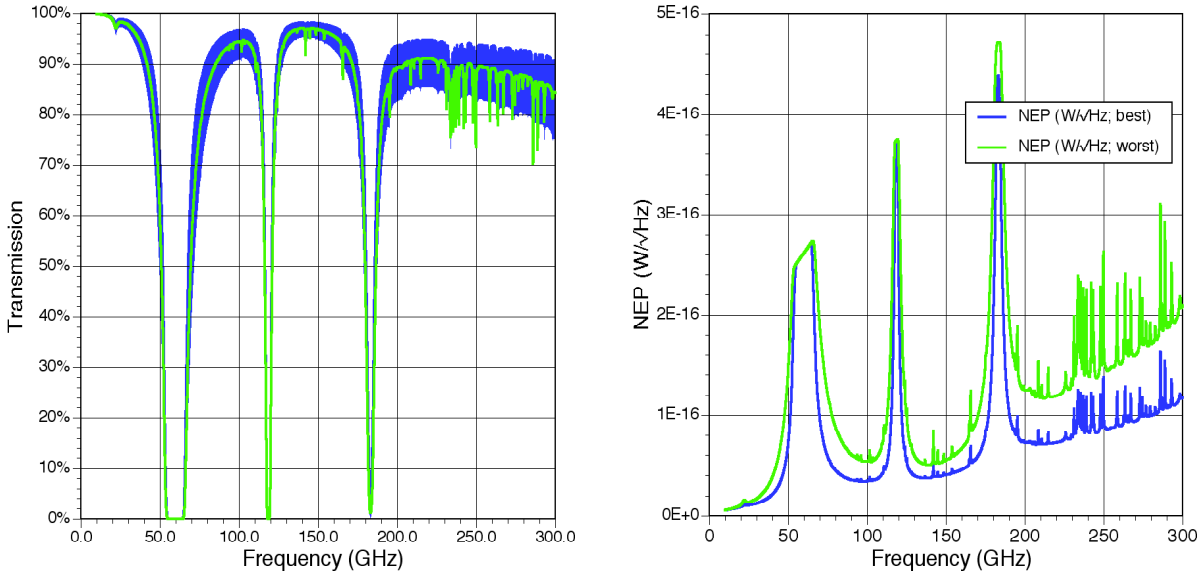

Figure 9. (Left) Atmospheric transmission and (Right) NEP for representative ranges of West Virginia weather.

In order to satisfy this requirement, a TES is used to read out the detector temperature. A TES bolometer has a faster response time than an identically designed, same-sensitivity semiconducting bolometer (or a more sensitive bolometer for the same response time) due to the strong negative electrothermal feedback intrinsic in a voltage-biased TES (Irwin 1995). TES bolometers are inherently low impedance devices, so they are well-matched to being read out by DC SQUID amplifiers (Welty & Martinis 1993). These amplifiers have a large noise margin over the bolometer noise. This permits the bolometer to be read out in a multiplexed fashion by a suitable SQUID multiplexer (Chervenak et al. 1999), reducing the amplifier size and wire count. Because SQUID amplifiers operate at the base temperature of the bolometer, they can be coupled very closely, removing the complex mechanical-thermal interfaces necessary with semiconducting bolometers.

A TES bolometer is fundamentally no different from a semiconducting bolometer, other than a change in the thermistor that has substantial implications. Infrared light is absorbed in the bolometer and converted into heat which warms the detector of heat capacity C above its nominal temperature T_{bias} (Figure 10). This temperature change is converted into a resistance change which is measured electrically. The heat is conducted away through a thermal conductance G to a heat sink at T_{bath}. A superconducting transition at temperature T_C yields an extremely sharp but continuous change in resistance from near zero to the normal state resistance (Figure 11). A unitless measure of the sharpness of the transition is defined as the sensitivity α:

$$\alpha \equiv \frac{d\log R}{d\log T} = \frac{T}{R}\frac{dR}{dT} \approx \frac{2T_C}{\Delta T}$$

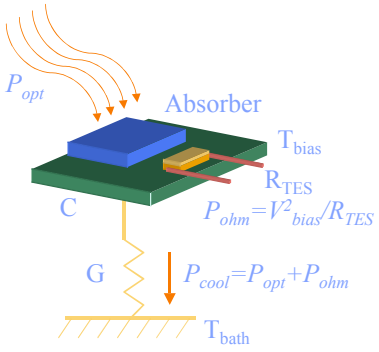

Figure10. Schematic of the operation of a TES bolometer.

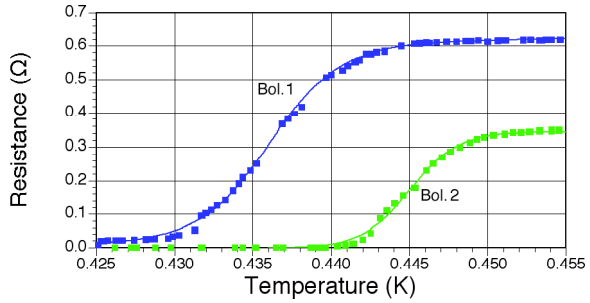

Figure11. R_{TES} vs. T_{bias} for representative bolometers.

where ΔT is the approximate transition width. The response time of a bolometer is typically the thermal time constant, $\tau=C/G$. However, TES bolometers can be faster by means of electrothermal feedback. When biased onto the transition, power is dissipated in the thermistor as $P=V^2/R$. When optical power is applied, the thermistor warms up, increasing its resistance dramatically. The bias power drops to compensate, bringing the TES back towards the stable bias point. The effective time constant is then approximately $\tau_{eff}=\tau n/\alpha$, where n is the temperature index of the thermal conductance. At low frequencies ($(\omega\tau_{eff})^2\ll1$), the Johnson noise is suppressed through the action of the electrothermal feedback by a factor of $(n/\alpha)^2$. The end result of this is that the intrinsic noise of a TES bolometer is typically dominated by the phonon noise alone.

One downside of TES bolometers is that, above some optical loading, the superconductor is driven normal and the detector responsivity goes to zero. This poses an interesting fundamental limit. The saturation power of a superconducting bolometer is $P_{sat}\approx GT_C/\eta$, where G is the thermal conductivity and $\eta\sim5$. The phonon noise is given by $NEP_{phonon}=(4kT^2G)^{1/2}$. The photon noise is given by $NEP_{phonon}=(\zeta 2Ph\nu)^{1/2}$, where $\zeta\approx2$ when photon bunching is significant. Assuming operation at $T=T_C$ and $P=P_{sat}$, we can rearrange to find that photon and phonon noise are equal when $T_C=(\zeta h\nu/2k\eta)$. At 90GHz, this point is at T_C=860mK. The ratio of noise scales as $T_C^{1/2}$, so operating well below this point is necessary.

Superconducting transitions can be made in several ways. In order to produce a thermistor with a tunable T_C and with a known resistance, we manufacture superconducting-normal bilayers. The superconductor, in this case a thin film of molybdenum, has its transition temperature reduced by proximity to a thin film of a normal metal such as gold. This process is described more fully by Chervenak et al. (2003) and Allen et al. (2003). The thermistor is manufactured by deposition and photoetching to produce a small (50μmx100μmx0.1μm) active volume. Such a thermistor is shown in Figure 12.

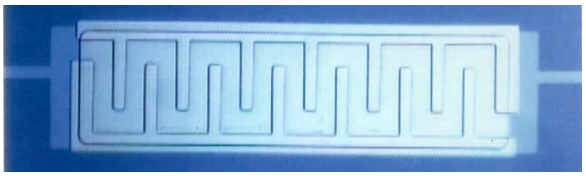

Figure 12. TES bilayer with lateral noise-suppression bars.

The voltage-current characteristic of a TES bolometer is quite different from that of a semiconducting bolometer. If we consider a voltage-biased TES cooling down from the normal state, the device exhibits a constant resistance ($I=V/R$). If we lower the bias voltage, at some point the bias power becomes too little to keep the device in the normal state, and it will begin to drop in resistance. Because the transition width is small, the TES is nearly isothermal at any point on the transition, and so the total dissipated power must be constant. In this case, the current becomes a hyperbolic function of the voltage, $I=P/V$. At some point, the bias current reaches a maximum value (set by electronics) and the TES becomes superconducting. The responsivity of a TES on its transition is approximately $1/V$ (A/W).

The function of a SQUID readout is more complex than of a FET, due to the fact that a SQUID's output is a periodic rather than linear function of the input. A SQUID transduces a measurement of magnetic flux into a voltage with extreme sensitivity. We use a voltage-biased TES sensor, so that the current varies as the resistance changes. This current couples through an inductor into the SQUID, which produces a voltage that is periodic in the input current. We then place a second inductor, called the feedback coil, next to the SQUID, and introduce a current exactly opposite the measured current in the input coil. As the input coil current changes (i.e., as the TES resistance changes), the SQUID reads a differential current. The feedback current is changed based on this difference to result in a nulled flux through the SQUID. The SQUID output is now a linearized function of the input, and the feedback current is always equal to the current through the TES.

A crucial element in the design of a large-format array is the multiplexer. As a collaborative effort between NASA-Goddard and NIST-Boulder we have, over the past few years, made substantial progress in the use of SQUID multiplexers for the readout of low-impedance devices. An eight-input SQUID multiplexer/amplifier (Chervenak et al. 1999) has been used to demonstrate Johnson-noise-limited readout (Staguhn et al. 2001), detection of infrared light with TES bolometers (Benford et al. 2000), and operation in an astronomical application (Benford et al. 2001). There is now a 32-input SQUID multiplexer with a more advanced architecture (Irwin et al. 2001), shown below in Figure 13. This multiplexer operates using time-domain multiplexing, and can operate at rapid switching rates with

low channel-to-channel crosstalk. A second stage SQUID amplifier is included on this chip to provide sufficient output to drive the multiplexed signal to a SQUID amplifier located elsewhere.

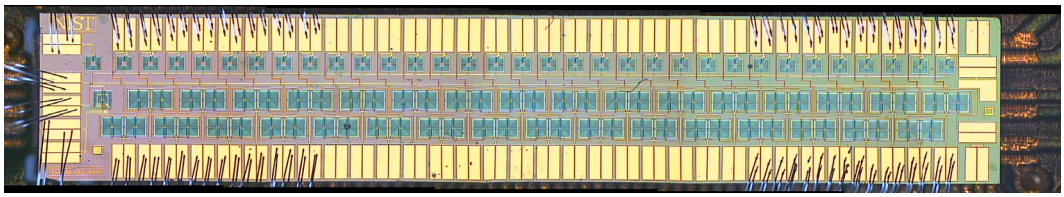

Figure 13. 32-input SQUID multiplexer chip manufactured at NIST-Boulder.

In the case of a multiplexed SQUID readout, several inputs are read through one output. Under control by a computer, a given input SQUID is turned on and its differential current (the signal minus the feedback) is read out. This difference current is then nulled by changing the feedback current, and its value – equal and opposite to the TES current – is stored for the future. The next SQUID is read out similarly, until all inputs have been read. On the next cycle, the previous readout of the TES current is looked up from memory, and its current is nulled with the previous feedback value. The SQUID then reads out the difference between the previous reading and the present reading, providing a linearized response. There is a flexible, compact, and modular analog / digital data acquisition subsystem to control and read out this complex but capable multiplexed amplifier array (Benford et al. 2003; Reintsema et al. 2003; Forgione et al. 2004).

The mechanical design for the detectors uses a 3.3mm-pitch, planar silicon membrane, 1μm thick, suspended by low thermal conductance legs. This is shown in Figure 14. The pitch was chosen to permit absorbers of ~λ in size, permitting the use of a filled-sheet absorber rather than an antenna.

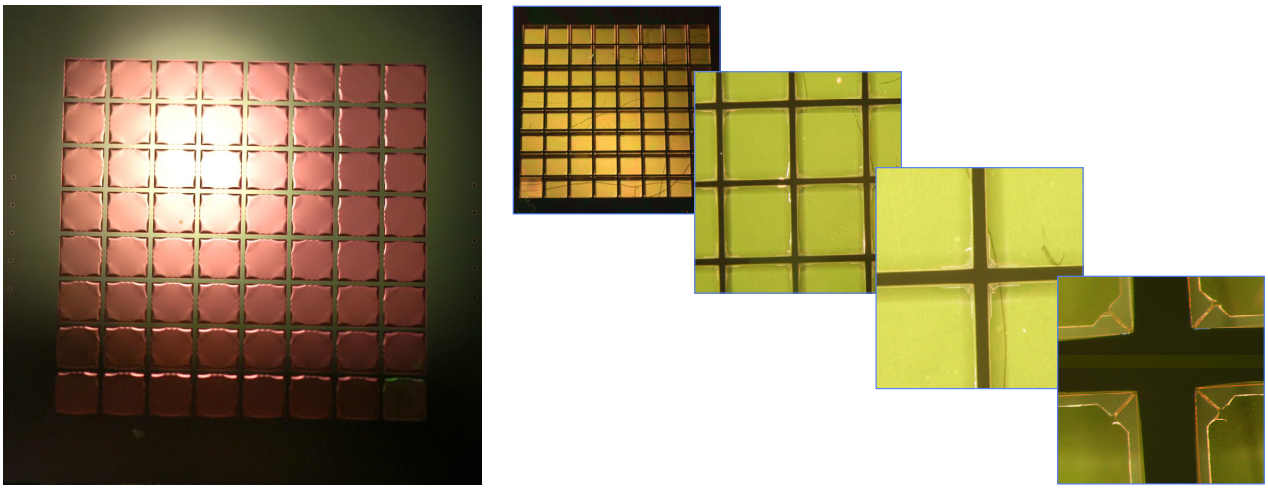

Figure 14. Mechanical model of the PAR 8x8 bolometer array, showing the overall design and the details of the thermal attachment of the membrane at the corner.

Detector Characterization

The PAR bolometers are in a development stage where variations of the bolometers are being characterized. The results presented here are taken from samples of 1×8 arrays consisting of 1mm^2 pixels. More detailed discussions of these detectors are presented elsewhere by Staguhn et al. (2004). The dark noise is within a factor of <2 of the theoretical prediction of 10^{-17} W/√Hz, the dynamic range is around a factor of $5 \cdot 10^5$, and the time constant is 1ms.

In Figure 15, we show the calibrated current vs. voltage for a set of detectors taken on several multiplexed bolometers simultaneously. The normal portion of the curve is a straight line, becoming hyperbolic at lower bias voltages as the detector resistance drops down the superconducting transition curve. At right in Figure 16, we show the response of several detectors to a blackbody source of known temperature. The response is calibrated by a multiplicative factor to account for the unknown coupling to the source. Over a range of three octaves in optical loading, the bolometers respond similarly to their predicted behavior.

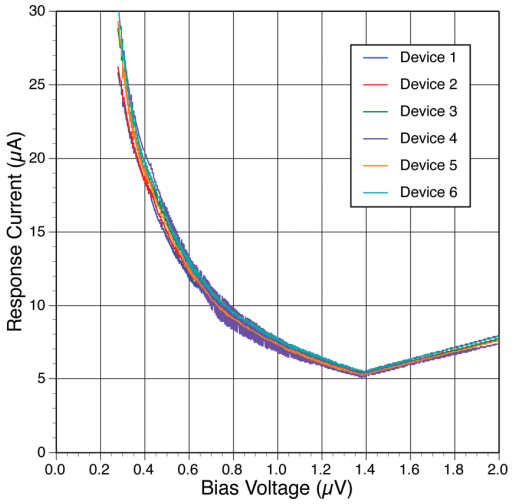

Figure 15. Current vs. voltage for several bolometers.

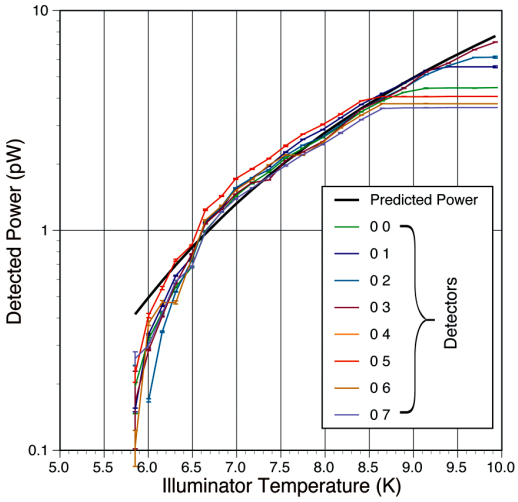

Figure 16. Optical response to blackbody illumination.

References

R.M. Prestage & R. Maddalena, *"Green Bank Telescope: Status and Early Results"*, Proc. SPIE #4837, pp. 944-953 (2003).

A.W. Blain, I. Smail, R.J. Ivison & J.-P. Kneib, *"The History of Star Formation in Dusty Galaxies"*, MNRAS 302, pp. 632-648 (1999).

A.W. Blain, I. Smail, R.J. Ivison, J.-P. Kneib & D.T. Frayer, *"Submillimeter Galaxies"*, Phys. Reports 369, pp. 111-176 (2002).

A.W. Blain, private communication (2004).

T.J. Ames, *"XML in an Adaptive Framework for Instrument Control"*, Proc. 2004 IEEE Aerospace Conference, in press (2004).

Cryomech Inc., PT-405; Falso Drive, Syracuse, NY 13211 USA; 1-315-455-2555.

M.J. Devlin, S.R. Dicker, J. Klein & M.P. Supanich, *"A High Capacity Completely Closed-Cycle 250mK ^{3}He Refrigeration System Based on a Pulse Tube Cooler"*, Cryogenics, in press (2004).

W.S. Holland et al., *"SCUBA: A Common-User Submillimeter Camera Operating on the James Clerk Maxwell Telescope"*, MNRAS 303, pp. 659–672 (1999).

J.G. Staguhn, D.J. Benford, S.H. Moseley & C.D. Dowell, *"Astronomical Results from SHARC-II"*, NIMPR-A 520, pp. 384-386 (2003).

D.J. Benford et al., *"Superconducting Bolometer Arrays for Submillimeter Astronomy"*, ASP Conference series #217, "Imaging at Radio through Submillimeter Wavelengths", pp. 134-139 (1999).

E.N. Grossman, *"AT-Atmospheric Transmission Software User's Manual, v1.5"*, Airhead Software, 2069 Bluff St., Boulder, CO 80302 (1989).

K.D. Irwin, *"An Application of Electrothermal Feedback for High Resolution Cryogenic Particle Detection"*, Appl. Phys. Lett. 66 (15), pp. 1998-2000, (1995).

R.P. Welty & J.M. Martinis, *"Two-Stage Integrated SQUID Amplifier with Series Array Output"*, IEEE Trans. on Applied Superconductivity 3 (1), pp. 2605-2608, (1993).

J.A. Chervenak, K.D. Irwin, E.N. Grossman, J.M. Martinis, C.D. Reintsema & M.E. Huber, *"Superconducting Multiplexer for Arrays of Transition Edge Sensors"*, Appl. Phys. Lett. 74 (26), pp. 4043-4045, (1999).

J.A. Chervenak et al., *"Fabrication of Transition Edge Sensor X-ray Microcalorimeters for Constellation-X"*, NIMPR-A 520, pp. 460-462 (2003).

C.A. Allen et al., *"A Dry-Etch Process for Low Temperature Superconducting Transition Edge Sensors for Far Infrared Bolometer Arrays"*, Low Temperature Detectors #10, Elsevier, in press (2003).

J.G. Staguhn et al., *"TES Detector Noise Limited Readout Using SQUID Multiplexers"*, AIP–CP #605, Low Temperature Detectors, pp. 321-324 (2001).

D.J. Benford et al., *"Multiplexed Readout of Superconducting Bolometers"*, IJIMW 21 (12), pp. 1909-1916 (2000).

D.J. Benford et al., *"First Astronomical Use of Multiplexed Transition Edge Bolometers"*, AIP–CP #605, Low Temperature Detectors, pp. 589-592 (2001).

Irwin, K.D. et al., *"Time-Division SQUID Multiplexers"*, AIP–CP #605, "Low Temperature Detectors", pp. 301-304, (2001).

D.J. Benford, G.M. Voellmer, J.A. Chervenak, K.D. Irwin, S.H. Moseley, R.A. Shafer & J.G. Staguhn, *"Design and Fabrication of Two-Dimensional Superconducting Bolometer Array for SAFIRE"*, Proc. SPIE #4857, pp. 125-135 (2002).

J. Forgione, D.J. Benford, E.D. Buchanan, S.H. Moseley, J. Rebar & R.A. Shafer, *"Enhancements to a Superconducting Quantum Interference Device (SQUID) Multiplexer Readout and Control System"*, Proc. SPIE #5498, submitted (2004).

C.D. Reintsema et al., *"Prototype System for Superconducting Quantum Interference Device Multiplexing of Large-Format Transition-Edge Sensor Arrays"*, Rev. Sci. Inst. 74 (10), pp. 4500-4508 (2003).

J.G. Staguhn, D.J. Benford, S.H. Moseley, C.A. Allen, T.A. Stevenson & W.-T. Hsieh, *"A Comparison of Device Characteristics of Mo/Au TES Bolometers with Different Normal Metal Bar Geometries"*, Proc. 15th Int. Symp. Space THz Tech., in press (2004).

Frequency Selective Bolometers - Progress and Projections

G.W. Wilson[a], T.C. Chen[b], E.S. Cheng[c], D.A. Cottingham[b], T.M. Crawford[e], T. Downes[e], F.M. Finkbeiner[f], D.J. Fixsen[f], D.W. Logan[a], S. Meyer[e], T. Perera[e], E.H. Sharp[b], and R.F. Silverberg[d]

[a]University of Massachusetts, Dept. of Astronomy, Amherst, MA, 01003, U.S.A.
[b]Global Science and Technology, NASA/GSFC, LASP, Greenbelt, MD, U.S.A.
[c]Conceptual Analytics, Glenn Dale, MD, U.S.A. [d]NASA/GSFC, Greenbelt, MD, U.S.A.
[e]Univ. of Chicago, Chicago, IL, U.S.A.
[f]SSAI, Greenbelt, MD, U.S.A.

ABSTRACT

We describe recent progress in the modeling and production of Frequency Selective Bolometers operating in the frequency range of 150-1500 GHz. The Frequency Selective Bolometer (FSB) functions by incorporating a bolometer element into a resonant structure to control the range of frequencies over which it absorbs. Both the bolometer absorber and the backshort are planar metal layers with periodic patterns that resonate at the desired frequency. The bolometer layer is resistive and absorbs the incident radiation at the desired frequency while the backshort is a low resistivity resonant pattern. The transmission, reflection, and absorption spectra of this two-layer structure are predicted with a numerical model and controlled by the design of the characteristics of the patterns. The key advantage to the FSB bolometer lies in the fact that the radiation not absorbed on the bolometer is transmitted through the device and passed on to subsequent FSB elements that are tuned to other frequencies. Thus a stack of FSB elements enables a multi-spectral single pixel with a geometry that can be close packed into an array of pixels.

We describe the electromagnetic modeling and measurements of FSBs spanning 150 to 1500 GHz. The discussion is focused on two issues: prediction and control of the FSB passband and the projected high frequency limit of FSBs currently being produced. Results from FSBs produced for the SPEctral Energy Distribution (SPEED) receiver (150-350 GHz) are shown along with corresponding results from prototype FSBs for the Explorer of Diffuse high-z Galactic Emission (EDGE) telescope (300-1500 GHz).

Keywords: Bolometer Camera, FIR Detectors, Cosmology, LMT

1. INTRODUCTION

The past five years has witnessed a growing effort by both ground and space-based millimeter and sub-millimeter wave observatories to build large-format bolometer arrays. Pioneering work by the SCUBA team in constructing a 128 element bolometer camera for the JCMT[1] has been followed by the 37 detector MAMBO instrument for the IRAM 30 m telescope, the 144 element BOLOCAM[2] and 384 element SHARC II[3] instruments on the CSO as well as the sub-orbital BLAST arrays (280 elements) and the 270 element SPIRE arrays on the Herschel satellite.[4] With the advent of multiplexed transition-edge superconducting (TES) detectors, this trend of larger detector arrays is expected to continue with several TES arrays currently in the construction phase including the approximately 10,000 element SCUBA II array for the JCMT.[5]

In contrast to these dramatic advances in array size, technologies that efficiently increase the spectral range of bolometer cameras have received relatively little attention. In fact, the cameras above which observe simultaneously in more than one band do so at great expense in complexity, mass, and detector efficiency by combining

Direct correspondence to G.W.
E-mail: wilson@astro.umass.edu
Telephone: 1 413 545 0460

the beams of multiple monochromatic detector arrays using complex schemes of dichroic filters and re-imaging optics or by sharing the focal plane between detectors illuminated by different feed horns. Instruments limited to one pass band at a time change frequencies either by replacing the upstream filters and array backshort (BOLOCAM) or by utilizing a filter wheel (SHARC II).

Herein we describe our progress in developing the Frequency Selective Bolometer (FSB) technology which addresses the desire for array receivers to spectrally multiplex the large bandwidth available at a telescope focal plane in a compact and efficient manner. This technology is planned to be demonstrated in two future instruments: the SPEctral Energy Distribution (SPEED) camera[6,7] and the Explorer of high-z Diffuse Galactic Emission (EDGE) experiment.[8] SPEED observes in four bands, between 2.1mm and 0.85mm, simultaneously in four pixels from a ground-based telescope. EDGE is a balloon-borne experiment which will observe in eight bands, from 300 GHz to 1.5 THz, simultaneously in seven pixels.

This paper is organized as follows. In Section 2 we describe the FSB concept and its implementation. In Section 3 we briefly outline the optical modeling of FSBs and show model/measurement comparisons. In Section 4 we describe the fabrication of the detectors with emphasis on the transition-edge superconducting sensors and on the limitations of the current processing for pushing FSBs to high frequencies.

2. FREQUENCY SELECTIVE BOLOMETERS

Traditionally, bolometric continuum detectors have used broad bandwidth absorbers (usually thin sheets of Au or Bi) and have left the definition of the system passband to upstream optics. While this approach results in detectors which can be used to observe different spectral passbands (BOLOCAM and SHARK II), in practice one finds that the optimal detector parameters for a particular passband are a strong function of the total power loading on the detector. Thus, ultra-broad bandwidth detectors only achieve their maximum sensitivity over a much smaller bandwidth of operation.

Frequency selective bolometers utilize a frequency selective surface to define the passband at the detector. Incorporating a pair of resonant arrays of dipole antennas as shown in the inset of Figure 1, the frequency selective bolometer absorbs only over a well defined passband while allowing radiation outside of that band to pass (see Figure 1). The bolometer is backed by a similarly resonant frequency selective backshort, spaced at $\lambda/4$ behind the absorber. The backshort functions to steepen the cutoff of the passband and to increase the coupling efficiency of the bolometer. By cascading a series of FSBs with successively lower passband frequencies, a multi-spectral pixel is created. There are several significant advantages to this design over the broad bandwidth absorber approach:

- The detector array geometry can be compact and light-weight.
- The lack of dichroic and bandpass filters results in a more efficient optical path with fewer elements contributing to scattering.
- Several passbands may be stacked at high efficiency in a single array.
- The system passbands are defined at the detector level, minimizing the complexity of optical alignments and cooling of external filters.
- The detectors are optimized for the passband they are designed to accept.

Over the past two years we have realized a series of prototype frequency selective surfaces and frequency selective bolometers ranging in frequency from 150 GHz to 1.5 THz. Both absorptive (bolometers) and reflective (backshorts) surfaces have been studied in transmission using Fourier Transform Spectrometers (FTS) at the University of Chicago and the University of Massachusetts. All prototype devices were fabricated using the Detector Development Laboratory at the Goddard Space Flight Center. The prototype optical devices were generated in order to test and calibrate our numerical model of frequency selective surfaces (see Section 3). The prototype bolometers were fabricated to explore the thermal properties of large detectors (see Section 4).

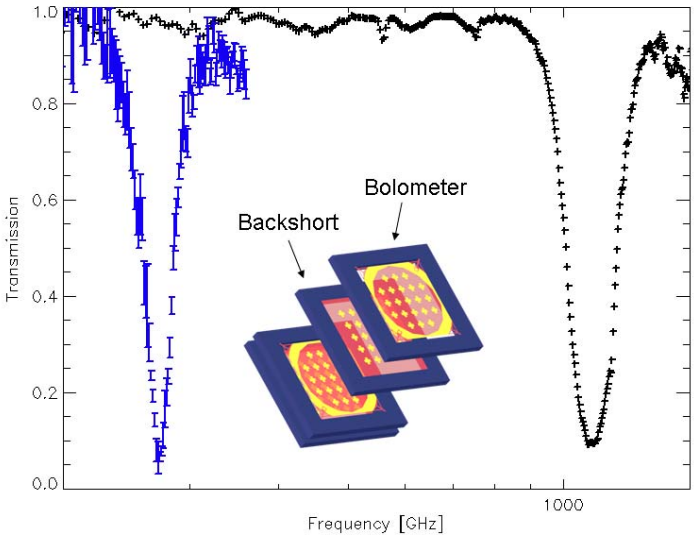

Figure 1. Plot: Transmission of a pair of FSBs. Note that these devices were measured individually, not in a stack configuration. The high low-frequency transmission of the 1150 GHz device (black data points) allows lower frequency FSBs to be placed directly behind yet still achieve high coupling efficiency. Note also that the high frequency FSB will act as a band-stop filter for subsequent lower frequency devices. Inset: A cartoon of an exploded pair of FSBs.

3. MODELING OF FREQUENCY SELECTIVE SURFACES

Significant analytical modeling of frequency selective surfaces dates back to studies of tuned surfaces utilized to diminish the bandwidth of reflectivity of military radar antennas in the 1950s.[9] In the case of this research, optical performance of FSBs is predicted and optimized using Ansoft's High Frequency Simulation Software (HFSS) v.8.5 on a 4 Xeon 1.5 GHz processor computer. HFSS is a finite element solver that calculates Maxwell's equations at all points on a generated mesh.

FSBs are optically large devices and even a simple model of the electric field around a single cross requires a large dynamic range in the solver. To numerically solve the case of an incident plane wave on an FSB, one must mesh the geometry finely enough to accurately represent the fields while not exceeding the memory and processing limits of the computing platform. This places a constraint on the overall range of scales in a given geometry. For our prototype FSBs, the ratio of largest to smallest feature is 2×10^4. To make the problem of modeling an array of crosses tractable, we model a single pair of crosses (an absorbing and a reflecting cross) with periodic boundary conditions that mimic an *infinite* array of cross pairs.* To further simplify the geometry, each cross is modeled as a 2-dimensional structure since the typical thickness of the crosses (0.2μm) is one part in 1000 of the shortest wavelength simulated.

The left side of Fig. 2 shows an exploded cartoon view of a model unit cell. The model consists of each cross located on a surface of 0.5 μm thick silicon nitride and separated by a distance of $\lambda/4$. The ends of the model are capped with a Perfectly Matched Layer (PML) that, by construction, absorbs all the incident radiation and terminates the cavity. The crosses are excited by a plane wave traveling along the z-axis and the transmission and reflection of the cross pair are calculated at the planes labeled "In" and "Out" by integrating the Poynting vector of the scattered fields at these planes. The backshort cross is modeled as a perfect conductor and the absorbing cross is modeled with a sheet resistance of 1.6 Ω/square. The 0.5 μm silicon nitride sheet on which the crosses are laid down is modeled as a finite thickness sheet with a relative permittivity of 7.5.

*Modeling a unit cell with periodic boundary conditions restricts the model to the wavelength range $2g \leq \lambda \leq g/2$ where g is the periodicity of the array. For this reason we are only able to model FSBs near their resonance.

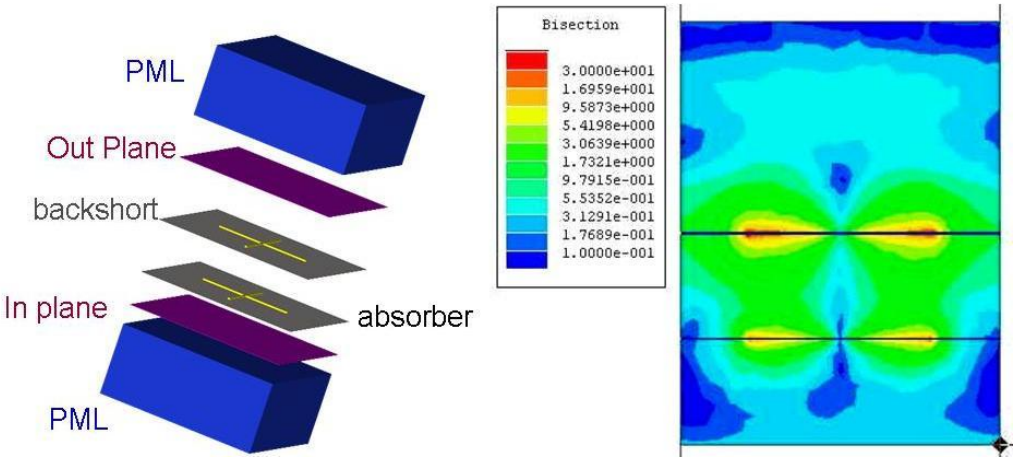

Figure 2. Left: An exploded cartoon view of an FSB unit cell as modeled in Ansoft's HFSS v8.5. Right: Sectional view of the scattered electric field amplitude. The units of the key are V/m.

The right side of Figure 2 shows the scattered electric field distribution for a model at frequencies near the resonance. The coupling of evanescent fields between the bolometer and backshort is clearly visible in the figure. Note that this behavior is not modeled in transmission-line calculations of layered frequency selective surfaces and yet, as shown below, is essential to accurately predicting the spectral response of the surfaces.

3.1. Models and Measurements

We have fabricated a series of FSB prototype devices to test the validity of the HFSS model. Optical models of frequency selective surfaces were produced at the NASA/GSFC Detector Development Laboratory and measured in transmission at the University of Chicago. We designed these devices to have physical properties as similar as possible to those desired for the SPEED and EDGE detectors so that we could both test the GSFC fabrication process and the frequency selective surface modeling.

The optical models were made on 200 μm silicon wafers coated with a 0.5 μm silicon nitride film. In all cases the active surface of the test devices was 1 cm in diameter, circumscribed by a 1.2 cm square (inside dimension) Si frame. The devices are mounted in a 1 cm light pipe which is fed with a pair of back to back Winston cones (4.5 mm^{2}sr or 14 mm^{2}sr) which serve to define the throughput of the incident radiation. The pair of cones was illuminated by a Fourier Transform Spectrometer. A 4K bolometer downstream of the test devices measured the transmitted radiation. Since this setup is inherently uncalibrated, all measurements are the ratio of the transmitted power with and without the test devices in the setup.

Below we describe results of this testing with emphasis on aspects related to the scaling of FSBs to THz frequencies.

Bolometer/Backshort Alignment

We have empirically demonstrated the importance of the modeled evanescent field coupling between the absorber and backshort layers to the passband shape by measuring actual FSBs with the bolometer intentionally misaligned with the backshort. As shown at left in Figure 3, misalignment of the surfaces causes significant deviations in the spectral behavior of the device. This set of empirical tests shows that for narrow transmission profiles the relative cross alignment must be better than $g/4$ where g is the periodicity of the cross array. For an FSB at 1.5 THz, $g/4 \sim 38\mu$m which should be straightforward to achieve under a microscope.

Scaleability of FSBs

To test the frequency range of the FSB production process a series of four prototype devices ranging from 0.2 to 1.1 THz was fabricated and tested in transmission. Model and measurement results are shown for these devices

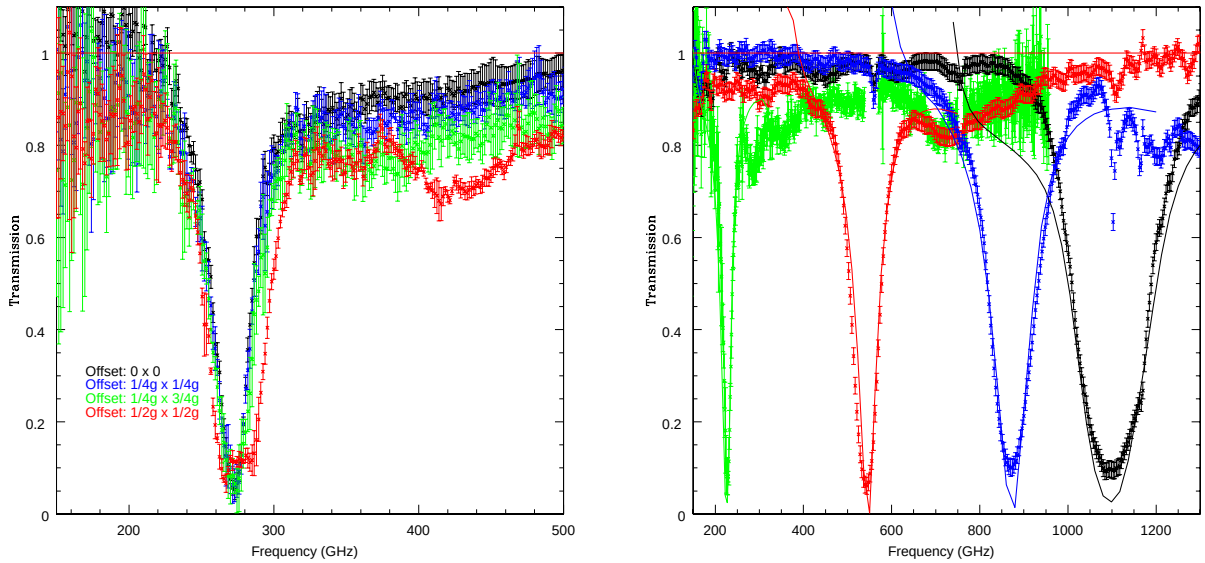

Figure 3. Left: Transmission of a 270 GHz FSB with four alignments of the bolometer and backshort layers. Significant deviation from the aligned case is seen for misalignments greater than $g/4$. Right: Transmission responses of FSBs tuned to different resonant frequencies from 0.2 to 1.1 THz.

in Figure 3. As expected, the transmission of the FSBs far from resonance approaches unity. Unfortunately, we were not aware of the importance of layer alignment at the time of measurement and the relative alignment of layers is nearly random. Thus, the asymmetry in the transmission between the low and high frequency sides of the resonance is likely due to misalignments though we can not yet rule out a contribution from additional mode coupling due to the finite optical opening angle of the lightpipe. Note however that the passband shapes shown in Figure 3 are already suitable for continuum measurements from balloon-borne platforms such as the EDGE experiment.

Qualitatively the predicted transmission of the FSBs matches the measured transmission closely through the resonance. The deviations between the model and the measurements illuminate the shortcomings of the model and the challenges of assembling FSBs at THz frequencies. Although it is possible to tweak individual models to better match the observed spectra, the power of the HFSS model is to predict the bandpass of many such FSBs without fabricating many prototype devices. By creating simulations, we are able to efficiently explore a wide range of parameters and designs for the optical behavior of future FSBs.

4. BOLOMETER DESIGN

In parallel with the optical prototype devices described above we have fabricated complete bolometer elements to test the thermal properties of the FSBs *independently* of their optical properties. This process included the development of a new approach to constructing TES sensors[10, 11] as well as new techniques to fabricate large free-standing membranes of silicon nitride. Figure 4 shows a prototype bolometer. Below we describe these prototype bolometers along with the challenges we are now working to overcome.

The cross arrays for both the bolometers and backshorts are in the same design as for the test pieces referred to in the previous section. The crosses are made of gold on a 0.5 μm silicon nitride substrate. The gold on the backshorts is 200 nm thick, to give high conductivity; on the bolometers it is 20 nm, which tunes it to optimum absorptivity. In both cases the gold is patterned using a lift-off process. This gives much sharper edge definition than a gold-etch process; the edge definition is important because the currents are highest near the edges of the gold and degradation of conductivity there would result in degradation of the passbands.

For the bolometers, the absorbing area must be partially thermally isolated from the frame temperature. This is achieved by a reactive ion etch of the silicon nitride film to cut it away from the frame except for four

narrow legs. In addition, because the thin nitride film tends to curl, additional support legs are formed to maintain an appropriate tension in the film.

The temperature of the absorber is sensed with TES sensors placed outside the optical path. The prototypes have two TES sensors located on opposite edges of the disk. The sensors are formed of Au/Mo. Our current prototypes use the Mo layer as the electrical leads, bolstered with additional sputtered Mo on top. The leads run down the support legs to the frame, where they terminate in bonding pads. The leads are the primary thermal conduction path from the disk to the frame, and are thus the primary contributor to the bolometer G.

Silicon nitride is not a very good thermal conductor, and this has led to some challenges in the prototype bolometers. In the classical model of a bolometer, the absorber disk is perfectly isothermal, and the bolometer can therefore be modeled as a heat capacity C connected to the thermal bath through a conductivity G. If the absorber is not isothermal, two general problems arise. First, if the conductivity across the disk is not much greater than the conductivity down the legs then the temperature signal at the TES is attenuated and the sensitivity is decreased. Second, if the characteristic thermal time constant of the disk is not short compared to the bolometer time constant there is additional thermal noise; in the literature this is often referred to as a "hanging heat capacity." A third problem more specific to our situation is that poor conduction across the disk leads to electrical response of the TES out to high post detection frequencies; if this response continues into the vicinity of $f \approx R/(2\pi L)$, where L is the SQUID inductance and R is the TES resistance, an instability occurs. These problems are exacerbated in our case by the fact that we are designing these bolometer for ground-based telescopes, where the high background environment forces a high G.

All three problems clearly could be resolved by using a different substrate with higher conductivity, such as Si. However, this would give up the advantage of the low optical impact of the various silicon nitride sheets in the optical path. To mitigate the problems described above in our prototypes, we are experimenting with a gold ring that outlines the optically active portion of the bolometer. This ensures that at least the part of the bolometer outside the optical path is isothermal. It of course does nothing about the first problem listed above, but potentially can solve the other two by adding enough heat capacity in contact with the TES to slow the devices down to the point where the "hanging heat capacity" will not contribute noise, and the SQUID instability is not reached. Note that, unlike traditional semiconducting bolometers, these devices are sufficiently fast due to their electrothermal feedback that one can choose to slow the devices by a factor of 10 without impacting operational performance at the telescope.

5. CONCLUSION

We have described recent progress in the modeling and implementation of frequency selective bolometers. The construction and characterization of prototype optical devices and of prototype bolometers has revealed non-

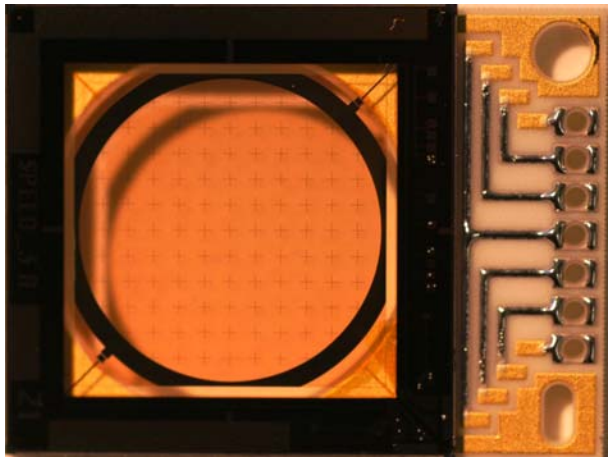

Figure 4. Photograph of an FSB bolometer layer.

intuitive characteristics of the devices which are now accounted for in the optical and thermal models. At present, there appears to be no significant roadblock to the implementation of FSBs at THz frequencies, though at some frequency above 1.5 THz we expect that the limitations in the lift-off process will limit the quality of the device passband.

ACKNOWLEDGMENTS

This work is supported by NASA grant S20052896400000 and the Five College Radio Astronomy Observatory under NSF grant AST-0228993. The FSB devices were fabricated using the exceptional facilities of the Detector Development Laboratory at NASA/GSFC.

REFERENCES

1. W. S. Holland, C. R. Cunningham, W. K. Gear, T. Jenness, K. Laidlaw, J. F. Lightfoot, and E. I. Robson, "SCUBA: a submillimeter camera operating on the James Clerk Maxwell Telescope," in *Proc. SPIE Vol. 3357, p. 305-318, Advanced Technology MMW, Radio, and Terahertz Telescopes, Thomas G. Phillips; Ed.*, pp. 305–318, July 1998.
2. J. Glenn, P. A. R. Ade, M. Amarie, J. J. Bock, S. F. Edgington, A. Goldin, S. Golwala, D. Haig, A. E. Lange, G. Laurent, P. D. Mauskopf, M. Yun, and H. Nguyen, "Current status of Bolocam: a large-format millimeter-wave bolometer camera," in *Millimeter and Submillimeter Detectors for Astronomy. Edited by Phillips, Thomas G.; Zmuidzinas, Jonas. Proceedings of the SPIE, Volume 4855, pp. 30-40 (2003).*, pp. 30–40, Feb. 2003.
3. C. D. Dowell, C. A. Allen, R. S. Babu, M. M. Freund, M. Gardner, J. Groseth, M. D. Jhabvala, A. Kovacs, D. C. Lis, S. H. Moseley, T. G. Phillips, R. F. Silverberg, G. M. Voellmer, and H. Yoshida, "SHARC II: a Caltech submillimeter observatory facility camera with 384 pixels," in *Millimeter and Submillimeter Detectors for Astronomy. Edited by Phillips, Thomas G.; Zmuidzinas, Jonas. Proceedings of the SPIE, Volume 4855, pp. 73-87 (2003).*, pp. 73–87, Feb. 2003.
4. M. J. Griffin, B. M. Swinyard, and L. G. Vigroux, "SPIRE - Herschel's Submillimetre Camera and Spectrometer," in *IR Space Telescopes and Instruments. Edited by John C. Mather. Proceedings of the SPIE, Volume 4850, pp. 686-697 (2003).*, pp. 686–697, Mar. 2003.
5. W. S. Holland, W. Duncan, B. D. Kelly, K. D. Irwin, A. J. Walton, P. A. R. Ade, and E. I. Robson, "SCUBA-2: a new generation submillimeter imager for the James Clerk Maxwell Telescope," in *Millimeter and Submillimeter Detectors for Astronomy. Edited by Phillips, Thomas G.; Zmuidzinas, Jonas. Proceedings of the SPIE, Volume 4855, pp. 1-18 (2003).*, pp. 1–18, Feb. 2003.
6. G. Wilson, T. C. Chen, E. S. Cheng, D. A. Cottingham, T. Crawford, D. J. Fixsen, F. M. Finkbeiner, D. W. Logan, S. Meyer, R. F. Silverberg, and P. T. Timbie, "Spectral energy distribution camera for the LMT," in *Millimeter and Submillimeter Detectors for Astronomy. Edited by Phillips, Thomas G.; Zmuidzinas, Jonas. Proceedings of the SPIE, Volume 4855, pp. 583-593 (2003).*, pp. 583–593, Feb. 2003.
7. D. A. Cottingham, A. Bier, B. Campano, T. C. Chen, E. S. Cheng, T. Crawford, F. M. Finkbeiner, D. J. Fixsen, D. W. Logan, S. Meyer, E. Sharp, R. F. Silverberg, and G. Wilson, "Development of frequency selective bolometers for ground-based MM-wave astronomy," in *Millimeter and Submillimeter Detectors for Astronomy. Edited by Phillips, Thomas G.; Zmuidzinas, Jonas. Proceedings of the SPIE, Volume 4855, pp. 192-200 (2003).*, pp. 192–200, Feb. 2003.
8. S. S. Meyer, E. S. Cheng, D. A. Cottingham, D. J. Fixsen, L. Knox, R. F. Silverberg, P. T. Timbie, and G. Wilson, "The EDGE Project," in *Airborne Telescope Systems II. Edited by Ramsey K. Melugin, Hans-Peter Roeser . Proceedings of the SPIE, Volume 4857, pp. 204-216 (2003).*, pp. 204–216, Feb. 2003.
9. B. Munk, *Frequency Selective Surfaces: Theory and Design*, John Wiley & Sons, Inc., 2000.
10. T. C. Chen, A. Bier, B. A. Campano, D. A. Cottingham, F. M. Finkbeiner, C. O'Dell, E. Sharp, R. F. Silverberg, and G. W. Wilson, "Development of molybdenum-gold proximity bilayers as transition edge sensors for the speed camera," in *Nuclear Instruments and Methods in Physics Research Section A: Accelerators, Spectrometers, Detectors and Associated Equipment*, 2003.

11. R. F. Silverberg, S. Ali, A. Bier, B. A. Campano, T. C. Chen, E. S. Cheng, D. A. Cottingham, T. M. Crawford, T. Downes, F. M. Finkbeiner, D. J. Fisxen, D. Logan, S. S. Meyer, C. O'Dell, T. Perera, E. Sharp, P. T. Timbie, and G. W. Wilson, "A bolometer array for the spectral energy distribution (speed) camera," in *Nuclear Instruments and Methods in Physics Research Section A: Accelerators, Spectrometers, Detectors and Associated Equipment*, 2003.

A Comparison of Device Characteristics of Mo/Au TES Bolometers with Different Normal Metal Bar Geometries

Johannes G. Staguhn,[a,b,*] Dominic J. Benford,[a] S. Harvey Moseley,[a] Christine A. Allen,[a] James A. Chervenak,[a] Thomas R. Stevenson,[a] Wen-Ting Hsieh[a,c]

[a] *NASA/Goddard Space Flight Center, Greenbelt, MD 20771, USA*
[b] *SSAI, 5900 Princess Garden Pkwy. Lanham, MD 20706, USA*
[c] *Raytheon ITSS, Forbes Blvd., Lanham, MD 20706, USA*

ABSTRACT

Recent efforts in the Transition Edge Sensor (TES) bolometer/calorimeter community have focused on developing detectors whose noise properties are near the fundamental limits. Those include the in-band phonon noise, the out-of-band Johnson noise, and the 1/f noise. We have investigated the noise performance of Mo/Au-bilayer TES bolometers designed for infrared detectors. These detectors use normal metal regions for the suppression of excess noise. A set of devices with variations in geometry were fabricated at the NASA/GSFC detector development facility. These detectors have different bilayer aspect ratios (providing differing normal state resistances and current densities), and have varieties of normal metal regions to study the effects of geometry on noise. These normal metal regions are oriented either parallel to or transverse to the directioon of current flow, or both. The lowest noise detectors are found to have normal metal regions oriented transversely. For about a dozen different devices, we have measured a large set of parameters by means of a suite of tests. These include complex impedance measurements to derive time constants; IV curves to determine resistance and power; thermal conductance measurements; noise measurements as a function of device resistance; and direct resistance vs. temperature measurements.

We compare the detailed noise measurement and quantitative analysis of the noise level in each device as a function of the detector resistance. The best detector design features only moderate excess noise in both the in-band region and in the out-of-band region.

INTRODUCTION

The development of large format (>100 element) cryogenic bolometer arrays is a requirement for future astronomical imaging and low resolution spectroscopy in the far-infrared and submillimeter. Recent research has led to a new approach to building arrays of many bolometers. Instead of a semiconducting thermistor, a superconducting transition edge sensor (TES) is used to read out the detector temperature. A TES bolometer has a faster response time than an identically-designed, same-sensitivity semiconducting bolometer (or a more sensitive bolometer for the same response time) due to the strong negative electrothermal feedback intrinsic in a voltage-biased TES [1]. TES bolometers are inherently low impedance devices, so they are well matched to being read out by DC SQUID amplifiers [2]. These amplifiers have a large noise margin over the TES Johnson noise and bolometer phonon noise. This permits the bolometer to be read out in a multiplexed fashion by a suitable SQUID multiplexer [3], potentially vastly reducing the amplifier size and the wire count. In light of these advantages, we have been developing the technologies for fabricating multiplexed superconducting TES bolometer arrays.

Attempts to find robust materials systems and fabrication methods for transition edge sensor (TES) microcalorimeters and bolometers have encountered differing amounts of noise magnitudes and functional dependences. The phonon-noise limit predicted for TES devices has been approached for certain devices and proved elusive to other designs [1]. The approaches that have been tried include a variety of materials, geometries, and fabrication techniques [2], [3]. These have resulted in constraints on bias conditions, quantum efficiency of photon detection, etc. Ideally, the

* Johannes Staguhn. Tel.: +1-301-286-7840; fax: +1-301-286-1617; e-mail: staguhn@stars.gsfc.nasa.gov.

mechanisms for noise in TES bolometers will be elucidated so that, for example, an imposed geometric ordering can quell the noise sources in more of the materials, independent of deposition method, film quality, etc. A less ideal situation would be a higher degree of constraints on materials, deposition techniques, or detector geometries. In this work, we have taken a system of materials that intrinsically has a large excess noise source. We have shown that certain geometries of normal metal boundary conditions imposed on the bilayer reduce the excess noise problems. This result may be relevant to other materials systems and detector geometries.

BOLOMETER DESIGN

The bolometers we have produced for our performance studies are based on a linear 1x8 design, using a pop-up-detector architecture first presented elsewhere [4] (Figure 1). The TES consists of a molybdenum and gold superconducting bilayers. Each pixel has a different Au normal metal bar geometry; two different 1x8 arrays were manufactured. The thermal conductivity G of these devices was about a factor of ten higher than in those devices produced for astronomical observations. A subset of the resultant 16 geometries is shown below in Figure 2. A description of the fabrication process is given elsewhere [5].

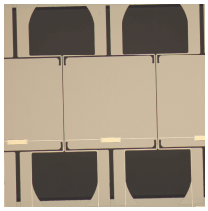

Figure 1. Photo of single bolometer in a linear 1 by 8 array.

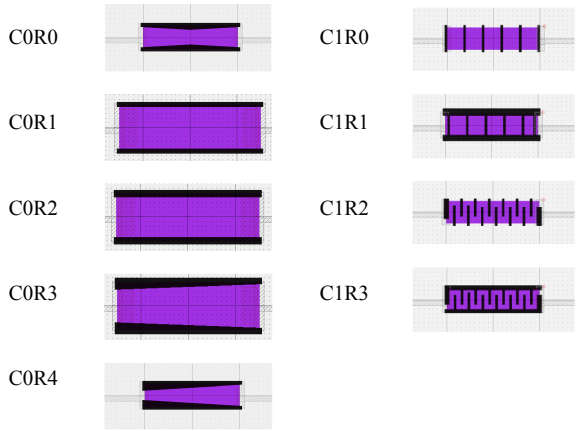

Figure 2. Devices tested to date, showing (L) lateral bars and (R) interdigitated transverse normal metal bars (black).

DEVICE CHARACTERIZATION

Several standard measurements were used to characterize the devices. These include: *a.* four-wire resistance vs. temperature measurements, with variable current excitation; *b.* current-voltage (IV) curves, with variable base temperatures; *c.* complex impedance measurements, with variable bias conditions, as described by Lindeman et al. [6]; *d.* noise measurements, with variable bias conditions. Some representative results of these measurements are tabulated in Table 1; We show below a sample of R(T), R vs. V, P vs. V, G(T), noise measurements, and Z(ω) measurements (Figure 3).

Devices from chip C0 have more uniformity of parameters, and sharper R(T) transitions. Devices labeled C1 have less sharp transitions and have less noise (Figure 4). A relation between sharpness of the transition and the amount of excess noise of TES was also observed elsewhere [7].

Table 1. Summary of measurements on TES bolometers.

Geometry	R_N [mΩ]	T_C [K]	α	$G(T_C)$ [W/K]	Bias Power [pW]	τ_e [ms]	Excess Noise†
C0R0	539	504.5	5506	$0.84 \cdot 10^{-9}$	61		~3.5×
C0R1	419	505.8	2771	$1.10 \cdot 10^{-9}$	65		~2.5×
C0R2	500	506.0	6787	$0.87 \cdot 10^{-9}$	63		~2.5×
C0R3	422	~490	-	$1.12 \cdot 10^{-9}$	52		~2.5×
C0R4	554	~490	-	$0.92 \cdot 10^{-9}$	60		~7.5×
C1R0	361	-	-	-	31		-
C1R1	212	436.1	89	-	30		-
C1R2	420	445.0	148	$0.44 \cdot 10^{-9}$	37		≤50%
C1R3	401	~435	-	$0.38 \cdot 10^{-9}$	35		≤50%

† Excess noise is estimated maximum noise level relative to the theoretical prediction, at any frequency in the range 100Hz-25kHz.

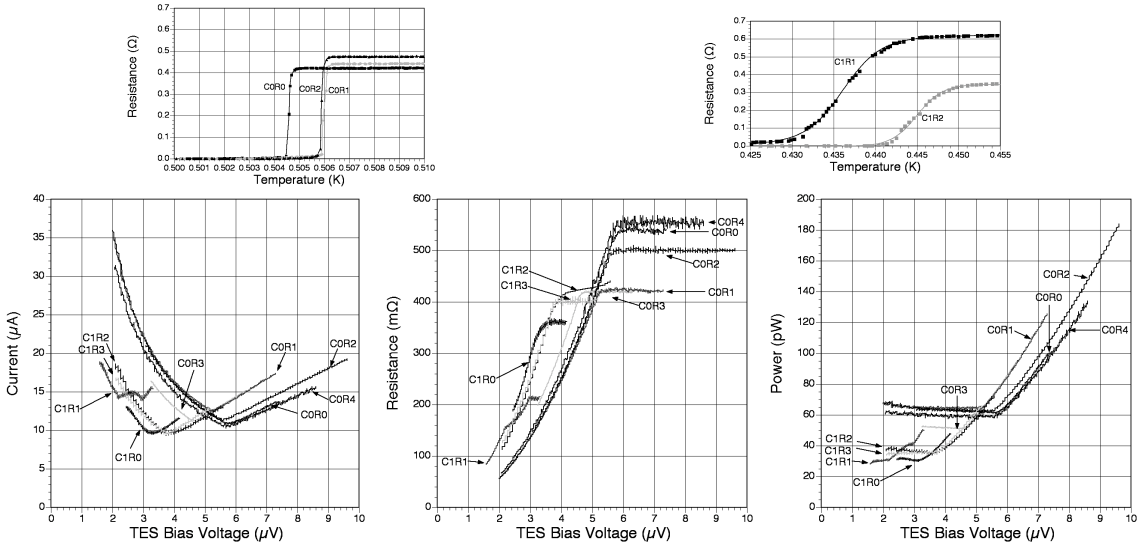

Figure 3. Measurements of devices, illustrating parameter variations.

NORMAL METAL BAR GEOMETRIES

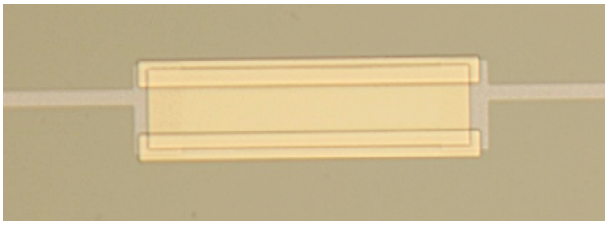

Figure 4. Photo of the Mo/Au TES with normal metal bars brighter at the edges along the direction of current flow. The length of the device is ~2 mm.

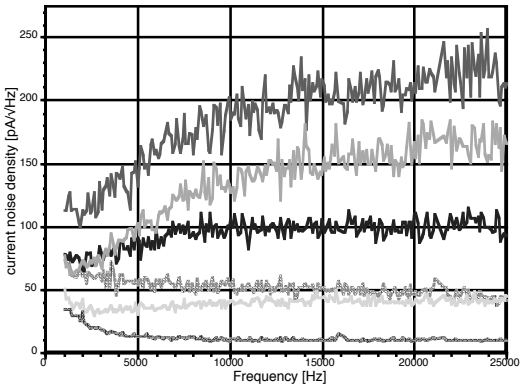

Figure 5. Measured current noise density of the bar device shown in Fig. 4. The solid lines are measurements on the transition, the darkness corresponds to a quasi-logarithmic magnitude of the bias current through the detector with TES resistance ranging from ~5 mΩ (dark) to ~ 300 mΩ (light grey). The light dashed line corresponds to the superconducting state, the dark dashed line shows the noise in the normal state.

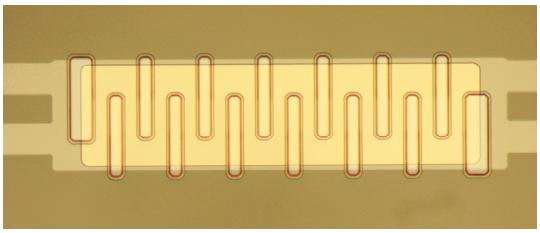

Figure 6. Photo of the Mo/Au TES with normal metal bars perpendicular to the current flow. The length of the device is ~2 mm.

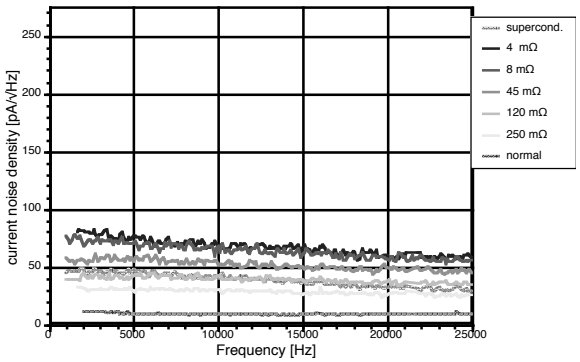

Figure 7. Measured current noise density of the "modified Zebra" device shown in Fig. 6.

By placing normal metal regions in the active region of the superconducting detector the boundary conditions for the superconducting order parameter can be constrained. Two ideas have circulated concerning the use of normal metal regions. NIST's normal metal edge conditions [8] and SRON's normal metal regions placed over the inner regions of the bilayer [9] are used to separate superconducting and normal regions. Until recently our group has used normal metal bars at the edge of the TES that are parallel to the current. The mask set used for those devices is similar to C0R2 in Figure 2. Figure 4 shows a picture of the tested device with this bar geometry. The noise measurements of the device in the superconducting state, on the transition and in normal state (the normal resistance of this device is 480 mΩ) are displayed in Figure 5. The significant excess in the out-of-band (> 4.5 kHz) noise in the data taken on the transition is

evident. Other parameters can be found in Table 1. Figure 6 shows a picture of our "modified Zebra" (C1R2 in Figure 1) with normal metal bars oriented perpendicular to the current flow direction. The device was fabricated on the same wafer as device C0R2. A drawback of a conventional "Zebra" detector, where the normal stripes span the width of the film, is the creation of parasitic normal resistance when biased low on the transition. Our "modified Zebra" pattern has attempted to utilize the boundary conditions imposed on the interior of the superconducting region of the detector without creating regions of parasitic normal resistance. Figure 7 shows the noise measurements for this device in the superconducting state, on the transition, and in the normal state (420 mΩ). A significant reduction in excess noise, particularly out-of-band noise, is observed. This indicates that the normal metal bar geometry confines regions driven normal by the bias current, and makes them sufficiently spaced to prevent interaction; hence it is an efficient method for excess noise reduction. The device shown in Figure 6 had a 400 Ω/square Bi film for broadband submillimeter absorption added, which did not result in the increase out-of-band excess noise. Figure 8 shows the fundamental noise expected for this device which was calculated by using the following parameters: T_{base}= 300 mK, T_c= 445 mK, R_{shunt} = 3.7 mΩ, R_{stray} = 3.7 mΩ, stray inductance L_{stray} = 55 nH, I_{SQUID_noise} = 6 pA/√Hz, and perfect electrothermal feedback on transition with an electrical time constant yielding a bandwidth of 6.0 kHz [10]. The excess in the measured noise of the "modified Zebra" device approaches a factor of two over the fundamental noise level only at the high resistance part of the transition where the fundamental noise of the TES is lowest.

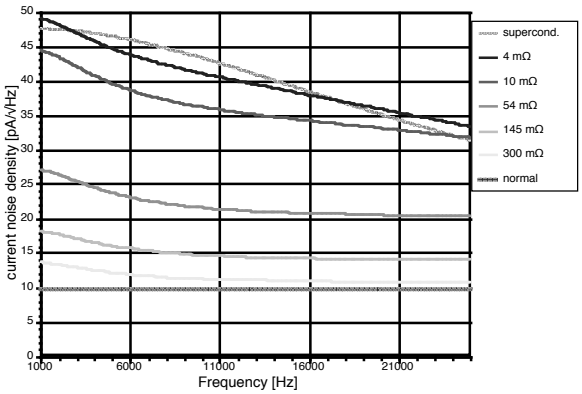

Figure 8. Theoretical noise of the device shown in Fig. 6. The parameters used for the calculations can be found in the text.

CONCLUSION AND OUTLOOK

One of the physical processes considered responsible for the creation of excess noise in TES is the random motion of superconducting and normal regions in these devices which creates a broadband noise source that appears as out-of-band excess noise. We have investigated methods for geometric ordering of the normal regions within the superconductor by means of depositing normal metal bars perpendicular to the current direction on dedicated devices. Indeed our measurements show that TES test devices with normal metal bars perpendicular to the current flow have significantly reduced excess noise as compared to devices with normal metal bars only deposited along the edges of the device. The reduction of noise goes along with a broadening of the transition, which, however, practically does not impact the performance of the TES. The new bilayer/normal metal bar design is being implemented in current and future astronomical instruments, including FIBRE [11], SPIFI [12], SAFIRE [13], and the GBT 3 mm camera [14]. We are furthermore improving our model of the tested devices by calculating the noise without the assumption of perfect electrothermal feedback on the transition close to the superconducting state. The excess noise model for the "modified Zebra" device will include a hanging heat capacity of the low T_c Mo leads (C_{Mo}/C_{TES} ~ 0.2). The superconducting boundary condition at the edge of this device may also create some excess noise. It is likely that further improvements in the TES design will allow the production of TES devices which will perform at the fundamental noise limit.

REFERENCES

[1] K.D. Irwin, APL 66 (15), 1995, 1998

[2] R.P. Welty & J.M. Martinis, IEEE Trans. On Applied Superconductivity 3 (1), 1993, 2605.
[3] K.D. Irwin et al., American Institute of Physics Conference Proceedings (AIP), 605, 301.
[4] D.J. Benford et al., IRMMW, 21 (12), 2000, 1909.
[5] J.A. Chervenak et al., 2004, Nuclear Instruments and Methods in Physics Research, Section A (NIMPA), 520, 460.
[6] M. Lindeman et al., 2003, submitted.
[7] Ullom, J. N. et al., 2004, ApPhL., 84. 4206
[8] Hilton, G. et al., 2001, IEEE Appl. Supercond., 11(1), 739.
[9] Bergmann Tiest, W.M., et al., 2002, American Institute of Physics conference Proceedings (AIP), 605, 199.
[10] Benford, D.J., et al., 2004, Nuclear Instruments and Methods in Physics Research, Section A (NIMPA), 520, 270.
[11] Staguhn, J.G. et al., 2003, SPIE, 4855, 11.
[12] Nikola, T. et al., these proceedings.
[13] Benford, D.J., Moseley, S.H., Shafer, R.A., Stacey, G.J., Staguhn, J.G., 2003, SPIE, 4875, 13.
[14] Benford, D.J. et al., these proceedings.

Tunable All-Solid-State Local Oscillators to 1900 GHz

John Ward, Goutam Chattopadhyay, Alain Maestrini [1], Erich Schlecht, John Gill,
Hamid Javadi, David Pukala, Frank Maiwald and Imran Mehdi

California Institute of Technology, Jet Propulsion Laboratory, MS 168-314,
4800 Oak Grove Drive, Pasadena, CA 91109

[1] Now at LISIF - Université Paris VI, 4, place Jussieu, 75252 Paris, France

ABSTRACT

We present a status report of an ongoing effort to develop robust tunable all-solid-state sources up to 1900 GHz for the Heterodyne Instrument for the Far Infrared (HIFI) on the Herschel Space Observatory. GaAs based multi-chip power amplifier modules at W-band are used to drive cascaded chains of multipliers. We have demonstrated performance from chains comprised of four doublers up to 1600 GHz as well as from a x2x3x3 chain to 1900 GHz. Measured peak output power of 23 μW at 1782 GHz and 2.6 μW at 1900 GHz has been achieved when the multipliers are cooled to 120 K. The 1900 GHz tripler was pumped with a four anode tripler that produces a peak of 4 mW at 630 GHz when cooled to 120 K. We believe that these sources can now be used to pump hot electron bolometer (HEB) heterodyne mixers.

I. INTRODUCTION

The Herschel Space Observatory is a 3.5 meter diameter passively-cooled telescope that will focus light onto three science instruments (PACS, SPIRE, and HIFI) to observe the cosmos from 450 to 5000 GHz (60 – 670 μm) [1]. Band 6 of the Heterodyne Instrument for the Far-Infrared (HIFI) [2] is a heterodyne spectrometer to cover 1410 to 1910 GHz. Four local oscillator chains operating at 120 K will each pump a pair of orthogonally-polarized HEB mixers. Table 1 provides a brief summary of the four local oscillator chains that will be required to cover this band.

When the development of heterodyne receivers for the Herschel Space Observatory was initiated, state-of-the-art submillimeter sources typically consisted of cascaded whisker-contacted Schottky-diode frequency multipliers driven by phase-locked Gunn oscillators [3,4]. Frequency tuning was achieved with mechanical tuners, and multipliers were mechanically fragile. Above about 900 GHz, the available power was too low to pump a mixer, and so compact solid-state sources gave way to FIR lasers. These lasers are massive, bulky, difficult to operate, require large amounts of power, and only operate at specific discrete frequencies. Thus, the recent development of tunable solid state THz sources represents a major advancement for the THz field.

The results presented here are for planar Schottky diode multipliers electronically tunable with about 10% bandwidth. Power amplifiers driven by commercial synthesizers produce 100 to 150 mW in the 70 to 106 GHz band [5,6]. One to four frequency doublers and/or triplers are cascaded after the W band source. All multipliers are balanced designs implemented with monolithic circuits mounted in split-waveguide blocks. The frequency doublers each have two parallel branches of diodes, while the triplers each have two anti-parallel branches. The low frequency multipliers (below 1 THz) use "substrateless" technology implemented with 1 to $2 \cdot 10^{17}$ cm^{-3} doped GaAs, while the multipliers above 1 THz are fabricated on 3 μm thick GaAs membranes with $5 \cdot 10^{17}$ cm^{-3} doped active layers [7-10]. The first stage multipliers have 3 anodes in series in each branch (for 6 anodes total), and the second stages have 2 series anodes in each branch (for 4 anodes total). All multipliers above 700 GHz have only 1 anode per branch, or 2 anodes per multiplier. Multipliers with output frequencies above 1 THz have diagonal horns integrated into the waveguide split blocks. Further details on the multiplier designs are given in [11]-[15]. A model of a complete chain is shown in Figure 1.

Band	Chain	Amp Freq.	Multiple	Output Freq.	Required Power
Band 6 Low	6a	88-99.5 GHz	x2x2x2x2	1414-1592 GHz	3 µW
	6b	92-106 GHz	x2x2x2x2	1472-1696 GHz	2.5 µW
Band 6 High	6c	94.6-106 GHz	x2x3x3	1704-1908 GHz	2.5 µW
	6d	94.6-106 GHz	x2x3x3	1704-1908 GHz	2.5 µW

Table 1. Frequency and configuration of the four local oscillator chains being developed for Band 6 of the HIFI instrument on the Herschel Space Observatory.

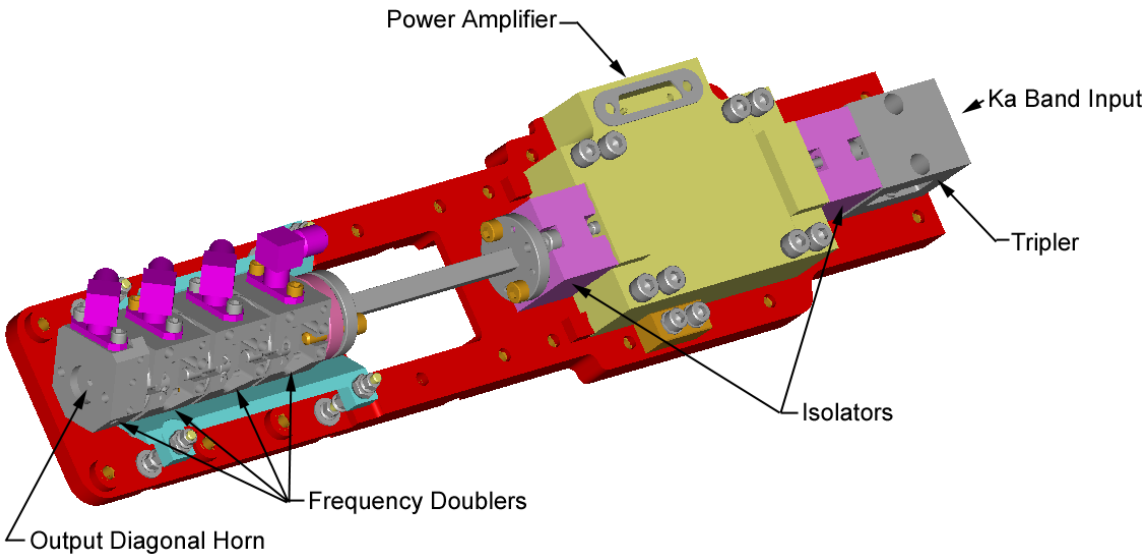

Figure 1. Model of a x2x2x2x2 local oscillator chain. The maximum envelope is smaller than 250x60x40 mm. The signal flows from right to left, with the output at the 48th harmonic of the Ka band input. The four frequency doublers are biased through SMA connectors.

II. MEASURED RESULTS

The measurements were performed at room temperature and at 120 K. The output power of the W band power amplifier was monitored with a directional coupler and power meter. A waveguide calorimeter [16] was calibrated with a DC load and used for all room temperature power measurements below 1.4 THz. A Keating meter was calibrated with a DC square wave and lock-in amplifier, and used for cryogenic power measurements below 1.4 THz. Above 1.4 THz, measurements were made optically with a Golay cell calibrated against the Keating meter. All optical measurements were corrected for the losses in Mylar windows, where applicable, but were not corrected for other optical losses including non-ideal mirror reflectivity and water vapor absorption. Waveguide measurements were not corrected for loss in the connecting waveguides between the device under test and the meter. A summary of typical measured efficiencies and output powers is given in Table 2.

A. 300 & 375 GHz Chains. Figure 2 shows preliminary 295 K results of a new 300 GHz chain consisting of two cascaded frequency doublers. This chain produced high power levels suitable for driving further stages of multiplication, such as a doubler to 600 GHz or a tripler to 900 GHz. The first stage doubler to 150 GHz has six planar anodes divided into two parallel branches and produced a peak of over 45 mW from 150 mW input. The second stage doubler to 300 GHz has four planar anodes divided into two parallel branches and produced a peak output power of nearly 10 mW at 292 GHz. Both devices are implemented with $1{\cdot}10^{17}$ cm^{-3} doped GaAs. We expect the output power of this chain to increase significantly when the multipliers are cooled.

Output Frequency	Multiple	Intended Use	Typical Efficiency	Typical Power
176 – 199 GHz	2	Chain 6a, stage 1	30%	30 mW
352 – 398 GHz	2	Chain 6a, stage 2	* 15%	* 4.5 mW
704 – 796 GHz	2	Chain 6a, stage 3	* 8%	* 400 µW
1408 – 1592 GHz	2	Chain 6a, stage 4	4%	30 µW
184 – 212 GHz	2	Chain 6b, stage 1 Band 6 high, stage 1	30%	30 mW
368 – 424 GHz	2	Chain 6b, stage 2	20%	6 mW
736 – 848 GHz	2	Chain 6b, stage 3	10%	1 mW
1472 – 1696 GHz	2	Chain 6b, stage 4	Not demonstrated	
552 – 636 GHz	3	Band 6 high, stage 2	9%	3 mW
1704 – 1908 GHz	3	Band 6 high, stage 3	0.3%	10 µW
152 – 159 GHz	2	Not used	* 27%	* 40 mW
304 – 318 GHz	2	Not used	* 20%	* 8 mW

Table 2. Typical measured efficiencies and output powers demonstrated with moderate bandwidth. The temperature was 120 K unless noted with an asterisk (*), in which case the measurements were performed at room temperature. W band input power ranged from 100 to 150 mW. In all cases the best measured peak efficiencies and powers were significantly higher than the values listed here.

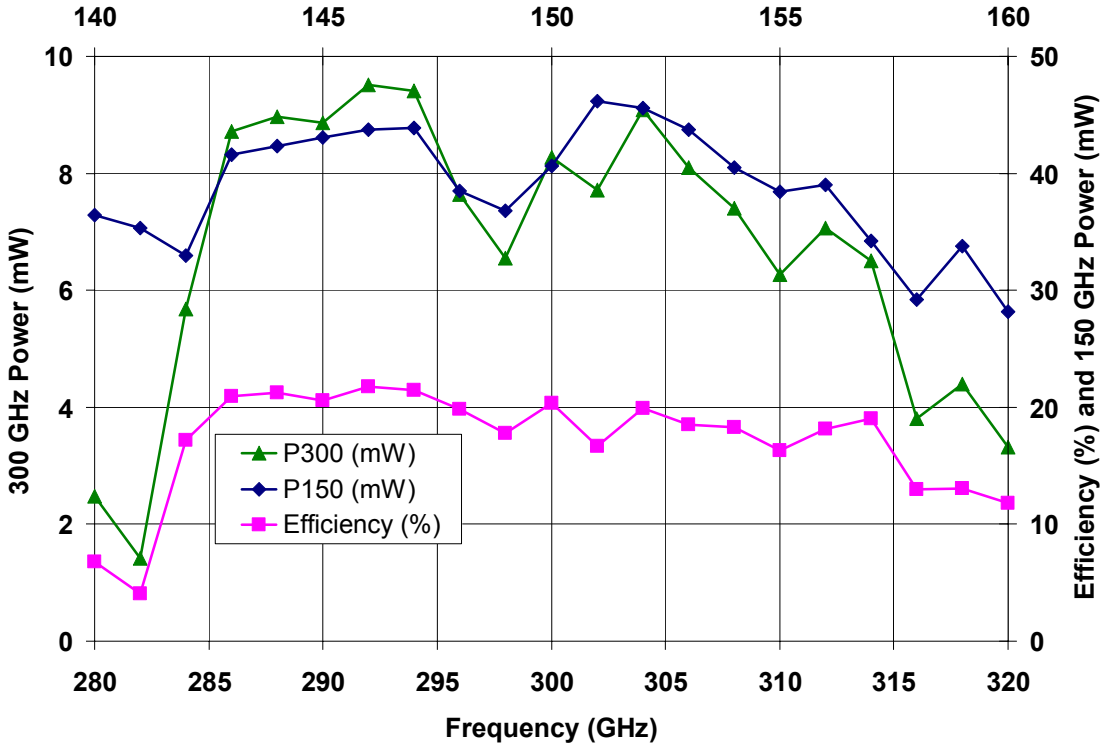

Figure 2. Measured room temperature performance of 150 and 300 GHz balanced doublers. The power of the 70-80 GHz input was 150 mW.

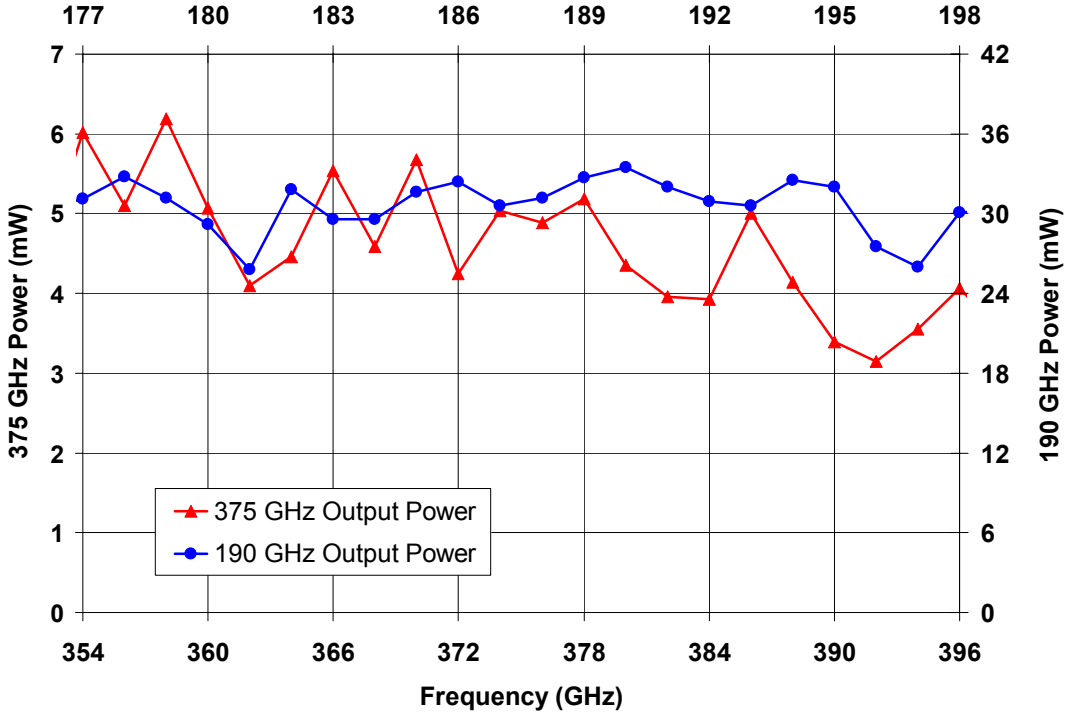

Figure 3. Measured room temperature performance of 190 and 375 GHz balanced doublers. The power of the 88.5-99 GHz input was 100 mW.

Figure 3 shows recent 295 K measurements of a chain to 375 GHz. Like the 300 GHz chain shown in Figure 2, both doublers are implemented with $1 \cdot 10^{17}$ cm^{-3} doped GaAs, with six anodes in the first stage to 190 GHz and four anodes in the second stage to 375 GHz. The drive power in the 88 to 99 GHz band was 100 mW. The efficiency of the first stage is flat to better than ±0.6 dB.

B. 600 GHz Tripler. Early in this project, it was recognized that for a local oscillator chain to produce adequate power at 1.9 THz to pump a pair of orthogonally-polarized mixers, the power produced by the lower frequency driver multipliers must be as high as possible. With this requirement in mind, a novel four-anode tripler to 600 GHz was designed to drive a final tripler covering the 1.7-1.9 THz band. Dividing the drive power across four anodes effectively doubles the power that can be safely handled by the multiplier as compared to previously-existing two-anode balanced triplers; an overview of the failure mechanisms of Schottky varactor multipliers and what limits the maximum safe power is given in [17]. Figure 4 shows the device mounted in the waveguide block with a close-up of the anode region. It can be seen from Figure 5 that the performance of these triplers is very uniform among units. The 295 K measurements were made with about 23 mW of drive power in the 200 GHz band. The efficiency is in the 4 to 8% range. The performance improves dramatically with cooling, with 120 K peak output power of 4 mW at 630 GHz and efficiency ranging from 7 to 13%. Detailed information about this design will be given in [18].

C. THz Chains. Figure 6 shows the current performance of the flight-like multiplier chains for all of Band 6. Although significantly higher peak power has been produced around 1.5 THz, the performance displayed for the 6a chain was optimized for bandwidth and reliability. The curves above 1.7 THz are for x2x3x3 chains including a 600 GHz tripler as shown in Figures 4 and 5 and a 1900 GHz tripler described in [19]. Peaks of 24 μW at 1780 GHz and 9 μW at 1820 GHz represent the highest power measured to date for solid state sources. The authors believe that with continued effort the power above 1820 GHz can be substantially increased.

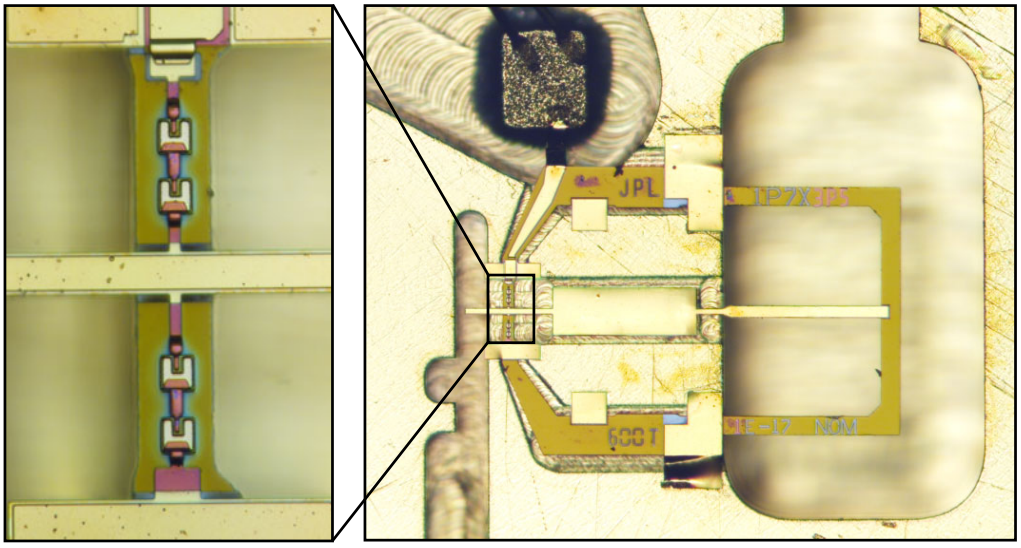

Figure 4. A four anode balanced 600 GHz tripler. The device is about 1 mm long. The 200 GHz input signal enters from the upper right. Four diodes lie near the output waveguide to the lower left. A frame minimizes the amount of GaAs in the channel between the input and output waveguides. The four anodes are biased in series from the discrete capacitor to the upper left.

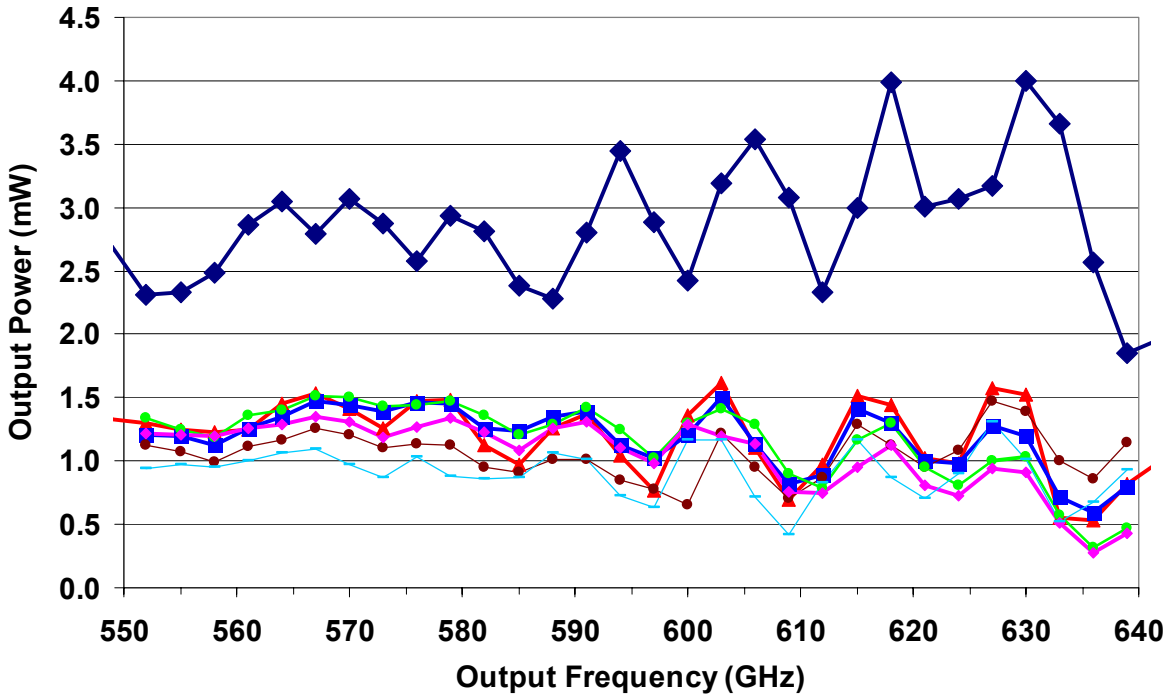

Figure 5. Measured performance of six different 600 GHz triplers. The lower family of curves was measured at room temperature with about 23 mW of input power in the 200 GHz band. The upper curve shows the 120 K performance of one of these units when the chain was driven with 150 mW at W band. The ripple is caused by interaction between the two stages of multiplication.

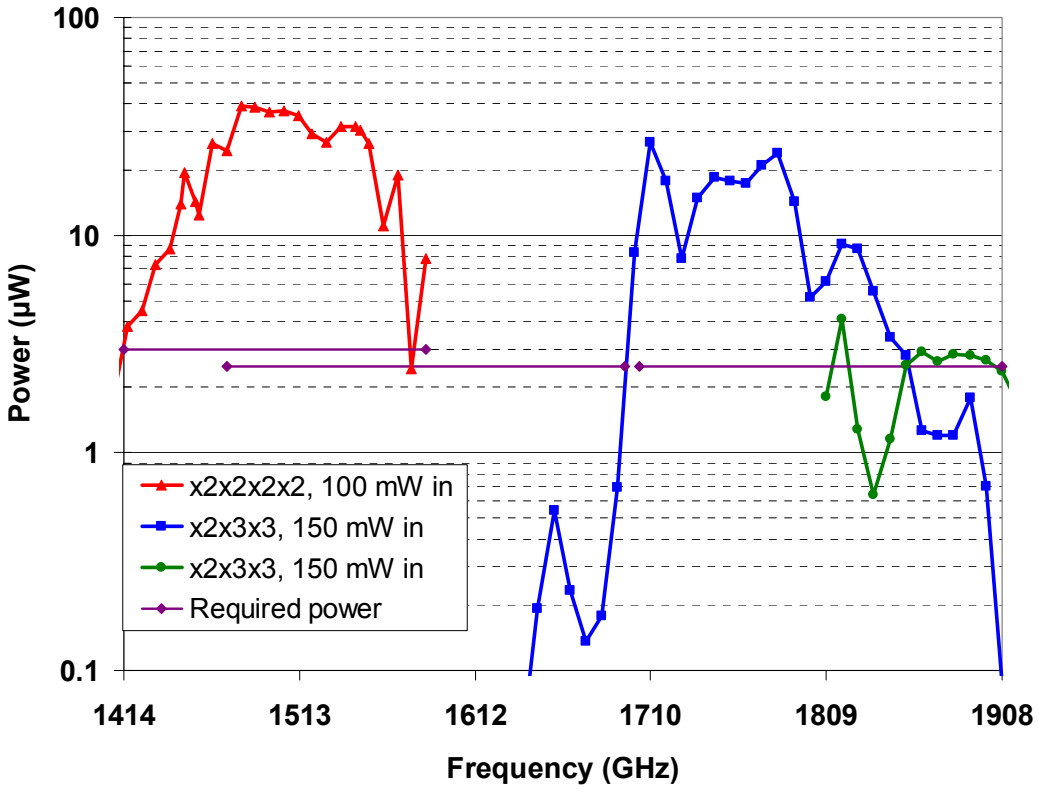

Figure 6. Results measured at 120 K. For comparison, reported measurements of the optimum LO power incident on the HEB mixer lens at these frequencies ranges from about 0.2 to 1 μW [20,21]. The required power of 2.5 to 3 μW shown in this figure is expected to be adequate to pump two mixers with orthogonal polarizations with a single LO chain, and to compensate for all optical losses in the system including beam mismatch, diplexer loss, etc.

III. CONCLUSIONS

Solid-state, electronically tunable, broadband sources suitable for use as local oscillators in heterodyne receivers have been demonstrated up to 1908 GHz. These sources are flight qualified, and have been optimized to be compact, low mass, low power, tunerless, and mechanically robust. A novel four-anode frequency tripler has produced 4 mW at 630 GHz, and 24 μW of continuous power was produced by a x2x3x3 chain at 1.78 THz. Three-quarters of the 1414-1908 GHz band has been demonstrated with output power over 2.5 μW. Remaining challenges include filling in a gap in frequency coverage from 1580 to 1700 GHz.

ACKNOWLEDGEMENTS

The authors wish to acknowledge the significant contributions of Ray Tsang, Robert Lin, Brad Finamore, William Chun, Luis Amaro, Alex Peralta, Ed Luong, and Jim Velebir. We also thank Peter Bruneau, James Crosby, and Hal Janzen for the superb fabrication of the many high frequency waveguide blocks needed for this project. Technical discussions with Neal Erickson of the University of Massachusetts are gratefully acknowledged. Finally, this work would not have been possible without the continued support of John Pearson and Peter Siegel. The research described in this publication was performed at the Jet Propulsion Laboratory, California Institute of Technology, under a contract with the National Aeronautics and Space Administration.

REFERENCES

[1] G.L. Pilbratt, "The Herschel Mission, Scientific Objectives, and this Meeting," Proceedings of The Promise of the Herschel Space Observatory Symposium, 12-15 December 2000, Toledo, Spain, eds. G. L. Pilbratt, J. Cernicharo, A. M. Heras, T. Prusti, R. Harris, ESA SP-460, pp. 13-20, 2001.

[2] N. D. Whyborn, "The HIFI Heterodyne Instrument for FIRST: Capabilities and Performance," Proc. ESA Symp., The Far Infrared and Submillimetre Universe, ESA SP-401, 1997.

[3] John E. Carlstrom, Richard L. Plambeck, and D. D. Thornton, "A Continuously Tunable 65-115 GHz Gunn Oscillator," IEEE Transactions on Microwave Theory and Techniques, Vol. MTT-33, No. 7, July 1985.

[4] Neal Erickson, "High Efficiency Submillimeter Frequency Multipliers," IEEE MTT-S Digest, 1990.

[5] H. Wang, et al., "Power-Amplifier Modules Covering 70-113 GHz using MMICs," IEEE Trans. Microwave Theory and Techniques, vol. 49, pp. 9-16, 2001.

[6] Robert R. Ferber, John C. Pearson, Todd C. Gaier, Lorene A. Samoska, Frank W. Maiwald, Mary Wells, April Campbell, Gerald Swift, Paul Yocom, and K. T. Liao, "W-Band MMIC Power Amplifiers for the Herschel HIFI Instrument," Proceedings of the Fourteenth International Symposium on Space Terahertz Technology, Tucson, 22 April 2003.

[7] S. Martin, B. Nakamura, A. Fung, P. Smith, J. Bruston, A. Maestrini, F. Maiwald, P. Siegel, E. Schlecht and I. Mehdi, "Fabrication of 200 GHz to 2700 GHz Multiplier Devices Using GaAs and Metal Membranes," IEEE MTT-S International Microwave Symposium, Phoenix, Arizona, May 20-25, 2001.

[8] A. Maestrini, J. Bruston, D. Pukala, S. Martin and I. Mehdi, "Performance of a 1.2 THz Frequency Tripler Using a GaAs Frameless Membrane Monolithic Circuit", Proceedings of the IEEE MTT-S, Vol. 3, pp. 1657-1660, Phoenix, Arizona, May 20-25, 2001.

[9] E. Schlecht, J. Bruston, A. Maestrini, S. Martin, D. Pukala, R. Tsang, A. Fung, R. P. Smith, I. Mehdi, "200 and 400 GHz Schottky Diode Multipliers Fabricated with Integrated Air-Dielectric 'Substrateless' Circuitry," Proceedings of the Eleventh International Symposium on Space Terahertz Technology, Ann Arbor, Michigan, May 2000.

[10] J. Bruston, S. Martin, A. Maestrini, E. Schlecht, P. Smith, and I. Mehdi, "The Frameless Membrane: a Novel Technology for THz Circuits," Proceedings of the Eleventh International Symposium on Space Terahertz Technology, Ann Arbor, Michigan, May 2000.

[11] G. Chattopadhyay, E. Schlecht, J. Gill, S. Martin, A. Maestrini, D. Pukala, F. Maiwald, and I. Mehdi, "A Broadband 800 GHz Schottky Balanced Doubler," IEEE Microwave and Wireless Components Letters, vol. 12 no. 4, pp. 117-118, April 2002.

[12] E. Schlecht, G. Chattopadhyay, A. Maestrini, A. Fung, S. Martin, D. Pukala, J. Bruston and I. Mehdi, "200, 400 and 800 GHz Schottky Diode 'Substrateless' Multipliers: Design and Results," IEEE Int. Microwave Symp. Digest, pp. 1649-1652, Phoenix, Arizona, May 2001.

[13] A. Maestrini, J. Ward, John Gill, G. Chattopadhyay, F. Maiwald, K. Ellis, H. Javadi, and I. Mehdi, "A Planar-Diode Frequency Tripler at 1.9 THz," Proceedings of the IEEE MTT-S, Philadelphia, Pennsylvania, June 8-13, 2003.

[14] G. Chattopadhyay, E. Schlecht, J. Ward, J. Gill, H. Javadi, F. Maiwald, and I. Mehdi, "An All Solid-State Broadband Frequency Multiplier Chain at 1500 GHz," IEEE Transactions on Microwave Theory and Techniques, vol. 52, no. 5, pp. 1538-1547, May 2004.

[15] A. Maestrini, J. Ward, J. Gill, H. Javadi, E. Schlecht, G. Chattopadhyay, F. Maiwald, N. Erickson, and I. Mehdi, "A 1.7 to 1.9 THz local oscillator source," IEEE Microwave and Wireless Components Letters, vol. 14 no. 6, June 2004.

[16] N. Erickson, "A Fast and Sensitive Submillimeter Waveguide Power Sensor," Tenth International Symposium on Space Terahertz Technology, pp. 501-507, Charlottesville, VA, 1999.

[17] F. Maiwald, E. Schlecht, R. Lin, J. Ward, J. Pearson, P. Siegel, and I. Mehdi, "Reliability of cascaded THz frequency chains with planar GaAs circuits," Proceedings of the Fifteenth International Symposium on Space Terahertz Technology, Northampton, MA, April 2004.

[18] A. Maestrini, J. Ward, J. Gill, H. Javadi, E. Schlecht, C. Tripon-Canseliet, G. Chattopadhyay, and I. Mehdi, "A 540-640 GHz High Efficiency Four Anode Frequency Tripler," submitted to the IEEE Transactions on Microwave Theory and Techniques.

[19] A. Maestrini, J. Ward, J. Gill, G. Chattopadhyay, F. Maiwald, K. Ellis, H. Javadi, and I. Mehdi, "A Planar-Diode Frequency Tripler at 1.9 THz," To appear in the 2003 IEEE MTT-S International Microwave Symposium Digest, 2003.
[20] J. Baselmans, M. Hajenius, J. Gao, P. de Korte, T. Klapwijk, B. Voronov, and G. Gol'tsman, "NbN phonon cooled hot electron bolometer mixers with improved interfaces: noise temperature and LO power requirement," Proceedings of the Fifteenth International Symposium on Space Terahertz Technology, Northampton, MA, April 2004.
[21] S. Cherednichenko, P. Khosropanah, T. Berg, H. Merkel, E. Kollberg, V. Drakinskiy, B. Voronov, and G. Gol'tsman, "Optimization of HEB mixer for the Herschel Space Observatory," Proceedings of the Fifteenth International Symposium on Space Terahertz Technology, Northampton, MA, April 2004.

Reliability of cascaded THz frequency chains with planar GaAs circuits

Frank Maiwald, Erich Schlecht, Robert Lin, John Ward, John Pearson, Peter Siegel, and Imran Mehdi

Jet Propulsion Laboratory, California Institute of Technology, MS 168-314, 4800 Oak Grove Drive, Pasadena, CA 91109

Abstract — **Planar GaAs Schottky diodes will be utilized for all of the LO chains on the HIFI instrument for the Herschel Space Observatory. A better understanding of device degradation mechanisms is desirable in order to specify environmental and operational conditions that do not reduce device life times. Failures and degradation associated with ESD (Electrostatic Discharge), high temperatures, DC currents and RF induced current and heating have been investigated. The goal is to establish a procedure to obtain the safe operating range for a given frequency multiplier.**

1. Introduction

Planar GaAs Schottky devices have been developed for fixed-tuned broadband frequency doublers and triplers [1-4] with output frequencies ranging from 140 to 1900 GHz for the Heterodyne Instrument for Far-Infrared (HIFI) on the Herschel Space Observatory (HSO). In order to obtain satisfactory amounts of RF power especially at the high end of this spectrum, it is important to pump the first multiplier stage in a cascaded chain with 100-200 mW of power. These power levels are now available due to recent developments in W-band power amplifiers [5]. For instance, for a cascaded chain to 1200 GHz, the 200 GHz stage is pumped with 100 to 200 mW at WR-10 band, the 400 GHz stage with 30 to 50 mW, and the final stage with 3 to 10 mW. For the purpose of space qualification, a solid understanding of the risks associated with diode failures has to be achieved. Therefore, the reliability of planar GaAs Schottky diodes has been systematically investigated with the goal to define guidelines for determining the safe operating range of varactor diode frequency multipliers.

The work described in this paper is based on the investigation of various failure mechanisms that might occur in the device based on environmental and operational conditions. In most cases there is no redundancy in the LO chains and thus a failure of one device represents a single point failure causing that whole frequency band to be non-operational. It is also important to understand these failure mechanisms so that environmental and operational precautions can be appropriately placed to mitigate risk.

Failure mechanisms associated with ESD, high temperatures, and current (both DC and RF) have been investigated in some detail. Our investigations into these failure modes will now be presented in some detail. However, it should be kept in mind that the goal of this study is to establish a safe operating range for the HIFI diodes in particular and to establish some general procedures that can be used as guidelines for any given frequency multiplier.

2. Degradation due to Electrostatic Discharge (ESD)

ESD is perhaps the single most common failure mechanism in high frequency diodes. This is unfortunate since this risk is also quite easily mitigated by sound engineering procedures. For a quantitative analysis, the ESD susceptibility of five planar GaAs devices was measured in forward as well as in reverse bias for a number of different dopings. The ESD measurement was performed with a human body model (HBM) ESD simulator circuit, based on MIL-STD-883 Method 3015.7 [6]. The HBM is modeled by a 100 pF capacitor discharging through a switching device and a 1500 ohm resistor in series to the DUT (Device Under Test). The discharge produced a double exponential waveform with a rise time of 25 ns and a pulse-duration of approximately 250 ns. This test simulated the conditions when ESD sensitive hardware is handled without protection, such as proper grounding of operator and hardware. The ESD voltage pulse was increased in steps of 10 V or 20 V in the forward direction and –5 V or -10 V in the reverse direction. After each ESD pulse the diode voltage for ± 1 μA was measured. A failure was defined as a 10% change in this voltage in either direction.

A comparison between pulses in the forward and reverse direction indicated that the device is more susceptible to pulses in the reverse direction, consistent with results reported for large area Schottky diodes [7]. In forward a nominal

diode can withstand ESD pulses that were 2 to 4 times higher than reverse. However, since it is impossible to predict the ESD pulse polarity the upper limit is taken to be the pulses in the reverse direction. The voltage magnitude that results in damaging the diode (in reverse) for a number of different dopings is shown in Figure 1(a). After the failure of the device (as defined above), an inspection at 500x magnification of the individual anodes showed no visual evidence of damage. The damage to the device is probably due to localized heating under the anode metallization or metal migration. Since the devices are extremely sensitive to ESD, they have to be classified as Class I ESD Sensitive Devices per MIL-STD-883. In order to mitigate the ESD risk, the implementation of sound engineering practices such as proper grounding, ESD safe working space and elimination of ground loops is highly recommended. A number of possible approaches can be used to reduce sensitivity to ESD [8].

A possible filter circuit that consists of two RC filters in series is shown in Figure 1 (b). The capacitors also help to reduce high frequency noise on the bias line. When biased through this circuit the diode was able to withstand ESD pulses up to 2000 V (upper limit reached by measurement apparatus), as shown in Figure 1(c).

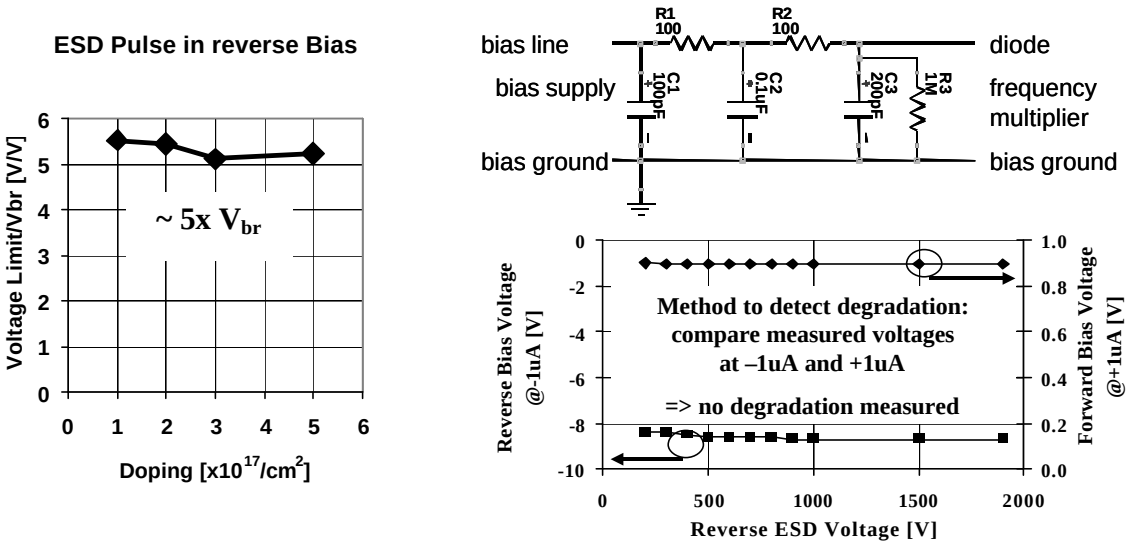

Figure 1: (a) ESD pulse magnitude in the reverse direction (normalized to the breakdown voltage) is plotted as a function of doping for onset of degradation. (b) T*he circuit diagram of the filter used to suppress ESD shock, and (c) the measured peak ESD pulse voltage for both positive and reverse directions when the ESD is applied through the protection circuit.*

3. Temperature induced failures

Metal diffusion into the semiconductor can degrade diode performance. High temperature, high electric fields or a combination of the two can accelerate this process. A quantitative analysis of thermally activated failures can be done by measuring time-to-failure (MTTF) for these devices at different elevated temperatures. The observed failure times are plotted on an Arrhenius plot allowing one to extrapolate mean-time-to-failure for any given operational temperature.

In earlier experiments, the activation energy of similar GaAs Schottky diodes was estimated to be between 0.6 and 1.2 eV [9]. The mission lifetime specification for HIFI is about 1500 operational hours at 120 K ambient temperature, but with RF power the devices will be heated to higher temperatures. Thermal modeling (to be discussed below) shows that the device will never experience temperatures above 350 K when operated at 120 K ambient. By conservatively assuming an activation energy of 0.5 eV, we can plot the required mission lifetime as a function of diode temperature. This is shown in Figure 2. Multiplier diodes from the most recent batches to be used for HIFI were tested for times-to-failure at 220 °C, 225 °C, and 250 °C. The failure criteria were defined as a change relative to the pre-test value of more than 15% of the ideality constant η, 20% of series resistance R_s, 20% of forward bias voltage (V_0) at +1 μA, or 50% of reverse bias voltage (V_{br}) at –1 μA. Results from these long-term failure tests are plotted in Figure 2. Figure 2a shows that the measured MTTF for JPL GaAs Schottky diodes is greater than five times the required mission lifetime. More-

over, many tests did not result in any failures even at 10 times the mission lifetime. Times tested for diodes without any failures are shown in Figure 2b. However, it is important to state that these tests were done without the presence of any DC or RF power and are thus more akin to measuring the shelf life of the diodes. To determine more realistic operational MTTF times for these diodes it is important to determine the hottest point of the chip in the presence of RF power.

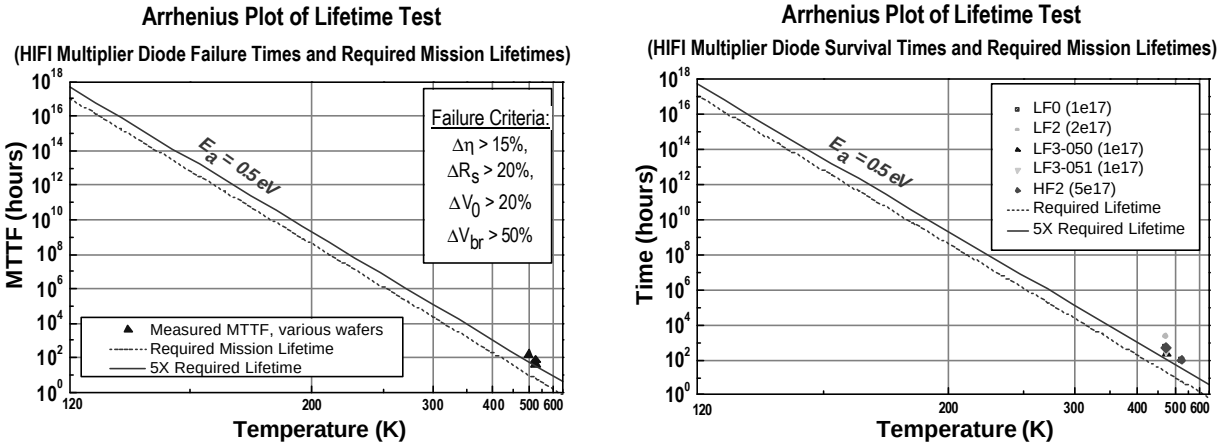

Figure 2: Results from lifetime tests of JPL diodes at 200C, 225C, and 250C. (left) Failure time, (right) Survival time.

A simple model was used to predict the heating of the chip due to RF [2]. This model is based on the topology of the diode chip and uses a temperature dependent thermal conductivity of GaAs, since GaAs devices are susceptible to thermal runaway problems. A preliminary verification of the diode thermal model was done by mounting a varactor device in a open waveguide block, biasing with DC current that mimics RF induced heating and measuring the temperature rise of the chip via a recently available infrared camera with a spatial resolution of 2.8 μm (15x lens) [10]. This measurement closely matched our predicted results based on the simple model.

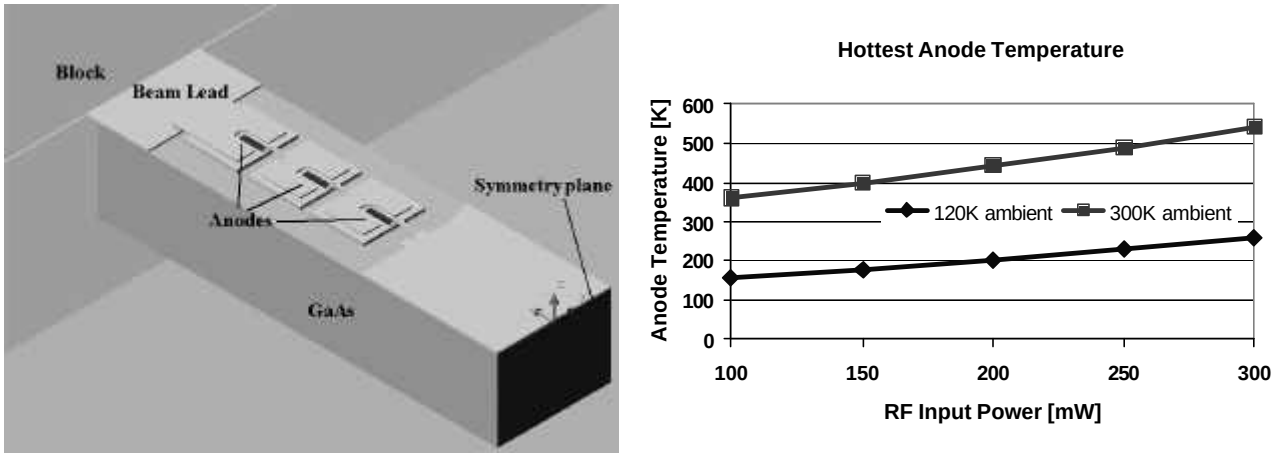

Figure 3: *Schematic of one-half of a nominal 200 GHz doubler chip used for the thermal analysis. The predicted temperature of the hottest anode on the chip is plotted as a function of input power. The multiplier is assumed to be 25% efficient in converting the input power to the output power. It was assumed that the rest of the power is dissipated equally by the six anodes on the chip.*

Based on the simple model one can now determine the operational lifetime of the diodes based on the hottest temperature point on the chip. For 150 mW of pump power the hottest anode temperature is determined to be 400 K

when the block temperature is at room temperature. This would indicate that the expected lifetime would be ~ 300 days. However, when the block temperature is set to 120 K (operational temperature for HIFI) the expected temperature of the hottest anode is only 177 K assuming 150 mW of input power. This would indicate that the lifetime of the diodes would be in excess of 1 million years, significantly higher than the mission lifetime.

Use of the MTTF given from the Arrhenius plot is helpful in increasing the confidence that one can place in the integrity of the device fabrication process. Process degradations such as lack of diffusion barriers, impurities, and infant mortality can be exposed by such experiments. However, accurate device thermal modeling is needed to determine the actual device temperature and this should be used to extrapolate the MTTF for the given device.

4. DC current induced damage

DC current-voltage characteristics are the most widely used health check for Schottky diodes. However, it is often not obvious what current maximums can be applied without fear of degradation. For each wafer lot, five devices were selected for the forward current ramp test, and five additional devices for the reverse current ramp test. For each device the I-V characteristic was measured before each incremental step in the current ramp. The current was iteratively increased by 0.5 mA in forward and by 0.010 mA in reverse with a dwell time of 2 minutes. The test continued until a catastrophic failure was detected. The failure was defined by a change of more than 50% on any of the DC parameters, i.e., ideality factor η, series resistance R_s, turn-on or forward voltage V_f(1 μA), and reverse voltage V_r(-1 μA).

The current density resulting in diode failure in the forward direction is shown in Figure 4(a) as a function of doping. The allowable current density increases drastically with doping. The measured maximum of the forward DC current is limited by the diode's ability to dissipate heat. Bias conditions below these limits guarantee that the diode will not be damaged. To be safe, the highest nominal current density in the forward bias direction was selected as 0.5 mA/μm^2, which is about one tenth of the value that results in damage. It is also highly recommended that the I(V) curve of the diode be measured in a pulsed mode to avoid the measurement being tainted by self heating.

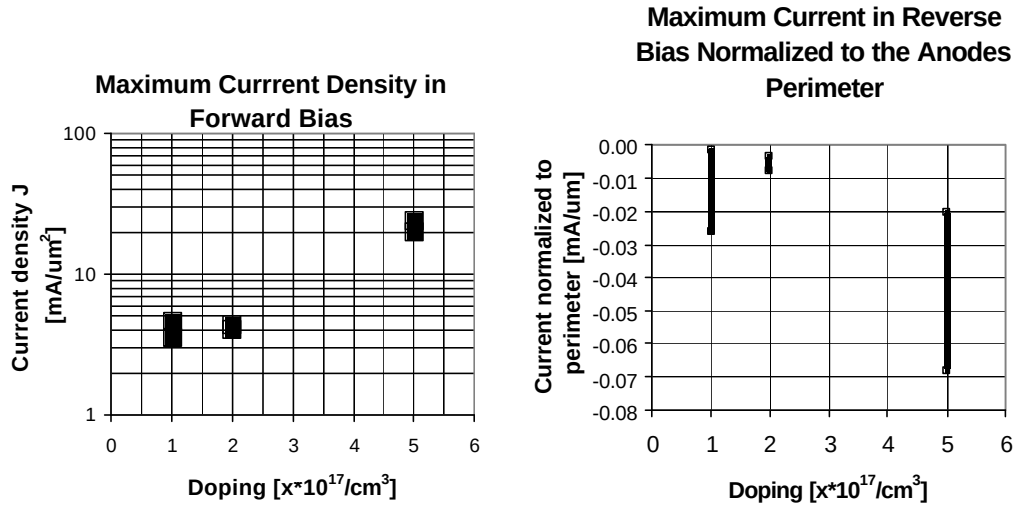

Figure 4*: (left) The current density in the forward direction that results in device degradation is plotted as a function of doping. (right) The reverse current that results in degradation is plotted normalized with respect to diode periphery. In both cases multiple data points are measured for each doping.*

In the reverse direction, due to the high electric field it is expected that most of the current will pass through the diode periphery rather than the diode area. This was confirmed by matching the actual measured reverse currents to a current model that takes into consideration the current through the diode periphery. This phenomenon is also well

documented for FET devices [11] and GaAs diodes [12]. The current per unit periphery for different dopings is shown in Figure 4(b). The large variation in the measured diode indicates that the actual current through the anode perimeter is very sensitive to microscopic variations in the anode/GaAs and passivation/GaAs interfaces. Even small amounts of currents in the reverse direction can permanently alter the device I(V). However, breakdown voltage is often quoted as an important device characteristic and it is necessary to pass reverse current to measure this voltage. It has been shown that the device I(V) is sensitive to both the magnitude as well as the duration of the reverse current [13], thus it is recommended to define the breakdown voltage for very small reverse currents (less than 0.01mA/μm) and to not excessively measure the breakdown voltage for a given anode. This degradation is probably due to the presence of traps at the GaAs/passivation interface. A calculated potential profile for an anode under reverse bias shows high electric fields at the edge that can cause energetic electrons to create traps at the interface. Impact ionization from electrons accelerated in the high field produces high-energy holes and electrons that can also be trapped near the nitride/GaAs interface. Hole trapping in this region will increase the field further, causing higher reverse currents.

5. RF induced failures and the determination of the safe operating range

In order to understand failure modes associated with the application of RF power it is instructional to visualize the different RF induced currents and voltages present in a multiplier when it is being pumped. A harmonic balance simulation coupled with a 3-D electromagnetic simulator can be used to determine the various currents in a given multiplier. An example is presented in Figure 5. A 200 GHz anode with a breakdown voltage of 10.4 V and 25 mW of input power is assumed. The various currents in the diode, forward current peak (Ipeak fwd), reverse current peak (|Ipeak rev|), forward average (Iavg fwd) and reverse average (|Iavg rev|) currents along with the calculated diode efficiency (%) are plotted. Moreover, the reverse peak bias voltage (Vpeak rev) is also plotted. For high efficiency operation the calculated reverse voltage peaks approaches close to the breakdown voltage, resulting in a large reverse current peak. While the bias voltage and average bias current are measurable, there is no easy way of measuring the reverse and forward peak currents. Simulations such as these are highly dependent on the circuit design and strongly frequency dependent. Multipliers can also be designed to be optimally biased further away from the breakdown voltage, but in order to obtain higher output power; the design simulated in Figure 5 is more typical.

Determining the safe operating zone for a given multiplier boils down to finding the bias range where no significant reverse current is present. The following procedure can be used to determine the safe operating range. A multiplier is biased at a reverse bias voltage and the coupled RF input power to the diode is increased monotonically. When the measured bias current indicates a value of −5 μA in the reverse direction the bias conditions and the coupled power are recorded and the RF power is reduced to zero. The coupled power can be measured with a bi-directional waveguide coupler. Next a slightly more positive bias voltage is selected and the input power is again increased slowly to determine the coupled power and bias voltage for −5 μA of current. This process is repeated for a number of bias values. Then the bias voltage is plotted with respect to the square root of the coupled power. Such a plot is shown in Figure 6.

The linear like behavior of the coupled power with the bias voltage allows one to extrapolate the data. With 100 mW of coupled power the bias voltage is approximately −11 V. However, at this bias voltage the measured bias current is -5 μA indicating that the reverse bias current peak is probably closer to −50 μA. Such a large reverse current peak is not suitable for long-term operation since cumulative degradation has been shown for reverse constant current stress [13, 14]. Thus the recommended bias voltage is derated by approximately 25% to −8 V. This is also close to the optimum bias voltage. The limit of −8 V was set to ensure that the operation is within the safe bias range with power levels up to 100 mW. This establishes the envelope of the maximum reverse bias voltage to eliminate risk due to the large reverse peak current. In the forward direction the envelope is determined by the maximum current that can be sustained by the diode with damage as discussed earlier (approximately $0.5\text{mA}/\mu\text{m}^2$). Thus, between these two boundary conditions lies the safe operating zone of this particular multiplier.

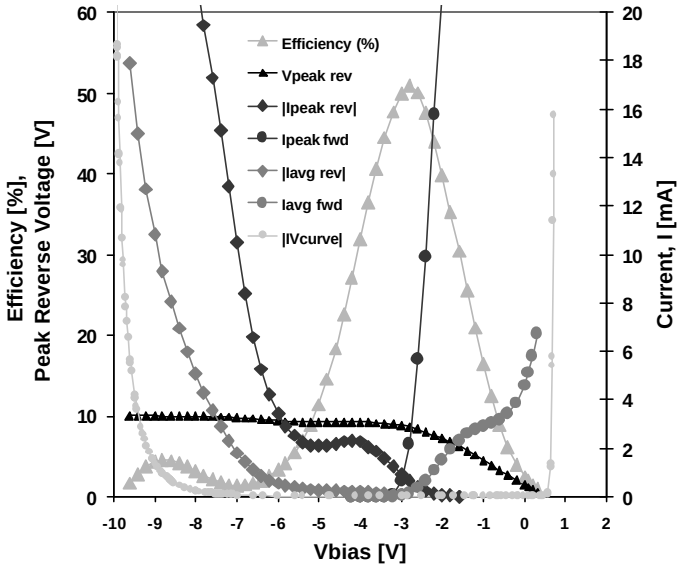

Figure 5: *Simulation of a 200 GHz doubler with 25 mW of input power (breakdown voltage is 10.4 V). Multiplier efficiency and various currents through the diode are depicted.*

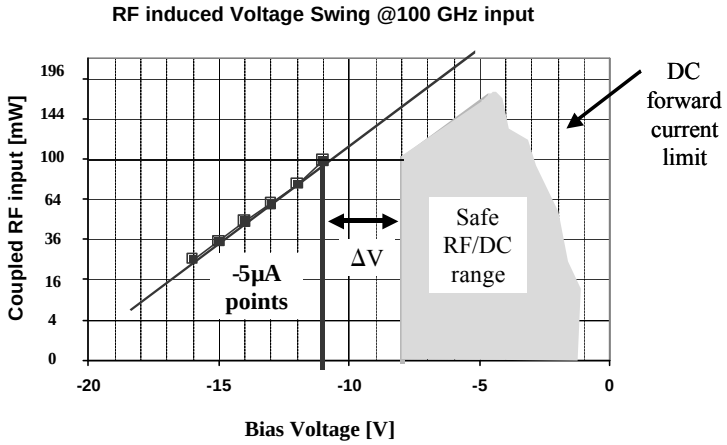

Figure 6: *Proposed procedure for determining the safe operating range of a 200 GHz doubler. The bias voltage is plotted as the square of coupled power for -5 µA of reverse current.*

CONCLUSION

A comprehensive reliability study of planar GaAs diodes with relatively high RF power capability has been conducted. ESD, high temperature, DC, and RF induced failures have been investigated. It has been shown that failure risk due to ESD, temperature, and DC currents can be substantially mitigated by proper engineering procedures. Failures due to excessive RF induced currents are intimately related to the circuit design and the magnitude of the RF induced peak reverse current is difficult to measure directly. A general procedure has been proposed that is based on monitoring the bias current of the multiplier and then derating the bias voltage to reduce the reverse current through the anode.

By following these guidelines one can ensure that the multiplier diodes operate in a safe zone where failure risks have been reduced.

ACKNOWLEDGEMENTS

We thank Neal Erickson (U-Mass) and Goutam Chattopadhyay (Caltech) for many fruitful discussions and insights regarding high frequency multiplier behavior. The team at MPIfR (Max Planck Institut fuer Radioastronomie) in Bonn, Germany for fruitful discussions and providing filter circuits. Ronald Ruiz (JPL) helped perform the measurements with the IR camera. Further we appreciated the huge support by the Submillimeter-Wave Advanced Technology Group (SWAT), especially the contributions of Raymond Tsang, Bradley Finamore, William Chun, and Alejandro Peralta. This work was performed at the Jet Propulsion Laboratory, California Institute of Technology, under a contract with the National Aeronautics and Space Administration (NASA).

REFERENCES

1. Neal Erickson, "Diode Frequency Multiplier for THz Local Oscillator Applications," *SPIE Conference on Advanced Technology MMW*, Radio and Terahertz Telescopes, SPIE Vol. 3357, pp. 75-84, March 1998.
2. E. Schlecht, G. Chattopadhyay, A. Maestrini, A. Fung, S. Martin, D. Pukala, J. Bruston and I. Mehdi, "200, 400 and 800 GHz Schottky Diode 'Substrateless' Multipliers: Design and Results," *2001 Int. Microwave Symp. Digest*, Phoenix, AZ, May 2001.
3. G. Chattopadhyay, E. Schlecht, J. Ward, J. Gill, H. Javadi, F. Maiwald, and I. Mehdi, "An All Solid-State Broadband Frequency Multiplier Chain at 1500 GHz," *IEEE Trans. On Microwave Theory and Tech.*, Vol. 52, No. 5, May 2004, pp. 1538-1547.
4. Alain Maestrini, John Ward, John Gill, Goutam Chattopadhyay, Frank Maiwald, Katherine Ellis, Hamid Javadi, and Imran Mehdi, "A Planar-Diode Frequency Tripler at 1.9THz," *IEEE MTT-S Int. Microwave Symp.*, Philadelphia, Pennsylvania, June 13, 2003.
5. L. A. Samoska, T. C. Gaier, A. Peralta, S. Weinreb, J. Bruston, I. Mehdi, Y. Chen, H. H. Liao, M. Nishimoto, R. Lai, H. Wang, and Y. C. Leong, "MMIC power amplifiers as local oscillator drivers for FIRST," *Proc. SPIE*, vol. 4013, San Diego, CA, Aug. 2000, pp. 275–284.
6. Sponsor: Surge-Protection Devices Committee of the IEEE Power Engineering Society, "IEEE Guide on Electrostatic Discharge (ESD): ESD Withstand Capability Evaluation Methods for Electronic Equipment Subassemblies," *IEEE Standards Board*, approved October 24, 1994.
7. Y. Anand, R.J. Malik, "Electrostatic Failure of GaAs Planar Doped Barrier Diodes," *EOS/ESD Symp.* 93-1003.
8. J.E. Vinson, J.J. Liou, "Electrostatic Discharge in Semiconductor Devices: Protection Techniques," *Proc. of the IEEE*, Vol. 88, No. 12, December 2000.
9. R. Lin, A. Pease, R. Dengler, D. Humphrey, T. Lee, S. Kayali, I. Mehdi, "Quartz-based GaAs Schottky Diodes -- Lifetime and Failure Analysis," *Proc. of the 9th Int. Symp. on Space Terahertz Technology*, pp. 511-520, March 1998.
10. Quantum Focus Instrument Corporation (QFI), Denman D. Kessler at QFI.
11. S. Takatani, H. Matsumoto, J. Shigeta, K. Ohshika, T. Yamashita, and M. Fukui, "Generation Mechanism of Gate Leakage Current to Reverse-Voltage Stress in i-AlGaAs/n-GaAs HIGFET's," *IEEE Trans. On Electron Devices*, Vol. 45, No. 1, January 1998, pp. 14-20.
12. P. Dodd, T.B. Stellweg, M.R. Melloch, and M.S. Lundstrom, "Surface and Perimeter Recombination in GaAs Diodes: An Experimental and Theoretical Investigation," *IEEE Trans. On Electron Devices*, Vol. 38, No. 6, June 1991, pp. 1253-1261.
13. Frank Maiwald, Erich Schlecht, John Ward, Robert Lin, Rosa Leon, John Pearson, and Imran Mehdi, "Design and operational considerations for robust planar GaAs varactors: A reliability study," *Int. Symp. on Space THz Technology*, Tucson, April 22, 2003.
14. M. Schuessler, V. Krozer, K.H. Bock, M. Brandt, L. Vecci, R. Losi, and H.L. Hartnagel, "Pulsed Stress Reliability Investigations of Schottky Diodes and HBTS," *Pergamon, Microelectron. Reliab*. Vol. 36, No. 11/12, pp. 1907-1910, 1996

AM Noise in Drivers for Frequency Multiplied Local Oscillators

Neal Erickson
Astronomy Dept.
University of Massachusetts
Amherst, MA 01003 USA

Abstract AM noise on local oscillators which have been power amplified in W band are measured and compared with the needs of heterodyne receivers for the submillimeter. The noise is measured only in the 77-110 GHz range but it is shown that one may predict the expected noise that will appear in the THz output signal. In general it is found that AM noise may be low enough to be negligible for driving SIS or HEB mixers as long as the final amplifier is very strongly saturated. PM to AM noise conversion may substantially degrade the noise in some cases where strong frequency variation is seen in the response of following multiplier stages.

Introduction

Heterodyne receivers for mm-and submm wavelengths are generally based on single ended mixers which are susceptible to amplitude (AM) noise originating on their LO source. These mixers act as total power detectors as well as mixers and thus their IF output contains a term which is sensitive to the instantaneous LO power. Balanced mixers eliminate this total power sensitivity, but they are too complex to build in the submm, although this situation may change in the near future. In most receiver systems the AM noise originating from the LO is not readily measured, since there is no way to separate the LO noise from the mixer noise. In lower frequency systems highly resonant filters may be used to clean up the LO, and provide a measure of the LO noise, but these are too lossy in most cases, and they require careful mechanical tuning. In most mm-wave LO systems, InP Gunn oscillators are used as the primary LO source and these have sufficiently low AM noise that there is no need to apply additional filtering. While these oscillators must be phase locked to a low frequency reference, the properties of the reference have no effect on the AM noise (at large offset frequencies) produced by the oscillator since the phase lock loop bandwidth is generally much less than any receiver IF. Similarly the lock loop affects the phase noise only within the loop bandwidth, so the oscillator acts as a narrow band filter.

In the new generation of frequency multiplier based LO sources for THz frequencies, Gunn oscillators have too little power output to be useful as drivers, and also require mechanical tuning which is inconvenient in many applications. Herschel HIFI will use direct frequency synthesis with amplification and passive multiplication to reach frequencies as high as 2 THz. The highest frequency amplifier is within the 75-110 GHz band, where a power output of up to 300 mW may be produced using GaAs HEMT MMIC amplifiers over 10% bandwidths. Given that HIFI is intended to be wideband, it is impractical to provide any significant noise filtering at any point in the chain except near the lowest frequencies. This allows AM noise to grow enormously within the chain since there are several amplifiers involved and none of them have particularly low noise. In the WR10 power amplifiers alone there may be a gain of 30 dB. While data has been obtained in a few specific cases [1,2] showing that the noise level in such amplifiers is low enough to not significantly degrade receiver noise there has been no systematic study. This work was begun to measure the details of AM noise on the output of such an LO chain, and its behavior vs output power, particularly in the limit where the final amplifier saturates and the noise is expected to decrease.

AM and PM noise

All noise in any oscillator system may be characterized as either amplitude or phase noise. Pure amplitude noise consists of a carrier with precise frequency (as defined by zero crossings), but with a modulated amplitude. Pure PM noise consists of a carrier with precisely constant amplitude but with a modulated phase.

$$\text{AM noise: } V = (1+V_n)\sin\omega t$$
$$\text{PM noise: } V = \sin(\omega t+\Phi_n)$$

where V_n and Φ_n are noise voltage and phase terms, respectively.

Pure AM and PM noise must both have two equal sideband components, and they differ only in the relative phase of the two sidebands. AM sidebands are in phase, PM sidebands are 180° out of phase. In the case of a wideband white noise spectrum having no correlation between sidebands, the noise is exactly half AM and half PM. There is no way to distinguish AM from PM noise on a spectrum analyzer, since such an instrument does not look at the phase relationship between sidebands. Any single sideband modulation on a carrier must also be half AM and half PM. While noise may be classified as one form or the other, it may also convert between forms if there is any element which alters either the amplitude or phase relationship between the sidebands. Despite their similarity, only AM noise affects the IF noise of a single ended mixer. The phase noise influences the linewidth of the LO as far as spectral resolution is concerned but is otherwise not observable.

AM noise corresponds to simple amplitude fluctuations in a carrier, and one obvious way to reduce it is to overdrive an amplifier so that its output voltage is saturated and the output approximates a square wave. This process, of course, generates harmonics and intermodulation products, but these are all predictable and may be chosen to fall at unused frequencies. Possibly the overdrive may produce noise through other mechanisms, and saturation is not a sharp process in RF amplifiers, so the object of this study was to determine how effective this saturation mechanism is in reducing AM noise.

Since we are considering a frequency multiplier chain we must also know what will happen to a given noise level within a multiplier. In general, optimized multipliers operate at a power level where the conversion efficiency is nearly independent of input power, so they may be considered linear devices for AM noise purposes. In extreme cases the slope of the input-output characteristic may vary by a factor of two from linear, so that a multiplier may either increase or decrease amplitude fluctuations by as much as 3 dB. In spectral behavior, the input spectrum appears at the output unchanged as long as the multiplier has a flat frequency response. Multiplier behavior to phase noise is entirely different, since phase errors are due to time errors in zero crossings, and so phase noise grows as the multiplication factor squared.

AM noise measurement setup

A definition of the required noise level is needed to bound the measurements in this study. We assume that we are interested in an SIS mixer at 1 THz. The required LO power at the junction is believed to be 200 nW (-37 dBm), while the mixer noise referenced to the junction input is 2kT = 100 K (DSB). An optimum LO should add <5% to the mixer noise or 5K (-192 dBm/Hz in spectral density). This means our desired noise relative to the carrier should be below –155 dBc/Hz (DSB). If we instead consider an HEB mixer, the LO power should be less while the mixer noise tends to be higher so the LO noise may be higher as well [3]. In either case we must realize that LO power depends on many factors including junction area, so these numbers are not firm, and apply largely to devices optimized to require relatively low LO power.

The AM noise on various power amplifiers was measured with a setup shown in Fig. 1. An amplifier following a synthesizer was used to drive a single ended diode mixer in W band with a constant LO power near 1 mW. The IF noise was measured and related to the noise from the amplifier through a radiometric calibration. A test system was assembled which approximates the method to be used within Herschel HIFI to produce the LO. A 50 GHz synthesizer (HP86350L) was used to drive a 50 mW power amp in Ka band which in turn drives a tripler to WR10 band. The tripler produces 0.5-1.0 mW and drives a wideband low power amplifier boosting the level to 4 mW. Following this amplifier a variable attenuator was used to set the input level to the power amplifier under test to any needed level from 10 μW to 4 mW. Following this, a directional coupler sampled the input power to the power amplifier. Another directional coupler sampled the output power, and a variable attenuator was used to set the level going to the mixer to a constant value. The mixer was actually a fast detector (Pacific Millimeter model W-D) which acts as a single ended mixer with a wideband IF. The detector/mixer is biased with a wideband bias T, and followed by an L band IF strip with an input isolator, and a narrow band filter at 1.4 GHz to define the IF band. The mixer operated self-biased, and the bias current was measured and used to keep the LO drive constant during the measurements. Bias current was 0.7 mA for all tests, corresponding to an LO power of ~1 mW, which produced nearly the minimum conversion loss of ~10 dB.

Calibration

It is difficult to accurately measure the low level noise on an LO source due to the shot noise originating in a mixer when it is driven by an LO source. The best measure of this noise floor is to drive the mixer with a known quiet LO source but this not easy to establish. Another problem is simply establishing a power scale referenced to the input of the mixer, taking into account the conversion loss and IF gain. This is best done by using the receiver as a radiometer, although absolute power calibrations can also be done using an RF signal source and power meters. This receiver was converted to a radiometer by adding a 13 dB coupler to the mixer input and injecting the LO though the coupled arm with a feed horn on the input. The LO came from an InP Gunn oscillator, known to have very low AM noise. LO power was set at 0.7 mW and the noise temperature was measured using hot/cold loads in front of the horn. Assuming no LO noise, the 0 of input power is determined by extrapolating the IF power to 0 K input. Another way to measure the zero of noise is to turn off the LO, and measure the IF power (with the IF strip terminated in 295K by the input isolator). This presumes that the mixer produces shot noise of exactly room temperature. The difference in the input zero power measured these ways is about 200 K (referenced to the input). There is no way to readily assign this noise to either shot or AM noise, but since this corresponds to a noise level of –174 dBc/Hz, it is low enough to be neglected relative to the requirements of this study.

This hot/cold measurement was used to calibrate the receiver at all of the frequencies were data were obtained The calibration is DSB and all of the data presented here is DSB as well. For simplicity, the noise zero was assumed to be that measured with the LO off (assumed RT shot noise), which may lead to errors of as much as 3 dB in the very lowest noise measured on some sources.

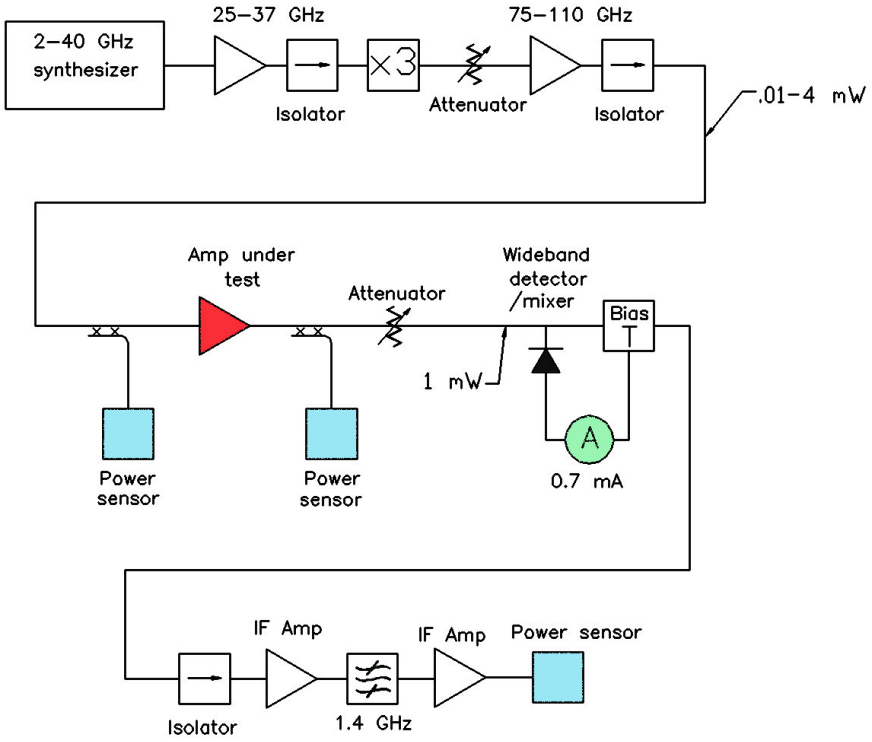

Figure 1. Test setup for measuring AM noise on an amplified LO signal.

Measurements

Several power amplifiers were measured at various frequencies to determine typical performance. All amplifiers were fabricated as GaAs MMIC's and were produced at TRW (now NGST) with designs primarily from JPL [1,4]. The first tests were of the low power driver amplifier, which was established to have AM noise below –170 dBc/Hz in the complete setup. This was necessary to be sure that it is practical to build a low noise driver using generic components, and that any noise measured would be from the power stages. The next set of power

amplifiers were measured at a frequency of 77 GHz, and the data is shown in Fig 2. The small signal gain was 33 dB as can be seen from the initial slope of the input output curve. At low power this set of amplifiers shows very high noise as is expected when the carrier is weak, but the noise drops very rapidly as the power increases. For small signals the noise to carrier ratio (N/C) should drop linearly with the carrier strength, since the noise is constant. For stronger signals the N/C drops much faster than the increase in strength of the carrier as the amplifier begins to saturate. Overall an increase by a factor of three in power results in a factor of 1000 reduction in N/C so it is easy to see the great effect of saturation. At an input power near 1 mW, the N/C ratio is below –155 dBc, and so meeting the required noise is possible. It should be noted that in this test a Ka band driver amplifier was used that was very old and known to be quite noisy compared to more modern amplifiers, and yet the noise may still be made adequately low.

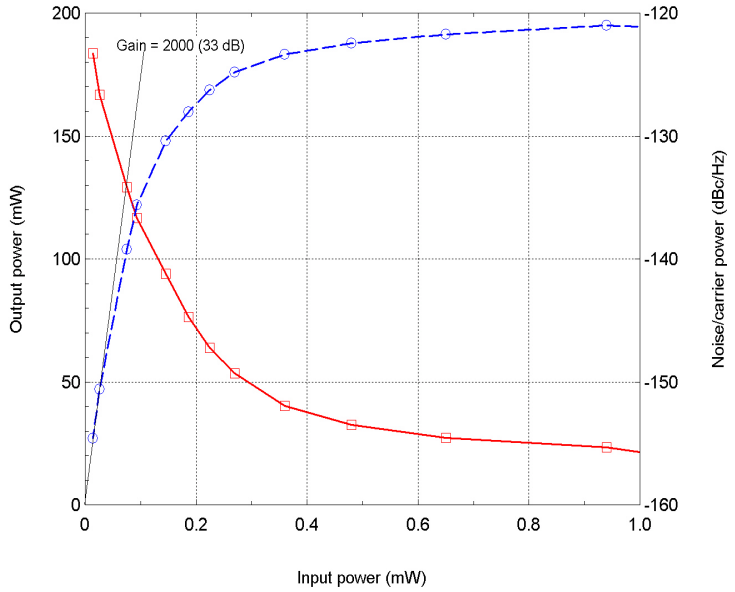

Figure 2. DSB spectral density of noise relative to carrier power for an LO signal amplified with 33 dB gain, as a function of input power to the amplifier. Output power is shown as well, with the straight line being a fit to the small signal gain. Frequency is 77 GHz.

The next set of tests was also done with the same set of amplifiers at 77 GHz, but with a lower noise Ka band driver. Results are shown in Figure 3. In these tests, the final high power stage was initially removed, and the noise of the driver amplifier was measured as well as its power output. As can be seen this amplifier never reaches strong saturation and so its noise drops rapidly up to the highest input power measured. Then the high power stage was added, and its 10 dB gain was sufficient to result in a moderate degree of saturation over the full input power range used. It is interesting to note that this amplifier produces a dramatic reduction in noise on its output as it begins to saturate, and that the output noise is less than the input over the full power range tested.. Under substantial overdrive conditions the output actually begins to decrease with input power, and the noise too increases. This behavior is typical of overdriven amplifiers but the effect is small and the noise never increases significantly.

Figure 4 shows tests on an amplifier with similar MMIC designs but assembled (at NGST) as an engineering model (EM) for the Herschel HIFI LO module [4]. The amplifier tunes 94-110 GHz with >100 mW power output, but the required band is somewhat less. The noise behavior of this amplifier is shown for two frequencies in band, one near minimum noise and the other near maximum. In both cases the noise drops to a very low level with sufficient input power and the difference appears to be just a difference in gain at the two frequencies. This amplifier was stepped across its band with 0.5 mW input at all frequencies and the variation in noise is shown in Fig. 5. This test was done at a physical temperature of 120 K as will be the case with the HIFI LO amplifiers, and the results show that there are no unacceptably noisy spots in the required band of 95-106 GHz. The ripple in noise probably arises from variations in the small signal gain due to interactions between gain stages.

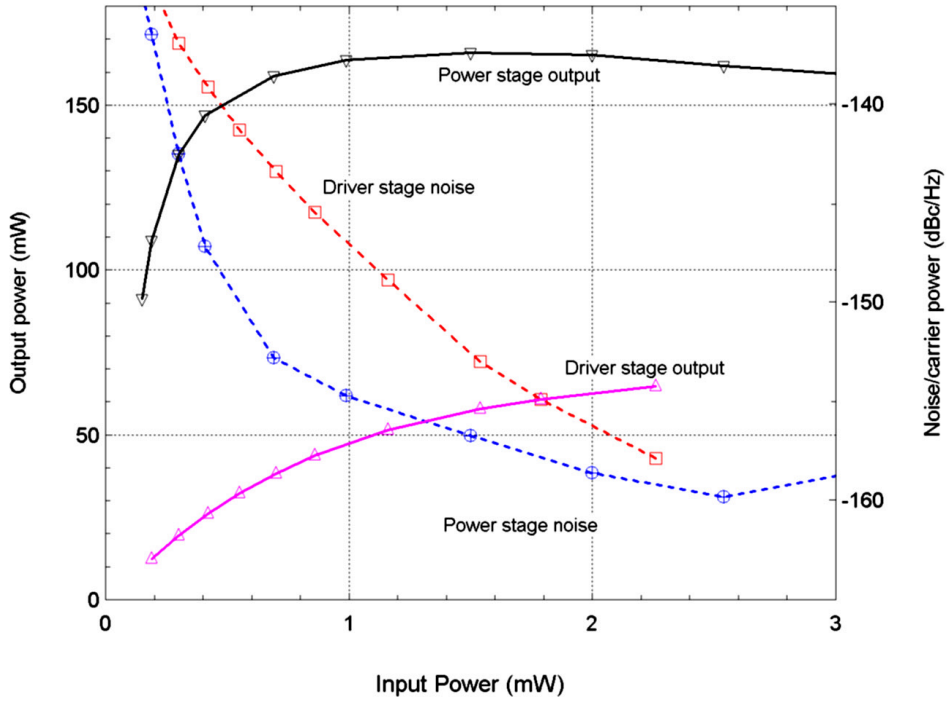

Figure 3. Output power and DSB noise/carrier ratio from a driver amplifier and high power amplifier as a function of input power to the driver amplifier. Frequency is 77 GHz and the small signal power amplifier gain is 10 dB.

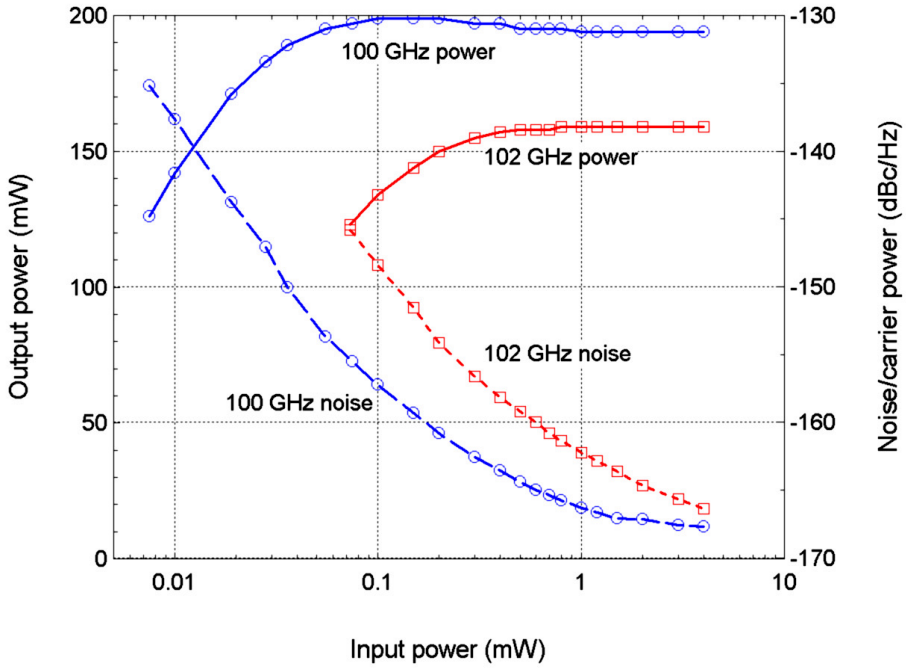

Figure 4. Output power and DSB noise/carrier ratio from a HIFI EM power amplifier at two frequencies in band representing the highest and lowest noise.

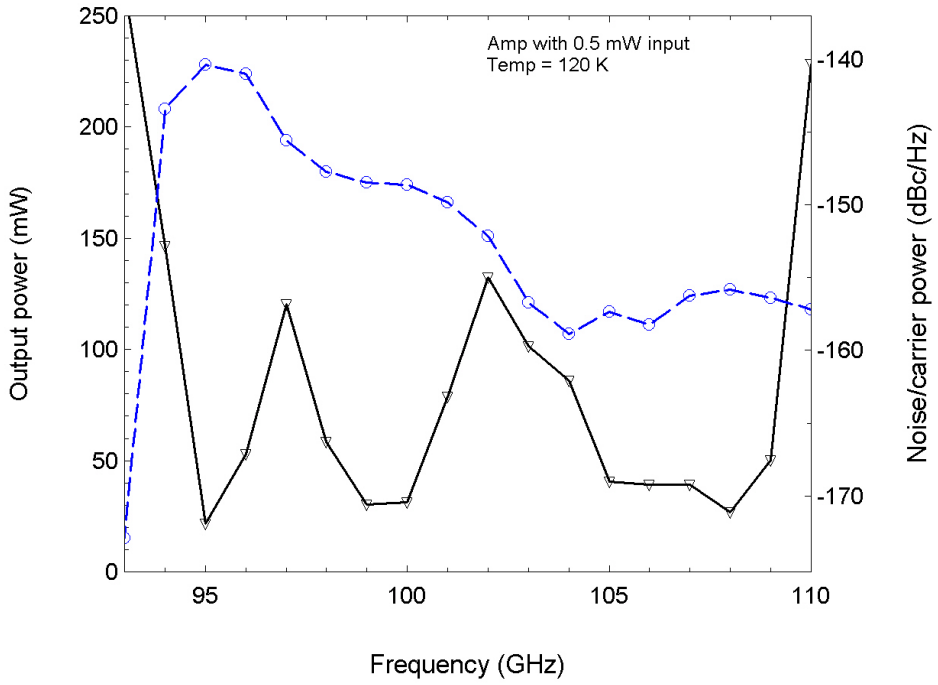

Figure 5. Output power and DSB noise/carrier from power amplifier across the full useful frequency band with a constant input power of 0.5 mW. Amplifier is operated at 120 K, as would be the case in HIFI.

Similar results were obtained with another set of amplifiers of different design at 100 GHz. All of these results show that very low AM noise may be produced through saturation of the final power amplifiers, but the required input power greatly exceeds the amount required for nominal operation. In every case the input must be at least 10 dB in excess of the small signal gain (10 dB compression), and in some cases 20 dB compression results in even lower noise. This points out that any such systems should have a large gain margin in the power amplifiers.

Power control with bias

These results show that it is not practical to control the output power of an amplifier chain by varying the input power. It is possible to attenuate the output, but such attenuators require mechanical setting, and introduce a significant loss at minimum. A better alternative is to vary the drain bias on the last power amplifier so that its saturation power varies. This will work as long as the output power drops as fast as the small signal gain of this stage, and in general the power is more sensitive to drain bias than the gain.. The results for the HIFI EM LO amplifier are shown in Fig. 6, where the power may be varied by a factor of 4 with less than a 1 V bias change, while the noise remains nearly constant over the power range. Varying the drain bias produces a very smoothly varying output power that could be incorporated into an power control loop. This same test was done on three sets of amplifiers and the results were similar

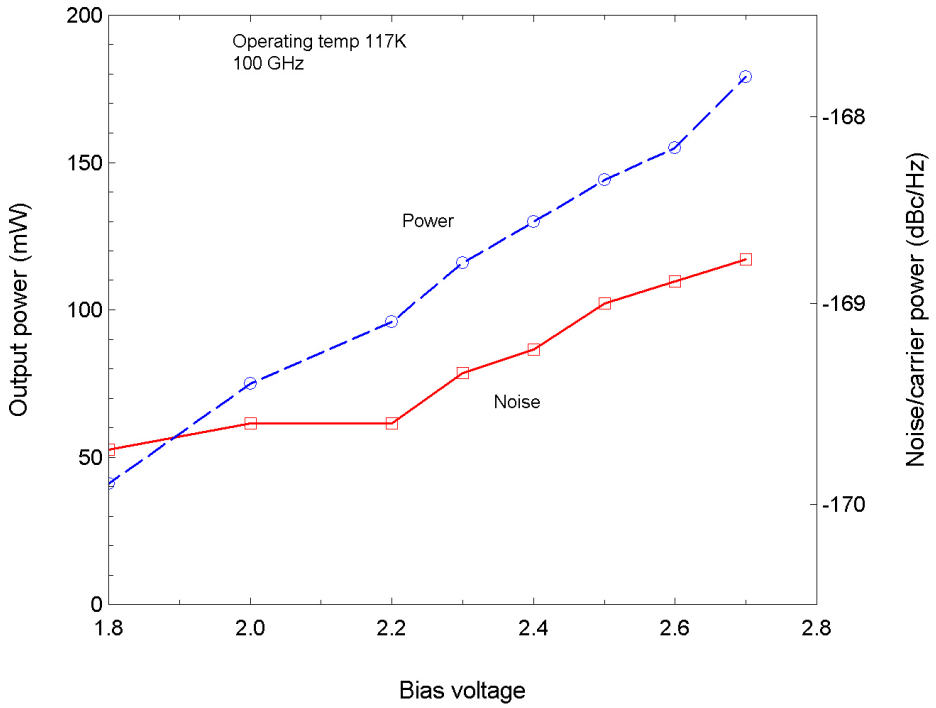

Figure 6. Power output and DSB noise/carrier from a power amplifier as a function of dc drain bias voltage on the final stages. Amplifier is operated at 117 K but similar results are obtained at room temperature.

Conversion of PM to AM noise

In any system where noise is present it may appear as AM or PM noise and may convert between them. In the highly saturated amplifiers described above, the AM noise is reduced to a very low level but the PM noise is unchanged (assuming no amplitude dependent phase shifts in the amplifier). Since conversion in later multipliers is possible it is helpful to see how large the PM noise may be. While it is not directly measured by a mixer, it is easy to convert this noise to AM using a filter which strips off one sideband. Such a filter rejects half of the input noise and converts the remainder to half AM and half PM. In the limit where the input noise is dominated by AM the output AM level would drop 6 dB, while if PM dominates then the AM level will increase to 6 dB below the input PM level. While a filter is the simplest way to measure the conversion, any gain or phase slope will have a similar (but lesser) effect, and so such conversion is likely in any system.

To measure the level of PM noise that might be present in such a system, a set of amplifiers producing low AM noise was altered by simply adding a high pass filter to their output, with the passband edge set to reduce the lower sideband by 10 dB relative to the upper, before driving the mixer as before. The before and after curves are shown in Fig. 7. In the ideal case the AM noise should drop ~6 dB with the addition of the filter, but because the filter attenuates the carrier somewhat (it is on the edge of the passband), the noise may not drop as much. What is actually seen is an 8 dB increase in noise over the upper part of the power range tested, showing that the PM noise before the addition of the filter is ~14 dB above the AM noise. In the region where the AM noise is large, the noise does drop as expected with the addition of the filter although the drop is only about 3 dB. Even in this nearly worst case situation the noise drops to an adequately low power, showing that with a good synthesizer and a reasonable choice of other components, there should be little added noise.

In a multiplier chain there are many opportunities for PM to AM conversion, given that the passband is not very flat and there may be phase dispersion as well. These are not a serious problem if the conversion occurs in the first stage but the problem becomes significantly worse if the PM noise has grown after multiplication. Fortunately the later stages are typically those with the most total bandwidth and the lowest Q so that they are less likely to suffer from rapid changes in response vs frequency.

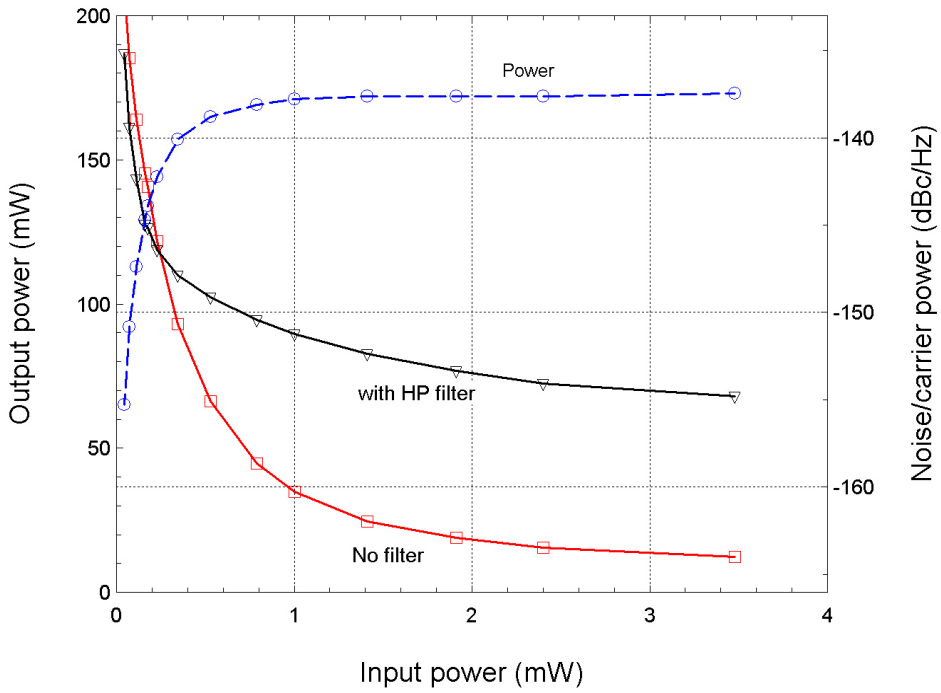

Figure 7. Output power and DSB noise/carrier for a power amplifier with and without the addition of a high pass filter with a band edge at the LO frequency. The increased noise with the filter is due to PM to AM noise conversion.

Conclusions

We have measured the AM noise on the output of GaAs HEMT power amplifiers within W-band under a range of input drive conditions. The output AM noise is below –155 dBc/Hz in all cases as long as the input is sufficiently saturated, but a very high degree of saturation is required to meet this requirement. In most cases this will require >10 dB of overdrive to reduce the noise sufficiently. It is also found that reduction of the drain voltage is a good way to reduce the amplifier output power while maintaining low AM noise.

Acknowledgement

This work was supported by the Jet Propulsion Laboratory under contract 1239274.

References

[1] I. Mehdi, T. Gaier, J. Kooi, B. Fujiwara, and R. Lai, "A W-band HEMT based power amplifier module for millimeter-wave LO multipliers," *Ninth Int. Symp. on Space Terahertz Tec*h., (Pasadena, CA), pp. 573-578, Mar 1998.

[2] E. W. Bryerton, D. L. Thacker, K. S. Saini, and R. F. Bradley, **"**Noise Measurements of YIG-Tuned Oscillator Sources for the ALMA LO," ALMA Memo No. 311**,** August 2000

[3] N. Whyborn, "HIFI LO Requirements Analysis" (HIFI memo), Mar 2004

[4] R.R. Ferber, T.C. Gaier, J.C. Pearson, L.A.. Samoska, M. Wells, A. Campbell, G. Swift, P. Yocom, and K.T. Liao, "W Band MMIC Power Amplifiers for the Herschel HIFI Instrument," *14th Int. Symp. on Space Terahertz Tec*h., pp. 73-82, Tucson, Apr. 2004.

Continuous THz-Wave Generation using Uni-Traveling-Carrier Photodiode

Hiroshi Ito, Tomofumi Furuta, Fumito Nakajima, Kaoru Yoshino, and *Tadao Ishibashi

NTT Photonics Laboratories, NTT Corporation
3-1 Morinosato Wakamiya, Atsugi-shi, Kanagawa 243-0198, Japan
*NTT Electronics Corporation, 1841-1 Tsuruma, Machida-shi, Tokyo 194-0004, Japan

Abstract

Photonic generation of millimeter/sub-millimeter waves up to THz range using an antenna-integrated uni-traveling-carrier photodiode is investigated. A test device measured on-wafer exhibits a record maximum output-power of 2.6 μW at 1.04 THz with good linearity. A quasi-optical module fabricated for practical use generates almost the same output power as the chip at around 1 THz and operates at frequencies of up to 1.5 THz. These are record results for photonic THz-wave generation using photodiodes operating at 1.55 μm.

Introduction

The generation of continuous millimeter(mm)/sub-mm wave signals using photonics technology is promising for various applications, such as high-speed measurements, spectroscopy, and the local signal supply for radio telescopes [1]. Among the photomixers that can generate such high-frequency signals, a photoconductive switch utilizing low-temperature-grown GaAs (LT-GaAs) is the most widely used. To date, sub-mm wave generation at up to 5 THz [2] has been reported using such a device. Although the response is very fast, this device utilizes short-wavelength ($\lambda \approx 0.8$ μm) light signal. Thus, it cannot use the abundant optical components developed for optical communications systems. A more convenient approach is to use a standard photodiode (PD) operating at a long-wavelength ($\lambda \approx 1.55$ μm). This enables us to use various optical components, such as optical fiber amplifiers and wavelength-tunable lasers. Sub-mm wave generation at up to 1 THz has already been reported using a conventional pin-PD [3]. A problem with this approach is that a conventional pin-PD has the inevitable trade-off between output and bandwidth [4]. In fact, the obtained output powers at around 1 THz are only a few nW [3], which has to be increased for practical applications.

The uni-traveling-carrier photodiode (UTC-PD) [5] is one of the best ways to improve the output power because it provides a high 3-dB down bandwidth (f_{3dB}) [6] and a high-saturation-output power [7] simultaneously. An output power of 300 μW at 300 GHz [8] has already been demonstrated for an antenna-integrated UTC-PD chip [9]. In the present work, we have investigated a photonic mm/sub-mm wave generation from a UTC-PD integrating a planar log-periodic antenna to demonstrate the possibility of practical output power in the THz range. A quasi-optical UTC-PD module [10] was also fabricated and its characteristics compared with that of the chip.

Device fabrication

The epi-layers were grown by MOCVD. The absorption layer consists of p-InGaAs ($p = 4 \times 10^{17}$ /cm^3, 80 nm), p-InGaAs ($p = 1 \times 10^{18}$ / cm^3, 10 nm) and undoped InGaAs (8 nm), and the collection layer consists of undoped InGaAsP (16 nm), undoped InP (6 nm), n-InP ($n = 1 \times 10^{18}$ /cm^3, 7 nm) and n-InP ($n = 1 \times 10^{16}$ /cm^3, 253 nm). Double-mesa back-illuminated UTC-PDs with an absorption area of 13 m m^2 were fabricated by wet chemical etching and metal-lift-off processes. Each PD was then integrated with a planar antenna on a semi-insulating InP substrate. Figure 1 shows a micrograph of the fabricated device. The device integrates a UTC-PD and a self-complementary log-periodic toothed planar antenna, whose teeth correspond to frequencies from 150 GHz to 2.4 THz. The p- and n-type electrodes of the PD were connected to each wing of the antenna. The front side of the wafer was anti-reflection coated, and the backside, high-reflection coated. The intrinsic f_{3dB} of a fabricated UTC-PD was evaluated to be 170 GHz by pulse photoresponse measurements, and its CR-limited bandwidth was estimated to be 210 GHz. The responsivity was measured to be about 0.03 A/W.

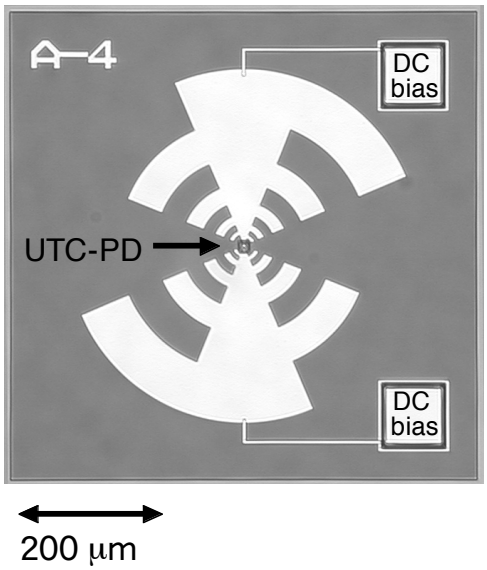

Fig. 1. Micrograph of the fabricated UTC-PD chip integrating a log-periodic toothed antenna.

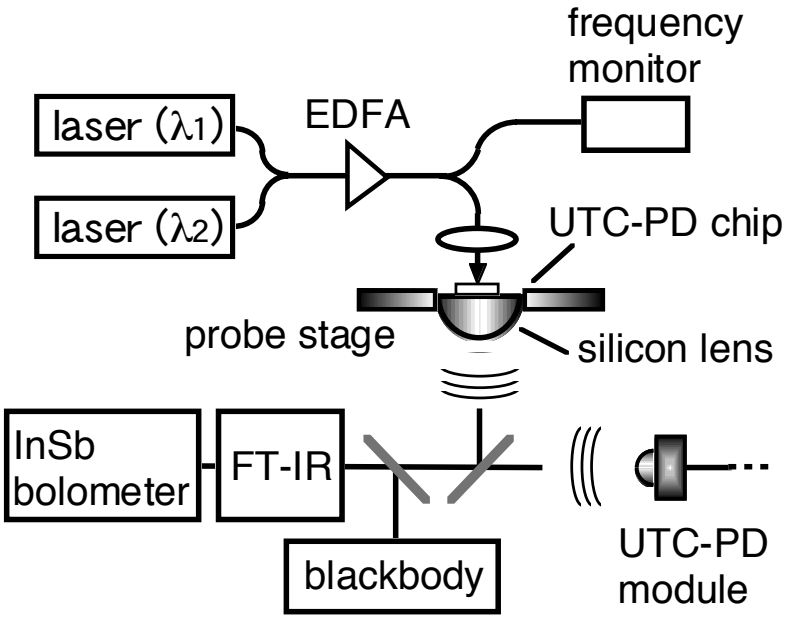

Fig. 2. Schematic drawing of the measurement setup.

Characterization

Figure 2 shows the experimental setup. The RF modulated optical signal was prepared by two-mode beating using two wavelength-tunable laser-diodes (WT-LDs) having λ_1 and λ_2 of around 1.55 μm. The optical modulation index of the optical signal measured was about 60 %. The device was placed on a hyper-hemispherical Si lens and measured on-wafer. The input optical signal introduced from the front side of the wafer was reflected at the backside, and then focused on the PD. The mm-wave was mainly emitted toward the backside of the wafer through the Si lens. The mm-wave power was alternately detected with a Schottky diode detector (Farran Technology, WD-03) with a feed-horn or with a Martin-Puplett-type Fourier transform spectrometer and InSb hot-electron bolometer. The absolute value of the output power was calibrated against blackbody. By using the same setup, we measured the output power from the module, so that we could quantitatively compare the output powers from both types of devices.

Experimental Results

Figure 3 shows the relationship between the measured mm-wave output power and the diode photocurrent for the device at 300 GHz for a bias voltage of -1.5 V. A wide linearity range is maintained up to a high output power of over 100 mW, and the saturated output power was 300 mW at a photocurrent of 20 mA. To our knowledge, this is the highest output-power directly generated from a PD in the 300-GHz band. Here, power losses due to the coupling efficiency of the horn antenna, absorption, reflection and divergence of the output signal, etc. were not excluded. Thus, the actual emitted power should be even higher.

Figure 4 shows the relationship between the measured output power and the photocurrent at 1.04 THz for a bias voltage of -2 V. Again, the output power increased linearly in proportion to the square of the photocurrent, and the maximum output power obtained was 2.6 μW at a photocurrent of 13 mA [10]. To our knowledge, this is also the highest output-power directly generated from a PD in the THz range. It is even higher than the highest output power reported for the LT-GaAs photoconductive switch [11] and more than two orders of magnitude higher than that obtained by a pin-PD [3]. The observed result includes power losses so that the actual emitted power should be even higher. More importantly, the bias voltage applied was about an order smaller than that required for the LT-GaAs photoconductive switch [2, 11]. Thus, the total power dissipation in the device is much smaller, which should be advantageous in regard to device reliability.

For practical use, we also fabricated the quasi-optic UTC-PD module shown in Fig. 5. We designed the module to be the same size as that of conventional semiconductor optoelectronic (O/E) devices [12] so that we could use standard assembly equipment. The PD chip was placed on a hyper-hemispherical silicon lens and electrically connected to the DC bias leads. Then, the photodiode was optically coupled to the optical fiber using a single-lens system. These optical parts were welded onto the package using a YAG laser, which assures the stability of the optical alignment. The size of the module is 12.7 mm × 30 mm × 10 mm (excluding the optical fiber and the leads).

Figure 6 shows the relationship between the detected output power and the photocurrent at 1.04 THz for a bias voltage of -0.75 V. The output power increased linearly in proportion to the square of the photocurrent, and the maximum output power obtained was 2.3 μW at a photocurrent of 13 mA. This is also the highest output-power directly generated from a PD module in the THz range. Noteworthy too is that the output power from the module is almost the same as that from the chip. This indicates that there is very small power penalty regarding the device assembly.

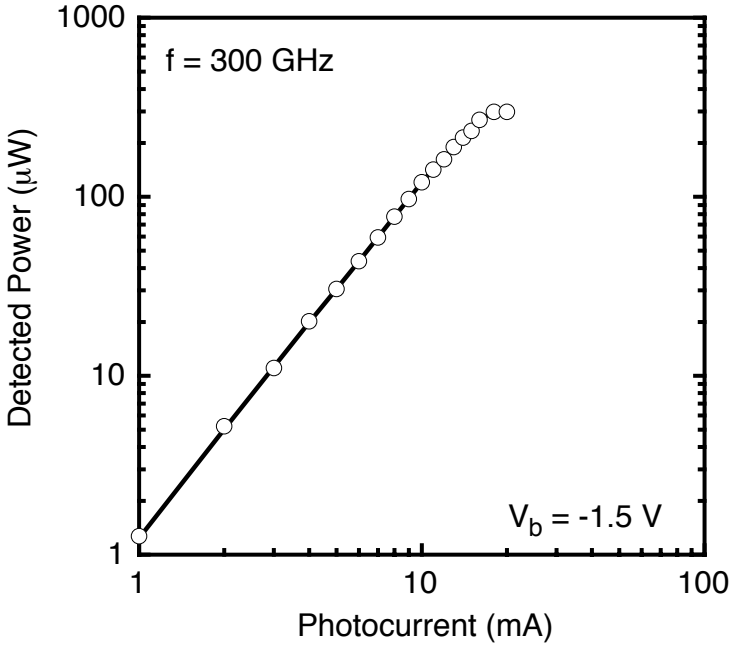

Fig. 3. Relationship between the measured mm-wave output power at 300 GHz and diode photocurrent for the antenna-integrated UTC-PD chip.

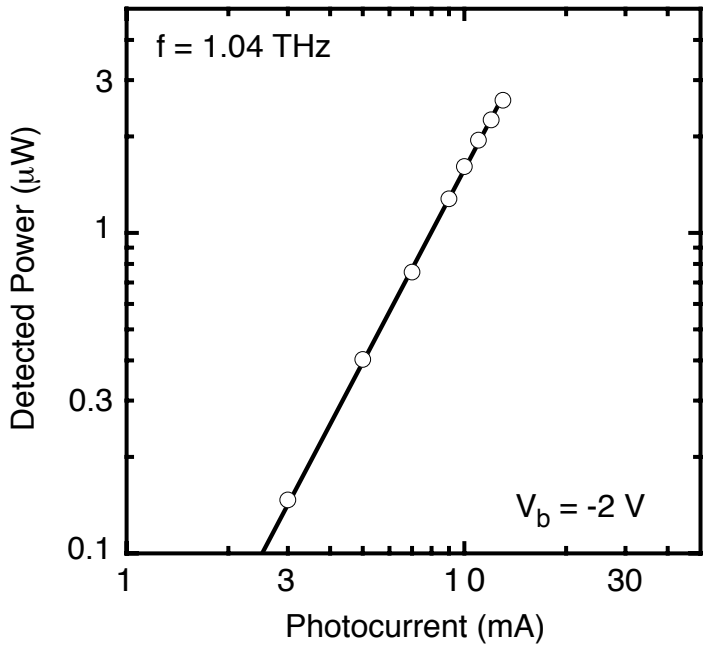

Fig. 4. Relationship between measured THz-wave output power and diode photocurrent for the UTC-PD chip.

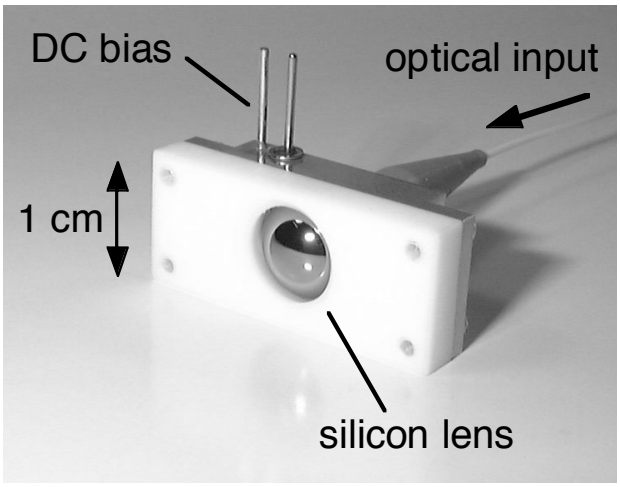

Fig. 5. Photograph of the fabricated quasi-optical UTC-PD module.

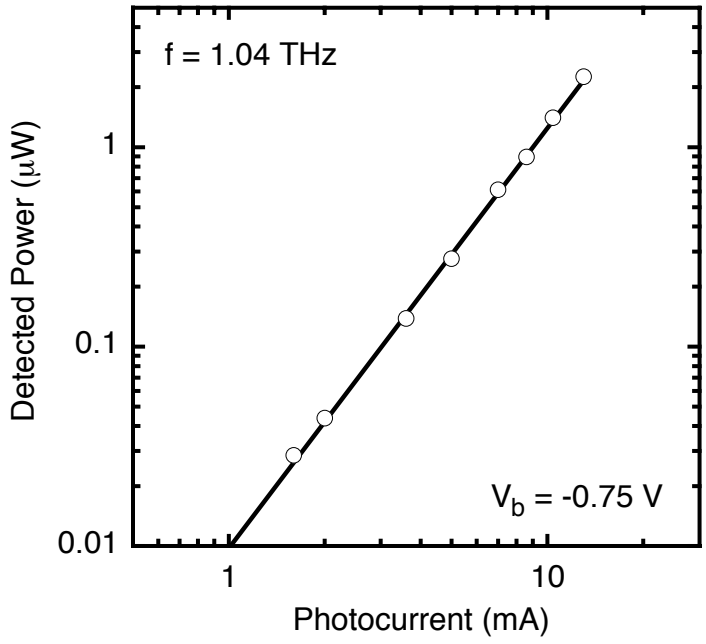

Fig. 6. Relationship between measured THz-wave output power and diode photocurrent for the quasi-optic UTC-PD module.

Figure 7 shows the frequency characteristics of the fabricated module for a photocurrent of 10 mA. The output power decreased gradually with increasing frequency, and we could detect sub-millimeter waves at frequencies of up to 1.5 THz. This is the highest operation frequency ever achieved by using a photodiode operating at 1.55 μm. The solid curve in the figure is a calculation, which only takes into account the CR-limited and transit-time limited bandwidths [9] of the UTC-PD with a constant loss. The experimental result agrees well with the calculation, indicating that only the device parameters of the PD are determining the basic frequency dependence and that the integrated antenna is very wideband. Thus, if we can eliminate the influence of the CR time constant by employing a resonating narrow-band matching circuit, it will be possible to obtain an output power of more than 10 μW at 1 THz, as indicated by the broken curve in the figure.

Figure 8 compares reported RF output powers above the 100-GHz range for UTC-PDs [8, 10, 12], pin-PDs [3, 13, 14], and LT-GaAs photomixers with a wideband design [11, 15]. The output power of a pin-PD has been reported to be inversely proportional to the fourth power of the frequency [3]. Although the results for UTC-PDs plotted in Fig. 8 are not for the same device, they well follow the trend for pin-PDs. More importantly, the output powers of UTC-PDs are about two orders of magnitude higher than those of pin-PDs, mostly due to their very high output saturation levels. The reason for the high output saturation level is that the space charge effect is less significant in a UTC-PD than in a pin-PD due to the difference in the accumulated carriers (electrons or holes). Moreover, the output power is even higher than those reported for LT-GaAs photomixers [11, 15]. These results clearly indicate that the UTC-PD is a promising and realistic device for generating a continuous THz wave with a practical output power, which is required in various applications.

Summary

We have investigated the generation of mm/sub-mm-waves at frequencies of up to the THz range by using an antenna-integrated UTC-PD. The fabricated device exhibits a record output power of 300 μW at 300 GHz and 2.6 μW at 1.04 THz, both with a good linearity. A quasi-optic module, which is the same size and has the same configuration as conventional O/E device modules, was also fabricated. The module exhibited output power similar to that of the chip, indicating the feasibility of the quasi-optic module. It could be operated at up to 1.5 THz, which is the highest operation frequency ever reported for the PDs operating at 1.55 μm. These results clearly demonstrate that the antenna-integrated UTC-PD is highly promising for use as a photonic mm-/sub-mm-wave generator in various practical applications in the THz range, such as sub-mm-wave spectroscopy, imaging, and a photonic local oscillator system in radio telescopes.

Acknowledgments

The authors thank T. Nagatsuma for his valuable discussions on the measurements, J. Yumoto and Y. Yoshikuni for their continuous encouragement, and Prof. M. Ishiguro of the National Astronomical Observatory of Japan for his stimulating discussions on photonic mm-wave sources.

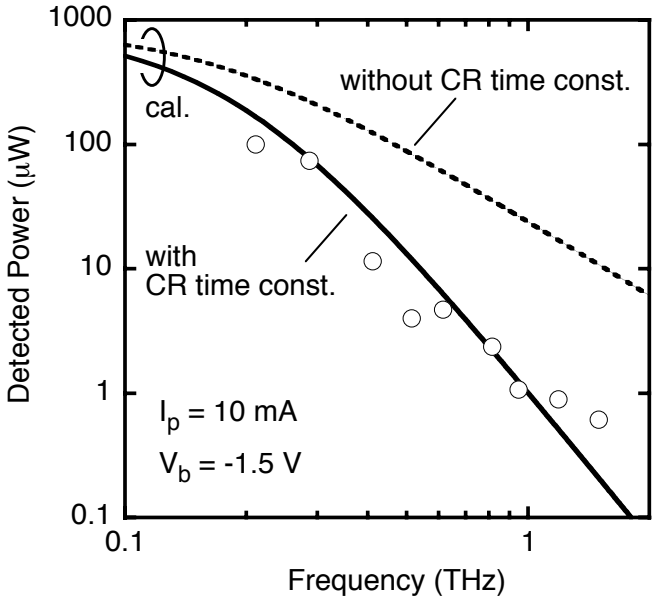

Fig. 7. Relationship between measured mm-/sub-mm-wave output power and frequency for the UTC-PD module.

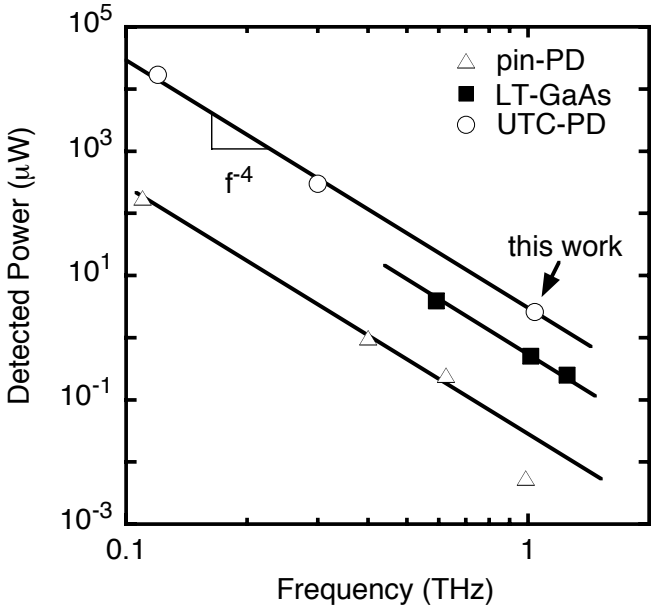

Fig. 8. Comparison of reported mm-/sub-mm-wave output power against the operation frequency for UTC-PDs, pin-PDs, and LT-GaAs photomixers.

References

[1] J. Payne, B. Shillue, and A. Vaccari, "Photonic techniques for use on the Atacama large millimeter array," Tech. Dig. Int. Topical Meeting on Microwave Photonics, pp. 105-108, 1999.

[2] K. A. McIntosh, E. R. Brown, K. B. Nichols, O. B. Mcmahon, W. F. Dinatale, and T. M. Lyszczarz, "Terahertz photomixing with diode lasers in low-temperature-grown GaAs," *Appl. Phys. Lett.*, vol. 67, pp. 3844-3846, 1995.

[3] A. Malcoci, A. Stöhr, S. Schulz, and D. Jäger, "Optical THz generation," Tech. Dig. Int. Topical Meeting on Microwave Photonics, pp. 179-182, 2003.

[4] K. Kato, S. Hata, K. Kawano, and A. Kozen, "Design of ultrawide-band, high-sensitivity p-i-n photodetectors," *IEICE Trans. Electron.*, vol. E76-C, pp. 214-221,1993.

[5] T. Ishibashi, N. Shimizu, S. Kodama, H. Ito, T. Nagatsuma, and T. Furuta, "Uni-traveling-carrier photodiodes," Tech. Dig. Ultrafast Electronics and Optoelectronics, pp. 83-87, 1997.

[6] H. Ito, T. Furuta, S. Kodama, and T. Ishibashi, "InP/InGaAs uni-travelling-carrier photodiode with 310 GHz bandwidth," *Electron. Lett.*, vol. 36, pp. 1809-1810, 2000.

[7] H. Ito, T. Nagatsuma, A. Hirata, T. Minotani, A. Sasaki, Y. Hirota, and T. Ishibashi, "High-power photonic millimetre-wave generation at 100 GHz using matching-circuit-integrated uni-travelling-carrier photodiodes," *IEE Proc. Optoelectron.*, vol. 150, pp.138-142, 2003.

[8] H. Ito and T. Nagatsuma, "High-speed and high-output-power uni-traveling-carrier photodiodes," Proc. SPIE, No. 4999, pp. 156-166, 2003.

[9] H. Ito, T. Furuta, Y. Hirota, T. Ishibashi, A. Hirata, T. Nagatsuma, H. Matsuo, T. Noguchi, and M. Ishiguro, "Photonic millimeter-wave emission at 300 GHz using an antenna-integrated uni-travelling-carrier photodiode," *Electron. Lett.*, vol. 38, pp. 989-990, 2002.

[10] H. Ito, F. Nakajima, T. Furuta, K. Yoshino, Y. Hirota, and T. Ishibashi, "Photonic terahertz-wave generation using an antenna-integrated uni-travelling-carrier photodiode," *Electron. Lett.* vol. 39, pp. 1828-1829, 2003.

[11] S. Verghese, K. A. McIntosh, S. M. Duffy, and E. K. Duerr, "Continuous-wave terahertz generation using photomixers," in *Terahertz Sources and Systems*, edited by R. E. Miles, P. Harrison, and D. Lippens, Kluwer Academic Publishers, Netherlands, pp. 157, 2001.

[12] H. Ito, T. Ito, Y. Muramoto, T. Furuta, and T. Ishibashi, "Rectangular waveguide output uni-traveling-carrier photodiode module for high-power photonic millimeter-wave generation in the F-band," *IEEE J. Lightwave Tech.*, vol. 21, pp. 3456-3462, 2003.

[13] P. G. Huggard, B. N. Ellison, P. Shen, N. J. Gomes, P. A. Davis, W. P. Shillue, A. Vaccari, and J. M. Payne, "Efficient generation of guided millimeter-wave power by photomixing," *IEEE Photonics Technol. Lett.*, vol. 14, pp. 197-199, 2002.

[14] P. G. Huggard, B. N. Ellison, P. Shen, N. J. Gomes, P. A. Davis, W. P. Shillue, A. Vaccari, and J. M. Payne, "Generation of millimetre and sub-millimetre waves by photomixing in 1.55 mm wavelength photodiode," *Electron. Lett.*, vol. 38, pp. 327-328, 2002.

[15] S. M. Duffy, S. Verghese, K. A. McIntosh, A. Jackson, A. C. Gossard, and S. Matsuura, "Accurate modeling of dual dipole and slot elements used with photomixers for coherent terahertz output power," *IEEE Trans. Microwave Theory and Tech.*, vol. 49, pp. 1032-1038, 2001.

PHOTON-COUNTING SUPERCONDUCTING DETECTORS FOR SUBMILLIMETER ASTRONOMY: RECENT RESULTS

J.D. Teufel, L. Frunzio, M. Shen, D.E. Prober, R.J. Schoelkopf
Depts. Of Applied Physics and Physics, Yale University, New Haven, CT

W.-T. Hsieh, , M.J. Li, F.A. Pellerano, G. Schneider,
C.M. Stahle, T.R. Stevenson, D.E. Travers, E.J. Wollack
NASA Goddard Space Flight Center, Codes 553 and 555, Greenbelt, MD

We are developing superconducting direct detectors for submillimeter astronomy that can detect individual photons. These Al-based STJ detectors count quasiparticles generated breaking Cooper-pairs by photon absorption in the submillimeter band. They could yield high quantum efficiency, microsecond response time, and sensitivities of 1e-20 W/rt(Hz). The use of antenna coupling to a small absorber also suggests the potential for novel instrument designs and scalability to imaging or spectroscopic arrays. The use of an RF readout scheme also naturally lends itself to wavelength-division multiplexing for simultaneous readout of large arrays. We describe device concept, fabrication and dark current characterization of these detectors. Measurements of the STJ dark current scale exponentially with temperature down to 200 mK and can be as small as 1 fA, corresponding to detector sensitivity less than 1e-20 W/rt(Hz). We are also developing hot-electron microbolometers that can be used as calibrated blackbody sources for characterizing the detector photoresponse. We will also present current work on RF readout, noise and sensitivity characterization. All of these developments will be key ingredients in scaling to large detector arrays.

CLOVER- A Novel Instrument for Measuring the CMB Polarization

G. Yassin[*], P. A. R. Ade[+], C. Calderon[+], A. D. Challinor[*], L. Dunlop[*], W. K. Gear[+], D. J. Goldie[*], K. J. B. Grainge[+], M. J. Griffin[+], M. E. Jones[*], A. N. Lasenby[*], B. Maffei[+], P. D. Mauskopf[+], S. J. Melhuish[+], A. Orlando[+], L. Piccirillo[+], G. Pisano[+], A. C. Taylor[*] and S. Withington[*]

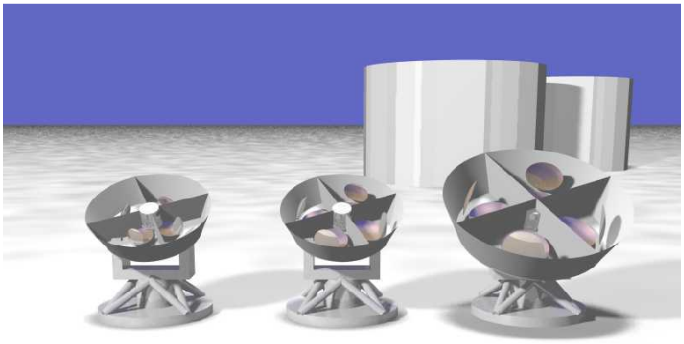

We describe the design and performance of a new fully-funded instrument, CLOVER, to measure the *B*-mode polarization of the cosmic microwave background. The instrument comprises three independent telescopes operating at 90, 150 and 220 GHz and is planned to be sited at Dome C, Antartica. Each telescope will fed by a focal plane array of 256 horns with background-limited detectors and will measure the polarization signal over angular multipoles $20< l<1000$. The unique design of the telescope and extremely low systematics should enable the *B*-mode signature from gravitational waves to be measured, or constrained to a lensing confusing limited tensor-to-scalar ratio $r \sim 0.005$.

1. Introduction

The Cosmic Microwave Background (CMB) provides direct information about the origin of the universe, and our current understanding of the cosmological evolution of the Universe is heavily based on measurements of the CMB radiation. Over the past 15 years a vast amount of information has been accumulated about the angular power spectrum of the CMB anisotropies. Ground-based, balloon-borne and satellite instruments such as COBE, CAT, DASI, VSA, Boomerang and WMAP have measured the CMB anisotropies at various angular

[*] Cavendish Astrophysics, University of Cambridge, UK
[+] Department of Physics and Astronomy, University of Cardiff, UK

scales and frequencies. The power spectrum obtained from these measurements agrees remarkably well with that predicted by the present cosmological models. The main cosmological parameters have been determined with impressive accuracy.

Despite these discoveries, it is now becoming clear that measurement of the temperature anisotropy alone will not provide the complete picture of the early universe. The anisotropy must be combined with additional information in order to break some degeneracies between cosmological models. This can only be done with the CMB alone by measuring its other defining characteristic, namely its polarization. Polarization of the CMB is caused by Thompson scattering of CMB photons at the last scattering surface (Hu and White, 1997). The signal can be decomposed into a curl and a curl-free component, known as the *B*- and *E*-mode respectively. The *E*-mode component is generated mainly as a result of density perturbations and has amplitude of approximately 10% of the temperature anisotropy. The *B*-mode signal however is generated entirely by primordial gravitational waves. It provides unique information about the early universe and would greatly increase our ability to place constraints on inflationary models. Unfortunately, the *B*-mode signal is at best an order of magnitude weaker than the *E*-mode component and its detection constitutes a major technological challenge. Recent advances in detector technology however, combined with better understanding of systematics have made this exciting prospect quite feasible.

In this paper we describe a novel instrument design with extremely low systematics that will be able to reach the sensitivity required for detecting the *B*-mode component to the limit set by contamination from gravitational lensing of the *E*-mode signal. The instrument comprises three completely independent telescopes, operating at 90, 150, and 220 GHz. Each telescope consists of four separate optical assemblies, fed by 265 background-limited detectors. The telescope beamwidth is 15' and will cover the range of angular multipoles $20 < l < 1000$. The division into four arrays, symmetrically distributed with respect to the cryostat axis, reduces aberrations substantially, and also helps to reduce cross polarization. A key feature of the instrument design is the employment of large-format arrays of antenna-coupled Transition Edge Sensors (TES). Power is fed to the TES via an antipodal finline taper that transforms the waveguide into a microstrip. The array symmetry allows us to feed groups of four channels, corresponding to horns pointing to the same direction in the sky and the same polarisation, to a single TES.

2. Science requirements

The polarization signal on the sky is a second-rank tensor that can be decomposed into a curl and a curl-free component, known as the *B*- and *E*-mode respectively (Kamionkowski, et al, 1997). The component generated as a result of density (scalar) perturbations has a characteristic zero-curl, i.e. *E*-mode, pattern**.** Polarization due to the metric perturbations of gravity waves has pure curl, i.e. *B*-mode, pattern. In addition, gravitational lensing by the intervening large-scale structure distorts the polarization field and converts power from one mode to the other. Since the *E*-mode has much higher amplitude, the important effect is to introduce a new *B*-mode component due to the lensing of the intrinsic *E*-mode.

The main science goal of CLOVER (Taylor *et al*, 2004) is to measure the power spectrum of B-mode polarization in the multipole range l =20–1000. We aim to make the measurement down to sensitivity limited by the contamination due to foreground lensing of the E-mode signal for multipoles $l \le 200$. From a two-year experiment, observing a near-circular survey region of radius 15 degrees we expect a thermal thermal noise level after subtraction of foregrounds of ~ 0.3 μK per resolution element (15-arcmin by 15-arcmin) to the Stokes parameters Q and U. For comparison, the expected r.m.s. of Q and U is 2.1μK at 15-arcmin resolution; 0.1μK of this arises from the B-mode polarization generated by lensing, and $0.3\sqrt{r}\ \mu$K from gravitational waves. The performance of CLOVER in measuring the total power B-mode spectrum for three different values of the tensor-to-scalar ratio is shown in Fig. 1. We find that the one-sigma error on r, computed from the errors on C_l^B in the null hypothesis $r = 0$, is Δr = 0.004, and is limited by the sample variance of the lensing signal. This sets the detection limit of gravitational waves from a measurement of B-mode polarization with CLOVER. A summary of the instrument specification is given in table 1.

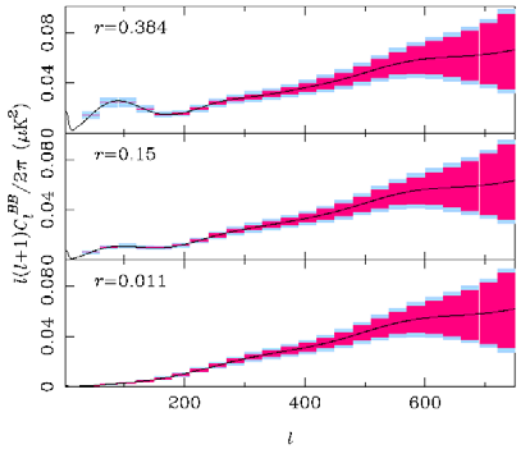

Figure 1: *Expected errors from CLOVER on the B-mode power spectrum for flat, ΛCDM inflation models. The upper panel has tensor-to-scalar ratio r=0.384 corresponding to the 68-per cent upper limit from CMB and large-scale structure data of (Leach & Liddle 2003). The middle panel is for ϕ^2 inflation, with r=0.15. The lower panel is for small-field, parabolic inflation with r=0.011. The inner error boxes are the contribution from instrument noise; the outer boxes also include sample variance (from gravitational waves and weak lensing).*

Table 1: Key specifications of CLOVER

Telescope frequency	**90 GHz**	**150 GHz**	**220 GHz**
Δf (GHz)	30	45	60
Photon NEP $W/\sqrt{Hz}$	2.7×10^{-17}	3.7×10^{-17}	5.8×10^{-17}
Detector NEP $W/\sqrt{Hz}$	$< 2\times10^{-17}$		
NET $\mu s\ s^{1/2}$	170	215	455
Array NET $\mu s\ s^{1/2}$	10.5	13.4	28.5
Number of horns	256	256	256
Number of modes	512	512	512

3. Instrument description

3.1 General layout

We have already indicated that CLOVER consists of three completely independent telescopes. The design of the array, optical assemblies and pseudo-correlator are shown in Fig. 2. Each telescope consists of four separate, co-pointed optical assemblies, each fed by an 8 *x* 8 array of feed horns. The signal from each horn is separated into the two independent linear polarization states, converted to circular polarization, phase modulated and then correlated. The two correlator outputs encode the Stokes parameters *I, Q* and *U*. The outputs from each corresponding pixel in the four telescopes are then summed incoherently before being detected by a TES bolometer. There are thus 256 horns per telescope but only 64 simultaneously observed pixels, since the optical assemblies are co-pointed. The sensitivity however is equivalent to 256 individually-detected pixels. Stokes parameters *Q* and *U* are measured instantaneously by the phase modulation in the polarimeter, while *I* is measured by scanning the telescope. The four optical assemblies are built around a single cryostat which houses all four horn/polarimeter arrays and the detector array, and are mounted on a common mount which allows altitude-azimuth tracking as well as rotation of the entire optical assembly.

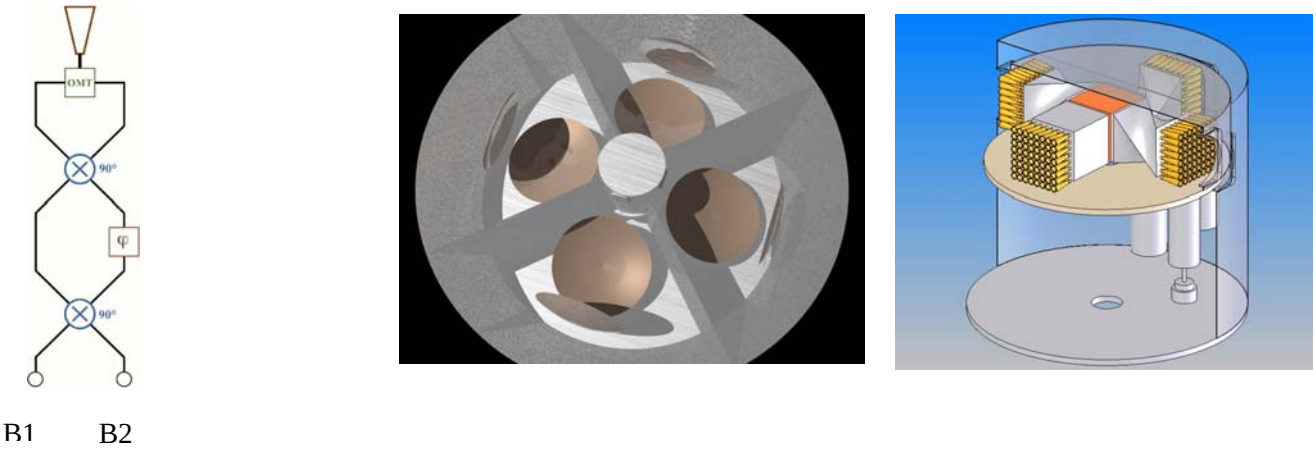

Figure 2: **Left:** Schematic view of the pseudo correlation receiver. **Middle**: A schematic view of a CLOVER telescope with four co-pointing Compact Range Antennas (CRA). Each CRA is fed by 64 horns. **Right**: The central cryostat containing four 64-feed arrays and the sections behind containing the hybrids and phase switches.

The division into four arrays distributed symmetrically with respect to the Cryostat axis reduces aberrations substantially, helps to minimise cross polarization and reduces the number of required TES devices by a factor of 4.

3.2 The pseudo correlation polarimeter

There are several advantages in utilizing a correlation receiver scheme for the imager. In particular, it allows determining the Stokes parameters *Q* and *U* simultaneously at the sky pixel, by taking the difference of the detector outputs, without moving the optics. To calculate the polarimeter outputs, the electromagnetic radiation incident on each antenna is written in terms of its Jones vector. Each component of the polarimeter shown in Fig. 3 is then expressed in terms of its Jones polarisation matrix and the total polarisation matrix is found by multiplying the individual matrices. It can be shown that the outputs of the two polarimeter detectors is given by:

$$B1 = I - Q \cdot \cos\varphi - U \cdot \sin\varphi$$

$$B2 = I + Q \cdot \cos\varphi + U \cdot \sin\varphi$$

The above equation tells us that our polarimeter is sensitive to *I, U* and *Q* Stokes parameters. By varying the phase difference from 0 to 90 degrees we can cycle the outputs between *Q* (-*Q*) and *U* (-*U*). If we chop the phase difference between 0 and 180 degrees, the U term is always zero and we can measure just *Q*.

3.2 Telescope optics

We have already indicated that each CLOVER telescope employs four optical assemblies, each is a Compact Range Antennas (CRA) which is an offset-fed design consisting of a hyperbolic secondary and an offset parabolic primary. This design exhibits low beam distortion and cross polarisation, hence is ideal for a large imaging array, since beams generated by feeds at the edges of the array suffer much less distortion than those obtained in offset Cassegrain or Gregorian systems. An important advantage of this design is that it allowed the choice of the reflectors dimensions to be entirely based on the required resolution (*l*-range) rather than to be artificially large in order to reduce aberrations. The *l*-range chosen for CLOVER was $20<l<1000$ corresponding to a 15-arcmin FWHM main beam. This could be obtained at 150 GHz with a main reflector diameter 800 mm, sub-reflector dimensions 735 mm *x* 700 mm and ideal hybrid feeds with flare angle 10 degrees and aperture diameter 15 mm.

Calculation of the radiation patterns of the antenna was made using the software package GRASP which employs the rigorous Physical Optics method. In Fig. 3 we show co-polar contour plots, both for the feed located at the centre of the array and also when the feed is offset by 50 mm in the focal plane. The cross polarization component for the central pixel is less than –60 db and for the outer pixel –35 db. The very low levels of cross-polarization and aberration of this optical system are a key advantage of the CLOVER design.

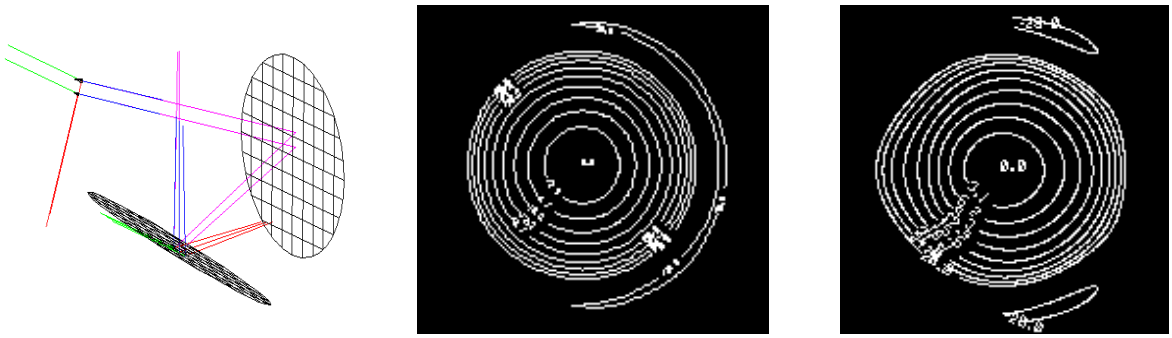

Figure 3. *Radiation patterns obtained when the feed is placed in the centre of the array (centre) and with the feed is moved 50mm in the positive x-direction (right). The Physical Optics simulated geometry of the CRA (left) is also shown.The rays are shown for clarity but are not used in the calculations.*

3.3 **Detector array**

3.3.1 *The single pixel*

A detector may be considered suitable for CMB polarization measurements if it satisfies the following requirements: (i) background limited sensitivity (ii) high dynamic range (iii) large bandwidth and (iv) easy to fabricate. The need for large bandwidth to enhance sensitivity makes bolometric detection appealing for CMB polarisation measurements. We aim to achieve a bandwidth of 30%, which is possible through careful design of all components. The single-pixel sensitivity required for detecting CMB polarization is high, and therefore it is essential to ensure that the sensitivity is limited by the sky background rather than the detectors themselves. Assuming that the background level at Dome C limits the sensitivity at 150 GHz to $s \approx 200\ \mu\mathrm{K\,s}^{1/2}$ and assuming an RF bandwidth of 50 GHz, the required NEP $\approx 4\times10^{-17}\ \mathrm{W}/\sqrt{\mathrm{Hz}}$ which is within the capability of modern TES bolometers operating at 300 mK.

Voltage-biased Transition Edges Sensors have recently been thoroughly investigated in view of using them in CMB instruments. A TES consists of a thin superconducting film deposited on a silicon nitride membrane. The device is biased at the middle of the transition region between the normal and superconducting states. Absorbed photons heat the quasiparticle gas, causing a sharp increase in the electrical resistance, and therefore a decrease in bias current. This electro-thermal feedback keeps the TES on the transition point and, as a by-product, decreases the effective time constant, making the devices very fast. The change in electrical current is read out by a SQUID. An important advantage of the TES over other widely-used detectors (eg NTD bolometers) is that it can be fabricated using lithography. This means that the detector itself and the feeding RF circuits can be fabricated at the same time using

miniature superconducting planar circuits. Moreover, the detector lends itself to frequency or time domain multiplexing which reduces the required readout components substantially. These properties become crucial for large format arrays such as for CLOVER. Finally the TES can be shown to have large dynamic range, hence it has all the properties that are required for high performance CMB instruments.

3.3.2 *The TES chip*

The design of the individual TES and the detector chip architecture is clearly chosen to suit the array configuration. In CLOVER, groups of four horns (one from each sub-array) are pointing at the same direction in the sky. Consequently, each TES is fed by four microstrip lines corresponding to the same polarimeter output, as shown in Fig. 4. Transition from waveguide to microstrip is made using an antipodal finline taper consisting of two superconducting fins of 300 nm Niobium separated by 400-nm SiO with the whole structure fabricated on a 200 μm silicon substrate (Yassin and Withington, 1995) . The width of the resulting microstrip is 3 μm, corresponding to a characteristic impedance of 20 Ω which is both electrically convenient and allows the fabrication of a large number of microstrip networks on a single substrate. Efficient coupling of power from the microstrip to the TES is achieved by terminating the microstrip with a resistor that heats the device. Details of the electric and thermal design of the antenna coupled TES have already been reported (Dunlop *et al*, 2004)

The detector operates from a bath temperature of 300 mK, and is modelled as a $50\times 50\ \mu\mathrm{m}^2$ Mo/Cu TES each of 50 nm thickness with 300 nm thick Cu edges - to ensure fully normal edges of the TES, with a total Nb volume of $200\times 200\times 0.5\ \mu\mathrm{m}^3$ representing the microstrip and TES bias lines. The total heat capacity for $T_c = 400\,\mathrm{mK}$ is estimated as $84\,\mathrm{fJ/K}$. Thermal isolation is provided by patterning the $0.5\ \mu$m thick Si_3N_4 into 8 bridges each of $20\ \mu$m width giving a total thermal conductance of $G = 58\,\mathrm{pW/K}$, an intrinsic time constant of 1.4 ms and a limiting NEP of $1.7\times 10^{-17}\ \mathrm{W}/\sqrt{\mathrm{Hz}}$ determined by the thermal conductance.

The detector array configuration is illustrated in Fig. 4. One possible layout is a rectangular wafer loaded with finline substrate transitions from 4 sides, each side fed by one of the four horn arrays. Each side of the wafer will therefore have 16 finline channels corresponding to 8 horns with two polarisations. In total, the wafer will have 64 microstrip channels and 16 TES detectors. Sixteen of the chips shown in Fig 4. are needed to populate the array, two for each horn array vertical layer. Alternatively the finline channels can be re-directed to two sides of the rectangular substrate thus avoiding microstrip crossings as shown in Fig. 4. Each group of 8 TESs is frequency multiplexed and read by a single wideband, low-noise SQUID.

3.3.3 *Readout and multiplexing*

Frequency multiplexing is obtained by AC biasing the TES devices with a comb generator, ΣV, which is a sum of bias voltages at the resonant frequencies. Each TES is modelled as an RLC circuit with a resonant frequency $f_i = 1/(2\pi\sqrt{LC_i})$ which is equal to the frequency of the voltage bias of the individual TES.

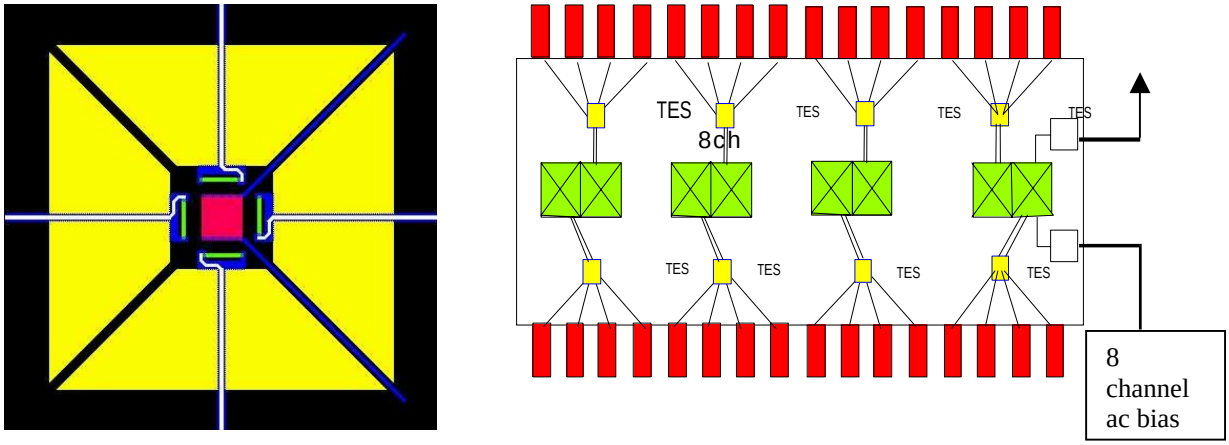

Figure 4: (a) *Scale layout of a single pixel with TES (red), Nb bias lines (blue), microstrip line (white on blue) and termination resistors (green). The nitride membrane is removed in the regions shaded yellow.* (b) *Schematic of a detector module. 32 fin-lines are coupled to 8 TES and a single 8 channel multiplexer. Read-out is by a single wideband, low noise SQUID.*

The half-width of the resonance $\Delta f_i = f_i / 2Q_i$ needs to be chosen to exceed both the detector thermal bandwidth $f_{thermal} = 1/2\pi\tau$, where the time constant includes the effect of electro-thermal feedback, and the signal bandwidth Δf_{sig}.

We assume a frequency spacing of 20 kHz and a minimum resonant frequency of 100 kHz. With a signal bandwidth of 1 kHz, the maximum required $Q_{\max} = f_{\max}/2\Delta f_{sig} = 120$. Assuming $R_{TES} = 0.5\,\Omega$ at the operating point, we require capacitor values in the range 11 to 64 nF. These can be achieved by anodization of thin film Nb with dimensions in the range 1.9 to 4.6 mm^2. Estimated power cross-talk is about -25 dB in this example. The resonant bias AC sources for the TESs also provide reference signals for the demodulation, cancelling phase noise to first order. Demodulated signals are low-pass filtered so that the sampling rate for each individual A to D needs to be $f_{sample} = 2 f_{bw}$ of order 2 kHz.

4. Observation strategy

It is intended that Clover will be installed at Dome C on the Antarctic Plateau at an altitude of 3200~m. This site is one of the premier locations for mm and sub-mm observations, providing dry and atmospherically stable conditions which are comparable to, if not slightly better than, the South Pole. In the first two years of operation we aim to observe a connected region of sky of a few hundred square degrees. We plan to implement a multi-cross scanning strategy consisting of observing a given patch of sky scanning over a fixed azimuth range while keeping the elevation constant for a 2-3-hour period. Once this time has elapsed, the centre azimuth and elevation are changed to follow the sky patch and constant elevation scans are repeated. This strategy results in a well cross-linked coverage of a single sky area. The

telescopes will also be periodically rotated about the pointing axis to calibrate out instrumental effects and improve the density and cross-linking of the sky coverage.

5. Conclusion

We have presented the design of a high performance imaging instrument, CLOVER, for measurement of the *B*-mode polarization component of the Cosmic Microwave Background. The focal plane array of CLOVER combines both the low systematics of corrugated feed and the simplicity and reliability of planar circuit technology. The novel design of the telescope optics allows 512 pixels (for two polarizations) to be used without substantial degradation in the radiation pattern. The large number of background-limited detectors combined with the well-known advantages of Dome C should allow CLOVER to reach the required sensitivity to detect gravity waves down to a tensor-to-scalar ratio $r \sim 0.005$, after two years of integration. The instrument will be fully operational by 2008. However, first light will be seen by a subset of the instrument at one frequency by the end of 2006.

Acknowledgements

CLOVER is UK-led instrument funded by the Particle Physics and Astronomy Research Council, in collaboration with the University of Rome and College de France.

References

1- W. Hu and M. White, astro-ph/9706147, (1997)
2- M. Kamionkowski, A. Kosowsky and A. Stebbins, *Phys. Rev. Lett*., **78,** 2058, (1997)
3- A. Taylor *et al*, in proceedings of XXXIXth Rencontres de Moriond, Editions Frontiers, (2004)
4- S. M. Leach and A. R. Liddle, *Phys. Rev.* D. **68**, 123508 (2003)
5- L. Dunlop *et al*, in proceedings of SPIE vol. 5498, Glasgow, UK, (2004)
6- G. Yassin and S. Withington, *J. Phys. D: Appl. Phys*., **28**, 1983, (1995)

Detection of 1.6 and 2 THz radiation with a Tunable Antenna-Coupled Intersubband Terahertz (TACIT) detector.

G. B. Serapiglia[a] , M. S. Sherwin[a], M. Hanson[b] , A. C. Gossard[b] and W. R. McGrath[c]

Physics Department and Iquest, University of California, Santa Barbara 93117[a]
Materials Department, UCSB[b]
Jet Propulsion Laboratory , Pasadena, California[c]

We have realized a new kind detector for Terahertz frequencies based on Intersubband Transitions in semiconductor quantum wells. Intersubband transitions in our case occur between carefully engineered quantum confined electron states in the conduction band of coupled GaAs quantum wells. The optically excited electrons thermalize rapidly, increasing the electron temperature and hence the resistance of a heterojunction channel. The resistance is measured between source and drain ohmic contacts using a current amplifier. Two 25 micron squared Schottky gates define the channel, and are used to tune the absorption resonance via the Stark effect and by varying the electron density. The intersubband transition linewidth of 100 GHz defines the detection bandwidth, and the center frequency can be tuned between 1 and 2.5 THz by applying gate voltages of order 1 Volt.

The detector was fabricated using flip chip microprocessing to integrate the quantum well absorbing region at the focus of a twin-slot dipole antenna. The antenna, RF filters and 5micron by 5 micron mesa were all patterned on a GaAs wafer, which was subsequently thinned to 0.7 microns in order to couple the quantum well most efficiently to the antenna leads and Schottky gates. The device was mounted on a silicon lens to couple light more efficiently to the antenna radiation pattern.

In order to test the device, we used highly attenuated, 5 microsecond pulsed plane waves from UCSB's Free Electron Laser (Figure 1). We scanned the gate voltages to tune the TACIT detector in and out of resonance with the laser tuned to either 1.6 or 2 THz. The data (Figure 2) shows that for a particular frequency, the device tunes into resonance for two stark fields, of equal magnitude but opposite sign, as it should for symmetrical biasing. The data also agree very well with theoretical calculations based on solving Schrodinger's equation. So far, working with non-optimized, first generation samples, we have achieved responsivities of order 1Volt/Watt at temperatures of 77K, and are working towards our theoretical prediction of 1kV/W. The detector is at least as fast as the 5 microsecond laser pulse length and this response time is currently limited by the amplifier electronics. Theory[1] predicts operation as a heterodyne mixer could achieve nearly quantum noise limited performance with IF frequencies exceeding 10GHz at temperatures above 77K. This work was supported by NASA under contract NAG10299.

Email: brendan@iquest.ucsb.edu

[1] M. S. Sherwin *Proceedings of Far-IR Sub-mm and mm Detector Technology Workshop* (April 2002)

Experimental Set up

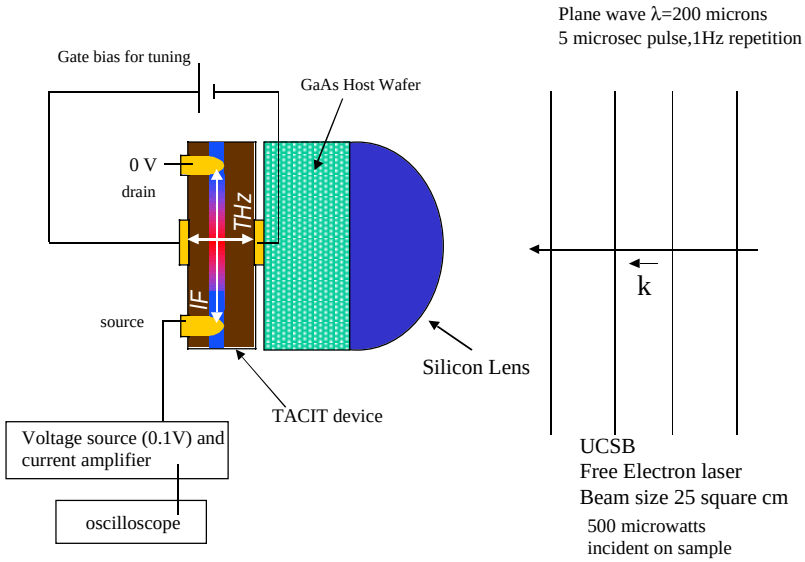

Figure 1

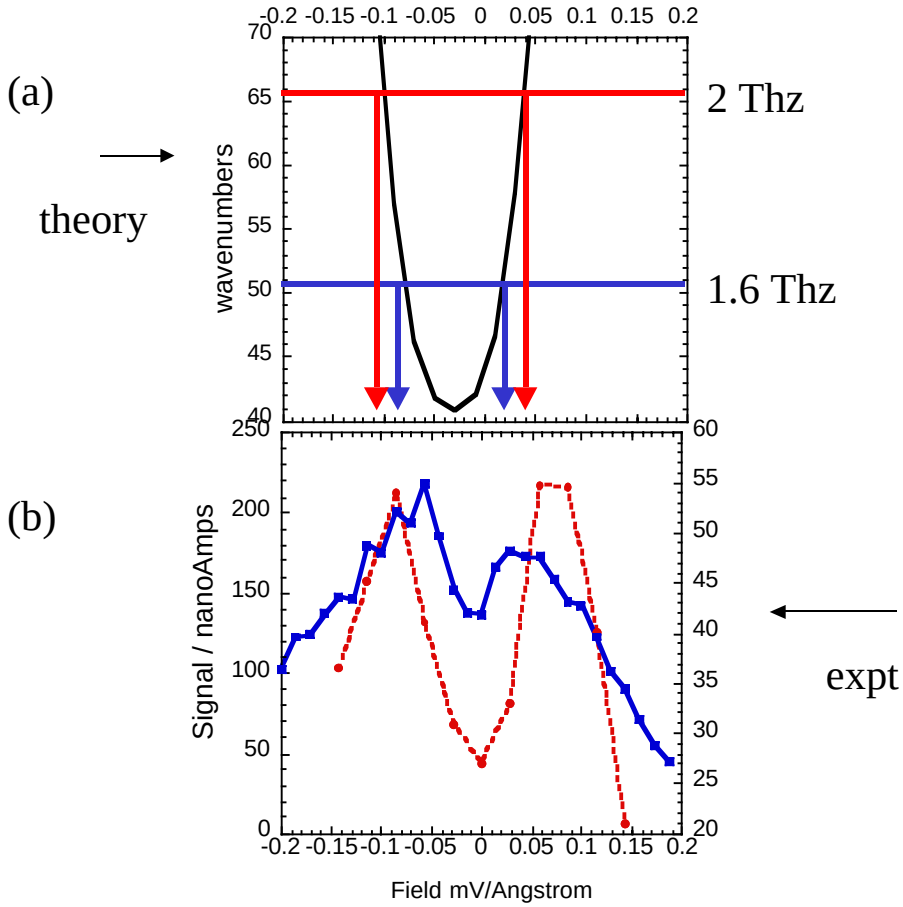

Figure 2 (a): Theoretical calculation for the frequency response as a function of applied DC field, based on solving Schrodinger's equation. **(b)** Signal as a function of gate voltage (DC stark field) for two different incident Terahertz fields at 2 THz (dotted curve) and 1.6 THz (solid curve). The double resonance occurs because DC fields of equal magnitude but opposite sign result in the same Stark shift.

Quantum Mechanical Mixing Model for Hot Electron Bolometers

Harald F. Merkel, P. Khosropanah, T. Berg, S. Cherednichenko, E. Kollberg
Chalmers University of Technology
412 96 Göteborg, Sweden

In recent experiments, quantum effects have become visible in the device noise of hot electron bolometers. Modelling attempts have been made to asses this additional noise [1] Here a model is presented, where the bolometer is associated with a photon counting operator. Since the local oscillator and the radio frequency signal are treated as photon flows, a stochastic fluctuation of the absorbed power in time is caused by the graininess of the incoming radiation. Applying counting operators to the downconverted signal and using a simple Poisson distribution for the presence or absence of a photon, a closed form expression for the quantum noise of the HEB is found that is similar to the relations given in [1]. Quantum noise is a substantial part in the mixer noise at larger THz frequencies and dominates the mixer noise of NbN phonon cooled HEB at frequencies around 8THz and above. Quantum noise contributions are found to be subject to the same electrothermal feedback process as fluctuation and thermal noise are. A way to minimize quantum noise contribution is one is achieved by a correct matching of the active part of the bolometer to the antenna. On the other side, for frequencies above the quasiparticle bandgap, the whole HEB must be matched to the antenna for optimum performance so the best mixer performance lies in between these extrema.

[1] S. Yngvesson, E. Kollberg, Proceedings 14th. ISSTT , 2003 Tucson, AZ

SUPERCONDUCTING HOT-ELECTRON BOLOMETER MIXER FOR TERAHERTZ HETERODYNE RECEIVERS

Alexei D. Semenov[a], Heinz-Wilhelm Hübers[a], Heiko Richter[a], Konstantin Smirnov[c], Gregory N. Gol'tsman[c], and Boris M. Voronov[c]

[a] DLR Institute of Planetary Research, 12489 Berlin, Germany
[c] Moscow State Pedagogical University, 119891 Moscow, Russia

A number of on-going astronomical and atmospheric research programs are aimed to the Terahertz (THz) spectral region. At frequencies above about 1.4 THz heterodyne receivers planned for these missions will use superconducting hot-electron bolometers as a mixers.

We present current results on the development of superconducting NbN hot-electron bolometer mixer and quasioptical radiation coupling scheme for GREAT (German Receiver for Astronomy at Terahertz Frequencies, to be used aboard of SOFIA) and TELIS (Terahertz Limb Sounder). The mixer is incorporated into hybrid antenna consisting of a planar feed antenna, which has either logarithmic spiral or double-slot configuration, and hyperhemispherical silicon lens. For the log-spiral feed antenna, the double side-band receiver noise temperature of 5500 K was achieved at 4.3 THz. The noise temperature shows less than 3 dB increase in the intermediate frequency band from 4 GHz to 7 GHz. The hybrid antenna had almost frequency independent and symmetric radiation pattern with the beam-width slightly broader than expected for a diffraction limited pattern. Results of FTS measurements in the direct detection regime agreed with the spectral dependence of the noise temperature for spiral antennas with different spacing of inner terminals.

Presenting author

Alexei Semenov
DLR Institute of Space Sensor Technology and Planetary Exploration
Rutherfordstrasse 2
12489 Berlin
Germany

Tel. +49 (30) 670 55-505
Fax +49 (30) 670 55-507
E-mail: Alexei.Semenov@dlr.de

Presentation form: Oral, if possible

A Prototype Focal Plane Array with HEB Mixer Elements and MMIC IF Amplifiers

F. Rodriguez-Morales[a], K.S. Yngvesson[a], E. Gerecht[a], N. Wadefalk[b] J.Nicholson[a], D.Gu[a], X. Zhao[a], T. Goyette[c], and J. Waldman[c]

[a]University of Massachusetts at Amherst
[b]California Institute of Technology
[c]Submillimeter Technology Laboratory, University of Massachusetts at Lowell

ABSTRACT

We describe the design, construction and testing of a 3-element prototype focal plane array (FPA) based on HEB superconducting mixers and wide-band MMIC IF amplifiers. This prototype is the first functional heterodyne FPA to be reported for any frequency above 1 THz. The FPA module makes use of a quasi-optical coupling scheme and incorporates all bias and IF circuitry in the same housing, resulting in a fairly compact design, with the MMIC amplifiers placed in the same plane as the HEB devices. We present novel experimental results regarding noise temperature and coupling efficiency of this array. We also discuss how the number of pixels can be enlarged considerably in the future by using a multi-level array architecture.

1. INTRODUCTION

The development of Hot Electron Bolometer (HEB) technology over the past decade has made possible the implementation of single-pixel observing platforms operating at terahertz frequencies. Instruments such as TREND, TELIS, GREAT, and HIFI, are current examples of heterodyne receivers based on this technology. Similarly, cryogenic IF amplifiers have evolved over the last two decades from GaAs Field Effect Transistors (FETs) to High Electron Mobility Transistors (HEMTs) and more recently to InP HEMTs [1]. Advances in modelling and fabrication technologies have brought forth Microwave Monolithic Integrated Circuit (MMIC) Low Noise Amplifiers (LNAs) with remarkable noise performance and low dc-power consumption [2]. In order to exploit the benefits of these ongoing technological efforts even further, it is worthwhile to consider the integration of HEB mixers and MMIC amplifiers into focal plane arrays. Such integration yields a substantial improvement in detection speed compared with single-pixel receivers. The low LO power consumption and near quantum noise limited performance of HEB mixers make them well suited for integration in multi-pixel FPAs.

We have developed a three element array based on the fly's-eye concept, as illustrated in Figure 1, where each detector element is placed in the focal plane of an objective lens or reflector. The implementation of the fly's eye concept utilizing HEB array receivers and MMIC amplifiers, was proposed in [3]. All the required DC-bias and RFI protection circuitry, are accommodated inside a split-block design that uses field-replaceable SMA connectors to extract the IF outputs for each pixel. The focal plane array prototype was designed to operate at 1.6 THz but can operate at any terahertz frequency by changing the design center frequency for the integrated antennas. This HEB FPA is fully operational and represents the state-of-the-art in receiver technology for terahertz frequencies.

2. DESIGN CONSIDERATIONS

Figure 2 illustrates the basic configuration for a single element in the array. This design is based on a single element receiver we have developed previously [4].

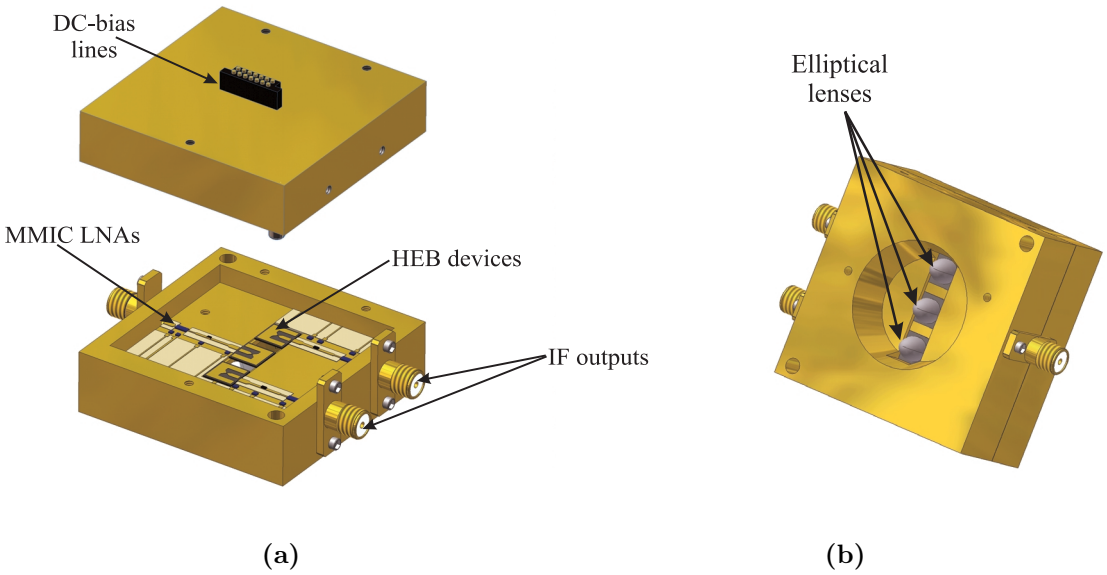

Figure 1: Concept for the 3x1 FPA: (a) Inside view; (b) Lens side.

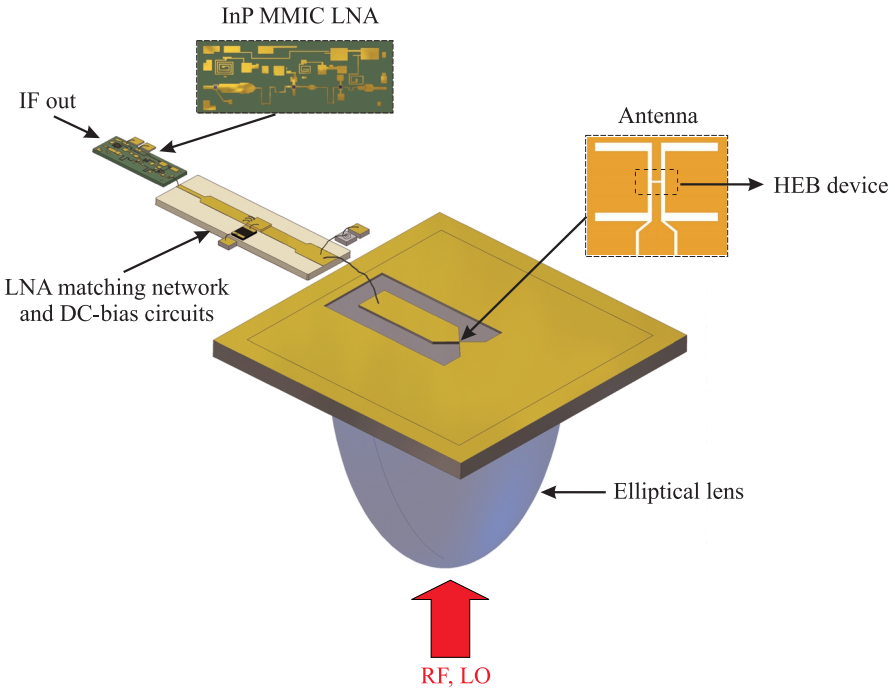

Figure 2: Concept of an integrated single-element THz receiver.

2.1 Quasi-Optical Considerations

We use a quasi-optical scheme to couple the incoming radiation to the detector, consisting of a silicon elliptical lens and a monolithic antenna. This configuration of a single pixel receiver was analyzed in [5] and [6]. Multipixel receivers for lower frequencies with a similar fly's eye configuration were described in [5] and [7]. A major advantage of this configuration is that it allows ample space for IF amplifiers, transmission lines, and bias lines. The active elements we use are phonon-cooled NbN HEBs fabricated on a 350 μm thick silicon substrate. The device chip size is 6 x 6 mm. We have previously developed a fabrication process for near quantum noise limited HEB devices integrated with either twin-slot or slot-ring antennas [8]. Both types of antennas were designed and tested at 1.6 THz.

2.2 MMIC IF Amplifiers

The MMIC chip utilized in our prototype was originally intended for use on the Allen Telescope Array [9]. It was developed and tested by Sander Weinreb and Niklas Wadefalk at JPL/Caltech. This amplifier (referred to as WBA-13) has three stages of InP transistors with 0.1 μm gate length, demonstrated gain of about 10 dB per stage and total noise temperature of less than 8K throughout the 1-10 GHz band. Figure 3a shows a picture of the MMIC chip (size 0.75 x 2 mm). The three capacitors shown on top are the pads for DC-bias of the transistors. Both the input and output pads are wire (ribbon) bonded to microstrip transmission lines placed at either end of the circuit. As can be seen in Figure 3b, the noise temperature of the WBA-13 is remarkably low and nearly independent of bias settings. This feature allows minimizing the power dissipation without paying the price in the total receiver noise temperature. Power dissipation will become a restrictive issue as the number of elements in the array becomes large.

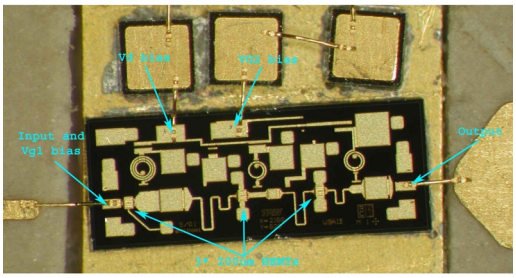

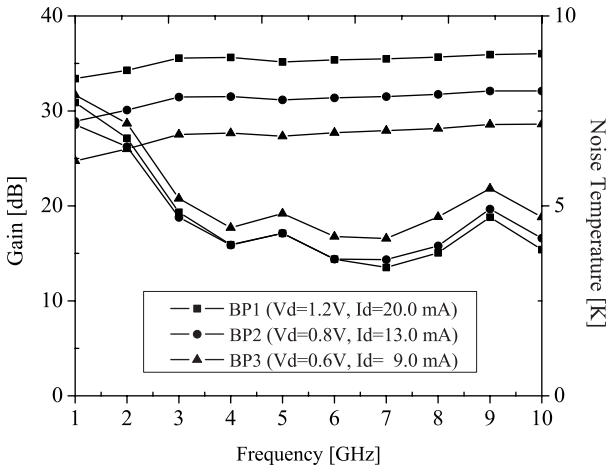

(a) **(b)**

Figure 3: WBA13 MMIC amplifier: (a) Close-up view of the chip; (b) Performance of the MMIC measured at 11K for different bias conditions.

2.3 MMIC/HEB Impedance Matching

In general, the impedance that a phonon-cooled HEB will present to the IF circuitry will be complex, yet predominantly real for frequencies below the *IF gain bandwidth*, i.e. the IF frequency at which the conversion efficiency of the mixer drops by 3 dB from its low IF value [4]. This IF impedance has been found to follow the differential slope in the IV curve for a particular bias point [4], [10]. Therefore the device impedance may be changed through the proper combination of LO power and DC voltage.

Consequently, it is reasonable to assume that the IF impedance of the HEB is close to 50 ohms, at least over the bandwidth of interest and in the vicinity of the optimum bias point. A multi-section matching transformer fabricated on microstrip line was placed at the input of each WBA-13 chip so that the impedance of the HEB is matched to the capacitive reactance presented by the MMIC input gate (see Figure 2).

2.4 DC-Biasing

The DC-biasing scheme for the HEB mixers in the FPA is a variation of the 4-wire concept used in the TREND instrument [11]. The matching network described in subsection 2.3 includes a series DC-blocking chip capacitor, which in conjunction with an RF-blocking spiral inductor, forms a broadband bias-tee for each mixer. A 50 kΩ resistor is used in order to inject the appropriate gate voltage to the first HEMT stage. Additional chip resistors are placed on a separate circuit board to monitor the voltage and current signals from the device, as well as for protection of the MMIC chips. A number of chip capacitors are soldered onto the same board to provide protection against RF interference and shunt transients to ground. All three elements are biased simultaneously using dedicated electronic circuitry interfaced using a computer running Labview® software.

3. FPA PROTOTYPE

The designed split-block structure was machined from OFHC copper (size 4.5 x 4.5 x 2.5 cm). All three MMIC amplifiers, silicon device chips and associated components were assembled together as shown in Figure 4. The spacing between elements was chosen to be 8.5 mm (Figure 4b) in order to avoid any interaction between radiating elements. The minimum possible spacing will be limited by diffraction effects [12], and will be investigated further in the future. The front half of the block (Figure 4c) contains part of the bias circuitry as well as the MMICs and the HEB devices, which were thermally contacted to the metallic block using small amounts of Stycast®. The electrical connections to the rest of the circuit were made using indium ribbon. Each MMIC was enclosed in a narrow rectangular cavity in order to minimize cross talk between amplifiers. The cavity is designed to have a cut-off frequency well above the maximum frequency of operation of the MMIC (75 GHz in this case). The input/output microstrip lines were not covered with a metallic structure. Instead, we used Eccosorb® microwave absorber to avoid exciting waveguide modes inside the block. These undesired modes lead to feedback effects that would otherwise drive the MMICs into oscillation.

All bias connections are routed from the front to the back half of the block (Figure 4d) using three multi-pin connectors. The back half of the module contains a circuit board with surface-mount components for DC-biasing. One main DC-connector located outside of the FPA provides the final interface to the liquid helium dewar wiring.

4. EXPERIMENTAL SETUP

Two different sets of tests were performed in order to characterize the noise temperature and optical coupling to the array elements. The LO source was a CO_2 laser pumped far-infrared (FIR) gas laser, operating on a 1.63 THz line in difluoromethane (CH_2F_2) gas with a typical power output of 30 mW. The power was injected through a six micron thick mylar beam splitter. We found that we had enough LO power to pump the three detectors simultaneously. This was achieved by defocussing the laser beam until it covered all elements. There are only two coaxial lines in our dewar. We were, therefore, unable to measure all three elements simultaneously. The noise temperature measurements were performed using the Y-factor method, where a hot/cold blackbody source is inserted into the signal beam path and the change in IF power is recorded [4]. The optical test was performed using sideband techniques, as described in [13]. An Offset-Axis Parabolic (OAP) reflector was used as the last focusing element. This mirror was mounted on a linear translator such that its vertical position could be moved. The incident beam to the OAP was the input signal, and this beam had been collimated to form a long waist. The OAP could thus be translated vertically while keeping the signal beam focused in the aperture plane of the two silicon lenses in the FPA, inside the cryostat.

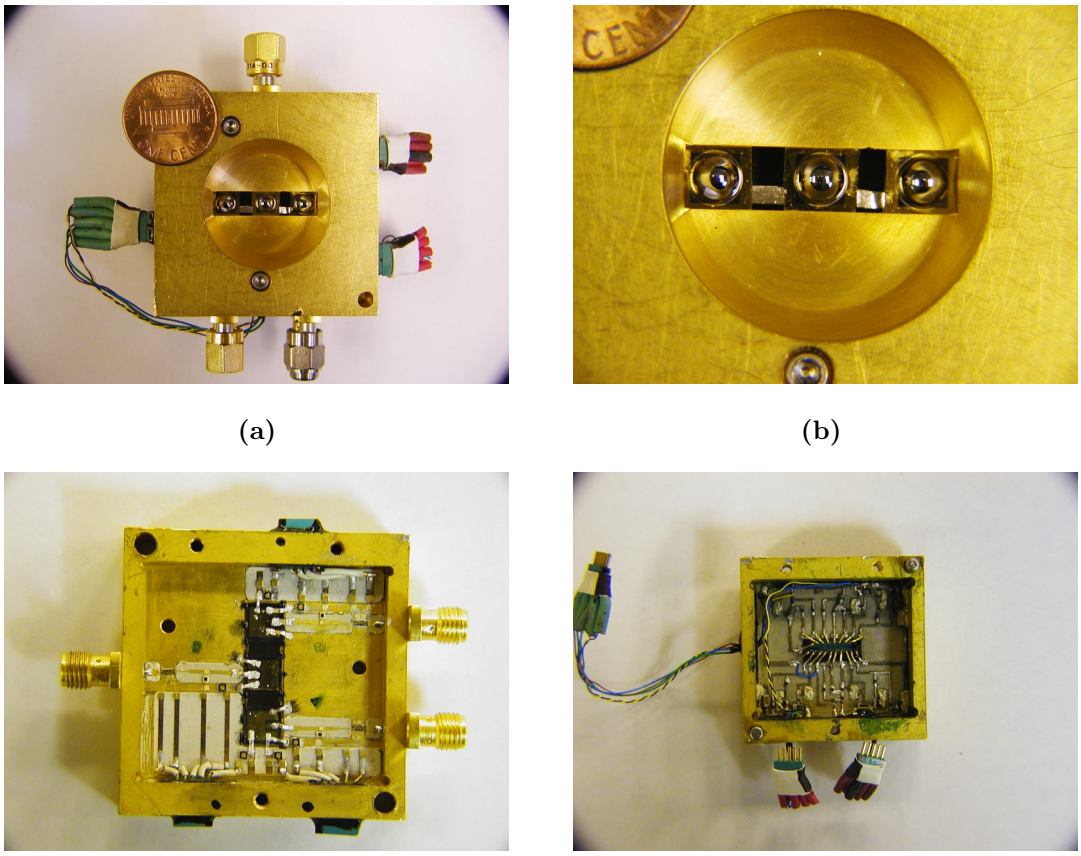

(a) **(b)**

(c) **(d)**

Figure 4: The three element FPA: (a) Seen from the lens side; (b) Close view of the lens side; (c) Inside of the front half; (d) Inside of the back half.

The FPA was mounted in the cryostat such that the two elements (designated A and C, respectively) were along the z-axis. The output signals from the two detectors under test were recorded on a spectrum analyzer. We used a convenient IF frequency of 2 GHz.

5. RESULTS AND DISCUSSION

We first performed noise measurements on one device installed in the FPA. This HEB device had been measured previously with the HEB device and the LNA on a separate module and connected through a short coaxial transmission line. The new configuration with the HEB much closer to the MMIC produced a different response, as can be seen in Figure 5a. The receiver noise temperature is essentially the same below the *noise bandwidth*[1] in both cases. The broadband matching of the HEB to the MMIC was affected by the FPA environment, causing a faster rise of the total noise temperature as the frequency grows. Nevertheless, we have successfully integrated an HEB and an MMIC in the same block for the first time and measured comparable noise temperatures over the useful bandwidth of the mixer.

In the next step, two HEB devices coupled with twin-slot antennas were measured simultaneously in the FPA unit. One element had a noise temperature of 1,200 K while the noise temperature of the second element was about 3,000 K, both at 1 GHz IF, as shown in Figure 5b[2]. The more sensitive device had a noise bandwidth of about 3.5 GHz (NB_1), versus 4.25 GHz (NB_2) for its counterpart.

[1]The frequency at which the noise temperature doubles with respect to its low frequency value [4].
[2]The second device had earlier been measured to have a similar noise temperature but had degraded.

The differences between the two elements are not unexpected since the IV characteristics were different. This is often due to NbN film inhomogeneity and fabrication issues. The final three element FPA module included a slot-ring device as the third detector. This specimen is expected to have a noise temperature of 2,000 K according to its IV characteristics.

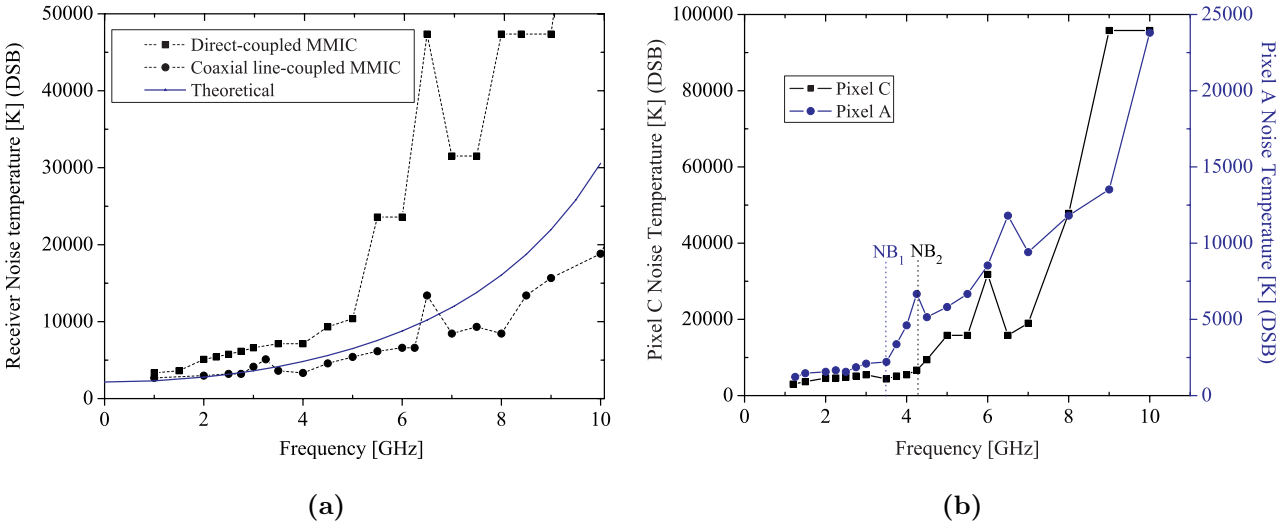

Figure 5: Measured IF response of the FPA: (a) Single element response; (b) Two elements pumped simultaneously.

Next, we performed the optical test using the general approach outlined above. The output power for both elements was recorded on a spectrum analyzer as the OAP displaced the signal beam along the z-axis. The data for this test are shown in Figure 6. The output powers were normalized to their respective peaks and are plotted on a linear scale. The dotted curve represents the expected response of the third element.

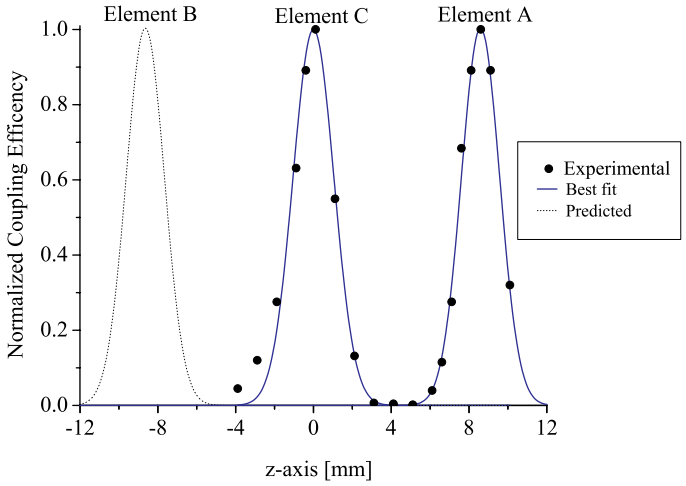

Figure 6: Measured response of two adjacent elements in the FPA.

We simulated the beams assuming a Gaussian shape for both the input sideband and the response of the individual elements. The Gaussian beam waists are assumed to be the same, as would be the case if the sideband were optimally focused on the elliptical lenses for the two FPA pixels. In the simulations we varied the Gaussian beam parameter, w, until a best fit to the measured data was obtained. This procedure produced a value for w very close to what we had calculated previously for the particular lens/antenna configuration, about 1.5 mm (see solid curve in Figure 6). The quasi-optical response is predicted to have a "Gaussicity" of about 94 %. The spacing between the two detected peaks also agrees well with the actual separation of the lenses, 8.5 mm. Furthermore, our simulations allowed us to estimate the minimum possible separation between contiguous pixels for future FPAs of this kind to be 4.25 mm.

6. CONCLUSIONS AND FUTURE WORK

We have designed, constructed and tested the first heterodyne focal plane array for any frequency above 1 THz. The design integrates three elements composed of MMIC IF amplifiers and NbN phonon-cooled HEBs. Isolators were not used in this design, which considerably reduced the size of the prototype. We showed the efficacious integration of an MMIC and an HEB for the first time. Very good noise temperatures were measured for low IF frequencies. Future investigation of the broadband matching mechanisms will allow us to extend the useful bandwidth of the receiver. We have successfully tested the optical coupling of contiguous elements in the FPA. The measured response showed a very good agreement with the theoretical prediction. The array presented here can in principle be extended to a larger number of elements. A large planar array, though, would lack adequate space for complete IF and DC-bias circuits and will present potential difficulties in thermal power dissipation [14]. To overcome these problems, we propose a multi-level architecture as illustrated in Figure 7. The lenses can be stacked with small clearance producing diffraction limited resolution. The device board consists of the HEB devices at the terminals of the antenna structure. The connections to the IF board above are done using indium bumps connected to the MMIC amplifiers through via holes. The bias board uses spring-loaded pins to contact a number of points in the IF board, thus providing the required bias voltages for both the HEBs and the IF amplifiers. All boards are assembled using special alignment pins. Future work will address all the issues and fabrication techniques involved in realizing this array architecture.

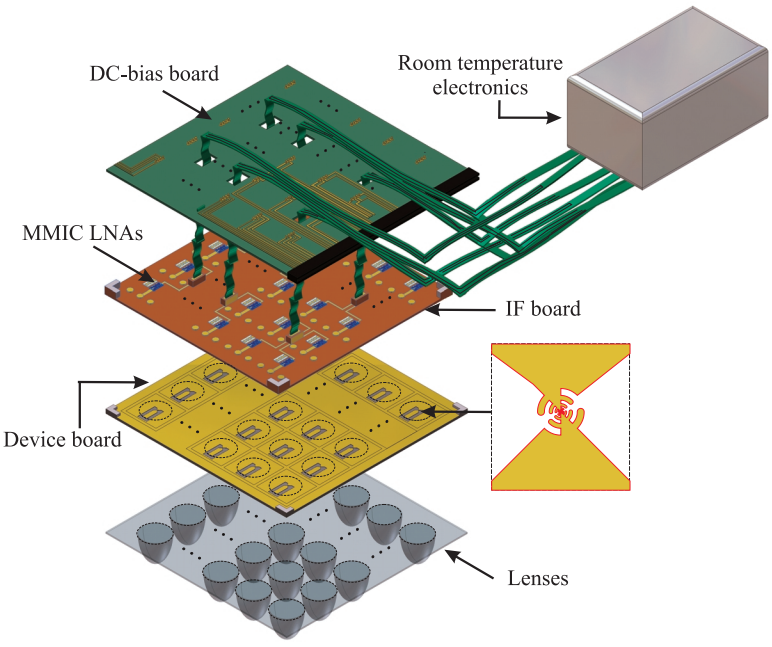

Figure 7: Conceptual focal plane array architecture with HEB devices.

ACKNOWLEDGEMENTS

This work was supported by the National Aeronautics and Space Administration (NASA) (Contract NAS1-01058) and the National Council for Science and Technology in Mexico (CONACyT). We are grateful to Dr. Sander Weinreb for supplying the MMICs.

REFERENCES

[1] I. Lopez-Fernandez et al. Wide Band, Ultra Low Noise Cryogenic InP IF Amplifiers for the Herschel Mission Radiometers. In *Astronomical Telescopes and Instrumentation SPIE Conference: Millimeter and Submillimeter Detectors*, 2002.

[2] I. Angelov, N. Wadefalk, J. Stenarson, E. Kollberg, P. Starski, and H. Zirath. On the Performance of Low Noise, Low DC Power Consumption Cryogenic Amplifiers. *IEEE Transactions on Microwave Theory and Techniques*, 50:1480–1486, June 2002.

[3] E. Gerecht, C.F. Musante, Y. Zhuang, K.S. Yngvesson, T. Goyette, J. Dickinson, J. Waldman, P.A. Yagoubov, G.N. Gol'tsman, B.M. Voronov, and E.M. Gershenzon. NbN Hot Electron Bolometric Mixers, a New Technology for Low-Noise THz Receivers. *IEEE Transactions on Microwave Theory and Techniques*, 47(12):2519–2527, December 1999.

[4] F. Rodriguez-Morales and K.S. Yngvesson. Impedance and Bandwidth Characterization of NbN Hot Electron Bolometric Mixers. In *Proceedings: 14th International Symposium on Space Terahertz Technology, Tucson, Az*, April 2003.

[5] M.J.M. van der Vorst. *Integrated Lens Antennas for Submillimetre-wave Applications*. PhD thesis, Technische Universiteit Eindhoven, The Netherlands, 1999.

[6] D. F. Filipovic, S. S. Gearhart, and G. M. Rebeiz. Double-Slot Antennas on Extended Hemispherical and Elliptical Silicon Dielectric Lenses. *IEEE Transactions on Microwave Theory and Techniques*, 41:1738–1749, October 1993.

[7] V. P. Koshelets and S. V. Shitov. Integrated Superconducting Receivers. *Superconductor Science and Technology*, 13:R53–R69, 2000.

[8] E. Gerecht, D. Gu, Z. Zhao, J. Nicholson, F. Rodriguez-Morales, and K.S. Yngvesson. Development of NbN Terahertz HEB Mixers Coupled through Slot-ring Antennas. This symposium.

[9] D.R. DeBoer and D.C.-J. Bock. The Allen Telescope Array: Splitting the Aperture. *IEEE Microwave Magazine*, 5(2):46–53, June 2004.

[10] H. Ekstroem, B.S. Karasik, E.L. Kollberg, and K.S. Yngvesson. Conversion Gain and Noise of Niobium Superconducting Hot-Electron Mixers. *IEEE Transactions on Microwave Theory and Techniques*, 43(4):938–947, April 1995.

[11] E. Gerecht et al. Deployment of TREND A Low Noise Receiver User Instrument at 1.25 THz to1.5 THz for AST/RO at the South Pole. In *Proceedings: 14th International Symposium on Space Terahertz Technology, Tucson, Az*, April 2003.

[12] S. Yngvesson et al. Development of Focal Plane Arrays with Hot Electron Bolometer Heterodyne Detectors for 3 to 10 THz. In *Proceedings: 2004 IEEE Aerospace Conference, Big Sky, MT.*, March 2004.

[13] F. Rodriguez-Morales, K.S. Yngvesson, E. Gerecht, J. Nicholson, T. Goyette, J. Waldman, D. Gu, and Z. Zhao. Bandwidth Measurements on HEB Mixers at Terahertz Frequencies Using Sideband Generators as well as Two Lasers. This symposium.

[14] P.F. Goldsmith, C.-T. Hsieh, G.R. Huguenin, J. Kapitzky, and E.L. Moore. Focal Plane Imaging Systems for Millimeter Wavelengths. *IEEE Transactions on Microwave Theory and Techniques*, 41(10):1664–1675, October 1993.

Design and Characterization of a Sideband Separating SIS Mixer for 85-115 GHz

V. Vassilev, V. Belitsky, C. Risacher, I. Lapkin, A. Pavolotsky, E. Sundin
Onsala Space Observatory, Chalmers University of Technology
† Institute of Applied Physics RAS, Nizhnij Novgorod, Russia

Abstract

This work presents results of the development and measurements of a heterodyne sideband separating SIS mixer for 85-115 GHz band. The sideband separation is achieved by using a quadrature scheme where a local oscillator (LO) pumps two identical mixer junctions with 90° phase difference.

A key component in the mixer is a waveguide to microstrip double probe transition used as a power divider to split the input RF signal and to provide transition from waveguide to microstrip line. The double probe transition enables the integration of all mixer components on a single compact substrate. The design also involves coupled lines directional couplers to introduce the LO power to the mixer junctions. An additional pair of SIS junctions is used to provide termination loads for the idle ports of the couplers.

Several mixer chips were tested and similar and consistent performance was obtained. The best single sideband noise temperature is below 40 K with IF bandwidth 3.4-4.6 GHz. The sideband suppression ratio is better than 12 dB for both sidebands across the entire RF band. The mixer was also successfully tested over a 4-8 GHz IF band.

Introduction

Any mixer receiving narrow band signals provides a higher signal-to-noise ratio if the image channel is terminated in a low temperature termination. The motivation for using sideband separating (2SB) mixers for radio astronomical applications at mm-wavelengths is that the noise performance of a double-side band (DSB) heterodyne receiver is often limited by the atmospheric noise fed into the system via the image band. Thus, to further increase the system sensitivity, 2SB or single sideband (SSB) operation is preferred.

Sideband separating Mixers

A 2SB mixer performance can be achieved using a quadrature scheme where the RF and LO signals are divided and introduced to two identical DSB mixers. The IF components of both DSB mixers are combined in an IF hybrid where the sideband cancellation takes place. The quadrature scheme does not use any tunable RF filters but requires 90^0 phase delay for either RF or LO signals in one of the mixer channels. Designs where the RF signal is applied with 90^0 delay and the LO in-phase is illustrated in the figure below and has been demonstrated for mm-wavelengths [1]-[4]. The RF power divider is normally a 4 port device - a branch-line coupler [1]-[4] or a magic-T [5]. The fourth port of the RF power divider is terminated in a low-temperature load that is also a source of RF thermal noise which is down-converted and present at the IF output ports.

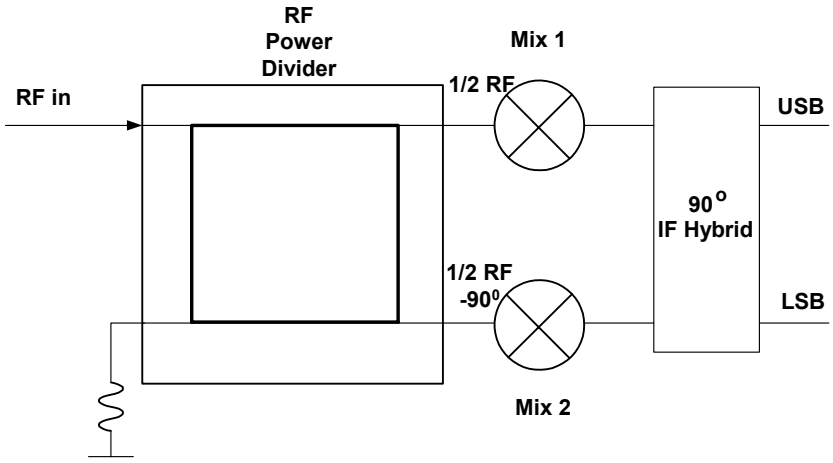

Figure 1 Block-diagram of the 2SB mixer demonstrated in [1]-[4]. The RF signal is divided and delayed by using a branch line coupler at the input, the LO power is applied in-phase to both mixers.

In the mixer design presented here we use an alternative way to achieve a 2SB operation. Instead of a RF branch-line coupler, we use a three-port structure, a waveguide to microstrip double probe transition, which divides the RF signal with a constant 180^0 phase difference [6], [7] and does not require any resistive termination. The LO power is divided with the required 90^0 phase delay by a waveguide branch-line coupler.

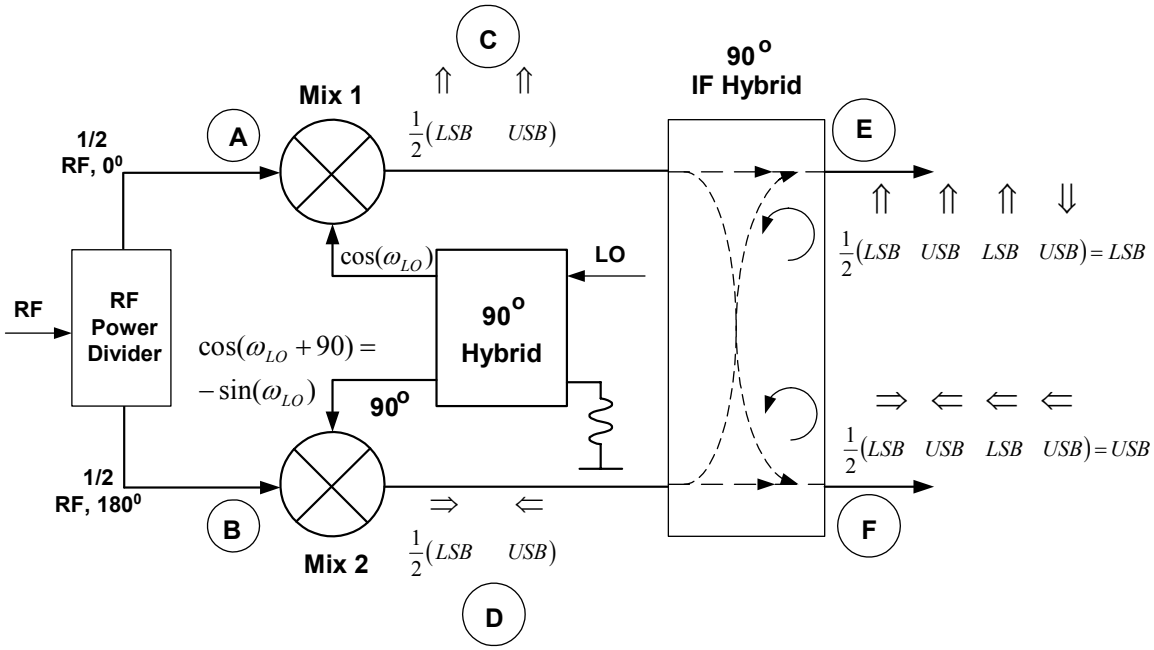

Figure 2 Block diagram of the suggested sideband separating mixer. To illustrate the sideband cancellation, the relative phases of the sideband signals at IF are shown at different points of the mixer. USB and LSB stand for Upper and Lower Side Band respectively.

Image products termination at RF

The output spectrum of a mixer excited with RF signal and pumped by a LO contains linear combinations of both frequencies. One of these combinations is an image component at RF. For example RF signal with frequency LO+IF will produce, through higher order conversion terms, a component with image frequency LO-IF. The way these combinations of frequencies are terminated by the mixer embedding circuitry is relevant to the conversion gain of the mixer.

In the case of a 2SB mixer using a four-port structure to divide the RF (Figure 1), these RF image components are dissipated at the input of the mixer. To illustrate how the corresponding image components are terminated in the suggested mixer design in Figure 2, we give an example by considering the RF image products produced by a third order conversion term.

RF image products from Mixer 1

$$\left[\cos(RF)+\cos(LO)\right]^3 = \cos(RF)^3 + 3\cos(RF)^2\cos(LO) + 3\cos(RF)\cos(LO)^2 + \cos(LO)^3$$

The second term produces components with frequency LO±2IF, while the third term is responsible for the image components at RF. For example if the signal is in the USB we have:

$$\cos(LO+IF)\cos(LO)^2 = \cos(LO+IF)\left[1+\cos(2LO)\right]$$

producing a component

$$\cos(LO+IF-2LO) = \cos(LO-IF)\,, \tag{1.1}$$

which is a frequency in the LSB (an image product).

In the same way if the signal is in the LSB:

$$\cos(LO-IF)\cos(LO)^2 = \cos(LO-IF)\left[1+\cos(2LO)\right]$$

producing a component

$$\cos(LO-IF-2LO) = \cos(LO+IF) \tag{1.2}$$

which is also an image product.

RF image products from Mixer 2

Since the RF is applied to the mixers with 180^0 phase difference and the LO is delayed with 90^0 we have:

$$\left[-\cos(RF)-\sin(LO)\right]^3 = -\cos(RF)^3 - 3\sin(LO)\cos(RF)^2 - 3\sin(LO)^2\cos(RF) - \sin(LO)^3$$

The corresponding image components are: For signal in the USB

$$-\sin(LO)^2\cos(LO+IF) = -\left[1-\cos(2LO)\right]\cos(LO+IF)$$

giving rise to a component in the LSB

$$\cos(2LO-LO-IF) = \cos(LO-IF)\,. \tag{1.3}$$

If the signal is in the LSB:

$$-\sin(LO)^2\cos(LO-IF) = -\left[1-\cos(2LO)\right]\cos(LO-IF)$$

giving rise to a component in the USB:

$$\cos(2LO-LO+IF) = \cos(LO+IF)\,. \tag{1.4}$$

From the calculations above it follows that the considered image products at RF from both mixers are applied in *phase* to the outputs of the RF power divider (equations 1.1≡1.3 and 1.2≡1.4). Since the divider intrinsically produces 180^0 phase difference [5], *the same phase difference* is required to combine the image products and couple them to the input RF waveguide. Furthermore because the RF image components from both mixers are applied in phase, they will be reactively terminated in the structure and will not propagate in the input waveguide, i.e., the mixer behaves as an "image-enhanced" mixer where the image port is reactively terminated.

Mixer Design

The mixer block layout shown in Figure 3 consists of two identical parts dividing symmetrically all waveguide structures (split-block technique). The RF input is a corrugated horn divided into two sections to facilitate the machining. A waveguide 3dB hybrid is used to divide the LO power and to introduce the required 90^0 phase delay. The bottom part of the mixer block accommodates the mixer substrate, bias T filters to introduce DC bias for the junctions, and an absorber to terminate the idle port of the LO 90^0 hybrid. The LO power is then coupled to the ends of the substrate through waveguide to microstrip transitions.

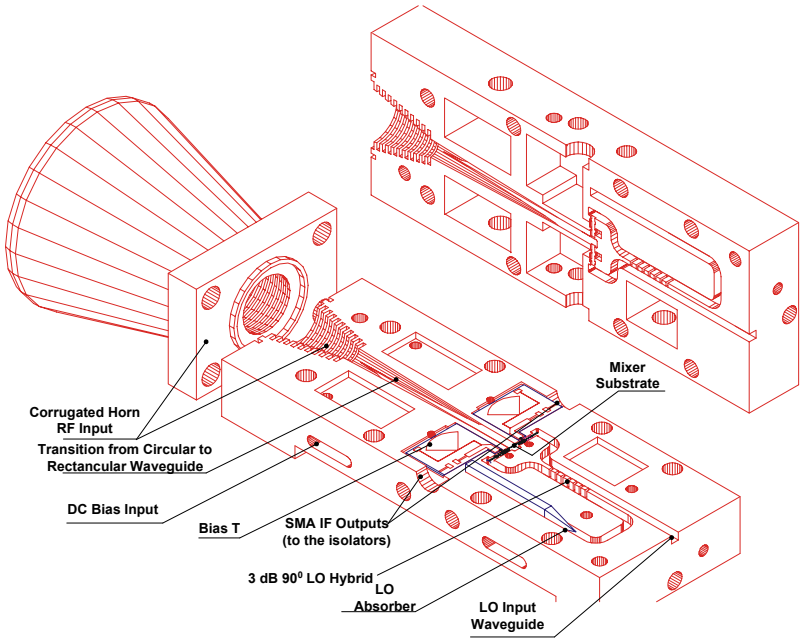

Figure 3 Layout of the sideband separating mixer. The mixer block consists of two identical parts dividing symmetrically all waveguide structures. Waveguide cross-section is 1.2/2.4 mm.

A closer look at the mixer substrate is presented in Figure 4. To ensure a high degree of symmetry in the SIS junction performance, most of the mixer components are integrated on the same compact substrate.

To divide the input RF signal and to couple it to the substrate we designed a special structure, a waveguide to microstrip double probe transition. The waveguide to microstrip double probe transition has a simple geometry and does not require any lumped termination load. Since the E field oscillates in parallel to the probes, the waveguide to microstrip double probe transition is naturally a 180^0 phase shifter introducing a constant phase difference for the divided RF signals. It also gives very good magnitude symmetry of the divided RF signal over the whole waveguide dominant mode, which is a critical requirement for obtaining a good degree of sideband separation. The measured magnitude and phase imbalance introduced by the waveguide to microstrip double probe transition is 0.3 dB and 0^0 in the band 85-115 GHz [6].

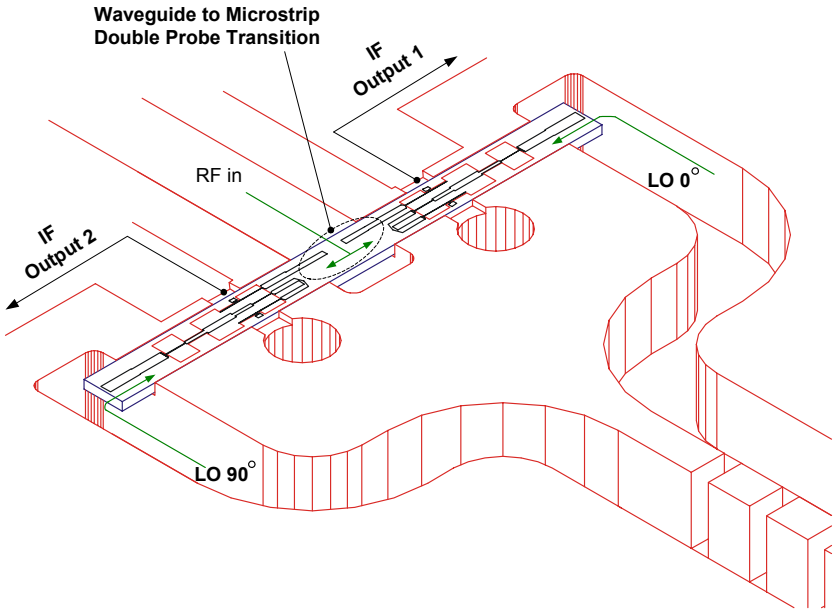

Figure 4 The mixer substrate coupled to the waveguides. The divided LO power is introduced at the ends of the substrate while the RF power is coupled to the substrate in the middle and divided between the two mixer junctions by the waveguide to microstrip double probe transition. The mixer substrate is a Z cut crystal quartz with dimensions 0.7/8.74/0.15mm (W/L/H). The substrate size is chosen such that it does not allow waveguide modes inside the substrate channel.

The divided LO power is coupled at the end of the substrate via an E-probe and transmitted to the 15 dB LO-directional coupler through a microstrip circuit. The RF and LO signals are then fed to each of the mixer junctions with its tuning circuitry. The rest of the LO power at the idle port of the coupler is terminated by a second SIS junction with its tuning circuitry. This SIS-termination absorbs 15 dB more LO power than the mixer junction and becomes over-pumped, its non-linear current-voltage (I-V) curve straightens and thus behaves as a lumped resistor Figure 6.

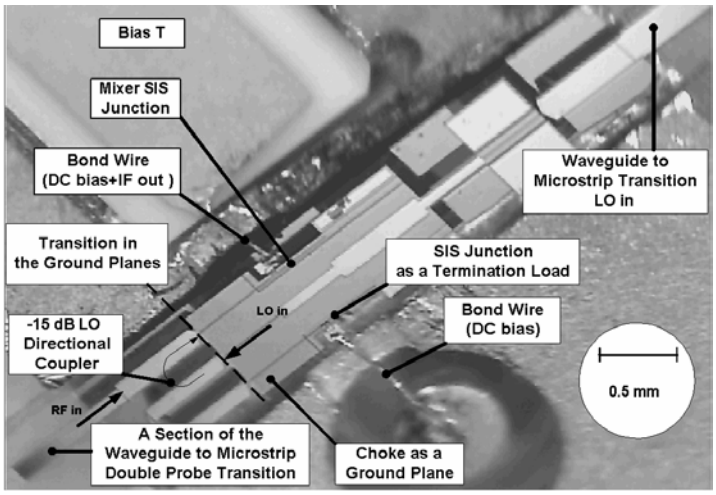

Figure 5 A closer view of the mixer components. In order to minimize the loss of RF power, the LO is injected to the RF line through a -15dB directional coupler. A second SIS junction and its tuning circuitry provides real impedance to terminate the rest of the LO at the idle port of the LO coupler. To avoid critically small spacing between the lines, the LO coupler uses the 0.15 mm thick crystal quartz substrate as a dielectric and substrate backside metallization as a ground plane. The choke serves as a ground plane for the rest of the circuitry.

The degree of sideband suppression is directly related to the magnitude and phase balance of the RF and LO power applied to the mixers and the symmetry of the circuitry. Therefore it is important to provide reflection-free terminations for the LO directional coupler because a part of a reflected LO signal from one branch of the mixer will be directed through the waveguide to microstrip double probe transition [6] to the other and thus degrade the sideband separation. For that reason we keep the possibility to independently bias the load junctions and thus compensate a possible minor impedance mismatch caused by, for example, a spread of the nominal value of junction's normal state resistance.

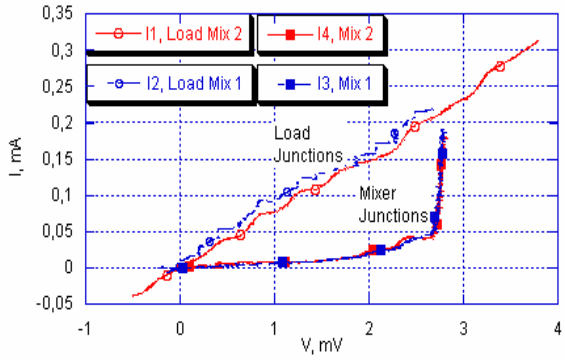

Figure 6 Junctions I-V curves in presence of LO power. The mixer junctions are pumped with optimum power for best sensitivity, while load junctions are over pumped being exposed to 15 dB higher power. The pairs of I-V curves show excellent symmetry giving good prospects for high degree of sideband separation.

Measurements

In order to characterize the 2SB mixer we measure the equivalent mixer noise temperature as a function of LO frequency using conventional Y-factor technique. In contrast to an ideal DSB mixer, a SSB mixer equivalent noise temperature T_{SSB} can not be measured without knowing sideband suppression ratios R_U, R_L. We calculate the T_{SSB} for USB and LSB using the T_{DSB} noise temperature derived from Y-factor measurements of the 2SB mixer, and the measured sideband suppression ratios:

$$T_{SSB,USB} = T_{DSB}\left(1+\frac{1}{R_U}\right),\ T_{SSB,LSB} = T_{DSB}\left(1+\frac{1}{R_L}\right)$$

Calculating the sideband suppression ratios requires measuring the mixer response to a continuous wave (CW) source placed at either the lower or upper sidebands. For example, a CW signal placed at the LSB ($f_{CW}=f_{LO}-f_{IF}$) of an ideal 2SB mixer should only be seen at the LSB IF output with no response at the USB port. Similarly, placing the CW at the USB should produce a peak at IF in the USB and give no response in the LSB output. Since real mm-wave mixers are not ideal, CW signal is seen at both IF outputs. In this case, measuring the sideband suppression ratios R_U, R_L results in measuring the difference in the observed peak value referred to the noise level at the corresponding output. In order to check the consistency in the measured sideband suppression ratios, R_U, R_L are calculated and compared for a number of CW frequencies in the USB/LSB. Our measurements show that the variation of R_U, R_L vs. IF frequency is in the range of 2-3 dB and can be related to asymmetry produced by the IF hybrid and cold amplifiers.

The 2SB mixer was measured in two configurations with IF 3.4-4.6 GHz and IF hybrid following the amplifiers, and with IF 4-8 GHz and amplifiers following the IF hybrid. The results from the measurements of SSB equivalent noise temperature and sideband suppression ratios are presented in Figure 7, 8.

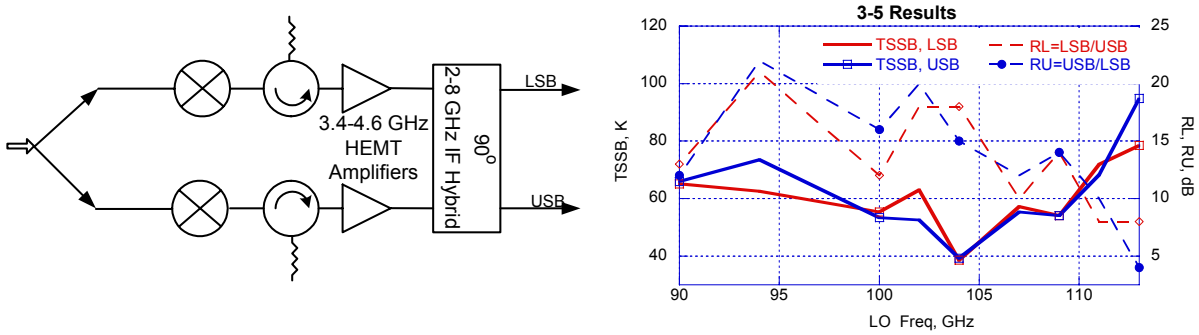

Figure 7 Measured SSB equivalent noise temperature T_{SSB} – solid lines, and sideband suppression ratios R_U, R_L-dashed lines vs. LO frequency, (equivalent to RF band of 86-118GHz with 4 GHz IF center frequency). IF band is 3.4-4.6 GHz and the IF hybrid follows the amplifiers.

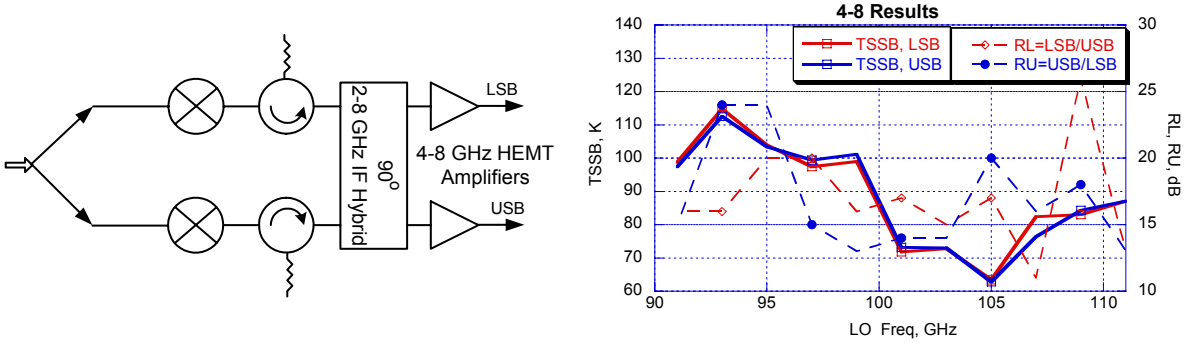

Figure 8 Measured SSB equivalent noise temperature T_{SSB} – solid lines, and sideband suppression ratios R_U, R_L-dashed lines vs. LO frequency, (equivalent to RF band of 85-117GHz with 6 GHz IF center frequency). IF band is 4-8 GHz and the IF hybrid is in front of the amplifiers.

Conclusions

Several mixer chips were tested and similar and consistent performance was obtained. The best single sideband noise temperature with IF 3.4 - 4.6 GHz (configuration 1 in Figure 7) is below 40 K with a sideband suppression ratio above 12 dB for both sidebands over the RF band. The noise contribution of the IF chain was measured to be 6 K.

Configuration 2 (Figure 8) gives about 20 K higher SSB noise temperature but also a better sideband suppression. This extra noise is partly associated with the fact that 4-8 GHz amplifiers are slightly noisier than 3.4-4.6 GHz, partly because the IF hybrid, placed in front of the amplifiers, introduce some extra loss. However we believe that it is this configuration that should be used for practical 2SB mixers (especially with 4-8 GHz IF band) since tuning the mixer for optimum noise/sideband suppression is to a large extent simplified compared to configuration 1, which requires very well balanced IF amplifiers. The IF noise contribution for this configuration is about 10 K.

The measured noise temperatures include losses in all passive components in front of the mixer: a 290 K vacuum window of the cryostat, a 77 K IR filter and a lens at 4 K, all made of PTFE.

Acknowledgments

Authors would like to acknowledge Professor R.S. Booth for his constant trust and support of our work. Thanks to Sven-Erik Ferm for his effort on fabricating the mixer block. This work is a part of the APEX Project, supported by the Swedish Research Council and the Wallenberg Foundation.

References

[1] A. R. Kerr, S.-K. Pan and H. G. LeDuc, "An integrated sideband separating SIS mixer for 200-280 GHz", Proc. of the Ninth Space Terahertz Technology Symposium, pp.215-222, Pasadena, USA, March, 1998.

[2] A. R. Kerr and S.-K. Pan, "Design of Planar Image Separating and Balanced SIS Mixers," Proc. of Seventh International Symposium on Space Terahertz Technology,pp. 207-219, March 12-14, 1996.

[3] S. M. X. Claude, C. T. Cunningham, A. R. Kerr, and S.-K. Pan, "Design of a Sideband-Separating Balanced SIS Mixer Based on Waveguide Hybrids", ALMA Memo 316, September 2000.

[4] S. Asayama, et al., "An Integrated Sideband-Separating SIS mixer Based on Waveguide Split Block for 100 GHz Band", ALMA Memo 453, http://www.alma.nrao.edu/memo/, April 2003.

[5] R. L. Akeson, J. E Carlstrom, D. P. Woody, J. Kawamura, A. R. Kerr, S. -K. Pan and K. Wan, "Development of a Sideband Separation Receiver at 100GHz", Proc of Fourth International Symposium on Space Terahertz Technology, pp.12-17, Los Angeles, USA, March, 1993.

[6] V. Vassilev, V. Belitsky, D. Urbain, S. Kovtonyuk, "A New 3 dB Power Divider for MM-Wavelengths", IEEE Microwave and Wireless Components Letters, page 30-32, vol.11, January 2001.

[7] V. Vassilev and V. Belitsky, "Design of Sideband Separation SIS Mixer for 3 mm Band", 12th International Symposium on Space Terahertz Technology, Feb. 2001.

[8] V. Vassilev, "Development of a Sideband Separating SIS Mixer Technology for MM-Wavelengths", Technical report No. 465, School of Electrical Engineering, Chalmers University of Technology, ISSN 1651-498X

ALMA Band 6 Prototype Cartridge: Design and Performance

G. A. Ediss, M. Carter[*], J. Cheng, J. E. Effland, W. Grammer, N. Horner, Jr.
A. R. Kerr, D. Koller, E. F. Lauria, G. Morris, S-K. Pan, G. Reiland and M. Sullivan

National Radio Astronomy Observatory[#]
2551 Ivy Road, Bldg. 4
Charlottesville, VA 22903

[*]Institut de Radio Astronomique Millimétrique
300 rue de la Piscine
38406 St. Martin d'Heres, France

Abstract: This paper describes the design and performance of the initial Band 6 (211-275 GHz) ALMA cartridges. The incoming beam is coupled by 4-K reflecting optics to a scalar horn followed by an orthomode transducer. Each polarization is down-converted in a sideband-separating SIS mixer integrated with a pair of 4-12 GHz IF preamplifiers. Stringent thermal management and LO loss requirements are satisfied by using an overmoded stainless-steel waveguide between the LO triplers on the 100-K stage and the 4-K mixers. For ease of maintenance, all connections into the vacuum vessel are "blind mating."

Introduction

The Atacama Large Millimeter Array (ALMA)[†] is a radio telescope with 64 antennas under construction in the Atacama desert in northern Chile. The front-ends for ALMA will each consist of a 4-K cryostat with ten insertable receivers (called cartridges) covering the frequency range 31 to 950 GHz. Each cartridge will operate simultaneously in two linear polarizations. A block diagram of the Band 6 (211-275 GHz) cartridge, showing the main interfaces, is given in Fig. 1, and an overall view of the cartridge is shown in Fig. 2.

The cartridge consists of three cold stages with operating temperatures of 4 K, 20 K, and 90 K, and a room-temperature base-plate which acts as the vacuum barrier. The stages are supported on cylindrical G-10 glass-epoxy spacers. The 90-K stage has mounted on it two LO triplers and heat sinks for the LO waveguide, IF coaxial cables and wiring. The 20-K stage has only heat sinks for the LO waveguide, coax cables and wiring, while the 4-K stage has the mirrors, horn, OMT, mixer-preamps, IF hybrids and heat sinking for the LO waveguide, coax cable and wiring.

The RF signal enters the cartridge through a vacuum window and infrared filters, which are part of the outer vacuum vessel. Two off-axis ellipsoidal mirrors mounted on the cartridge 4-K plate couple the beam to the scalar feed horn (see section on optics). The two polarizations are then split in an orthomode transducer (OMT). Each polarization channel uses a sideband-separating mixer-preamp containing two DSB component mixers. Each component mixer requires an independent, six-wire bias supply, and each preamplifier uses a nine-wire bias supply. Protection circuits are installed on the vacuum side of the hermetic connector to protect the mixers and the preamps from over-voltage and static discharge. The two IF outputs from the mixer-preamp are connected via phase-matched cables to a quadrature hybrid. This provides the two sidebands at separate outputs, both of which are brought out of the cartridge. Switching between sidebands can also be achieved by changing the polarity of the bias on one of the component mixers.

[†]The Atacama Large Millimeter Array (ALMA) is an international astronomy facility. ALMA is an equal partnership between Europe and North America, in cooperation with the Republic of Chile, and is funded in North America by the U.S. National Science Foundation (NSF) in cooperation with the National Research Council of Canada (NRC), and in Europe by the European Southern Observatory (ESO) and Spain. ALMA construction and operations are led on behalf of North America by the National Radio Astronomy Observatory (NRAO), which is managed by Associated Universities, Inc. (AUI), and on behalf of Europe by ESO.

[#]The National Radio Astronomy Observatory is a facility of the National Science Foundation operated under cooperative agreement by Associated Universities, Inc.

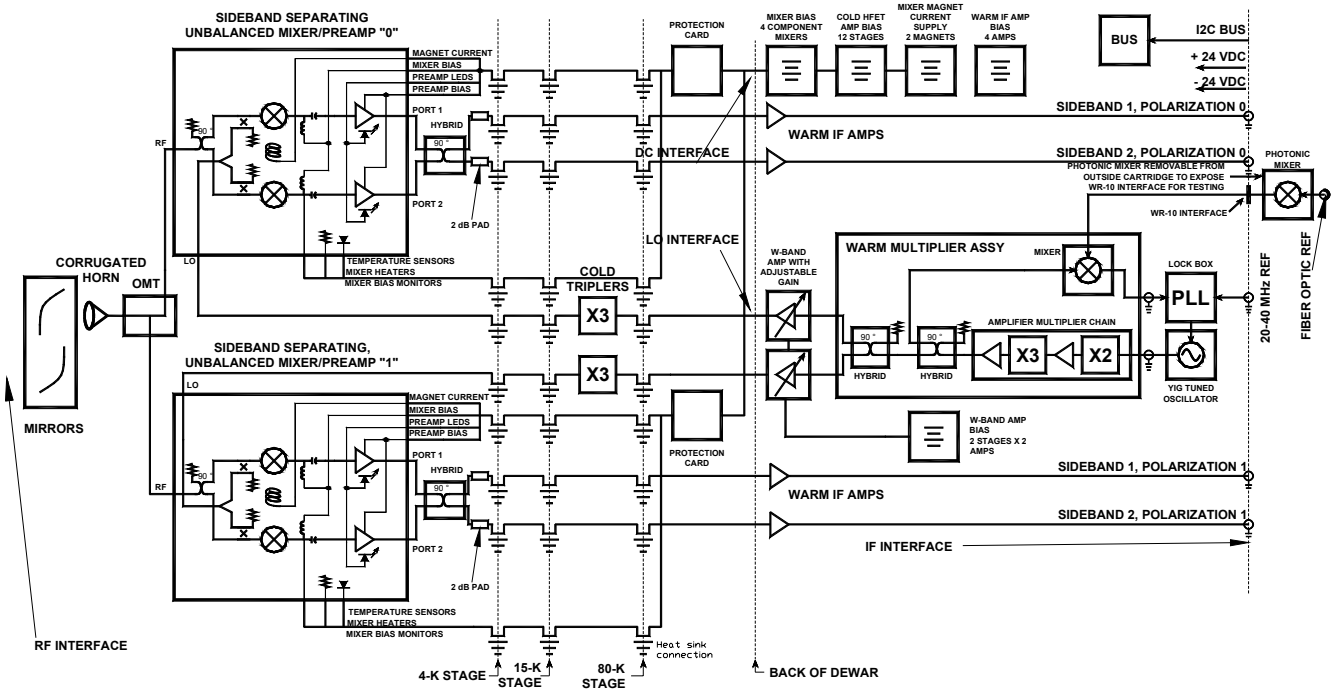

Fig. 1. Block diagram of cartridge.

< Quaternary mirror

< Feed horn

< Tertiary mirror

< 4 K plate

< 20 K plate

< 90 K plate

< Room temperature base-plate and vacuum flange.

Fig. 2. View of complete cartridge.

Temperature sensors are installed on each SIS mixer body and on the 90 K, 20 K and 4 K cartridge stages to facilitate troubleshooting the cartridge.

SIS mixers require a magnetic field across the junction to suppress Josephson currents. Each polarization uses a single superconducting coil and bifurcated pole pieces to concentrate the magnetic fields at each component mixer. Two independent magnet supplies are required per cartridge to deliver current to the superconducting coils.

On cooling, magnetic flux may be trapped in SIS mixers and can change the magnetic field required to suppress Josephson currents. In mixers with multiple junctions, such as the four-junction designs used in Band 6, trapped flux can affect the individual junctions to different degrees. Heating the mixer briefly above the superconducting critical temperature, typically to about 10 K for the niobium mixers used in this design, can eliminate trapped magnetic flux. Heaters are mounted on each mixer-preamp for this purpose.

In addition to the IF preamplifiers on the mixers, four additional amplifiers, one for each IF output, are located in the room temperature area on the back of the cartridge to increase IF output power levels prior to routing to the IF selector switch.

System Components

Optics and Horn

The RF signal enters the corrugated horn via two off-axis ellipsoidal mirrors thermally anchored to the 4-K plate. A Finite Element Analysis (FEA) indicates that the optical structure achieves better than the required deflections under gravity.

The original optics design was given in ALMA memo #362 [1]. This design was analyzed using GRASP software [2] which indicated that modification was required to obtain the desired performance. The new design [3] was manufactured and measured in the IRAM near-field antenna range. Measured results are shown in Figs. 3 and 4.

Figure 3 shows the beam waist radius (-8.7 dB radius) determined from the near-field measurements. Also shown are the expected waist radii for a Gaussian beam with 12 dB taper at the edge of the telescope secondary mirror, and the target of 10 dB edge taper from the Physical Optics (PO) calculations (curves overlap). Figure 4 gives the position of the waist (and the target position) relative to the mirror on the 4-K plate.

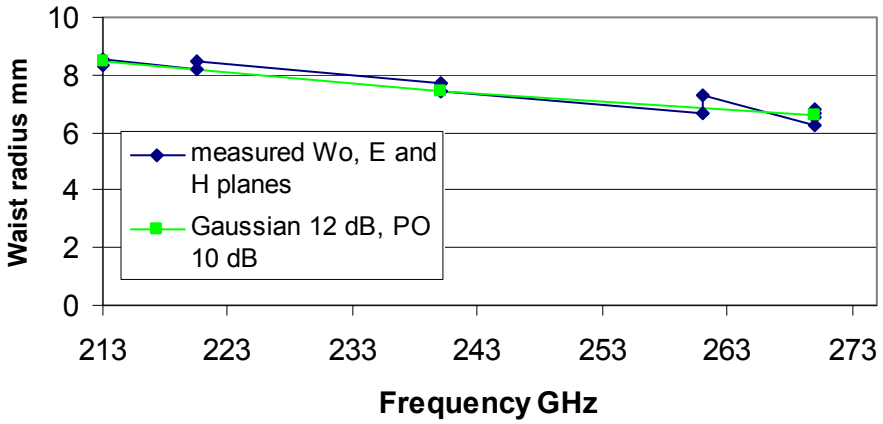

Fig. 3. Beam waist radii determined from the near-field measurements.

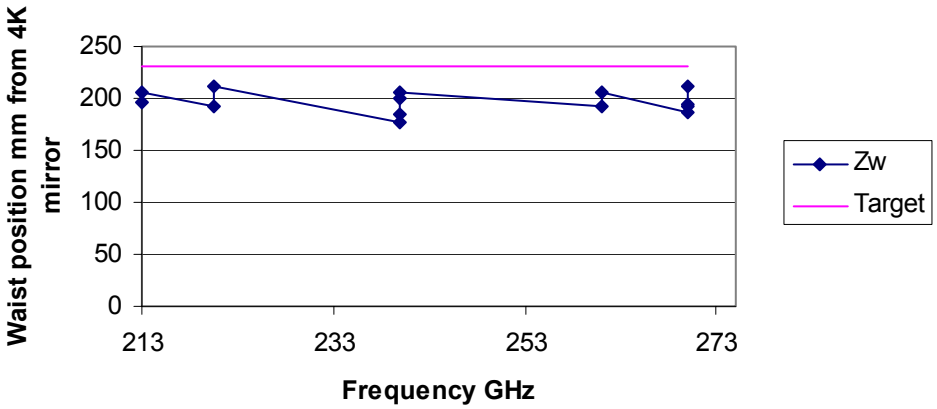

Fig. 4. Beam waist position (mm) above the 4 K tertiary mirror.

The original optics design also includes the requirements for the windows and infrared filters which are part of the outer vacuum container and not part of the cartridge. For the cartridge to meet the noise temperature specification, the window should have a loss of < 1% and a S_{11} < -20 dB, and each of the IR filters on the 90 K and 20 K shields should have a loss of < 1% and a S_{11} of < -20 dB [1].

Mechanical Finite Element Analysis of the Optical Mount

Fig. 5. Structure analyzed in FEA.

The Finite Element Analysis program MSC Patran was used to analyze the optics support structure shown in Fig. 5. The structure includes the frames and cross supports modeled as a single unit (*i.e.*, the frame was assumed to be a solid structure with no bolted sections), with masses of the components represented as point masses. These were 100g for the mirror directly above the mixer, 750g for all the components supported off the horn (OMT, mixer-preamps and one hybrid) and 20g for the hybrid attached on the right A frame. Two cases were analyzed, the first one with gravity in the *z* direction, and the second one with gravity in the *y* direction. Contour plots of the displacements in the *y* and *z* directions for both cases were made and Fig. 5 shows an example. The results indicate that the structure sags slightly in the -*z* direction under gravity in the -*z* direction. The quaternary mirror drops by 0.4 μm relative to the 4 K plate and the horn by 1.45 μm and both shift to the -*y* direction by approximately 0.8 μm. All other displacements in this case are less than 0.1 μm. With gravity in the *y* direction, both horn and mirror sag by approximately 0.8 μm with a shift in the *y* direction of 5.5 μm; all other displacements are less than 0.1 μm. According to the tolerance analysis for ALMA Band 6 [4], the horn may move relative to the quaternary mirror by 20 μm and the whole assembly relative to the tertiary mirror by 80 μm and relative to the base plate by 80 μm. So the calculated shifts are well within the tolerances for this band.

OMT

An orthomode transducer (OMT) is a passive waveguide device that separates the signal received by the feed horn into its two orthogonal linearly-polarized components. The original Band 6 design, as given in [5], has been modified to locate the two outputs opposite one another, thus allowing both mixer-preamps to be mounted directly on the OMT.

The goals for the OMT are: frequency range 211-275 GHz (fractional bandwidth > 0.4), with a return loss > 20 dB, an insertion loss < 0.2 dB, isolation > 40 dB.

The first OMT has been delivered and is being used in the prototype cartridge.

Mixers

The cartridge contains two sideband-separating SIS mixer-preamplifiers with separate signal and LO waveguide ports. There are no mechanical tuners. The design uses two simple DSB component SIS mixers in a single mixer block containing waveguide hybrids, LO power dividers and LO couplers (see paper by Kerr *et al.* in these Proceedings). Approximately -23 dB of the LO power is coupled to each of the building block mixers. Mixer heaters allow raising the physical temperature of the mixer junction above its critical temperature to remove trapped flux. The mixer heaters are Mini-Systems MSR thick-film resistors on alumina substrates with case size 2412 rated at 2W dissipation. The mixer heater is epoxied to a copper block which is bolted onto the mixer body.

Preamps

The IF preamplifiers directly connected to the IF ports of the SIS mixer are three-stage HFET MIC amplifiers with indium phosphide devices. The preamplifier covers 4 to 12 GHz when measured in a 50 Ω system, and has an equivalent noise temperature of 4-8 K with 30 dB of gain (see paper by Kerr *et al*. in these Proceedings).

IF

Four IF lines, two per polarization, are brought out of the cartridge on 2.18 mm (0.085 inch) outside diameter cable with stainless-steel inner and outer conductors. The interface between the cartridge and the rest of the system is at the rear of the base-plate of the cartridge, which holds the LO, bias, and monitor and control electronics. The interface for IF power is a “blind mate” BMA connector (Mil-Spec 83513).

To reduce passband ripple from VSWR effects, cold 2-dB attenuators are inserted at the outputs of the IF hybrids.

LO

There is a separate LO for each polarization to provide independent LO level control for each mixer. The LO interfaces on the base-plate of the cartridge are "blind mate" WR-10 waveguide flanges and include the waveguide vacuum window and waveguide feed-through. The "blind mate" interfaces simplify the removal of the cartridge warm electronics and LO modules by eliminating the need to open the cryostat. Inside the cartridge, there is a 75-mm stainless-steel WR10 waveguide between the 300 K base-plate and the 90 K stage for each polarization. Mounted to the 90 K stage is a settable attenuator (Custom Microwave LA10R –which consists of a movable piece of nichrome-metalized mylar, inserted in a section of WR10 waveguide) and another 75 mm section of coin-silver waveguide before the final multiplier (X3). The output of the final multiplier (WR-3) is tapered back to WR-10 for the stainless-steel waveguide run to the 4 K plate. For thermal reasons, this waveguide is stainless-steel but is over-moded to reduce losses (see [6]). The over-moded waveguide tapers back to WR-3.4 before the bends necessary to connect the waveguide to the mixer assembly. Fundamental waveguide modes are used in the bends to reduce the possibility of coupling to higher order modes which could lead to significant LO power loss from resonances.

Wiring

The Band 6 cartridge requires 96 wires between the vacuum flanges and the 4 K plate. Four ribbon cables are used; they consist of 36 AWG phosphor-bronze wires, twisted in pairs, and then 12 pairs (24 wires) are woven into a ribbon.

To reduce the risk of electrostatic discharge damaging the mixers, all bias wires to the mixers and preamps pass through a protection circuit mounted in the DC wiring, in vacuum but at room temperature.

All wiring is heat sunk at each of the stages (90 K, 20 K, and 4 K) to reduce the thermal loading on the following stage and on the mixers-preamps.

Thermal Considerations

Table 1 gives the allowed and achieved static heat loads for the cartridge. This includes the conduction of the 96 phosphor-bronze wires, four stainless-steel IF cables and the two LO waveguides.

Table 1: Cartridge thermal load with mixer-preamps and LO off.

Stage temperature	Allowed	Calculated
100 K	400 mW	375 mW
20 K	95 mW	69 mW
4 K	5 mW	1.8 mW

Table 2 gives the added loads when the cartridge is "on" – warming up or in operation.

Table 2: Additional cartridge thermal load with mixer-preamps and LO on.

Stage Temperature	Allowed	Calculated
100 K	833 mW	40 mW
20 K	67 mW	0
4 K	36 mW	36 mW

The "cartridge on" calculations include 7 mW of power dissipation in each preamp, the bias for the mixers and magnet currents at 4 K, and the LO power dissipated in the triplers operating at 90 K. All other loads (radiation, conduction between the stages) are excluded.

Measurements of the Prototype Cartridge

Typical measurements of single-sideband noise, sideband rejection, and gain (including cables to room temperature) for the mixer-preamp at a single LO frequency of 240 GHz are given in Fig. 6. The measurements were made at 1-GHz steps over the IF range (4-12 GHz). Figures 7 and 8 are the first measurements of a completed cartridge and show single-sideband noise temperature, sideband rejection, and gain. These data were collected with the LO frequency changed in 10-GHz steps and IF stepped by 1 GHz. The cause of the poor image rejection in polarization 1, not present in the mixer-preamp tested alone, is under investigation.

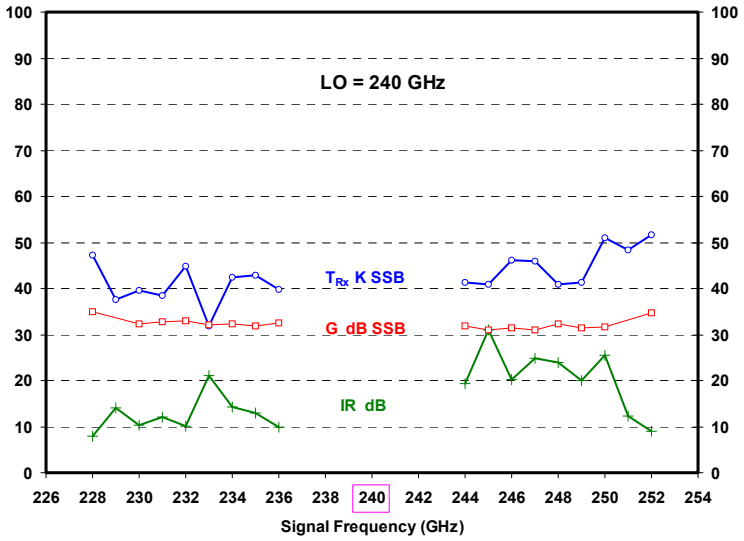

Fig. 6. Single-sideband noise, sideband rejection and gain of a mixer-preamp in both sidebands at an LO frequency of 240 GHz.

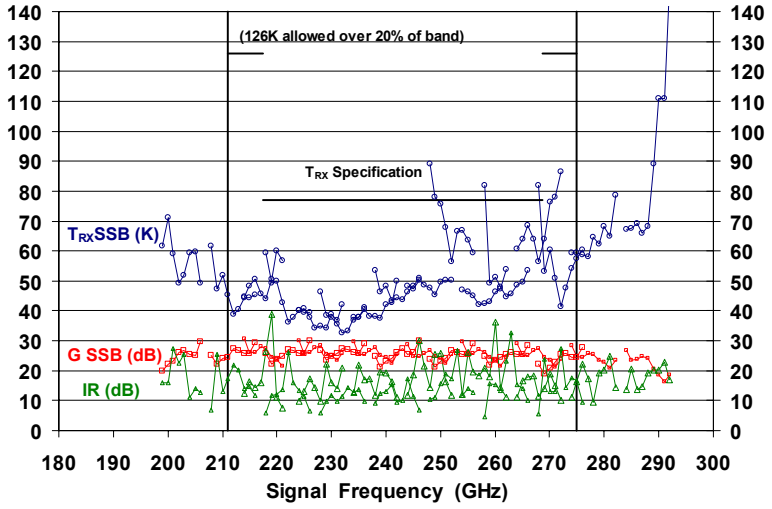

Fig. 7. Cartridge noise temperature, gain and image rejection for polarization 0, mixer heated to 4.2 K.

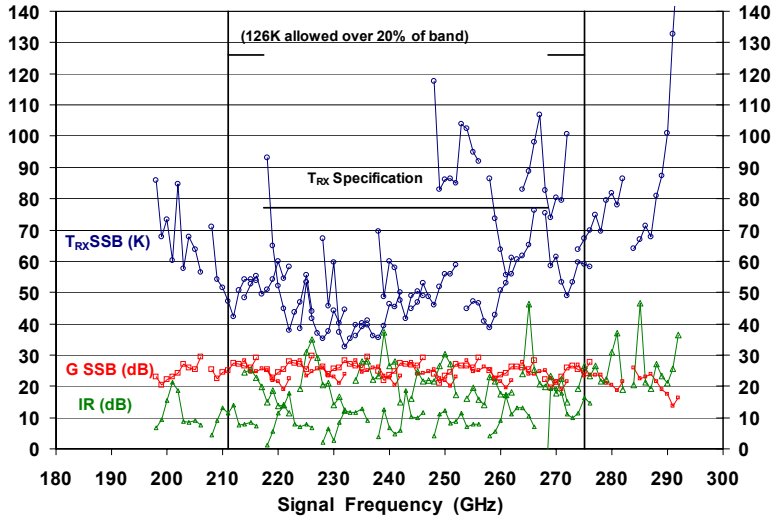

Fig. 8. Cartridge noise temperature, gain and image rejection for polarization 1, mixer heated to 4.2 K.

References

[1] J. W. Lamb, A. Baryshev, M. C. Carter, L. R. D'Addario, B. N. Ellison, W. Grammer, B. Lazareff, Y. Sekimoto and C. Y. Tham, "ALMA Receiver Optics Design," ALMA memo #362, 4/11/2001. http://www.alma.nrao.edu/memos/html-memos/abstracts/abs362.html

[2] C. Y. Tham and S. Withington, "Receiver Optics Design Electromagnetic Analysis," 09/04/2001. http://almaedm.tuc.nrao.edu/forums/alma/dispatch.cgi/iptfedocs/docProfile/100533/d20040216144724/No/t100533.htm

[3] C. Y. Tham and S. Withington, "Receiver Optics Design, Electromagnetic Analysis, Second Report (Bands 3, 6, 7 and 9)," 07/01/2003. http://almaedm.tuc.nrao.edu/forums/alma/dispatch.cgi/iptfedocs/docProfile/100532

[4] B. Lazareff, "Alignment Tolerances for ALMA Optics," ALMA memo #395, 10/25/2001. http://www.alma.nrao.edu/memos/html-memos/abstracts/abs395.html

[5] E. Wollack, "A Full Waveguide Band Orthomode Junction," NRAO Electronics Division Internal Report #303, 5/16/1996. http://www.gb.nrao.edu/electronics/edir/edir303.pdf

[6] G. A. Ediss, "Measurements and Simulations of Overmoded Waveguide Components at 70-118 GHz, 220-330 GHz and 610-720 GHz," *Proc. of the Fourteenth Int'l. Symp. on Space Terahertz Tech*., Tucson, AZ, 2003.

DESIGN CONSIDERATIONS FOR A TWO-DISTRIBUTED-JUNCTION TUNING CIRCUIT

Yoshinori UZAWA[1)], Masanori TAKEDA[1)], Akira KAWAKAMI[1)], Zhen WANG[1)], and Takashi NOGUCHI[2)]

1) Kansai Advanced Research Center, National Institute of Information and Communications Technology
588-2 Iwaoka, Iwaoka-cho, Nishi-ku, Kobe 651-2492, Japan
e-mail: uzawa@nict.go.jpT
2) Nobeyama Radio Observatory, National Astronomical Observatory of Japan
Nobeyama, Nagano 384-1305, Japan

Abstract

We describe a novel method of designing a tuning circuit with two half-wave distributed junctions separated by a half-wavelength microstripline, which analytically determines the circuit parameters such as the minimum current density of the junctions and the characteristic impedances of the distributed junctions and the microstripline. The tuning circuit was approximated by simple transmission theory and then simplified with ideal circuit components for analysis. We applied Chebyshev's band-pass filter theory, in part, to optimize the circuit design. The analytical results revealed that a high characteristic-impedance ratio between the distributed junctions and the microstripline is necessary to obtain broadband matching using low-current-density junctions. The experimental results for all-NbN SIS mixers we designed with this method demonstrated double-sideband (DSB) receiver-noise temperatures of 6-10 quanta from 710 to 810 GHz for a mixer with a current density of only 4 kA/cm^2 (estimated $\omega C_J R_N$ product of 37 at 750 GHz). The RF bandwidth was broader than that of a conventional full-wave distributed SIS mixer with the same current density.

1. Introduction

The quality of superconductor-insulator-superconductor (SIS) junctions strongly influences mixer noise. In general, the subgap leakage current of the junction tends to become large for high current density, which degrades mixer performance. It is better to use SIS junctions with a current density as low as possible to achieve low noise. However, SIS junctions have large specific capacitances C_S, of say 100 fF/μm^2 for typical junctions such as Nb/AlOx/Nb and NbN/AlN(or MgO)/NbN, which roughly limit the operational fractional bandwidth, $\Delta f/f_0$, to $1/\omega C_J R_N$ using a conventional tuning circuit design, where ω, C_J, and R_N are the signal angular frequency, geometrical junction capacitance, and normal resistance of the junction, respectively. To achieve a fractional bandwidth of 20%, for example, the $\omega C_J R_N$ should be 5 at the center frequency. The $\omega C_J R_N$ product is related to the current density, J_C, according to $\omega C_S I_C R_N / J_C$. Appling this relation to the highest band of the Atacama Large Millimeter Array (ALMA), which is the 787-950 GHz (band 10), high-current-density junctions of about 20 kA/cm^2 for Nb and 40 kA/cm^2 for NbN are necessary. Consequently, it is difficult to achieve ultra-low noise for the ALMA band 10 using a conventional tuning circuit faced with the expected low quality of SIS junctions with high current densities [1].

We previously proposed a novel tuning circuit with two half-wave distributed SIS junctions and theoretically and experimentally demonstrated that its performance enables a fractional bandwidth to be obtained that is broader than $1/\omega C_J R_N$ [2, 3]. Although the design principle behind the tuning circuit was founded on the idea of efficient reactance compensation for open-ended distributed junctions, the circuit designs were produced by varying many circuit parameters, through trial and error, to achieve optimization. Whether the tuning circuit was really optimized using the SIS junctions with the minimum current density was not certain. In this paper, we will explain that the circuit parameters can uniquely be determined with the new design method when the fractional bandwidth and maximum tolerable value for the reflection coefficient between the source and tuning circuit are given as well as filter design theory. The minimum current density of the junctions derived by the design method was much smaller than that of SIS junctions with a conventional tuning circuit. We also present experimental results on a comparison

between the two-distributed-junction and the conventional tuning circuit using NbN/MgO/NbN tunnel junctions and microstriplines.

2. Design method

Figure 1 (a) illustrates a two-distributed-junction tuning circuit, in which Z_J, γ_J (= $\alpha_J + j\beta_J$), and d_J respectively represent the characteristic impedance, propagation constant (α_J is the attenuation constant due to quasi-particle loss and β_J is the phase constant below the gap frequency), and length of the distributed junctions. As the microstripline between the junctions is treated as a loss-free transmission line with a characteristic impedance of Z_m and a length of d_m, the propagation constant is described by only a phase constant of β_m below the gap frequency. It looks like a band-pass filter structure consisting of low (distributed junctions) and high (microstripline) impedance sections when $\beta_J d_J$ and $\beta_m d_m$ are chosen to be π at center frequency. The difference in design between an ordinary band-pass filter and the tuning circuit is as follows:

1) Transmission lines composed of the tuning circuit have loss, but the filter circuit is loss free.
2) According to 1), the input and output impedances may be taken to have different values for the tuning circuit, but the same impedances for the filter circuit.

Therefore, we assumed a source impedance of Z_S, which can be any value to optimize the circuit. This assumption is reasonable when a quarter-wave transformer is added to the tuning circuit. Once Z_S is decided by optimization, then this value may easily be transformed to another impedance level that for a waveguide or quasi-optical antenna feed points by using the quarter-wave transformer.

Let us now investigate how to find the optimal solution so that the current density of the junctions is minimized under the design conditions of a fractional bandwidth and a maximum tolerable value for the reflection coefficient in the band between the circuit and Z_S. If the distributed junction has relatively low loss satisfying the following conditional equation

$$\sin(\alpha_J d_J) \cong \alpha_J d_J , \qquad (1)$$

the open-ended distributed junction is described by a loss-free transmission line end-loaded with pure resistance [2]. Another condition expressed by

$$\alpha_J d_J \tan(\beta_J d_J) << 1 \qquad (2)$$

may be satisfied around $\beta_J d_J = \pi$. Using these conditions, the circuit including loss, in part, (Fig. 1 (a)) is simplified with ideal circuit components of loss-free transmission lines and pure resistance as we can see in Fig. 1 (b). Normalizing the impedances to a terminating resistance of $R_L = Z_J/(\alpha_J d_J)$, the circuit in (b) is written as Fig.1 (c). The circuit observed from a-a' toward the load in the figure is just like a 3-section band-pass-filter structure for an input source impedance of unity (the output terminating impedance is now also unity). This part can be designed with the Chebyshev's band-pass filter theory [4]. The question is how

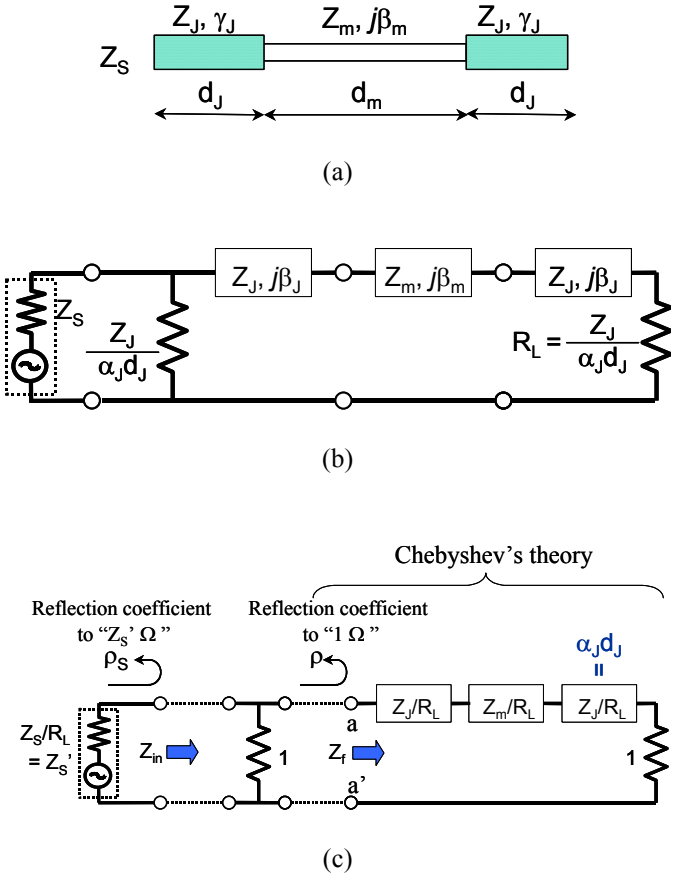

Fig. 1. (a) Diagram of tuning circuit with two half-wave distributed junctions connected by microstripline. (b) Simplified circuit model of tuning circuit. (c) Method of analyzing to optimize circuit parameters.

do we design Chebyshev filter to minimize the current density in the junctions?

The normalized characteristic impedance of the junctions equals $\alpha_J d_J$, which is the attenuation of the distributed junctions in Np. Since the guided wavelength in the distributed junction is almost independent of the junction current density for the same geometrical configuration, the normalized characteristic impedance of the junctions is dependent on the attenuation constant, α_J. Therefore, $\alpha_J d_J$ becomes lower along with decreasing current density, and this value is much less than unity because of the conditional Eq. 1. According to 3-section filter theory, the maximum tolerable value of the reflection coefficient should be large, when the impedance ratio between the terminating load and low impedance section is large. Therefore, to find the minimum current density, the maximum tolerable value in designing Chebyshev filter should be as large as possible under the given design conditions between Z_S and the tuning circuit, as previously mentioned. To find the solution mathematically, we denote the normalized input impedance of the filter as Z_f and the reflection coefficient as ρ, as shown in Fig. 1 (c). It is well known that the relation between Z_f and ρ is

$$\rho = \left| \frac{1 - Z_f}{1 + Z_f} \right| \tag{3}$$

and

$$Z_f = \frac{1 \pm \rho}{1 \mp \rho}. \tag{4}$$

Therefore, the normalized input impedance of the tuning circuit, Z_{in}, as represented in Fig. 1 (c) becomes

$$Z_{in} = \frac{1 \pm \rho}{2}. \tag{5}$$

The maximum reflection coefficient should be below ρ_S as one of the design conditions, hence the conditional equation using the normalized source impedance of Z_S' is obtained by

$$\rho_S \le \left| \frac{Z_S' - Z_{in}}{Z_S' + Z_{in}} \right|. \tag{6}$$

Accordingly, ρ is now written as a function of Z_S'. Thus, we can simultaneously find Z_S' and ρ so that ρ is maximized under the conditions. The actual design procedure is explained in the following example.

Design example:

Consider the design of a tuning circuit with a fractional bandwidth of 20% and having a reflection coefficient of 0.314 or less (-10 dB matching) in the tuning band. Plotting using Eqs.5 and 6 in the Z_S'-ρ plane (Fig. 2), the hatched area is valid for $\rho_S < 0.314$. From this graph, we can obtain $\rho = 0.58$ as the maximum value when $Z_S' = 0.41$. According to Chebyshev's theory, we can hereby easily design an ordinary 3-section band-pass filter for a maximum tolerable reflection coefficient of 0.58 with a fractional bandwidth of 20%. Figure 3 shows the calculated results based on theory. The details on the method to determine the circuit parameters are described elsewhere [4]. Thus, we theoretically determined the impedance ratio of R_L:Z_J(=$\alpha_J d_J$):Z_m:Z_S = 1:0.12:2.69:0.41 in Fig. 1 (b). This result tells us that the characteristics impedance of the micriostripline should be high

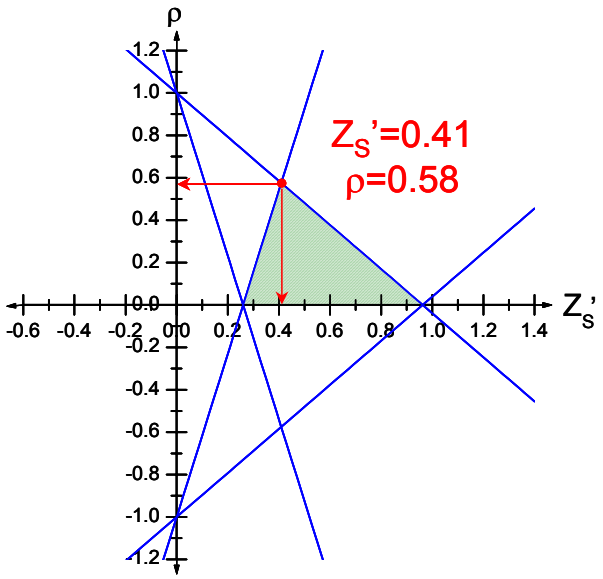

Fig. 2. Reflection coefficient ρ as a function of normalized source impedance Z_S', based on Eqs. 5 and 6. Hatched area indicates design condition of $\rho_S < 0.314$.

compared to those of the distributed junctions. Since it is difficult to achieve high characteristic impedance above 30 Ω using an ordinary configuration of superconducting microstriplines, the characteristic impedance of the distributed junctions should be less than 2 Ω.

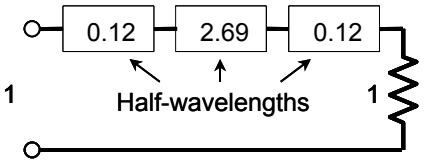

Fig. 3. Circuit parameters determined by ordinary Chebyshev's theory for conditions of $\rho < 0.58$ and $\Delta f/f_0 = 20\%$.

Using the derived impedance ratio, we calculated the frequency characteristics of the tuning circuit as plotted in Fig. 4. Figure 4 (a) is a Smith chart plot and (b) is plots the return loss in the tuning circuit. The frequency is normalized at center frequency. From (a), we can see that the designed tuning circuit optimally achieved –10 dB matching with the 20% bandwidth as we expected. As we can see from (b), the normalized source impedance for the tuning circuit was set to less than half the impedance of the terminating load, which made it possible to maximize the reflection coefficient in filter design under a circuit design condition of $\rho_S < 0.314$. Thus, we found the minimum value for $\alpha_J d_J$. The minimum current density of the distributed junctions can be derived from $\alpha_J d_J = 0.12$. Since the half-wavelength d_J is dependent on SIS junction parameters such as the specific capacitance and the penetration depth of the superconductors, we derived the current density in the actual mixer design based on NbN.

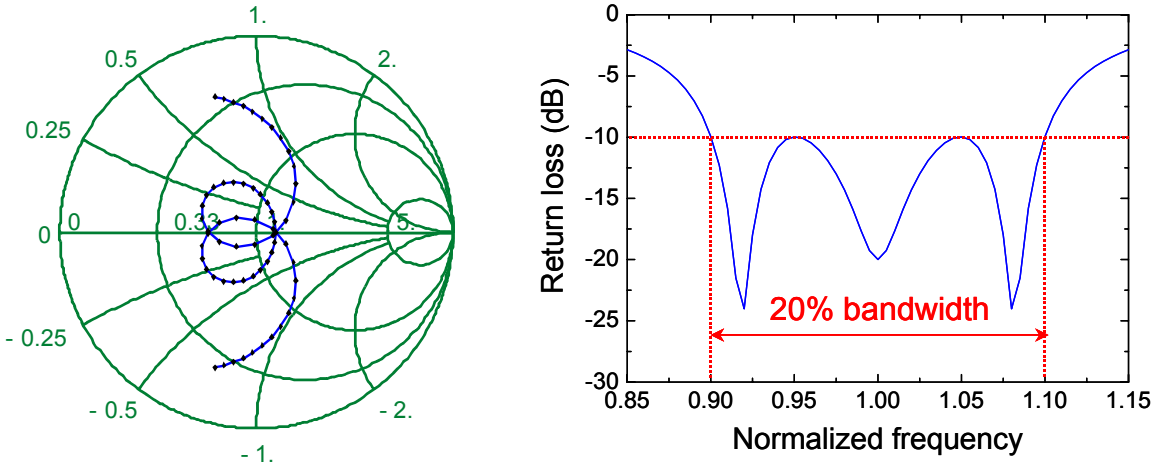

(a) (b)

Fig. 4. (a) Smith chart plot and (b) return loss plot of tuning circuit as a function of normalized frequency.

3. Mixer design

A quasi-optical coupling structure with an MgO substrate lens and a planar twin-slot antenna was used for the mixer input [5]. The feed point of the antenna was centrally positioned using coplanar waveguide transmission lines as can be seen in Fig. 5 (a). A tuning circuit was integrated with one side of the lines as its ground plane. The optical micrograph in Fig. 5 (b) shows that the tuning circuit consisted of two half-wave NbN/MgO/NbN tunnel junctions and NbN/MgO/NbN microstriplines grown epitaxially on a single-crystal MgO substrate [6, 7]. The circuit was connected to the feed point by a quarter-wave impedance transformer. To compare its performance with that of a conventional tuning circuit, we also prepared full-wave distributed junction mixers on the same substrates as seen in Fig. 5 (c).

We designed the tuning circuit to have a center frequency of 870 GHz and a fractional bandwidth of ~20% (ALMA Band 10) with –10 dB matching. The parameters used in our design process are listed in Table 1. The specific capacitance of the NbN/MgO/NbN junctions was assumed to be the same as that of NbN/AlN/NbN

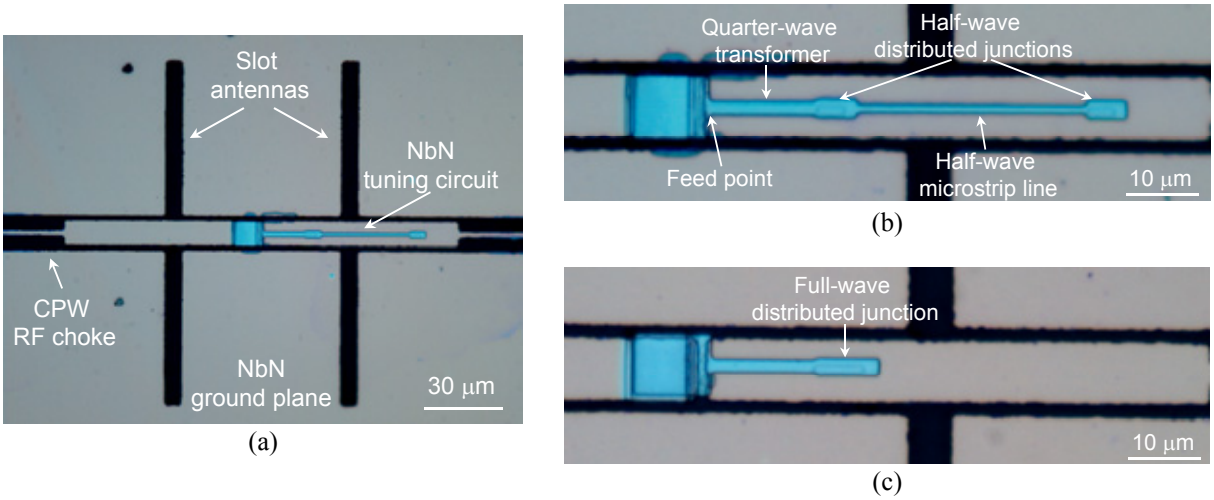

Fig. 5. Optical micrographs of (a) twin-slot antenna mixer, (b) novel tuning circuit with two half-wave SIS junctions, and (c) conventional tuning circuit with full-wave SIS junction.

junctions because the dielectric constants of their tunnel barriers were similar [8]. The method of calculating the characteristic impedance and propagation constant of the distributed SIS junctions, including the overhanging structure with the NbN/MgO/NbN microstrip line for wiring the SIS junctions, is described elsewhere [9]. The surface impedances of the upper and lower electrodes were calculated using the Mattis-Bardeen theory of the anomalous skin effect [10]. We derived the theoretical minimum current density according to the description in the former section. Figure 6 plots the dependence of attenuation ($\alpha_J d_J$) on current density for a distributed NbN junction with a width of 1 μm at a center frequency of 870 GHz. From this figure, the current density to satisfy $\alpha_J d_J$ = 0.12 is about 16 kA/cm^2 (calculated $\omega C_J R_N$ product of about 13) which is much lower than the 40 kA/cm^2 needed for conventional tuning-circuit design ($\omega C_J R_N$ product of about 5).

The diagram in Fig. 7 shows the tuning circuit we designed assuming a constant source impedance of 65 Ω. The impedance ratio of the circuit was taken to have

Table 1. Design parameters.

NbN gap frequency	1.4 THz
normal state conductivity	1.5 x 10^6 Ω^{-1}m^{-1}
upper electrode thickness	400 nm
lower electrode thickness	200 nm
MgO insulator thickness	200 nm
dielectric constant	9.6
NbN/MgO/NbN $J_C R_N A$ product	3.5 mV
Specific capacitance	71 $J_C^{0.16}$ fF/μm^2
MgO barrier thickness	1 nm

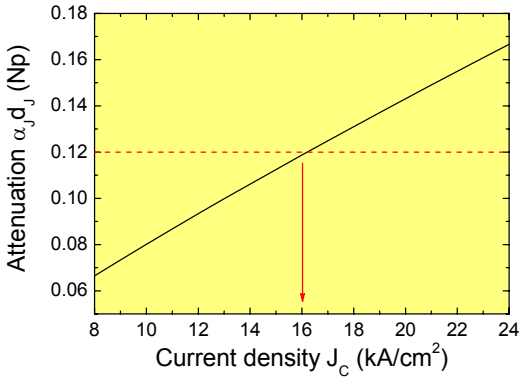

Fig. 6. Attenuation of distributed junction as a function of current density.

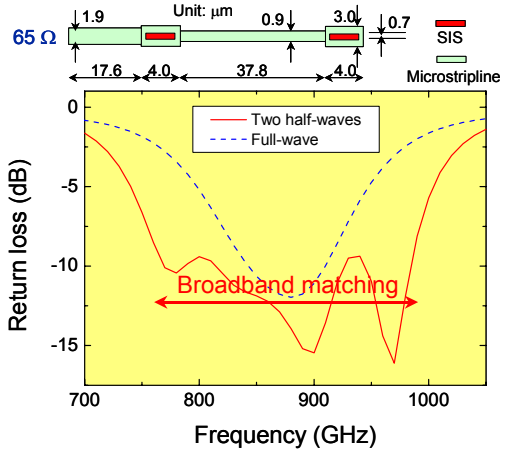

Fig. 7. Layout and theoretical return loss of tuning circuit.

approximately the same values derived above. The return loss of the circuit is also plotted in Fig. 7. A fractional bandwidth of 20% was achieved by using junctions with a current density of 16 kA/cm^2, as was expected theoretically. To compare this bandwidth with that of a conventional tuning method, we calculated the return loss of an SIS mixer with a full-wave junction having the same current density [11]. As we can see in Fig. 7, the fractional bandwidth of the mixer with two half-wave junctions was much broader than that with the full-wave junction.

4. Receiver performance

The mixer chips were fabricated using a process described elsewhere [6, 7]. The critical current density of the junctions was about 4 kA/cm^2, which was measured using other junctions with a large area on the same substrate. The mixer chips were placed on an MgO hyperhemisphere with a 50-μm-thick Kapton-JP anti-reflection cap. The receiver set-up was basically the same as described previously [12], except for the use of a backward-wave oscillator instead of an optically pumped far-infrared laser as the local oscillator (LO) source. The signal and LO power, coupled using a 9-μm-thick Mylar beam splitter, entered the Dewar through a 0.5-mm-thick Teflon vacuum window and Zitex infrared filters cooled to 77 K and 4.2 K, respectively. The intermediate frequency (IF) signal at 1.5 GHz from the mixer output was amplified by a low-noise HEMT amplifier with a 500-MHz bandwidth. A standard *Y*-factor method was used for the noise measurements. No corrections were made for losses in front of the receiver.

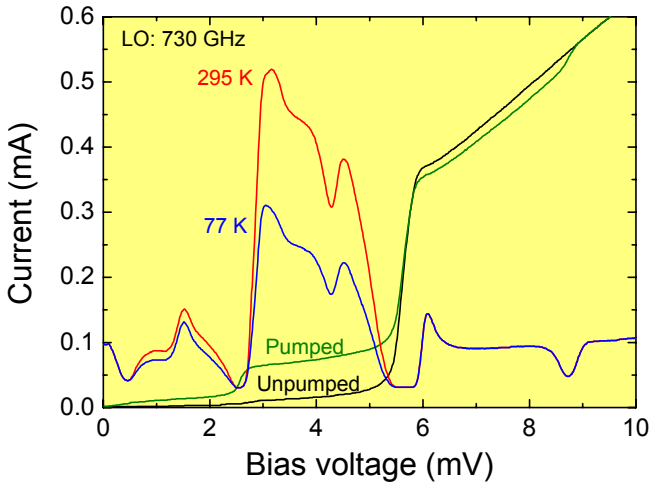

Fig. 8. Heterodyne response of receiver at 730 GHz. Shown are I-V characteristics of mixer with two half-wave SIS junctions with and without LO power. Also shown is IF power as a function of bias voltage for hot (295 K) and cold (77 K) loads.

Figure 8 shows a typical heterodyne response of the receiver at 730 GHz. Since the current density was fairly low, high-quality *I-V* characteristics with a large subgap-to-normal resistance ratio of about 15 were observed when no LO power was applied. Since the fabricated NbN junctions had a large gap voltage of about 5.6 mV, corresponding to 1.35 THz, a first voltage step by photon-assisted tunneling with 730-GHz irradiation clearly appeared at about half the gap voltage. Even though the current density was lower than the design value of 16 kA/cm^2, we observed distinct IF responses to hot and cold loads, indicating that the maximum *Y*-factor was 1.80 at a bias voltage of about 4 mV, corresponding to the double-side-band (DSB) receiver noise temperature of 195 K (about 6 hf/k_B, where h, f, and k_B are the Planck constant, frequency, and Boltzmann constant).

Figure 9 plots the DSB receiver noise temperature using the tuning circuit as a function of LO frequency. Although the measured center frequency was slightly lower than the design frequency of 870 GHz, a noise temperature below 10 hf/k_B was achieved between 710 and 810 GHz, corresponding to a fractional bandwidth of about 13%. It should be

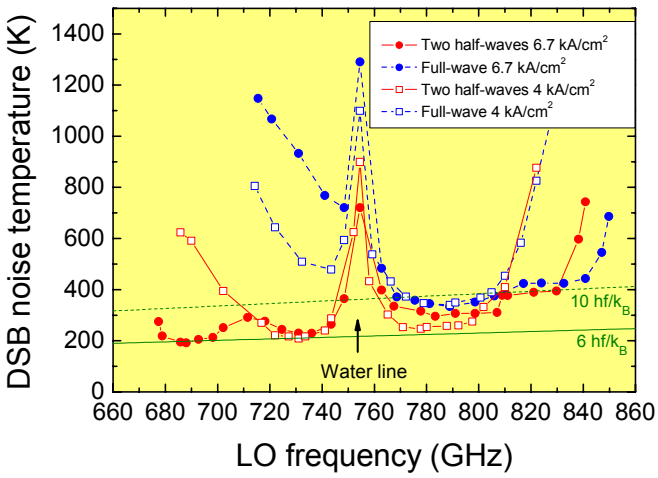

Fig. 9. DSB receiver noise temperature as a function of LO frequency. A 9-μm-thick Mylar beam splitter was used at all measured frequencies.

noted that the estimated $\omega C_J R_N$ product is about 37 using the parameters in Table 1. Also plotted in Fig. 9 is the dependence of receiver noise temperature on frequency when a conventional full-wave junction fabricated on the same substrate was used. The fractional tuning bandwidth with the two half-wave junctions was broader than that with the full-wave junction. In the figure, we also plotted the noise temperatures of other mixers with the current density of 6.7 kA/cm^2 that have been measured previously [3]. The noise temperature below 10 hf/k_B exhibited broadband characteristics from 675 to 830 GHz for the two-half-waves. The fractional bandwidth reached 20%, which also was broader than that with the full-wave junction as well as the results with 4 kA/cm^2. This suggests that new tuning method we developed is effective in reducing the current density of the junctions compared to the conventional method, as we had expected from the theoretical-design considerations.

5. Conclusion

We have developed a method of analytically designing a novel tuning circuit with two half-wave distributed junctions using a simplified circuit model, which uniquely determined the circuit parameters without having to depend on the experience of the designer. We theoretically derived a minimum current density, when actually designing the mixer, which is necessary for two-distributed-junction tuning circuit, and the value was much lower than that needed for a conventional tuning circuit. Experimental results using NbN-based SIS mixers supported our theoretical-design considerations. We feel certain that this type of mixer will improve performance at terahertz frequencies.

Acknowledgements

This work was supported in part by the ALMA Joint Research Fund of the National Astronomical Observatory of Japan.

References

[1] Y. Uzawa, A. Kawakami, S. Miki, and Z. Wang: IEEE Trans. Appl. Supercond. **11** (2001) 183.
[2] Y. Uzawa, M. Takeda, and Z. Wang: Jpn. J. Appl. Phys. **42** (2003) 91.
[3] Y. Uzawa, M. Takeda, A. Kawakami, and Z. Wang: Int. J. Infrared Millimeter Wave **24** (2003) 1749.
[4] R. E. Collin: *Foundations for Microwave Engineering* (McGraw-Hill, Inc., 1992) 2nd ed., Chap. 5, p.303.
[5] J. Zmuidzinas, N. G. Ugras, D. Miller, M. Gaidis, H. G. LeDuc, and J. A. Stern: IEEE Trans. Appl. Supercond. **5** (1995) 3053.
[6] A. Kawakami, Z. Wang, and S. Miki: IEEE Trans. Appl. Supercond. **11** (2001) 80.
[7] A. Kawakami, Z. Wang, and S. Miki: J. Appl. Phys. **90** (2001) 4796.
[8] Z. Wang, Y. Uzawa, and A. Kawakami: IEEE Trans. Appl. Supercond. **7** (1997) 2797.
[9] Y. Uzawa and Z. Wang, *Studies of High Temperature Superconductor*, ed. A. V. Narliker (Nova Science, Hauppauge, NY, 2002) Vol. 43, Chap. 9, p. 255.
[10] D. C. Mattis and J. Bardeen, Phys. Rev. **111** (1958) 412.
[11] T. Matsunaga, C. E. Tong, T. Noguchi, and R. Blundell: IEICE Trans. Electron. **E85-C** (2002) 738.
[12] Y. Uzawa, Z. Wang, and A. Kawakami: Appl. Supercond. **6** (1998) 465.

Sideband-Separating SIS Mixer at 100GHz Band for Astronomical Observation

S. Asayama[1], K. Kimura[2], H. Iwashita[3], N. Sato[1], T. Takahashi[3],
M. Saito[1], B. Ikenoue[1], H. Ishizaki[1], N. Ukita[1]

[1]*National Astronomical Observatory of Japan,*
[2]*Department of Earth and Life Sciences, Osaka Prefecture University, Japan*
[3]*Nobeyama Radio Observatory, Japan*

e-mail: asayama@nro.nao.ac.jp

ABSTRACT

We have developed an integrated sideband-separating SIS mixer at 100GHz based on waveguide split block with 4-8GHz IF. The measured receiver noise temperatures with 4-8GHz IF are less than 60K in the LO frequency range of 90-110GHz, and minimum value of around 45K is achieved at 100GHz. The image rejection ratios are more than 10dB in the LO frequency range of 90-110GHz in the laboratory measurements. The sideband-separating SIS mixer was installed into the cartridge-type receiver system on the Japanese prototype antenna, which is a 12m submillimeter telescope built as a prototype ALMA antenna. This antenna is located on the ALMA Test Facility (ATF) site. We detected continuum signals from the moon and planets (Mars and Saturn) at 98GHz (LSB observation), and successfully obtained a spectrum of ^{12}CO (J =1-0) (rest frequency = 115.27GHz, USB observation) from Orion KL by using a spectrum analyzer as the spectrometer. We confirmed that the image rejection ratio is as large as 13dB in the spectrum of ^{12}CO (J =1-0). This image rejection ratio is consistent with the measurement value in laboratory. These results show that a sideband-separating mixer is very promising for ALMA project.

Keyword: Sideband-Separating mixer, SIS mixer, ^{12}CO (J = 1 - 0) spectrum

INTRODUCTION

There is a strong interest in the millimeter astronomical and atmospheric community to operate low noise quasi-particle mixers in SSB mode in order to eliminate atmospheric noise in the image band during spectral line observations. To meet these demands we have been developing a sideband-separating mixer. In the microwave range, sideband-separating mixers have been available commercially for many decades. The usual implementation is to divide the signal and LO power into two mixers using a quadrature hybrid in either the signal or LO path. Here, the former option as shown in Fig. 1 is used in our SSB mixer. The IF outputs from the two mixers are combined in an IF quadrature hybrid and in principle, all the downconverted power from the upper and lower sidebands appears separately at the two output ports of the IF hybrid. Following this manner We developed an integrated sideband-separating SIS mixer (2SB mixer) at 100 GHz based on the waveguide split block. We installed the sideband-separating SIS mixer into the Cartridgetype receiver system on the Japanese prototype antenna, which is a 12 m submillimeter telescope built as a prototype ALMA antenna. The prototype antenna was assembled at ALMA Test Facility (ATF) site and is currently being tested. The antenna is designed to meet ALMA specification requirements, high surface and pointing accuracy, and fast position switching capability. The 2SB mixer developed by our group will be used for radiometric observations to evaluate the prototype antenna. In particular, the character of 2SB mixer, separating upper-sideband from lower-sideband, enables us to measure the beam size and other radiometric performance without frequency ambiguity. In this report we present brief design, performance, and test observation results using our 2SB mixer on the Japanese prototype antenna.

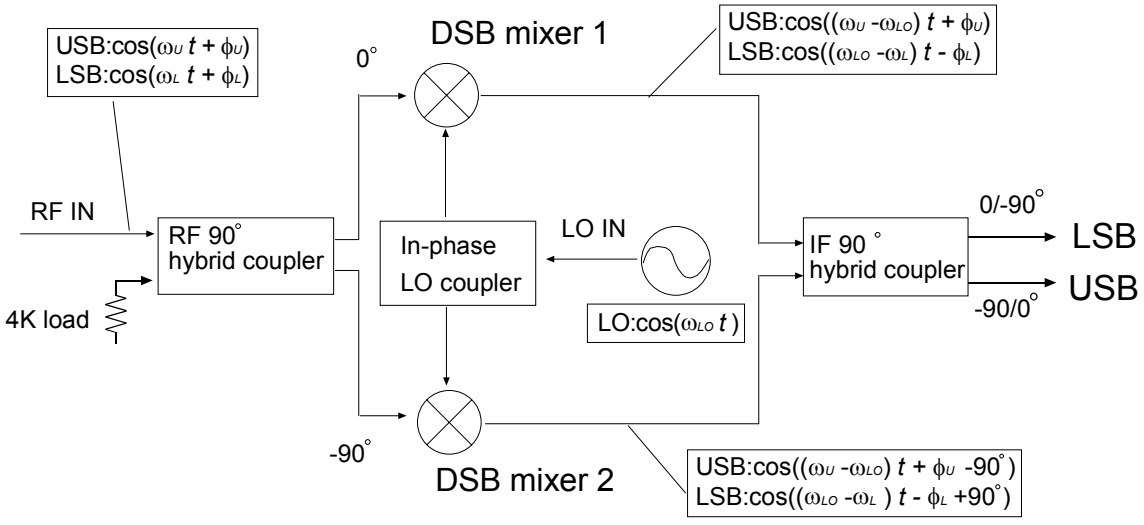

Fig. 1: Block diagram of the sideband-separating mixer

2. MIXER DESCRIPTION

Detailed structure of a split-block waveguide unit for our sideband-separating mixer is shown in Fig. 2. We adopted W-Band waveguide (2.54 x 1.27 mm) for our waveguide unit. The basic design of the sideband-separating SIS mixer is similar to that described by *Claude et al*. [1]. The split-block waveguide unit contains an RF quadrature hybrid, two LO directional couplers, a LO power divider, and 4 K cold image terminations. We also integrated two DSB mixers on the split-block waveguide unit through the waveguide taper transformer. The detail of this waveguide unit is written in MEMO 453 [2]. The DSB mixer adopted here was developed at Nobeyama Radio Observatory [3]. The measured DSB receiver noise temperature of the SIS mixer with 4.0–8.0 GHz IF is less than 25 K in the LO frequency range of 95–120 GHz, and a minimum value of around 19K is achieved. One end of the RF choke filter is connected directly to a 50 Ω IF line by a 25μm-diameter Al wire to extract the IF output and to supply DC bias. The slot of the other port of the channel is filled with indium and electrically grounded. The signal and the LO are fed to the feed point through a linearly tapered waveguide impedance transformer (full height to 1/5 reduced height). The IF signals from the two DSB mixers are combined in a commercial quadrature hybrid (Anaren Microwave, Inc.).

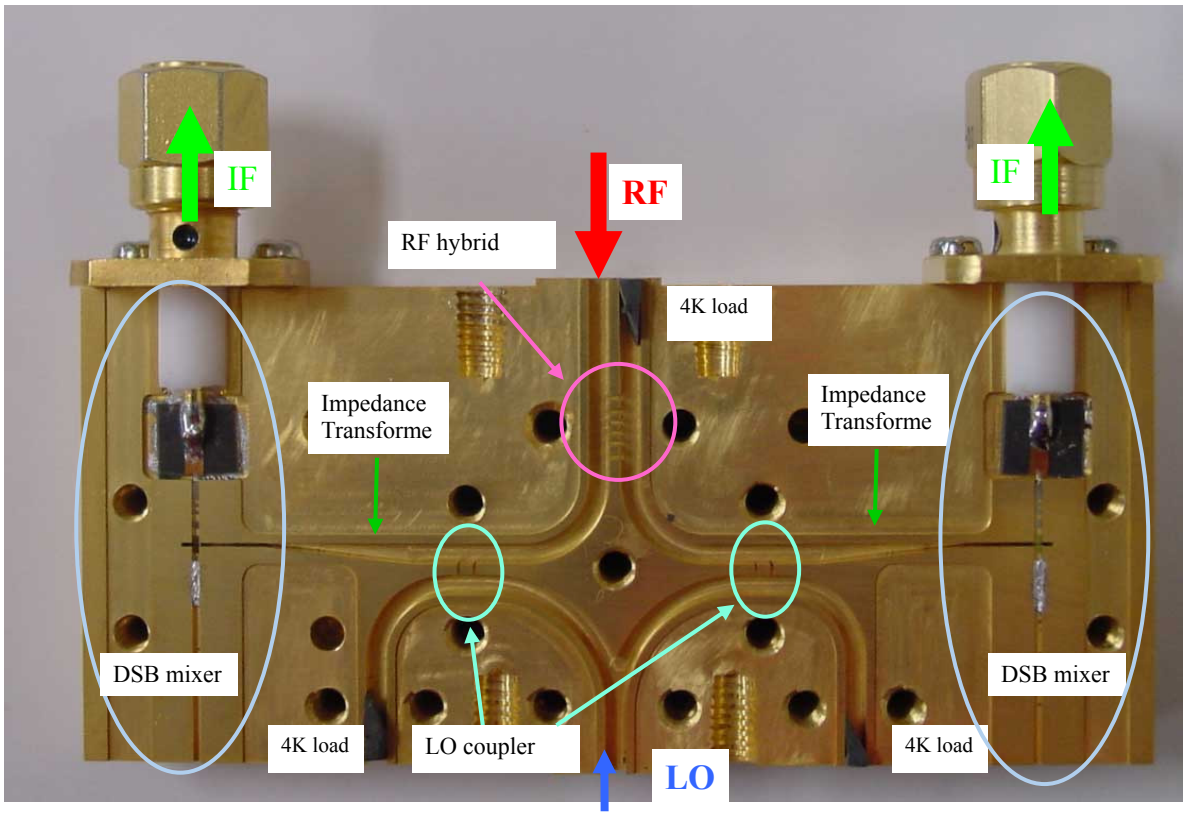

Fig. 2: A photograph of the split-block waveguide unit

3. MIXER PERFORMANCE

The noise temperature of the sideband-separating mixer with 4–8 GHz IF was measured by a standard Y-factor method. The mixer was mounted on the 4K cold stage in a SIS receiver evaluation cryostat. A Teflon film with a thickness 1.0 mm was used as a vacuum window. The IF output from the mixer was first amplified by a cooled High Electron Mobility Transistor (HEMT) amplifier, and then further amplified at room temperature. The equivalent noise temperature and gain of the HEMT amplifier associated with the isolator were about 15 K and 30 dB, respectively. The overall receiver noise temperatures of the receiver (including the noise contribution of the vacuum window, feed horn, and IF amplifier chain), measured on the first photon step below the gap voltage, are plotted in Fig. 3. The measured receiver noise temperatures are less than 60 K in the LO frequency range of 90–110 GHz, and a minimum value of around 45 K is achieved at 100 GHz.

In case of a sideband-separating mixer, the image rejection ratio can be measured accurately injecting CW test signals in the upper and lower sidebands, even when the relative power level of the test signals are not known [4]. Considering stability and repeatability, we adopted a cross guide coupler (CGC) for CW signal injection. The coupling efficiency of the CGC is -25 dB. The measured image rejection ratios are plotted in Fig. 4. The image rejection ratios are more than 10 dB in the LO frequency range of 85–110 GHz.

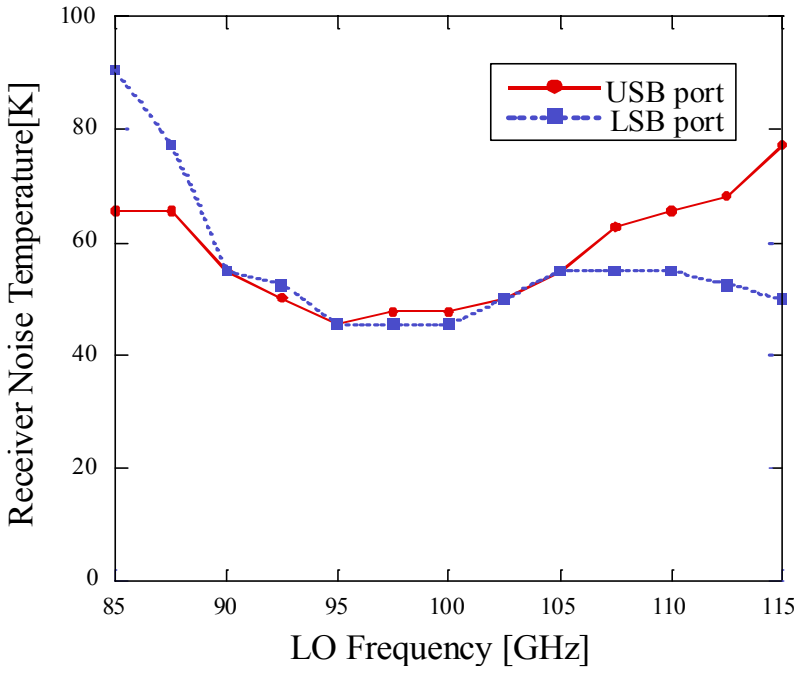

Fig.3: Receiver noise temperature as a function of frequency

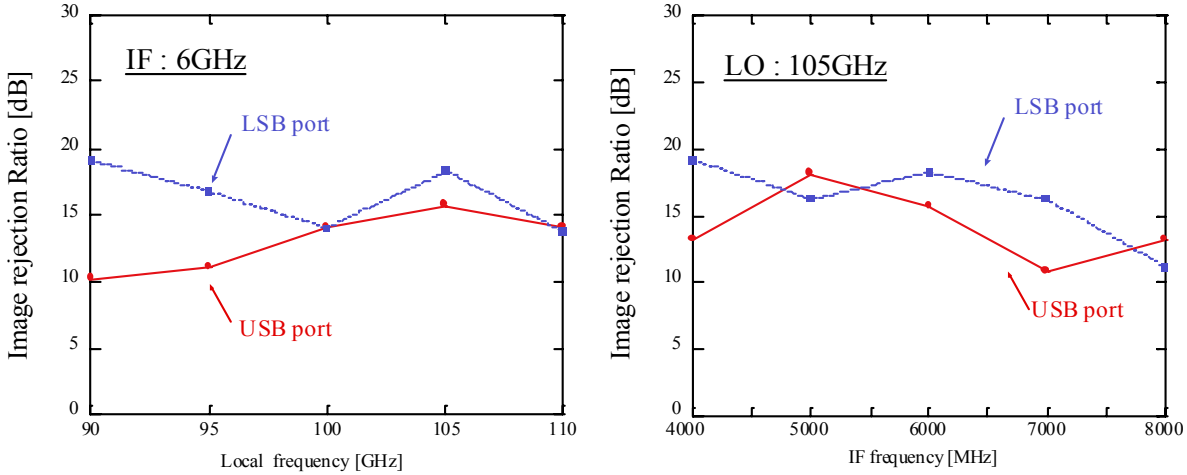

Fig.4: (a)Image rejection ratio at IF=6 GHz as a function of Local frequency. (b) Image rejection ratio at LO=105 GHz as a function of IF frequency.

3. FIRSTRIGHTS WITH SIDEBAND-SEPARATING SIS MIXER

The cartridge-type receiver cryostat for the Japanese prototype antenna is almost same as the cryostat tested on the Atacama Submillimeter Telescope Experiment (ASTE) [5]. The detail of the cryostat was described by Yokogawa et al. [6]. We developed Band 3 (100 GHz) and Band 6 (200 GHz) cartridge-type receivers for the Japanese prototype antenna. The picture of the cryostat, in which 2 cartridge-type receivers were installed, is shown in Fig. 9 (a). The cylindrical cryostat can accommodate two cartridges of 170 mm diameter and one cartridge of 140 mm diameter. The ϕ140 mm cartridge for Band 3 has been designed and developed by Osaka Prefecture University/Nagoya University [7]. The closeup of 4 K stage of the band 3 cartridge is shown in Fig. 9 (b).

In September 2003, the cartridge-type receiver cryostat was installed onto the Japanese prototype antenna. The antenna is equipped with RF Power Meter (Agilent E4419B dual channel powermeter with E9300A power sensors) and Agilent 8562EC Spectrum Analyzers in the receiver cabin. The beginning of October 2003, we detected continuum signals from the moon and planets (Mars and Saturn) at 98 GHz (LSB observation)with the Band 3 receiver. On 18 October 2003, we successfully obtained a spectrum of ^{12}CO (J =1-0) (rest frequency =115.27GHz, USB observation) from Orion KL by using a spectrum analyzer as the spectrometer (Figure 10). USB and LSB spectra were not observed at the same time, and the interval of those observations was less than ten minutes. In these observations, Doppler corrections were not applied. The Doppler frequency shift is less than 40 kHz in ten minutes. This frequency shift is almost negligible because the resolution bandwidth of these observations was 300 kHz. We can estimate that the image rejection ration of LSB port is more than 13 dB because the rms noise level of those observations is 0.4 μW. This image

rejection ratio is consistent with the measurement value in laboratory. Those results are the first astronomical observation with the waveguide type Sideband-Separating SIS mixer. We have confirmed that a sideband-separating mixer is very promising for ALMA.

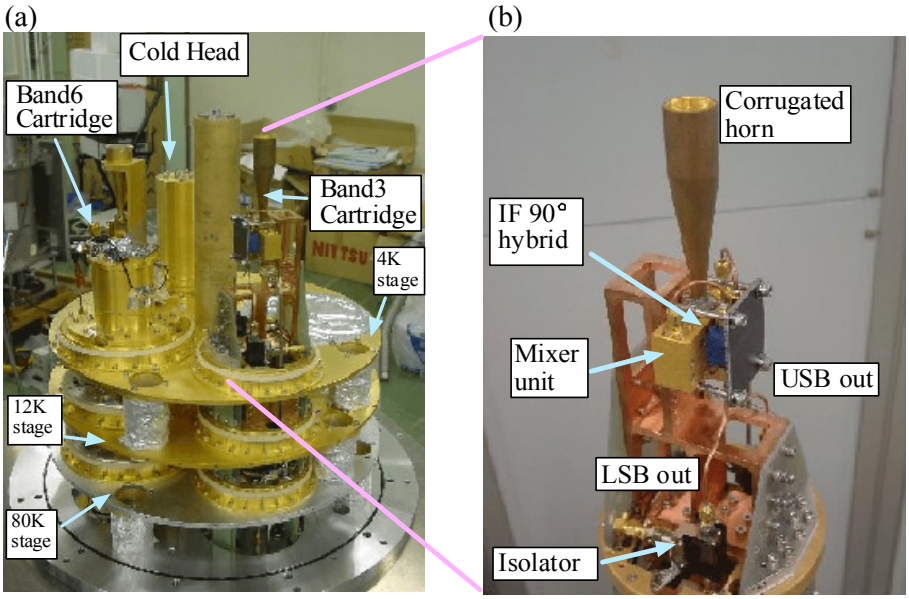

Fig. 5: (a) A photograph of the cryogenic system, in which 2 cartridge-type receivers were installed. The cryostat is composed of 3 stages (from up to down 4 K, 12 K, and 80 K stage). (b)The closeup of 4 K stage of the band 3 cartridge.

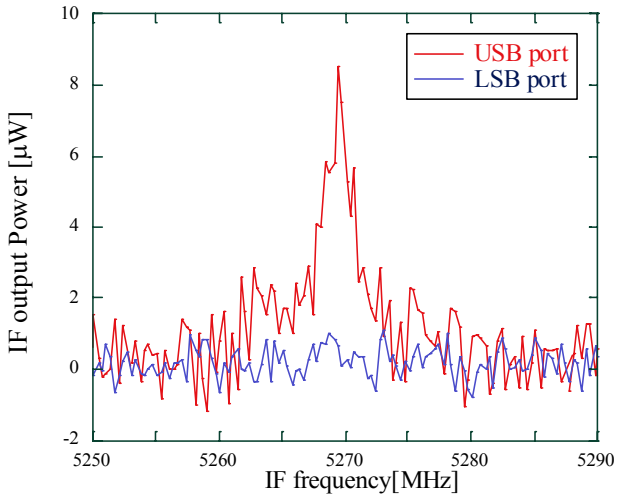

Fig. 6: Spectrum of ^{12}CO (J = 1- 0) from Orion KL by using a spectrum analyzer as the spectrometer. The Local frequency was 110 GHz (USB observation). The resolution and video bandwidth were 300 kHz and 3kHz, respectively. Average counts was 90 times.

ACKNOWLEDGEMENTS

We would like to thank T. Nakajima, N. Nakajima, J. Korogi, Y. Yonekura, H. Ogawa, Y. Sekimoto, T. Noguchi, and ALMA-J members. S. A. acknowledges the financial support from the Japan Society for the Promotion of Science (JSPS) for Young Scientists.

REFERENCES

[1] S. M. X. Claude, C.T. Cunningham, A.R. Kerr, S.-K. Pan, "Design of a Sideband-Separating Balanced SIS Mixer Based on Waveguide Hybrids," ALMA Memo 316

[2] S. Asayama, H. Ogawa, T. Noguchi, K. Suzuki, H. Andoh, and A, Mizuno, "An Integrated Sideband-Separating SIS mixer Based on Waveguide Split Block for 100 GHz Band," ALMA Memo 453

[3] S. Asayama, T. Noguchi, and H.Ogawa, "A fixed-tuned W-band waveguide SIS mixer with 4.0-7.5 GHz IF," Int. J. Infrared and Millimeter Waves, Vol.24, pp.1091-1099, 2003 .

[4] A. R. Kerr, S.-K. Pan, and J. E. Effland, "Sideband Calibration of Millimeter- Wave Receivers," ALMA Memo 357

[5] M. Sugimoto, Y. Sekimoto, S. Yokogawa, T. Okuda, K. Tatematsu, K. Kohno, H. Ogawa, K. Kimura, K. Suzuki, T. Minamidani, "Preliminary tests of Cartridge-Type Receiver System at Atacama Site," ALMA Memo 458

[6] S. Yokogawa, Y. Sekimoto, M. Sugimoto, T. Okuda, T. Sekiguchi, T. Kamba, K. Tatematsu, T. Nishino, H. Ogawa, K. Kimura, K. Noda, K. Narasaki, "Plug-In Cryogenic System for Cartridge-Type SIS Receivers," Publications of the Astronomical Society of Japan, Vol.55, No.2, pp. 519-525, 2003.

[7] H. Ogawa, Y. Yonekura, S. Asayama, K. Kimura, A. Mizuno, N. Mizuno, T. Minamidani, H. Maeda, K. Suzuki, Y. Fukui, H. Andoh, Y. Sekimoto, T. Noguchi, "ALMA Front-End System for Band 4," Proc. IAU 8th APRM, Vol. 289, pp. 23-24, 2003.

A Dual Polarization Sideband Separation SIS Receiver for the Large Millimeter Telescope

Gopal Narayanan[1]**, Ron Grosslein, Vikram Kodipelli, Vern Fath, Don Lydon, and Prachi Deshpande**
Department of Astronomy, University of Massachusetts, Amherst, MA 01002

Abstract

A dual polarization SIS heterodyne receiver is being built for use on the Large Millimeter Telescope (LMT). The LMT is a 50 m diameter millimeter-wavelength telescope being built in Mexico as a joint project between UMass and Instituto Nacional de Astrofisica, Óptica, y Electrónica (INAOE) in Mexico. The receiver is designed to operate in the 210 – 275 GHz atmospheric window, and will provide state-of-the-art sensitivity using a sideband separation scheme to separate the upper and lower sidebands. In each polarization, 8 GHz of effective bandwidth per sideband (16 GHz total) will be available without the use of cumbersome mechanical tuners. Due to the prevailing physical conditions in the interstellar medium of galactic and extra-galactic sources, the 1 mm band is expected to be the workhorse scientific band for the LMT. The SIS receiver will also handle the necessary requirements of a commissioning receiver.

The receiver will be mounted at the Cassegrain focus of the LMT, and will employ a waveguide-based OMT. Each polarization output of the OMT will enter a split-block waveguide mixer block, which will contain the passive in-phase and quadrature hybrids for the LO signal and RF signals respectively. Two single-ended SIS junctions of the same design as that used in the ALMA Band 6 mixers will be used. The IF outputs of the two mixers are amplified using 4–12 GHz IF amplifiers, and then passed through a quadrature IF hybrid to separate out the sidebands. The entire receiver system will be housed in a cryostat equipped with a closed-cycle 4 K refrigerator. A new generation of bias electronics has been designed, which is interfaced to the control computer using a simple 2-wire I^2C communication protocol. The design of the entire receiver system has been optimized to allow the individual subsystems to be scaled up to an eventual large-format focal-plane array receiver system at 1 mm wavelength for the LMT.

1 Introduction

The Large Millimeter Telescope (LMT) is a 50m diameter millimeter-wavelength telescope being built atop Sierra Negra, a volcanic peak near Mexico City (see Figure1a) [1]. The LMT will have a wavelength coverage of 4 mm to 1 mm (75 - 300 GHz). The telescope is being built in a collaboration between the University of Massachusetts, Amherst (UMass), and the Institito Nacional de Astrofisica, Óptica, y Electrónica (INAOE) in Mexico. Due to the prevailing physical conditions in the interstellar medium of galactic and extragalactic sources, the 1 mm band is expected to provide the most interesting science for the LMT/GTM. Figure 1b shows the transmission plot and some molecular lines of significant astrophysical interest for the Sierra Negra site, assuming a rather pessimistic water vapor column of 2 mm of PWV. The excellent atmospheric transmission provided by the site, coupled with a sensitive wideband 1 mm heterodyne receiver system will provide new perspectives on stellar, chemical, and galaxy evolution in present and past epochs. The proposed instrument will also handle the necessary requirements of a commissioning receiver.

The receiver is designed to provide state-of-the-art sensitivity using a novel sideband separation scheme to separate the upper and lower sidebands. In each polarization, 8 GHz of effective bandwidth per sideband (16 GHz total) will be available without the use of cumbersome mechanical tuners. The polarization diplexing will be performed using a novel waveguide orthomode transducer (OMT) [2,3]. The technology development of the initial 1 mm commissioning receiver is geared to serve as a stepping stone for a future 1mm focal plane array on the LMT.

2 Overview of the Receiver Architecture

The 1 mm SIS commissioning receiver will be mounted at the Cassegrain focus of the LMT with simple coupling optics. See Figure 2 for details of the system architecture. Figure 3 shows the schematic details of a single balanced sideband separation mixer (BSSM).

[1]e-mail: gopal@astro.umass.edu

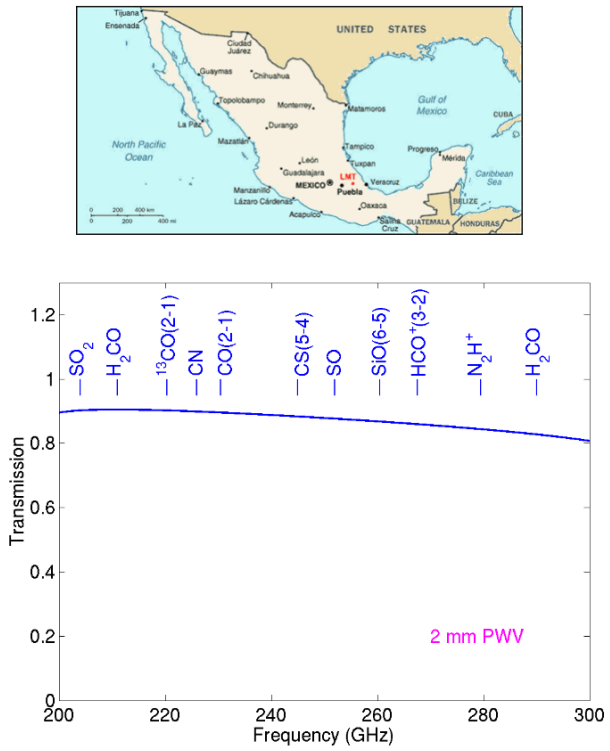

Figure 1: (a) Location of LMT in Mexico (b) Transmission plot for LMT site assuming 2 mm of precipitable water vapor. Also shown are the frequencies of important molecular lines in the 1 mm band.

The incoming dual-polarized signal is coupled into a corrugated feedhorn. A waveguide orthomode transducer (OMT) splits the signal into two orthogonal components, each of which is processed by a balanced sideband separation mixer (BSSM). Two sidebands of each polarization is amplified by 4 - 12 GHz low-noise IF amplifiers. The local oscillator signal is derived from a computer controlled frequency synthesizer, which is frequency multiplied by a chain of multipliers. The LO signal is split by a waveguide power divider and feeds each BSSM mixer block. Details of the BSSM are shown in Figure 3.

3 Design of Waveguide Hybrids

The entire BSSM will be assembled in one single split-block machined block, and will house the waveguide hybrids. Figure 4 shows the appearance of the split-block. The RF 90° coupler uses a branchline coupler. The design details and expected performances of the 4-section branchline coupler is presented in Figure 5. The design was performed with CST Microwave Studio and Ansoft HFSS. The optimized 4-branch line coupler shows good performance, and is easily machinable (and scalable to THz frequencies). The LO power divider design is based on a 3 dB 0° power combiner that was used in the OMT design described in [2]. This design was scaled, and then optimized for the 1mm band.

4 Prototype Single-Ended Mixer

Before building the full BSSM, a prototype single-ended mixer block has been constructed to test SIS junction mounting methods, characterize double-sideband noise performance, and new generation of bias electronics. The design of the LMT 1 mm SIS receiver employs the NRAO Band 6 low parasitic (with low output ca-

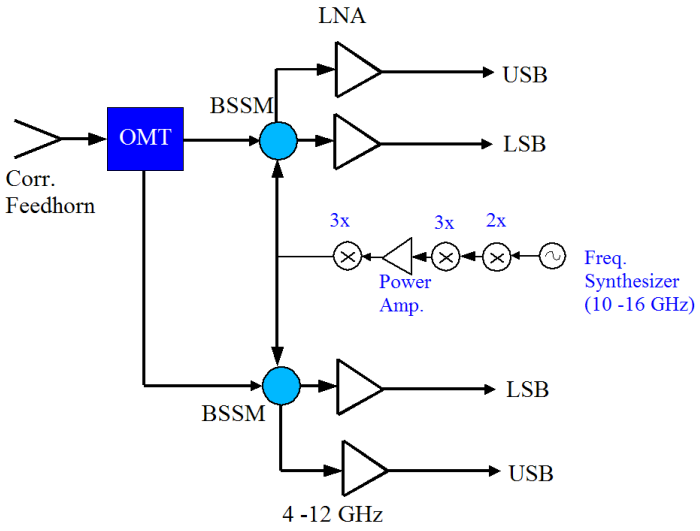

Figure 2: Schematic Block Diagram of 1mm SIS Receiver. See text for details of the receiver

pacitance and inductance) SIS junctions [4]. The mixer block (see Figure 6) was fabricated at UMass using a numerically-controlled NC micromachine [5]. The junction is mounted in suspended stripline channel cut orthogonal to the waveguide. The SIS junction has a coplanar waveguide section which needs to be grounded to the block. Two 20 mil (0.5 mm) long, 1 mil (25.4 μm) diameter gold wires are glued carefully to the shelves in the channel, after which the junction is mounted into channel. The gold wires are then crushed to provide a good ground return. A custom jig with glass-slides was constructed to crush the gold wires when mounting the SIS junction. A 0.5 mil (12 μm) goldwire is used to connect hot-side of junction to a 50 Ohm IF microstrip line. The IF line connects to a field-replaceable SMA connector at the top end of the block. A DC bias network (with a 100:1 voltage divider) consisting of chip resistors and chip capacitors is mounted on the mixer block, and a 4-wire bias network connector is soldered directly to the mixer block. Room temperature DC resistance tests show that SIS junction has the correct normal state resistance. Cryogenic DC IV test results are shown in Figure 7. RF Cryogenic tests will be performed soon. The single-ended mixer will be tested with a 4 – 8 GHz isolator mounted to the IF SMA, followed by a WBA13 type 4 – 12 GHz IF Low Noise Amplifier. A Sumitomo SRDK 415DE closed-cycle 4 K refrigerator system, with integral helium pot (for temperature stabilization of the 4 K stage) is being used. A custom square dewar will house the receiver.

5 Bias Electronics Systems With I^2C Control

A new generation of bias electronics for SIS/HEB receivers has been designed and built. Computer control of SIS, IF LNA, magnet, and IF total power is achieved by a two-wire serial bus called the I^2C (Inter-IC) bus [6]. Most of the bias cards are VME 6U based cards which will be housed in a VME chassis.

The SIS mixer bias control is divided into two circuit cards - an SIS bias card, and a SIS bias preamp card (which is mounted right outside the dewar in an RFI tight box). The SIS bias card has I^2C Xicor digital potentiometers with which bias voltage can be set. The bias cards contain 12-bit I^2C analog-to-digital converters to digitize the current and voltage sense outputs which originate from the bias preamp card. An I^2C general purpose IO chip is used to select between constant voltage mode or open-loop mode (for IV sweeps). Each SIS bias card and preamp card can bias 8 independent mixers. For laboratory testing, a Linux PC running a GTK+ based graphical user interface (GUI) with a MySQL database backend is used. Low-

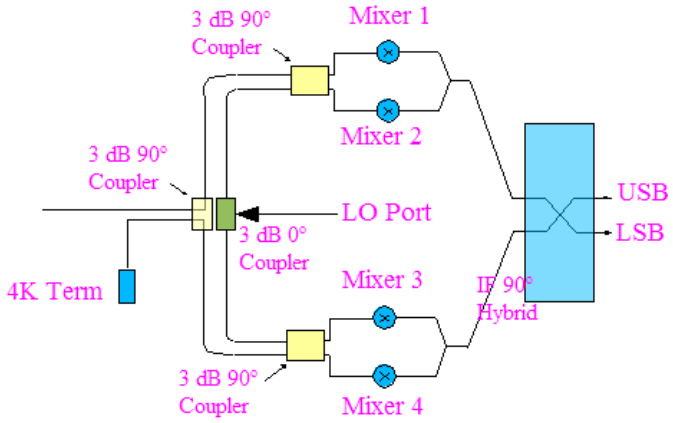

Figure 3: Schematic Block Diagram of a Balanced Sideband Separation Mixer (BSSM). The incoming RF signal is split by a 3 dB 90° coupler, while the LO goes through a 3 dB 0° coupler. The LO and RF couplers are implemented in waveguide hybrids (see §3). The top and bottom halves each contain a balanced mixer, implemented with two SIS mixers (biased with opposite polarity with respect to each other). The IF signals are amplified and combined with a IF 90° hybrid to separate out the upper sideband (USB) and lower sideband (LSB) signals.

level I^2C commands are encapsulated in user-callable libraries with a simple API (Application Programming Interface).

6 Wideband IF Amplifier

A connectorized 4 - 12 GHz WBA13 IF amplifier has been fabricated and tested (see Figure 8). These IF amplifiers have a noise temperature $\leq$ 6 K through most of the 4 - 12 GHz band. However, we find that for optimum noise, the power dissipation in these amplifiers can be rather high ($\sim$ 20 mW). NRAO has developed very low dissipation, low noise IF amplifiers which are well-matched with the SIS junctions, and require no isolators between it and the mixer [7]. The NRAO design uses a 3-stage design based on discrete InP HFET amplifiers (which are available at UMass from a previous TRW wafer run). Assembly of the amplifier can be somewhat complex. For the future 1mm focal plane array for the LMT, it might be desirable to design an IF amplifier with simpler assembly requirements. We are designing a new hybrid IF amplifier, which employs a single InP HFET amplifier in the first stage, and a TRW InP WBA5 MMIC amplifier (a 2-stage design) immediately following it. A preliminary design shows good noise performance with 30 dB gain (see Figure 8c).

7 Summary and Acknowledgements

- A dual-polarization, balanced, sideband separation SIS receiver for the 1mm wavelength band is being built for the LMT.
- The mixer block employs waveguide hybrids to perform the appropriate phasing to accomplish balanced, sideband separation.
- Wideband 4 – 12 GHz IF amplifiers will be used.
- The receiver will be fully computer controlled using I^2C 2-wire interfaces.

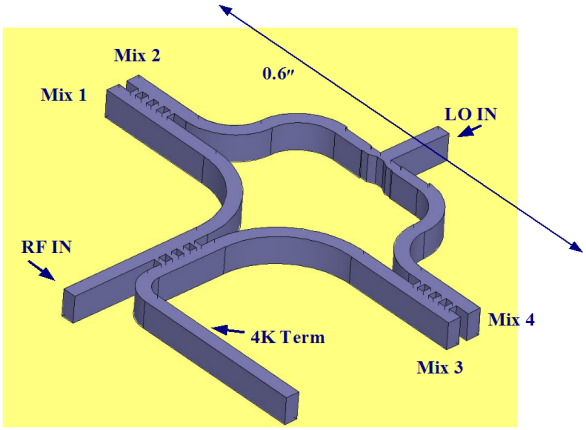

Figure 4: Waveguide Hybrid design for the BSSM. The block can be machined in split-block fashion, and measures $0.9 \times 0.9 \times 0.75$ inches in size.

Acknowledgements: This work was supported by NSF grant AST 02-28993 to the Five College Radio Astronomy Observatory. We wish to thank Tony Kerr at NRAO for providing the SIS junctions, and for many useful technical discussions. Gene Lauria at NRAO is also thanked for discussions on IF amplifier options, and for providing design details of the NRAO IF amplifier. We also thank Sandy Weinreb and Niklas Wadefalk for providing the WBA13 MMIC chip and mechanical design for the IF amplifier. We thank Neal Erickson for providing the local oscillator module for the receiver, and for many useful discussions. John Wielgus helped with wafer-probe measurements of the WBA5 MMIC amplifier.

8 References

[1] F. P. Schloerb, and L. Carrasco, “The Large Millimeter Telescope”, in Proc. of the 15th Int’l Symp. on Space Terahertz Technology, Northampton, MA, this volume.

[2] G. Narayanan, and N. R. Erickson, “A Novel Full Waveguide Band Orthomode Transducer”, Proc. of the 13th Int’l Symp on Terahertz Technology, Harvard Univ., March 2002, pp 504-514.

[3] G. Narayanan, and N. R. Erickson, 2003, “Full-Waveguide Band Orthomode Transducer for the 3mm and 1mm Bands”, in Proc. of the 14th Int’l Symp on Space Terahertz Technology, Tucson.

[4] A. R. Kerr, S.-K. Pan, E. F. Lauria, A. W. Lichtenberger, J. Zhang, M. W. Pospieszalski, N. Horner, G. A. Ediss, J. E. Effland, R. L. Groves, “The ALMA Band 6 (211-275 GHz) Sideband-Separating SIS Mixer-Preamp”, in Proc. of the 15th Int’l Symp. on Space Terahertz Technology, Northampton, MA, this volume.

[5] G. Narayanan, N. R. Erickson, and R. M. Grosslein, 1999, “Low Cost Direct Machining of Terahertz Waveguide Structures”, Proceedings of the 10th International Symposium on Space Terahertz Technology, ed. T. Crowe, U. of Virginia, pp 519 – 529.

[6] Website: http://www.semiconductors.philips.com/buses/i2c/index.html/

[7] E. F. Lauria, A. R. Kerr, M. W. Pospieszalski, S.-K. Pan, J. E. Effland and A. W. Lichtenberger, ”A 200-300 GHz SIS mixer- preamplifier with 8 GHz IF bandwidth,” IEEE Int. Microwave Symp. Digest, pp. 1645-1648, May 2001. See Memo 378 at http://www.alma.nrao.edu/memos/.

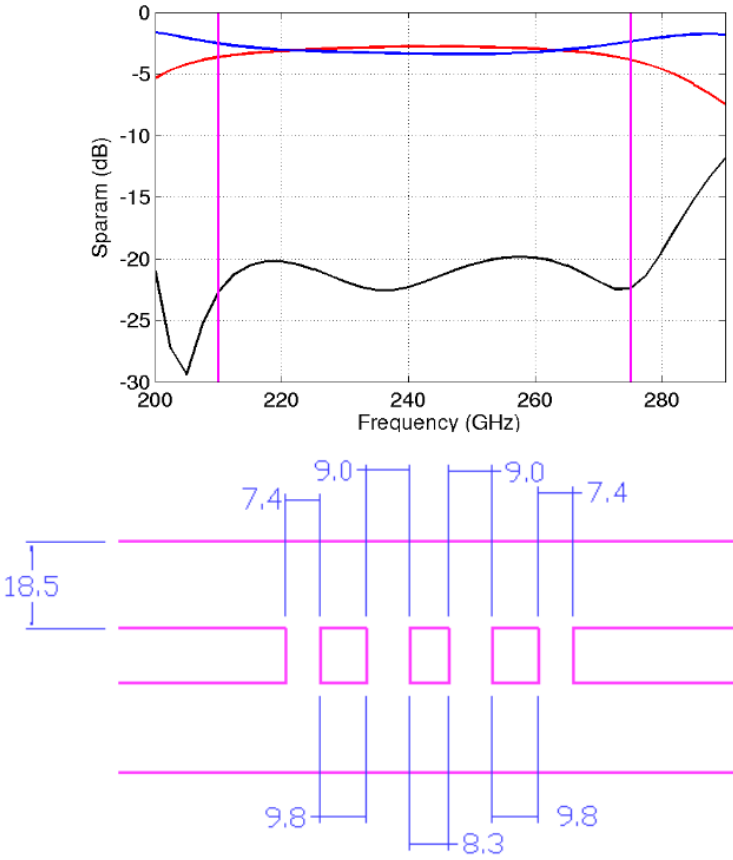

Figure 5: (a) Expected performance of the designed 4-branch line coupler. The designed band is 210 - 275 GHz. The red and blue curves show the coupling to the two output 3 dB ports, and the black curve shows the input match to the branchline coupler. (b) Details of the 4-branch line coupler. All dimensions are in mils. The width of the waveguides is 37 mils.

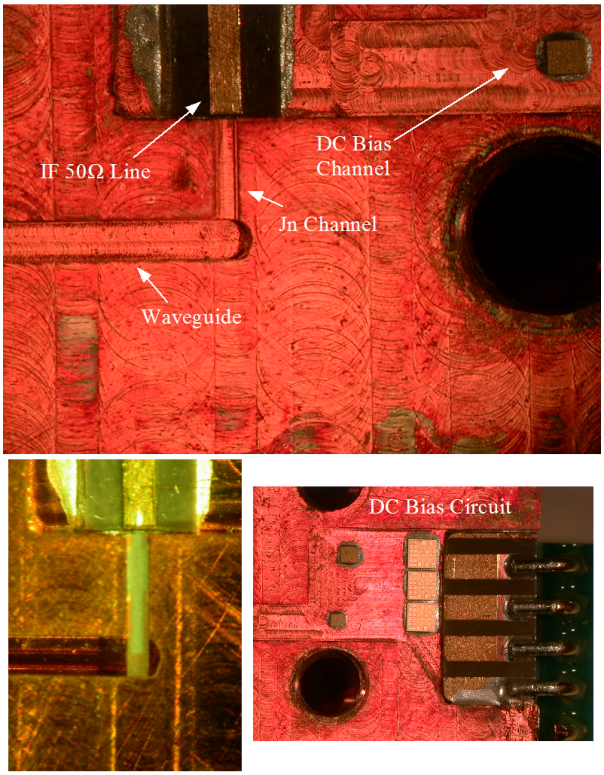

Figure 6: Single-ended SIS mixer block assembly details. Top picture: View of the waveguide, suspended stripline channel, and IF line before placing SIS junction. Bottom left: SIS junction in channel (with ground plane facing above). Bottom right: View of the DC bias circuit that includes, pins for current and voltage sense outputs.

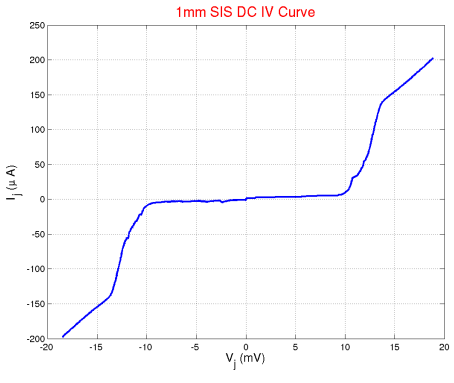

Figure 7: Single-ended SIS mixer Cryogenic I-V tests at $\sim$ 4 K. The measured I-V response of the single-ended SIS mixer showing low-leakage current.

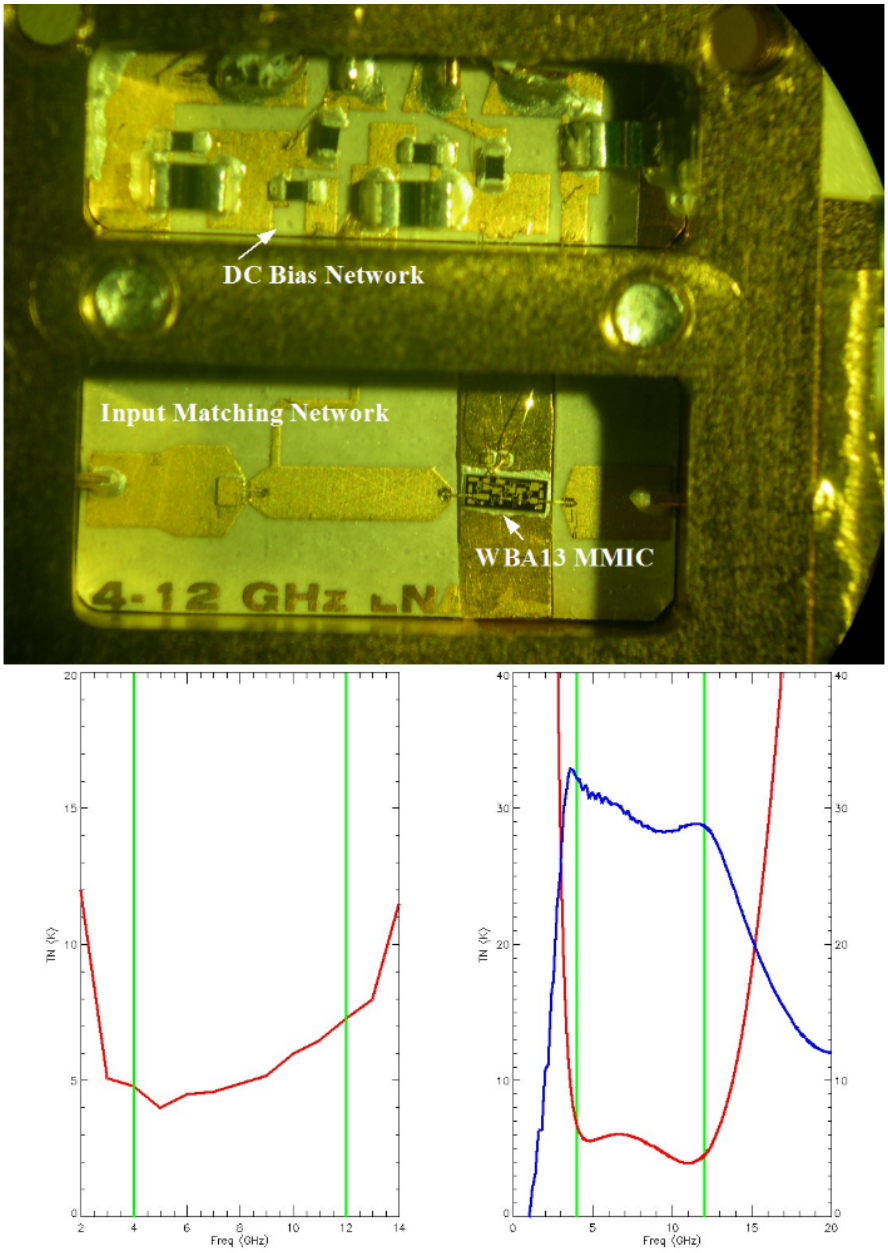

Figure 8: (a) Top: Photograph of the WBA13 IF amplifier built and assembled at UMass. A metal bridge provides isolation between the DC bias networks and the high frequency RF side of the amplifier. (b) Bottom Left: Measured Noise temperature of the WBA13 amplifier. Noise tests were done at 20 K in a test dewar equipped with a Variable Temperature 50Ω load (VTL). The plot shows an upper limit to the noise temperature as mismatch losses in the VTL have not been factored out. (c) Bottom Right: Simulated performance of a newly designed hybrid HFET/MMIC IF amplifier. The blue curve shows the gain in dB, and the red curve shows the anticipated noise temperature. Green lines denote the design bandwidth of the IF amplifier.

Design of a Balanced Waveguide HEB Mixer for APEX 1.32 THz Receiver

M. Pantaleev, D. Meledin, A. Pavolotsky, C. Risacher, and V. Belitsky
Onsala Space Observatory, Chalmers University of Technology,
Group for Advanced Receiver Development (GARD), MC2,
Chalmers University of Technology, S-412 96, Gothenburg, Sweden

Abstract

The prototype of a waveguide balanced Hot Electron Bolometer (HEB) Terahertz mixer is designed as a part of development for the APEX Project of Band T2 receiver for 1250-1390 GHz. The proposed mixer employs balanced scheme with two identical HEB devices. These individual mixers would be placed on two separate crystalline quartz substrates with dimensions of 1000μm x67μm x17 μm each with integrated RF choke filters, DC-bias and IF circuitry. A 3 dB quadrature waveguide directional coupler is needed to provide local oscillator (LO) injection and RF signal distribution between the two HEB mixers. We have designed the coupler to achieve the required frequency band, low insertion loss and symmetrical division of the RF and LO power within the band of interest. Initial design of HEB mixer layout is developed based on a previous development for a 345 GHz sideband separation mixer. We present also results of development of microfabrication technology of the waveguide hybrid employing micromachining approach combined with electroplating technique.

I. Introduction

This mixer is being developed for APEX 12m ground based single dish telescope located at Chajnantor, in the Northern Chile at an altitude of 5000 m [1], [2]. This site was selected according to detailed atmospheric transmission measurements [3] showing possibility to make astronomical observations at 0.85, 1.03, 1.30, and 1.50 THz frequencies with useful efficiency. The telescope will have both heterodyne and incoherent instruments covering the frequency range 211-1500 GHz. Presented in this paper mixer prototype is intended for APEX band T2, covering the frequency range 1250-1390 GHz with central frequency of 1320 GHz.

Most millimeter and submillimeter wavelength receivers in radio astronomy use single-ended mixers and LO injection is established using an optical beam splitter or a diplexer (for example, Martin-Pupplet interferometer). Using these schemes and accounting for very low available LO power in this frequency range, the coupling of LO power should be relatively large, e.g., in case of the beam-splitter about −10 dB. This leads to the signal loss and could make a noticeable contribution to the receiver noise temperature due to the thermal noise injected into the receiver input along with LO [4]. The use of balance mixer allows us to suppress LO amplitude modulation noise, provide better LO power handling capabilities, and reject unwanted spurious responses [5]. In addition, the balanced mixer use all available LO power. There is a number of balanced mixer designs has been reported for different frequencies operation, such as 90 GHz [6], 200-300 GHz [7], and 530 GHz [8]. However, no balanced mixers were proposed for frequencies above 1 THz.

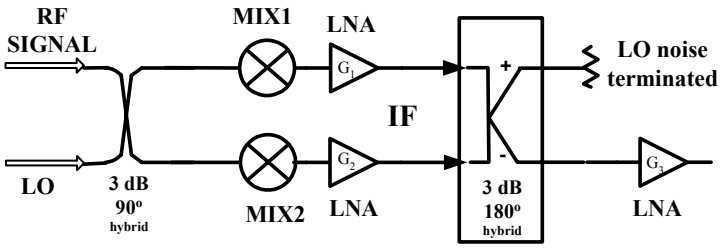

Fig. 1. Block diagram of the balanced mixer.

In the proposed design, waveguide balanced mixer is realized using a quadrature scheme shown in Fig.1. One of the key component is a 3 dB quadrature waveguide hybrid, which couples the signal and LO to the individual mixers. The mixer outputs at intermediate frequency (IF) are connected to cryogenic 2-4 GHz IF low noise amplifiers (LNA). In order to improve system noise temperature, we plan to use 50 Ω-matched inputs LNAs designed at our lab for this project (to be published elsewhere). A 180° IF hybrid combines IF outputs of the two mixers so that the IF signal appears at one output and then amplified by a cryogenic LNA (G_3). The amplitude component of the sideband LO noise is collected at the other port of the IF hybrid and terminated. Use of the LNAs before the IF hybrid improves the system noise performance significantly reducing additional noise due to insertion loss in the IF hybrid but requires 2 gain- and phase- matched amplifiers. The isolation of the balanced mixer depends on the amplitude and phase balance of the components.

II. Waveguide 90° Hybrid Design and Tolerance Requirements

A quadrature hybrid is a four port directional coupler providing LO injection and RF signal distribution between the two mixers with a 90° phase difference. In the ideal case, the incident power at the input ports of the hybrid is divided equally between the two output ports. The quadrature hybrid consists of two parallel waveguides coupled through a series of apertures or branch waveguides usually between the broad walls and approximately quarter of wavelength long. The hybrid design is compatible with the split-block technique with splitting trough the plane of symmetry at the center of broad walls of the waveguides with no surface currents flow across this plane of symmetry[9]. Furthermore, there is just a little concern about imperfect contact between the two halves.

The amplitude and phase imbalance at the outputs of the quadrature hybrid influences also on the LO injection. It is known that in order to ensure 20 dB isolation, the imbalance in the signal path has to be less than 1.7 dB or the phase imbalance should be less then 12° [4]. Part of this work is to design and fabricate a waveguide quadrature hybrid with the worst-case amplitude imbalance ≤0.5 dB and the phase imbalance ≤1° within the band of interest.

Designing a waveguide hybrid coupler for high frequency band involves a number of compromises given by fabricating constrains. To meet the required bandwidth of about 20% the central frequency, fewer sections are needed, e.g., 6 - sections layout was chosen for our coupler design. A larger number of branches would make the hybrid fabrication more difficult because the required dimensions became too small to be produced with sufficient accuracy.

Fig.2 shows drawing of the designed hybrid with 6 sections. The design variables are: the height of the branches (H_n), the spacing between branches (L_n), and the distance (K) between the main waveguides. The limit on the branch

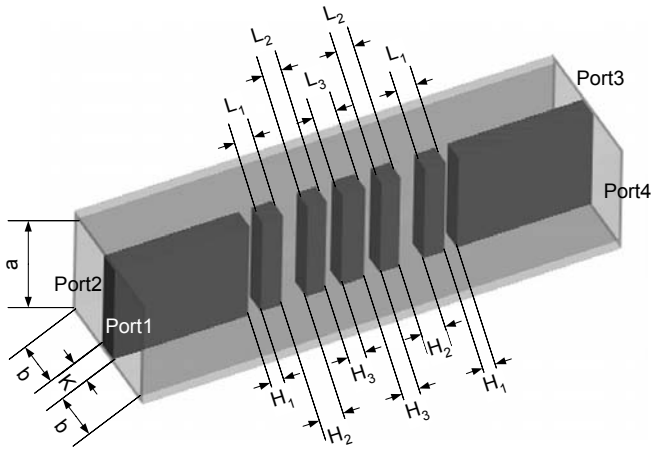

Fig. 2. Design of waveguide hybrid with a 6 branches coupler. The main waveguide height $b = a/2$ is fixed to be $b = 100$ μm.

guide height, H_n, is chosen to be 20 μm. In our design, we have kept the main waveguides at the full height ($b = a/2$) with fixed $b = 100$ μm. Therefore, for each half of split-block, the waveguide channel depth should be 100 μm. Indeed, to simplify the design and fabrication of the hybrid for THz frequencies, we might like to make all the branch lines with the same length and spacing in order to facilitate machining using, e.g., end-mill. However, to achieve maximum possible bandwidth and flat characteristics of the hybrid structure we need to follow classic ripple Chebyschev design, and vary the heights of the branch guides along with spacing between branches from section to section of the coupler.

Initially, the hybrid was simulated as a series of E-plane T-junctions, interconnected by waveguides. We employed a numerical matrix method using matrices based on the circuit theory [10], [11], [12]. For further optimization of the bandwidth, coupling and the return loss, we use High Frequency Structure Simulator (HFSS™) [13]. In Fig.3, the lines without markers show S_{21}, S_{31}, S_{11}, and S_{41} calculated by the numerical matrix analysis mentioned above. The curves of the circles, the squares, the triangles, and the inverted triangles demonstrate the S parameters obtained from HFSS™ simulations. Optimal configuration of the coupler has been achieved with the design variables as follows: K=41 μm, H_1=24 μm, H_2=46 μm, H_3=30 μm, L_1=38 μm, L_2=35 μm, L_3=42 μm. As can be seen from the Fig. 3, the matrix analysis results are well correspond to the data obtained from HFSS™ simulation. As we noted above, the amplitude and phase symmetry is critical to achieve the best possible performance of the balanced mixer. The results of HFSS™ simulations of the amplitude imbalance and the phase differences are shown in Fig.4.

Since the required manufacturing accuracy influences on a choice of a fabricating method, we studied how the manufacturing tolerances would affect the hybrid performance. For that, we varied design parameters around its optimal values and fed the changed geometry in the simulation program to obtain the S-parameters of such a hybrid. According to these simulations, the amplitude imbalance within the band of interest become worse when all structure dimensions are offset from the optimal level even as little as up to 2 microns.

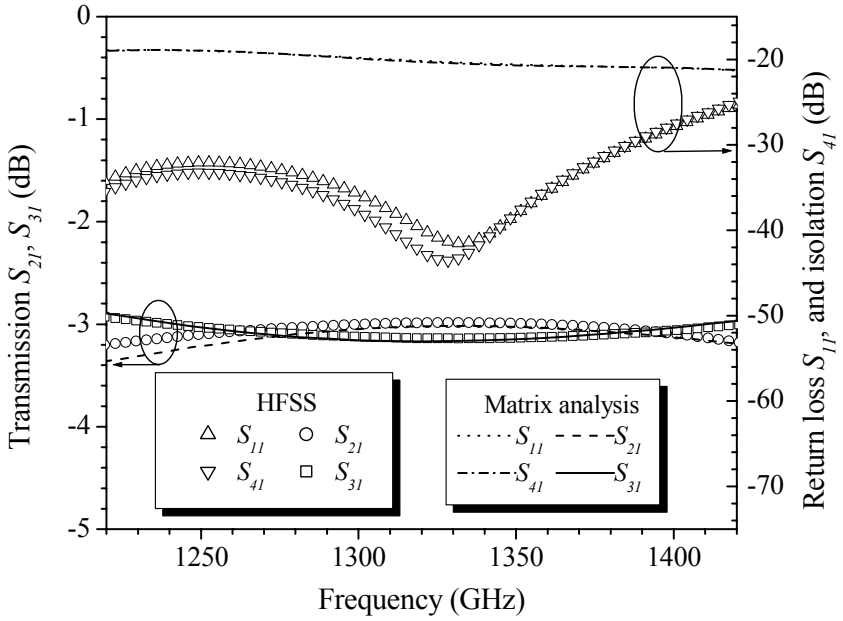

Fig. 3. Comparison of the results for magnitude of the hybrid S-parameters. Results of matrix analysis are shown by lines, results obtaining by HFSS™ simulations are demonstrated by open figures (○ – S_{21}, □ – S_{31}, Δ – S_{11}, ∇ – S_{41}).

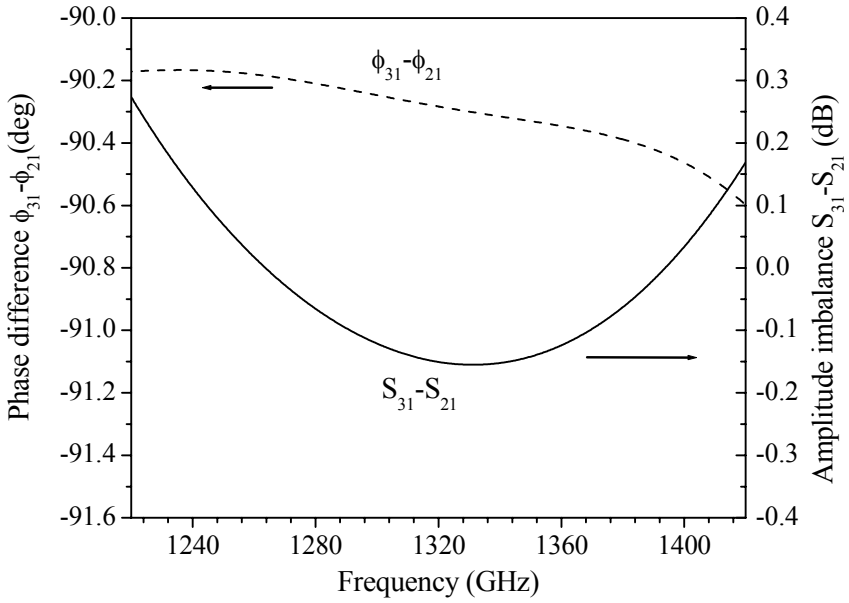

Fig. 4. HFSS™ simulated phase difference *(ϕ_{31}-ϕ_{21})* and amplitude imbalance *(S_{31}-S_{21})* of quadrature hybrid as a function of frequency.

Consequently, the machining of the mixer hybrid structure has to be done with linear dimension error less or about 1 μm in order to meet the required performance. In addition, 1.3 THz frequency operation necessitate very high surface quality in order to minimize the loss due to the waveguide wall roughness because of the skin depth is below 0.1μm at 1.3 THz. Clearly, a fine machining using end mill that was successfully used for longer wavelengths cannot be suitable for reproduction of sub-100 μm dimensions.

III. Micromachining of the Hybrid

Following the considerations above, we employed photolithography of thick photoresist combined with electroplating for fabricating of the waveguide hybrid structure. The scheme of the hybrid fabricating process is shown in Fig.5. In the processing, a 2" silicon wafer was used as a substrate. Release layer of PiRL-III [14] has been applied first at 3000 rpm spin and baked at 200°C for 5 minutes (Fig. 5a). Thick photoresist, SU8-2035 [15] has been applied afterwards. We found the subsequent spinning of the two layers at 2000 rpm with intermediate baking at 65°C for 20 minutes provides the best resist uniformity. After spinning of the second layer we applied soft baking at 65°C for 20 minutes followed by 95°C for 20 minutes. A pattern has been exposed with a contact mode i-line mask aligner with wavelengths shorter than 350 nm filtered out. Post - exposure baking at 65°C for 5 minutes and subsequently 95°C 10 minutes followed by developing in XP-SU8 developer for about 10 minutes have been carried out (Fig. 3b).

In order to get higher conductivity of the waveguide walls and to provide conductive seeding layer for the following electroplating, a 0.5 μm layer of Au, Pd or Al/Pd has been deposited by magnetron sputtering (Fig. 5c). Copper electroplating has been carried out with a *dc* power feed in proprietary solutions [16]. We have plated in two steps, first at a slow plating rate for fine gap filling, 20 μm at 0.5 A/cm^2, followed by thick plating of 500 μm at 2 A/cm^2 (Fig. 5d). After completion of the electroplating, we detached the silicon substrate by dissolving of the release layer at 60°C in an ultrasonic bath of alkaline developer (Fig. 5e).

To strip SU8 resist (Fig. 5f) we have tried Piranha (sulfuric acid + 2% of hydrogen peroxide) wet etching at 60°C and microwave plasma ashing in oxygen at 1 mbar with temperature kept below 120°C. Both methods provided reasonable results, but Piranha etching better removed resist from the narrowest gaps. Test pattern after copper plating and etching of SU8 resist is demonstrated in Fig.6.

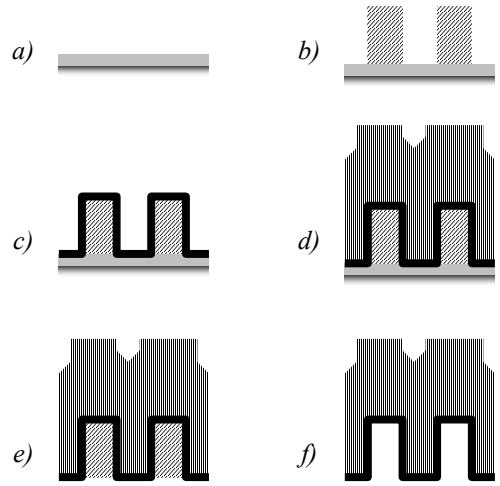

Fig. 5. Fabricating scheme of waveguide structure.

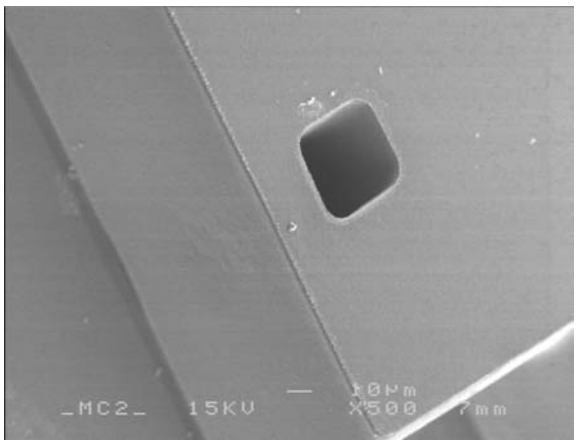

Fig. 6. SEM micrograph of produced test pattern after copper plating and stripping of SU8 resist.

Summarizing, the test pattern with characteristic dimension of 30 µm proved that the suggested technology meets the requirements on the precision for the patterned geometry and the surface quality.

IV. Initial HEB mixers layout

The heart of our balanced receiver is two phonon-cooled HEB mixers based on an thin NbN film and which are placed on separated substrates. In ideal case, the mixers has to be identical for complete rejection of LO noise contribution. Practically, DC and noise characteristic of them are wanted to be as close as possible, which can be producible by modern HEB technology.

Each of the HEB elements are planned to be integrated with RF choke filters and DC-bias and IF circuitry on individual chips of a crystalline quartz substrate of dimensions 1000 µm x67 µm x17 µm fit into suspended microstrip channel across full height waveguide of dimensions 200 µm x 100 µm. The mixer layout design is based on a previous development done for a 345 GHz sideband separation mixer [17]. The chosen "one-side" configuration of probe suspended in a full height waveguide achieves good match over a wide frequency band without reducing of waveguide height, which normally would increase resistive loss in the waveguide wall.

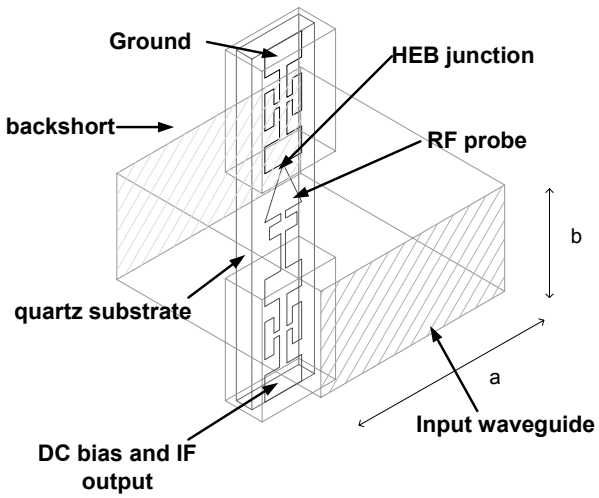

Fig. 7. Layout of the individual HEB mixer.

The central part of the individual HEB mixer layout is shown in Fig.7. It allows coupling of the input waveguide signal to the HEB junction via a radial E-type probe while having an isolated port at the opposite side of the substrate where the IF signal can be extracted and DC bias applied. The RF probe

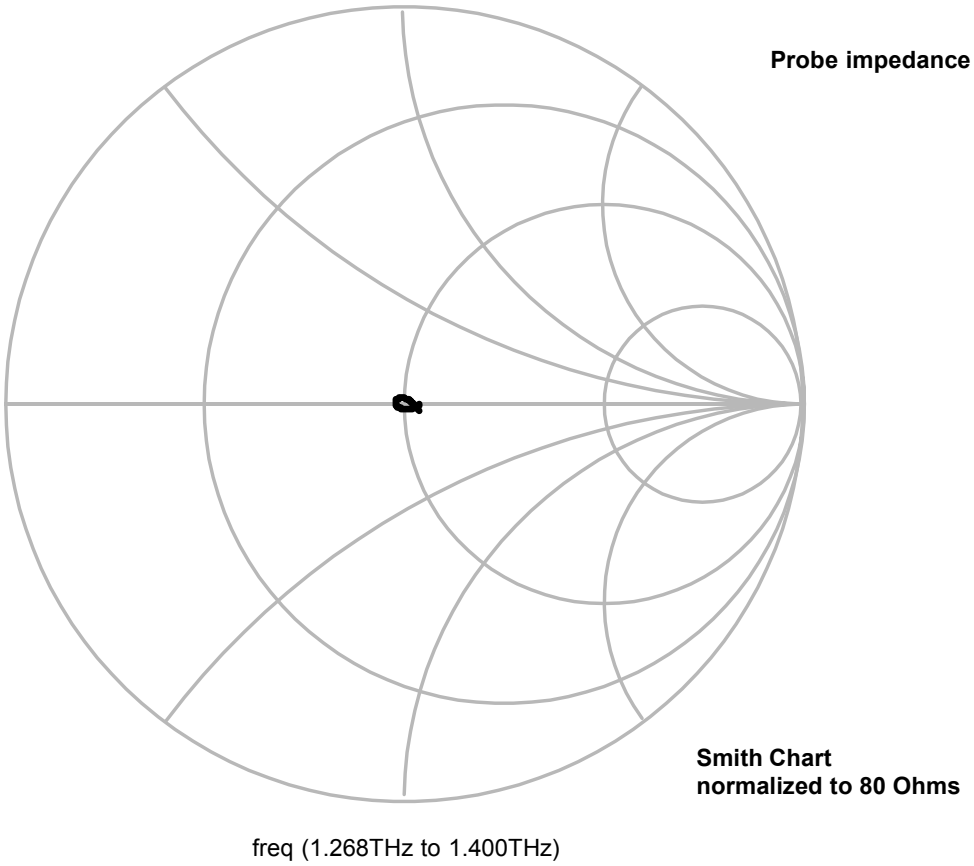

Fig. 8. The RF probe impedance at the HEB input is almost purely real of value about 80 Ohm between 1250 and 1390 GHz.

impedance at the HEB input is almost purely real according to our simulation and has a value of about 80 Ohm between 1250 and 1390 GHz as shown on the Smith chart, Fig.8. The length of the backshort section of the waveguide was chosen to provide good input match over the entire signal frequency band.

V. Summary

We have presented design for 3 dB waveguide hybrid along with initial design of individual HEB mixer layout. These results are based on detailed HFSS™ simulations. Required value of the amplitude and phase imbalance for the hybrid of 0.3 dB and 1 deg respectively have been achieved. We have successfully demonstrated processing technology suitable for the waveguide hybrid fabricating for 1.32 THz balanced heterodyne receiver.

VI. Acknowledgements

Authors would like to acknowledge Galvanord and Dr.B. Okholm for providing excellent possibilities for electroplating. Authors are thankful to Dr. A. Bogdanov for his idea of using SU8 thick photoresist for

micromachining of the hybrid. This work is part of APEX Project and is supported by Swedish Research Council and Wallenberg Foundation by their respective grants.

VII. References

[1]. J. Black, "Scientific drivers for APEX," presented on Masers and Molecules workshop, Sept. 18-19, 2003, Särö, Sweden.
[2]. APEX project at http://www.mpifr-bonn.mpg.de/div/mm/apex.html.
[3]. S. Paine, R.Blundell, D.C. Papa, J. Barrett and S.Radford A Fourier Transform Spectrometer for Measurement of Atmospheric Transmission at Submillimeter *Wavelengths Publication of the Astronomical Society of the Pacific*, vol. 112, pp. 108-118, 2000 January.
[4]. A. R. Kerr and S.-K. Pan, "Design of planar image separating and balanced SIS mixers," *Proc. Seventh Int. Symp. Space Terahertz Technolog*y, Charlottesville, VA, Mar. 12–14, 1996, pp. 207–219.
[5]. S. A. Maas, Microwave Mixers, 2nd edition. Boston, MA: Artech House,1993.
[6]. K. D. Stephan, N. Camilleri, and T. Itoh, "A quasioptical polarization-duplexed balanced mixer for millimeter wave applications," *IEEE Trans. Microwave Theor*y, vol. MTT-31, no. 2, pp. 164–170, Feb. 1983.
[7]. A. R. Kerr, S.-K. Pan, and H. G. LeDuc, "An integrated sideband-separating SIS mixer for 200-280 GHz," Proceedings of the Ninth International Symposium on Space Terahertz, Technology, pp. 215-221, 17-19 March 1998.
[8]. G. Chattopadhyay, F. Rice, D. Miller, H.G. LeDuc, and J. Zmuidzinas,"A 530-GHz Balanced Mixer," *IEEE Microwave and Guided Wave Lett*., vol. 9, no. 11, pp.467-469, Nov. 1999.
[9]. G. Matthaei, L. Young and E.M.T. Jones, (Reprint of the edition published by McGraw-Hill Book Company, Inc., 1951) Microwave Filters, Impedance-matching Networks, and Coupling Structures, Artech House, Inc. (1980) pp.775-842. (Reprint of the edition published by McGraw-Hill Book Company, Inc., 1964).
[10]. Hiroya Andoh, Shinichiro Asayama, Hideo Ogawa, et al., "Numerical matrix analysis for performances of wideband 100GHz branch-line couplers," *Int. Jour. of Infr. and Mill. Waves,* Vol. 24, No. 5, pp. 773-788, May 2003.
[11]. Reed J., "The multiple branch waveguide coupler*," IRE Trans.,* PGMTT-6, pp.398-403, October 1958.
[12]. N. Marcuvitz, *Waveguide Handboo*k, New York: McGraw Hill, 1951.
[13]. Agilent Technologies, 395 Page Mill Road, Palo Alto, CA 94304 USA.
[14]. Brewer Science, Inc., Specialty Materials Division 2401 Brewer Drive, Rolla, Missouri 65401 USA.
[15]. MicroChem Corp., 1254 Chestnut Street, Newton, MA 02464 USA.
[16]. Galvanord Galvano & PSB Teknik, Bybjergvej 7, DK-3060,Espergærde, Denmark.
[17]. Risacher et al., " Design of a 345 GHz Sideband Separation SIS mixer", 3rd ESA Workshop on Millimeter Wave Technology and Applications", May 2003, MilliLab, Espoo, WPP-212, pp. 629-623.

New Results on Bistability Effects in HEB Devices

Dazhen Gu, Yan Zhuang, Sigfrid Yngvesson
Department of Electrical and Computer Engineering, University of Massachusetts, Amherst, MA 01003

The Hot Electron Bolometric (HEB) mixer, employing NbN superconducting material, has been widely used as the terahertz (THz) receiver [1][2][3]. The essential part of the HEB device is a thin NbN film which is a fraction of a μm long and a few μm wide. Several models have been developed to predict its performance in the THz frequency range. The hot spot model, based on nonlinear heat transfer and self-heating, is the most popular theory and is the one that best fits the experimental results.

The operating condition for an HEB device is normally at liquid Helium temperature, which allows the NbN material to work as a superconductor. At some specific DC bias conditions, a hot spot is sustained by *Joule* heating, which is sufficient to raise the temperature above T_C, i.e. the critical temperature of superconductor. The rest of the NbN micro strip is still superconducting. This phenomenon can be explained by the heat balance equation holding at more than one temperature. Due to an external perturbation, the hot spot can recover to the superconducting state or vice versa. The device is thus *bistable* state. To understand the details of this mechanism will improve the hot spot model, since the optimal HEB device operating point for the mixer is just in this region.

1. Steady Hot Spot in a Superconduting Strip

The non-uniform thermal structure in a superconducting strip could be described as a hot region (hot spot), where electrons become normal, and a cold region, where they maintain their superconductivity. The heat balance equations for this strip can be represented as:

$$-\frac{\partial}{\partial x}\left(K_N \cdot \frac{\partial T}{\partial x}\right) + q = Q \qquad x<x<x_0, \text{ (normal region)} \quad \text{(1a)},$$

$$-\frac{\partial}{\partial x}\left(K_S \cdot \frac{\partial T}{\partial x}\right) + q = 0 \qquad x_0<x<L/2, \text{ (superconducting region)} \ \text{(1b)}.$$

Here, we assume a device of length L, width W, and thickness d with a normal region of length $2x_0$ and resistivity ρ_N. Q is the power of the *Joule* heating, q is the specific power due to heat transfer to a cold bath. K_N and K_S are the thermal conductivity in the normal region and superconducting regions respectively, which are assumed identical, equal to K and estimated from the resistivity by the *Wiedemann-Franz Law*:

$$K \cdot \rho_N = \frac{\pi^2}{3}\left(\frac{k_B}{e}\right)^2 \cdot T \qquad (2).$$

Solving Equation (1), we'll have an analytical solution for the non-uniform temperature distribution. A more rigorous approach has been applied by H. Merkel [4], who included the Andreev Reflection and localized device parameters in Equation (1).

2. A Dynamic Hot Spot in Superconducting Strip

Starting with the time-independent heat balance Equations (1a) and 1 (b), we can rewrite these including a time-dependence:

$$C\frac{\partial T}{\partial t} = \frac{\partial}{\partial x}\left(K\frac{\partial T}{\partial x}\right) + Q - q \quad (3),$$

where C is the heat capacity of the superconductor per unit volume. In a general case, the temperature-dependent Q and q are plotted in Figure 1. Self-heating in a superconductor has three parts: (1) when the temperature is lower than the effective critical temperature T_{Ceff} (obtained from the *Ginsburg-Landau* relation), there is no heating power, $Q=0$; (2) when the temperature is higher than T_C, the superconductor becomes totally normal, $Q=J^2\rho_N$. (3) when the temperature is in the range of (T_{Ceff}, T_C), $Q=J^2\rho_N(T-T_{Ceff})/(T_C-T_{Ceff})$. Here, J is the current density in the region of interest.

The uniform central temperature is determined by $Q=q$, since the values of $\partial T/\partial t$ and $\partial T/\partial z$ are both zero near the center. In other words, the current should be high enough to elevate curve Q to intersect with curve q, as shown in Figure 2. Of the two intersections (at T_1 and T_2), only T_2 is stable against small perturbations. Let's consider two cases for state 2: (1) if it is perturbed by a small increase in temperature, the cooling curve q will exceed the heating curve Q, and make the temperature fall back to T_2; (2) on the other hand, if it is perturbed by a small decrease in temperature, the heating curve Q will exceed the cooling curve q, and make temperature go up to T_2. As for state 1, a small increase in temperature will lead to temperature elevation to T_2 and a small decrease in temperature will cause the temperature to fall to T_b. Thus, for a stable normal zone, its central temperature must be at T_2.

Consider the domain wall (i.e. the transition region at the edge of the hotspot where the temperature goes from T_1 to T_2) propagating as: $z = x + v\cdot t$, substitute this into Equation (3), which yields:

$$-vC\frac{dT}{dz} + \frac{d}{dz}\left[K\left(\frac{dT}{dz}\right)\right] + Q - q = 0 \quad (4).$$

To derive the minimum propagating current I_p, set $v=0$ in Equation (4), then follow the same algebraic steps as in Reference [5]. We obtain the well-known equal-areas theorem for I_p:

$$\int_{T_b}^{T_2}(Q-q)dT = 0 \quad (5),$$

i.e., the two hatched areas in Figure 3 should be equal under the condition of minimum domain propagation.

When the current lies beyond (or below) the minimum propagating current I_p, the hot spot grows (or shrinks) due to more (or less) self-heating than heat transfer. Under the constant current bias condition, the propagating velocity is constant and the temperature profile at the edges of the hot spot does not change its shape with time. To calculate this velocity, we employ equation (4), using the heat flux, which is defined as $s=K(dT/dx)$:

$$-vCs + s\left(\frac{ds}{dT}\right) + K(Q-q) = 0 \quad (6).$$

To avoid the complexity of solving this equation, we make the following approximations: (1) replacing the three-part curve for Q by a two-part step function curve: $g(\Delta T)=\rho_N\cdot J^2$ for $\Delta T<(T_C+T_{Ceff})/2-T_b$ and $g(\Delta T)=0$ for $\Delta T>(T_C+T_{Ceff})/2-T_b$; (2) using *Newton*'s law of cooling $q=h\cdot\Delta T/d=h\cdot(T-T_b)/d$, where we ignore

the nonlinear case; (3) assuming K is temperature independent. The approximate analytical solution of the velocity is given by:

$$v = v_* \frac{C_0 - 1}{2\sqrt{\alpha}\sqrt{C_0}} \quad (7),$$

where, v_* is the characteristic thermal velocity: $v_* = \frac{2J_c}{C}\sqrt{\frac{K\rho_N}{\Delta T_c}}$; α is the so called *Stekly* number $\alpha = \frac{\rho_N J_c^2 d}{h\Delta T_c}$, which characterize the relative role of *Joule* self-heating in the superconductor; C_0 is a function dependent of the current density as: $C_0 = \frac{\alpha i^2 - (1 - i/2)}{1 - i/2}$, with normalized current density: $i=J/J_C$. The plots of the normalized velocity and the normalized current are shown in Figure 3.

3. Experimental Setup

The whole experimental setup for recording the device behavior is shown in Figure 4. The device is mounted on a circuit board in an Aluminum box. We bias the device through a low pass filter by a very low resistance voltage source. The box is immersed into Liquid Helium and is connected to two coaxial cables housed in a stainless steel tube.

With the aid of an oscilloscope, which has an upper limit of 1 GHz, we detect the voltage response from two SMA connectors on the box. One is the voltage across the reference resistor, which can be converted to the current through the device. The other is the total voltage across the device and the reference resistor.

Another experimental setup is employed for the domain velocity measurement. A pulse generator, paralell with the DC bias box, is added to drive the device from the superconduting state to the normal state, and vice versa. We also include a resistor with several hundred ohms between the bias box and device box . This resistor will enable us to measure the voltage and current waveform of the device more accurately.

4. Measurements on NbN Films

The devices used for instability measurements are NbN strips with several different lengths and widths, which are fabricated by standard UV lithography.

4.1 Self Sustained Oscillation

Figure 5(a) and 5(b) show the oscillations from a voltage-biased device with dimensions 1X2μm^2 at different bias points. At this point, we removed the reference resistor from the Aluminum box to check the pure voltage response of the device.

In the beginning, at the lower bias voltages, the oscillation response is similar to that in Figure 5(a). Besides the fast 25 MHz relaxation oscillation, there is another slow oscillation modulating on it, which we will call the slow repetition frequency. It separates the whole response into two parts: (1) the upper level oscillation, which means that the device is mainly “hot” and exhibits a voltage value; (2) the lower level

oscillation, which means that the device is mainly "cold" and the average voltage is zero. When we increase the bias voltage, the repetition frequency also increases, in other words, the adjacent upper levels become closer. However, the 25 MHz relaxation oscillation doesn't change with the bias.

The repetition frequency was also observed in other work, for example in [6] and in [7,8]. It can be shown [6,8] that this frequency depends on the inductance in series with the device, as well as the bias voltage, in quantitative agreement with experiment.

The voltage response of device, biased at some ***high*** voltage point, is shown in Figure 5(b), where the lower level oscillation disappears. We interpret the variation of the device voltage as being due to the (normal) hotspot varying periodically in size. The thermal domain (hot spot) in the device will propagate from infinitesimal to some finite length. Further increase of the bias voltage will only increase the amplitude of the oscillation, which corresponds to the maximum length of the domain.

We then I added the 20Ω reference resistor to investigate both the voltage and current response, which are shown in Figure 6(a). Both voltage and current show the 25MHz relaxation oscillation. However, no matter where the bias is set, we can't find the simple sinusoidal relaxation oscillation from this measurement setup. Our interpretation of this is that the reference resistance stabilizes the device, as was also observed in [7,8]. By switching the 20Ω resistor to a 5Ω resistor, we obtain the pure oscillation again, shown for both current and voltage in Figure 6(b).

We repeated the measurements on several different devices both on silicon substrate and on MgO substrate. From the results listed in Table 1 the 25 MHz relaxation oscillation seems to be an intrinsic property of the NbN film, independent of the device dimension and the device wafer. This oscillation nevertheless seems sensitive to the exact experimental setup, since in earlier measurements in a slightly different experimental arrangement we measured this frequency as about 5 MHz [7,8].

4.2 Fly-out Measurements

In this section, we describe a measurement to investigate the hot spot domain expansion, which we call "fly-out". The experimental setup is shown in Figure 4. There is a resistor of several hundred ohms in series with the device. The device has a second stable state at higher voltage and lower current, shown in Figure 7.

We bias the device is at 745μA, which is close to its critical current, and then apply a positive pulse to drive the device to its normal state, which will stimulate a hot spot domain in the device. The positive pulse has a small amplitude and short duration, which won't have any effect on the device after this short time. After the domain wall has expanded to its equilibrium state, a negative pulse makes the device go back to its superconducting state. With the aid of the oscilloscope, we record both the device voltage and reference voltage, which can be converted to the device current. Figure 8 shows the voltage and current waveforms. The device shifts repeatedly between superconducting and normal state under double pulses.

To prove that the response shown in Figure 8 is an intrinsic device property, we also measured the voltage waveform on a dummy resistor under the same pulse, shown in Figure 9. Comparing the responses

of the device and the resistor, we can confidently claim that the device responds to the pulse much more slowly, due to the hot spot domain wall propagation.

During the domain wall expansion, we assume that the hot spot resistivity is constant, which is equal to the resistivity of device in the low temperature normal state: $\rho = R_N \frac{A}{L}$ (8),

where A and L are device cross section area and length respectively, and R_N is the full device normal resistance at low temperature. Then the device resistance is proportional to its hot spot length. Thus the velocity of the domain expansion can be obtained by:

$$v = \frac{1}{2}\frac{dl_{domain}}{dt} = \frac{1}{2}\frac{d\left(R \cdot A/\rho_N\right)}{dt} = \frac{1}{2}\frac{L}{R_N}\frac{dV}{dt}\frac{1}{I} \quad (9).$$

Here, the factor 2 represents the fact that two domain walls are involved in the propagation. As the domain expands, the current shows small oscillations around a constant value. By varying this average current we can plot v as a function of I, or normalized v versus normalized I.

4.3 Fly-back Measurements

Besides fly-out measurements, we designed another measurement setup for testing the domain as its size was shrinking. Now we applied a DC bias to the device to set its current slightly smaller than the domain wall minimum propagation current I_p. Two pulses were then applied. The first pulse was about 0.3μs long and had large amplitude to stimulate a hot spot in the device. The second pulse resulted in a total current value slightly larger than I_p and was applied to the device with much longer duration to let the device be stable in the normal state. Following the second pulse, the hot spot domain is predicted to shrink by itself. We could observe the voltage waveform decreasing linearly until it reached zero, while the current stayed at an intermediate value for a short duration. We believe that this intermediate current is equal to I_p. The waveforms are shown in Figure 10. Because of this constant current level, we can't follow the same method for calculating the domain velocity as we do in the case of the fly-out.

From the recording of the voltage waveform, we can obtain the relaxation time τ of the domain wall shrinking under different DC bias. This relaxation time is found to be independent of the amplitude and width of the second pulse. However, it is dependent on the DC bias current. This agrees with the measurements by *Freytag* and *Huebener* [9], who made similar measurements on Sn film We assume that the current in the device is equal to the DC bias current after the second pulse. Thus we can approximately calculate the fly-back velocity as: $v(I_{DC}) = \frac{L}{\tau}$.

5. Discussion of Experimental Results

In order to fit the experimental velocity with the theoretical *v-i* curve (Figure 3), we need to obtain the characteristic thermal velocity v_* and the *Stekly* number α for this particular device. The calculated thermal velocity for this device is v_*=107m/s, and the *Stekly* number is α=36. By fitting the fly-out velocity shown in Figure 8, we find that the *Stekly* number is 13 for the best least square fit. This discrepancy may come from the measurements on critical current and the estimation of film thickness.

The experimental data agree well with the prediction based on Eq. (7) if we multiply the experimental resuls by a factor of 10, and normalize them to v_*. This big discrepancy may come from the thermal conductivity K of NbN film even after including the *Andreev* Reflection effect. This value is strongly related to the film thickness, substrate type and cryogenic condition. A more likely explanation is that the theory in [5] assumes a quasi-steady state in which the domain propagates at a constant velocity. The actual conditions are likely a good deal more nonlinear, which could slow the propagation of the domain [9].

On the other hand, we get some reasonable results from Figure 11. First, the minimum propagation current can be calculated from the plot by interpolating the curve: $0.347*I_C \approx 300\mu A$. This is very close to the result of the fly-back measurements, i.e., the constant current level in Figure 10. Secondly, the fly-back velocity grows much faster than the fly-out velocity, as the current deviates from I_p, based on the experimental results, which agrees with the theory very well. Third, the value of the AR factor α_{th} (from the best fitting curve) is very close to the theoretical value at 4K from theoretical value. Finally, if we calculate the relaxation oscillation frequency from the same domain velocity model, we obtain order-of-magnitude agreement; this oscillation is also *slower,* but by a factor of about 6 compared with the model. As a conclusion, the domain wall propagation model predicts the trend of the velocity curve very well, and the order-of-magnitude of the relaxation frequency. The maximum amplitude of the oscillation is also always less or equal to that obtained from a domain which fully fills the device length. To improve the agreement between theory and experiment, we have to put more emphasis on estimating accurate parameters for the device, such as thermal conductivity, heat transfer coefficient and device dimension. We also need to explore a more realistic nonlinear model for the domain dynamics.

Reference:

[1] E. Gerecht et al, Proc. 14th Intl. Symp. Space Terahertz Technology, Tucson, USA, April 2003.
[2] S. Cherednichenko, et al, Proc. of the Symp. on Astronomical Telescopes and Instrumentation, SPIE, Hawaii, USA, August 2002.
[3] D. J. Benford et al, Proc. 14th Intl. Symp. Space Terahertz Technology, Tucson, AZ, April 2003.
[4] H. Merkel, Proc. 13th Intl. Symp. Space Terahertz Technology, Cambridge, USA, April 2002.
[5] L. Dresner, "Stability of Superconductors", Plenum Press, NY, 1995.
[6] V. N. Skokov, Technical Physics Journal, 40, 562-565, 1995.
[7] Y. Zhuang et al, Proc. 14th Intern. Symp. Space THz Technology, Tucson, AZ, Apr. 2003.
[8] Y. Zhuang, PhD Thesis, UMass Amherst, 2002.
[9] L. Freytag and R. P. Huebener, J. Low Temp. Phys. 60 (1985) 377.
[10] H. Merkel, private communication.

Table 1: Relaxation oscillation frequency for different devices.

Substrate	Silicon						MgO	
Dimension (μm^2)	1X2	4X2	5X2	10X2	5X5	10X5	4X2	5X5
Frequency (MHz)	25.5	25.5	24.9	25.5	26.8	25.9	26.8	26.8

Figures

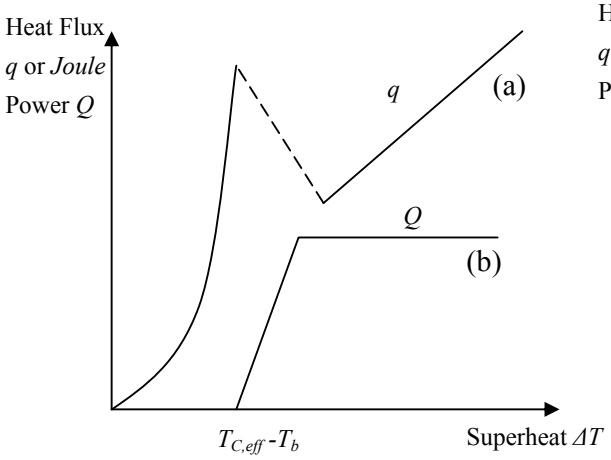

Figure 1: The steady state boiling heat flux with the three-part curve of *Joule* power.

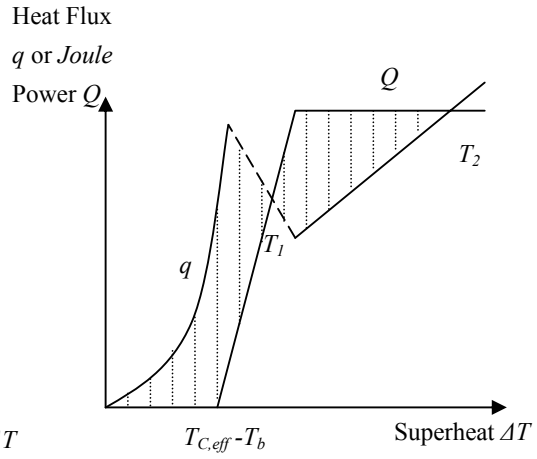

Figure 2: The steady state boiling heat flux intersects the three-part curve of *Joule* power. The equality of the two hatched region determines I_p.

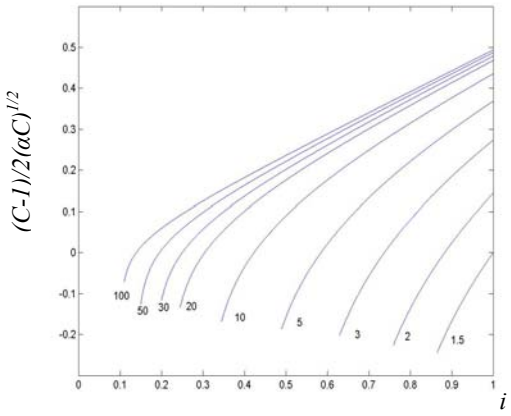

Figure 3: Normalized velocity versus normalized current under different *Stekley* number.

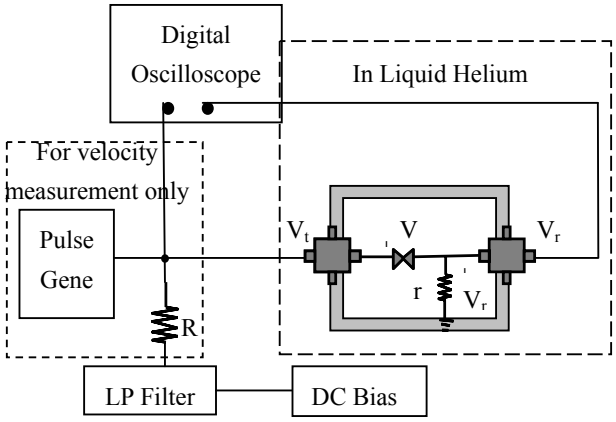

Figure 4: Experimental setup for the instability oscillation / (domain velocity) measurement.

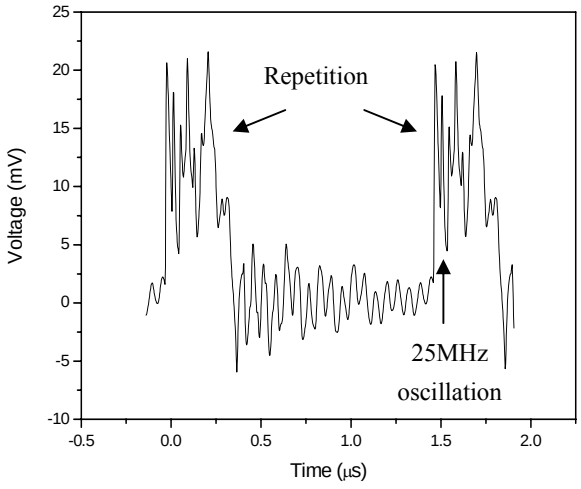

(a) Bias at 3.3 mV, 121μA.

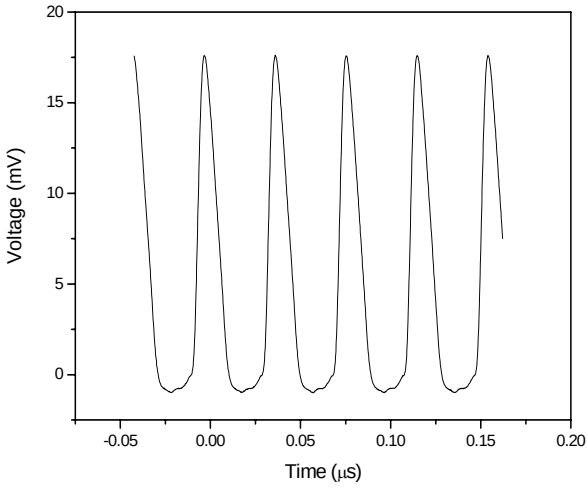

(b) Bias at 4.7 mV, 125μA.

Figure 5: Voltage waveform of one device (1X2μm^2) in unstable region without reference resistor.

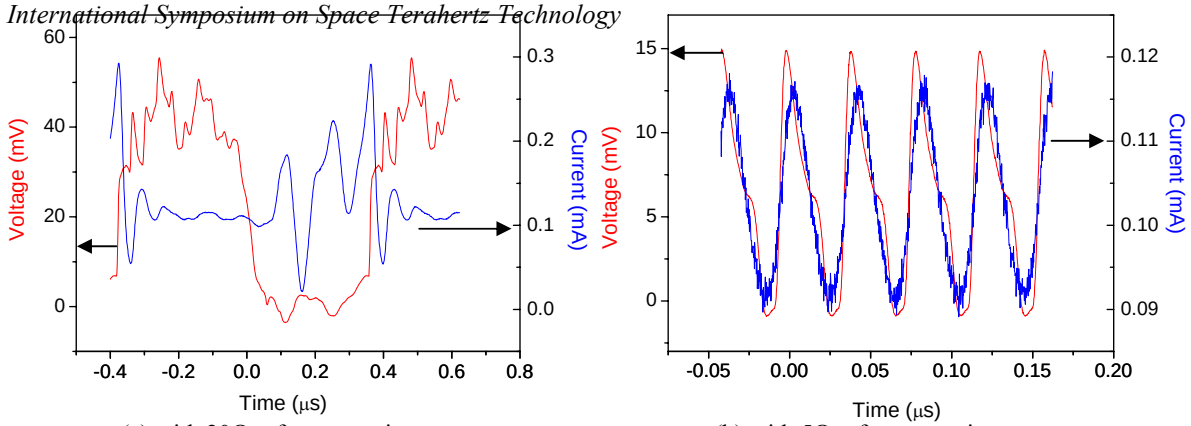

(a) with 20Ω reference resistor. (b) with 5Ω reference resistor.

Figure 6: Voltage and current waveforms of NbN device in unstable region with measurement setup in Figure 4.

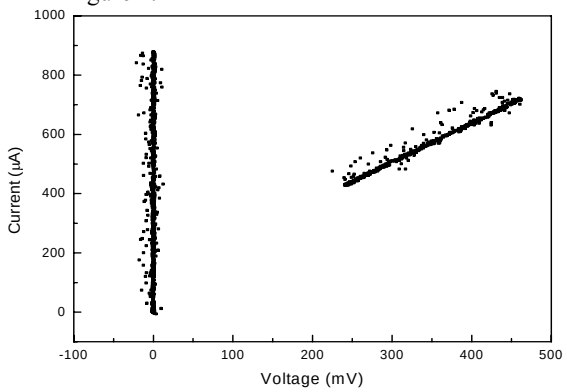

Figure 7: IV curve of the 5μm long device.

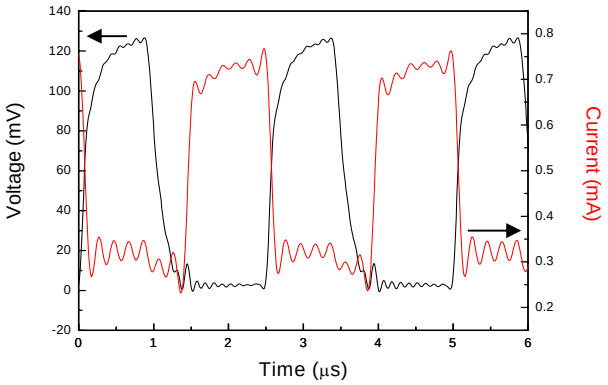

Figure 8: Voltage and Current response of device 5μm long device under double pulses.

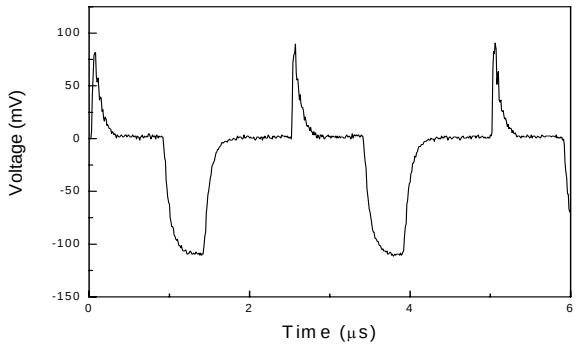

Figure 9: Voltage response of a dummy resistor under double pulses.

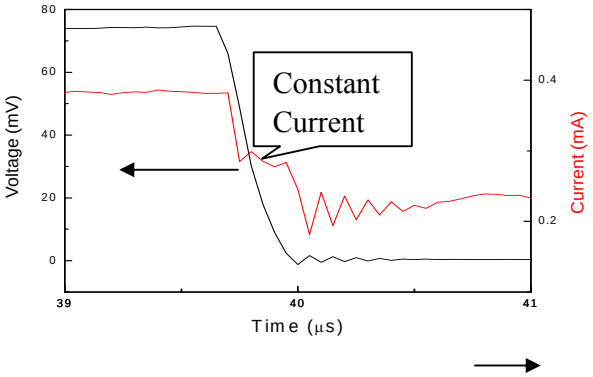

Figure 10: Voltage and current waveform in the fly back measurement 5μm long device.

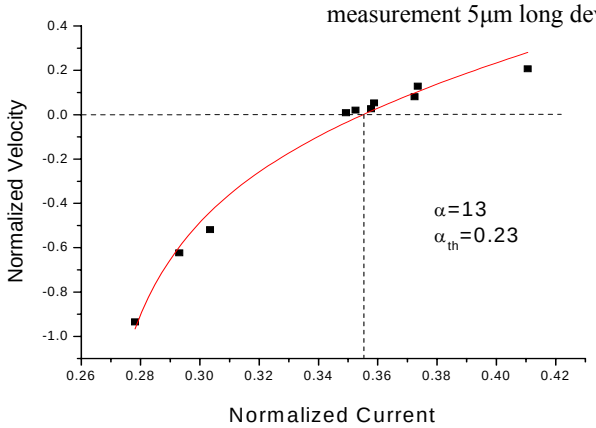

Figure 11:Comparison between the theory and the experimental results on fly-out and fly-back measurements for 5μm long device.

Bandwidth Measurements on HEB Mixers at Terahertz Frequencies Using Sideband Generators as well as Two Lasers

F. Rodriguez-Morales, K.S. Yngvesson, E. Gerecht, J. Nicholson, J. Waldman, T. Goyette, D. Gu, X. Zhao, and R. Zannoni
Department of Electrical and Computer Engineering, University of Massachusetts at Amherst, Amherst, MA 01003; yngvesson@ecs.umass.edu

ABSTRACT

Accurate characterization of the mixer conversion gain bandwidth in NbN Hot Electron Bolometer (HEB) mixers requires the use of at least one tunable source in the terahertz frequency range.

In this paper we present recent results obtained from such characterization. The measurements are performed using two types of tunable sources. In one case a variable microwave source is mixed with a fixed laser source to produce tunable sidebands, whereas two cavity-tuned FIR gas lasers are used in the second case.

The bandwidth characterization with the sideband generator is carried out over a 1-8 GHz IF band using quasi-optical coupling for the terahertz radiation and a single wide-band MMIC chip as the IF amplifier. Figure 1 shows some preliminary experimental results from measurements performed in this fashion.

On the other hand, the conversion gain at low IF frequencies up to about 10 MHz is measured using the two-laser approach.

The experimental results of both sets of measurements are used for comparison with those obtained from the standard model.

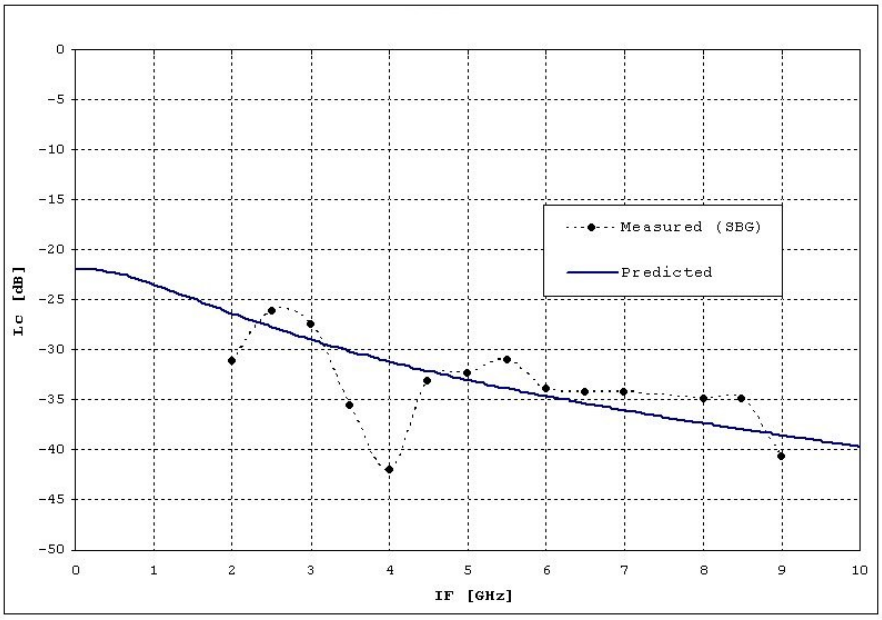

Figure 1. Measured and predicted mixer conversion gain vs. IF frequency

Ultimate Performance of a Cold-Electron Bolometer with Strong Electrothermal Feedback

Leonid Kuzmin
Chalmers University of Technology, Department of Microtechnology and Nanoscience 41296 Gothenburg, Sweden

ABSTRACT

A novel concept of the Cold-Electron Bolometer (CEB) with strong electrothermal feedback has been proposed. The concept is based on ***direct electron cooling*** of the absorber that serves as negative electrothermal feedback for incoming signal. This feedback is analogous to TES (transition-edge sensor) but additional dc heating is replaced by deep electron cooling to minimum temperature. It could mean a principle breakthrough in realization of supersensitive detectors. Noise properties are considerably improved by decreasing the electron temperature. The loop gain of electrothermal feedback could exceed 1000. The response time is reduced by electrothermal feedback to 10ns in comparison with the intrinsic e-ph time constant of 10μs.

The CEB gives opportunity to increase dynamic range by removing all incoming power from supersensitive absorber to the next stage of readout system (SQUID) with higher dynamic range. Saturation problems are not so severe for CEB as for TES: after exceeding the cooling power there is only slight deviation from linear dependence for voltage response. The full saturation comes at the level of 100pW when temperature of absorber achieves Tc of Al. Ultimate performance of the CEB is determined by shot noise of the signal readout. For background load P_0 =10fW and quantization level T_e= 50mK, the limit NEP is equal to 10^{-19}W/Hz$^{1/2}$. The estimations show that it is realistic to achieve ultimate NEP at 100 mK with SQUID readout system and NEP=10^{-18}W/Hz$^{1/2}$ at 300mK for background load of 10fW. Applicability of the CEB to post-Herschel missions looks very promising.

INTRODUCTION

As it has been recognized by Science [1], the Breakthrough of the Year has been ***"Illuminating the Dark Universe".*** The portraits of the earliest universe made in microwaves by the Wilkinson Microwave Anisotropy Probe confirm that the Universe is made up largely of mysterious ***dark energy and dark matter.*** To understand the nature of them, the future cosmology needs to get a more detailed picture of the **cosmic microwave background**. The proposed NASA missions SPIRIT, SPECS, and SAFIR will determine the highest level of requirements for bolometers in nearest future.

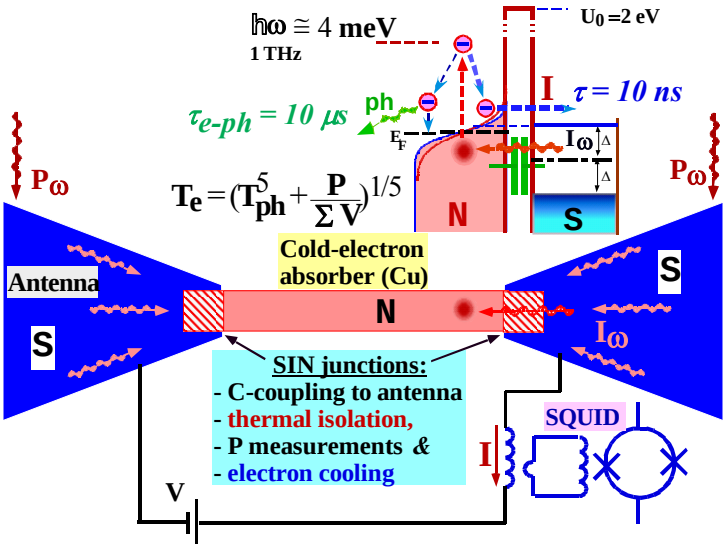

Fig. 1. Capacitively coupled Cold-Electron Bolometer with SIN tunnel junctions for direct electron cooling and power measurements. The signal power is supplied to sensor through capacitance of tunnel junctions, dissipated in cold-electron absorber, and removed back from the absorber as hot electrons by the same SIN junctions. The electron cooling serves as strong negative electrothermal feedback improving all characteristics of the CEB (time constant, responsivity) and NEP.

The detector goal is to provide **noise equivalent power down to 10^{-20} W/Hz$^{1/2}$** [2] over the 40 – 500 μm wavelength range in a **100x100 pixel detector array** with low power dissipation array readout electronics. ***No one existing technology could satisfy these requirements.*** Technological breakthrough should be done, first of all, to approach these requirements. The analysis shows that the proposed concept of ultimate CEB with strong electrothermal feedback has a real chance to become a leading concept in this development.

Decisive step in development of superconducting detectors has been innovation of a TES with strong electrothermal feedback [3,4]. However, the TES has some problems with excess noise, saturation, and the most

with artificial overheating by dc power for the feedback. This additional heating kills all efforts on deep cooling and does not give good perspectives for realization of limit performance of the bolometer. In contrast to this overheating, the principle new concept of a "***Cold-Electron" Bolometer (CEB)*** with direct electron cooling has been proposed by Kuzmin et al. [5-8]. The CEB is the only concept suggesting removing incoming background power from supersensitive region of absorber. The CEB avoids the main problem of TES, an *additional dc heating* for the electrothermal feedback, and replace it with *the direct electron cooling* of the absorber that could be a *turning point* in realization of modern supersensitive detectors. This cooling could be especially important for the realization of high sensitivity in presence of the realistic background power load. It could help to avoid full saturation when signal exceeds the level of dc bias power that is the great problem for the TES. The CEB could give a high dynamic range in combination with SQUID readout system having high dynamic range in closed-loop operation. All power of the signal is used for measurements. Possible objection that tunneling of electrons would increase shot noise is rejected by simple argument: if power is not removed by tunnel junctions, the same type of shot noise will be created by phonons through increased electron-phonon interaction.

Comparison of CEB and TES

The operation of CEB can be analyzed using heat balance equation [7,8]:

$$P_c(V, T_e, T_{ph}) + \Sigma\Lambda\,(T_e^5 - T_{ph}^5) + C_\Lambda \frac{dT}{dt} = P_0 + \delta P(t) \tag{1}$$

Here, $\Sigma\Lambda(T_e^5 - T_{ph}^5)$ is the heat flow from electron to the phonon subsystems in the normal metal, Σ is a material constant, Λ - a volume of the absorber, T_e and T_{ph} are, respectively, the electron and phonon temperatures of the absorber; $P_{cool}(V, T_e, T_{ph})$ is cooling power of the SIN tunnel junctions; $C_v = \gamma T_e$ is the specific heat capacity of the normal metal; and $P(t)$ is the incoming rf power. We can separate Eq. (1) into the time independent term, $\Sigma\Lambda(T_{e0}^5 - T_{ph}^5) + P_{cool\,0}(V, T_{e0}, T_{ph}) = P_0$, and time dependent: $(\partial P_{cool}/\partial T + 5\Sigma\Lambda T_e^4 + i\omega C_\Lambda)\delta T = \delta P$

The first term, $G_{cool} = \partial P_{cool}/\partial T$, is the cooling thermal conductance of the SIN junction that gives the negative electrothermal feedback (ETF); when it is large, it reduces the temperature response δT because cooling power, P_{cool}, compensates the change of signal power in the bolometer. The second, $G_{e-ph} = 5\Sigma\Lambda T_e^4$, is electron-phonon thermal conductance of the absorber. From Eq. (2) we define an effective complex thermal conductance which controls the temperature response of CEB to the incident signal power

$$G_{eff} = G_{cool} + G_{e-ph} + i\omega C_\Lambda \tag{2}$$

In analogy with TES [3,4], the effective thermal conductance of the CEB is increased by the effect of electron cooling (negative ETF). The current resposivity is given by

$$S_i = \frac{\partial I}{\partial P} = \frac{\partial I / \partial T}{G_{cool} + G_{e-ph} + i\omega C_\Lambda} = \frac{\partial I / \partial T}{G_{cool}} \frac{L}{(L+1)\left[1 + i\omega\tau\right]}, \tag{3}$$

where

$$L = G_{cool}/G_{e-ph} >> 1 \quad \text{is ETF gain and} \quad \tau = C_\Lambda/G_{e-ph} = \tau_0/(L+1) \tag{4}$$

is an effective time constant, $\tau_0 = C_\Lambda/G_{e-ph}$ ($\cong 10\mu s$ at 100 mK).

The principle of operation of CEB and TES in voltage-biased mode is shown in Fig. 2 and 3. The TES is heated to Tc by dc power P_{bias}. This temperature is supported during all range of operation (before saturation) due to electrothermal feedback. The principle of operation of the CEB is approximately the same but moving to another bias point in temperature: to absolute zero. Starting from the phonon temperature T_{ph}=100 mK, the cooling conductance, G_{cool}, decrease the electron temperature to the possible minimum level. Dependence of output power on signal power is shown in Fig. 3. For both concepts Pout is nearly equal to incoming power in the range of dc heating power (TES) and typical cooling power (CEB). Accuracy of removing (CEB) or compensation (TES) of incoming power is determined by the strength of the electrothermal feedback - loop gain L.

For TES, the L is determined by nonlinearity of R(T) dependence and could exceed 1000. For CEB, the L is determined as relation of thermal conductances (5). Typical dependence of L on incoming power is shown in Fig. 4. The saturation problem is very serious for TES: P_{sat} is exactly equal to applied dc heating power P_{bias} (Fig. 3). After

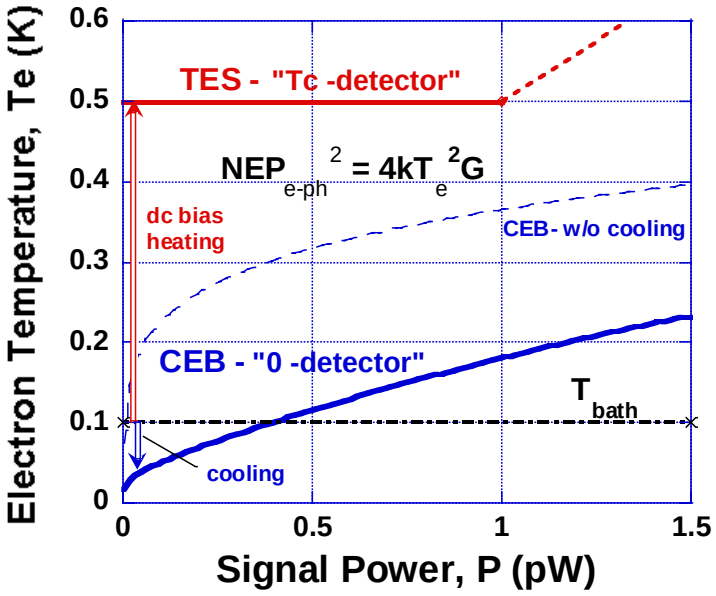

Fig. 2. Electron temperature as a function of signal power for T_{bath}=100 mK for CEB and TES. For CEB, the T_e is always cooled to possible minimum level. For P<0.4pW, the T_e of CEB is less than T_{bath} (real Cold-Electron Bolometer). For TES, the T_e is equal to T_C for all range of operation up to saturation power. After saturation there is uncontrollable increase of temperature.

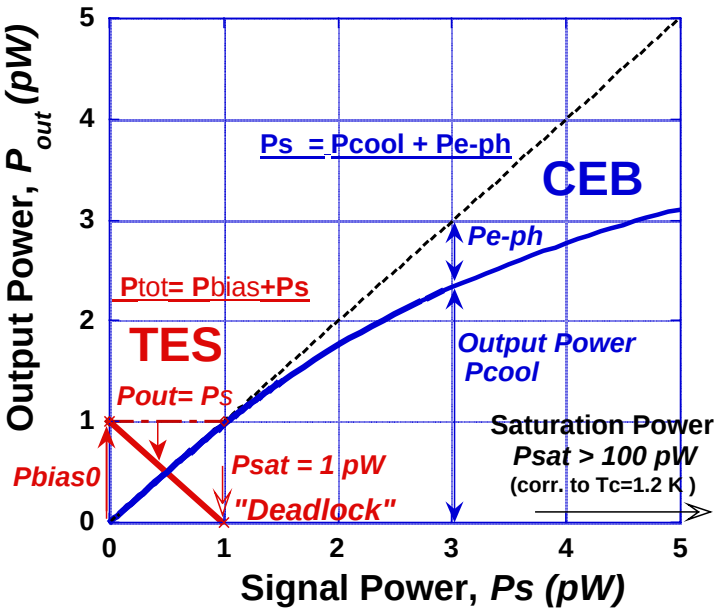

Fig. 3: Output power of CEB (Pcool) and TES (-δPbias) in dependence on Signal power. They are almost equal at small level of power. At higher level of power, the signal power P is split between Pcool and Pe-ph. The Saturation power would be achieved only after heating to Tc of Al electrode (P_{sat} is around 100 pW). Output power of TES is equal to reduce in bias power proportional to signal power. Saturation power is equal to zero bias power with full "deadlock" after this value.

saturation power, the TES fully stops operation. It is difficult to foresee the expected level of maximum power load and choose of P_{sat} is really complicated problem. Absolutely different situation is for CEB saturation: the output cooling power would simply deviate from the linear dependence Pcool(P). For the typical cooling power around 1 pW, the deviation from linear dependence $P_{out}(P)$ would be only several % at this level (Fig. 3). As signal power is further increased, the deviation will be larger but CEB still continue to work. It is the question of only calibration of this dependence. Final "deadlock" for CEB would be at the level of power around 100 pW when temperature achieves the critical temperature of the Al electrode.

Time constant

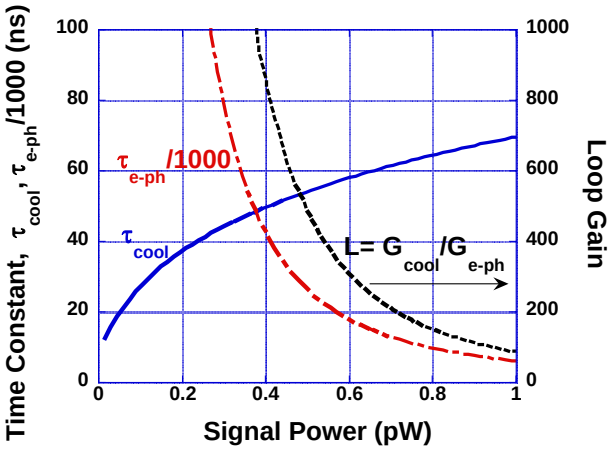

Fig. 4. Time constant of CEB, τ_{cool}, in dependence on signal power P_s. The electron-phonon time constant, $\tau_{e\text{-}ph}$, is shown for comparison (scaled 1000 times). The τ_{cool} is considerably shorter than $\tau_{e\text{-}ph}$ and difference is increased when we move to smaller signal power with stronger electron cooling. The loop gain L of negative electrothermal feedback is shown by dashed line. The loop gain is strongly increased for smaller P_s due to decrease of $G_{e\text{-}ph}$.

Time response of the CEB (4) in dependence on incoming power is shown in Fig. 4. As for TES, it is strongly reduced by loop gain L of electrothermal feedback (5). Cooling conductace G_{cool} is not dependent strongly on incoming power and slightly increased for smaller power (τ_{cool} is reduced). In contrast, the e-ph conductance , $G_{e\text{-}ph}$, is very dependent on power due to 4th power dependence on T_e and strongly reduced for low power (related $\tau_{e\text{-}ph}$ is increased). As final result, the L is considerably increased for smaller power and exceeds the level of 1000.
It is interesting to remark that the time constant of CEB in current-biased mode will be increased in comparison with intrinsic e-ph time constant [7]. The reason is in decrease of the total thermal conductance of a bolometer due to negative voltage response of the junction (positive electrothermal feedback).

Ultimate Noise Performance of the CEB. General Limit Noise Formula

Noise properties are characterized by the noise equivalent power (*NEP*), which is the sum of three different contributions, and is defined as follows [7-9]:

$$NEP_{total}^2 = NEP_{e-ph}^2 + NEP_{SIN}^2 + \frac{\delta I^2}{S_I^2}, \qquad NEP_{e-ph}^2 = 10 k_B \Sigma \Lambda (T_e^6 + T_{ph}^6) \qquad (6)$$

Here NEP^2_{NIS} is the noise of the NIS tunnel junctions, and the term $\delta I^2/S^2_I$ is due to the finite sensitivity of the amplifier (SQUID) δI. The noise of the NIS junctions has three components: shot noise $2eI/S^2_I$, the fluctuations of the heat flow through the tunnel junctions and the correlation between these two processes [7-9]:

$$NEP_{SIN}^2 = \frac{\delta I_\omega^2}{S_I^2} - 2\frac{< \delta P_\omega \, \delta I_\omega >}{S_I} + \delta P_\omega^2 . \qquad (7)$$

Due to this correlation the short noise is decreased at 30-70%. Similar correlation in TES decreases Johnson noise.

The question about ultimate noise performance has arisen in relation to highest requirements on NEP for future NASA missions [2]. The question is how realistic are these requirements on NEP=10^{-20} W/ $Hz^{1/2}$. Ultimate performance of CEB and other bolometers has been analyzed. Photon noise is not included in this analysis and should be added later as additional external noise. The NEP is determined by the shot noise due to the power load. The shot noise is treated in general sense including e-ph shot noise due to emission of phonons. Other sources of noise are neglected due to small values. For the level of P_0 =10 fW, this limit can be achieved using low temperatures (~ 100 mK) and small volume of the absorber ($\Lambda \leq 0.003$ μm^3) when we can neglect the electron-phonon noise component.
General ultimate NEP formula for shot noise limitation has been derived:

$$NEP_{shot} = (2 P_0 \, E_{quant})^{1/2} \qquad (8)$$

where E_{quant} is an energy level of P_0 quantization:
$E_{quant} = k_B T_e$ –for normal metal absorber, $E_{quant} = \Delta$– for superconducting absorber.

Ultimate NEP can be estimated for different bolometers for relatively low power load $P_0 = 10$ fW:

Type of bolometer	Energy of quantization	Characteristic parameter of absorber	NEP_{shot}
CEB	$k_B T_e$ =9 μeV	T_e = 50 mK	$1*10^{-19}$ W/$Hz^{1/2}$
TES	Δ=73 μeV	T_C = 500 mK	$4*10^{-19}$ W/$Hz^{1/2}$
KID [11,12]	Δ=200 μeV	T_C = 1.2 K (Al)	$7*10^{-19}$ W/$Hz^{1/2}$

The lowest NEP can be achieved for CEB with lowest level of quantization. However, even these extreme parameters of P_0 and E_{quant} show that it's rather unrealistic to achieve NEP=10^{-20} W/ $Hz^{1/2}$ announced in NASA requirements for future missions [2].
Systems with linear on T thermal conductance
- Spider-web TES with conductance through the legs
- CEB with cooling through SIN tunnel junctions (weak dependence on T: G ~$T^{1/2}$),
Limit shot noise is described by general formula (8) with numerical coefficient 2.
Systems with dominant e-ph thermal conductance (strong nonlinearity on T: $G_{e\text{-}ph}$ ~T^4):
- all bolometers on plane substrates with e-ph conductance
- antenna-coupled TES on chip with Andreev mirrors, - NHEB with Andreev mirrors.

Due to strong nonliniarity of e-ph conductance the limit shot noise is described by modified general formula with five times increased coefficient 10:

$$NEP_{shot-e-ph} = (10 P_0 \; E_{quant})^{1/2} \tag{9}$$

That means if we leave the system for normal relaxation of energy through e-ph interaction, the shot noise is increased due to strong nonlinear dependence of electron-phonon thermal conductance on temperature in contrast to linear systems with weak dependence on temperature (or absence of it). These formulae (8,9) can be effectively used for estimation of ultimate parameters of CEB and other bolometers for given parameters of detector systems.

Quantum efficiency

Limit shot noise formula (9) gives estimation of the NEP in dependence of two parameters: background power P_0 and energy of quantization E_{quant}. Dependence on the P_0 is rather evident: the more incoming power is applied the higher noise of sensing element for any realization. Usually we could not change too much this parameter and realization is determined by external conditions. The second parameter, E_{quant}, is considerably more important for realization of limit NEP. This level of energy characterizes the quantum efficiency of bolometers (Fig. 5). Excitation of an electron for typical frequency of 1 THz to the level of 4 meV after consumption of the energy quantum is the same for all concepts. Then, relaxation of energy due to e-e interaction occurs to different energy levels.

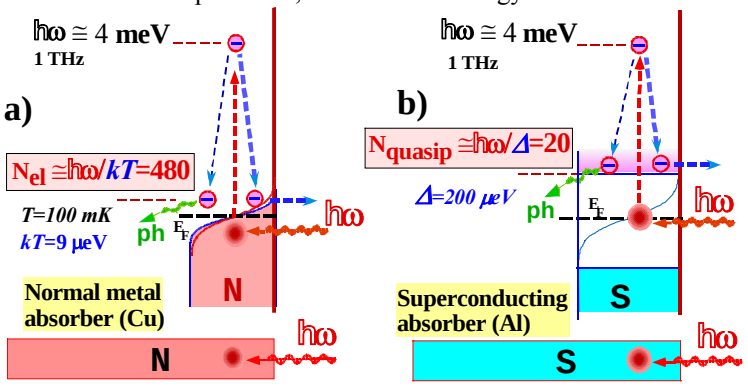

Fig. 5. Quantum efficiency of normal metal (a) and superconducting (b) absorber. An electron is excited after absorption of photon to the same energy level (4 meV for 1 THz signal) in both absorbers. Then electron is relaxed due to e-e interactions and energy is distributed between hot electrons at quantization level $E_{quant} = kT$ for normal metal (a) and between quasiparticle at quantization level $E_{quant} = \Delta$ for superconductor (b). The quantum efficiency is equal to 480 for normal metal and 20 for superconductor.

For CEB the energy will be distributed between electrons at the level of kT= 9 μeV (Fig. 5a). It gives number of electrons and quantum efficiency after absorption of one quantum: N=480 el/quant for electron temperature 100 mK. For TES and KID the relaxation of energy is stopped at the level of superconducting gap (Fig.5 b) that gives the following quantum efficiency: N= 96 for TES (with Δ=45 μeV) and N= 20 for KID (with Δ=200 μeV). Thus introduction of superconducting absorber considerably decreases the quantum efficiency that leads to higher shot noise and require more sensitive readout electronics.

Electron-phonon noise of superconducting and normal metal absorbers

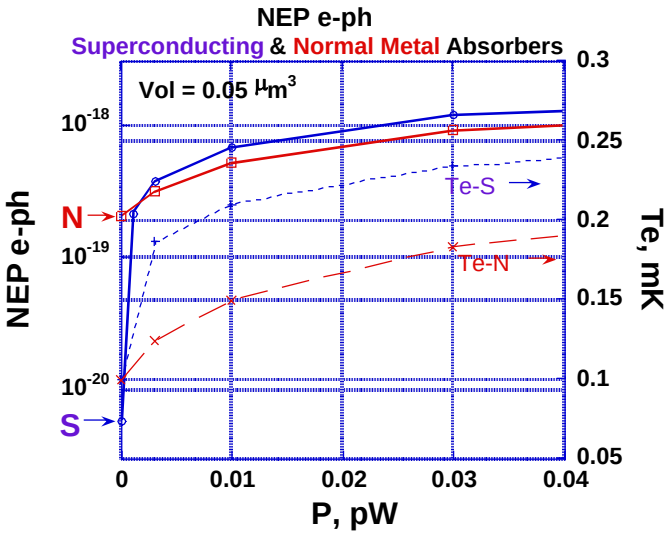

Application of superconducting absorber for different bolometers is rather widespread due to opportunity of superconductor to absorb high frequency signals with energy quantum more than superconducting energy gap [10-14]. The theory of electron-phonon interaction in superconductors is complicated and an approximate scheme has been used for analysis of electron-phonon noise in

Fig. 6. Electron-phonon Noise Equivalent Power (NEP) for superconducting and normal metal absorbers in dependence on power load. Effective electron temperature is shown for illustration of overheating of the absorbers. Phonon temperature is equal to 100 mK. Dependence of electron temperature for uncooled CEB is shown for comparison.

superconductor [15] based on kinetic equation proposed in Ref. [16]. To illustrate complicated nature of superconducting absorber, the electron-phonon noise is compared for both superconducting and normal metal absorbers in dependence on power load (Fig. 6). The NEPe-ph has been estimated for phonon temperature T=100 mK and volume of the absorber equal to 0.05 μm^3. Dependence of NEP for normal metal absorber does not show any unpredictable behavior: starting from NEP=$2*10^{-19}$ W/ $Hz^{1/2}$ it is monotonically increased for higher power. The superconducting absorber shows very low noise at zero power: NEP=$0.8*10^{-20}$ W/ $Hz^{1/2}$. It corresponds to some protection by superconducting gap against any excitations with energy less than Δ (Fig. 5b). However, even for very low applied power (> 1 fW), the noise is quickly increased to the level higher than NEP for normal metal. The reason of this noise is the same as discussed in previous paragraph. The quasiparticles excited by incoming signal are stopped at the level of Δ. Then recombination to superconducting state is accompanied by emitting of energetic phonons that lead to increased noise. Thus, protection of absorber by the gap without power load turns round in stopper of incoming energy at this higher level of the gap that leads to increased noise.

Optimal performance of the CEB

Our analysis of influence of the background power load on noise performance for different configurations of the CEB shows that the optimal configuration of the bolometer is the CEB with voltage-biased SIN tunnel junctions and current readout by a SQUID [8]. For analysis of ultimate performance, the high parameters of bolometer are accepted: a volume of absorber is equal to 0.01 μm^3, which is realistic for modern technology, the current noise of SQUID is equal to 5 $fA/Hz^{1/2}$ [18]. The typical junction resistance (R) equal to 1 kΩ has been used for simulation. The results are shown in Fig. 9 for the level of microwave background power P_0 = 0.01 pW. The latter figure is a relatively low level of background power load P_0 and used for analysis of limit characteristics of the CEB. The total NEP = $1.2x10^{-19}$ W is determined mainly by shot noise of NIS tunnel junctions due to incoming power load. Electron-phonon component and amplifier noise are lower than noise of the NIS junction that corresponds to background limited case. Resposivity S=dV/dP has maximum value of 150 nA/pW and is determined mainly by electron temperature of the absorber (energy of quantization) and finally by quantum efficiency of the CEB. For comparison, the similar figure, S= 200 nA/pW can be achieved for TES for the case of relatively low bias voltage V_b = 5 μV.

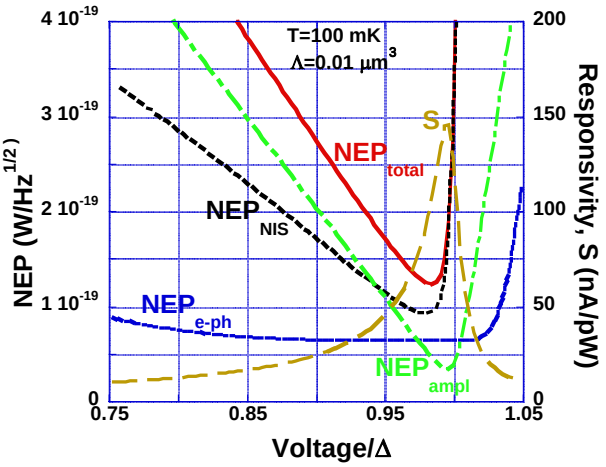

Fig. 7a. NEP of an optimal bolometer in presence of the background power load 0.01 pW for Λ= 0.01 μm^3, R= 1 kΩ, S_{SQUID} =5 $fA/Hz^{1/2}$, and for bath temperature 100 mK.

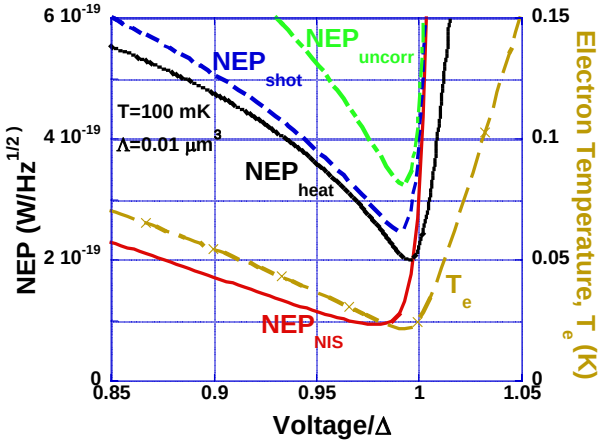

Fig. 7b. NEP_{SIN} with partial cancellation of the shot noise NEP_{shot} by the heat flow noise NEP_{heat} of SIN tunnel junction (7); NEP_{uncor} is shown for comparison.

It is interesting to analyze the correlated NEP_{SIN} (Fig. 7b) and uncorrelated NEP_{uncorr} including the first and third terms in equation (7). The shot noise and heat flow noise (7), partly compensate each other due to mutual correlation and lead to reduction of NEP_{SIN} in comparison with NEP_{shot}. The reduction of noise is especially considerable when bias point deviates from delta more than kT_e and removed quantum of energy are more uniform that leads to closer values of shot and heat flow components and more effective compensation. This compensation is possible only in voltage-biased mode; in current-biased mode there would be opposite effect of increase of the noise higher than uncorrelated noise NEP_{uncorr} [7-9].

We have analyzed the concept of the optimal CEB for 300 mK operation in the presence of the final background power load (P_0 = 0.1 pW) and for fixed parameters of the SQUID-amplifier [8]. The optimal regime can be realized when thermal "cooling conductance" through the tunnel junctions predominates over "fundamental" electron-phonon conductance. In these circumstances, an NEP level of 10^{-18} W/Hz$^{1/2}$ at 300 mK can be achieved in presence of P_0 = 0.1 pW for typical parameters for junction resistor R= 1 k□, S_{SQUID} =10 fA/Hz$^{1/2}$, and a volume of the absorber □□0.005 □m^3□□□□□□□□. This volume of the absorber □ is close to the technological limit.

Superconducting Cold-Electron Bolometer (SCEB) with Proximity Traps

Optimization of the CEB [8] has shown that the best values of NEP can be achieved the for volumes less than 0.005 μm^3 representing the limit of technology that meet some problems in realization. Proposed concept of the SCEB with proximity traps (Fig. 8) helps to overcome these problems [18]. The best properties of the superconducting absorber without power load and normal metal absorber under power load (Fig. 6) are combined in this concept.

The bolometer consists of a superconducting antenna coupled by tunnel junctions to a narrow absorber with two proximity traps formed by square normal metal underneath the superconducting strip. The THz signal is concentrated by antenna and absorbed by superconducting strip having energy gap less than photon quantum (Fig. 8). The released heat diffuses to normal metal traps provided by the proximity effect in bilayer of superconductor-normal metal. The normal metal trap is simultaneously a top electrode for the SIN tunnel junction. Thermal isolation is provided by a potential barrier of the SIN tunnel junction (2eV) that should give perfect isolation up to optical range. SIN tunnel junctions remove the heat from the traps very effectively due to small volume of the normal metal. Tunnel junctions realize near 100% efficiency (!) as electron cooler (relation of area of the tunnel junction to the area of cooled absorber).

The NEP of the SCEB can be estimated using results of analysis of optimal bolometer in paragraph 3 [8]. Superconducting part of the absorber will not contribute to noise due to weak electron-phonon interaction for temperatures considerably lower than the gap. The typical volume of normal metal part of absorber is Λ= 0.004 μm^3 (0.5x0.5x0.02 μm^3) and is close to optimal value for best noise performance. The total NEP ([8]) for P_0= 0.1 pW, R= 1 kΩ, S_{SQUID} =10 fA/Hz$^{1/2}$, and T= 300 mK is at the level of 1.5x10^{-18} W/Hz$^{1/2}$. In reality the effective volume of the traps can be even smaller due to proximity effect.

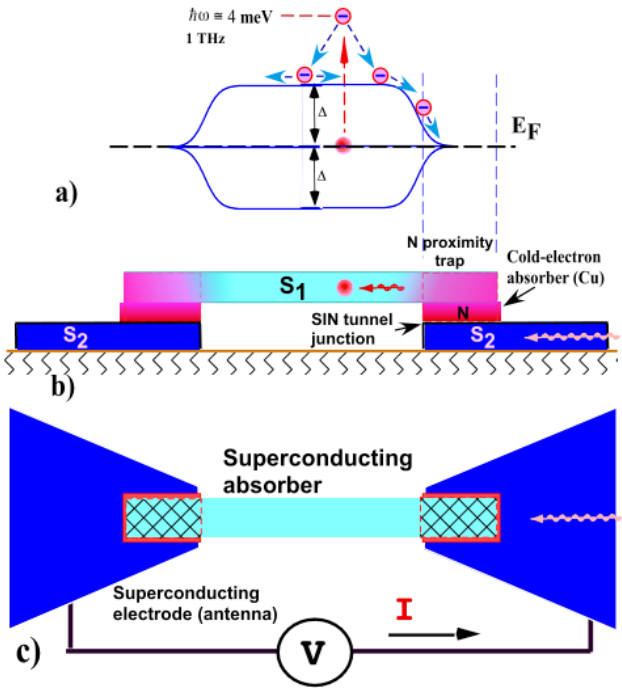

Fig. 8. Schematics of the cold-electron bolometer (SCEB) with superconducting absorber and proximity traps for very efficient electron cooling by the SIN tunnel junctions. a) The THz signal is concentrated by an antenna and absorbed by a superconducting strip having an energy gap less than the photon quantum. The released heat diffuses to normal metal traps provided by the proximity effect in bilayer of superconductor-normal metal. Side view b) and top view c) show layout of the bolometer. The SIN tunnel junctions remove a heat from the traps very effectively due to small volume of the normal metal forming top electrode of the tunnel junction and 100% area efficiency of cooling junctions.

Superconducting cold-electron nanobolometer (SCEB) with proximity traps and capacitive coupling to the antenna can be used in voltage-biased and current-biased modes. The voltage-biased mode could be optimized using more complicated parallel collection of tunnel junctions (twice increase of output current) [18].

Readout system.

The SQUID readout system with superconducting transformer and ferromagnetic core (Fig. 1) is under development [19]. Sensitivity of system is realized at the level of 30 fA/Hz$^{1/2}$. However , the main disadvantages of the system are large time constant, □$_{tr}$, and excess noise of the ferromagnetic core. The large □$_{tr}$ closes a way to realization of full cooling ability of the CEB demanding time constant less than e-ph time constant. The large □$_{tr}$ close a way to

realization of multiplexing schemes with large number of channels.The SQUID with resonance circuit (instead of transformer) could help to overcome these difficulties and realize all advantages of CEB with very short time constant. Voltage-biased mode of CEB operation with modulation of bias voltage could be used in this case. This mode could be realized by using small voltage bias resistor $R_S << R_I, R_b$. The voltage V_S is applied to the CEB and the task is to measure RF component of current ***I*** through the CEB with maximum sensitivity. The optimal realization is parallel resonance circuit (with resonance of currents) connected in parallel to current measuring resistor R_I. The optimal value of $R_I = 1k\Omega$ for typical bolometer dynamic resistance from 1 to 10 kΩ. For quality factor Q =100, current SQUID sensitivity could be improved from 1pA/Hz$^{1/2}$ to 10 fA/ Hz$^{1/2}$ that is a goal of current measurements. For modulation frequency 5MHz and input SQUID inductance L_{in}=0.3 μH, we would get inductive impedance $Z_L = \omega L$=10 Ω and C_r= 3 nF. This impedance gives a searched quality factor Q= R_I/Z_L=100. This schematic gives opportunity to get high sensitivity of readout system and select channels for frequency domain multiplexing.

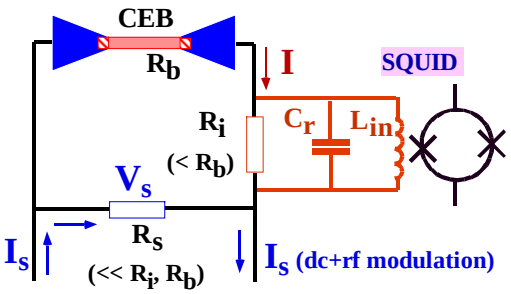

Fig. 9. SQUID readout system with RF modulation of the bolometer bias and resonance selection of the signal by input inductance of the SQUID and additional parallell capacitance. Quality factor of 100 ca be easy realized for typical parameters of the SQUID (using input inductance), additional capacitance C_r= 3 nF and current measuring resistor R_I = 1kΩ.

Conclusions

The concept of a cold-electron bolometer with strong electrothermal feedback is a turning point in development of supersensitive detectors from artificial bias heating to effective electron cooling. This concept could give the ultimate noise performance in presence of a realistic background power load. Due to strong electrothermal feedback, all incoming power is removed with high accuracy from the absorber increasing dynamic range of the system. The CEB does not suffer from the problem of saturation showing only some deviation from the linear response for power higher than characteristic cooling power. The time constant of CEB could be considerably reduced by the loop gain of negative electrothermal feedback (similar to TES) to the level of 10 ns. The CEB concept could be very promising for future post-Herschel space telescopes.

The author would like to thank Paul Richards, Dmitri Golubev, and Michael Tarasov for stimulating discussions. The work was supported by VR and SI Swedish agencies.

1. BREAKTHROUGH OF THE YEAR 2003: "*Illuminating the Dark Universe*". Science, **302**, p.2038 (2003).
2. D. Leisawitz et al., "Scientific motivation and technology requirements for the SPIRIT and SPECS far-infrared/submillimeter space interferometers", SPIE 2000.
3. K. Irwin. Applied Physics Letters, **66**, (1995) 1998.
4. A. Lee, P. Richards, S. Nam, B, Cabrera, K. Irwin, Applied Physics Letters, **69**, (1996) 1801.
5. L. Kuzmin, Proceeding of the 9th International Symposium on Space Terahertz Technology, Pasadena, pp 99-103, March 1998; Physica B: Condensed Matter, **284-288**, (2000) 2129.
6. L. Kuzmin, I. Devyatov, and D. Golubev. Proceeding of SPIE, v. 3465, pp. 193-199 (1998).
7. D. Golubev and L. Kuzmin. Journal of Applied Physics. **89**, 6464-6472 (2001).
8. L. Kuzmin and D. Golubev. Physica C **372-376**, pp 378-382 (2002).
9. S. Golwala, J. Johum, and B. Sadoulet, Proceedings of the VIIth International Workshop on Low Temperature Detectors, July 1997, Munich, Germany, pp 64-65.
10. B. Mazin, P. Day, J. Zmuidzinas, and H. LeDuc, AIP Conference Proceedings **605**, pp. 309-312, July 2001.
11. A. Sergeev, V. Mitin, and B. Karasik, Appl. Phys. Lett. **80**, 817-819 (2002).
12. A. Peacock et al., Nature **381**, (1996) 135.
13. R.J. Schoelkopf et al., IEEE Transactions on Applied Superconductivity, **9** (1999) 2935.
14. A.D. Semenov, G.N. Gol'tsman, and A.A. Korneev, Physica C, **351** (2001) 349.
15. D. Golubev and L. Kuzmin, "Superconducting hot-electron bolometer", to be published.
16. J. Clarke, in Nonequilibrium superconductivity, ed. by D. Langenberg and A. Larkin, Elsevier S.Publ (1986).
17. F.Gay, F.Piquemal, G.Geneves, Rev. Sci. Instr., V. 71, N 12, 4592-4595 (2000).
18. L. Kuzmin, Microelectronic Engineering, **69**, 309-316 (2003).
19. M.Tarasov, S.Gudoshnikov, A.Kalabukhov, H.Seppa, M.Kiviranta, L.Kuzmin, Physica C 368, 2002, p. 161-165.

Noise temperature measurements of NbN phonon-cooled Hot Electron Bolometer mixer at 2.5 and 3.8 THz.

Yu. B. Vachtomin, S. V. Antipov, S. N. Maslennikov, K. V. Smirnov, S. L. Polyakov, N. S. Kaurova, E. V. Grishina, B. M. Voronov and G. N. Goltsman

Moscow State Pedagogical University, Moscow 119992, Russia

ABSTRACT

We present the results of noise temperature measurements of NbN phonon-cooled HEB mixers based on a 3.5 nm NbN film deposited on a high-resistivity Si substrate with a 200 nm - thick MgO buffer layer. The mixer element was integrated with a log-periodic spiral antenna. The noise temperature measurements were performed at 2.5 THz and at 3.8 THz local oscillator frequencies for the 3 μm x 0.2 μm active area devices. The best uncorrected receiver noise temperatures found for these frequencies are 1300 K and 3100 K, respectively. A water vapour discharge laser was used as the LO source. We also present the results of direct detection contribution to the measured Y-factor and of a possible error of noise temperature calculation. This error was more than 8% for the mixer with in-plane dimensions of 2.4 x 0.16 μm^2 at the optimal noise temperature point. The use of a mesh filter enabled us to avoid the effect of direct detection and decrease optical losses by 0.5 dB. The paper is concluded by the investigation results of the mixer polarization response. It was shown that the polarization can differ from the circular one at 3.8 THz by more than 2 dB.

1. INTRODUCTION

Today, many terahertz radio astronomy projects and research efforts are aimed at studying the atmosphere of the Earth. Generally, if such a project is directed to the measurements at frequencies over 1.2 THz then HEB mixers that have no competitive analogues for this frequency range are used. As a rule, astronomical and atmospheric missions require a receiver of linearly polarized radiation in a relatively narrow frequency band which matches the LO frequency. In this case the optimal solution is to use a mixer with a well-studied plane polarized twin slot antenna for which the band is centered to a given frequency. This is the direction of the research efforts of diverse scientific groups. In particular, such projects as TELIS [1] and HERSCHEL [2] in the terahertz frequency rang are oriented to building a heterodyne receiver which has a 1.8 THz channel and a heterodyne spectrometer which has two channels at 1.41-1.91 THz, respectively.
The measured noise temperature versus frequency dependence is well linearly approximated by 8-10ħω/k for the frequencies less than 2.5 THz. However, the solution of a series of some scientific tasks is concerned to the fabrication of the mixers that are optimized to operate at higher frequencies (more than 2.5 THz) for which the performance of twin-slot antennas is poor. In fact, the only investigation of the HEB mixers at the frequencies over 2.5 THz is the one in which the noise temperature of the mixer was measured at frequencies up to 5.2 THz [3]. These measurements show that the sensitivity of the mixer drops and the noise temperature versus frequency dependence significantly differs from 10ħω/k. That is why further feasibility studies are needed to find out if the performance of heterodyne receivers directed to higher frequencies can be improved. In this work we investigated quasioptical mixers both at the well studied frequency of 2.5 THz and the frequency of 3.8 THz where very few measurements had been taken previously. In particular, we studied polarization properties of the mixers integrated with a spiral antenna at 3.8 THz. Besides, many similar problems are unsolved yet for both frequencies less than 2.5 THz and higher frequencies. One of them is the effect of direct detection, which causes an experimental error of Y – factor measurement in laboratory and real astronomical experiments. When mixer sizes are reduced, the effect of direct detections becomes more significant, hence the experimental error value of Y – factor measurement is increased. It can lead to a spectral line distortion in radioastronomical investigations.

2. HEB FABRICATION AND EXPERIMENTAL SETUP

HEB mixers were manufactured from a 3.5 nm thick superconducting NbN film on Si substrates with a MgO buffer layer. A 200 nm thick MgO buffer layer was deposited by e-beam evaporation from MgO pellet. Ultrathin NbN films have been deposited by reactive dc magnetron sputtering in the Ar + N_2 gas mixture. The quasioptical mixer was made by lift-off e-beam lithography and photolithography. A scanning electron microscope (SEM)

image of the central part of one of the devices is shown in Fig.1. Typically, the mixers based on 3.5 nm thick NbN films on silicon substrates with an MgO buffer layer have a superconducting transition temperature between 10 K and 11 K.

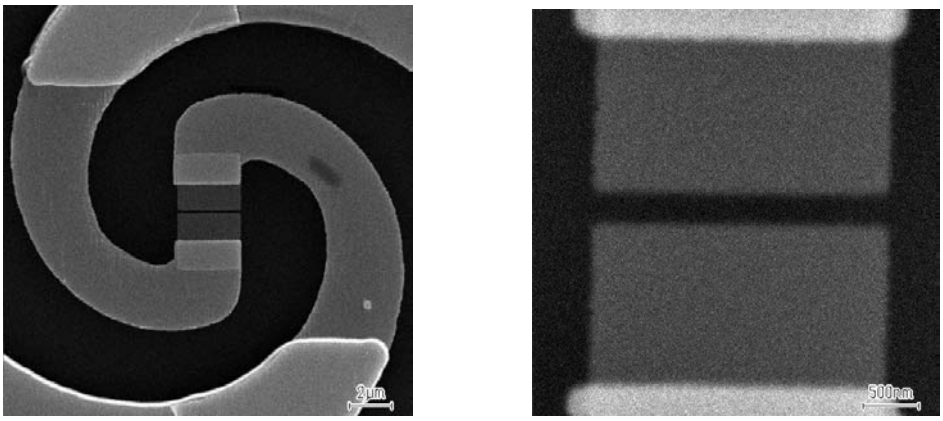

Figure 1. SEM micrograph of the spiral antenna (left) and central part of the spiral antenna with an NbN bridge (right).

The experimental setup for noise temperature measurements is presented in Fig2. The hyper-hemispherical lens fabricated from high-resistivity silicon with a HEB positioned on the flat side of the lens were mounted on a copper holder which in its turn was tightly bolted to the 4.2 K cold plate of an LHe cryostat. The cryostat has a wedged 0.5 mm thick high-density polyethylene window. A 0.35 mm thick black polyethylene IR filter was mounted on the 77 K shield. The intermediate frequency (IF) signal was guided out of the HEB via a 50 Ω coplanar line, which was soldered to an SMA connector. A bias tee followed by an isolator was used to feed the bias to the mixer and to transmit the IF signal to a low noise (5 K) 1.2-1.8 GHz HEMT amplifier (30 dB gain at 1.5 GHz). The bias tee, the isolator and the amplifier were also mounted on the cold plate of the cryostat. The output of the amplifier was filtered at 1.5 GHz with a bandwidth of 40 MHz, further amplified and finally rectified with a crystal detector.

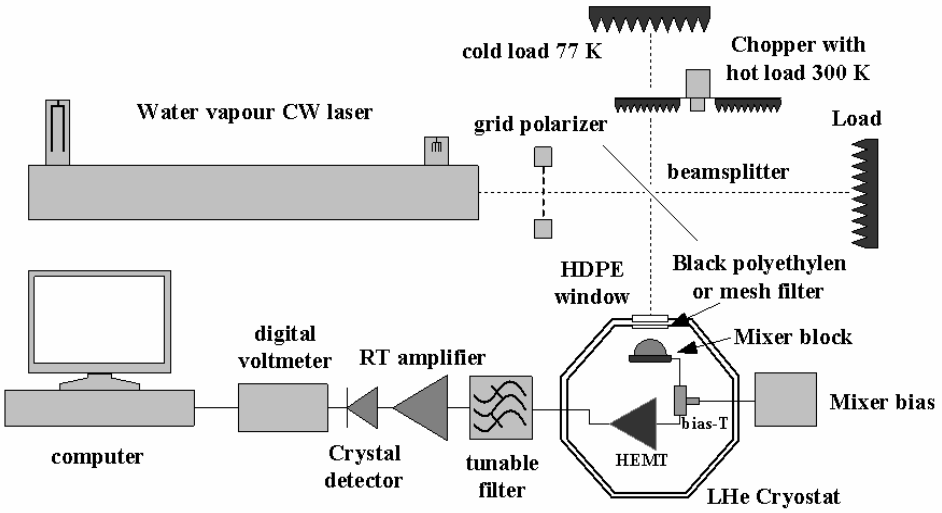

Figure 2. Experimental setup for noise temperature measurements.

The measurements were performed using the CW gas discharge water-vapor laser as a local oscillator. The laser operates on the terahertz transitions of 2.529 THz, 3.826 THz and 3.792 THz. The intensity of transition line at 3.792 THz is essentially weaker than one of the line at 3.826 THz, and the difference between the frequencies of these lines is about 34 GHz. That is why only the 3.826 THz transition line was used in the experiments. The laser was constructed from a straight quartz tube having two openings for the electrodes and for pumping and reflectors against its ends. One of the reflectors was a concave spherical mirror with a 6 meter curvature radius, driven longitudinally to the laser cavity for fine tuning by differential screw arrangement, and the other was a square nickel mesh of wires 10 μm thick, with centre-to-centre spacing of 30 μm (a transmission coefficient of 0.5-1% at 80-120 μm). The laser used a flowing mixture of water vapor and helium (1:2) at a total pressure near 1 Torr. It was excited at an applied voltage of about 2.5 kV. The axial discharge current might be changed over the range of

0.5-1.2 A by current stabilized power supply. High-density polyethylene was used to cover the mesh coupler. The measured diameter of the Gaussian laser beam at half maximum of the intensity profile obtained by scanning the Golay cell across the laser beam at a distance of 1m from the output mesh is 16 mm and 13 mm at 2.5 and 3.8 THz, respectively. The signal and the LO radiation were superimposed by a 10 μm thick Mylar beam splitter. DSB receiver noise temperatures were determined using the Y-factor technique. Ecosorb was used as a hot and cold load. The temperature of the hot and cold loads was 293K and 77K, respectively. The laser systems were stable enough to measure the noise temperature either by putting alternately the hot load and the cold load in the signal path behind the beam splitter or by chopping between the hot and cold loads using a lock-in technique.

3. RESULTS OF NOISE TEMPERATURE AND DIRECT DETECTION EFFECT MEASUREMENTS

Two types of planar antennas are widely used in quasioptical mixers at the moment: twin-slot and log-periodic spiral ones. The log-periodic spiral antenna is the most appropriate to operate at frequencies over 2 THz. This type of antenna has a rather wide input band. Besides, significant variation of spiral sizes leads only to an inconsiderable variation of the antenna bandwidth [4]. On the one hand, this fact enables us to perform noise temperature measurements at various frequencies in a rather wide range. For the best device 180#14 we measured 1300 K at 2.5 THz and 3100 K at 3.8 THz (see Fig. 3).

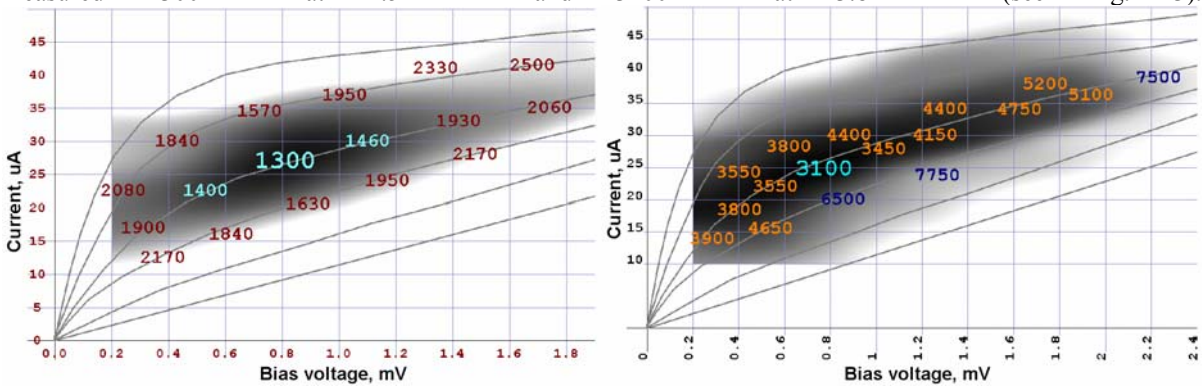

Figure 3. Pumped IV-curve and bias dependence of noise temperature at 2.5 THz (left) and 3.8 THz (right) for device 180#14.

These results are given for the silicon lens without antireflection coating. If the antireflection coatings [5] would be used for each frequency of 2.5 and 3.8 THz the noise temperature values would be about 1050 K and 2500 K respectively. On the other hand, it brings about an additional heating of the mixer electron subsystem and a noticeable variation of the mixer bias current when hot and cold loads are swapped in the signal path of the receiver.

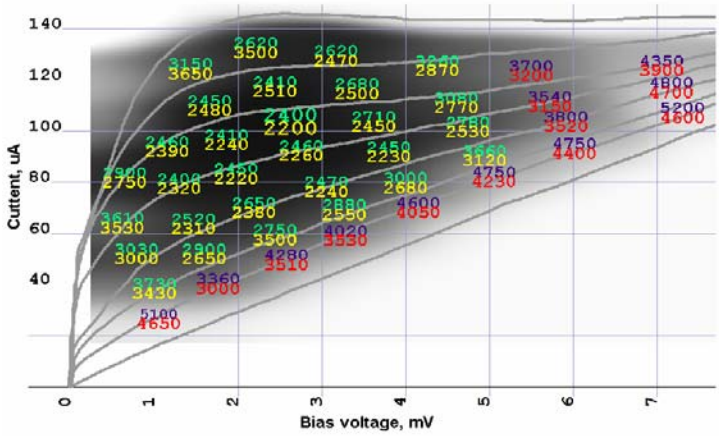

Figure 4. Pumped IV-curve and bias dependence of uncorrected receiver noise temperature at 2.5 THz with black polyethylene used as IR-filter (top) and corrected to direct detection one (bottom) for device 567/1#8.

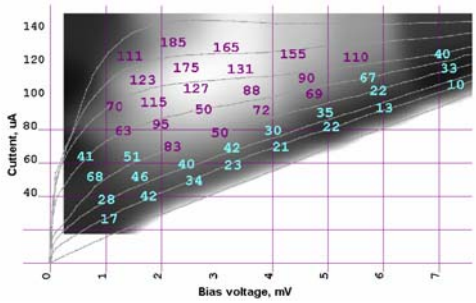

Figure 5. Pumped IV-curve, bias current variation due to the effect of direct detection [in nA] and output IF power P_{out} (shown by brightness) for device 567/1#8.

This effect is known as the effect of direct detection [6]. Since the output power of the mixer is dependent on bias operating point, it leads to a Y – factor measurement error. The error value can be derived from the measured bias current variance value (ΔI) and the derivative dP_{out}/dI taken at the operating point, where "P_{out}" is output IF power of the mixer and "I" is the bias current. The $P_{out}(I)$ dependence and dP_{out}/dI value can be obtained by varying the LO power. ΔI and Y – factor values are measured simultaneously by swapping cold and hot loads. If this experimental error is taken into account, the corrected Y – factor can be roughly expressed as $Y_{cor} = (P_{hot} \pm (dP_{out}/dI) * \Delta I) / P_{cold}$, where P_{hot} and P_{cold} are output power values measured when the hot and cold loads, respectively, are placed in the signal path of the receiver. The contribution of the direct detection effect to the measurement error of mixer noise temperature was studied for a typical mixer 567/1#8. The bias dependence of the noise temperature derived from the directly measured Y – factor is shown in Fig. 4 (above). The minimum value of the directly measured noise temperature is 2400 K. In order to estimate the contribution of direct detection effect, ΔI and P_{out} (Fig. 5) versus bias dependencies were obtained. The estimation of the noise temperature derived from corrected Y – factor is shown in Fig. 4. It is seen that the noise temperature is negatively corrected if the bias current is less than the one corresponding to the maximum of the output IF power. If bias current is more than that corresponding to the maximum of output IF power the noise temperature value is corrected positively. To avoid an error of Y –factor

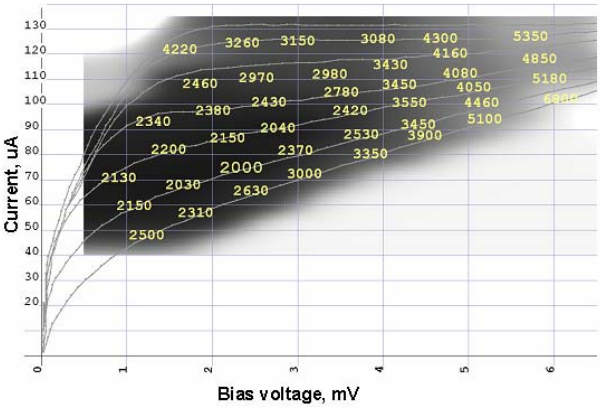

Figure 6. Pumped IV-curve and bias dependence of uncorrected receiver noise temperature at 2.5 THz with a cold input mesh filter.

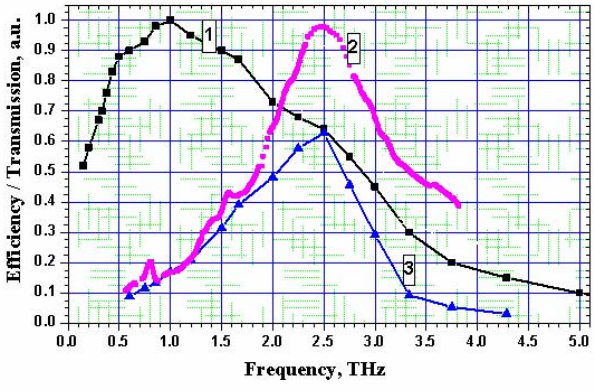

Figure 7. FTS spectra of log-spiral antenna (1), frequency dependence transmission coefficient of the mesh-filter (2) and product of multiplication of these two curves (3)

measurement, an additional input cold IR filter with the bandwidth significantly narrower than that of the spiral antenna can be used. Such a filter must also have low losses at the LO frequency. One of the most appropriate filters is a metal mesh. It is known that a mesh filter with square cells has its transmission versus frequency dependence of a bell curve form. The central frequency of the mesh filter is expressed by $f_{max} \sim 1.2\ d$ in which d is the period of the mesh. In our experiment a square nickel cell mesh filter with d = 100 μm and a filling factor of 0.15 was mounted on the helium shield of the cryostat instead of the traditionally used black polyethylene IR filter. The mentioned filling factor is the ratio of the wire diameter to the mesh period. The transmission vs. frequency dependence of the filter is shown in Fig. 7. When the mesh filter is used, ΔI is decreased until it is less than 10 nA at the optimal noise temperature point, and the error of the noise temperature measurement becomes negligible. Furthermore, the replacement of a black polyethylene IR filter by a mesh filter caused a noticeable decrease of the noise temperature of the receiver. The noise temperature versus bias dependence for the receiver with a cold input mesh filter is shown in Fig. 6. At the optimal operating point the directly measured noise temperature is about 2000 K which is even less than the noise temperature obtained by Y – factor correction for the same receiver with polyethylene input IR filter. Hence, the use of the cold input mesh filter not only enables us to avoid the effect of direct detection but also decreases optical losses.

4. POLARIZATION MEASUREMENTS

Polarization measurements of the mixer integrated with a spiral antenna were done using the experimental setup shown in Fig. 8. Linearly polarized radiation of FIR water vapor laser passed through the rotator of the polarization plane and applied to the mixer fixed on hyperhemispherical lens inside the helium cryostat. The rotator of the polarization plane used is based on a 3 – mirrors reflector. The rotation of the polarization plane was due to rotation of the reflector, as shown in Fig. 8. The laser output power was calibrated by the Golay cell.

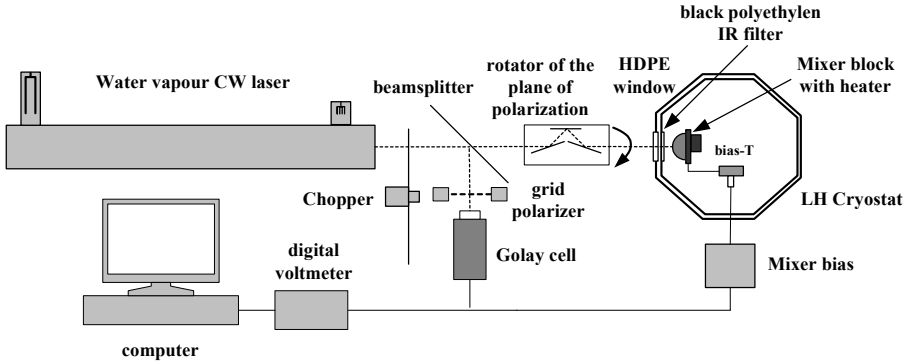

Figure 8. Experimental setup for polarization measurements.

The temperature of the mixer was maintained around the critical value by a heater. The laser radiation was chopped at a frequency of 20 Hz. The mixer was biased by a current source, and the amplitude of the mixer voltage oscillation at the chopping frequency was the measured signal value, which in its turn was reduced to

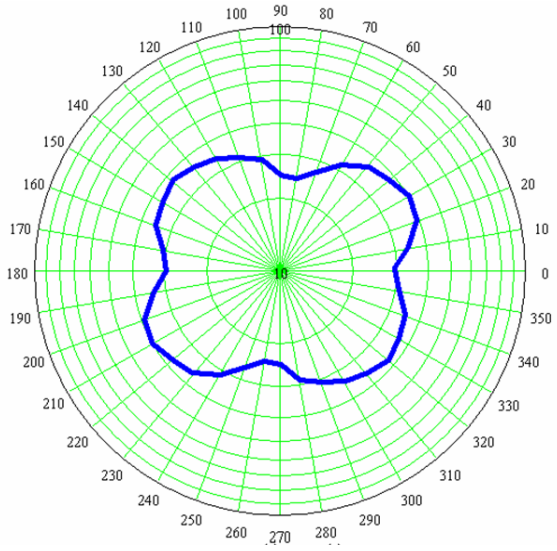

Figure 9. Polarization response of NbN HEB mixer integrated with log - periodic spiral antenna at 3.8 THz LO frequency.

the value of absorbed power. The results of the polarization measurements at 3.8 THz are presented in fig.9. As seen from the Figure, absorbed power can vary more than 2 dB when the polarization plane of the input radiation is rotated. Hence, the noise temperature of the receiver significantly depends on the polarization of the input radiation even if a spiral antenna - coupled mixer is used.

5. CONCLUSION

Direct detection contribution to the measured Y-factor leads to an error of noise temperature calculation of more than 8% for the mixer with in-plane dimensions of 2.4 x 0.16 μm^2.

Polarization of mixer integrated with log-periodic spiral antenna can differ slightly from the circular one at a frequency over 2.5 THz and is about 2 dB at 3.8 THz.

The measured receiver noise temperatures are 1300 K at 2.5 THz LO frequency and 3100 K at 3.8 THz. It should be stated that the obtained noise temperatures are based on the measurements with a lens without an antireflection coating and without regard to the contribution of direct detection. Taking into account the optical

losses due to reflection on the silicon lens [6] the corrected receiver noise temperatures are 1050 K and 2500 K at 2.5 and 3.8 THz, respectively.

REFERENCES

[1] TELIS home page: http://telis.af.op.dlr.de/
[2] HERSCHEL home page: http://astro.estec.esa.nl/SA-general/Projects/Herschel/
[3] J. Schubert, A. Semenov, G. Gol'tsman, H. Huebers, G. Schwaab, B. Voronov, E. Gershenzon, "Noise temperature and sensitivity of a NbN hot-electron mixer at frequencies from 0.7 THz to 5.2 THz", Proc. of 10th International Symposium on Space Terahertz Technology, pp. 189-199, 1999
[4] Alexei Semenov, Heiko Richter, Konstantin Smirnov, Boris Voronov, Gregory Gol'tsman and Heinz-Wilhelm Huebers, "The development of terahertz superconducting hot-electron bolometric mixers", Supercond. Sci. Technol. **17** (2004) pp436-439
[5] M. Hajenius, J.J.A. Baselmans, J.R. Gao, T.M. Klapwijk, P.A.J. de Korte, B. Voronov, and G. Gol'tsman, "Improved NbN phonon cooled hot electron bolometer mixers", Proc. of 14th International Symposium on Space Terahertz Technology, Tucson, USA, March 2003
[6] S. Svechnikov, A. Verevkin, B. Voronov, E. Menschikov, E. Gershenzon, G. Gol'tsman, "Quasioptical phono-cooled NbN hot-electron bolometer mixer at 0.5-1.1 THz ", Proc. of 9th International Symposium on Space Terahertz Technology, pp. 45-51, 1998

Superconducting Single Photon Detectors Array Based on Hot Electron Phenomena

S. Ryabchun, A. Korneev, V. Matvienko, K. Smirnov, P. Kouminov, V. Seleznev, N. Kaurova, B. Voronov, G.N.Gol'tsman
Moscow State Pedagogical University, Malaya Pirogovskaya 1, Moscow, 11992, Russia
S. Polonsky
Picosecond Imaging Circuit Analysis, Optical Communications and High Speed Test, IBM T.J. Watson Research Centre

Abstract

In this paper we propose to use time domain multiplexing for large format arrays of superconducting single photon detectors (SSPDs) of the terahertz, visible and infrared frequency ranges based on ultrathin superconducting NbN films. Effective realization of time domain multiplexing for SSPD arrays is possible due to a short electric pulse of the SSPD as response to radiation quantum absorption, picosecond jitter and extremely low noise equivalent power (NEP). We present experimental results of testing 2×2 arrays in the infrared waveband. The measured noise equivalent power in the infrared and expected for the terahertz waveband is 10^{-21} $WHz^{-1/2}$. The best quantum efficiency (QE) of SSPD is 50% at 1.3 μm wavelength.

Introduction

Radioastronomy missions require detectors, which provide ultimate (background limited) sensitivity in the submillimeter wavelength range even when exposed to relatively weak background radiation. Several research groups are currently developing low noise superconducting detectors – both integrating direct detectors [1, 2] and quantum counting detectors [3, 4] – for terahertz range. Direct and quantum counting detectors have different detection mechanisms. In continuous integrating detectors energy of a large number of absorbed photons is distributed among a far larger number of elementary thermal excitations. Thus individual photons can not be distinguished. The response is effectively integrated over the response time of the detector. The number of excitations measures average radiation power that the detector absorbs. In a quantum, or photon, detector one photon creates excitations, which are collected and counted before they relax and before another photon is absorbed. Thus, each absorbed photon is registered. The number of collected excitations measures the energy of absorbed photon. These detectors can be compared in terms of Noise Equivalent Power (NEP). Integrating direct detectors can be of various types, for example, superconducting tunnel-junction detectors [5], or tungsten-based superconducting transition-edge sensors [6]. In this paper we present superconducting single photon detector (SSPD) potentially capable of operating in the infrared to terahertz waveband. The measured value of the SSPD NEP in the visible and infrared wavebands is $10^{-21}WHz^{-1/2}$.

Future submillimeter and far-infrared space telescopes will need large-format (of order of 10^3 elements) imaging detector arrays to perform astronomical observations. When the number of elements in array increases to order of thousand it becomes virtually impossible to realise an individual layout for every element. Various multiplexing systems were proposed; among them is one where elements are coupled with resonant circuits with different natural frequencies and multiplexing is realised by frequency dividing a signal [7]. Another approach [8] uses a frequency domain multiplexing scheme of the bolometer array. The bolometers are biased with ac currents whose frequencies are individual for each element and are much higher than the bolometer bandwidth. In another variant each detector is individually biased by dc of alternate polarities [9].

In this paper we present time domain multiplexing for SSPD arrays with all the detectors connected in series. Multiplexing is realised by comparing time delays between pulses coming from the opposite ends of an array. It should be noted that short response time of the SSPD (~200 ps [10]), low dark counts rate (less than 1 s^{-1}) [11], planar layout and relatively simple SSPD fabrication technology favour the integration of single detectors into an array with subsequent time domain multiplexing.

SSPDs photon-detection mechanism

For a detailed treatment of single photon detection we refer to [12, 13], here we only give a brief outline of the mechanism involved in the process. The mechanism of single photon detection by thin superconducting films biased close to the critical current of the film consists in the formation of the hot spot in the place of photon absorption resulting in voltage pulse generation which can be easily measured.

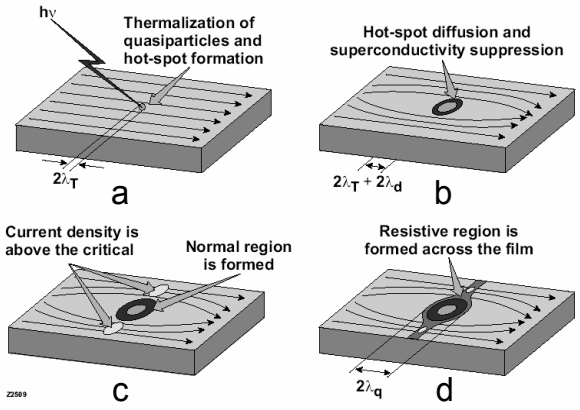

Fig. 1. Schematics of a hotspot-generated and supercurrent-assisted formation of a resistive barrier in an ultrathin and submicrometer-width superconducting stripe, kept at temperature far below T_c. The arrows indicate the flow direction of a supercurrent biasing the stripe.

SSPD consists of a superconducting stripe of a submicrometer width (comparable with the hotspot size) whose thickness is less than the electron thermalization length. The device is maintained at a temperature much lower than that of superconducting transition T_c and biased close to the device critical current I_c. The photoresponse mechanism is presented in Fig. 1. The collective action of the hotspot formation and I_b redistribution results in the appearance of the macroscopic resistive barrier across the SSPD stripe [12, 13]. As is illustrated in Fig. 1, after the localized hotspot is created [Fig. 1(a)], it then grows as quasiparticles diffuse out of the hotspot core. Simultaneously, the biasing supercurrent I_b is expelled from the resistive hotspot volume and concentrated in the "sidewalks" near the edges of the film [Fig. 1(b)]. Thus, I_b exceeds the critical value outside the hotspot, and phase-slip centres are created in quasi-one-dimensional sidewalks [Fig. 1(c)]. As a result, the superconductivity is destroyed, and a resistive barrier is formed across the entire cross-section of the stripe [Fig. 1(d)]. The resistive barrier gives rise to a voltage signal with the amplitude proportional to I_b. After its growth phase, the hotspot decreases due to the relaxation and out-diffusion of quasiparticles. Thus, after the quasiparticle relaxation time the hotspot in the stripe collapses, superconductivity (a zero resistance state) is restored, and the detector is ready to register another photon. As is seen from the above discussion the operation frequency range of the detector is determined by the ratio of the quantum energy to the energy gap of a superconductor. Low energy photon can not produce concentration of unpaired electrons that sufficient for superconductivity suppression. Quantum efficiency turns to be larger in a superconducting material with a smaller transition temperature as the superconducting energy gap decreases with transition temperature decrease. Thus, the use of a material with a smaller transition temperature will shift the cut-off towards longer wavelength [14].

SSPD array time domain multiplexing

A short response time of the SSPD (~200 ps [10]), low dark counts rate (less than 1 s^{-1}) and a short jitter (~30 ps) allow not only developing detectors of wide frequency range but also integrating them into large arrays with subsequent multiplexing, specifically, recognizing the signal with a two-channel read-out system. Figure 2 presents the principle of the time domain multiplexing of an SSPD array. All the SSPDs in the array are connected in series with delay lines and thus form a 50 Ω transmission line (Fig. 2). At the moment of any detector response there are two simultaneous voltage pulses propagating along the transmission line in the opposite directions. Both ends of the transmission line are loaded by the input of amplifiers A1 and A2. Their outputs are connected to the S(et) and R(eset) inputs of an SR-trigger. The time intervals between the pulses coming to the S and R inputs are different for each detector as they depend on the electro-magnetic lengths difference between the detector and amplifiers A1and A2 which are determined by the delay lines. Multiplexing of SSPD array elements will be

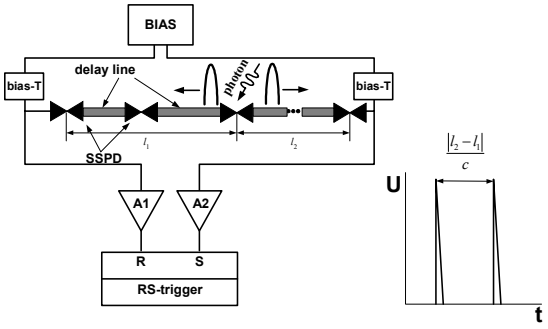

Fig.2. Time Domain Multiplexing of SSPD array

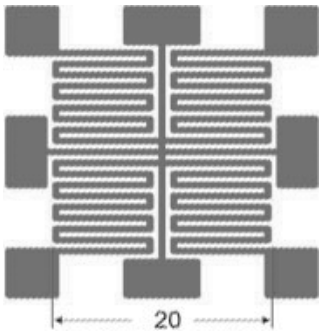

Fig.3. SSPD array layout. Active area – 4 pixels, pixel size - 10×10 μm^2, stripe width – 100 nm, thickness – 3.5 nm, filling factor – 0.5.

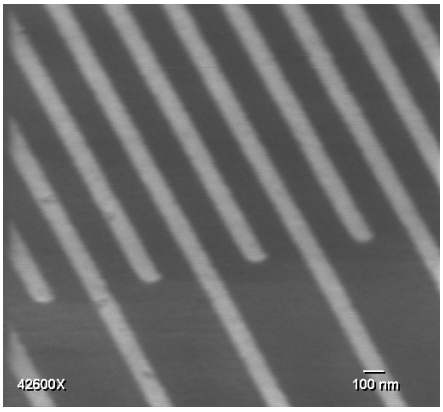

Fig. 4. Scanning electron microscope image of a small area of SSPD. 10×10 μm^2 3.5-nm-thick SSPD, the superconducting stripe width is ~100 nm.

realised by the determination of the pulse duration at the SR-trigger output. For successful time domain multiplexing of the system it is necessary the jitter be much shorter than delay times which eventually determine the rate of the array.

SSPD array fabrication

We manufactured SSPDs of the visible and infrared frequency ranges from 3.5-nm-thick NbN superconducting films, deposited on optical-quality sapphire substrates by dc reactive magnetron sputtering. The films are characterized by T_c = 10 to 11 K, superconducting transition width ΔT_c ~ 0.3 K, and critical current density j_c = 6 to 7×10^6 A/cm^2 at 4.2 K. Single devices are patterned into stripes with a nominal width of 80 to 100 nm. Our fabrication procedures, namely patterning based on the direct-electron-beam lithography, followed by reactive ion etching with a photoresist mask, are presented in detail in Ref. 15. To maximize the detector's active area, we have chosen a meander-type geometry with a device area of 10×10 μm^2 and a filling factor (the ratio of the active meander area to the nominal detector area) of up to 0.5. Thus, the total meander length is ~500 μm. Considering that for successful detector operation it is critical the superconducting stripe be uniform (effective deviation from the mean stripe width throughout the whole length should be such as to ensure uniform bias current density), manufacturing even single detector is not too easy a technological task. By the effective width of the stripe we understand not only its geometry but also its discontinuity which is determined by the raw superconducting film. When several detectors are integrated into an array the uniformity requirement holds true for all the detectors of the array.

To gain experience in the array fabrication technology and study time domain multiplexing capabilities we chose one of the simplest variants – a 2×2 array (fig. 3). Four elements (with a 10×10 μm^2 active area and a filling factor of 0.5) have a common ground contact. The other electrode between the two ground contacts is made so as to couple the matrix with a coplanar line. The layout also allows connecting the detectors in series in pairs as well as parallel connection. Figure 4 presents a micrograph of our 3.5-nm-thick SSPD with a filling factor of 0.5 etched in an interdigitated manner.

SSPD performance

As the uniformity of a meander is critical for optimal operation of our devices, we measured the

Table 1. SSPD 2×2 array characteristics: R_{300} – room temperature resistance, I_c – critical current at 2 K, QE – quantum efficiency of SSPDs at 2 K for 1.3 μm.

#	R_{300}, MOhm	I_c, $\times 10^{-6}$ A	QE, %
1	0.95	14.3	10
2	1.05	14.5	12
3	1.1	14.0	9
4	1.2	13.9	16

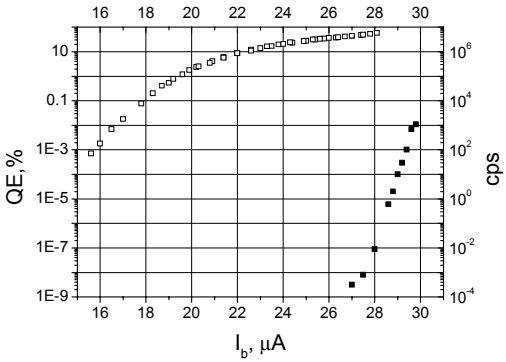

Fig. 5. Single SSPD quantum efficiency (open squares) and dark counts rate (solid squares) versus bias current at 2 K.

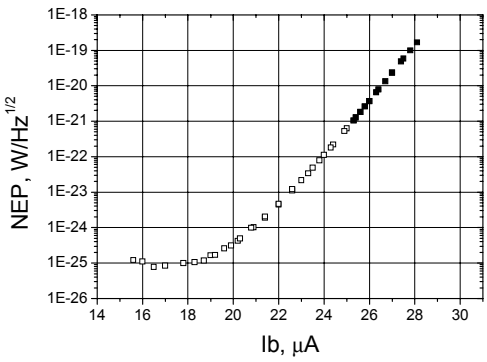

Fig. 6. Single SSPD NEP versus bias current 2 K – squares. The solid are measured data, the open are extrapolated date.

main parameters of our samples in an array, specifically, the room temperature resistance and critical current density. The values of these parameters for a 2×2 array are presented in table 1 where the first column shows the detector ordinal number. The 5 % spread in values of the samples characteristics at the constant current took place for other arrays as well and meets the time domain multiplexing requirements.

Another important characteristic of the SSPD is its quantum efficiency. Quantum efficiency (QE) is defined as the ratio of the number of photons registered by the detector to the number of photons incident on it. Figure 5 presents the quantum efficiency of the best single SSPD versus the bias current (I_b) for 1.3 μm wavelength at 2 K operating temperature. As radiation sources we used a continuous-wave laser diode. The same figure shows dark counts rate (R) dependence on the bias current at 2 K. As is seen from figure 5 the R versus I_b dependence obeys exponential law. For QE versus I_b dependence the slope decreases with I_b increase and for I_b close to I_c the dip of the QE curve is relatively slow. In the vicinity of the critical current QE goes up to ~50 %. We also measured QE of each detector of a 2×2 matrix for 1.3 μm wavelength at temperature 2 K. Table 1 shows the results of the measurement - all the four elements have high and almost equal quantum efficiency about 10%. The results obtained are important not in terms of high but in terms of equal values of QE of all the SSPDs in the array.

For comparison of direct and quantum counting detectors noise equivalent power (NEP) is introduced. The photon-counting process brings some peculiarities into signal processing. Because there is no integration time for a photon counter, a direct comparison of integrating detectors and quantum detectors in terms of their noise equivalent power is not possible. However, for quantum devices a parameter equivalent to NEP can be introduced as:

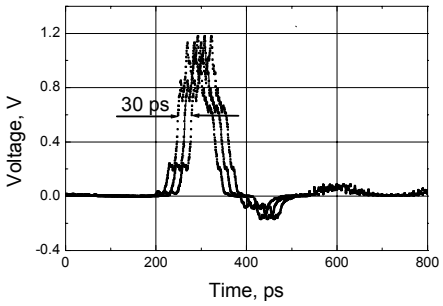

Fig. 7. SSPD jitter.

$$NEP = \frac{h\nu}{QE}\sqrt{2R} \qquad (1)$$

Figure 6 presents NEP versus I_b obtained using Eq. (1) and the experimental results for both QE and R presented in Fig. 6 for 2 K. The best achieved NEP value is of the order of 10^{-21} W/Hz$^{1/2}$ for 1.3 μm at 2 K. To our knowledge, this is the best sensitivity in the near-IR range ever reported for a single-photon detector. As we can see in fig. 6 the NEP rapidly decreases with the bias decrease, since close to I_c, R is a much stronger function of I_b than QE. The measured NEP is limited not by the detector properties but the measurement technique – integration time. The extrapolated values of dark counts rate lead to NEP values that reach 10^{-25} W/Hz$^{1/2}$ for 1.3 μm at 2 K.

We also measured one of the time characteristics of the SSPD – the jitter. The array time domain multiplexing will be restricted by SSPD jitter as it will set the lower limit of delay lines length between the elements of an array and thus determine the rate of the whole system. Figure 7 shows a time-resolved response pulse from our SSPD. The transient was taken at incident flux of about 10^3 photons per pulse with a bias current density of $0.6j_c$ and the oscilloscope working in the accumulation mode. The total system jitter was found to be about 30 ps. The value of the jitter includes the jitters of the laser system (20 ps), the output circuit and the oscilloscope (20 ps). Thus, the intrinsic SSPD jitter should be much less than 30 ps.

5. Conclusion

The method of array multiplexing presented in the paper can be realised for hot-electron single photon detectors of the visible, infrared and terahertz wavebands. This method enables us to develop an array detecting system outperforming a single SSPD in terms of 2D area scanning speed, which is certainly an advantage in the terahertz waveband or for large integrated circuits analysis.

The manufactured 2×2 SSPD array of the infrared waveband based on thin NbN superconducting film meets all the requirements of the time domain multiplexing. The characteristics of the best SSPD are the following: QE~50%, jitter < 30 ps, NEP ~ 10^{-21} WHz$^{-1/2}$. Increasing integration time determined by low dark counts rate will enable us in principle to reach SSPD noise equivalent power ~ 10^{-25} WHz$^{-1/2}$.

References

1. D. Chouvaev, L. Kuzmin, M. Tarasov, *Supercond. Sci. Technol.* **12**, 985, 1999.

2. B.S. Karasik, W.R. MacGrath, M.E. Gershenson, and A.V. Sergeev, *J. Appl. Phys.* **87**, 7586, 2000.

3. R.J. Schoelkopf, S.H. Moseley, C.M. Stahle, P. Wahlgren, and P. Delsing, *IEEE Trans. Appl. Supercond.* **9**, 2935, 1999.

4. S. Komiyama, O. Astafiev, V. Antonov, T. Kutsuwa, *Microelectronic Engineering*, **63,** 173-178, 2002.

5. de Bruijne, J. H. J., Reynolds, A. P., Perryman, M. A. C., Favata, F., and Peacock,A., 2002, *Opt. Eng*., **41**, 1158–1169.

6. Cabrera, B., Clarke, R. M., Colling, P., Miller, A. J., Nam, S., and Romani, R. W., *Appl. Phys. Lett*., **73**, 735–737, 1998; Miller, A. J., Nam, S. W., Martinis, J. M.,and Sergienko, A. V., *Appl. Phys. Lett*., **83**, 791–793, 2003.

7. P.K. Day, H.G. LeDuc, B.A. Mazin, A. Vayonakis, J. Zmuidzinas, *Nature*, **425**, 817-821, 2003.

8. J. Yoon, J. Clarke, J.M. Gildemeister, A.T. Lee, M.J. Myers, P.L. Richards, and J.T. Skidmore, *Appl. Phys. Lett.* **78.** 371 (2001).

9. B. Karasik and William R. McGrath, *Proc. 12th Int. Symp. on Space Terahertz Technol*., 436- 446, 2001.

10. Roman Sobolewski, A. Verevkin, G. N. Gol'tsman, A. Lipatov, and K. Wilsher, *IEEE Trans. Appl. Supercond*.,**13**, 1151-1157, 2003.

11. A. Verevkin, J. Zhang, W. Slysz, R. Sobolewski, A. Lipatov, O. Okunev, G. Chulkova, A. Korneev, K. Smirnov, G. Gol'tsman, A. Semenov, Proc. 13th Int. Symp. on Space Terahertz Technol., 105-112, 2002.

12. G.N. Gol'tsman, O. Okunev, G. Chulkova, A. Lipatov, A. Semenov, K. Smirnov, B. Voronov, A. Dzardanov, C. Williams, and Roman Sobolewski, *Appl. Phys. Lett*., **79**, 705–707, 2001.

13. A.D. Semenov, G.N. Gol'tsman, and A. Korneev, *Physica C* **351**, 349, 2001.

14. G. Gol'tsman, A. Semenov, K. Smirnov, B.Voronov, Proc. 12th Int. Symp. on Space Terahertz Technol., 469-475, 2001

15. G.N. Gol'tsman, K. Smirnov, P. Kouminov, B. Voronov, N. Kaurova, V. Drakinsky, J. Zhang, A. Verevkin, and R. Sobolewski, *IEEE Trans. Appl. Supercond*., **1**3, 192–195, 2003.

Compact 1.6-1.9 THz local oscillator as stand-alone unit for GREAT

M. Philipp[1], U.U. Graf [1] , F. Lewen [1], D. Rabanus [1], A. Wagner-Gentner [1], P. Müller [2] and J. Stutzki [1]

[1]KOSMA, I.Physikalisches Institut, Universität zu Köln, Zülpicher Str. 77, 50937 Köln, Germany
[2]RAIUB, Universität Bonn, Auf dem Hügel 71, 53121 Bonn, Germany
E-Mail: philipp@ph1.uni-koeln.de

ABSTRACT

The German Receiver for Astronomy at Terahertz Frequencies (GREAT) is a first generation PI instrument for the Stratospheric Observatory For Infrared Astronomy (SOFIA), developed by a collaboration between the MPIfR[1], KOSMA[2], DLR[3] and the MPAe[4]. GREAT is designed as a dual-channel, tri-band receiver, covering the frequencies of 1.6-1.9 THz, 2.4-2.7 THz and 4.7 THz . Each of the first three institutes named above contribute one heterodyne receiver channel, respectively. A later upgrade with an e.g. 1.4 THz channel will follow.

The GREAT instrument is designed to observe with any two of the three frequency channels simultaneously and to be able to quickly switch between different flight configurations. This demands a high modularity and flexibility on our receiver concept. For this purpose, we must be able to exchange the cryostats containing the mixer devices, the optical benches and the local oscillator subsystems (LO). Especially the LO systems are built as stand-alone units and integrated into compact boxes. KOSMA contributes GREATs heterodyne receiver channel operating at a frequency of 1.6-1.9 THz. We present an overview of the 1.6-1.9 THz LO system, and a detailed description of its internal parts.

Radiation of 1.9 THz is generated by means of a Backward Wave Oscillator (BWO) followed by a frequency tripler. The estimated output power at 1900 GHz is about 1μW. To correct the BWO's considerable elliptical output beam pattern we developed astigmatic off-axis mirrors to achieve maximum beam coupling into the tripler's feed horn antenna. All mirrors are manufactured in-house on a 5 axis CNC milling machine at KOSMA. To phase-lock the BWO we use a custom-made two-stage PLL system with a Gunn oscillator as intermediate LO. The PLL system is located in a small compartment in the front of the LO-box. Schottky mixers for 633 GHz have been manufactured at KOSMA. The required magnetic field of about 1.25 Tesla for the BWO-tube is provided by a permanent magnet. This solution makes the oscillator independent from high current electromagnets as well as helium infrastructure for superconducting magnets. The BWO-tube produces approximately 150 Watt of excess heat. We integrated a high efficiency chiller into the LO-box designed to dispose of this heat with a minimum additional power consumption and space requirement. The complete LO-system fits into a small box with 21cm x 24cm x 100cm in size and consumes only 230 Watts of power.

1. SCIENTIFIC BACKGROUND

Improving THz astronomy will complete our knowledge about planetary atmospheres and the interstellar medium in the galaxy. Furthermore, investigations related to the early universe will be possible. THz observations are expedient at places only where the atmospheric transmission of the spectral range is high and not blocked due to water vapor absorption. Thus, excellent sites for THz observations have to be extremely dry like space applications or in our case we will use the Stratospheric Observatory For Infrared Astronomy (SOFIA) operating at an altitude of about 13km.

The GREAT receiver attacks the long standing gap in the far infrared spectral range up to 4.7 THz. The KOSMA 1.9 THz detector will provide information about the atomic fine-structure transition of ionised carbon CII

[1] Max-Planck-Institut für Radioastronomie
[2] Kölner Observatorium für Sub-Millimeter Astronomie
[3] Deutsches Zentrum für Luft- und Raumfahrt
[4] Max-Planck-Institut für Aeronomie

(158 μm) which is the most important cooling line of the interstellar medium. In addition, C+ is found to be abundant in photo-dissociated regions (PDR), where FUV photons from the interstellar radiation field and/or emitted from young stars dissociates molecules such as CO and ionize carbon. Thus, the 1.9 THz receiver channel in conjunction with the 4.7 THz channel of the DLR (64 μm, fine-structure line of neutral atomic oxygen OI) makes it possible to verify our recent models on PDRs.

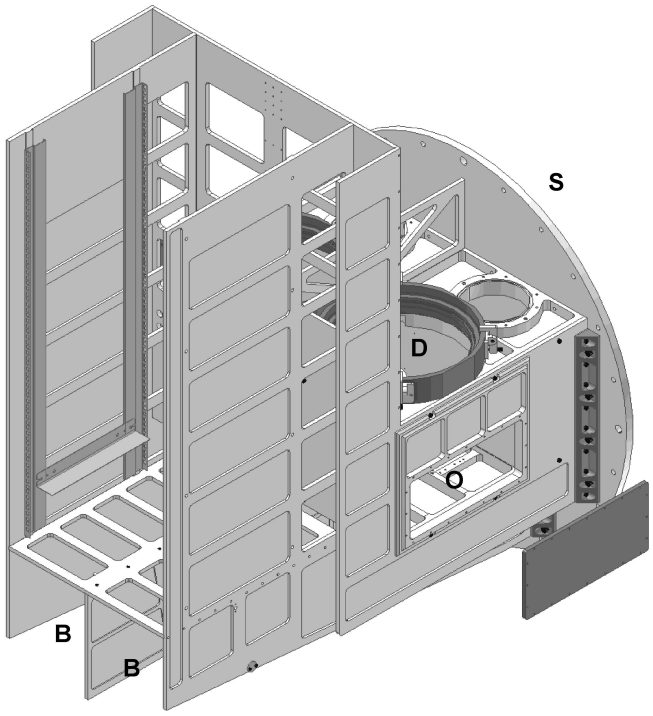

Figure 1: The GREAT structure: (S) SOFIA instrument flange; (O) common optics plate, (D) dewar mounting for cold optics and mixer; (B) local oscillator slots

2. GREAT RECEIVER CONCEPT

GREAT is a single pixel heterodyne receiver carrying two independent receiver channels at once. A total of three receiver channels, contributed by the MPIfR, KOSMA and the DLR are available (1.6-1.9 THz, 2.4-2.7 THz and 4.7 THz). Depending on the scientific purpose of a mission, two channels are selected and will be in operation simultaneously. This requires a high degree of modularity for the receiver system and for the common optics needed. To ensure the interchangeability, each channel contains its own exchangeable local oscillator box, a specific optical bench mounted on the common receiver optics and a cryostat containing the mixer device. When swapping receiver channels, all three subcomponents have to be replaced. Each receiver channel can operate in either receiver slot.

Pumping all three receiver channels with only one type of LO is not possible at present. At GREAT we will use three completely different types of local oscillators. A standard solid-state LO provides 2.4-2.7 THz. The upper band of 4.7 THz is covered by an OPFIRL and radiation at 1.6-1.9 THz is generated by a Backward Wave Oscillator (BWO) followed by a frequency tripler. To make these three systems interchangeable, they were designed to fit in small boxes with 21cm x 24cm x 100cm in size located at the bottom of the GREAT structure (see Figure 1). Each LO-box has to contain the whole LO-subsystem including the control electronics to work as an independent and exchangeable THz source. The boxes are inserted into the LO-slots, clamped and automatically aligned precisely to guarantee a reproducible coupling of the THz beam into the common optics. Interchangeability of the receiver channels results in additional requirements to the mechanical setup but it opens up the possibility to upgrade them easily to the newest technology by modifying either the LO subsystem, the corresponding optics bench or the mixer inside the cryostat as well as adding completely new receiver channels.

3. THE 1.9 THZ LOCAL OSCILLATOR SETUP

The detection frequency of the KOSMA receiver channel will be in the range of 1.6-1.9 THz (158-188 micron). This wavelength is a serious gap for the design of local oscillator sources with sufficient output power even to pump a single mixer device (about 1μW). Solid state LOs attack this gap from the lower frequency side. LOs based on mixing two IR-lasers are well under development. Using a laser LO is not possible for our application due to the insufficient tuning range of such a laser. Quantum cascade lasers (as we may use in the SOFIA Terahertz Array Receiver: STAR) developed for this frequency range require superconducting magnets and liquid helium cooling, which is not easy to accommodate in the modular LO-box of GREAT.

In our case radiation of 1.9 THz is generated at 633 GHz with a Backward Wave Oscillator (ISTOK, Russia, model No. OB-80) followed by a frequency tripler. Figure 2 shows the general setup. The BWO-tube is mounted inside a cylindrical permanent magnet (1.25 Tesla) to focus the electron beam for oscillation. The 633 GHz beam leaves the BWO output horn, passes an astigmatic optics and is coupled into the tripler's feed horn antenna (see section 4, Optics Design). The tripled 1.9 THz beam is then focused by an off-axis mirror and leaves the LO-box through a hole in the back of the top lid. A small fraction of the 633 GHz beam is coupled out by a beam splitter and fed into a PLL system to stabilize the BWO frequency (see section 5).

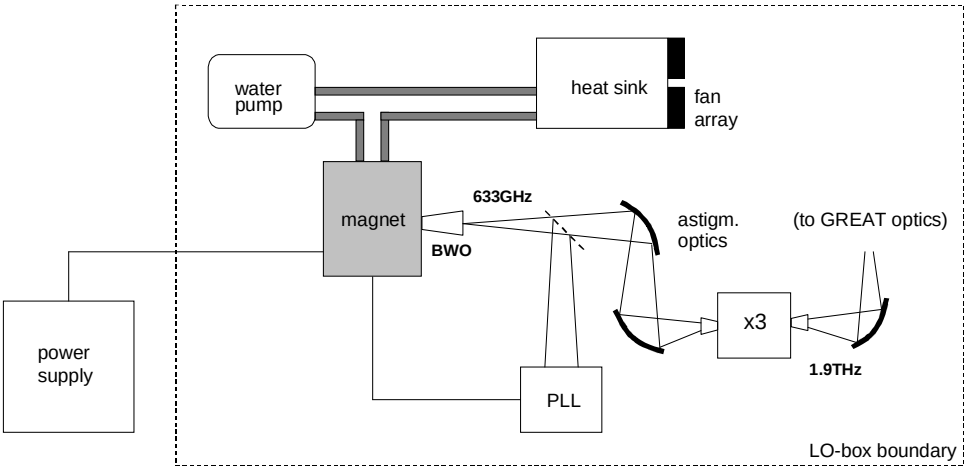

Figure 2: The local oscillator setup

An external high voltage supply (HVS) provides the cathode heating current (6ACV, 1A) as well as the acceleration voltage necessary for the BWO-tube (4000V). Since the acceleration voltage directly determinates the frequency of the BWO output beam, it has to be very clean and is filtered to a voltage ripple of <10mV. The cathode current is about 30mA at 4000V. In addition to the heating power of about 8 Watts the BWO-tube dissipates 130 Watt. For this reason water cooling is required. We implemented a custom-made chiller into the LO-box to dump this excess heat with a power consumption of only 50 Watts and a minimum space requirement. It consists of a fan array, a specially manufactured heat sink and a small aquarium water pump. The air is taken into the LO-box at the bottom and blown out through a slit in the front plate. Using this subassembly we are completely autonomous from external commercial chillers with a typical power consumption of 2000 Watt and the burden of additional safety regulations on SOFIA. A typical flight air pressure of 750mbar and a BWO excess heat of 130 Watt leads to a water heating of only 5K. The interconnection between high voltage, water and the IF-processing as well as phase lock and control electronics require additional safety systems all integrated in the LO-box and discussed in section 6.

4. OPTICS DESIGN

Radiation of 1.9 THz is generated by means of a Backward Wave Oscillator (BWO) followed by a frequency tripler. The output power of the BWO is between 5-20 mW at 633 GHz. The output beam pattern is considerably elliptic

with different beam waists in horizontal and vertical direction. The fraction of power in the fundamental Gaussian beam mode is about 89.9%. To achieve maximum beam coupling into the tripler's feed horn antenna we developed astigmatic off-axis mirrors manufactured in-house at KOSMA.

An astigmatic off-axis mirror is defined by three phase centres resulting in two different focal lengths for the ellipsoidal and spherical direction. If the positions and even the horizontal and vertical waists w_{0x} and w_{0y} of the beam are exactly known, the radii of curvature (R) at an arbitrary plane can be computed. Via the law for small lenses, in Gaussian optics valid for R, the focal lengths of adequate off-axis mirrors can be calculated to reimage the waists at a given distance z.

Numerical simulation show excellent imaging properties of our astigmatic optics. First results of the *measured* corrected BWO beam profile demonstrate an increase in gaussicity up to 98.9% in comparison to only 89.9% in the uncorrected beam (see Figure 3). This illustrates that astigmatic optics can be calculated and manufactured with high precision and could be also useful for more severe elliptic beams from sources such as quantum cascade lasers as we intend to use in the SOFIA THz Array Receiver (STAR) from KOSMA.

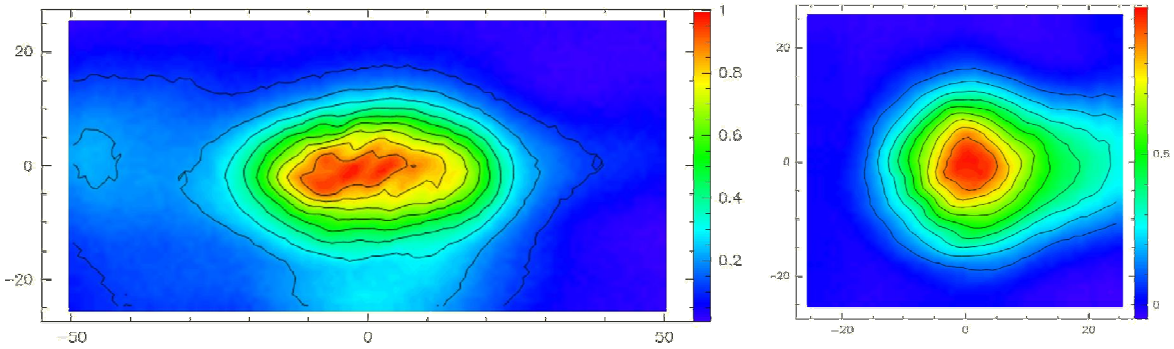

Figure 3: Measured BWO beam pattern at a distance of 335mm from the output feed horn (left). The right hand picture shows the corrected beam. Note, that our first measurements are based on a rude and visual aligned $4w_0$ mirror optics only which can explain deviation of a perfect Gaussian beam profile in conjunction with the distorted BWO input beam pattern.

The corrected 633GHz beam is then coupled into the tripler's feed horn antenna, a potter horn with a centre frequency of 600GHz. The tripler itself will be based on a coaxial design made by Radiometer Physics GmbH, Germany, with an estimated output power of about 1µW at 1900 GHz. The output beam is focused by an off-axis mirror, leaves the LO-box through a hole in the top lid and enters the common optics plate of GREAT from the bottom. A 2mm thin high density poly ethylene window inside the GREAT structure separates the inner compartment of GREAT from the LO-box, since the common optics is at outside air pressure whereas the LO-boxes are at cabin pressure. To guarantee correct beam coupling into the common optics, the last mirror inside the LO-box is adjustable. After switching a channel, adjustments can be made even during flight if the SOFIA telescope is caged. The complete optics is located at the back side of the LO-box and vertically orientated, for minimum space requirement.

5. PHASE LOCK ELECTRONICS

The BWO has an inherent 3dB line width of less than 1kHz. However, fluctuations of the supply voltage directly affect the BWO frequency and broaden the signal to ~20MHz. To avoid this, one has to control the 4000V cathode voltage with a maximum noise of 10µV over a cable distance of 25 meter (BWO to HV-supply). As a solution we implemented a PLL system into the LO-box (Figure 4). Instead of controlling the high voltage, frequency regulation is achieved by shifting the BWO's *ground* potential. In this way, the PLL system can be placed very close to the BWO to obtain best performance. The result is shown in Figure 5. We achieved a SNR of 50dBc for Δf=10kHz. Even for the frequency tripled 1900 GHz beam, this is enough to benefit from the full resolution of the chirp transform spectrometers (CTS) on GREAT (Δf=45 kHz).

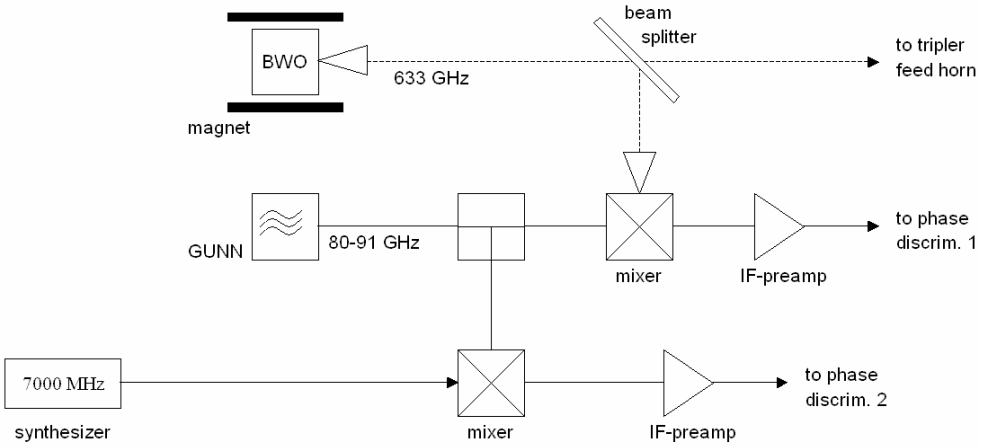

Figure 4: The setup of the dual-PLL system. For explanation see text.

We use a Gunn oscillator as stable reference for the PLL loop. A small fraction of the BWO beam is coupled out via a beam splitter and feed into a harmonic mixer. The signal is combined with the 7th harmonic of the Gunn and forms the IF-signal for the PLL. The complete IF processing chain is integrated on the PLL card and designed to be extremely low-noise (0.9 dB). To function as a stable reference, the Gunn oscillator is stabilized by a second PLL circuit, which uses the 13th harmonic of a high precision frequency synthesizer as the Gunn reference oscillator.

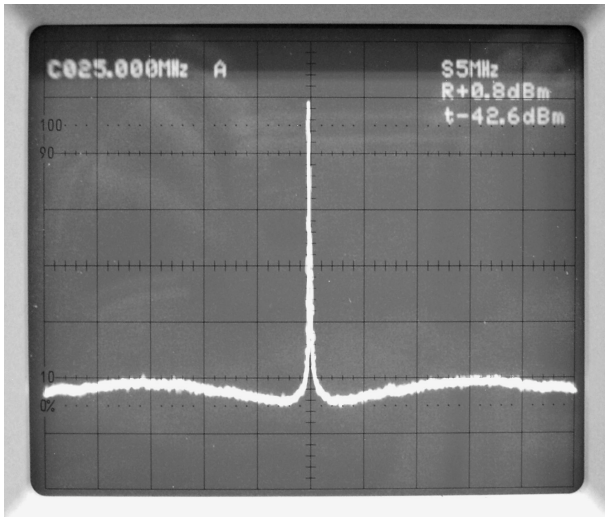

Figure5: The measured BWO IF-Signal.

Temperature fluctuations affect the Gunn frequency with about 1MHz/K and may result in loosing the lock of the PLL. We effectively increased the holding circuit range with an additional feed-back loop. The correction signal of the PLL is monitored and used to control the main Gunn voltage within a range of 7-10 volt, corresponding to a frequency drift of 1.5 GHz. Doing this the Gunn PLL appears to be ultra stable against long time temperature variations and can not loose the lock in any case.

6. SAFETY CONSIDERATIONS

The interconnection between high voltage, water and sensitive electronics inside the LO-box leads to the possibility of many different kinds of hazards. This becomes a serious problem, since the SOFIA airplane is built to be a science platform and to carry additional *civil* passengers for education and scientific motivation. For this reason, all science instruments on SOFIA have to meet the whole spectrum of safety regulations for airworthiness certification of the FAA (Federal Aviation Administration). We implemented several systems to guarantee a safe operation of the LO-box:

The high voltage supply (HVS) of the BWO contains an emergency circuit (*crow bar*) which is controlled by measuring the output current of the HVS. In case of a short circuit, the supply current will increase exceeding a fixed predetermined value. As a result, the high voltage will be switched off and the output capacitors of the HVS will be discharged within 50µs. The small shut-down time protects the electronics as well as crew members by limiting the discharge energy to a maximum of 0.5 Joule.

There is the possibility that an arc discharge develops inside the BWO-tube. In this case, its internal resistance drops to below one Ohm and the high voltage of 4000 Volt would be directly applied to the PLL output circuit. Although this is limited by the crow bar, the electric surge would be enough to damage the PLL and following electronics. To avoid this, we implemented a "protection circuit", placed between the BWO and the PLL. If the voltage at the PLL output rises above 15 Volt, the current will be dumped into large capacitors. Thus, the voltage will be kept below 20 Volt at all times causing no harm to the electronics.

The fast emergency switch-off circuit can be externally triggered, too. Various sensors measure e.g. the water flux and the water temperature of the chiller. If the water circuit is interrupted or the water temperature exceeds a maximum value for sufficiently cooling the BWO, the electronics will send a trigger pulse to the HVS to deactivate the high voltage to prevent overheating of the tube.

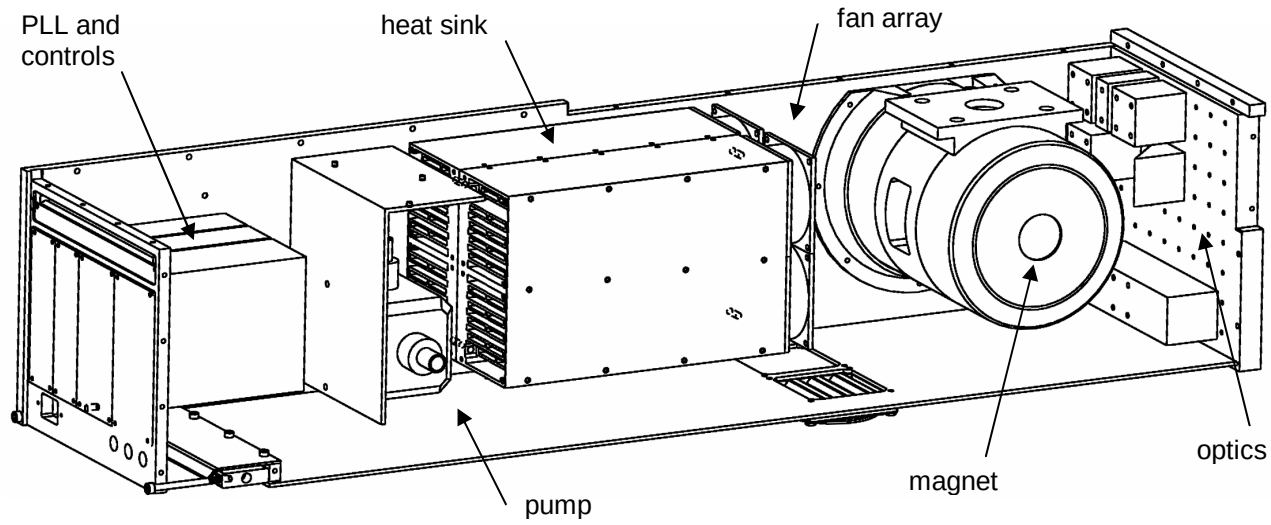

Figure6: Chart of the assembled LO-Box

7. CONCLUSION

We described the 1.6-1.9THz local oscillator for the GREAT receiver. The system is designed to be an exchangeable plug-in device and fits in a box with 21 x 24 x 100cm in size. It contains no helium infrastructure and needs no external chiller. The system power consumption is only 230 Watt and the estimated output power will be 1µW at 1900 GHz. We meet the SOFIA airworthiness safety regulations. A schematic of the assembled LO-box is shown in Figure 6.
We developed a theory of astigmatic off-axes mirrors to correct the BWO output beam pattern.

ACKNOWLEDGMENTS

This work is supported by the *Deutsche Forschungsgemeinschaft* through grant SFB 494 and by the ministry of science of the state Nordrhein-Westfalen.

REFERENCES

1. A. Krupnov, "Phase lock-in of mm/submm backward wave oscillators: development, evoulution and applications", *International Journal of Infrared and Milimeter Waves* **22**, pp. 1-14, 2001.
2. J. Murphy, "Distortion of a simple gaussian beam on reflection from off-axies ellipsoidal mirrors", *International Journal of Infrared and Milimeter Waves* **8**(9), pp. 1165-1187, 1987.
3. R.Timmermann, B. Köster and J. Stutzki, "[CII] 158 and [OI] 63 microns ISO-observations of L1457*", *Astron. Astrophys.* **336**, pp L53-L56, 1998.
4. P.F. Goldsmith, *Quasioptical Systems*, IEEEE Press, New York, 1998.
5. R. K. Melugin and H.-P. Röser, eds., "GREAT – the first generation german heterodyne receiver for SOFIA", *Proceedings of SPIE: Airborne Telescope Systems* **4014,** MPIfR, KOSMA, DLR, MPIAe, Rolf Güsten, P. v.d. Wal and A. Wunsch, 2000.
6. R. K. Melugin and H.P. Röser, eds., "The SOFIA telescope", *Proceedings of SPIE: Airborne Telescope Systems* **4014**, Alfred Krabbe, 2000
7. H. Ito, T. Furuta, F.Nakajima, K. Yoshino and T. Ishibashi, "Continous THz wave generation using uni-carrier photodiode", *proceedings of the 15th Inter. Symp. of Space THz Technology* 2004.
8. E.A. Michael, R. Schieder, M. Mikulics, M. Marso and P. Kordos, "Large-area traveling-wave photonic mixers for increased continous terahertz power", *submitted* 2004
9. J. Ward, E. Schlecht, G. Chattopadhyay, A. Maestrini, J. Gill, F. Maiwald, H. Javadi, and I. Mehdi, "Capability of THz sources based on Schottkey diode frequency multiplier chain", *accepted for the 2004 IEEE MTT-S International Microwave Symposium, Fort Worth, TX*, June 2004
10. A. Maestrini, **J. Ward,** J. Gill, H. Javadi, E. Schlecht, G. Chattopadhyay, F. Maiwald, N. R. Erickson, and I. Mehdi, A 1.7-1.9 THz local oscillator source", *IEEE Microwave and Wireless Components Letters*, 2003.
11. U. U. Graf, S. Heyminck, D. Rabanus, K. Jacobs, R. Schieder, J. Stutzki, "STAR: SOFIA Terahertz Array Receiver**",** *SPIE Airborne Telescope Systems II*, Vol. **4857**, 2002.
12. H.W. Hübers, S.G. Pavlov, A.D. Semenov, A. Tredicucci, R. Köhler, H.E. Beere, E.H. Linfield, D.A. Ritchie,"THz quantum cascade laser as local oscillator in a heterodyne receiver", *proceedings of the 15th Int. Symph. of Space THz Technology*, 2004.
13. P. Hartogh, "High resolution chirp transform spectrometer for middle atmospheric microwave sounding", *Satellite Remote Sensing of Clouds and the Atmosphere II, Proc. of SPIE* Vol. **3220**, p. 115-124, 1997.
14. A. Wagner-Gentner, U. Graf, R. Güsten, P. Hartogh, H.W. Hübers, M.Philipp, D. Rabanus and J. Stutzki, "GREAT Optics", submitted to *Proceedings of SPIE – Astronimical Telescopes and Instrumentation*, 2004.
15. "RPG Radiometer Physics GmbH", Birkenmaarstrasse 10, 53340 Meckenheim, Germany

Improving the Efficiency of Quasi-optical Analysis and Design of Terahertz Systems

Marcin L. Gradziel[1], David White[2], J.A. Murphy[1], S. Withington[3]

1. Department of Experimental Physics, National University of Ireland Maynooth, Ireland
2. Department of Computing, Institute of Technology, Tallaght, Dublin, Ireland
3. Astrophysics, Cavendish Laboratory, Madingley Road, Cambridge CB3 OHE

Introduction

The aim of long wavelength analysis is to understand the unique behaviour of terahertz (300 GHz - 30 THz) quasi-optical systems, and since most THz systems have small Fresnel numbers, a modal approach to analysis is appropriate. In this paper in particular we discuss the extension of a powerful approach based on Singular Value Decomposition (SVD) [1] for improving the efficiency of the application of Gaussian Beam Mode Analysis (GBMA) to complex optical systems. We compare the efficiency of the SVD approach with the overlap integral approach, and also validate the technique by comparison with test cases computed using physical optics code. This work was inspired by the need for efficient numerical schemes as part of the development of a software package for quasi-optical analysis and design of terahertz systems at NUI Maynooth (MODAL).

GBMA is particularly suited to analysing long wavelength systems and has been applied extensively in the design and analysis of both coherent and partially coherent quasi-optical systems in the millimeter and submillimeter wavebands [2]. Beam Modes can be thought of as the beam-guide analog of conventional waveguide modes, where a beam guide consists of a number of refocussing elements which ensure that the propagating beam remains quasi-collimated. The strength of Gaussian beam-mode analysis is that it is straightforward to model propagation through beam guide systems with apertures, mirrors and lenses, and build them up in a modular way, while at the same time keeping track of the evolution of the beam. Generally the source fields can be represented to high accuracy by a finite sum of only a few beam modes underlining the potential efficiency of the modal description.

However realistic optical components disturb the pure modal propagation through truncation and aberrational effects just as a step does in a waveguide. At such optical components power is scattered between modes and for a high accuracy description of beam propagation one needs to keep track of this scattering [3]. However, when there is a significant amount of power scattering between modes the number of integrations required to derive a scattering matrix in a straightforward way can be quite prohibitive. This has limited the efficiency with which GMBA has been applied to practical optical configurations.

An example of this is the calculation of Gaussian-mode scattering matrices at focussing mirrors [4]. If an off-axis mirror is treated as an inclined phase transforming plane, then it is necessary to determine the mode coefficients of the scattered field over the plane, but Gaussian-beam modes are only orthogonal over planes that are orthogonal to the direction of propagation and the direct evaluation of the scattering matrix turns out to be computationally extremely intensive. In fact many scattering matrices suffer from this kind of limitation [5]. Therefore such systems could be analysed much more efficiently if a more economical numerical method for determining the expansion coefficients over complex surfaces was available [6].

Modal Analysis

In Gaussian Beam Mode (GBM) theory a monochromatic coherent beam can be represented by a scalar field E, which can be written as a linear combination of independently propagating modes Ψ_m. The field at any plane z is then given by:

$$E(x,y,z)=\sum A_m \Psi_m(x,y;W(z),R(z)), \tag{1}$$

where W and R are beam parameters that depend on z and A_m are the mode coefficients [7]. To analyse optical systems in 3-D it is most convenient to use the Hermite-Gaussian modes $\Psi_{\mu,\nu}(x,y,z)$ of the form:

$$\Psi_{\mu,\nu}(x,y,z)=\sqrt{\frac{1}{\pi W(z)^2 \mu!\nu! 2^{\mu+\nu-1/2}}}H_\mu\left(\frac{\sqrt{2}x}{W(z)}\right)H_\nu\left(\frac{\sqrt{2}y}{W(z)}\right)\exp\left(-\frac{x^2+y^2}{W(z)^2}\right)$$
$$\times\exp\left(-jk\left(\frac{x^2+y^2}{2R(z)}\right)\right)\exp(-jkz)\exp\left(j(\mu+\nu+1)\Delta\Phi_0(z)\right), \tag{2}$$

where all the symbols have their usual significance and where $H_i(s)$ is the Hermite polynomial of order i [7]. The beam width parameter W, phase radius of curvature R and phase slippage term $\Delta\Phi_0$ are functions of position z, which is taken to be zero at a waist of the mode. The Hermite-Gaussian modes propagate through an optical system without scattering and the output field at the image plane can be reconstructed by resumming the modes using (1).

In theory, if the field E_0 is known at some reference plane z_0, the mode coefficients can be calculated by the appropriate overlap integrals of the general form:

$$A_m=\iint E_0(x,y,z_0)\Psi_m^*(x,y;W(z_0),R(z_0))\,dx\,dy\,. \tag{3}$$

Element boundaries are inherently accounted for, because the field is taken to be zero outside of the element aperture. For most applications the overlap integrals A_m have to be evaluated by numerical integration. This requires sampling of the field to be sufficiently fine to avoid numerical artefacts, such as aliasing. The minimum sampling period is given by the Nyquist's theorem ($\lambda/2$), but in most cases finer sampling is needed to obtain convergence. This means that the evaluation of the overlap integrals is computationally intensive and therefore inherently slow.

Alternative fast methods of modal decomposition are desirable for optics design and analysis tools, that would still retain the accuracy of the overlap technique. We can attempt to fit a linear combination (coefficients $\tilde{A}$) of the mode set functions Ψ_i to the known field $\boldsymbol{E}$, sampled on a limited number of points $\boldsymbol{r}_j$. In matrix formulation the approximate field $\tilde{\boldsymbol{E}}$ is given by:

$$\tilde{\boldsymbol{E}}=\begin{bmatrix}\tilde{E}(\boldsymbol{r}_1)\\ \tilde{E}(\boldsymbol{r}_2)\\ \vdots\\ \tilde{E}(\boldsymbol{r}_N)\end{bmatrix}=\begin{bmatrix}\Psi_1(\boldsymbol{r}_1) & \Psi_2(\boldsymbol{r}_1) & \cdots & \Psi_M(\boldsymbol{r}_1)\\ \Psi_1(\boldsymbol{r}_2) & \Psi_2(\boldsymbol{r}_2) & \cdots & \Psi_M(\boldsymbol{r}_2)\\ \vdots & \vdots & \ddots & \vdots\\ \Psi_1(\boldsymbol{r}_N) & \Psi_2(\boldsymbol{r}_N) & \cdots & \Psi_M(\boldsymbol{r}_N)\end{bmatrix}\begin{bmatrix}\tilde{A}_1\\ \tilde{A}_2\\ \vdots\\ \tilde{A}_M\end{bmatrix}=\Psi\,\tilde{\boldsymbol{A}} \tag{4}$$

and we determine the best approximation $\tilde{A}$ by minimising the norm of the residual $\boldsymbol{E}-\tilde{\boldsymbol{E}}$:

$$|\boldsymbol{E}-\tilde{\boldsymbol{E}}|=|\boldsymbol{E}-\Psi\,\tilde{\boldsymbol{A}}|=\inf_{\boldsymbol{A}\in\Omega_A}|\boldsymbol{E}-\Psi\,\boldsymbol{A}|\quad. \tag{5}$$

This approach, for the usual choice of the norm for the residual, reduces the problem of calculating the mode coefficients to a *linear least squares* (LLS) problem [8]. We can express it in a simple form using the Moore-Penrose pseudo-inverse Ψ^+ of the *mode matrix* Ψ:

$$\tilde{\boldsymbol{A}}=\Psi^+\boldsymbol{E} \tag{6}$$

Effective routines for solving LLS problems are readily available (e.g. LU decomposition, Gauss-Jordan elimination [1], [9]). SVD is one of the most powerful and interesting techniques that can be used to solve a LLS problem. The SVD method is based on the linear algebra theorem which states that any NxM matrix $\boldsymbol{M}$ can be written as the product of three matrices: a column-orthogonal NxM matrix $\boldsymbol{U}$, a diagonal MxM matrix $\boldsymbol{W}$, and a transpose of an orthogonal MxM matrix $\boldsymbol{V}$ [1]:

$$\boldsymbol{M}=\boldsymbol{U}\,\boldsymbol{W}\,\boldsymbol{V}^{\boldsymbol{T}}\,. \tag{7}$$

SVD allows the pseudo-inverse to be calculated as:

$$\boldsymbol{M}^+=\boldsymbol{V}\,\boldsymbol{W}^{-1}\boldsymbol{U}^{\boldsymbol{T}} \tag{8}$$

even if some of the *singular values* w_i on the diagonal of the matrix $\boldsymbol{W}$ are zero. If that is the case, the corresponding elements in the inverted matrix $\boldsymbol{W}^{-1}$ need to be set to zero. SVD is numerically stable, handles both over- and under-determined systems, and provides diagnostic information about the mode set (through the singular values) [1].

Mode set considerations

In all practical cases, we try to reduce the computational complexity of the propagation problem by representing the field using as few modes as possible. The choice of W and R are crucial in this case. Often they are chosen such that the power in the fundamental mode is maximised i.e. $|A_0|^2$. In the case of a uniformly illuminated aperture (top hat) we get W=0.891a, where a is the aperture radius. R is chosen to match the radius of curvature of the beam (i.e. infinity for a plane wave). With this choice, however, the remaining power is spread over a large number of higher order modes. Individually, they contribute little power, but all of them are required to accurately approximate the field.

The more appropriate choice of W should therefore take into account the form of the higher order modes. As the mode number increases, its spatial frequency spread is higher and hence it will perform better in modelling an edge. The choice of W should reflect this. The modes can be characterised in terms of their *effective extent*. Because of the gaussian envelope, the effective extent of the mode is finite, and is approximately given by $W\sqrt{1.5\,N}$. Figure 1 shows the mode profile and its extent for N=*10* and N=*20*.

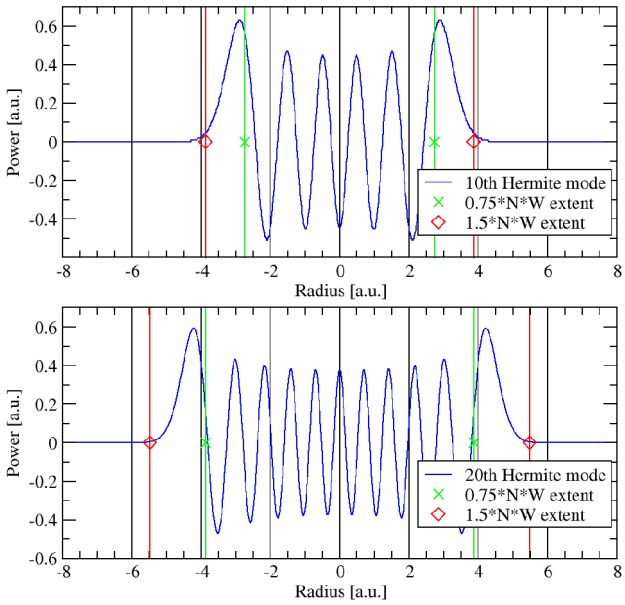

Figure 1: The effective extent of the 10th and 20th order Hermite-Gaussian modes.

To accurately reproduce the discontinuity at the aperture edge, we match the position of the last zero crossing of the mode to the extent of the aperture. If we look just at the position of the last zero crossing, the extent of the mode is approximately given by $W\sqrt{0.75\,N}$. This gives us the following rule for selecting W:

$$W = \frac{a}{\sqrt{0.75\,N}} \tag{9}$$

We have to remember however, that the actual extent of the highest order mode is $W\sqrt{1.5\,N}$ rather than $W\sqrt{0.75\,N}$. As a result, we must ensure that in any fitting routine the field is explicitly set to zero at all points outside the aperture, at least as far as $W\sqrt{1.5\,N}$. This suppresses spurious side-lobes that would otherwise emerge there.

Examples

First we will consider the modal decomposition of a top hat field of unit amplitude with an aperture of radius a = 1, in one dimension, using N = 50 modes. Figure 2 shows a comparison of the reconstruction (here using accurate overlap integrals) with W selected using both approaches discussed above.

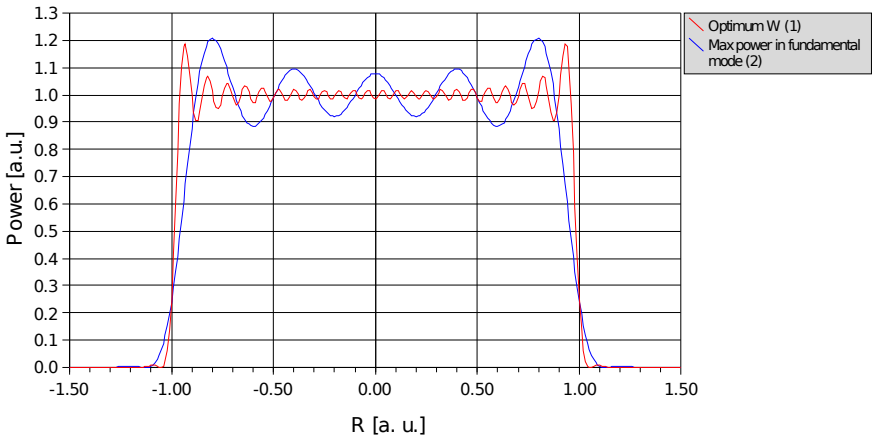

Figure 2: Top hat reconstruction using 50 modes. *W* was chosen to maximise power in the fundamental mode (i), and using mode extent matching (ii).

In figures 3 and 4 we show the results of modal reconstruction of a top hat field and a corrugated horn field, respectively. The aperture radius was 2.5 mm. The decomposition was done using both the overlap integral approach and the faster SVD technique. Selected mode amplitudes are also presented.

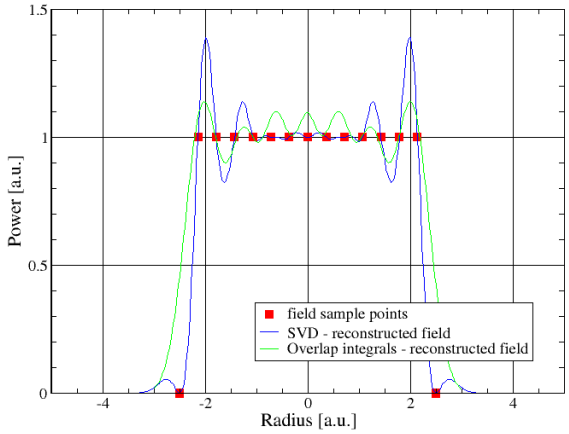

Mode μ	ν	Overlap $\|A_{\mu\nu}\|^2$	SVD $A_{\mu\nu}\|^2$
0	0	3.74170	3.60405
0	2	1.86868	1.80212
0	4	1.38604	1.34569
0	6	1.08402	1.06871
0	8	0.73789	0.73270
0	10	0.30206	0.28936
0	12	0.01705	0.02069
0	14	0.03572	0.03989
2	2	0.92413	0.89816
4	4	0.37946	0.40652
6	6	0.00737	0.02618
8	8	0.01131	0.00635
10	10	0.00559	0.00287
12	12	0.00236	0.00401
14	14	0.00049	0.00315

Figure 3: Comparison between SVD and overlap integral calculations: top hat field reconstruction. Selected non-zero mode coefficients are listed in the table.

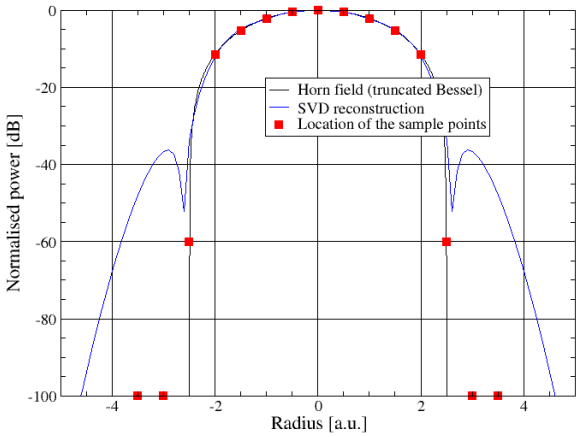

Mode μ	ν	Overlap $\|A_{\mu\nu}\|^2$	SVD $A_{\mu\nu}\|^2$
0	0	4.04409	4.04388
0	2	0.55084	0.55008
0	4	0.04844	0.04762
0	6	0.00026	0.00054
0	8	0.00302	0.00385
2	2	0.03231	0.03163
4	4	0.00155	0.00284
6	6	0.00022	0.00059
8	8	0.00004	0.00002

Figure 4: Corrugated horn mouth reconstruction and selected non-zero mode coefficients for 15 modes using SVD and overlap approaches.

Quasi-optical analysis

SVD approach to modal field decomposition can be used in quasi-optical analysis of optical systems in the terahertz region of the spectrum. In its simplistic version, where only one element is considered at a time, the method can be summarised as follows:

- The mode set to be used to decompose the source field needs to be determined. This has been discussed earlier in this paper. It is worth mentioning however that in the case of multi-element optical systems system-wide factors (optical throughput of the system) can be taken into the account to optimise the mode set.
- Source field decomposition using SVD approach.
- Propagation of the source field to the next optical element (mirror) using simple propagation characteristics of the Gaussian Beam Modes. This can be done very easily since only the mode parameters W and R evolve. Mode amplitudes are unchanged.
- Re-composition of the field at the next element. This element becomes the new source and the whole loop can be repeated.

We keep track of *W* and *R* of the fundamental mode to aid the mode set selection. Only these parameters and the size the current element (aperture) are used in the selection of the mode set. The throughput of the system is not considered (we take one element at a time). The method itself is general, and can be applied to both on-axis and off-axis elements. The determination of the optimal mode set however, is more difficult for off-axis systems.

Test systems

To test the SVD approach to quasi-optical system analysis, we applied it to the simple one- and two- ellipsoidal mirror test cases. Curvature of the mirrors was chosen to be significant to emphasise some of the potential problems. The simulated feed was a corrugated conical horn with an aperture radius of 2.5 mm and a slant of 15.4 mm. The wavelength chosen for the tests was 0.625 mm. The polarisation was perpendicular to the plane of the system (relevant for the benchmark PO calculations, see below). Other details of the geometry of the test systems are shown in figure 5.

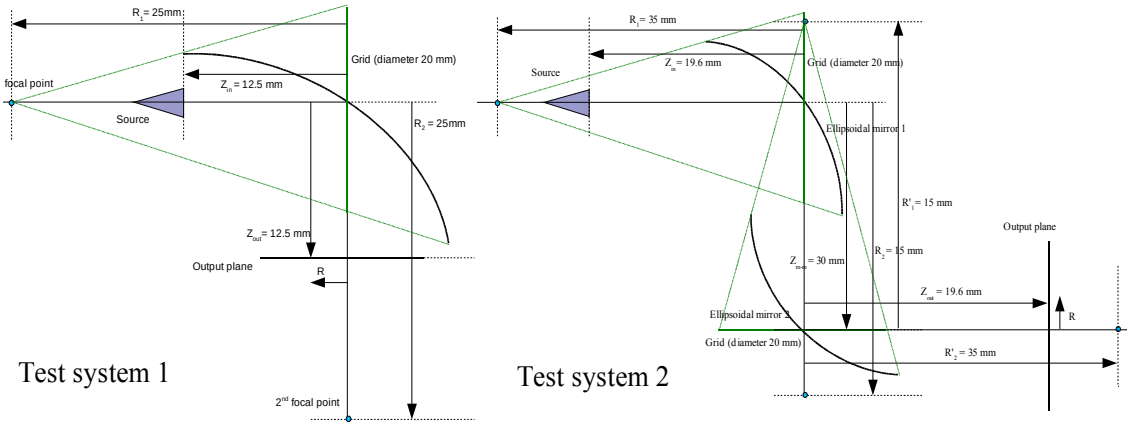

Figure 5: Geometry of the test cases. Please note that the systems are not drawn to scale.

The results of the SVD analysis of the test cases are shown in figures 6-9, in terms of two orthogonal cuts across the selected output plane (shown in the figures). Several combinations of the following parameters of the SVD method were tested:

- number of field sampling points: 40x40, 20x20, 10x10,
- number of modes used for decomposition: 10 or 15, and
- number of additional zero field points beyond the element (expressed in terms of the *padding* parameter – extent of the added part of the grid as a fraction of the extent of the main element sampling grid).

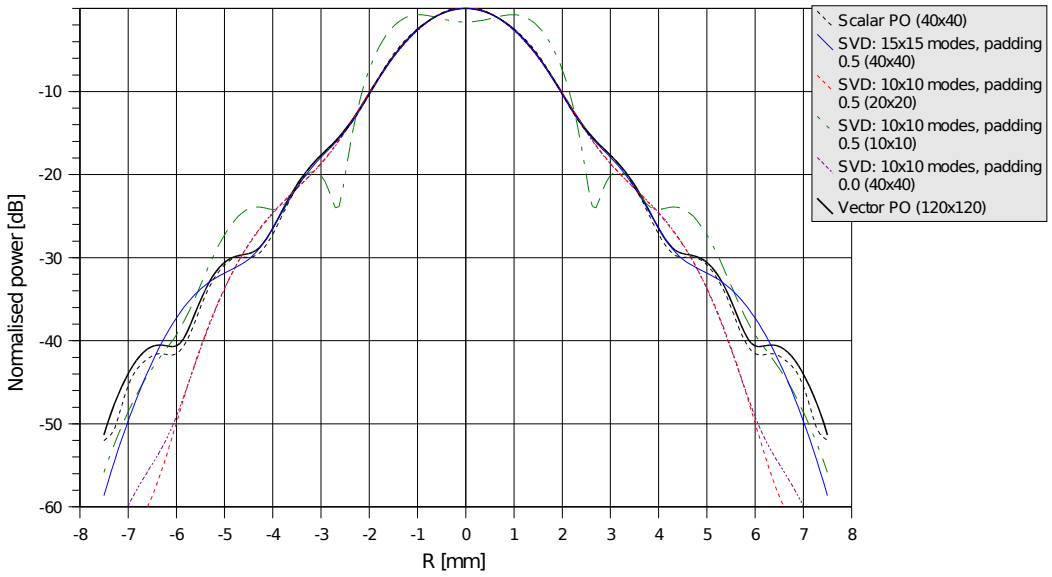

Figure 6: Symmetric cut across the output plane of the first test system (single ellipsoidal mirror). The power is normalised to the vector PO result at the centre. In the legend, the numbers in brackets are the mirror grid sizes in points. The field at the source mouth was always represented on a 24x24 main grid.

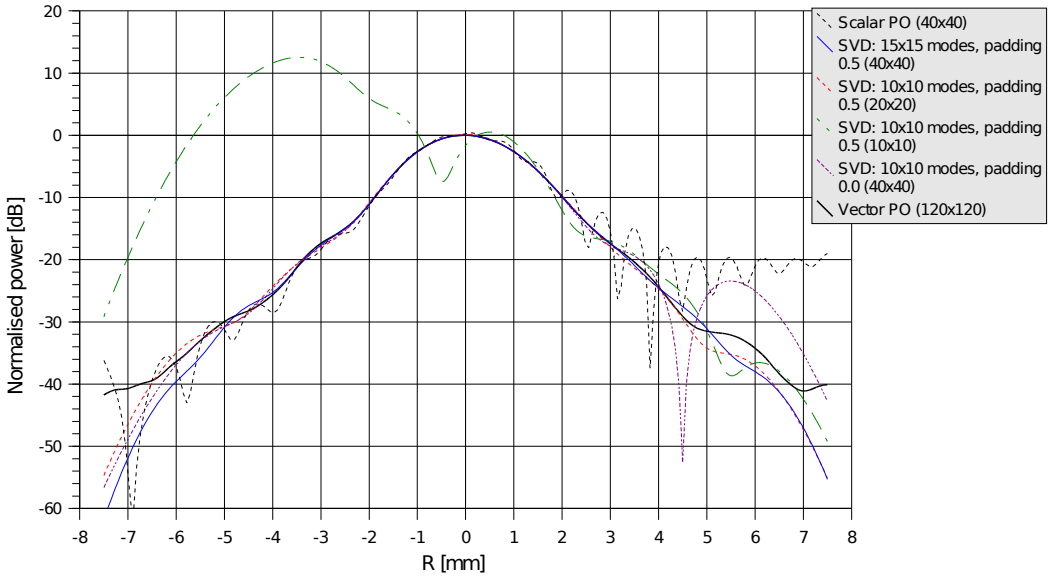

Figure 7: Asymmetric cut across the output plane of the first test system (single ellipsoidal mirror). Other details as in figure 6.

The SVD results were compared to results of Physical Optics (PO) calculations, in two versions:

1. Simplified scalar approach (Fresnel-Kirchhoff diffraction, polarisation not accounted for) on a 40x40 grid. These results were included as an example of an approximate PO calculation (that could be used in an interactive design package). The calculation time was comparable to the most computationally intensive SVD case tested here (15x15 modes on 40x40 grid with 0.5 padding).
2. Full vector approach (typical PO [10], as implemented in GRASP8 [11]). These results, calculated on a bigger grid (120x120 PO points, which is in our case big enough to ensure convergence), constitute a benchmark the other results can be compared to.

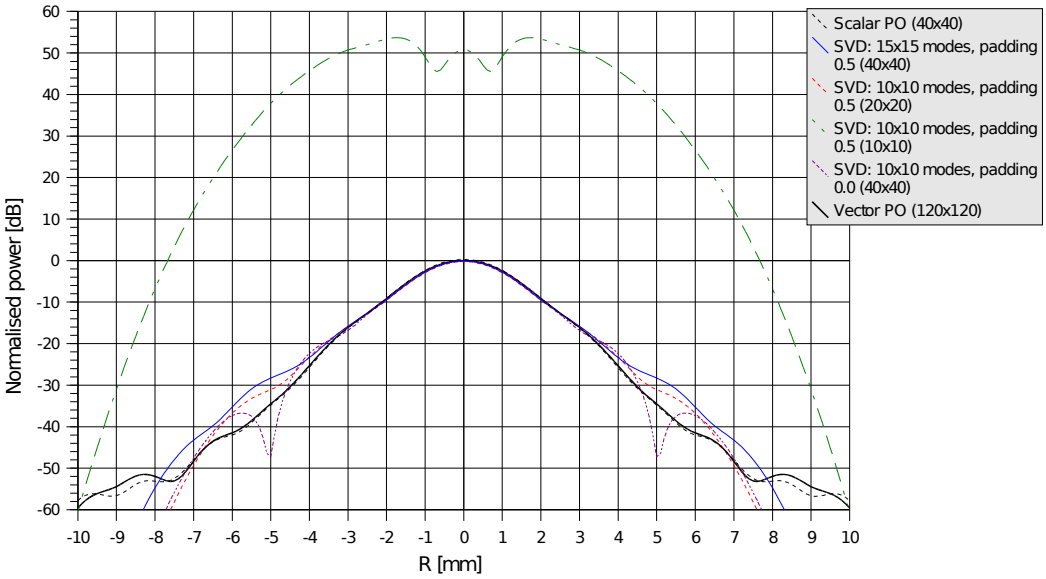

Figure 8: Symmetric cut across the output plane of the second test system (two ellipsoidal mirrors). Other details as in figure 6.

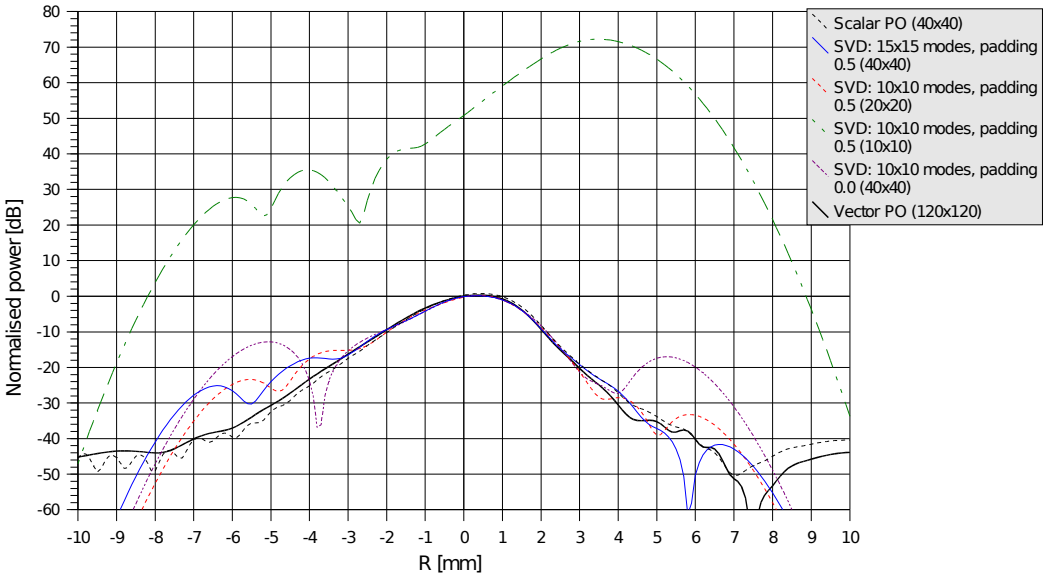

Figure 9: Asymmetric cut across the output plane of the second test system (two ellipsoidal mirrors). Other details as in figure 6.

All results were generated using MODAL, a design and analysis package being developed in-house in Maynooth [12]. This allowed all methods to be applied using exactly the same definition of geometry of the system. The accuracy of the vector PO engine in Modal favourably compares to that of GRASP8.

Analysis of the test results

Several general observations can be made if one analyses the SVD results:

- Apart from the 10x10 grid case, the SVD results agree rather well with the accurate PO calculation, down to -20 dB. The big advantage of the SVD method is its speed - here SVD calculations were a factor of 20-1000 faster (depending on the parameters) than the vector PO calculation.

- The SVD approach can yield a completely wrong result, if the field sampling is too coarse. This becomes a real problem if the phase changes quickly across the mirror, because aliasing effects can lead to physically incrrect results. In our test calculations the 10x10 grid case was included specifically to illustrate this issue. In other systems such grid size can be perfectly adequate.
- SVD results are much more regular than the scalar PO results, and do not suffer from spatial aliasing for small grid sizes (apart from 10x10 case, as discussed above).
- Increasing the number of modes (10x10 -> 15x15) to some extent improves the field reproduction, but gains are not very significant here.
- Adding zero field points around the main grid slightly improves the reproduction of the field in the centre of the beam, and also reduces the appearance of extra side-lobes.

Conclusions

Fast methods based on SVD Gaussian Beam Mode decomposition are potentially a very useful tool for analysing quasi-optical systems. There are many potential problems however that need to be studied in greater detail, before SVD approach to modal analysis reaches sufficient maturity to be considered a reliable method of quasi-optical analysis. The aspects of the SVD method that we aim to address in the near future include:

- optimisation of the mode set,
- minimum density of field sampling points,
- weighting of field sampling points in the fitting procedure,
- optimal number, and distribution, of the added zero field points,
- handling of polarisation.

Our view is that significant progress can be made in these areas. However, even at this early stage of its development, the SVD approach is useful in practical applications. In particular it can be implemented in designer tools, where it can be used to quickly generate useful results at the system design stage.

Acknowledgments

We would like to thank Science Foundation Ireland for supporting this work financially.

References

[1] Björck, Å., *Numerical Methods for Least Squares Problems*, Society for Industrial and Applied Mathematics, Philadelphia 1996
[2] S. Withington, S., Yassin, G. , and Murphy, J. A. 2001, *Dyadic Analysis of Partially Coherent Submillimeter-Wave Antenna Systems*. IEEE Transaction on Antennas Propagation, 49, 1226-1234
[3] Murphy, J. A., Withington, S., and Egan, A. 1993, *Mode conversion at diffracting apertures in millimetre and submillimeter-wave optical systems*. IEEE Trans. Microwave Theory Techniques, 41, 1700-1702
[4] Withington, S., Murphy, J.A., Isaak, K.G. 1995, *Representation of mirrors in beam waveguides as inclined phase-transforming surfaces*. Infrared Physics & Technology, 36, 723-734
[5] Murphy, J.A., Withington, S. 1996. *Perturbation analysis of Gaussian-beam-mode scattering at off-axis ellipsoidal mirrors*. Infrared Physics & Technology, 37, 205-219
[6] Withington, S., Hobson, M. P., Berry, R. H. 2004. *Representing the behavior of partially coherent optical systems by using overcomplete basis sets*. JOSA A, 21, 207-217
[7] Goldsmith, P. F., *Quasioptical Systems. Gaussian Beam Quasioptical Propagation and Application,* IEEE Press, New York 1997
[8] Usmani, R. A., *Applied Linear Algebra*, Marcel Dekker, Inc., New York and Basel 1987
[9] Radhakrishna Rao, C., and Toutenburg, H., *Linear Models. Least squares and alternatives*. Springer-Verlag, New York 1999
[10] Diaz, L., Milligan, T., *Antenna Engineering Using Physical Optics: Practical CAD Techniques and Software*, Artech House 1996
[11]http://www.ticra.com/swindex.htm
[12]http://www.may.ie/academic/physics/modal/modal.html

Instrument for Measurements of HEB Receiver Noise Temperature with Cold and Hot Loads Internal to the Cryostat

Ric Zannoni, Sigfrid Yngvesson
Department of Electrical and Computer Engineering
University of Massachusetts, Amherst MA

A significant obstacle to the accurate measurement of detector noise temperature is the effect of optical losses. Attenuation in warm components such as beamsplitters, focusing elements, and the laboratory atmosphere adds to the measured noise temperature. Traditionally these losses have been accepted as part of the measurement or estimated so a corrected value can be used. However, as detector performance improves, the contribution of optical losses becomes a significant part of the measured value. Thus, a new instrument that suppresses optical loss is needed. SwitCHLE, a device under development, addresses these concerns.

Most of SwitCHLE's components are located in the interior of the cryostat. The LO source is the only exterior component which enters through a 300K window on the cryostat wall. The LO then passes through a 4K attenuator. The RF originates from one of two sources within the cryostat, a 300K source on the wall or a 4K source at the cold plate. An electromechanically-actuated mirror switches between the sources. The RF and LO are combined in a 4K beamsplitter and then go on to the detector. The detector is housed within its own 4K shield, which is fitted with a 4K filter. The full SwitCHLE design has an integral controller for chopped measurements up to 1 hertz. Presented here is a prototype using manual control and a preliminary comparison of SwitCHLE measurements to those obtained using an external measurement system.

Modal Analysis and Experimental Study of High-Order Mode Contribution to Standing Waves in Quasi-Optical Systems

Willem Jellema[1,4], Stafford Withington[2], Neil Trappe[3], J. Anthony Murphy[3], Wolfgang Wild[1,4]

[1]Space Research Organization of the Netherlands (SRON), P.O. Box 800, 9700 AV Groningen, the Netherlands
[2]Cavendish Laboratory, Madingley Road, Cambridge CB3 0HE, United Kingdom
[3]National University of Ireland Maynooth, Co, Kildare, Maynooth, Ireland
[4]Kapteyn Institute, P.O. Box 800, 9700 AV Groningen, the Netherlands

In many submillimeter-wave optical systems performance is in some way affected by the presence of standing waves. Usually these effects are studied empirically or only modeled to first-order by assuming a quasi-sinusoidal variation with distance and wavelength. In this paper we present an analytical technique to calculate the coupling between two corrugated horns including the total transmission and reflection properties. In our model we have combined the waveguide mode matching technique with a Gaussian beam mode description of the free space propagation. We illustrate the approach for the case of two coupled corrugated horns as the distance between them is varied. We furthermore present experimental test results confirming that multiple reflections do not always result in a classical periodic standing wave pattern. In particular when the horns are close together and the fields are not well matched, high Q cavity effects are observed resulting in irregular standing wave patterns. These cavity effects can be attributed to high-order modes which get trapped between transmitting and receiving horn. We finally discuss the consequences of our observations for a few examples of typical quasi-optical arrangements illustrating that the presented effects can have important consequences for submillimeter-wave optical systems.

Integrated submillimeter system

Dr. Anders Emrich, Omnisys Instruments AB
Gruvgatan 8, 41230 Västra Frölunda, Sweden
ae@omnisys.se, Tel. +46 31 7343401, Fax +46 31 7343429

ABSTRACT

Traditionally, many radiometer systems have been designed and developed in collaboration between several groups, often residing in different countries. The reasons are obvious, but there are disadvantages, the major one is perhaps to achieve a high level of system integration and optimization.

Omnisys has started a project, funded by the Swedish National Space Board, with the goal to demonstrate the performance of a complete sub-millimeter radiometer, designed as an integrated instrument. It will be demonstrated in lab environment, but capable of operation in balloon, or low cost satellite environment. The radiometer will cover 320-360 GHz and incorporate high resolution as well as broadband spectroscopy capability. This scientific requirement specification is very similar to Mambo (radiometer for Mars), VEMEX (radiometer for Venus) and STEAM (multibeam radiometer for aeronomy).

To our knowledge, the ODIN payload is the only frequency agile submillimeter radiometer in space, but this system will show much improved bandwidth coverage, while providing state of the art performance (for non cryogenic systems). The spectrometer will be able to cover both the Herschel/HIFI high resolution and wide bandwidth specifications, with a power budget of less than 10 W and mass of 600 grams.

SYSTEM

The radiometer consists of three sections; the front-end block, the local oscillator subsystem and the spectrometer back-end. The front-end is based on a VDI mixer block and passive doublers, together with a LNA (Gain 50 dB and NF 2 dB). The local oscillator chain is based on a synthesized YIG source, followed by active multipliers and amplifiers. The spectrometer back-end consists of four spectrometer blocks, covering a bandwidth of 4 GHz with 4096 channels.

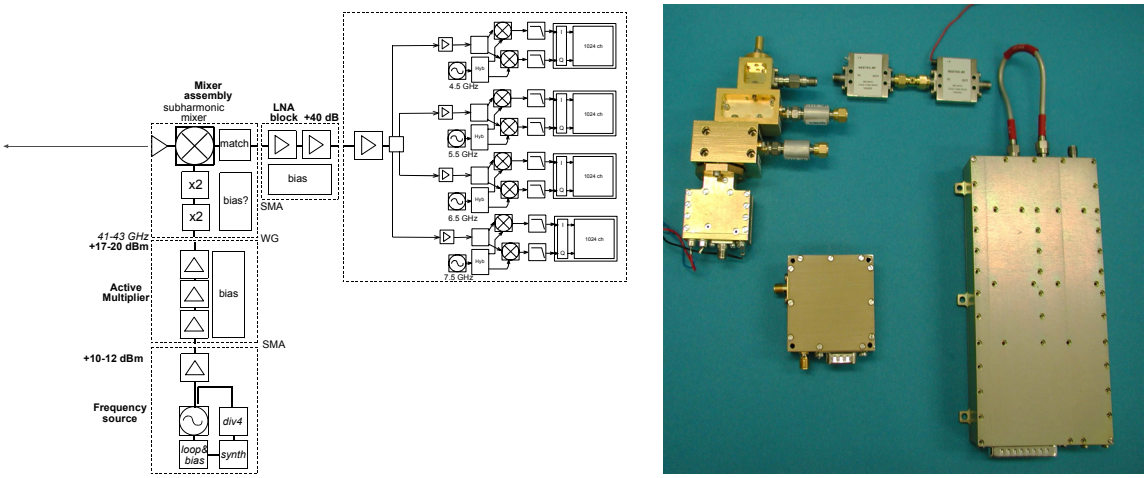

Fig 1a an 1b. The radiometer block diagram on the left, with physical blocks on the right.

Function and performance:

Input frequency:	300-380 GHz
T_{sys}:	2000 K
IF bandwidth:	2-18 GHz
Processed bandwidth:	4 GHz
Resolution:	1 MHz - 10 MHz
#channels:	4096
Mass:	1.2 kg
Power consumption:	5-13 W

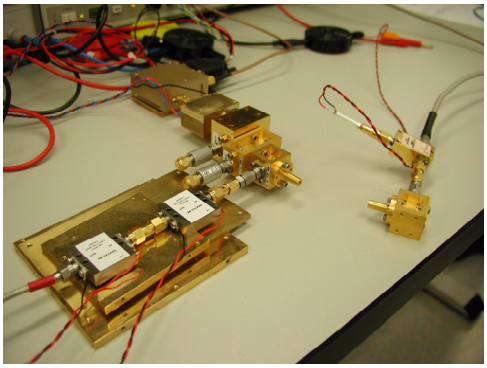

ACTIVE MULTIPLIER

The active multiplier block is based on one multiplier MMIC and one power amplifier, covering the frequency band of 33-45 GHz. The integrated bias supply allows for simple system integration, as well as providing local protection as filtering functions.

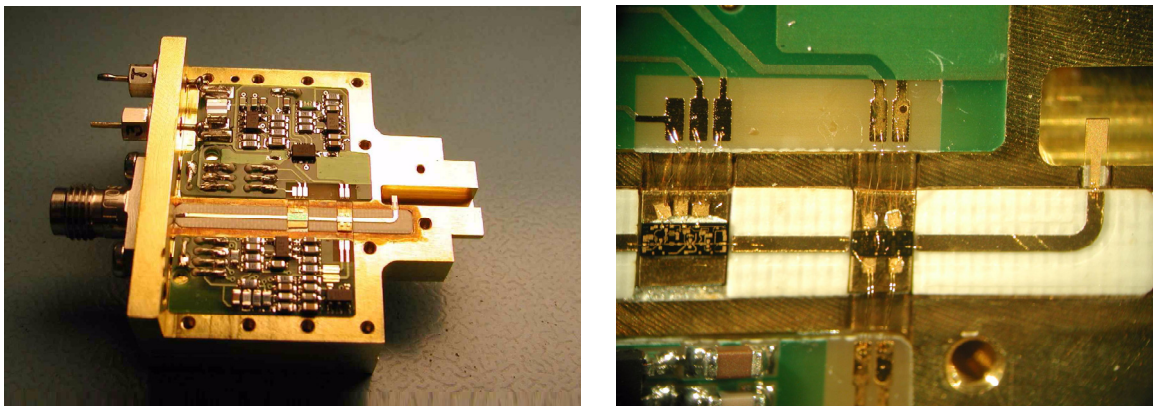

Fig 2a and 2b. Active multiplier block with the cover of to the left, and close up of the MMIC's on the right.

Input frequency:	8-11 GHz tested
Output frequency:	32-44 GHz tested
Output power level:	22 dBm (max)
Power supply:	1600 mW
Mechanical:	40x38x18 mm

FREQUENCY SOURCE

The frequency synthesizer/source design can be configured for output frequencies between 2-16 GHz, with resolutions of 0.1-1 MHz, and is based on a phase locked custom YIG oscillator. The IntRad configuration covers 10-11 GHz with 1 MHz resolution.

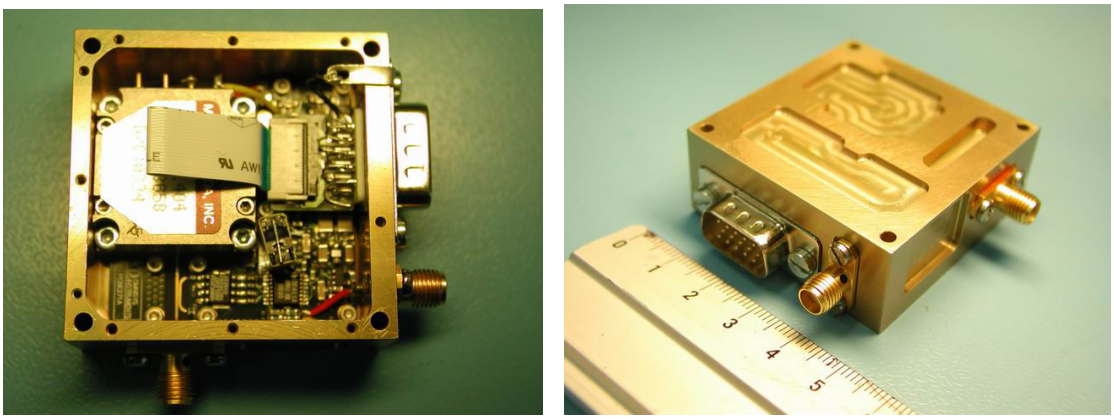

Fig 3a and 3b. The frequency source.

Output frequency:	2-16 GHz (10-11 GHz tested)
Output power level:	10 dBm
Power supply:	800 mW
Mechanical:	49x48x21 mm
Mass:	116 gram
Phase noise:	-113 dBc/Hz @ 100 kHz

SPECTROMETER

The spectrometers have been through a tremendous development over the last decade. The correlator chip set power consumption has been reduced by a factor of 3600 in one decade by Omnisys, and it is a factor of 25 better than current US and French designs. On system level, the bandwidth per chip set has been increased with a factor of 100. However, the spectrometer does not only rely on the correlator core, the complete spectrometer must be designed and developed to fulfill the end user requirements, and the complete spectrometer must be optimized together.

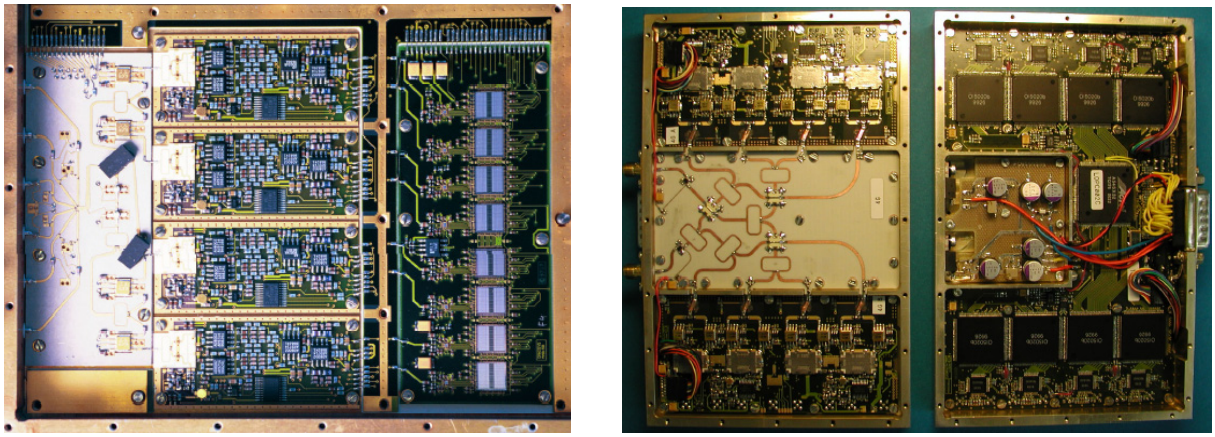

Fig 3a and 3b. The ODIN spectrometer on the left and the TELIS spectrometer to the right.

	ODIN (SATELLITE):	**TELIS (BALLOON)**	**IntRad (demo):**
Bandwidth:	100-800 MHz	2x 2 GHz	0.1-6 GHz
resolution:	0.13-1.1 MHz	2 MHz	0.01-1 MHz
mass:	1050 grams	950 grams	700 grams
size (mm):	220x180x30 mm	170x210x35 mm	152x77x24 mm
power:	18 W	20 W	10.2 W
basic technology	two full custom ASIC's	two full custom ASIC's	two full custom ASIC's
packaging:	Chip on board and parylene	Plastic QFP	MCM
use:	aeronomy & astronomy	aeronomy	demonstration
note	2 in orbit since february 2001	2 will fly in 2005	demonstration

The new spectrometer is based on four spectrometer modules, each covering bandwidths between 10 MHz-1.5 GHz, with center frequencies between 1-12 GHz. For the resolution, each module is software controlled to use between 128-1024 channels. For the IntRad project, the spectrometer covers the 4-8 GHz band. There are several configurations that will reduce the power consumption from the nominal 10 W, even down to less than 5 W.

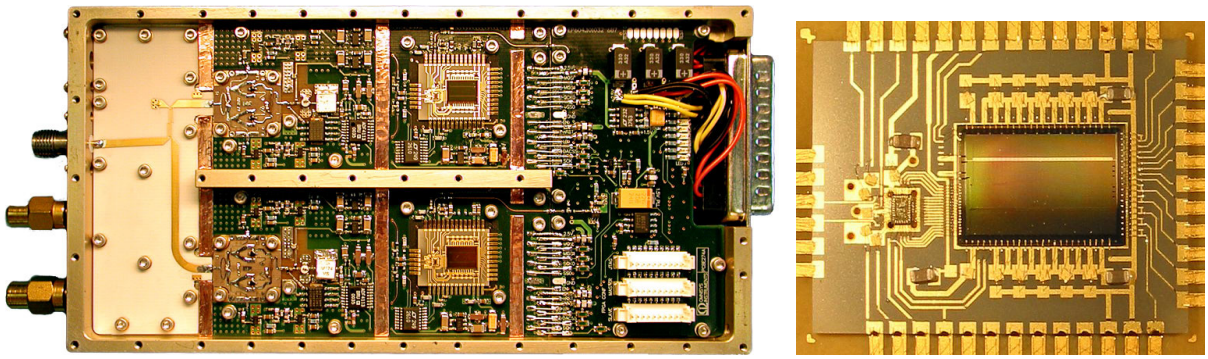

Fig 4. IntRad spectrometer with one lid removed on the left and a close up of the correlator MCM on the right.

STEAM

STEAM is a concept that is studied by a team from Sweden, France, Canada and the UK. It is a 8-16 beam, 320-360 GHz limb scanning mission with 8 GHz / 512 channel spectrometers for each beam.

For the STEAM project, it is has been found that it is possible to provide a 16 beam receiver system instead of a single receiver, by removing the cryostat and operate in ambient temperature, with improvements in mass, size and power budgets. This further shortens development time as well as system integration efforts by a large factor, and for space projects: **Time = cost.** This makes the 8-16 beam system lower cost than the single beam cryostat system.

Major features

- Multi-beam (simplified optics)
- Developed as an integrated instrument
- 8-16 front-ends at 320-360 GHz, DSB
- 8 front-ends at 490-505 GHz, DSB ?
- 8x8 GHz + 8x4 GHz = 96 GHz of spectrometers
- (HIFI/Herschel = 8 GHz)
- ambient temperature instrument
- 2000 K Tsys
- less than 10 kg, 60-70 W
- on-board, near real-time signal processing (Linux)

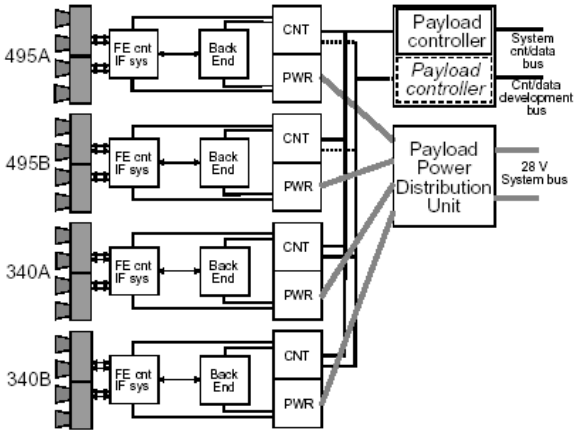

INTERSTELLAR PROBE RADIOMETERS

There has been several submillimeter radiometers proposed for interstellar probes, Mambo, Vemex and others. If we look at possible realization for the Mambo (Mars) radiometer, a fully redundant system is shown below. The major lines that will be covered are: CO at 345.796 GHz, 13CO at 330.588 GHz, H2O at 325.153 GHz, HDO at 335.395 GHz, O3 at 326.901 GHz and H2O2 at 326.981 GHz.

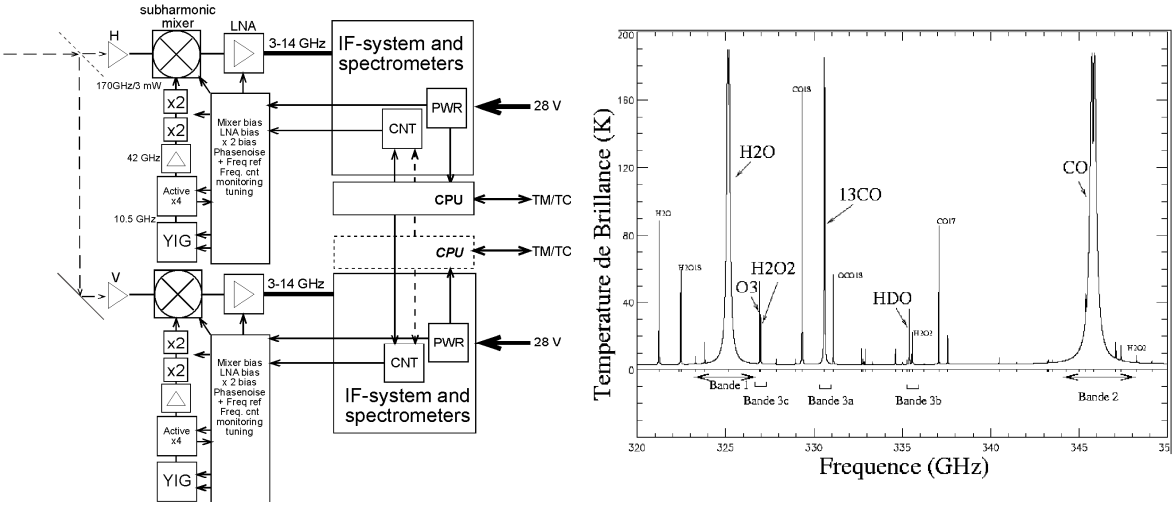

Fig 7. A possible Mambo realization is shown to the left, and the frequency coverage to the right.

DEMONSTRATOR SYSTEM CONSIDERATIONS

The radiometer system requirements enclose several aspects apart from the obvious ones like frequency coverage etc. Other important aspects are performance issues like stability and calibration, with solutions including thermal stabilisation and hot&cold load implementations. Several solutions have been investigated, but the selection will have to wait until the platform and the application have been decided.

The design has targeted on a radiation total dose tolerance of 30 kRAD+ with latch-up free operation. The system allows for graceful degradation, following the ODIN radiometer design philosophy. As for vibration, chock and thermal cycling tolerance, the requirements for the ODIN project has been used as a baseline for the design.

The power and control system for the radiometer is developed in a parallel project at Omnisys. The power system is more advanced than a collection of simple DC/DC converters, including protection mechanism as well as monitoring and control functions. The control system is based on a 32-bit CPU, running Linux, with several design features used to make the design compatible with the space environment. The mass of the power and control systems should be much less than 800 grams, the power system would operate with 75-80% efficiency and the CPU should end up in the 2-4 W class, depending on configuration, type of system interface etc.

The 32-bit CPU with the correct software promise to provide between 10-50 data compression compared with standard compression techniques, i.e. potentially providing an order of magnitude science output improvement, if the instrument is data link limited. The idea is to let the scientist and instrument providers provide an instrument specific data compression algorithm. This will of course be flexible, on and board software update capability will be one of the main features in the design.

The radiometer can also be operated as a stupid subsystem without the control cpu, as all blocks use simple serial interfaces for control and readout.

In addition, the radiometer will also need some optical interface to the observed object. This could be based on a lens or horn, or more advanced antenna solutions. This will also be determined on a platform&application basis.

CONCLUSION

We have demonstrated a complete, frequency agile submillimeter radiometer, including a wide bandwidth spectrometer in the 1 kg / 10 W class. This is an improvement in mass and power consumption with an order of magnitude, extremely important for space projects. Omnisys view is that it is vital that the SpaceTHz community looks at the cost and complications of using THz technology in Space.

The 4-8 GHz/4096 channels spectrometer specification can easily be modified for other requirements, i.e. using several different sub-bands with different resolutions, implementing flexible bandwidth/resolution combinations etc.

The front-end shows a bandwidth of 300-380 GHz, without any bias or mechanical tuning operation, just utilizing a simple digital command.

The LO source shows extremely good phase noise in combination with low mass and power consumption. The design covers any frequency between 2-16 GHz. The combination of the source and active multiplier block produce a 33-45 GHz, 20 dBm synthesizer function with a power budget of 2.5 W and a mass budget of 250 grams.

All parts have been designed with space requirements being considered. This includes environmental aspects, i.e. radiation, vibration etc. as well as performance aspects such as stability. One of the major design parameters has been to allow for simple and fast system integration and validation testing on the spacecraft.

The 1 kg class radiometer also makes the instrument compliant with interstellar probes. We have then the tradeoff between an ambient temperature radiometer in orbit around Mars or Venus, and a cryogenic radiometer in our lab.

Regarding Atmospheric and Mechanical Stability Requirements of (LO-Pumped) Mixers

J. W. Kooi[1], R. Schieder[2], J. Baselmans[3], M. Hajenius[4], A. Baryshev[5], R. Hesper[5]

[1]California Institute of Technology, MS 320-47 Pasadena, California 91125, USA.
[2]Physikalisches Institute, Universität zu Köln, Germany.
[3]SRON, Sorbonnelaan 2, 3584 CA, Utrecht, The Netherlands.
[5]Netherlands and Faculty of Applied Sciences, Delft University of Technology,
Lorentzweg 1, 2628 CJ Delft, The Netherlands
[4]Kapteyn Astronomical Institute, Univ. Groningen / NOVA / SRON,
Landleven 12, 9747 AD Groningen, The Netherlands

Abstract

In this paper we discuss atmospheric and mechanical stability requirements of heterodyne mixers. Though the analyses is general to any heterodyne system, we are particularly interested in "short" wavelength's (≤ 200 μm) mixers where instabilities due to atmospheric and mechanical path length fluctuations become significant. We hope to draw attention to the stringent mechanical and atmospheric tolerance requirements of (HEB) mixers operating at terahertz frequencies.

Keywords

Hot electron bolometer (HEB) mixer, atmosphere and mechanical stability, standing waves, terahertz frequencies, Allan variance method, continuum vs. spectroscopic measurements, and LO power fluctuations.

I. Introduction

At submillimeter and terahertz frequencies the required LO power is typically coupled to the mixer by optical means. This is regardless of mixer type, e.g. waveguide or quasi-optical. LO injection is often performed by a thin beamsplitter that acts as a directional coupler, though it is also possible to use a Martin-Puplett, Fabry-Perot interferometer, or a narrow band Etalon beam combiner. Typically, the submillimeter or teraherz heterodyne mixer and LO source (be it a FIR laser or solid state LO) are separated spatially with air as the medium between the two. Due to physical constraints, the mixer and LO source have a finite input return loss. Inevitably, the LO and RF reflected signals generate a standing wave in the telescope and LO path cavity. It is the standing wave in the LO-mixer path that we concern ourselves with in this paper. As the LO-mixer path length changes, be it due to air or mechanical fluctuations, the standing wave between the two will change in amplitude and modulate the LO signal. In turn this causes short and long term gain instability (1/f noise and drift) at the IF output of the mixer. Hence the concern.

II. LO path length loss

If the LO Electric field propagating in the z direction is described as

$$E_{lo} = E_{lo}(0) \cdot e^{-\gamma z} \cdot e^{j\omega t} \tag{1}$$

TABLE I
OPACITY AND PATH LENGTH VARIATION FOR A 1 METER COLUMN OF AIR.

P_{atm}=990 mBar, T=29 °C, and relative humidity 30 %.

Parameter	**1.519 THz**	**1.544 THz**	**1.630 THz**
Opacity (np)	0.0642	0.1351	0.3529
Change in optical path length, ΔL (μm)	41.5	47	83

where γ is the complex propagation constant $\alpha + j\beta$. Then the time averaged power density can be found as

$$P_{lo} = P_{lo}(0) \cdot e^{-2\alpha z} \tag{2}$$

α is the opacity/meter, and Plo(0) the peak LO power at z=0 meters.

The opacity and change in optical path length in a 1 meter column of air was calculated by Juan Pardo [1]. Here we define ΔL as the path length increase due to water vapor in a 1 meter column of air. In the case of turbulent air, it is not the absolute path length we concern ourselves with, but the variation in ΔL. The conditions Pardo used were as follows: Atmospheric pressure 990 mBar, temperature 29 °C, and relative humidity 30 %.
The change in optical path length due to the refractive index (n) of air is

$$\Delta L = (n-1) \cdot z \tag{3}$$

so that n=(z+ΔL)/z, which for z=1 meter equals 1+ΔL. Uncertainty in opacity is estimated to be no more than 5%. The LO signal attenuation per meter of air is therefore

TABLE II
LO SIGNAL ATTENUATION / METER OF AIR

Parameter	**1.519 THz**	**1.544 THz**	**1.630 THz**
Attenuation (dB)	0.557	1.174	3.066

III. STANDING WAVES IN THE LO-MIXER PATH

Aside from the above mentioned atmospheric attenuation of the LO power, there will also be a LO induced standing wave present between the mixer and (FIR-laser or solid state) LO source. This is due to non-zero reflections at the mixer and LO ports. It is of interest to access the sensitivity of LO power fluctuation to small changes in path length by, for example, atmospheric turbulence and/or mechanical instability in the setup. Following Schieder & Goldsmith analyses [2] [3], we define the incident LO power on the mixer as:

$$P_{lo} = |r_{bs}|^2 \cdot P_{lo}(0) \cdot A_i(\nu_{lo}) \tag{4}$$

where $|r_{bs}|^2$ is the beam splitter power reflection coefficient, $P_{lo}(0)$ the incident LO power, and $A_i(\nu_{lo})$ the Airy function that describes the fractional transmitted power ($|T|^2 = I_t/I_0$). From literature, $A_i(\nu_{lo})$ equals:

$$A_i(\nu_{lo}) = \frac{1}{1 + Fsin^2(\frac{\delta}{2})}, \qquad \delta = \frac{4\pi nz}{\lambda} \tag{5}$$

where n is the refractive index of air, and F the finesse coefficient of the mixer - LO cavity.

$$F = \frac{4|r|^2}{(1-|r|^2)^2} \tag{6}$$

$|r|^2$ represents internal reflections, in this case the mixer - LO cavity. Rewriting Eqn 6 to include loss, we substitute $r \to re^{-\alpha z}$ so that

$$F = \frac{4|r|^2 e^{-2\alpha z}}{(1-|r|^2 e^{-2\alpha z})^2} \tag{7}$$

Now substituting Eqn 7 into Eqn 5, and expressing the Airy function in terms of the the propagation constant β gives:

$$A_i(\nu_{lo}) = \frac{(1-|r|^2 e^{-2\alpha z})^2}{(1-|r|^2 e^{-2\alpha z})^2 + 4|r|^2 e^{-2\alpha z} sin^2(\beta nz)} \tag{8}$$

And finally, expressing $|r|^2$ in terms of the mixer reflection coefficient $|r_m|^2$, the LO reflection coefficient $|r_{lo}|^2$, and the beam splitter reflection coefficient $|r_{bs}|^2$

$$A_i(\nu_{lo}) = \frac{(1-|r_{bs}|^2\sqrt{|r_m^2 \cdot r_{lo}^2|}e^{-2\alpha z})^2}{(1-|r_{bs}|^2\sqrt{|r_m^2 \cdot r_{lo}^2|}e^{-2\alpha z})^2 + 4|r_{bs}|^2\sqrt{|r_m^2 \cdot r_{lo}^2|}e^{-2\alpha z} sin^2(\beta nz)} \tag{9}$$

Looking at Eqn. 9, we see that the Airy function (standing wave interference pattern between LO and mixer) has a ripple period of $\beta nz = \pi$. In sections V and VI we examine the importance of tuning to the peak of the LO-Mixer cavity standing wave ($\beta nz = 0,\ \pi,\ 2\pi, \cdots$), rather than on steep slope ($\beta nz = \pi/4,\ 3\pi/4, \cdots$).

IV. Estimate of allowed LO Power fluctuations

To get an estimate of the level of LO power fluctuation that may be tolerated, one has to consider the sensitivity of the mixer IF output power with respect to the input LO power (dP_{if}/dP_{lo}). Assuming that the mixer acts as a standard square law detector, $Acos(\omega_s t) \cdot Bcos(\omega_{lo} t)$, the IF output will be proportional to changes in the input signal ($V_{if} = ABcos(|\omega_s \pm \omega_{lo}|)t$). If tiny LO fluctuations (am noise) modulate the IF output, they will be manifest themselves at the output of the mixer as instability. This is certainly true in standard total power (continuum) measurements, when for example performing a Y-factor measurement (Phot/Pcold). Under these conditions the sensitivity, and stability, of essentially all HEB and SIS mixer to date are measured. If however LO power instability is correlated across the entire IF band (for example due to microphonics in the LO beam-splitter) then a spectroscopic measurement (Eqn. 10) maybe more meaningful. In this case

total power measured in two (or more) statistically uncorrelated sub-bands in the IF are differenced, and LO induced fluctuations common to both channels subtract away.

$$z_i = \frac{1}{\sqrt{2}}\left[\left(\frac{x_i}{< x >} - \frac{y_i}{< y >}\right)+1\right]\cdot\frac{< x > + < y >}{2} \tag{10}$$

z_i is the difference signal, x_i and y_i signals from independent bins, and <x> and <y> their mean expectation value.

In section's V & VI, we show the effect of atmospheric and mechanical fluctuations on LO power, and indirectly on the mixer IF output signal. Tolerances are seen to be very tight, and for mixers operating in the terahertz regime it may well be advisable to perform Y-factor and stability measurements in a spectroscopic, rather than in continuum mode as is typically the case in the submillimeter.

Of course, the level of improvement depends on the intrinsic HEB stability. Recent measurements suggest (Baselmans *et.al*) that LO-pumped HEB mixers have significant gain fluctuation (Fig. 10). The atmospheric, mechanical, and thermal effects described in this paper manifest themselves as 1/f and drift noise, and care should be taken to keep these on longer timescales than the intrinsic HEB stability. Note that 1/f noise does integrate down, though not at the same efficiency as white (radiometric) noise. If science goals call for the receiver to be used in continuum mode, than spectroscopic stability measurements may mask actual performance. What method is relevant thus depends on the science goals of the instrument.

V. Sensitivity to atmospheric turbulence

Consider that recent (SRON, Chalmers, Umass, AST/RO) stability measurements of HEB mixers indicate an Allan variance minima of 0.2-0.3 seconds in a 80 MHz noise fluctuation

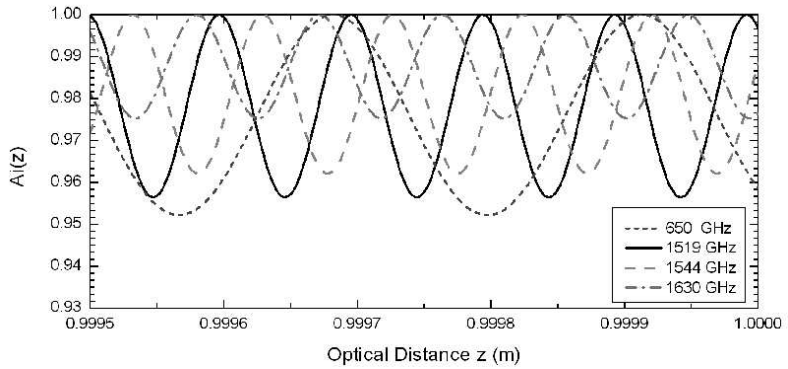

Fig. 1. Standing wave (Ai) for a cavity path length of z=1 meter. Note the effect of atmospheric loss (damping) on the standing wave. Shown here are the last 500 μm. In the example $|r_m|^2$ was taken to be 0.10 (-10 dB), $|r_{lo}|^2$ 0.16 (-8 dB), and $|r_{bs}|^2$ 0.10(-10 dB) for all four frequencies shown. If there were no atmospheric loss (space, or a high dry mountain site), the peak-to-peak standing wave amplitude in the example would be 4.934%. Solid curve is for ν_{lo}=1.519 THz, dashed 1.544 THz, dash-dot 1.630 THz, and dotted 650 GHz. We include 650 GHz as a reference where the loss is taken to be 4x less than at 1544 THz. At this frequency SIS receivers in the laboratory are known to be stable to 100 seconds in a 1 MHz resolution bandwidth[5].

bandwidth. In this case, we find from the radiometer equation

$$\sigma = \frac{< x(t) >}{\sqrt{B \cdot T_{int}}} \tag{11}$$

that LO signal fluctuations in excess of 0.025% of P_{lo} become visible at the mixer IF output. Given a typical spectrometer noise fluctuation bandwidth of 1.5 MHz, $\sigma / < x >$=0.025% corresponds to a Allan variance stability time [4] of $\approx$ 10 seconds. For comparison sake, a typical laboratory operated submillimeter SIS receiver has, in the same bandwidth, an Allan variance stability time on the order 80-100 seconds [5].

The absolute path length change in air for three different frequencies is tabulated in Table I. From this data we obtain an estimate of the LO power fluctuation in the presence of air turbulence. It should be stressed that we do not concern ourselves with the absolute optical path length change, but with optical path length fluctuations due to changes in the refractive index of air. Thus is it useful to plot the change in LO power (Eqn. 9) against the percentage change in optical path length. If the air were to be absolutely stable, or humidity very low as would be the case on a high mountain, we'd expect $dP_{lo} \rightarrow$ zero. Note also that the loss term in Eqn. 9 has a damping effect on the LO standing wave. Thus, if a mixer is operated close to a water line, the path length turbulence will be more significant. This is however somewhat compensated by the decaying (loss) standing wave amplitude (Fig. 1). The increase in sensitivity to air turbulence with frequency is therefore not only related to wavelength, but also to the increase in atmospheric loss. This is demonstrated in Fig. 2.

Consider as an example a typical mixer with an input reflection coefficient of -10 dB ($|r_m|^2$=0.10), a LO source reflection coefficient of -8 dB ($|r_{lo}|^2$=0.16), and a beam splitter

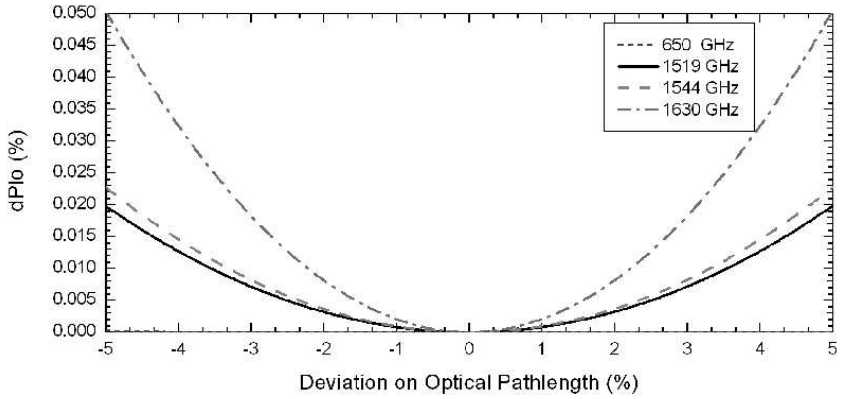

Fig. 2. LO power change (%) as a function of optical path length deviation for a z=1 meter cavity. The LO-mixer standing wave is tuned to a peak ($dP_{lo}/dz = 0$). $|r_m|^2$ was taken to be -10 dB, $|r_{lo}|^2$ -8dB, and $|r_{bs}|^2$ -10 dB. Solid curve is for ν_{lo}=1.519 THz, dashed 1.544 THz, dash-dot 1.630 THz, and dotted 650 GHz (barely visible at the bottom of the graph). For a 0.025 % LO power fluctuation, the allowed atmospheric path length turbulence at 1.519 THz & 1.544 THz (30% humidity, 990mBar atmospheric pressure) can be up to $\pm$ 6%. At the 1.63 THz CH_2F_2 FIR laser line (close to a water absorption line), the effect of air turbulence is quite a bit more significant ($\pm$ 3.5% for dP_{lo} = 0.025%.) At 650 GHz the atmosphere has essentially NO influence on the LO, as may be expected. Reducing the path length and atmospheric humidity level (high mountain) will considerably improve the situation.

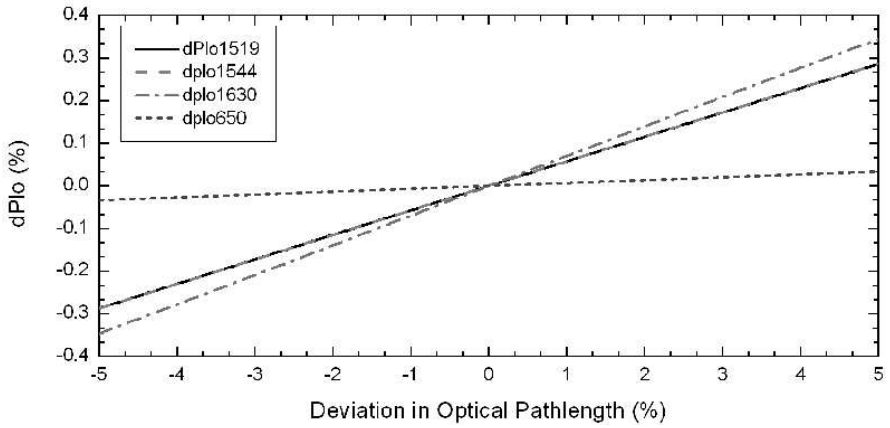

Fig. 3. Percent LO power change as a function of percent optical path length fluctuation, but now tuned to a maxima on dP_{lo}/dz. All else the same as in Fig. 2. With the LO tuned in this manner, it is essentially impossibly to get the LO power stable to better than 0.025%, with the exception of the 650 GHz frequency receiver. One should be careful therefore to always tune to a maxima (or minima) of the inevitable standing wave in the LO path. This usually means moving the dewar to or from the LO source, or by shifting the LO frequency to be on the peak of the standing wave. Note that LO power fluctuations maybe highly correlated across the IF band. If so, spectroscopic rather than continuum stability measurements are needed to separate atmospheric instability from mixer instability.

reflection 10% (-10 dB). In Fig. 1 we plot the Airy function(Eqn 9) for the last 500 μm of a 1 meter LO-mixer cavity path length. If there would be no atmospheric loss (space), the

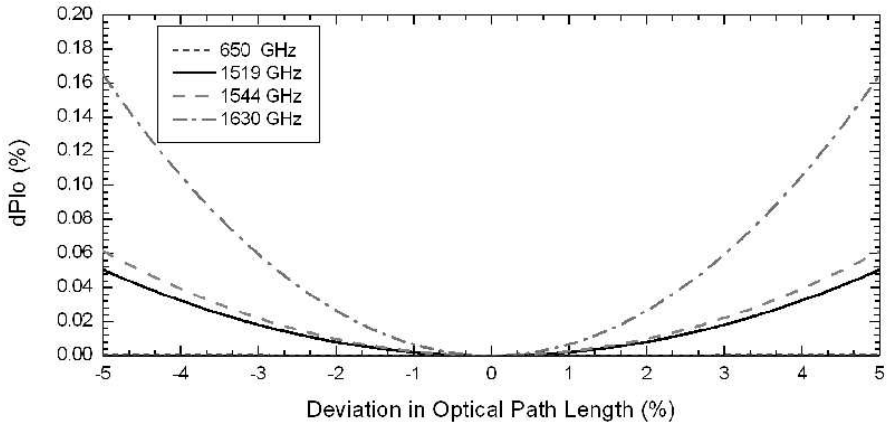

Fig. 4. Change in LO Power (%) as a function of optical path length deviation for a 0.5 meter total path length Martin Puplett LO injection scheme. $|r_m|^2$ was taken to be 0.10 (-10 dB), $|r_{lo}|^2$ 0.16 (-8 dB), and $|r_{bs}|^2$ 0.10(-10 dB). Solid curve is for ν_{lo}=1.519 THz, dashed 1.544 THz, dash-dot 1.630 THz, and dotted 650 GHz. To achieve a system imposed 0.025% LO power stability, the optical path length change due air turbulence at 1.519 THz & 1.544 THz (30% humidity, 990mBar atmospheric pressure) should be less than $\pm$ 3.5%. For the 1.63 THz CH_2F_2 FIR laser line (close to a water absorption line), the path length change due turbulent air must be kept less than ($\pm$ 2.2% for $dP_{lo} = 0.025\%$.) At 650 GHz the atmosphere has essentially no influence on the LO power stability, as expected. Reducing the path length and atmospheric humidity level (high mountain) will considerably improve the situation.

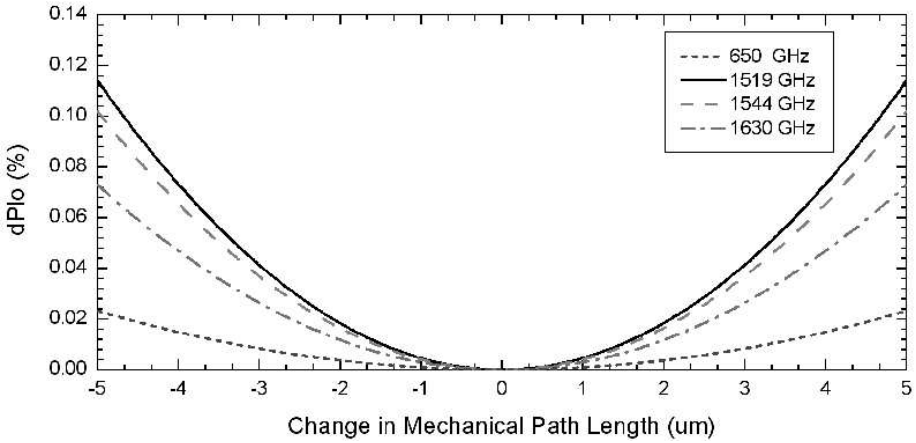

Fig. 5. LO power sensitivity as a function of path length change for a z=1 meter LO-mixer cavity length. $|r_m|^2$=0.10, $|r_{lo}|^2$=0.16, and $|r_{bs}|^2$=0.10. Solid curve is for ν_{lo}=1.519 THz, dashed 1.544 THz, dash-dot 1.630 THz, and dotted 650 GHz. To achieve a hypothetical 0.025% stability in LO power at 650 GHz, the allowed mechanical path length fluctuation will be on the order of $\pm$ 7 μm, which is easily achieved. A typical 650 GHz SIS receiver has a stability of $\approx$ 80-100 seconds in a 1 MHz spectral bandwidth. In this case micron level mechanical stability is to be required, which in general is accomplished by minimizing temperature drifts. At ν_{lo}=1519 GHz the situation has significantly degraded, and we find that for a system imposed 0.025% LO power fluctuation, that the mechanical stability needs to be better than $\pm$ 2.5 μm. Interestingly, at the 1630 GHz CH_2F_2 FIR laser line at sea level, the situation has actually slightly improved even though this is much closer to a water absorption line. This is due to atmospheric loss (Table 2) which dampens the LO-mixer cavity standing wave. Of course at a dry site, this advantage goes away and the sensitivity to mechanical fluctuations increases to $\pm$ 1.5μm in this particular example.

peak-to-peak amplitude variation for the given parameters would be 4.934%. In actuality, for a z=1 meter path length, the standing wave amplitude has damped to $\approx$ 4.8% for a 650 GHz LO signal, and 2.4% for the 1.63 THz CH_2F_2 FIR laser line, located near a water absorption line. Interestingly, a 5% standing wave value agrees well with measurements at 230 GHz, 352 GHz, 690 GHz, and 807 GHz obtained at the Caltech Submillimeter Observatory (CSO) in December 2003. A nice confirmation that the assumed mixer, LO source, and beam splitter reflections are reasonable. From Eqn. 9 it is clear that as $r_{bs} \rightarrow 0$ that the LO-mixer standing wave vanishes to zero. Thus it is advantages to use very low reflective (thin) beam splitters. Of course at terahertz frequencies, except for when an FIR laser is employed, this is not practical. In Fig. 2 the Airy function is evaluated for a mixer - LO path cavity of z=1 meter, a 10% reflecting beam splitter, and with the LO-Mixer standing wave tuned to a peak. This is the most stable LO configuration. In Fig. 3 we tune the LO to the most sensitive part of the standing wave, where dP_{lo}/dz is the largest. And finally, in Fig. 4 we plot LO power sensitivity at the mixer for a 0.5 meter optical path length Martin-Puplett LO injection scheme. Here the MP is assumed to have a 1 dB loss and is tuned to maximum transmission so that $sin^2(\beta nz) = 0$. Though not shown here, it is absolutely critical as far as receiver stability goes, that the mixer-LO cavity is tuned to a peak of the (inevitable) LO power standing wave. This is also the case for a dry-air mountain site.

VI. Sensitivity to mechanical fluctuations

As an example of the effect of mechanical path length fluctuations, consider the same mixer with an input reflection coefficient of -10 dB ($|r_m|^2$=0.10), LO source with an reflection coefficient of -8 dB ($|r_{lo}|^2$=0.16), and a LO path beam splitter reflection of 10% as before. Evaluating Eqn. 9 at 1.544 THz, we again find a peak-to-valley standing wave amplitude of 4.934%. By evaluating Eqn. 9 for small perturbations in z, we get an estimate for the allowed optical path length change of the Lo-Mixer cavity. Figures 5 and 6 show the mechanical stability requirement of a mixer system that uses a beamsplitter for LO injection. Fig. 7 shows the stability requirement in the case of Martin-Puplett (MP) LO injection scheme. The Martin-Puplett is assumed to be tuned to maximum transmission which would be the most stable configuration. Loss in the interferometer is taken to be 1 dB. In the case of a MP interferometer LO injection scheme, mechanical stability requirements on the order of 0.5μm (or less) are needed in the tereahertz regime. This specification places very stringent thermal requirements on the hardware. For example: Given a thermal expansion of Aluminum at room temperature of $2.25 \cdot 10^{-5}\ K^{-1}$, a LO power drift of 0.025%, and a 1.5 MHz spectrometer noise bandwidth. Then we find (Eqn. 11) a maximum allowed temperature drift of 0.25°C/minute. At a physical temperature of 100°K the situation improves by approximately a factor of 2, due to a decrease in thermal expansion of Aluminum. In practice this means that thermal fluctuations of the LO - mixer assembly are to be kept to a minimum. Of course tuning to the most sensitive part of the LO standing wave when using a Martin-Puplett is horrendous, and should be avoided. This means in practice that if the mixer-LO cavity length is fixed (LO and Mixer cannot be moved) that one should only observe at discrete frequencies such that βnz is a multiple of π radians. This is the free spectral range, which for z=1 meters equals 150 MHz.

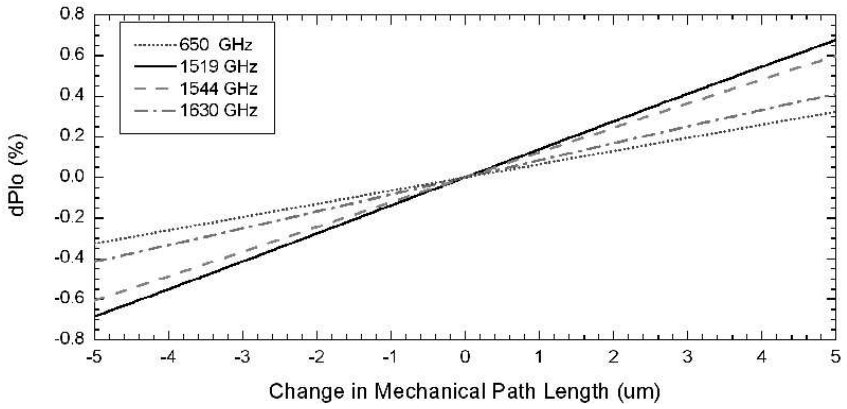

Fig. 6. LO power sensitivity as a function of percent path length change, but now with the LO position tuned to a maxima on the dP_{lo}/dz slope. All else being the same as in Fig. 5. With the LO tuned in this manner, it is essentially impossibly to get the LO power stable to better than 0.025%, even for the 650 GHz frequency receiver. One should be extremely careful therefore to always tune to a maxima (or minima) on the standing wave in the LO - mixer path. Typically this can be done by moving the dewar or LO source, though it is also possible to move the LO frequency such that βnz is a multiple of π radians (Eqn 9).

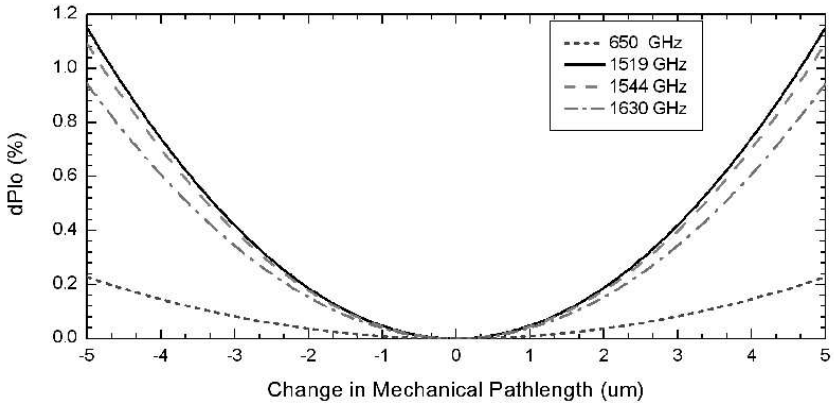

Fig. 7. LO Power sensitivity to path length change of a 0.5 meter Martin Puplett. Loss is taken to be 1 dB. $|r_m|^2$=0.10, $|r_{lo}|^2$=0.16, and $|r_{bs}|^2$=0.80. Solid curve is for ν_{lo}=1.519 THz, dashed 1.544 THz, dash-dot 1.630 THz, and dotted 650 GHz. To achieve a 0.025% stability in LO power, the path length change should be no more than a fraction of a micron during the time of a observation scan. This can only be achieved by keeping the MP temperature well stabilized. As before, depending on how dP_{lo} correlates across the IF, spectroscopic rather than continuum stability measurements may be needed to separate mechanical from mixer instabilities. For the 1630 GHz CH_2F_2 FIR laser line, at sea level, the situation has actually slightly improved due to atmospheric loss, even though this is much closer to a water absorption line. On a dry site, this advantage reverses itself and the sensitivity to mechanical fluctuations increases to roughly $\pm$ 0.3μm at 1.63 THz.

At this point, it should be clear that mixers operating at terahertz frequencies will, by their very nature, always be extremely sensitive to mechanical vibrations and atmospheric turbulence. It is probably not a good idea therefore to try to use these mixers as continuum detectors.

VII. Measured Results

A. Setup

To illustrate the issues discussed in the previous sections, we measured the Allan variance stability time of phonon cooled NbN hot electron bolometer mixers pumped at two different LO frequencies; 673 GHz and 1.52 THz. The expectation being that the effect of atmospheric and mechanical instability at 673 GHz is negligible, and that intrinsic HEB noise characteristics maybe measured directly. The drawing of the measurement setup is given in Fig. 8. We use a quasi-optical injection scheme for the LO, in which we glue the HEB die to the back of an elliptical Si lens. As LO source a solid-state multiplier chain, coupled to a phase locked Gunn Oscillator was used. The LO is attenuated using a wire grid, focused using a Teflon lens, and coupled reflectively to the Si lens of the mixer block through a 7 % reflective (14 μm) beam splitter. For the experiment at 1.52 THz we used a x16 multiplier chain from JPL[6], coupled to the same XL microwave Phase Locked Loop system. In this case the total output power of the HIFI test LO, 7 μW, is just barely enough to reach the optimal pumping level of the mixer. Hence the LO was coupled directly to the mixer lens without using a beam splitter or wire grid. At the output, the IF signal from the HEB passes through a Bias T, a 1-2 GHz isolator and a 1-2 GHz Berkshire low noise amplifier

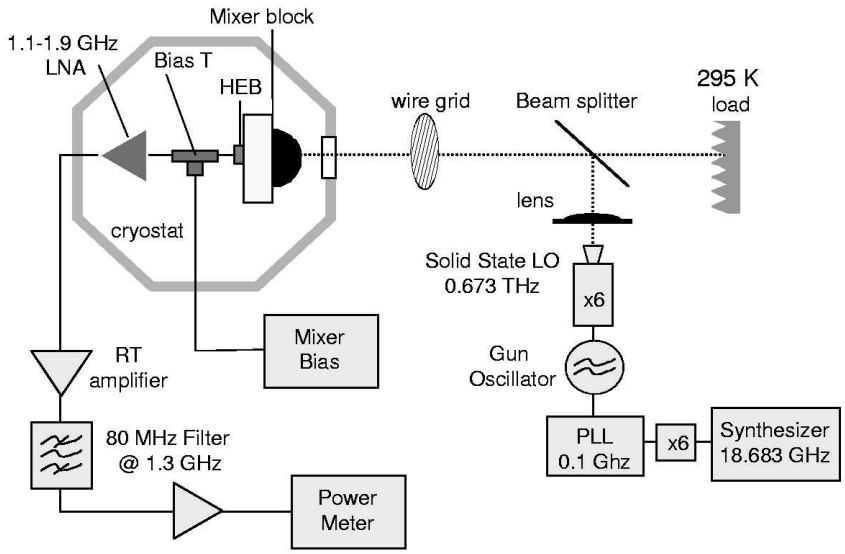

Fig. 8. Measurement setup used to measure the Allan variance. Shown here is the setup using a 673 GHz LO with a 7% reflective beamsplitter. For the high frequency experiment we used the same PLL with a x16 JPL multiplier chain to reach a LO frequency of 1.52 THz. In this case the LO is coupled directly into the cryostat, without the use of a beam splitter or wire grid, due to the limited output power of the LO chain at this high frequency.

(GaAs HEMT's), all thermally anchored to the 4.2 K plate of a liquid Helium dewar. The signal is further amplified at room temperature with a commercial Miteq amplifier and is measured in a 80 MHz bandwidth around 1.3 GHz using an Agilent E4418 B power meter at 200 samples/second. A computer program is used to calculate $\sigma_A / < x(t) >$ from this data.

B. HEB Stability

In Fig. 9 we show the measured HEB stability for different LO pump levels. A small volume 0.15 x 1 μm HEB mixer, with clean contact pads [7] and a twin slot antenna optimized for 1.6 THz was used in the experiment. At the measurement frequency of 673 GHz the antenna response is reduced by a factor two with respect to the antenna center frequency [8]. We measured a receiver noise temperature ($T_{N,DSB}$) of 1100 K at 673 GHz and used the exact same setup to measure the HEB mixer stability. This indicates that the mixer still has a reasonable sensitivity at a frequency in which the Allan variance is taken. A detailed description of the noise performance, LO power requirement and direct response of this device can be found in Ref. [8]. In Fig. 9 we plot in the left panel the normalized Allan variance ($\sigma_A / < x(t) >$) for several bias points along the optimally pumped IV curve (673 GHz). In the right panel we show the unpumped and optimally pumped IV curves, the 1.63 THz DSB receiver noise temperature (dots) along the optimally pumped IV, and the points at which the Allan variance has been taken (stars). At the optimal bias point, corresponding to a DC bias voltage of 0.8 mV, we obtain an Allan time of roughly 0.5 sec in a 80 MHz noise spectral bandwidth. Observe that the Allan time increases slowly with

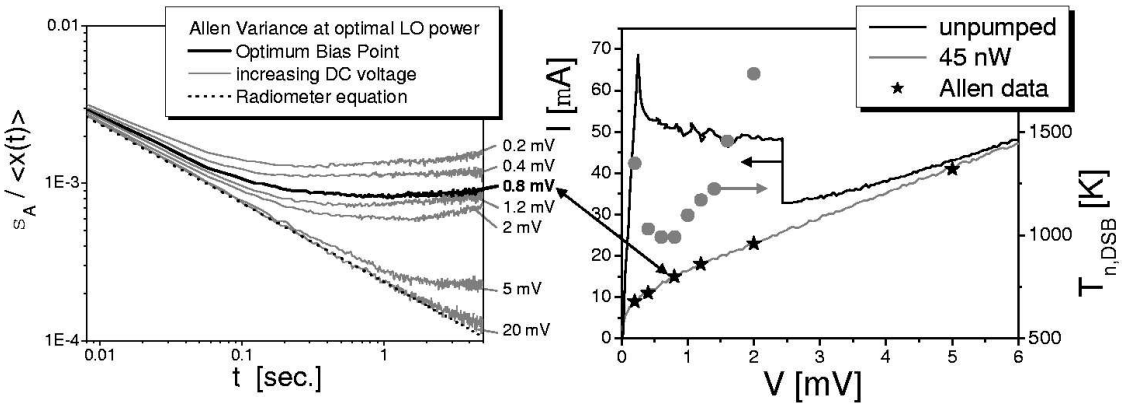

Fig. 9. 673 GHz HEB Allan variance stability measurements as a function bias voltage at optimal pump level with a 0.15 x 1 μm area twin slot NbN HEB mixer. Left panel: Normalized Allan variance ($\sigma_A / < x(t) >$) as a function of integration time t for different values of the DC bias voltage along the optimally pumped IV curve. Right panel: Unpumped (black) and optimally pumped (grey) IV curve of the HEB, together with the measured double sideband receiver noise temperature (dots) at 1.63 THz, the center frequency of the antenna. The optimally pumped IV curve corresponds to a LO power of 30 nW according to the isothermal technique, however, the power needed to pump the device is significantly higher (see [8]). The black stars indicate the bias points at which the Allan variance was measured along the optimally pumped IV.

increasing DC bias, and decreases with decreasing DC bias. For the lowest line in the left panel, obtained at a high DC bias of 20 mV, no heterodyne response is measurable. The explanation being that at a very high bias the HEB mixer conversion gain $\rightarrow 0$, and thus we measure the IF response of our setup. At about 5 seconds of integration time we see the 20 mV bias line deviate from the radiometer equation (Eqn. 11) which is indicated by the dotted line. This deviation is due to gain instability of the GaAs LNA and warm IF amplifier chain ($\approx$ 45 seconds in a 1 MHz resolution BW). Being so far out, it does not effect the HEB mixer stability measurements.

The plateau after reaching the system's Allan time indicates that short term gain fluctuations (1/f noise) are limiting the stability of the HEB mixer. The strong bias dependence of the gain fluctuations is another indication that we are observing a property of the HEB, and not some spurious noise sources in the system. Especially so since the expected LO-mixer standing wave is only 3%, and that short time scale mechanical path length changes of up to $\pm$ 5 μm are allowed (Fig. 5). Other measurements, where the DC bias voltage is kept constant but the LO power is increased indicate that an increase in LO power has the same effect as an increase in DC voltage; i.e. an increase in stability [8]. This indicates that fluctuations in the LO output power are very likely not influencing these measurements as well. Therefore we conclude that the mixer gain fluctuations observed are a fundamental property of NbN phonon cooled HEB mixers. The physical cause of the gain instability is likely related to stochastic modulation, due to for example heat or quantum noise, of the "hot spot" mixing area internal to the mixer. It is not inconceivable that device geometry and/or magnetic field can play an important role in minimizing HEB gain fluctuation noise. As such, small differences in the Allan time minima maybe expected between the different

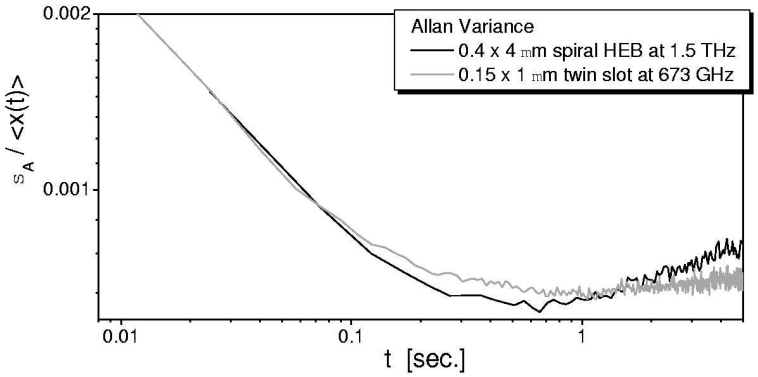

Fig. 10. Allan variance stability measurements with two different HEB mixers measured at 1.5 and at 673 GHz

mixer groups. The reported measurements are in good agreement with other reported stability measurements (these proceedings) on similar devices, taking into account variations in (noise) bandwidth[9], [10].

In addition to the discussed measurements, we have also performed similar measurements using a large volume (4 x 4 μm) spiral antenna HEB mixer at 1.52 THz, at its optimal operating point. The $T_{N,DSB}$ of this mixer is 750 K at 1.89 THz and 950 K at 2.5 THz, and estimated to be of the order of 700 K at 1.52 THz [7]. The result of this measurement is shown in Fig. 10. In the same graph we reproduce the result obtained at 673 GHz using the small volume twin slot HEB. From the figure it is clear that the stability is roughly identical for both devices, indicating again that the observed stability is a device property and not something in our setup. However, looking at longer integration times it is obvious that for the black line representing the data taken at 1.52 THz, no 1/f plateau is observed. Instead, we see an increase in the variance, associated with drift, which we believe can be attributed to mechanical and/or atmospheric instability in the setup. At 1.52 THz, due to available LO power, the LO was injected directly into the mixer. This being the case of a Martin-Pupplet LO injection scheme (Fig. 7). Interestingly, because of the relatively short time scale gain fluctuations, the measured Allan variance stability time does not appear to be limited by mechanical or atmospheric fluctuations at 1.52 THz. However at the 1.63 THz CH_2F_2 FIR laser line, when using more stable mixers, or by measuring at higher terahertz frequencies, the receiver stability will almost certainly be dominated by the setup. Thus a proper design approach should be taken to minimize atmospheric and mechanical fluctuations in the terahertz regime.

VIII. Conclusion

In this paper we have studied the effect of atmospheric and mechanical stability on terahertz mixers from the point of view of the LO - mixer "cavity" standing wave. There are of course many other mechanisms that can cause a mixer to behave unstable or erratic, such as temperature drifts of the mixer/LNA and low frequency noise on bias lines [5] [4]. As far as the LO standing wave is concerned; mechanical, thermal, and atmospheric tolerances for mixers operating in the terahertz regime have been found to be much more stringent

than for mixers operating in the submillimeter. Even with proper mechanical engineering principles in mind, it will be difficult to use terahertz heterodyne (LO pumped) receivers in continuum mode.

As a direct result of the analyses, it has been found that phonon cooled HEB's have significant short term (mixer) gain fluctuations, and that up to at least 1.5 THz they tend to dominate the mixer stability budget. The physical origin of the gain fluctuation noise is unclear, however it conjectured that it maybe related to thermal and/or quantum hot-spot modulation inside the mixer. For this reason it maybe advisable to establish stability, and possibly sensitivity, of terahertz mixers via spectroscopic, rather than continuum means.

The level of improvement that can be gained from using the spectroscopic measurement (statistically differencing two or more uncorrelated IF channels) will depend on how correlated the noise is across the HEB IF band. If science goals call for the receiver to be used in continuum mode, than spectroscopic stability measurements may mask actual performance. Whatever method is relevant thus will depend on the science objectives of the instrument.

In regards to the use of a Martin-Pupplet LO injection scheme, one should be very careful to only tune to the peak of the LO power standing wave. If the mixer-LO cavity length is fixed (LO and Mixer cannot be moved) than one should tune the LO at discrete frequencies such that βnz is a multiple of π radians. This is the free spectral range, which is for z=1 meters 150 MHz.

IX. Acknowledgements

We wish to Serguei Cherednichenko and Therese Berg for very helpful HEB performance discussions, Juan Pardo for his help in modeling atmospheric conditions encountered in the laboratory, and Wolfgang Wild for his unwavering support &coordination. This work was supported in part by NSF Grant# AST-0229008.

References

[1] Juan Pardo "Private communication"
[2] Rudolf Schieder "Private communication"
[3] Paul F. Goldsmith "Quasioptical Systems, Chapter 9"
[4] R.Schieder, C.Kramer Optimization of Heterodyne Observations Using Allan variance Measurements, *A&A 373,* 746-756 (2001)
[5] J.W. Kooi, G. Chattopadhyay, M. Thielman, T.G. Phillips, and R. Schieder, "Noise Stability of SIS Receivers," *Int J. IR and MM Waves,* Vol. 21, No. 5, May, 2000
[6] G. Chattopadhyay, E. Schlecht, J. Ward, J. Gill, H. Javadi, F. Maiwald, and I. Mehdi "An All Solid-State Broadband Frequency Multiplier Chain at 1500 GHz," *IEEE Trans on Microwave Theory and Techniques, Vol. 52, No. 5, May2004*
[7] J.J.A. Baselmans, J M.Hajenius, R. Gao, T.M. Klapwijk, P.A.J. de Korte,B. Voronov, G. Gol'tsman "Doubling of sensitivity and bandwidth in phonon cooled hot electron bolometer mixers" *Appl. Phys. Lett,* 84, 1958, 2004
[8] J.J.A.Baselmans, M.Hajenius, J.R. Gao, A. Baryshev, J. Kooi, T.M. Klapwijk, P.A.J. de Korte, B. Voronov, and G. Gol'tsman "Hot Electron Bolometer mixers with improved interfaces: Sensitivity, LO power and Stability," *These Proceedings (2004)*
[9] T.Berg, S. Cherednichenko, V.Drakinskiy, H.Merkel, E. Kollberg, J.W.Kooi "Stability measurements of NbN HEB receiver at THz frequencies," *These Proceedings (2004)*
[10] Alexei D. Semenov, Heinz-Wilhelm Hbers, Heiko Richter, Konstantin Smirnov, Gregory N. Gol'tsman, and Boris M. Voronov "Superconducting Hot-Electron Bolometer for Terahertz Heterodyne receievers," *These Proceedings (2004)*

BSMILES - A Balloon borne Superconducting Submillimeter-Wave Limb-Emission Sounder for Atmospheric Research

Yoshihisa Irimajiri, Takeshi Manabe, Satoshi Ochiai, Harunobu Masuko
National Institute of Information and Communications Technology (NICT), Japan
Takamasa Yamagami, Yoshitaka Saito, Naoki Izutsu, Michiyoshi Namiki
Japan Aerospace Exploration Agency (JAXA), Japan

Abstract
A Balloon-borne Superconducting Submillimeter-Wave Limb-Emission Sounder (BSMILES) to measure vertical profile of stratospheric minor constituents was developed. BSMILES carries a 300mm-diameter offset parabolic antenna, a 650-GHz heterodyne SIS receiver, and an acousto-optical spectrometer. The SIS junction chip consists of two Nb/AlOx/Nb junctions connected by a tuning inductance in parallel. The DSB receiver noise temperature of the SIS receiver is about 200 K. BSMILES was launched from Sanriku Balloon Center of Japan Aerospace Exploration Agency on August 30, 2003. The gondola was carried to an altitude of 31-33.8 km by a balloon of 80,000 m^3 in volume and the observations were made for 3 hours. All systems operated normally and the emission line spectra of ozone at 650.733 GHz and chlorine monoxide at 649.45 GHz were measured. After the observations, the gondola was dropped and splashed on the Pacific Ocean and retrieved. Almost all systems were waterproofed and it turns out that they are reusable.

I. INTRODUCTION

Heterodyne detection of stratospheric molecules at millimeter and submillimeter wavelength is useful technique. We can measure vertical profile of stratospheric minor constituents such as ozone and a number of key species related to ozone destruction by observing thermal emission line from these species. The strength of the emission line spectra becomes strong at the submillimeter-wave, however, the observation at this wavelength becomes difficult due to absorption by water vapor in the troposphere. Therefore a good method uses a balloon or an airplane. A balloon has the advantage that it can reach higher altitude in order to observe by high vertical resolution.

BMLS (Balloon-borne Microwave Limb Sounder) [1] [2] is the first balloon experiment to observe molecules in the middle atmosphere at millimeter wavelength. It carries shottkey diode mixer at 200/270 GHz band to measure O_3 and ClO. SLS (Submillimeterwave Limb Sounder) [3] observed O_3, ClO, HCl, HO_2 by using shottkey diode mixer. PIROG (Pointed InfraRed Observation Gondola) [4] [5] carries a superconducting low noise SIS mixer at 425/441 GHz and observed O_2, O_3. A Balloon OH [6] measured stratospheric OH at 2.5 THz. SUMAS (Submillimeter-wave Atmospheric Sounder) family [7] [8] [9] is airborne system which carries 625-650 GHz SIS mixer to observe O_3, ClO, HCl etc. The planned TELIS (TErahertz and submm LImb Sounder) [10] carries 500 GHz/600-650GHz SIS mixer and HEB mixer at 1.8 THz. Some balloon experiments have been performed also as a preliminary experiment of observations from space. Satellite-borne systems developed for observations of earth atmosphere are MLS (Microwave Limb Sounder)/UARS (Upper Atmospheric Research Satellite) [11] and SMR (SubMillimeter Radiometer) on board the Odin satellite [12], and EOS (Earth Observing System)-MLS (Microwave Limb Sounder)/Aura [13] and JEM/SMILES [14] [15] are planned.

A balloon-borne superconducting submillieter-wave limb-emission sounder (BSMILES) was developed to measure vertical profile of stratospheric minor constituents at submillimeter wavelength. An O_3 spectral line at 650.733 GHz and a ClO line at 649.450 GHz were selected for simultaneous measurement. The BSMILES uses limb sounding technique which has the advantages of high sensitivity and high vertical resolution. The instrument will act as validation tool for future JEM/SMILES mission.

II. INSTRUMENT DESCRIPTION

Fig. 1(a) shows system block diagram of the BSMILES. The system comprises of antenna system, optics system, receiver system, IF system, a spectrometer, data acquisition and operation system, attitude detection system, batteries command/telemetry system etc. Gondola size is about 1.35 m x 1.35 m x 1.26 m (Fig. 1(b)) and total weight is 490 kg. The whole surface is covered with 100-mm thick Styrofoam except for the signal window for heat insulation at the time of launch. This material will enable the gondola to float when it falls into the sea. Lithium battery cells of a few Ah to 30 Ah are used as a power supply. Battery packs were designed for each subsystem with a retention time of about 20 hours. Since a three-terminal regulator is used to stabilize the voltage, the heat from regulator and subsystems will be released to heat sinks, such as the pressurized chamber and the gondola itself. Total power consumption is 150 W.

The pressurized chamber was used to IF system, PLL electronics, a spectrometer, data acquisition and operation system (CPU), attitude detection system, and SIS/HEMT bias circuits for waterproofing. It serves also as a noise shield for CPU, and vacuum operation for the CPU, IF system, and SIS/HEMT bias circuits. Air in this chamber is to be replaced by dry nitrogen gas. Pressurized chambers maintain a vacuum of several Torr for 24 hours.

Since the gondola hangs from rope connected to a balloon, the attitude of the gondola may not be stable. Therefore, gondola attitude is measured by three-axis fiber-optical gyroscope, three-axis accelerometer, and a geoaspect sensor.

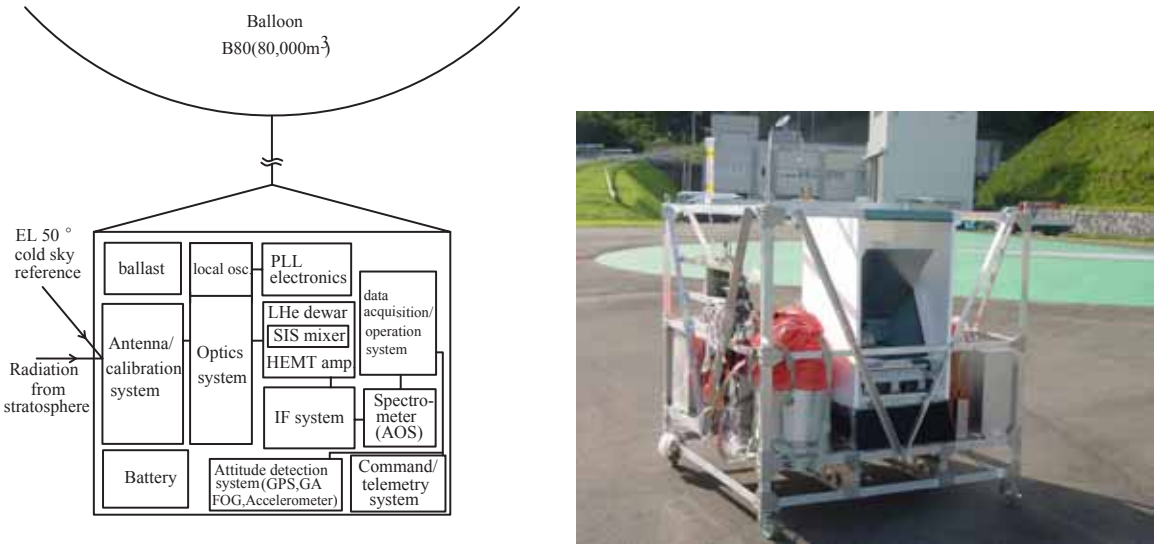

(a) (b)

Fig. 1: (a) System block diagram of the BSMILES. (b) Photograph of the BSMILES. The whole surface is covered with Styrofoam at the time of launch.

A. The antenna and optics system

The antenna system (Fig. 2) consists of an offset parabolic antenna with an aperture of 300 mm, a subreflector,

a flat mirror (L 630 mm x W 350 mm) for beam scanning, and a switching flat mirror. The size of the beam of the parabolic antenna is about 0.12 degree, corresponding to vertical resolution of about 1 km at a tangent height of 16 km. The parabolic antenna is fixed, while the flat mirror is moved by a stepping motor to perform beam-scanning in the elevation angle. The beam is scanned in a range between -8 and +4 degrees, with an interval of approximately 18 seconds. At each scan, a flat switching mirror switches the beam to obtain calibration data from calibrated hot load (CHL), and from cold sky at an elevation angle of 50 degrees.

As shown in Fig. 3, the optics system comprises five focusing mirrors, a wobbler, a Martin-Puplett interferometer for sideband separation, a local oscillator (LO), a PLL electronics, and a LO diplexer. Elements of the optics system are designed by fundamental Gaussian beam with an edge level of -40 dB. Signals from the switching mirror are reflected by the focusing mirror D into a wobbler and introduced by the focusing mirror C into the MPI. The image sideband signals are terminated to the cold load (TK RAM [16]) placed on 4-K stage within a liquid helium cryostat. The sideband separation ratio of the MPI is about 15 dB. The separated signals are reflected

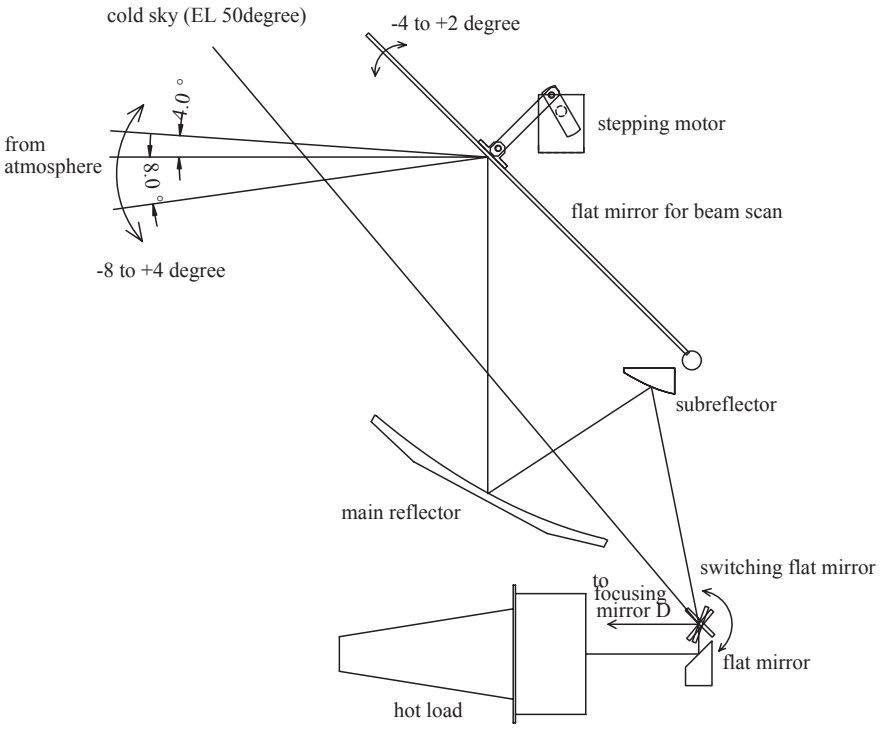

Fig. 2: Antenna system design.

by the focusing B mirror and introduced into a liquid helium cryostat through a LO diplexer. Then they are reflected by the focusing mirror A placed on a 4-K stage into the SIS mixer. The local oscillator consists of a Gunn oscillator followed by a doubler and a tripler, and a harmonic mixer for phase-locking. LO signals are guided to the LO diplexer through the focusing mirror E. Its output power is about 120 μW at 644 GHz. By using a Zitex G-108 film as the LO diplexer, about 2 % of the output power is introduced to the SIS mixer from outside of the vacuum window. The LO frequency is fixed at 644.273 GHz. Stabilization of phase-lock and optimization of the output power are important in terms of observation. Since temperature variation has an effect on the LO output power, the temperature of the Gunn oscillator was stabilized by using a heater. A CPU is used to monitor and control the state of the phase lock so that when it becomes unlocked, phase will return to the locked state. The local oscillator and

some elements of the optics system are contained in a waterproof optics box. This box is airtight, and is filled with nitrogen gas.

B. The receiver system

The SIS mixer operating in the 650-GHz band was designed and manufactured based on one for the 200-GHz band. As with other 200-GHz band devices, to produce a value of 4 for $\omega RnCj$ (equaling a current density of 3.5 kA/cm^2), we have to construct an SIS junction of about 10 kA/cm^2 in current density. Since such a high-density junction leaks a large amount of current, it is difficult to construct one of high quality. Therefore, we set the value of $\omega RnCj$ at 8 (designed with Rn = 10.6 Ω and an SIS junction area of 1.56 μm^2). In this case, the current density is 5.5 kA/cm^2, making it easier to produce an SIS junction. Since the specific band is slightly narrow (12.5 percent), a deviation of the center frequency from the designed value lowers the performance in the required band. Since the center frequency depends on the junction area, care should be taken in constructing the SIS junction in question. To cancel the junction capacity, we constructed a parallel-connected twin junction (PCTJ) [17] [18]. The junction was installed into a waveguide-type tuner less mixer mount with a corrugated horn. Fig. 4(a) shows the Nb/AlOx/Nb SIS junction and the mixer mount, and Fig. 4(b) shows measured (uncorrected) DSB receiver noise temperature. In the 650 GHz band used for observation of O_3, ClO, the noise temperatures was between 150 K and 200 K [19]. IF signal with the frequency range of 5 GHz to 7 GHz is amplified by a HEMT amplifier with an isolator, and then taken out of the cryostat. A permanent magnet is used to reduce the Josephson current for the SIS mixer. The HEMT amplifier is attached with an aluminum plate to the 4-K stage. The power consumption of the HEMT amplifier is 52.5 mW. Experiment revealed that the amplifier was cooled to a steady-state temperature of about 15 K. The HEMT amplifier performs gain of 30 dB, gain deviation of ±1.5 dB, input equivalent noise temperature of 18 K (a standard value, including noise from the isolator), and input VSWR of 1.4 (standard value).

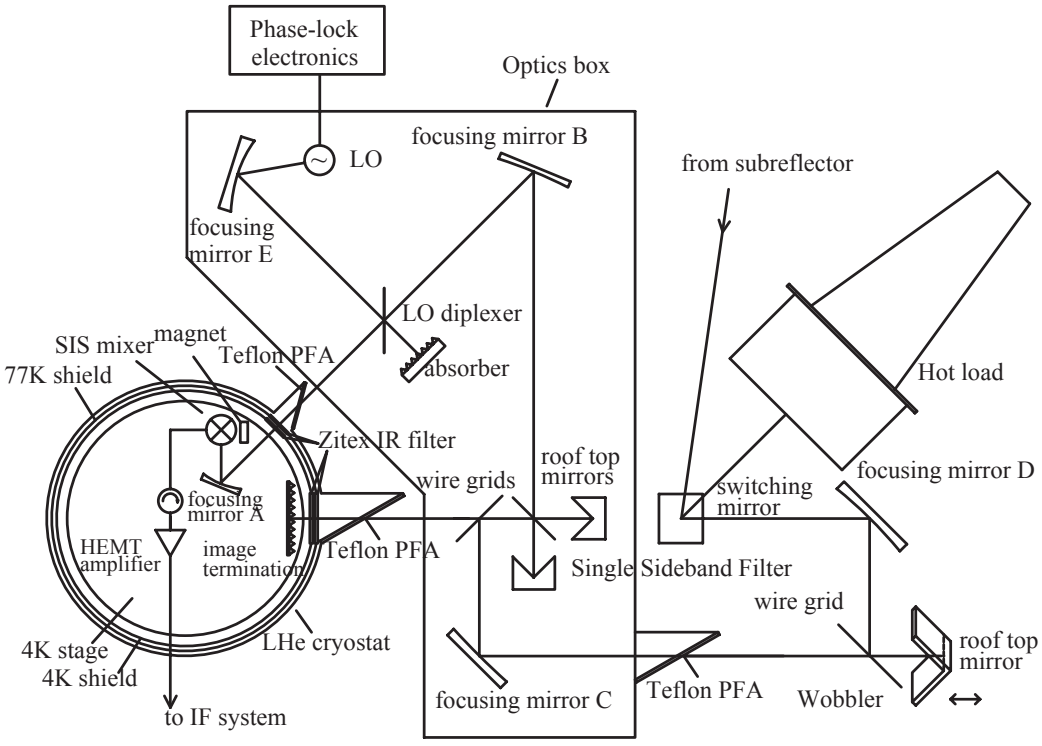

Fig. 3: Optical layout

The cryostat has a 1-inch diameter window for signal input and a 2-inch diameter window for image termination. Zitex G108 films are attached at the temperature shield as an infrared filter, while Teflon PFA 500-μm thick is used as a vacuum window. The transmission loss of PFA is measured to be about 2 percent at 650 GHz. The vacuum window is attached at nearly a Brewster angle (60 degrees) that will reduce reflection. To avoid a risk that dew will form on the window and freeze, causing a loss in signal intensity, the window flange is covered with a sealed cylinder that is connected to the optics box. This structure prevents moisture from direct contact with the window, so that no dew may form on the cold window. The capacity of liquid helium and nitrogen is 7 liters and 4 liters, respectively. It was shown that the liquid helium tank is large enough to retain liquid helium for about 14 hours as a result of the experiment. It may be possible that more helium will be lost through the decrease in pressure during ascent, thus shortening the retention time. To prevent this from occurring, a pressure valve is attached to the liquid-helium filling port (and to the liquid-nitrogen filling port) to maintain the internal pressure at about 1.2 atmospheric pressure. On the other hand, a decrease in pressure further cools the SIS mixer to 2 K, thus improving the performance and stability of the receiver. If the liquid helium holding time would be longer enough than required, it could be possible to operate at 2 K.

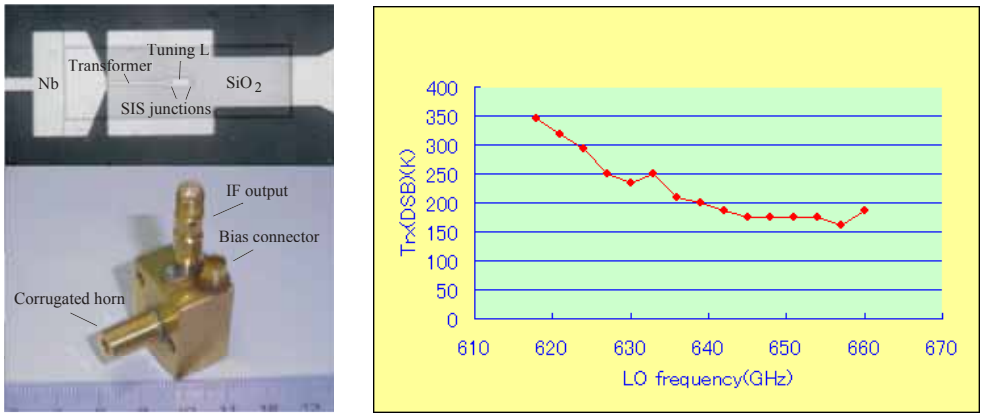

(a) (b)

Fig. 4: (a) Photograph of the SIS junction chip and the mixer mount with a corrugated feed horn. (b) Measured DSB receiver noise temperature (uncorrected).

C. The IF system and spectrometer

Taken out of the cryostat, the first IF signals are guided to the intermediate frequency (IF) system. In this system, an O_3 band and ClO band are picked up and converted to the second IF signal to be combined into an acousto-optical spectrometer (AOS). Fig5 (a) shows system block of the IF system. A power divider divides the IF signals (5 to 7 GHz) into two series of signals. For each series, a band-pass filter sorts signals either as first-band signals (5.03 to 5.53 GHz for ClO band) or as a second-band signals (6.313 to 6.813 GHz for O_3 band). Then, for each band, an additional mixer converts into the second IF signals. Finally, these bands are combined and output into a spectrometer. The second LO frequency is 3.430 GHz and 4.213 GHz for the ClO band and O_3 band, respectively. The final bands are 1.85 GHz ± 250 MHz for ClO band and 2.35 GHz ± 250 MHz for O_3 band. A CPU-controlled switch outputs a comb signal at a step-frequency of 100 MHz to calibrate the frequency of the spectrometer.

The bandwidth and the resolution of the AOS are 1 GHz and 1 MHz, respectively. CCD integration time was set to 15 milliseconds. The time interval of data acquisition of 180 milliseconds includes data-saving time at each spectrum. A measured absolute stability of the Allan variance of the receiver is about 30 seconds.

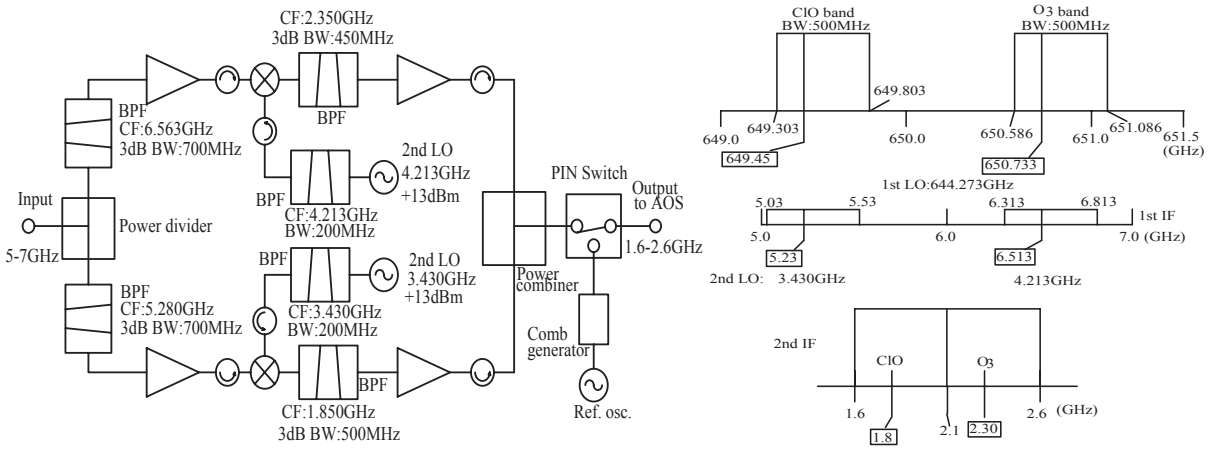

Fig. 5: (a) Block diagram of the IF system. (b) Heterodyning arrangement.

D. Data acquisition and operation system

Three CPUs performed data acquisition and operation of the observations. These CPUs operate at a clock frequency of 66 MHz with a RAM of 32 MB under MS-DOS version 5. The CPU-1 unit performs spectrum data acquisition from the AOS. The CPU-2 performs HK data acquisition and control the stepping motor that drives the antenna. The CPU-3 performs attitude data acquisition as well as antenna-position data (stepping-motor address data). The acquired data are recorded on a PC card, attached to the CPU unit with its capacity of 2 GB for CPU-1. The observed data is collected after the gondola lands in the sea. The HK data consist of temperature and voltage data for various components. Only the HK data is sent to earth using a telemeter in a rate of 1200 bps. A command can be sent from ground to reset power supply of the CPU and subsystems.

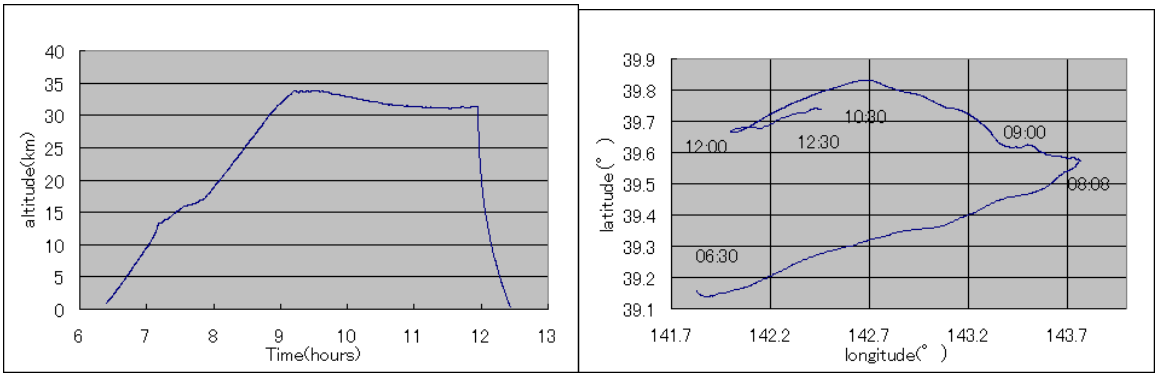

Fig. 6: (a) Altitude profile of the BSMILES flight. (b) Flight locus of the BSMILES shown at longitude and latitude

III. BSMILES FLIGHT AND EXPERIMENTAL RESULTS

The BSMILES was launched from Sanriku Balloon Center of Japan Aerospace Exploration Agency at the east coast of Japan, on August 30, 2003. The gondola was carried to an altitude of 33.8 km by a balloon of 80,000 m^3 in volume. The limb sounding observations were made for 3 hours (from 9:00 to 12:00) lowering an altitude to 31 km over the Pacific Ocean. Altitude profile of the BSMILES flight and flight locus are shown in Fig. 6 (a) (b). All systems operated normally by keeping their temperature within the limit of operation (Fig. 7). The SIS bias voltage was kept almost constant during the observations. The temperature of LO and AOS was stable in the accuracy of less than 1 degree C. The gondola temperature was about 20 - 25 degree C. The attitude of the gondola was stable

in the accuracy of about 0.005 degree rms. The system noise temperature was about 1,000 K. After the observations, the gondola was dropped and splashed on the Pacific Ocean by a parachute at 40 km offshore of the east coast of Japan, and retrieved by using a boat and a helicopter. Almost all systems were waterproofed and it turns out that they are reusable.

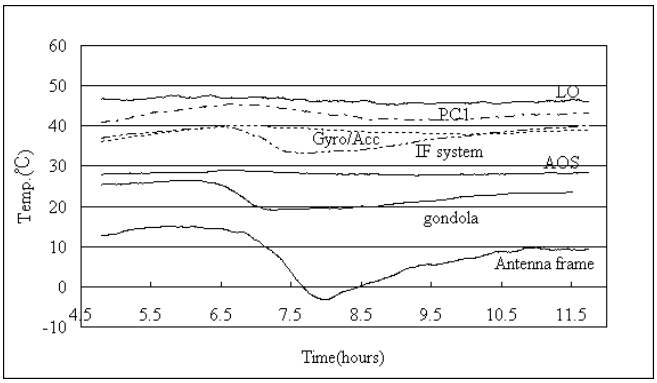

Fig. 7: Measured temperature variations on subsystems during the BSMILES flight.

The emission line spectra of ozone and chlorine monoxide were detected at different elevation angle (Fig. 8 (a)). Fig. 8 (b) shows the retrieved vertical profile of O_3 and ClO. The obtained ozone height profile is in good agreement with that measured by ozone zonde on September 13.

From the data analysis, we found there are some points which should be improved such as antenna efficiency, effective observation time, and observing bandwidth etc. We are planning the second balloon experiment in the summer of 2004 also in Japan after improving the system. Stratospheric molecules at 620 GHz band mainly O_3 (625.37 GHz) and HCl ($H^{37}Cl$; 624.98 GHz, $H^{35}Cl$; 625.92 GHz) with 2 GHz bandwidth in total will be observed.

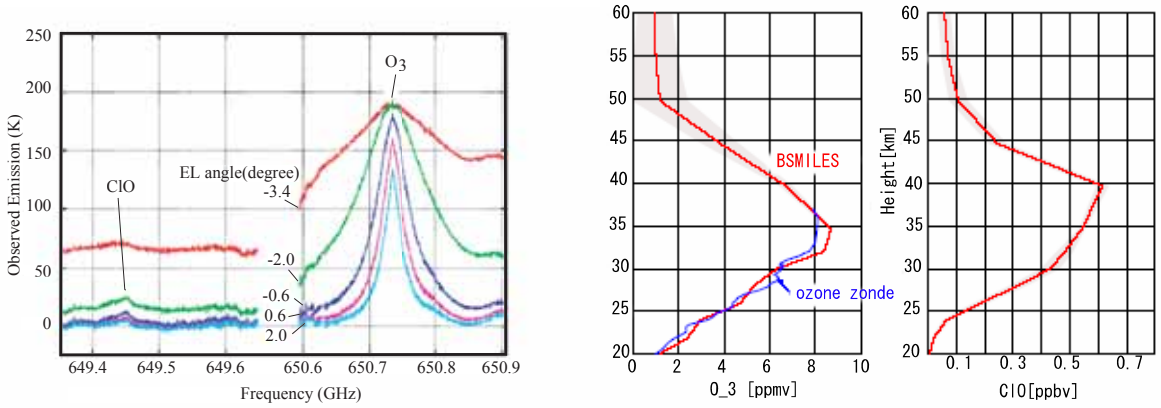

(a) (b)

Fig. 8: Measured emission line spectra of O_3 and ClO at different elevation angle. (b) Retrieved height profile of O_3 and ClO.

ACKNOWLEDGMENT

The authors would like to thank I. Murata (Tohoku University) for providing vertical profile data of ozone measured by the ozone zonde.

REFERENCES

1. J. W. Waters, J. C. Hardy, R. F. Jarnot, H. M. Pickett, and P. Zimmermann, “A Balloon-borne Microwave Limb Sounder for Stratospheric Measurements”, *Journal of Quantitative Spectroscopy & Radiative Transfer*, Vol. 32, No. 5/6, pp.407-433, 1984.
2. J. W. Waters, R. A. Stachnik, J. C. Hardy, and R. F. Jarnot, “ClO and O_3 Stratospheric Profiles: Balloon Microwave Measurements”, *Geophysical Research Letters*, Vol. 15, pp.780-783, August 1988.
3. R. A. Stachnik, J. C. Hardy, J. A. Tarsala, J. W. Waters, and N. R. Erickson, “Submillimeterwave Heterodyne Measurements of Stratospheric ClO, HCl, O_3, and HO_2: First Results”, *Geophysical Research Letters*, Vol. 19, No. 19, pp.1931-1934, October 2, 1992.
4. A. Dechamps, P. Encrenaz, P. Febvre, H. G. Floren, S. George, B. Lecomte, B. Ljung, L. Notdh, G. Olofsson, L. Pagani, J. R. Pardo, I. Peron, M. Sjokvist, K. Stegner, L. Stenmark, J. Tauber, and C. Ullberg, “Results of the PIROG 8 Balloon Flight with an Embarked Experiment Based on a 425/441 GHz SIS Receiver for O_2 Search”, *Ninth Int. Symposium of Space Terahertz Technology*, pp.253-261, Pasadena CA, March 1998.
5. J. R. Pardo, L. Pagani, G. Olofsson, P. Febvre, J. Tauber, “Balloon-borne Submillimeter Observations of Upper Stratospheric O_2 and O_3”, *Journal of Quantitative Spectroscopy & Radiative Transfer*, Vol. 67, pp.169-180, 2000.
6. B. J. Drouin, H. M. Pickett, “Laboratory and Field Studies in Rotational Spectroscopy at the Jet Propution Laboratory”, Proceedings of International Workshop on Critical Evaluation of mm-/submm-wave Spectroscopic Data for Atmospheric Observations, pp.10-13, 2004.
7. J. Mees, S. Crewell, H. Nett, G. de Lange, H. van de Stadt, J. J. Kuipers, and R. A. Panhuyzen, “ASUR - An Airborne SIS Receiver for Atmospheric Measurements of Trace Gases at 625 to 760 GHz”, *IEEE Transactions on Microwave Theory and Technologies*, Vol. 43, No. 11, Nov. 1995.
8. J. Urban et al., “Recent Airborne Heterodyne Receivers for the Submillimeter- wave Range”, *International Workshop on Submm-wave Observation of Earth’s Atmosphere from Space*, pp.1-13, Jan., 1999.
9. T. Wehr, S. Crewell, K. Kunzi, J. Langen, H. Nett, and J. Urban, “Remote sensing of ClO and HCl over northern Scandinavia in winter 1992 with an airborne submillimeter radiometer”, *Journal of Geophysical Research*, Vol. 100, No. D10, pp.20,957-20,968, Oct. 1995.
10. P.L. Yagoubov et al., “TELIS-development a new balloon borne THz/submm heterodyne limb sounder”, *Proceedings of 14th International Symposium on Space Terahertz Technology*.
11. J. W. Waters, ``Microwave Limb Sounding," in *Atmospheric Remote Sensing by Microwave Radiometry* (M. A. Janssen, ed.), *ch. 8, New York: John Wiley*, 1993.
12. F. von Sche’ele, “The Swedish Odin Satellite to Eye Heaven and Earth”, *Swedish Space Corporation Report (http://www.ssc.se/ssd/papers/odeye/odeye.html)*, 1996.
13. J. W. Waters et al., “An Overview of the EOS MLS Experiments”, *JPL D-15475, Ver. 1.1, (http://mls.jpl.nasa.gov/)*, Oct. 1999.
14. Inatani et al., "Submillimeter limb-emission sounder JEM/SMILES aboard the Space Station", *Proceedings of SPIE Symposium on Remote Sensing of the Atmosphere, Environment, and Space*, Oct. 2000.
15. JEM/SMILES mission plan, http://www2.nict.go.jp/dk/c214/smiles/Mission_Plan/
16. Thomas Keating Ltd.., http://qmciworks.ph.qmw.ac.uk/
17. J. Zmuidzinas, H. G. LeDuc, J. A. Stern, and S. R. Cypher, 'Two-junction tuning circuits for submillimeter SIS mixers', *IEEE Trans. Microwave Theory Tech.*, vol. 42, no. 4, pp. 698-706, April 1994.
18. T. Noguchi, S. C. Shi, and J. Inatani, 'An SIS mixer using two junctions connected in parallel', *IEEE Trans. Applied Superconductivity*, vol. 5, no. 2, pp. 2228-2231, June 1995.
19. Y. Irimajiri, T. Noguchi, S.-C. Shi, T. Manabe, S. Ochiai, and H. Masuko, "A 650-GHz Band SIS Receiver for Balloon-Borne Limb-Emission Sounder", *Int. J. of Infrared and Millimeter Waves*, Vol. 21, No. 4, pp. 519-526, April 2000.

ALMA cartridge-type receiver system for Band 4

K.Kimura1, S.Asayama4, T.Nakajima1, N.Nakashima1, J.Korogi1,
Y.Yonekura1 ,H.Ogawa1, N.Mizuno2, K.Suzuki2, Y.Fukui2, H.Andoh3,
Y.Sekimoto4, T.Noguchi4 and A.Yamamoto5

1Osaka Prefecture University, Japan

2Nagoya University, Japan

3Toyota National College of Technology, Japan

4National Astronomical Observatory, Japan

5Mitsubishi Electric Tokki System

We are developing the ALMA (Atacama Large Millimeter/Sub-millimeter Array) Band4(125--163GHz) receiver. Individual ALMA frequency bands are implemented asself-contained cartridges. The cartridge-type receivers are mounted in the 4 K dewar on theCassegrain receiver cabin of ALMA 12m telescope. The receivers are asked to receive two linearly polarized orthogonal signals. The diameter of the Band 4 cartridge is 140 mm.

Specifications

- Freq 125—163GHz
- Trx(SSB) over 80% _ 47K (goal 26K) any freq _ 76K (goal 40K)
- Two linear orthogonal polarizations
- Max. cross-polarization -20dB
- Sidebands DSB or 2SB (10dB image band suppression)
- IF bandwidth 4GHz 2SB,upper and lower sideband

ALMA Band4 cartridge-type receiver

Block diagram

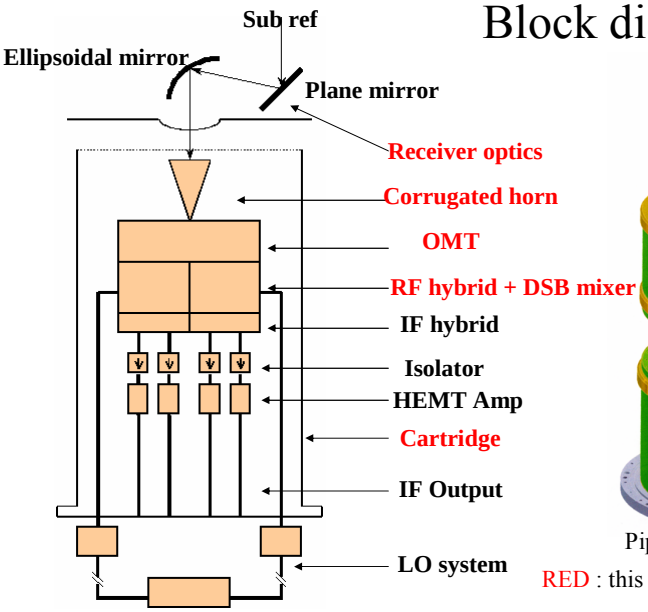

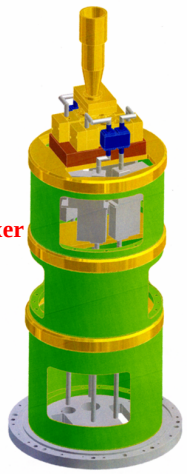

Pipe type cartridge

RED : this poster reports

ALMA dewar

Ten cartridge-type receivers are equipped with in ALMA dewar.
Band 4 receiver is located in 335mm offset from the center of dewar.
A position of band 4 receiver is symmetric with band 3 receiver.

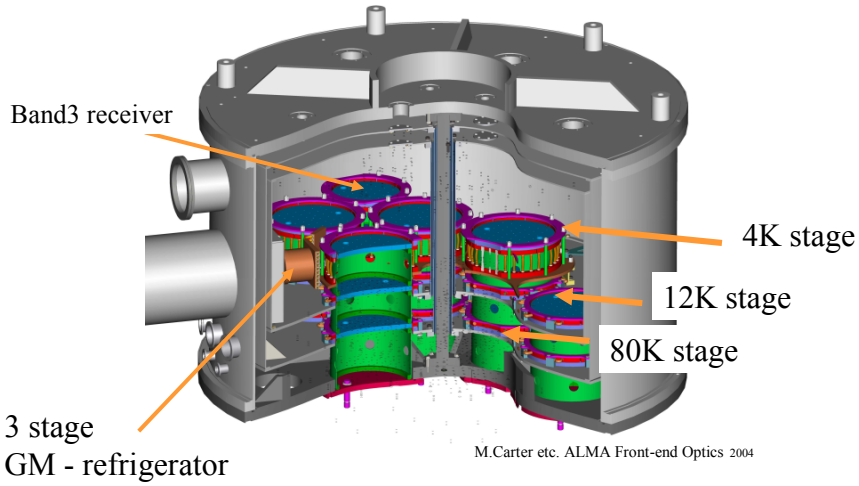

ALMA Band4 optics

05/09/2003

Composition

Warm optics
- plane mirror
- ellipsoidal mirror

Cooled optics
- corrugated horn

Performance goals of receiver optics

Minimize window apertures

Minimize added noise

Maximize aperture efficiency: Reduction < 5%

Aberrations: < 1%

Truncation loss: < 1%

Dissipative losses: < 1%

Scattering losses: < 1%

Polarization loss: < 1%

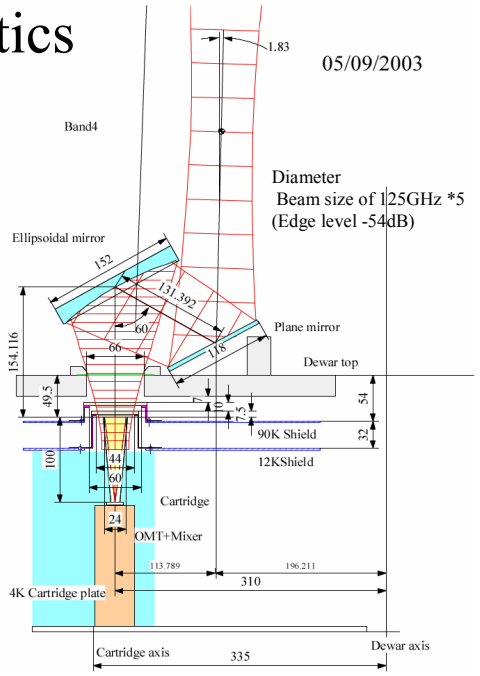

Optics parameter(Band4)

Frequency (GHz) (mm)	Design Parameters	125 2.398340	144 2.081892	163 1.839218
Horn diameter	24.0			
Horn axial length	100.040			
Horn slant length	100.757			
Horn waist, w_0		6.103	5.760	5.431
Horn waist offset, $z(w_0)$		-37.8211	-44.704	-50.923
Waist at horn aperture, w_{ha}		7.722	7.722	7.722
d_1 15	4.116			
R_{s1} 21	1.417	204.339	211.423	217.416
f_1 15	0.474			
R_{f1}	522.006	570.832	521.972	488.714
Waist at mirror 1, w_{M1}	(dia. = 152)	24.773	23.590	22.761
1	60.0			
d_2	128.268			
Waist at mirror 2, w_{M2}	(di a. = 118)	19.496	18.033	16.981
2	61.834			
$z_{w(Cass.)}$ 24	5.188	248.091	245.107	243.102
$w_{Cass.}$		14.343	12.453	11.004
$d_{mirror\text{-}subref1}$		6367.356	6367.356	6367.356
$w_{subref1}$	(dia. = 750)	319.035	319.035	319.035
$R_{subref1}$	6000.00	6000.000	6000.000	6000.000
Edge Taper (dB)	12.00	12.00	12.00	12.00
Multimode E. Taper (dB)		9.50	9.50	9.50

Dimensions in mm.

This optics are calculated by the frequency independent matching of gaussian beam(TA-SHING 1983 IEEE) . In any frequencies, Shape of a beam becomes equal in a sub-ref and horn aperture.

Design of corrugated horn (Band4)

Now We are producing the corrugated horn by a method of electro-former or machining.

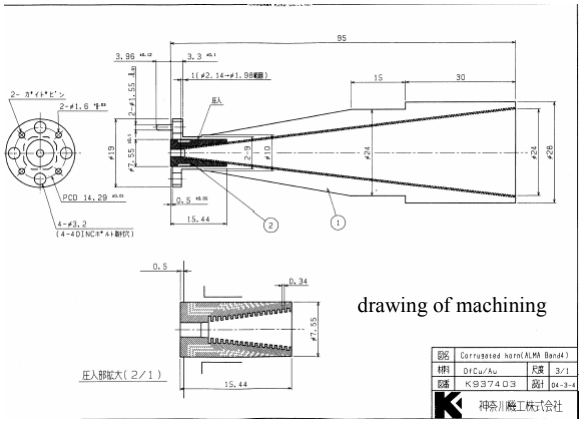

drawing of machining

Slot width 0.34mm
Ridge width 0.34mm
Slot depth
slot1=0.80mm
slot2=0.68mm
slot3=0.60mm
slot4=0.55mm
slot5--aperture(134)=0.52mm

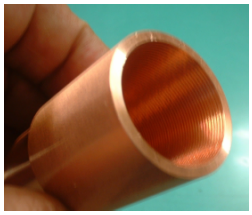

horn made by machining

Simulation of radiation pattern

A pattern of corrugated horn and an antenna pattern do simulation by GRASP8(TICRA).
GRASP8 is based on well-established analysis techniques such as Physical Optics (PO) supplemented with the Physical Theory of Diffraction (PTD), Geometrical Optics (GO) and Uniform Geometrical Theory of Diffraction (GTD).

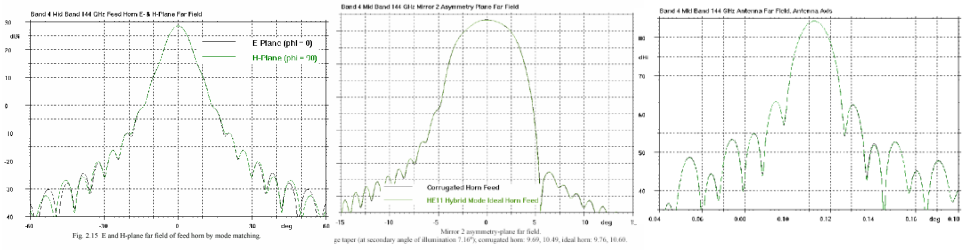

Horn beam pattern　　Beam pattern for sub-ref　　Antenna beam pattern

Simulation by C.Y.Cham etc. (University of Cambridge,UK)

Band4 Ortho Mode Transducer (OMT)

Higher mode TE_{11},TM_{11} excitation → "small"

Goals of performance

Insertion loss	**<0.2dB**
Return loss	**> 20dB**
Isolation	**> 30dB**

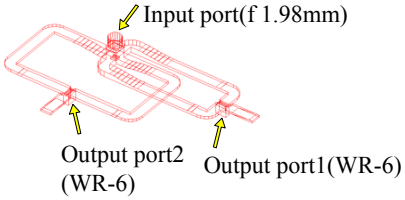

front

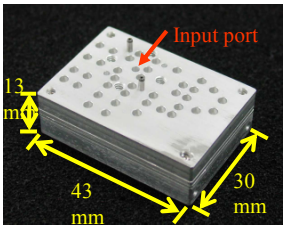

rear

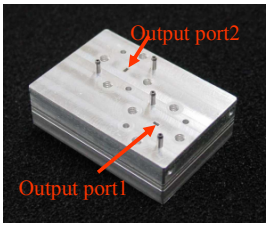

OMT measurement performance

We measured OMT by MVNA.

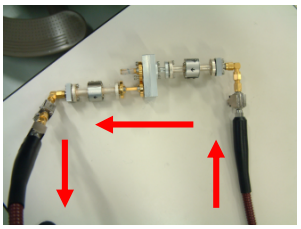

S21 Insertion loss

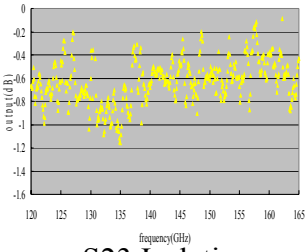

S11 Return loss

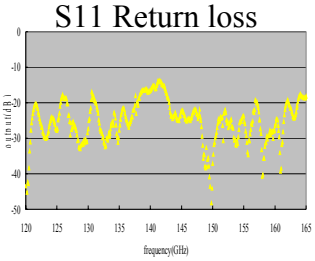

S23 Isolation

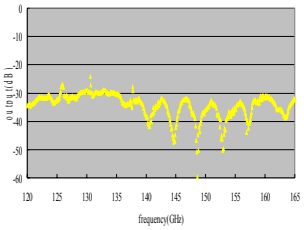

Half reduced height mixer mount for ALMA Band4

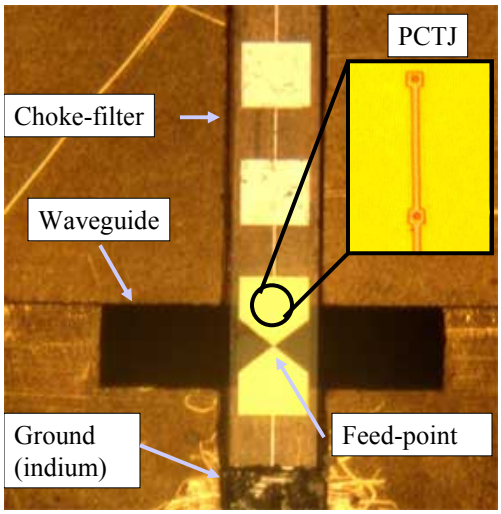

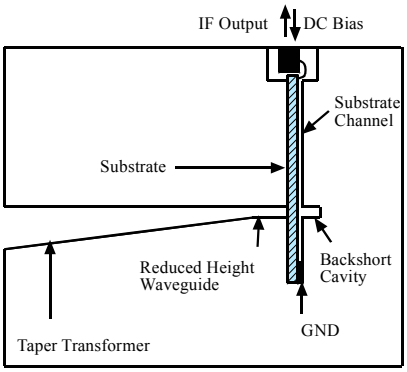

Band4 DSB mixer results

We measured the Band4 DSB mixer by Y-factor method.

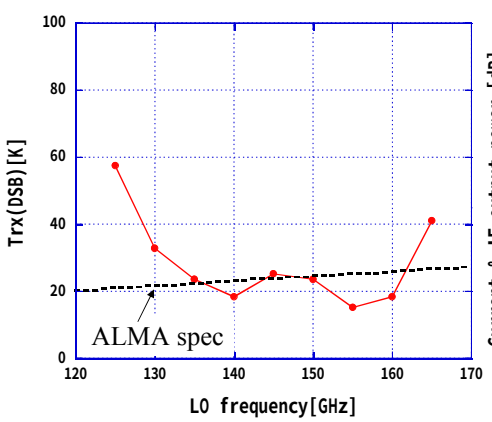

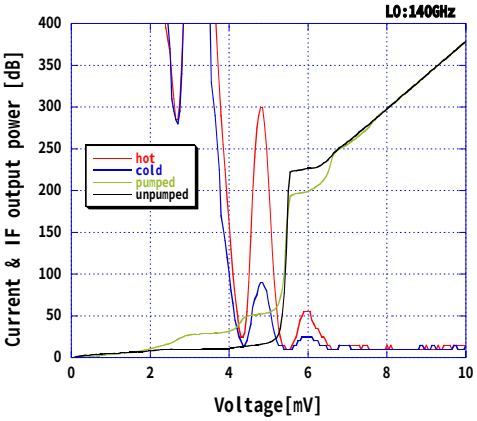

Sideband-Separating Mixer Unit for ALMA BAND 4

The Sideband-Separating Mixer Unit contents two LO coupler, an RF blanch line coupler and LO divider.

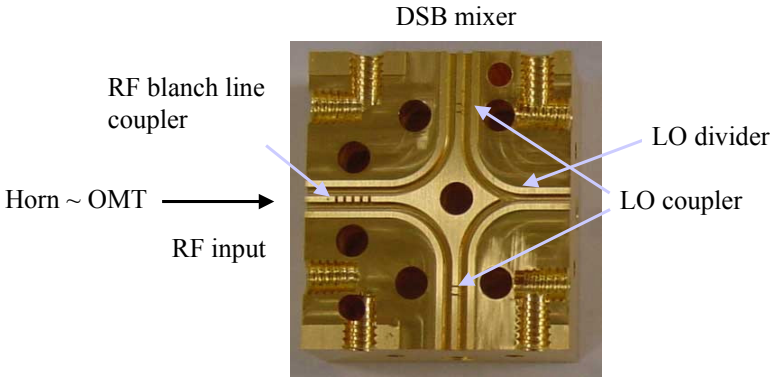

Receiver noise temperatures of ALMA Band4 Sideband-Separating Mixer

principle, the image rejection ratio of a receiver can be measured by injecting CW signals of known relative amplitudes into the upper and lower sideband measuring each IF response. At millimeter wavelengths, however, it is difficult to determine with sufficient accuracy the relative amplitudes of two RF signals separated in frequency by twice the IF frequency. In case of a sideband-separating mixer, the image rejection ratio can be measured accurately injecting CW test signals in the upper and lower sidebands, even when the relative power level of the test signals are not known (*). In a ideal sideband-separating mixer, CW signals
into the upper sideband and lower sideband appears separately at the two output ports. Since the image rejection ratio of an actual mixer is not perfect, a CW signal into one sideband appears at both IF output ports. In this case, the image rejection ratio can be determined by measuring the difference in the peak value referred to the noise revel at the corresponding output.

* Shin'ichiro Asayama (OPU/NRO), et al.
"Preliminary Tests of Waveguide Type Sideband-Separating SIS Mixer for Astronomical Observation " ALMA Memo 481
http://www.alma.nrao.edu/memos/index.html

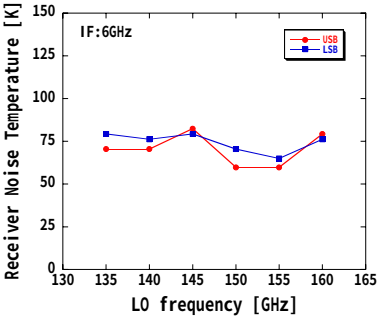

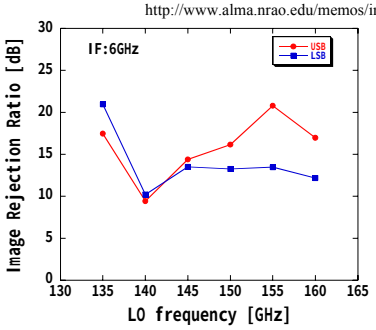

The measurement of cartridge distortion

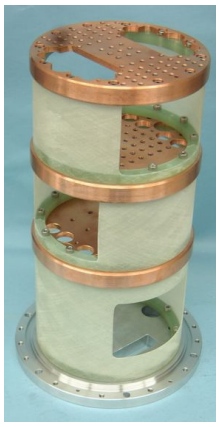

Pipe-type f140 cartridge

We adopted a pipe-type(thick 2mm) cartridge.
Because this type is strong to incline.

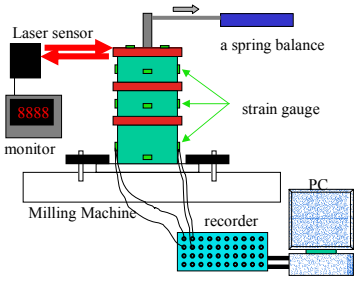

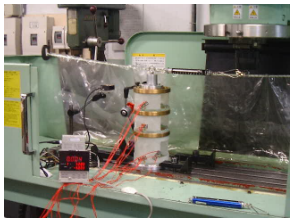

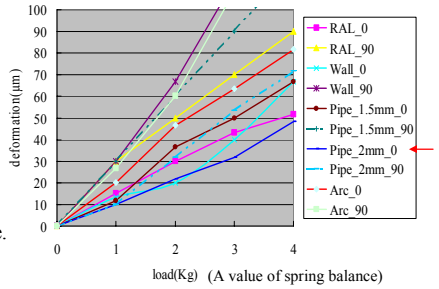

Conclusion

We are developing the ALMA Band4 cartridge-type receiver.

Development

+ Receiver optics	Design is end .
+Corrugated horn	In evaluation of a prototype.
+OMT	In evaluation of a prototype.
+ Sideband-Separating Mixer	In evaluation.
+Cartridge	Decision of a design. In production.

We are designing and assembling the receiver systems.
We aim at production of the first receiver system within 2004.

A Dual-Frequency Mixer Array for CHAMP+

R.Hesper[1], H. Schaeffer[1], G. Gerlofsma[1], C. Kasemann[2], A. Baryshev[1]

[1]Kapteyn Astronomical Institute, University of Groningen / NOVA / SRON, Landleven 12, 9747 AD Groningen, The Netherlands. [2]Max-Planck-Institut für Radioastronomie, Auf dem Hügel 69, D-53121 Bonn, Germany
Email: hesper@sron.rug.nl

ABSTRACT

We present the design, construction and prototype measurements of two seven-mixer arrays for the new CHAMP+ instrument, which is being built by MPIfR-Bonn.

CHAMP+ is a dual-frequency multipixel heterodyne receiver to be mounted on the APEX telescope (Atacama Pathfinder Experiment) recently installed at 5000 meters altitude in the Atacama Desert in northern Chile. The two observing bands are centred at 650 GHz and 860 GHz, and the arrays will consist of seven pixels each, in a hexagonal configuration. The mixer arrays are developed at NOVA/SRON in close collaboration with MPIfR.

Because of the required small spacing between the pixels, a very tight and compact design was called for, which could lead to undesired consequences in the form of cross-talk between the Josephson-suppression magnets and deflux heaters of neighbouring mixers. Another requirement was that the mixers should be individually replaceable without disassembling large parts of the instrument. For these reasons, a two-mixer prototype was built and tested, with very promising results. Subsequently, the design of the full seven-pixel arrays commenced, and production is underway at the moment of writing.

Apart from being a contribution to a valuable instrument in its own right, the production of a series of matched mixers can also be seen as a pilot project for the future series production of large numbers of mixers for the ALMA project.

THE TELESCOPE

The APEX (Atacama Pathfinder Experiment) telescope is a modified ALMA antenna, produced by Vertex Antennentechnik. Main differences with the ALMA antennas are the addition of two observing cabins at the Nasmyth foci and an improved surface accuracy.

Some specifications:

Diameter	12 m
f/D	8
Surface accuracy	18 microns
Pointing accuracy	2 arcseconds
Total mass	125 tons

THE CHAMP+ INSTRUMENT

The CHAMP+ receiver (Fig. 1) is a dual band heterodyne array, to be mounted in one of the Nasmyth foci of the telescope. It consists of two times seven mixers, each cluster in a hexagonal layout. By orienting the mixer array (by way of the telescope's K-mirror) at a certain angle with respect to the scan direction, seven equidistant traces can be mapped on the fly.

These are the ranges for the two observing bands:

Low band	600-710 GHz
High band	790-950 GHz

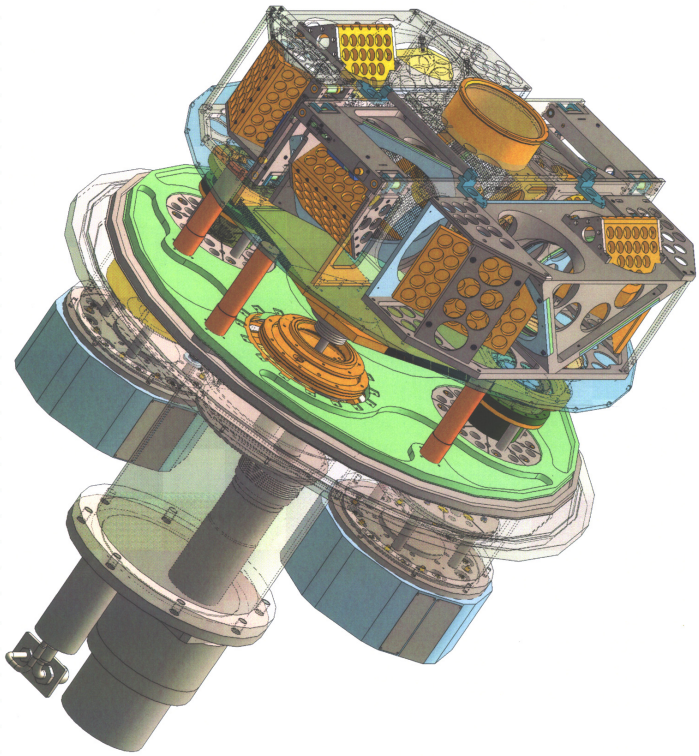

Fig. 1 The CHAMP+ instrument

Note that these bands correspond approximately with ALMA bands 9 and 10, respectively. The IF band of the system ranges from 4 to 8 GHz.

In the instrument, as shown in Fig. 2, the telescope beam is distributed over the two mixer arrays by a cross grid, implying that the two frequency bands have orthogonal polarizations on the sky. After the cross grid, each channel passes a Martin-Puplett SSB filter and a diplexer for LO injection. Before the diplexer, the LO beam is split into seven sub-beams be a holographic diffraction grating.

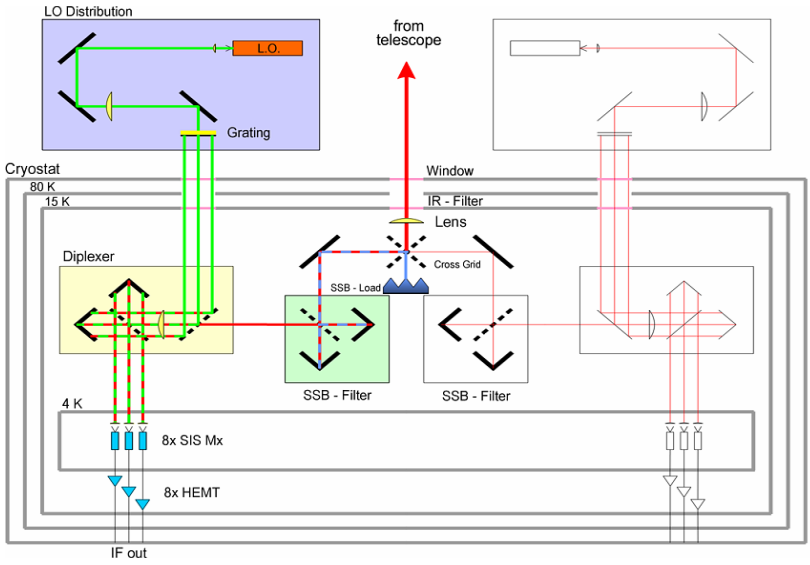

Fig. 2 CHAMP+ system design

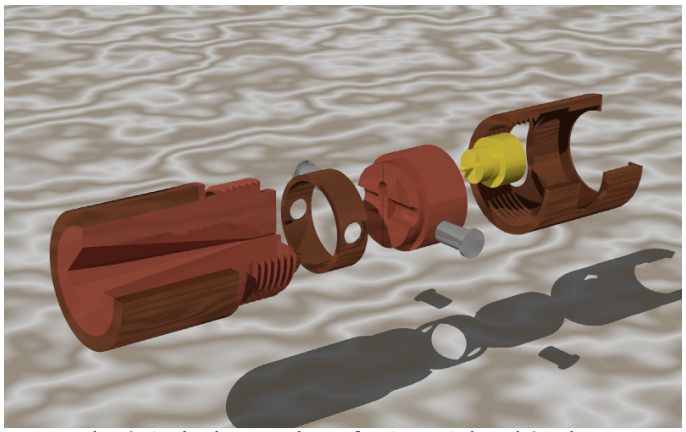

Fig. 3 Artist impression of a ALMA band 9 mixer

The following are the goals for the mixer noise temperatures:

Low band	150 K (80% of the band)	200 K (full band)
High band	300 K (80% of the band)	400 K (full band)

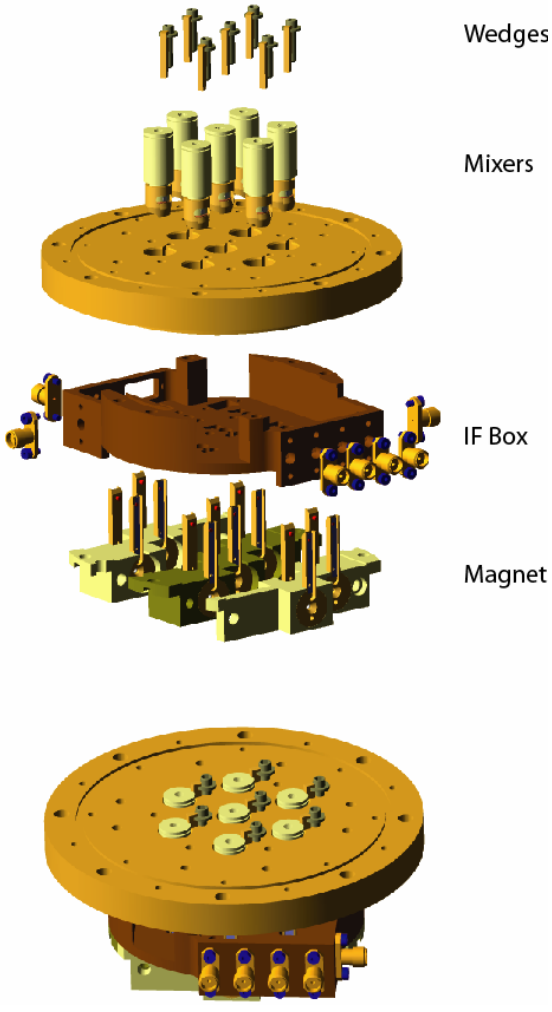

Fig. 4 Design concept of the CHAMP+ low band mixer array

THE CONCEPT: A CLUSTER OF 7 MIXERS

The CHAMP mixer arrays consist of modified ALMA band 9 mixers, as developed by NOVA/SRON. For the low band, only the horn and the outer envelope of the mixers are slightly different from the ALMA mixers. The concept is shown in Fig. 3. The mixer consists of two main parts: a corrugated feedhorn and a backpiece with a backshort cavity and the SIS device. Also in the backpiece are a miniature coaxial IF connector, a deflux heater and two magnetic poleshoes. The backpiece and the horn are aligned within a few microns with respect to each other by a centring ring. The angular alignment is provided by the poleshoes. A capnut holds the horn and the backpiece together.

In the case of the high band, the basic mixer design is the same, but the RF structures in the horn and backpiece are scaled appropriately and the ALMA SIS device is substituted by a HIFI band 3 device.

The design of the low-band mixer cluster is shown in Fig. 4. The high-band cluster will be slightly different because of the smaller spacing between the mixers. Within the array, the mixers have to be positioned with an accuracy of 20 microns with respect to each other, with a maximum angular alignment error of 0.045 degrees. Also, the mixers have to be individually replaceable without taking apart the rest of the instrument. To achieve these goals, the mixers are placed into a copper plate with accurately machined holes, honed to a diameter to fit the mixer horns closely. Each mixer is clamped into its hole by a wedge that is held in place by a screw. When the screw is loosened, the wedge is pulled out by a collar under the head of the screw, and the mixer can be extracted either by hand or by a tool fitting into a slot in the top of the horn. The longitudinal position of the mixers is determined by a stop plate below

the mixer plate (not visible in the figure).

When the mixer is inserted, its IF connector blind-mates with a connector in the IF box by way of a so-called bullet or barrel. At the same time, a leaf spring contacts the deflux heater in the mixer backpiece. The magnetic field, required for suppressing the Josephson current in the mixer device, is generated by a superconducting coil below the IF box, and led upwards by two magnetic conductors. At the top of these are spring-loaded poleshoes that contact the poleshoes integrated into the mixer.

In the IF box there will be a PCB with the IF connectors mating to the mixers, micro striplines to guide the signals to SMA connectors on the sides of the IF box, and the posts with leaf-spring contacts for the heaters.

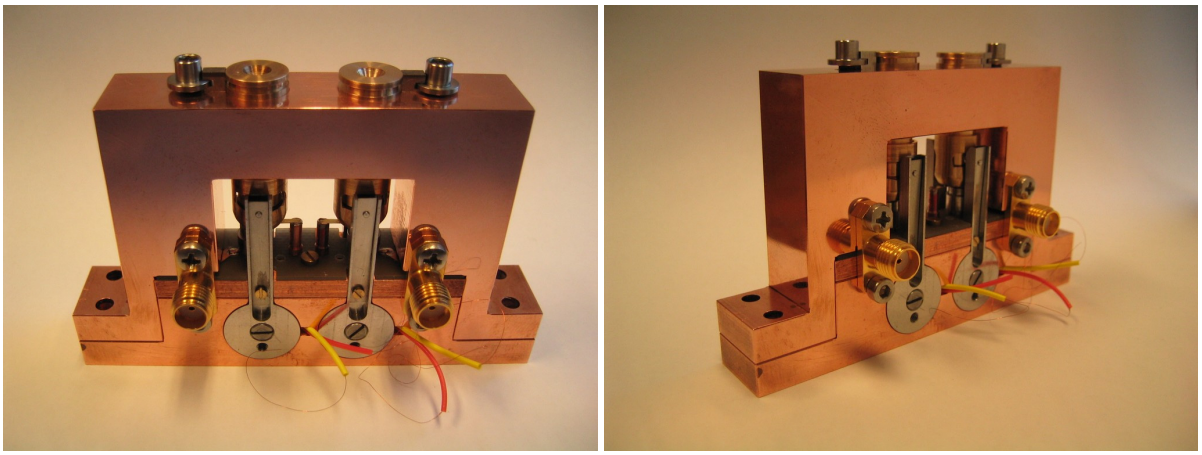

Fig. 5 Two-mixer prototype for testing the plug-in concept as well as investigating the thermal and magnetic cross-talks

THE PROTOTYPE

In order to test the plug-in concept, as well as to investigate the degree of magnetic and thermal cross-talk between the closely spaced mixers, a two-mixer prototype was constructed, as shown in Fig. 5. After several small but important modifications the mechanics of the plug-in concept turned out to work beautifully.

To test the thermal response time of a single mixer, the device was current-biased at a point halfway up the superconducting transition, after which a heat-pulse was applied by way of the deflux heater. Figure 6 shows the

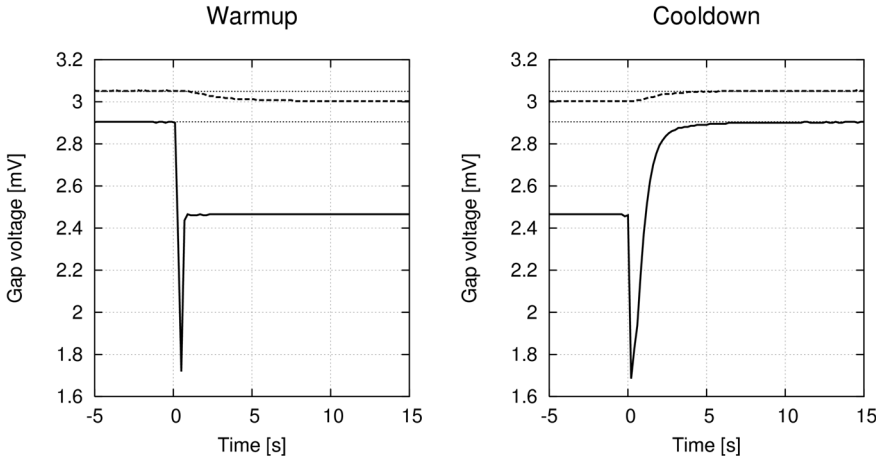

Fig. 6 Thermal relaxation and cross talk when heating mixer 1. Solid line: response of mixer 1; dashed line: response of mixer 2

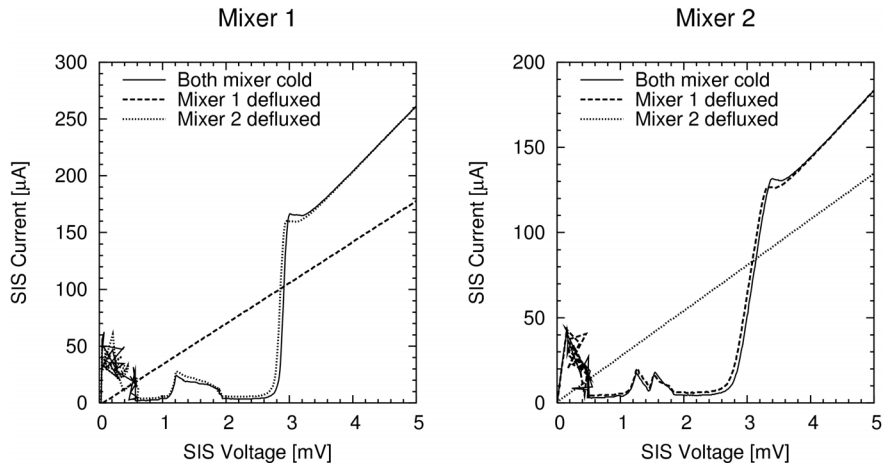

Fig. 7 I-V curves of the two mixers showing the thermal cross talk between them.

voltage over the device when at t=0 the heater current is switched on and off (left and right panel, respectively). The lower traces belong to the mixer that is being heated, the upper traces to the other mixer. Upon applying heat, first the voltage drops as the gap of the tunnel junction is suppressed, after which the voltage goes up again when the entire stripline structure of the device goes out of superconductivity. In the mixer that is not heated (upper trace), only the gap is slightly suppressed, but the entire structure remains superconducting. Also visible is that after removing the heat input, the mixer is fully recovered within, say, 10 seconds.

The full I-V curves of the mixers are shown in Fig. 7, each in the three situations: no mixers heated, mixer 1 heated and mixer 2 heated. Note that mixer 2 has a slight series resistance, which is not relevant for the present investigation. Also here is visible that the gap of the neighbouring mixer is suppressed by less than 0.1V.

Figure 8 shows the suppression of the critical current as function of the coil current. The first minimum is reached at about 10mA from the central maximum, the second minimum at about 18 mA. In the left panel, the current was swept from -40 mA to +40 mA, back to -40 mA, and forward to +40 mA once more. A clear hysteresis of about 7 mA is observed, due to the remanent field of the Vacoflux yoke material. The two forward curves almost exactly coincide. In practice, this hysteresis is usually not of great concern, since only small adjustments around the minimum are made. It is important, however, to set the field to the point of maximum critical current when defluxing the junction, to avoid freezing in extra field lines upon cooldown. Since the local flux at the junction is likely to change at this point (that is the primary goal of defluxing, after all), the operation should be repeated a few times, each time readjusting the coil current for maximum critical current.

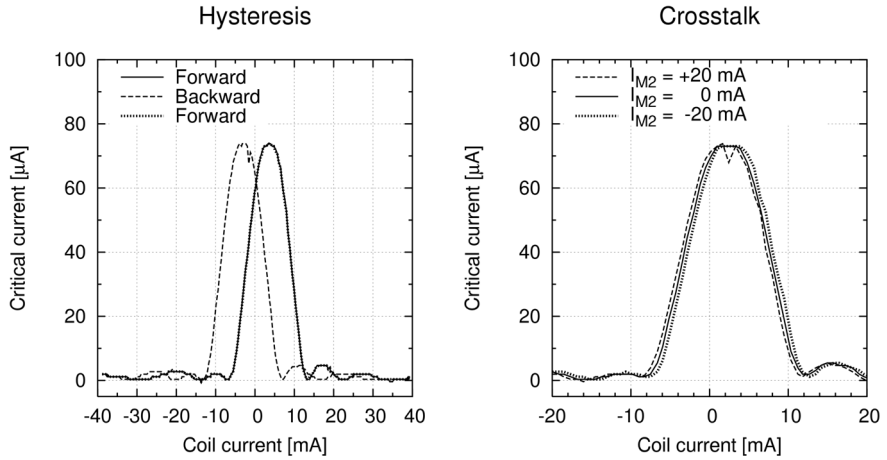

Fig. 8 Magnetic hysteresis of mixer 1 and cross-talk between mixer 1 and 2

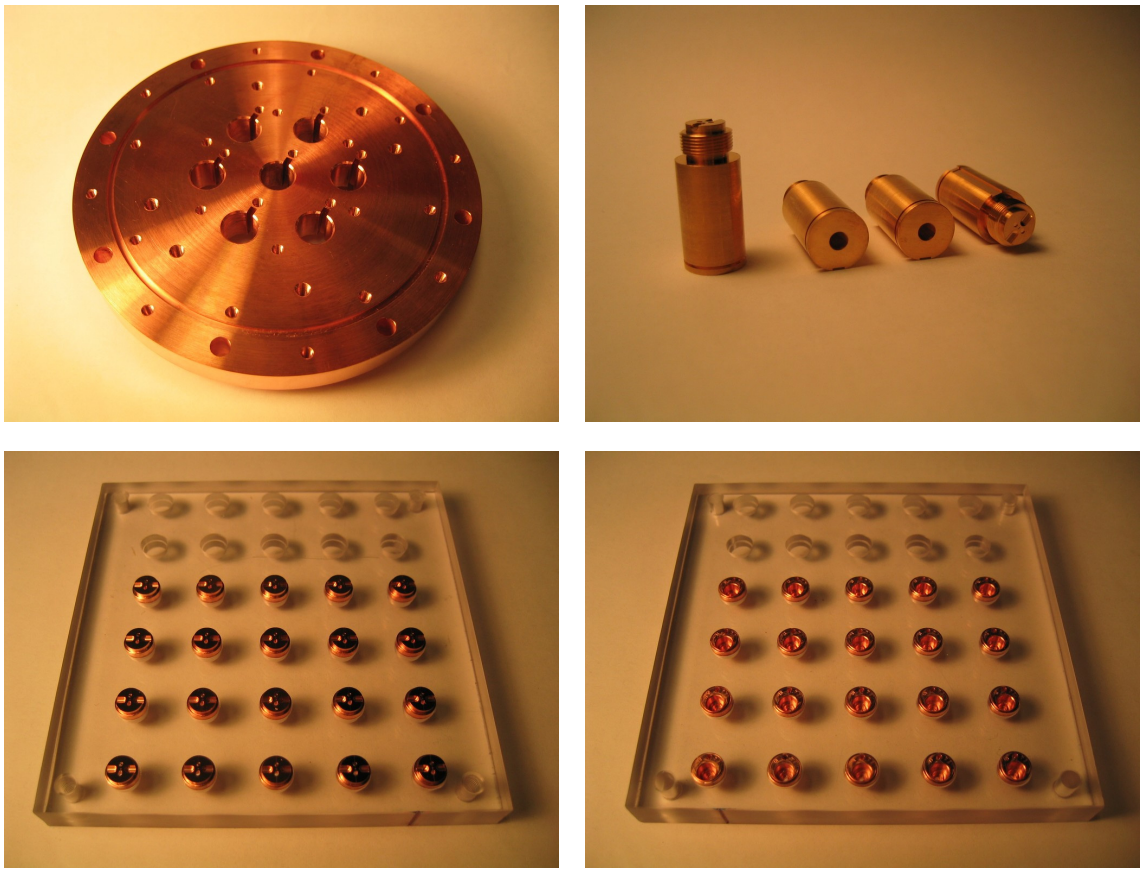

Fig. 9 Manufactured parts for the CHAMP+ low band array. Left to right, top to bottom: mixer clamp plate; corrugated horns; mixer back pieces front view and back view.

The right panel of Fig. 8 shows the effect on the suppression current of mixer 1 when the coil current of mixer 2 is changed from -20 mA to 0 mA to +20 mA. A crosstalk of about 10% is observed. Although this level of crosstalk is acceptable for operation, it probably will make it necessary to obtain optimal suppression in all seven mixers in an iterative way. In the final design we shall try to decrease the magnetic coupling, mainly by modifying the shape of the magnetic conductor components. For the high band, the coupling is likely to be much smaller, since in the high-band array, the coils are in line, contrary to the low-band array, where they are in parallel. When the coils are in line, there is much less opportunity for field lines to form closed loops through the neighbouring mixer.

THE METAL

Several actually manufactured components for the low-band mixer cluster are shown in Fig. 9. At the moment of writing more components are arriving, and assembly and testing are about to begin. The final design for the high band array is also nearing completion, and several components (backpieces and corrugated horns) arrived already.

CONCLUSIONS

A prototype two-mixer array was constructed to test the mechanics of the CHAMP+ plug-in concept and the degree of thermal and magnetic crosstalk between the mixers. Both goals were successfully met, and several design modifications were incorporated in the seven-mixer design as a result. The seven mixer cluster for the low band of the CHAMP+ instrument was designed and for the high band is being finalized. Components for both arrays are in the process of being manufactured.

THE LARGE MILLIMETER TELESCOPE

F. Peter Schloerb[1] and Luis Carrasco[2]

[1] Five College Radio Astronomy Observtory, Department of Astronomy, University of Massachusetts-Amherst, USA; [2] Coordinación de Astrofísica, Instituto Nacional de Astrofísica, Óptica, y Electrónica, Mexico

We present a summary of the Large Millimeter Telescope (LMT) Project and its present status. The LMT is a 50m-diameter millimeter-wave antenna which has been designed for best performance in the 1-4mm band. The telescope is being built in a collaboration between the University of Massachusetts at Amherst (UMass) in the USA and the Instituto Nacional de Astrofísica, Óptica y Electrónica (INAOE) in Mexico. The LMT site is Volcan Sierra Negra, an extinct volcanic peak in the state of Puebla, Mexico, approximately 100 km east of the city of Puebla. Erection of the antenna at the site is now well underway, and it is expected to be completed in early 2006. The LMT will have nearly 2000 m^2 of collecting area with an overall surface accuracy of 70 microns rms. Thus, its sensitivity will exceed that of existing millimeter-wavelength telescopes by a significant margin. As a completely filled aperture, the LMT will have the optimum sensitivity to low surface brightness emission at an angular resolution of 6-12 arcsec, which is comparable to that of the maps presently made with present interferometric arrays. Consequently, we expect the LMT to take a valuable place in the world's complement of millimeter-wave facilities.

A Multi-path Far-Infrared and Sub-millimetre Gas Cell for Spectral Tests of Herschel/HIFI

D. Teyssier
SRON-Groningen/ESA, Landleven 12,
9747 AD Groningen, the Netherlands

E. Dartois, D. Deboffle, J.-P. Crussaire, Y. Longval, F. Boulanger
IAS, Université Paris-Sud, bâtiment 121, 91405 Orsay, France

M. Pérault
LERMA/ENS, 24 rue Lhomond, 75005 Paris, France

***Abstract* – We present the design and operation of a gas cell developed in the framework of the Herschel/HIFI instrument-level ground-based test campaign. This cell is aimed at acting as a representative spectral source by feeding the system with signal from molecular lines excited by radiometric loads. Its main goal is to measure the sideband ratio of the double-side-band mixers used in the HIFI instrument. The design makes use of multiple reflection optics to increase the total path length through the gas sample while keeping the overall device size into reasonable limits. The system is operated under vacuum to get rid of any water line absorption along the line of sight. It offers a front-to-end 1:1 optical magnification and is designed to keep the beam waists within a 4*w* criterion for the HIFI test setup case. We present the first outcomes of the current test measurements at the SRON premises in Groningen.**

I. INTRODUCTION

HIFI (the Heterodyne Instrument for the Far-Infrared) is one of the three instruments to be launched on the Herschel Space Observatory (HSO) and will operate between 160 and 625 microns (480-1910 GHz). The detectors used in this instrument are based on the heterodyne mixer technology (SIS and HEB) and have the particularity to work in Double Side-Band mode (DSB). Each of these side-bands will contribute to the final spectra with a given gain, which may be strongly frequency-dependent along the mixer tuning range. Observational techniques exist to restore the signal detected in each of the bands but they cannot provide estimates of the side-band ratio (ratio between the gains of the two respective bands) to the accuracy required for the HIFI calibration. In the framework of the AIV/ILT (Assembly, Integration and Verification / Instrument Level Tests), dedicated measurements need to be performed on the HIFI development and flight models.

Several options can be considered to measure the side-band ratio. One common practice consists in using absorption cells filled with adequate gases for the frequency range of interest. This system proved to be very efficient during the SWAS [1] and Odin [2] test phase and allowed to check several detector characteristics (e.g. side-band ratio, mixer compression). It has the additional advantage to provide simulation of astrophysical spectra to the integrated instrument and to test many of the observing modes and reduction schemes. In particular it should help to validate dedicated algorithms to deconvolve the signal between the two side-bands. Alternative systems exist, mostly based on Fabry-Perot or Fourier-Transform spectrometers. They have the advantage to provide as many frequency measurement points as required (monochromatic signals), but are more expensive, hard to calibrate and significantly complex and time-consuming to design.

II. THE LESSONS FROM SWAS

Design recommendations can be found in a report by R. Schieder on gas cell measurements for SWAS tests [3]. The cell should be sufficiently long (30-100 cm) and filled with a gas which provides saturated lines. The pressure should be relatively low (undefined but typically a few mbar) but higher pressures might help to saturate lines with blended structures. The measurements are performed against hot and cold loads which look through empty and filled cells for calibration purpose. Glass cells seem more suitable

than metal cells because molecules are expected to stick more in the later case. The cell window, preferably made of Teflon to avoid internal fringes, shall be tilted to reduce standing waves. The absorption by water vapour along the light pass significantly affects the measurements. Vacuum isolation is not mandatory but dry air conditions would be required in the frequency range of interest (480 to 1910 GHz). Fig. 1 illustrates the expected water vapour spectral contamination for a 1 meter path computed with the ATM software [4].

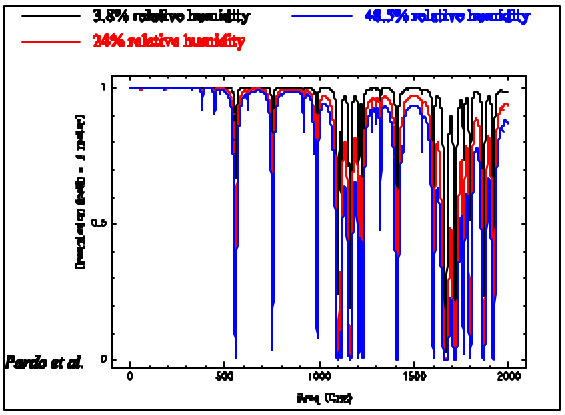

Fig.1: Computed water vapour absorption along a 1 meter path in the 0 to 2000 GHz frequency range (courtesy of Pardo). The transmission is computed for three values of the relative humidity. It shows that spectral measurement above 1 THz requires perfectly dry air conditions.

III. PRINCIPLES

In a given LO (Local Oscillator)- and mixer bias-setting, the side-band ratio measurement is based on the comparison of two signals taken successively through a filled and an empty cell. The measurements are performed against hot and cold loads, and the differential signal, if done fast enough, should be free from system noise contribution. The frequency range is chosen such that an absorption line affects only one of the side-bands and can be compared to the absolute continuum level. The following equations illustrate the basics for the ratio derivation and allow to assess the accuracy of a measurement. We assume that an absorption line (of opacity τ) is seen in the lower side-band, while the spectra in the upper side-band is not affected by any spectral feature. The differential measurements are then respectively:

$$S_{filled} = G_u(J_{hot} - J_{cold}) + G_l(J_{hot} - J_{cold})\mathrm{e}^{-t}$$

and

$$S_{empty} = G_u(J_{hot} - J_{cold}) + G_l(J_{hot} - J_{cold})$$

where G_u and G_l stand for the upper and lower side-band gains respectively, including all transmission elements along the optical path, and J_{hot} and J_{cold} are the effective (Rayleigh-Jeans) hot and cold load temperatures of a black body of temperature T and frequency ?.

Using the measurements described above, the side-band ratio is finally given by:

$$R_G = \frac{G_l}{G_u} = \frac{1 - S_{filled} / S_{empty}}{S_{filled} / S_{empty} - e^{-t}}$$

The opacity needs to be accurately known, unless the line is saturated (high τ), in which case R_G simply writes S_{empty}/S_{filled} - 1. Typically, a side-band ratio of unity would be observed for S_{empty}/S_{filled} = 0.5 at the line peak position, i.e. an absorption line of half the continuum level in a normalized spectra.

Based on this simple formalism, the measurement accuracy depends on the accuracy of the opacity knowledge (if lines are not saturated) and on the spectra rms noise. One can prove that a 1% uncertainty on the opacity is small enough to be neglected in the final measurement accuracy. This level is reasonably reached, depending on the species used. In order to reach a goal of 1% accuracy on R_G, the relative error on each individual spectrum has to be smaller than 2.5×10^{-3}. The temperature difference between hot and cold loads has thus a critical impact on the accuracy. Given the pressure conditions envisaged here (some mbar), expected line widths are of the order of 200 MHz, so that a 15 MHz spectral resolution is adequate. With detector operated under vacuum, relatively low DSB system temperatures are reachable, allowing to get the required sensitivity in a couple a seconds, far below the expected system drift time constants.

IV. CALIBRATION GASES

The choice of the gases depends on the type of measurement to be done. For side-band ratio measurements, gases with high line strengths and lines nicely distributed over the instrument frequency range should be considered. For the specific HIFI case, species such as OCS, N_2O, H_2CO or CO are of particular interest. When the gas cell is used as molecular line source aiming at mimicking lines of sight observed towards the cosmos, more complex molecules (symmetric and asymmetric tops) are well suited as they possess much more transitions and multiplet line structures. Typical examples are methanol (CH_3OH) or acetonitril (CH_3CN), which can

be used in order to exercise extensive frequency surveys (see Fig.10) across the instrument bands, and consequently optimise dedicated reduction tools necessary to recover the signals arising from either of the upper and lower side-bands.

V. TECHNICAL DESCRIPTION

In contrast to other similar systems operated in the millimetre and sub-millimetre domain (e.g. at University of Cologne), this cell was built following the multi-path concepts commonly used at visible and Near-Infrared wavelengths (e.g. [5]). The overall device is shown in Figs.2 and 3, and consists mainly of two parts: a lower cavity, that we call *connection chamber,* providing the mechanical interface to the input and output ports, and an upper glass cavity (*the cell*) hosting the gas sample. The interface between these two entities consists of two thin (50 microns) Mylar windows adequately tilted in order to avoid any back reflection along the signal path.

An Offner relay located inside the cell (mirrors M1 and M2 on Fig.2) allows a total path of more than 1 metre in a very compact (less than 30 cm high) configuration, easing thus operations and integration in a variety of measurement setups. In order to reduce the efforts on the glass cavity, the plate holding the M1 mirror, and located above the cell, is sustained by 4 stainless-steel bars directly screwed onto the connection chamber (see Fig.4 for an overview). This rigid interface also allows for a reproducible alignment even when the glass cell needs to be removed for any reason. In particular, it keeps constant the distance between M1 and M2, as well as their relative positions.

The optics are designed to control and keep the beam waists in required ranges at the input and output ports (here 4*w* criterion for the HIFI beams). They offer a 1:1 magnification, allowing the system to be operated with any microwave detection system whose beam properties would fit within the constraints of the gas cell optics. This versatile spectral source can be interfaced to the HIFI detection chain in such a way

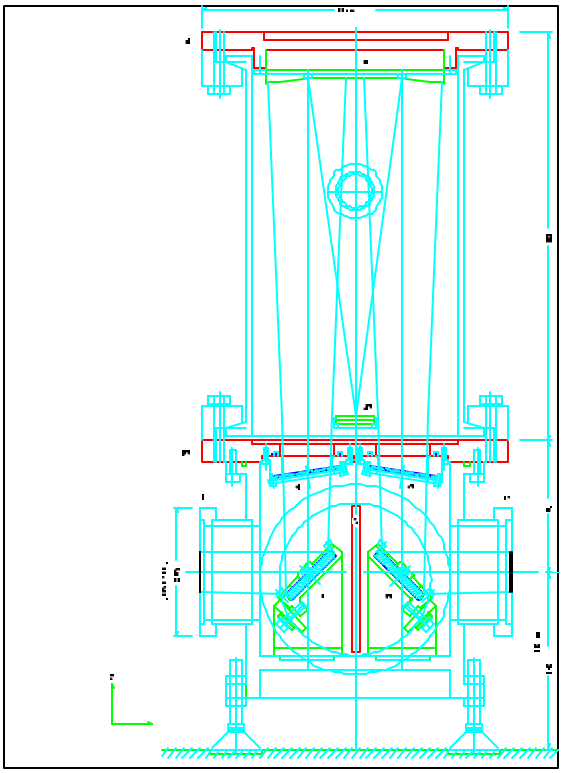

Fig.2: Drawing from the cell as seen laterally. Chief-ray and 4*w* beam envelopes are shown along the entire optical path. Indicated on this figure are the two folding mirrors P1 and P2, as well as the Offner relay consisting of spherical mirrors M1 and M2. Also shown are the tilted Mylar windows (F1 and F2).

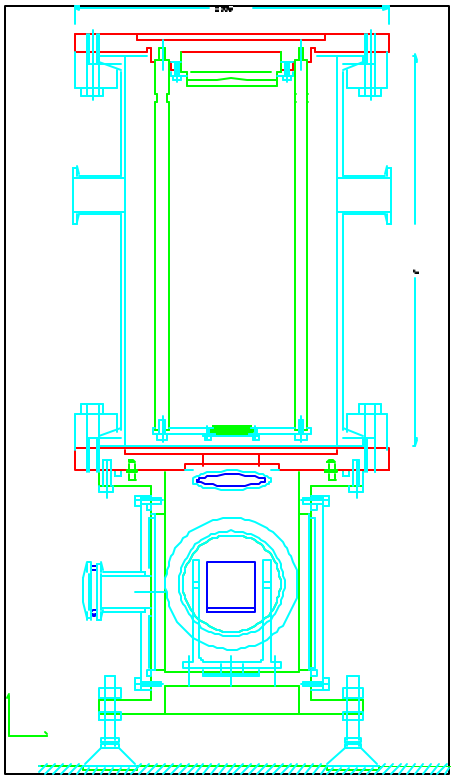

Fig.3: Drawing from the cell as seen from the input (or output) beam. Shown on the cell are two pipes dedicated to the filling and emptying of the gas sample (see next section). Also shown is the pipe at the side of the connection chamber (see text for details).

Fig.4: Picture of the gas cell (left) and of the hot/cold load source (golden cryostat) mounted onto the HIFI test setup.

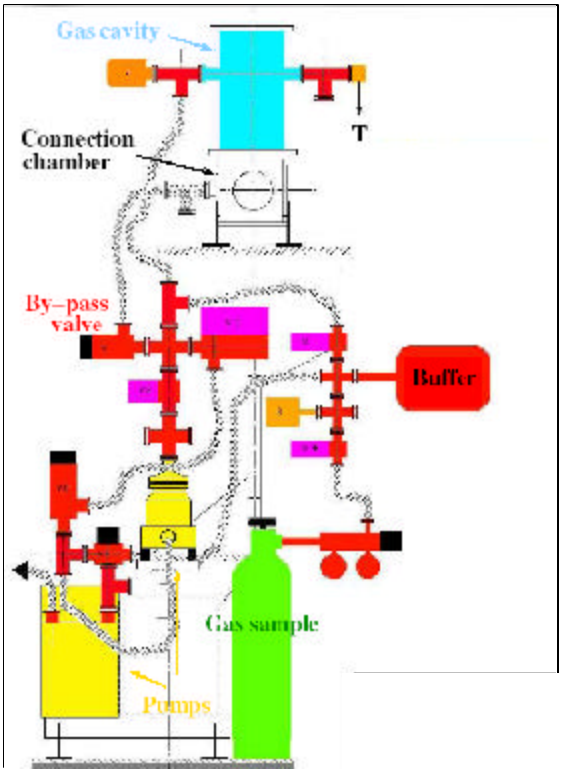

Fig.5: Scheme of the gas handling rack. Valves 1 to 4 are automated devices, while valve 5 serves as a by-pass between the cell and the connection chamber cavities.

that measurements can be performed under vacuum conditions, cancelling thus the contribution from the line-of-sight water lines over the whole operating frequency range, and reaching low noise temperatures compared to open-air systems.

A dedicated pipe was added on one side of the connection chamber in order to allow balancing of the pressure between the two cavities during the initial pumping out, permitting to protect the thin Mylar windows from too strong pressure difference on either side.

VI. OPERATIONS

The gas cell setup (partially shown on Fig.4) makes use of a dedicated gas handling rack allowing to perform the gas transfers and evacuation in a reproducible manner (see Fig.5). To that purpose, we designed a circuit making use of electronically controlled valves to be commanded automatically from the test control environment. Since the gas cavity and the chamber hosting the folding mirrors P1 and P2 (Fig.2) are separated by thin windows, the two volumes need to be connected during the initial pumping out. Once under vacuum, a by-pass valve is closed to isolate the gas sample from the rest of the test setup. As gases are planned to be used in the pressure range 0.1 mbar to 100 mbar, a buffer is necessary in order to thermalize the gas (initially at very high pressure) prior to injection into the gas cavity. Using the combination of primary and secondary pumps, the typical time for a complete measurement cycle is of the order to 10-20 sec., while the evacuation of the gas cavity takes 2-3 min. depending on the pressure contrast required between filled and empty cell spectra.

The system also allows for using species under liquid form, such as methanol or acetonitril. The gas pressure in the cell is then controlled by adapting the ratio between the volumes in the buffer and in the cell cavity respectively, the pressure in the buffer being constant and driven by the vapour pressure of the considered molecule.

The source feeding the cell consists of a cryostat hosting two identical trapping cavities at ambient and liquid nitrogen temperatures respectively (see Fig. 6). These cavities are coated by a mix of SiC grains and Stycast shown to offer specular reflection of 10^{-4} over a wide range of incidence angles, and an emissivity of

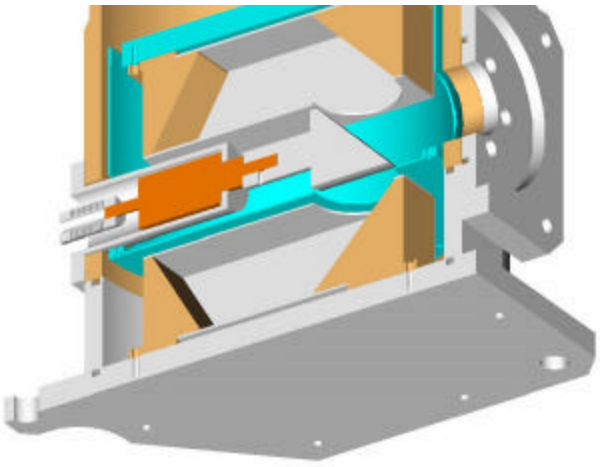

Fig.6: Partial drawing of the hot/cold source connected to the gas cell. Shown are the two identical trapping cavities serving as hot and cold loads, located above and below a switching mirror controlled by a stepping motor

0.93 [6]. Its dimensions are also chosen to respect the 4*w* beam truncation criterion.

VII. MEASURED SPECTRA

We present here some representative spectra obtained during the first measurement campaign conducted with the gas cell integrated onto the HIFI test setup. Details about these tests can be found somewhere else in these proceedings [7]. Fig.7 shows a sketch of the gas cell connected to the hot/cold switch and the some other equipment interfaced to the instrument prototype. The instrument was hosting the so-called band 1 mixer, working in the range 480-640 GHz [8], but the operating range was limited to 460-490 GHz by the LO Gunn actually available at that time. The spectra were sampled by an Acousto-Optical Spectrometer (AOS) developed at the University of Cologne [9], providing a instantaneous sampling of the 4 GHz IF band with 1 MHz resolution channels.

We show in Fig. 8 to 10 examples of the spectra measured during this first campaign. Fig. 8 illustrates the case of a side-band ratio measurement using acetonitril at a LO frequency of 484 GHz. In this case, the pressure was increased on purpose in order to broaden lines and achieve high optical depth through line blending. The dip of the absorption is here measured to be 0.497, translating into a side-band ratio of 1.01. However, another absorbed line measured in the same band indicates a ratio of 0.95. Unless rapid side-band ratio variations occur on GHz-scale, which is unlikely, we are probably witnessing side-band ratio

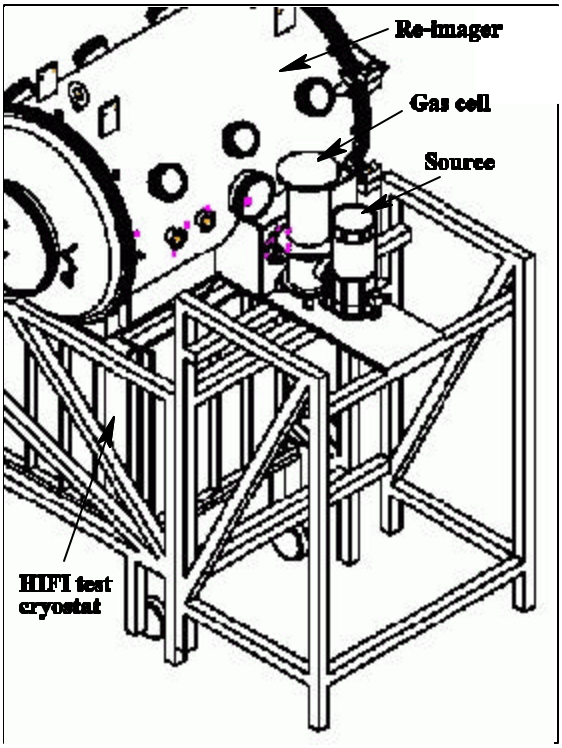

Fig.7: Sketch from the test setup used during the gas cell measurement of the HIFI test campaign. Shown are the re-imager used to focus all HIFI beam at a common position and waist at the cell entrance, as well as the cell itself and the source. The cryostat hosting the HIFI prototype stands below the re-imager.

modulation arising from standing waves generated between the mixer and the LO horns. This phenomenon has been extensively described by [10] and severely limits the accuracy of such measurements if precise knowledge of the shape of this modulation is unknown. Still, the value of the measured ratio is remarkably good considering the fact that we sit at the edge of the mixer working domain, where sideband imbalance is expected to be the worst.

Figs.9 and 10 illustrate another powerful use of the gas cell in order to simulate representative spectra of molecular lines. Both of them correspond to line survey, where the LO frequency is changed by small to larger steps in order to get sufficient spectral redundancy at the time of recovering the Single Side-Band (SSB) spectra from the DSB measurements [11]. The survey of Fig,9 is performed without LO retuning as such since only the synthesizers frequency was changed in a range keeping the phase locked. It shows very well the lines in upper and lower side-bands respectively moving in opposite direction as the LO frequency is changed. Fig.10 is obtained with larger LO frequency steps of order 1.5 GHz.

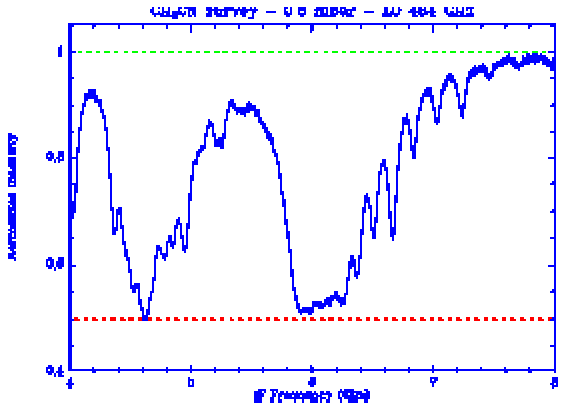

Fig.8: Example of side-band measurement at LO frequency 484 GHz, using acetonitril (CH_3CN). See text for details. Dashed lines indicate the respective 1 and 0.5 levels of the normalized spectrum.

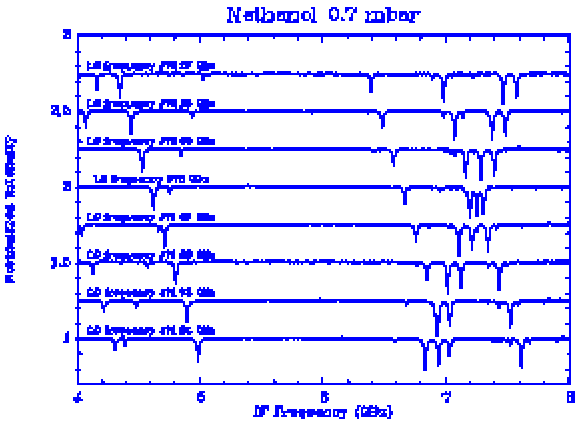

Fig.9: Example of small spectral survey in a LO range of about 600 MHz using methanol (CH_3OH). See text for further details.

VIII. CONCLUS IONS

In the framework of the Herchel/HIFI AIV/ILT campaign, we have developed an absorption gas cell aiming at providing representative spectral lines to the detector, as well as at measuring the side-band ratio along the HIFI frequency range using saturated lines. The system consists of multi-reflection optics, allowing long optical path through the gas sample while keeping the instrument compact. It is operated under vacuum and is thus insensitive to water vapour absorption. By acting as a 1:1 optical system, it can in principle be used with any system meeting the beam waist requirement at input and output ports (4*w* waists of 30 mm in that precise case, located at the gas cell port). More outcomes of this device are expected in the course of the HIFI qualification campaigns over the coming years.

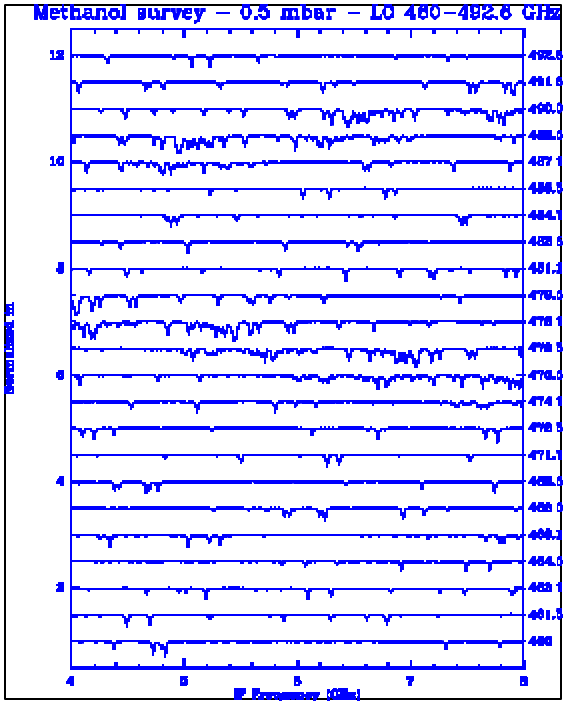

Fig.10: Same as Fig.9 on a larger LO frequency range (460-492 GHz) with tuning steps of order 1.5 GHz. The LO frequency is indicated on the rightmost column.

IX. ACKNOWLEDGMENTS

It is a pleasure to thank Paul Goldsmith and Rudolf Schieder for the numerous discussions and advises they gave us in the various design phases of this project. We are also grateful to the HIFI teams in Groningen and Utrecht for all their support during integration and operation of the system. This project was funded by the CNES, the French space agency.

X. REFERENCES

[1] V. Tolls, G.J. Melnick, M.L.N. Ashby, E.A. Bergin, et al., 2004, ApJ 152, 137, *SWAS performance on the ground and in orbit*

[2] U. Frisk, M. Hagström, J. Ala-Laurinaho, S. Andersson, et al., 2003, A&A 402, L27, *The Odin Satellite. I. Radiometer design and test*

[3] R. Schieder, 1993, SWAS/TM-4027, *The usefulness of a gas cell for performance testing*

[4] J. Cernicharo, 1985, IRAM technical report, *ATM, a program to compute atmospheric opacities between 0 and 1000 GHz*

[5] J. Ballard, K. Strong, J.J. Remedios, M. Page, W.B. Johnston, 1994, J. Quant. Spectrosc. Radiat. Transfer, Vol. 52, No. 5, pp. 677-691, *A coolable long path absorption cell for laboratory spectroscopic studies of gases*

[6] M.C. Diez, T.O. Klassen, C. Smorenburg, V. Kirschner, K.J. Wildeman, Astronomy 2000: Astronomical Telescopes and Instrumentation 2000, 29-31 March 2000, Münich, Germany, SPIE 4013 (2000), 129-39, *Submillimeter absorbing coatings*

[7] N. Whyborn, T. de Graauw, E. Caux, T. Phillips, J. Stutzki, this conference, *Development status of Herschel-Heterodyne Instrument for the Far-Infrared (HIFI)*

[8] M. Salez, Y. Delorme, I. Peron, B. Lecomte, et al., 2003, SPIE, Millimeter and Submillimeter Detectors for Astronomy, Vol. 4855, pp.402-414, *A 30% bandwidth tunerless SIS mixer of quantum-limited sensitivity for Herschel/HIFI Band 1*

[9] R. Schieder, J.M. Horn, O. Siebertz, C. Moeckel, et al., 2003, 1998, SPIE, Advanced Technology MMW, Radio and Terahertz Telescopes, *Design of large-bandwidth acousto-optical spectrometers*

[10] O. Siebertz, C. Honing, T. Tils, C. Gal, et al., 2002, IEEE Transactions on Microwave Theory and Technics, Vol. 1, No. 12, December 2002, *The impact of standing waves in the LO path of a heterodyne receiver*

[11] C. Comito, P. Schilke, 2002, A&A 395, 357, *Reconstructing reality: Strategies for sideband deconvolution*

Tunable Heterodyne Mixer using Plasmon Modes in a Grating Gated Double-Quantum-Well Field Effect Transistor

Mark Lee, Michael C. Wanke, and John L. Reno
Sandia National Laboratories, P.O. Box 5800, Albuquerque, NM 87185

Double quantum well (DQW) semiconductor heterostructures fabricated from high-mobility two-dimensional electron gases (2DEGs) can serve as tunable, sensitive, and possibly fast millimeter- and submillimeter-wave detectors by exploiting long wavelength photons to promote coupling of interwell charge excitations. Recently, DQW field-effect transistors (FETs) in which the gates are periodic metal gratings have been shown to function as tunable incoherent direct detectors between 500 to 700 GHz.[1] These DQW-FETs showed resonant photoconductance with $Q \sim 20$ at frequencies selected by the fixed (for a given device) grating period and the continuously variable gate voltage. A device with a 4 μm gate grating period could be tuned from 570 to 660 GHz by varying the DC gate bias between -1.5 to -0.5 V. This photoresponse was determined to arise from the excitation of plasmon modes in the DQW system. The gate bias depletes the electron density thereby changing the plasmon resonance frequency, initially in the upper quantum well at small negative biases and subsequently in both quantum wells. The gate grating period selects discrete plasmon wave vectors, leading to harmonic resonances in the photoresponse. Interestingly, the strength of the resonant photoresponse was observed to be maximal at temperatures between 25 to 40 K, decreasing at both lower and higher temperature. The composite plasma oscillation of the coupled quantum wells under illumination is complicated and as yet remains incompletely understood. The presence of both quantum wells appears to be necessary to produce the tunable resonant photoresponse.

The use of a DQW-FET in coherent detection as a tunable heterodyne mixer has not previously been addressed. Several properties of the DQW-FET indicate that it may function well in mixer applications requiring electrical tunability, low LO power, and modestly wide IF bandwidths for a resonant detector. The resonant response of these devices suggests that proper coupling of the electromagnetic field to the DQW system can lead to relatively small required LO powers. Current rise-and-fall time measurements have shown that the DQW-FET's direct response time is less than 0.7 μs, which was the limit of the light source and measurement equipment time constants. These devices also have relatively low sheet resistances and can be designed to operate near 50 Ω for impedance matching purposes.

We will present measurements of a grating-gated DQW-FET operating as a heterodyne mixer. The devices are fabricated from a modulation doped GaAs/AlGaAs DQW heterostructure with 20 nm wide wells separated by a 7 nm barrier. The nominal charge densities in the wells are 1.7×10^{11} cm^{-2} in the upper (closer to the gate) and 2.6×10^{11} cm^{-2} in the lower well. The grating gates are 70 nm thick TiAu patterned into gratings with periods between 4 to 16 μm. The devices will be tuned to resonate near the 94 GHz center frequency of a tunable Gunn oscillator. The basic properties of the mixer will be discussed and analyzed, including the conversion gain, required LO power, IF bandwidth, and temperature dependence.

[1] X. G. Peralta, S. J. Allen, M. C. Wanke, N. E. Harff, J. A. Simmons, M. P. Lilly, J. L. Reno, P. J. Burke, J. P. Eisenstein, Appl. Phys. Lett. **81**, 1627-1629 (2002)

A Broadband Finline Ortho-Mode Transducer for TeraHertz Applications

Christopher Groppi[1], Christian Drouet d'Aubigny[2], Christopher Walker[2] & Arthur Lichtenberger[3]
[1] National Radio Astronomy Observatory, 949 N. Cherry Ave., Tucson, AZ 85721
[2] University of Arizona, 933 N. Cherry Ave., Tucson, AZ 85721
[3] University of Virginia, 351 McCormick Rd., Charlottesville, VA 22904
email: cgroppi@nrao.edu

Abstract

At low frequencies, the preferred method for implementing a dual polarization, low-noise receiver for radio astronomy applications is the Ortho Mode Transducer, or OMT. This waveguide junction allows compact, low loss coupling of two detectors, each sensitive to a single linear polarization, to the (usually) randomly polarized signal. While these devices are the de-facto standard for receiver systems below 100 GHz, most systems built for the sub-mm and THz frequency range use quasi-optical polarization diplexers like the linear wire grid, or are single polarization systems. We plan to fabricate and test an OMT capable of operation at 1 THz and beyond. Recent advances in both electromagnetic simulation and micro-fabrication techniques allow construction of far more ambitious waveguide structures at high frequencies. Successful Bøifot type designs have been scaled to frequencies above 100 GHz, but these devices will be difficult to realize at frequencies significantly over 1 THz. A design using finline waveguide could prove to be far simpler to fabricate at THz frequencies. The proposed design is a finline OMT operating from 750 GHz to 1150 GHz. This design could be fabricated using laser micromachining techniques at frequencies above 1 THz, or with classical CNC micromilling techniques below 1 THz. The finline is a photolithograpically defined thick gold fin, fabricated on a thin Silicon-On-Insulator (SOI) substrate, with beamlead grounding. Losses are ~1 dB or less from 750-1150 GHz, with -20 dB input match. Crosspolarization is at the -50 dB level. Testing will be done optically using a Fourier transform spectrometer and a ^{4}He bolometer system. The prototype OMT will be equipped with horns at all three ports to facilitate testing, with the eventual goal of integrating both mixers and the input horn with the OMT in a single block.

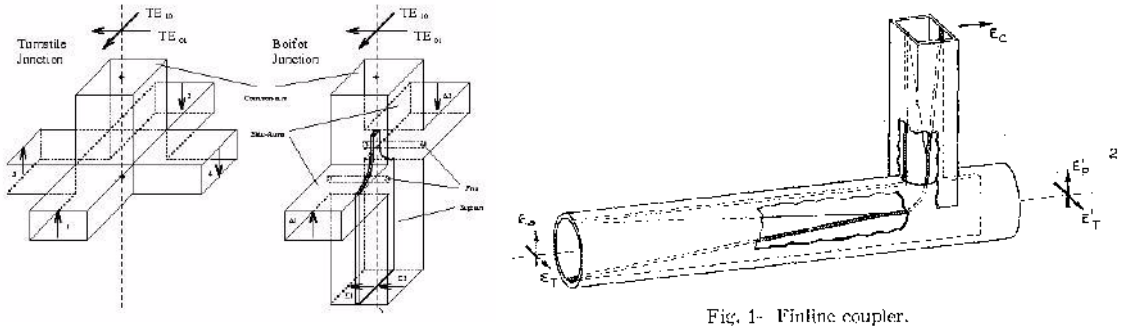

Wollack et al. 2002 *Robinson 1956*

Figure 1: The Bøifot OMT (left) and Robinson finline OMT (right) designs.

Introduction

The design of symmetric ortho-mode transducers at mm-wave frequencies has been discussed extensively by Wollack (2002, 2003). This design, referred to as the Bøifot OMT, is based on the 5 port turnstyle junction (Meyer and Goldberg, 1955), folded into a more compact shape (Figure 1). Recently, Narayanan and Erickson (2002, 2003), have

developed a Bøifot type design replacing the capacitive pins used in previous designs with a capacitive step. This and other refinements make the design far easier to fabricate and make it suitable for scaling to frequencies as high as 1 THz. These waveguide designs offer very low loss, good crosspolarization performance and excellent isolation, but are fundamentally three dimensional. Another design exists, using finline to extract one polarization from the square or round input guide. This design was originally proposed by Robinson (1956) and was recently pursued by Chattopadhyay and Carlstrom (1999) (Figure 1). This design is planar, and could be easily fabricated at THz frequencies using micromachining techniques for the waveguide, and photolithographic techniques on a silicon substrate for the finline. This structure does suffer from somewhat higher loss than the Bøifot design due to ohmic losses in the fin. For operation at frequencies below the bandgap of NbTiN (1.4 THz), the fin could be fabricated from this superconducting material if the losses in a normal metal fin prove to be too high. With a fin of zero resistivity (PEC) the losses in the device are significantly reduced.

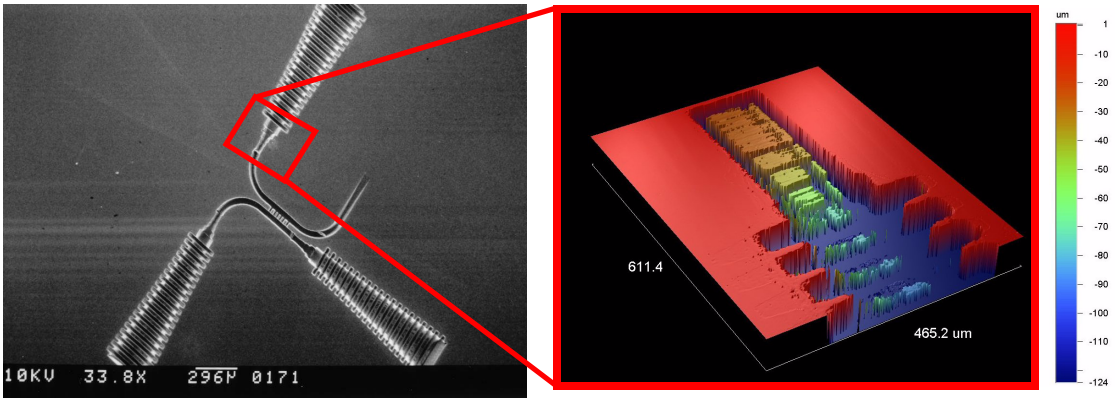

Figure 2a: Laser micromachined 1.5 THz coherent beam combiner with corrugated feedhorns

Figure 2b: 3-D image of quarter-wave transformer and horn throat made with the Veeco optical profiling system.

In the past, the ability to fabricate waveguide structures at high frequency was limited by available machining technology. Electroforming techniques allow construction of high frequency waveguide components, but this technique is extremely costly and time consuming. Today, classical CNC micromachining equipment is available commercially, and micromachining techniques have been pioneered by the JPL Sub-mm Wave Advanced Technology group and the University of Massachusetts (Narayanan et al. 1999). In addition, the Steward Observatory Radio Astronomy Lab has developed a laser micromachining system that uses a He-Ar laser to machine structures in silicon. This technique is a non-contact process, with no debris field. The silicon vaporized by the laser is reacted with chlorine gas in the milling chamber producing silicon tetrachloride gas. Additionally, silicon melted at the etching site re-grows epitaxially as it cools, producing high surface quality (Drouet d'Aubigny et al. 2003). The current system has the potential for fabricating waveguide structures at frequencies beyond 5 THz. Figure 2 shows example structures made via this process at the University of Arizona. A Veeco optical profiling system is used to measure structure depth and surface roughness to accuracies better than 100 nm. In addition to their laser micromachining and metrology capabilities, SORAL is equipped with a Coherent/DEOS far infrared laser system. This THz source is complimented by a Fourier Transform Spectrometer (FTS) system and an Infrared Laboratories ^{4}He bolometer.

OMT Design

Two design features have prevented scaling successful Bøifot type OMT designs to higher frequencies: the septum and the capacitive pins used to compensate the septum. As shown in Figure 1, the septum is a thin metallic plate that acts like a splitting junction for one polarization of the input guide, directing that mode into the two side arms. A thin septum disrupts the orthogonal polarization very little, allowing it to pass by the septum to a square to rectangular waveguide transition. The presence of the septum requires capacitive compensation for broadband performance in the side arms. In the newest NRAO design for use in ALMA, these pins are realized as thin gold wire run through holes in the guide walls. At high frequencies, these pins are nearly impossible to fabricate. The design by Narayanan and

Erickson has eliminated these pins in favor of capacitive steps in the waveguide walls. Fabrication of the septum poses little problem if made from silicon using photolithographic techniques, but fabrication of the capacitive steps in the waveguide walls, and the out of plane output waveguide pose significant challenges at THz frequencies. The capacitive steps could be too small to reliably etch at frequencies above 1 THz. Laser etching is limited in the depth of structures it can fabricate with straight walls, since the beam of the laser has a finite *f* number. This makes etching the out of plane guide a difficult task. Also, this design requires that the feedhorn or mixer assembly for the out of plane port be made as a separate block.

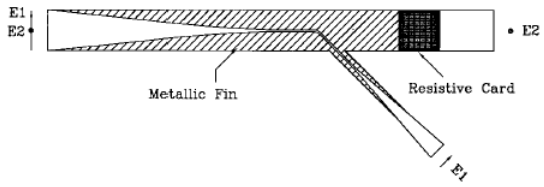

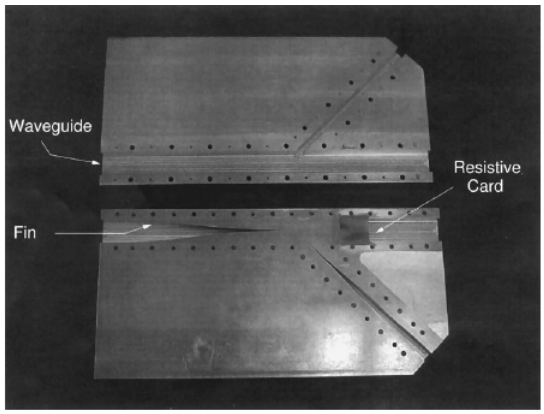

Fig. 2. A picture of the X-band finline OMT.

Figure 4: The Chattopadhyay and Carlstrom finline OMT design (1999). Above is a schematic diagram, below is the X-band scale model realization.

An OMT design proposed by Robinson in 1956 (Figure 1) has the potential to be the superior approach for THz applications. This design has been investigated at lower frequencies by Skinner and James (1991), and was also considered for mm-wave applications by Chattopadhyay and Carlstrom (1999), who tested a scale-model device at X-band (Figure 4). This device is planar, unlike the Bøifot type designs. A single split block structure contains all the necessary waveguide components, and will allow integration of horns and mixers.

In the Chattopadhyay scale model design, the fins were realized as two separate metallic plates, held at the proper separation with alignment pins. Scaling their design to 1 THz, the fin gap is ~5 μm. Since construction of freestanding fins would be exceptionally difficult, the finline structure for the proposed design will be fabricated using photolithographic techniques on a thin dielectric substrate. A thick substrate requires a transition from waveguide to dielectric loaded waveguide, then a transition from dielectric loaded waveguide to finline (Uhde et al. 1990). Since silicon has a very high dielectric constant (ε_r~11.66), even relatively thin membranes can require a vacuum to dielectric loaded waveguide transition. Simulations with CST microwave studio show that a 1 μm thick substrate requires no transition at 1 THz, producing S11 less than -25 dB from 800-1200 GHz. The match degrades as the substrate thickness is increased. When the thickness exceeds ~5 μm, a transition becomes needed. The 5 μm fin gap and 5 μm thickness limit on the substrate at 1 THz should allow scaling of this design to ~5 THz. In addition, the use of silicon as a substrate material will allow easy realization of the resistive card at the end of the finline noted in Figure 4. Current simulations show that a lossy card may not be necessary to suppress unwanted modes in the square waveguide, in which case the card could be a simple silicon tab. If a lossy card proves to be necessary, a resistive film can be deposited on the silicon substrate.

Figure 5: CST Microwave Studio model of the Robinson OMT design for THz applications. The design consists of a laser machined silicon split-block structure, with a gold on SOI finline chip grounded via beam leads.

The Robinson OMT design has been fully simulated using CST microwave studio, including conductor losses for both the waveguide and the fin, dielectric losses for the silicon substrate and losses due to waveguide roughness. We assume that the conductivity of gold is increased by 30% to simulate operation at 4K, and assume 25 nm RMS surface roughness in the waveguide (typical of Si micromachined waveguide after an isotropic polishing etch). The design consists of two waveguide to finline transitions connected via a 45 degree, 1/2 wave radius finline bend. Chattopadhyay and Carlstrom found that a 45 degree finline bend minimized mode conversion, improving crosspolarization performance. The through-arm transitions from square to full height rectangular waveguide via a three section matching transformer, while the full height rectangular side arm uses a mitered 45 degree bend to bring both output guides to the same plane. A 40% height waveguide iris is used at the junction between the side and main arms to minimize the effect of the side arm on the horizontal polarization, while not disturbing the finline guide mode. The waveguide structure will be fabricated using a split-block, with the finline chip sandwiched between the block halves (See Figure 5). As shown in Figure 6, the device offers good performance from 750-1150 GHz, fully including ALMA band 10 (787-950 GHz). The input match is approximately -20 dB across the band for both polarizations. Insertion loss for the horizontal (through) polarization is ~0.5 dB, while the loss for the vertical (side) polarization is ~1.3 dB. Crosspolarization performance of the design is good, with crosspolarization levels of less than -50 dB. Because the current density in the fin near the narrow gap is relatively high, conductor losses in the fin increase the loss in the side arm. These losses could be eliminated by fabricating the fin using NbTiN rather than gold. The bandgap energy of this superconductor is ~1.4 THz, so the material would behave like a PEC in the frequency band of interest. Losses would be dramatically reduced, at the cost of increased difficulty in fabrication. For the prototype, we plan to fabricate and test only gold fins. If the measured losses prove to be too high, a design with superconducting fins can be developed in the future, with losses of less than 0.5 dB (Figure 7).

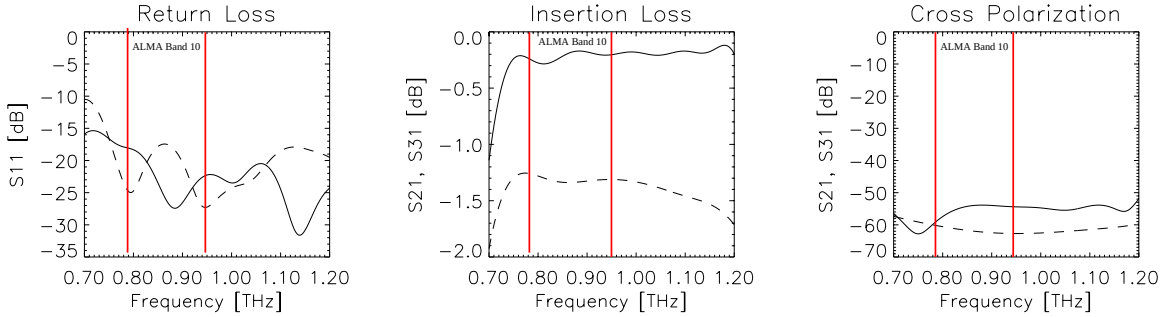

Figure 6: OMT simulation results. Frequency range is 700-1200 GHz for all plots. Return loss, insertion loss and crosspolarization are shown for horizontal (solid) and vertical (dotted) polarizations. These CST Microwave Studio simulations include conductor, dielectric and surface roughness losses, assuming operation at 4K.

The design will also allow easier integration of mixer chips for future development as an integrated dual polarization mixer. Since both output ports are in the same plane and very close to one another (600 μm), two mixing devices and their associated waveguide probes and tuning structures can be fabricated on a single chip for integration with the OMT/feedhorn assembly. The small separation between ports, with all output ports in the same plane and axially aligned with the input port allow this design to be used in large, two dimensional focal plane array applications. An example of a compatible mixer design is shown in Figure 7. This design was developed to be compatible with both HEB and SIS devices, and is scalable to frequencies as high as 5 THz. The mixer is entirely fabricated from laser machined and photolithographically processed silicon (Walker et al. 2003).

OMT Fabrication

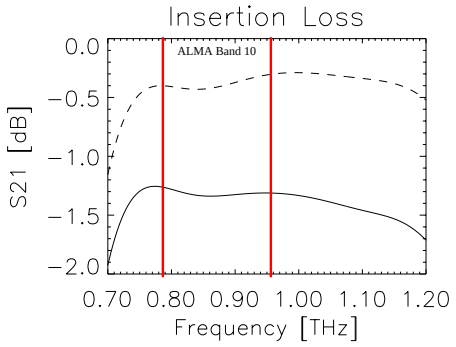

Figure 7: Comparison of insertion loss for the side arm of the Robinson OMT with NbTiN superconducting fins (dotted) and gold fins (solid).

We plan to fabricate the OMT waveguide circuit using a standard split-block approach and laser micromachining technology. The finline chip will be fabricated using photolithography on a 1 μm thick SOI substrate. Beamleads will be used to ground the device to the block. Beamleads are thin, freestanding metallic tabs fabricated on a substrate that is later etched away. They are thick enough to act as handles for manipulating the structure, and offer very good RF grounding performance. During assembly, a beam lead device is placed in a split-block waveguide structure, suspended by the beam leads. When the split-block is assembled, the gold beam leads are crushed between the block halves providing grounding. Beam lead devices are used extensively in the multipliers used in the Hershel HIFI LO system, as well as in many modern SIS and HEB detector designs. SOI (Silicon-On-Insulator) wafers allow silicon membranes thinner than 1 μm to be produced. The thin membrane is attached to a carrier wafer. After fabrication of the structure, the back side carrier wafer is released from the thin membrane. Silicon membranes are fairly flexible, and are much easier to handle than quartz wafers of the same thickness. Prototype devices will be fabricated with a feedhorn at each port for quasi optical testing with a FTS and a ^{4}He bolometer. Eventually, the OMT could become part of an integrated dual polarization mixer, with the input feedhorn, OMT and both mixers integrated into a single, flangeless block (see Figure 8).

Because there is no out of plane guide, milling the waveguide split block for the Robinson OMT is relatively straightforward. There are no small, tuned structures (i.e. capacitive steps) in the design, relaxing fabrication tolerances. In addition, the entire device can be made from a single split block, including input and output horns. The design of the waveguide block, including the side arm iris, is compatible with fabrication using the SORAL laser micromachining system. Alignment crosses are machined into the silicon away from the waveguide structure during the milling process to facilitate assembly with a flip-chip bonding tool. After laser machining, the waveguide split block halves are gold plated with an e-beam evaporator (the alignment crosses are masked off during plating). The finline chip is a straightforward fabrication task compared to a SIS junction; only a single gold metallization layer needs to be deposited on the substrate. The finline will be defined using standard photolithographic processes on the SOI wafer, using thick photoresist techniques. A 1:1 aspect ratio of finline gap width to metallization thickness realizable with these techniques. In addition, the design is not sensitive to the metallization layer thickness; variations of over 1 μm can be tolerated with almost no qualitative impact on the device performance. The planar beamlead structure is dropped (by hand) into a pocket milled into the bottom of the split-block. The precision milled pocked registers the chip. No electrical contacts need be made, since the beam leads will contact when the split block is closed. Alignment of the top split block with the bottom is achieved with an infrared semiconductor alignment tool or flip-chip bonder. This tool holds both the top and bottom halves of the chip in air chucks on precision motion stages. An IR microscope looks through the (transparent) silicon at the location of the alignment crosses to allow registration of the top and bottom of

the structure. The air chucks then clamp the halves together. The Van der Waals forces between the gold metallization layers bond the split block together. The silicon block is then glued into a copper fixture for use. This design is also well suited for fabrication via direct micromilling in a metal block, for frequencies as high as 1.5 THz. Only small modifications to the design are necessary to compensate for finite sized tools.

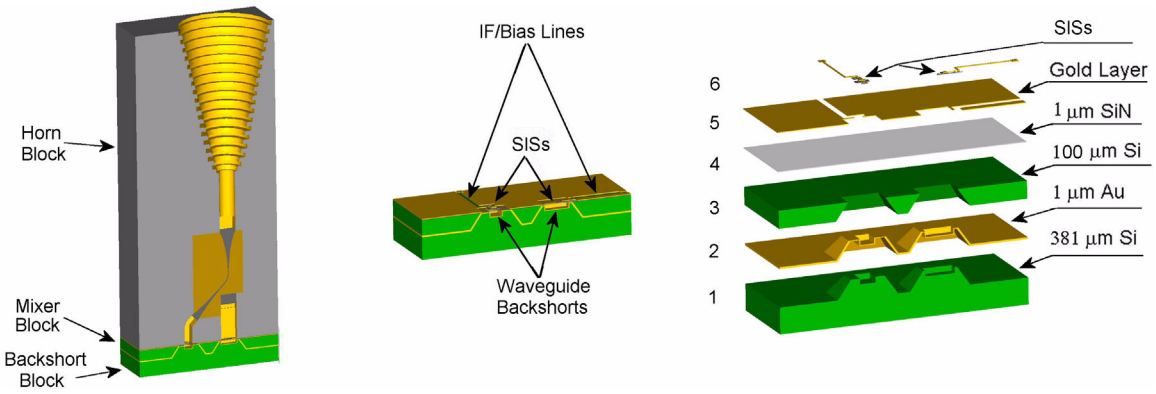

Figure 8: A laser micromachined, SiN membrane mixer mount (Designs for beamlead/SOI devices also exist). This device, consisting of 4 blocks, has 33% bandwidth at 1 THz, and is made entirely of micromachined and photolithographically processed silicon.

OMT Testing

For testing, horns will be laser machined at both the input and output ports, integrated with the OMT. In addition, a back to back feedhorn structure will be fabricated to allow measurement of the loss of the feedhorn structures. The FTS in the SORAL lab has a broadband FIR source. Combined with a IR Laboratories ^{4}He bolometer system, measurements can be made throughout the sub-mm and FIR. We can measure insertion loss, crosspolarization and isolation of the OMT structure through comparison with the back-to-back feedhorn structure. With some additional optics, it is also possible to measure return loss from the device as well. Measurement with a FTS does not provide the same accuracy expected from a scalar network analyzer at lower frequencies, but should be able to verify the performance of the device. A block diagram of the proposed test set is shown in Figure 9. If the dynamic range of this test set proves to be too small to measure the crosspolarization and isolation signals, the FIR laser can be used in place of the FTS to measure these properties at discrete frequencies.

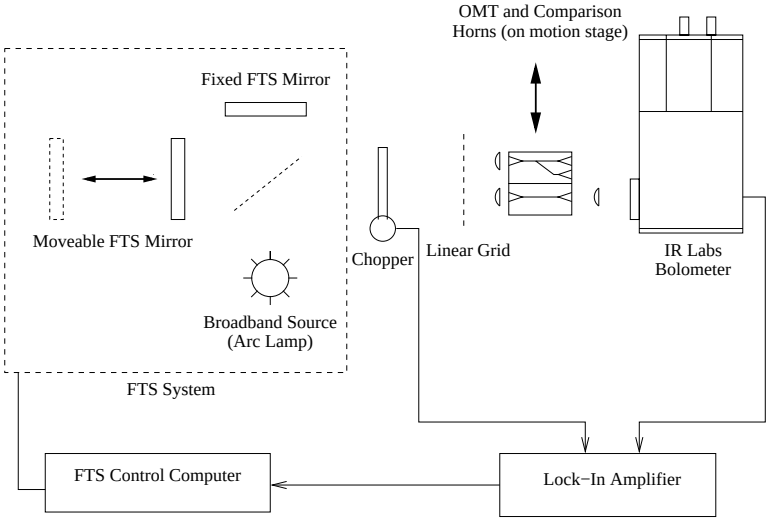

Figure 9: A block diagram of the measurement system proposed for the THz OMT. This test set can measure throughput, isolation and crosspolarization of the OMT by comparison to a back-to-back feedhorn structure.

Conclusion

We have designed and plan to fabricate and test a 40% bandwidth orthomode transducer capable of operation from 750-1150 GHz. This design is scalable to frequencies as high as 5 THz. Recent advances in micromachining and electromagnetic simulation allow the realization of such a structure. A laser micromachining system at SORAL and the

University of Arizona will allow low cost and high precision waveguide structures to be milled directly in silicon. A finline OMT design first proposed by Robinson in 1956 is planar and relatively easy to fabricate. Simulations of an OMT based on this design demonstrate good performance from 750-1150 GHz. This design uses laser machined silicon waveguide components with a photolithographically defined finline circuit on a thin SOI substrate with beamlead grounding. Waveguide structures fabricated at SORAL will be combined with planar structures fabricated at the University of Virginia, and assembled at either UVa or SORAL. Testing will be done using a Fourier transform spectrometer and ^{4}He bolometer system, allowing measurements of throughput, isolation and crosspolarization. Eventually, the OMT could become part of a dual polarization mixer, with the feedhorn, OMT and mixers integrated into a single, flangeless block.

References

Chattopadhyay, G. & Carlstrom, J.E., *Finline Ortho-Mode Transducer for Millimeter Waves*, IEEE Microwave and Guided Wave Let., vol. 9, no. 9, pp. 339, 1999.

Drouet d'Aubigny, C.Y., Walker, C.K., Golish, D., Swain, M.R., Dumont, P.J, & Lawson, P.R., *Laser Micro-machining of Waveguide Devices for Sub-mm and Far IR Interferometry and Detector Arrays*, Proc. SPIE., vol. 4852, pp. 568, 2003.

Meyer, M.A. & Goldberg, H.B., *Applications of the Turnstyle Junction*, IRE Trans. MTT, vol. 3, no.6, pp. 40, 1955.

Narayanan, G. & Erickson, N., *Full-Waveguide Band Orthomode Transducer for the 3mm and 1mm Bands*, 14th International Symposium on Space Terahertz Technology, In Press, 2003.

Narayanan, G., & Erickson, N.R., *A Novel Full Waveguide Band Orthomode Transducer*, 13th International Symposium on Space Terahertz Technology, Harvard University, 2002.

Narayanan, G, Erickson, N.R., & Grosslein, R.M., *Low Cost Direct Machining of Terahertz Waveguide Structures*, 10th International Symposium on Space Terahertz Technology, pp. 518, 1999.

Robinson, S.D., *Recent Advances in Finline Circuits*, IRE Trans. MTT, vol. MTT-4, pp. 263, 1956.

Skinner, S.J, & James, G.L., *Wide-Band Orthomode Transducers*, IEEE MTT, vol. 39, no. 2, pp. 294, 1991.

Walker, C.K., Groppi, C.E., Drouet d'Aubigny, C.Y., Kulesa, C., Hedden, A.S., Prober, D.E., Siddiqi, I., Kooi, J.W., Chen, G, & Lichtenberger, A.W., *Integrated Heterodyne Array Receivers for Submillimeter Astronomy*, Proc. SPIE, vol. 4855, pp. 349, 2003.

Wollack, E.J., & Grammer, W., *Symmetric Waveguide Orthomode Junctions*, 14th International Symposium on Space Terahertz Technology, In Press, 2003.

Wollack, E.J., Grammer, W. & Kingsley, J., *The Bøifot Orthomode Junction*, Alma Memo #425, 2002.

Chip for autocorrelation spectrometer applications with integrated digitizer

L. Landén, A. Emrich, S. Andersson, J. Dahlberg
Omnisys Instruments AB, Gruvgatan 8, 421 30 Göteborg, Sweden

INTRODUCTION

A chip for autocorrelation spectrometer applications has been designed. The chip contains both a digitizer and a digital signal processor. The digitizer transforms an analog baseband signal to digital information and the digital signal processor calculates the autocorrelation function for the data that the digitizer provides. The autocorrelation spectrometers built today contains two different chips for these two circuit functions. The chip is being manufactured using a 0.18 µm SiGe BiCMOS process. This paper will first describe an autocorrelator system, and then describe the two main functions of the chip. At last, the pros and cons of higher integration is described.

THE AUTOCORRELATION SPECTROMETER SYSTEM

The autocorrelation function of a discrete sequence, *x(n)*, of length *N* is defined as:

$$R_{xx}(l) = \sum_{l=0}^{N-1} x(n)x(n-l), l, n \in Z$$

By applying the discrete Fourier transform to the autocorrelation function the power spectrum is obtained. The resolution of the spectrum is improved by increasing the length, *l*, of the function. The autocorrelation function can be easily realized using a digital integrated circuit. The input to the spectrometer is some analog frequency band that is being observed. This band is down converted and split into subbands . The subbands are individually down converted to baseband. The baseband information is quantized by the digitizer and then fed to the autocorrelation circuit.

THE DIGITIZER

The baseband signals are analog and need to be converted to digital data in order to be manageable by the digital autocorrelator. For this, a digitizer is used. Time multiplexing may be used since the quantization is possible to achieve at higher frequencies than the following digital signal processing. The digitizer was designed using the bipolar transistors in the process. The reason for this is that the bipolar transistors gives the possibility to design high speed high precision comparators. In order to reduce the influence of noise on the data and reference ports, a differential output was chosen.

THE AUTOCORRELATOR

The serial output data from the digitizer is fed to the autocorrelator. This data is then split in two identical parts and fed to a multiplier that calculates the autocorrelation function for zero delay, *l*=0. One of the serial data paths is then delayed one clock cycle and multiplied with the initial data to produce the function for *l*=1. This procedure is then repeated until the desired resolution is obtained. Synchronization blocks have been introduced every sixteen delay block in order to synchronize the data and the clock.

BENEFITS OF BiCMOS AND CONCLUSIONS

The first and most obvious benefit of higher integration using SiGe BiCMOS is the reduction of the complex I/O between the two circuits. This interface is rather complex to manufacture when building the spectrometer. The SiGe HBTs have higher maximum frequency of operation than the bipolar transistors that have been used in the past. Also the CMOS part is faster than before, this mans that the bandwidth possible to analyze has been increased. One step in technology also means smaller devices and less power consumption.

T-SHAPED EMITTER METAL HETEROJUNCTION BIPOLAR TRANSISTORS FOR SUBMILLIMETER WAVE APPLICATIONS

Andy Fung, Lorene Samoska, Jim Velebir, Peter Siegel
California Institute of Technology Jet Propulsion Laboratory, Pasadena, CA 91109
Mark Rodwell, Vamsi Paidi, Zach Griffith, Miguel Urteaga, Department of Electrical and Computer Engineering, University of California,
Santa Barbara, CA 93106
Roger Malik, RJM Semiconductor, Berkeley Heights, NJ 07922

Abstract

We report on the development of submillimeter wave transistors at JPL. The goal of the effort is to produce advance-reliable high frequency and high power amplifiers, voltage controlled oscillators, active multipliers, and high-speed mixed-signal circuits for space borne applications. The technology in development to achieve this is based on the Indium Phosphide (InP) Heterojunction Bipolar Transistor (HBT). The HBT is well suited for high speed, high power and uniform (across wafer) performance, due to the ability to tailor the material structure that electrons traverse through by well-controlled epitaxial growth methods. InP with its compatible lattice matched alloys such as indium gallium arsenide (InGaAs) and indium aluminium arsenide (InAlAs) provides for high electron velocities and high voltage breakdown capabilities. The epitaxial methods for this material system are fairly mature, however the implementation of high performance and reliable transistors are still under development by many laboratories. Our most recently fabricated, second generation mesa HBTs at JPL have extrapolated current gain cutoff frequency (F_t) of 142GHz and power gain cutoff frequency (F_{max}) of approximately 160GHz. This represents a 13% and 33% improvement of F_t and F_{max}, respectively, compared to the first generation mesa HBTs [1]. Analysis based on the University of California, Santa Barbara (UCSB) device model, RF device characteristics can be significantly improved by reducing base contact resistance and base metal contact width. We will describe our effort towards increasing transistor performance and yield.

Background

Indium phosphide (InP) heterojunction bipolar transistors (HBTs) are one of the highest speed transistor technologies available. The advantages of this technology are enabled from the precise control of the semiconductor epitaxial properties that electrons traverse through. In HBTs, electrons move in the direction of epitaxial growth, as a result, the environment of the electrons at each region of transport in the transistor can be more easily and accurately controlled for optimum performance within the narrowest spatial dimensions. Because of this, InP HBTs can be grown with a large bandgap emitter region to reduce injection of holes from the base into the emitter that decreases gain with increasing base doping for reducing base resistance; the emitter-base junction can be alloy graded to minimize turn-on voltage; an alloy or doping graded base region can be grown in the epitaxy to produce a built in electric field to increase electron transport velocity through the base. Also through epitaxial growth for the collector region of the transistor, a high electric field breakdown material such as InP can be deposited so that the transistor may operate at higher voltages while maintaining short electron transport distances for speed. In contrast, other high speed transistor technologies, such as high electron mobility transistors (HEMTs), the electrons travel perpendicular to the direction of epitaxial growth and are confined to particular material layers with fixed properties. Modifications for material properties in the direction of electron transport for improving performance can only be done via processes after epitaxial growth, generally with less precision and more complications. Silicon Germanium HBTs, another high-speed technology, consists of semiconductor

materials with lower breakdown voltages and are less suitable for power applications. InP HBTs are well suited for both high speed and high output power operation, which are desired for our applications.

Motivation

The goal of the effort at JPL is to develop the fastest reliable transistor process beyond what is available from industry and have the capability to easily add features for performance not typically allowed in foundry services that are fixed. We are pursuing HBTs as they have shown very high power gain, >20dB at 100GHz [2] and higher power handling capability due to epitaxial engineering of the collector region of the transistor, in contrast to HEMTs. We expect that HBTs will provide more power per unit area at higher frequencies than HEMTs, and will yield higher transistor count ICs due to its particular fabrication procedures. Recent studies have reported HBTs with F_t of 509GHz and F_{max} of 219GHz [3], and in another study F_{max} of 478GHz with F_t of 154GHz [4]. To date, InP HBTs have demonstrated single stage power amplifiers with 7.5mW output power at 172GHz and 5dB associated gain [5]. ICs with transistor counts approaching five thousand have also been demonstrated [6]. Upon implementation of an ultra-high-speed and high-power HBT process we plan to fabricate power amplifiers to provide more power to local oscillator chains for space heterodyne systems [7]. Additionally, high-frequency voltage controlled oscillators can potentially be fabricated to simplify local oscillator chains by reducing component count and size. Ultimately we would like to have a high yield process so that we can develop ultra-high speed mixed-signal ICs. Systems that we would like to utilize this technology in are for THz imaging systems, which are in development at JPL [8], and also future space hardware such as advanced autocorrelators for high-resolution remote sensing spectral analysis.

Development of Mesa InP HBTS

At JPL, we recently completed fabrication of second-generation mesa HBTs with extrapolated F_t and F_{max} of approximately 142 and 160GHz, respectively. The epitaxial wafer used consisted approximately of a 120nm InP silicon doped emitter, 30nm carbon doped InGaAs base layer and a 210nm InGaAs/InAlAs alloy graded to InP silicon doped collector layer. HBTs fabricated on this epitaxial structure had submicron emitter features of 0.3x4, 0.5x4 and 0.7x4μm^2 defined with electron beam lithography. All other transistor features are fabricated with 2 μm minimum feature size contact lithography, wet etching and electron beam metal evaporation. Polyimide is used for planarization and passivation. For RF characterization, on-wafer measurements are performed with an Agilent 8510C vector network analyzer. Through-Line-Reflect (TRL) on-wafer standards are used to calibrate the measurement setup. S-parameter measurements are taken between 10 and 50GHz. S-parameters as a function of frequency are converted to current gain (H21) and Mason's unilateral gain (U) as a function frequency. A -20dB/dec extrapolation from H21 and U is used to determine F_t and F_{max}, respectively, at the frequencies where the gains extrapolate to 0dB (see Figure 1 (b)). This standard extrapolation is based on the behavior expected from the hybrid-pi model.

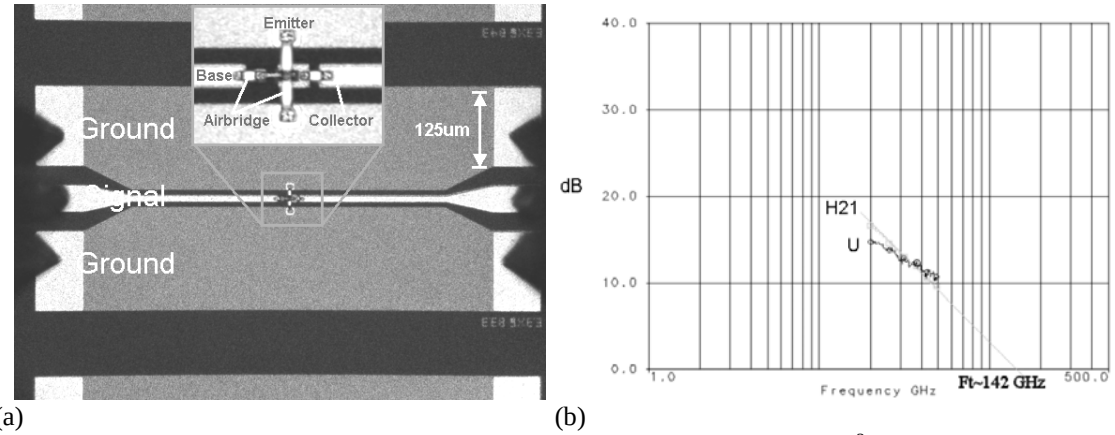

(a) (b)

Figure 1: (a) Optical photo of an InP mesa HBT. (b) Gain plots of a 2x0.7x4μm^2 InP mesa HBT calculated from S-parameter measurements. F_t and F_{max} are 142 and 160 GHz, respectively. Bias condition for the emitter current density J_e is 190 kA/cm^2 and collector-emitter voltage is 1.25V.

Since the RF and DC measurements of the second generation HBTs and test patterns, we have performed analysis of the device structure to determine how performance can be improved. Using the UCSB device model, we find that performance can be substantially improved by reducing parasitic resistances and capacitances associated with base contact resistance and base metal contact width (base-collector capacitance). Figure 2 (a) and (b) show the general trend of F_t and F_{max} as a function of base contact resistance and base contact width of the next generation of HBTs we are presently developing. To realize improvements in performance we are also currently examining UCSB's base metal fabrication process, which can provide for specific contact resistances of 20 ohm·μm^2 or less. To reduce base metal contact width, the JPL in-house process is being migrated from contact lithography to stepper projection lithography, so that smaller 1μm minimum feature size structures can be produced.

To improve HBT yield we have implement T-shaped emitter metal structures at the beginning of the second generation of HBTs fabricated at JPL. Electrical measurements of first generation HBTs indicated that yield is greatly reduced during the base-emitter junction fabrication process. Scanning electron microscopy in some cases showed that while some emitters are properly etched some still did not have complete undercut etching around the entire periphery of the emitter metal stripes. As a consequence, after deposition of the self-aligned base metal, many emitter-base junctions would be electrically shorted. The T-emitter metal structure is implemented so that an additional spacer is provided to keep evaporated base metal from shorting to the emitter epitaxy (see Figure 3). Additional benefit of this structure is that it allows the base metal thickness to be increased, reducing electrical and thermal resistance, and reducing the inductance of the base metal.

Summary

JPL is developing an in-house advanced mesa InP HBT and Transferred Substrate HBT process [1], in collaboration with UCSB and RJM Semiconductor. These processes can be utilized to produce components to improve systems for future astrophysics, planetary and Earth science THz missions. At JPL we have demonstrated, second generation emitter mesa HBTs with F_t of 142GHz and F_{max} of 160 GHz, first generation mesa HBTs with F_t of 126GHz and F_{max} of 120GHz, and first generation Transferred Substrate HBTs with F_t of 110GHz and F_{max} of 150GHz. Performance of the HBTs will improve by reducing parasitic resistances and capacitances, and reducing the distance electrons need to travel through the device. These requirements can be addressed through the minimization of base contact resistance, the reduction of base metal width, and the scaling of epitaxial layers.

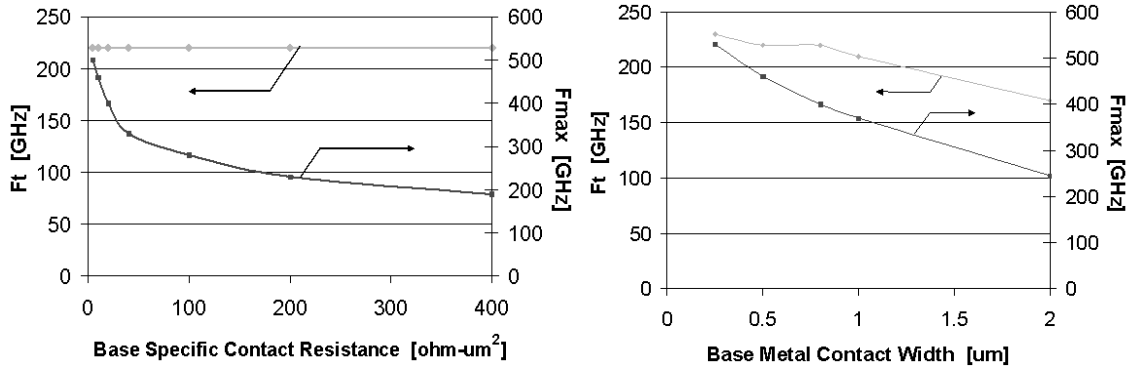

Figure 2: Simulations for the next generation of mesa HBTs based on the UCSB device model. Emitter area is 0.7x12 um^2 and emitter to base metal spacing is 0.25 um. Base-emitter voltage bias is 0.68V and collector-emitter voltage bias is 1.2V. (a) Cutoff frequencies versus base contact resistance for a HBT with 0.8 um base metal width. (b) Cutoff frequencies versus base contact width for a HBT with 20 ohm-um^2 specific base contact resistance.

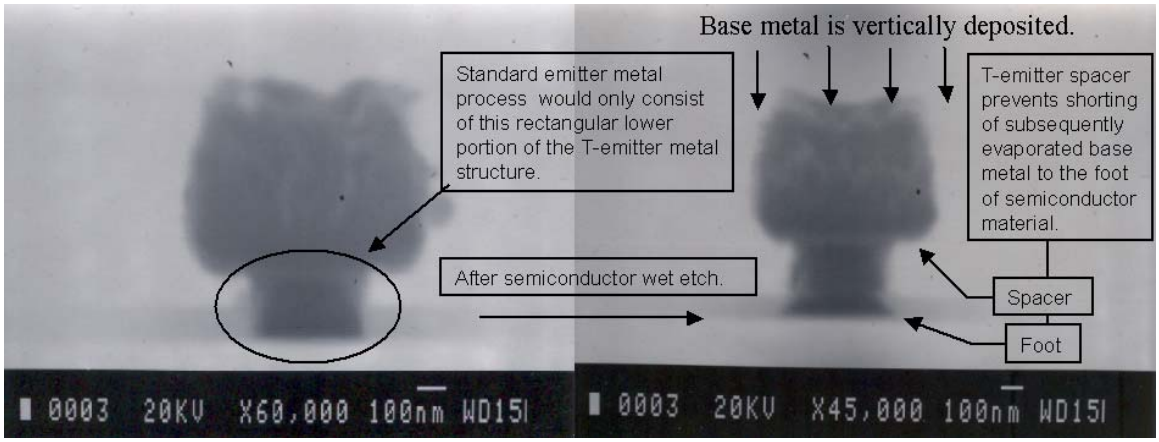

Figure 3: Scanning electron photos of the T-emitter metal structure. Standard rectangular emitter metal structures require more control to obtain enough undercut of the semiconductor emitter epitaxy so that the emitter metal can properly shadow mask the subsequently vertically deposited base metal from shorting to the foot of the semiconductor emitter epitaxy. In this example it can be seen that the foot of the semiconductor emitter material protrudes out enough that without the spacer provided by the T-emitter metal, evaporated base metal would short to the emitter.

Acknowledgments

The research and development presented in this paper was carrier out at the California Institute of Technology Jet Propulsion Laboratory, a federally funded research and development center under a contract with the National Aeronautics and Space Administration, and by MDA under contract DTRA-01-03-C-0033, managed by DTRA. The authors thank Richard Muller and Pierre Echternach at JPL for providing electron beam lithography.

References

[1] A. Fung, L. Samoska, P. Siegel, M. Rodwell, M. Urteaga, V. Paidi, and R. Malik, "Transferred Substrate Heterojunction Bipolar Transistors for Submillimeter Wave Applications," 14th International Symposium on Space TeraHertz Technology, Tucson, Arizona, 2003.
[2] M.J.W. Rodwell, M. Urteaga, T. Mathew, D. Scott, D. Mensa, Q. Lee, J. Guthrie, Y. Betser, S.C. Martin, R.P. Smith, S. Jaganathan, S. Krishnan, S.I. Long, R. Pullela, B. Agarwal, U. Bhattacharya, L. Samoska, and M. Dahlstrom, "Submicron scaling of HBTs," IEEE Trans. Electron Devices, vol. 48, Nov. 2001.
[3] W. Hafez, J. Lai, and M. Feng, "InP/InGaAs SHBTs with 75nm collector and Ft > 500GHz," Electronics Letters, vol. 39, Oct. 2003.
[4] D. Yu, K. Lee, B. Kim, D. Ontiveros, K. Vargason, J. Kuo, and Y. Kao, "Ultra High-Speed InP-InGaAs SHBTs With Fmax of 478 GHz," IEEE Electron Device Lett., vol.24, June 2003.
[5] V. Paidi, Z. Griffith, Y. Wei, M. Dahlstrom, N. Parthasarathy, M. Urteaga, M.J.W. Rodwell, A. Fung, and L. Samoska, "Common Base Amplifier with 7-dB gain at 176 GHz in InP mesa DHBT Technology," Proceedings IEEE RFIC Symposium, June 2004.
[6] Previously posted at http://www.vitesse.com/news/20030113.shtml, "Vitesse is First to Offer Indium Phosphide HBT Foundry Services Through MOSIS; Partnership Will Assist with the Adaption of the Emerging Technology," Jan. 2003.
[7] J. Ward, G. Chattopadhyay, A. Maestrini, E. Schlecht, J. Gill, F. Maiwald, and I. Mehdi, "Tunable All-Solid-State Local Oscillators to 1900 GHz," Proceedings 15th International Symposium on Space TeraHertz Technology, Northampton, Massachusetts, 2004 (to be published).
[8] P.H. Siegel, "Submillimeter-Wave Camera," JPL New Technology Report NPO20718, June 1, 1999.

Device Technology for SIS Mixers in the 1 – 1.5 THz Band

M. Kroug[1], J. Eroms[1], T. Zijlstra[1], A. Baryshev[2], T.M. Klapwijk[1]
[1]*Kavli Institute of Nanoscience, Delft University of Technology*
[2]*SRON – National Institute for Space Research*
The Netherlands

Superconductor–insulator–superconductor (SIS) mixers have been developed to operate in the THz regime with the highest frequency reported so far being 1.2 THz [1]. Best results are obtained by using low–loss normal metal tuning circuits and junctions with extremely high current density.

We are developing a technology to fabricate SIS mixers which should be capable to give low noise performance well abve 1 THz. We follow up on earlier work [2,3] where the embedding circuit is an Al / SiO_2 / Al micro strip. For the ground plane of the micro strip we use single crystalline Al films on Si (111) substrates deposited in a molecular beam epitaxy system. Apart from their high conductivity, $\sigma_{4\,\mathrm{K}} > 5 \cdot 10^8/(\Omega\,\mathrm{m})$, implying low rf losses, these Al films provide a very smooth surface for the subsequent growth of the SIS trilayer. We find that this is an important issue for making high quality junctions in terms of a low leakage insulating barrier. The junctions are based on Nb / AlN / NbTiN trilayers and have a sum gap voltage of $V_{\mathrm{gap}} = 3.5$ mV, setting the maximum operating frequency to $1.7 \cdot e\,V_{\mathrm{gap}}\,/\,h \simeq 1.5$ THz. Lithographic definition of the junction makes use of direct e-beam writing and dry etching techniques. The junction area can be made as small as 0.3 $\mu\mathrm{m}^2$, current densities are 20 – 30 $\mathrm{kA/cm}^2$ with the subgap to normal resistance ratio ≥ 10.

RF absorption losses in high quality Al are not expected to increase strongly with frequency making this type of circuit suitable for THz SIS receivers. We discuss the possibility to use higher gap junctions based on NbTiN / AlN / NbTiN which could operate up to ~ 2 THz.

References

[1] Karpov et al, these proceedings
[2] Bin et al, Appl. Phys. Lett. **68** (12) 1996
[3] Gao et al, Proceedings 7th ISSTT 1996

A Phase-Locked Terahertz Quantum Cascade Laser

A.L. Betz, R.T. Boreiko
Center for Astrophysics & Space Astronomy, UCB 593,
University of Colorado, Boulder, CO 80309

B. S. Williams, S. Kumar, and Q. Hu
Department of Electrical Engineering and Computer Science &
Research Laboratory of Electronics,
Massachusetts Institute of Technology, Cambridge, Massachusetts 02139

J. L. Reno
Sandia National Laboratories
Department 1123, MS 0601, Albuquerque, New Mexico 87185-0601

ABSTRACT

Progress in coherent receiver development at terahertz frequencies has been hindered by the lack of a suitable local oscillator source that can be qualified for space missions. Space systems now in development rely on harmonic multipliers of microwave sources. Multipliers have achieved usable performance up to 1.6 THz, and probably, with a lot of work can be extended to 2.0 THz, but above that hope dims. The science driving the development of THz spectral line receivers requires capability up to at least 4.75 THz (the neutral oxygen line). Ideally, the THz LO should be some type of tunable semiconductor laser that can be locked to a harmonic of a millimeter-wave source. In the early 1990's a new type of semiconductor laser was developed called the quantum-cascade-laser. This device is unipolar in that only transitions of electrons between sub-levels in the conduction band are needed to produce laser emission. Although the QCL was originally developed as an infrared laser operating well above the 8-9 THz reststrahl band of GaAs/GaAlAs, it was eventually realized that operation below the reststrahl band was also possible, but much more difficult. The first terahertz QCL was demonstrated two years ago at 4.4 THz, and now devices work as low as 2.1 THz, with even lower frequencies envisioned. State-of-the-art QCLs require only LN_2 cooling and a DC bias power as low as 2 W, and yet produce > 500 μW of CW power from a chip no bigger than a transistor.

In order to demonstrate the potential of a QCL to serve as a THz local oscillator, we have phase-locked a QCL to a 3.1 THz methanol laser line. This particular QCL emits about 160 μW at an operating temperature of 81 K. Spectra of the IF signal at the 3250.000 MHz offset frequency indicate a QCL linewidth of 350 kHz (FWHM) for this initial attempt. The lineshape is Lorentzian and has considerable fine structure, which suggests that bias current fluctuations are broadening a much narrower line. We expect to achieve a factor of 10 improvement to a 30 kHz linewidth (1 part in 10^8 fractional bandwidth) after improved bias source and lock electronics are implemented.

Introduction

Compact THz sources are critically needed as local oscillators in space-qualified heterodyne receivers. LO applications require oscillators that are frequency programmable, have good amplitude stability and a linewidth consistent with observational objectives. For interstellar clouds, Doppler gradients can be a low as 0.1 $km \cdot s^{-1}$, and so an LO fractional linewidth < 1 part in 10^7 is desirable. Phase noise should also be low so that LO noise is not detected in the IF band. Fixed-frequency gas lasers have the required frequency stability, but their relatively large size and required CO_2 pump source preclude their use in space applications, aside from one application in NASA's Microwave Limb Sounder instrument. Tunable millimeter wave sources also have good frequency stability and low phase noise under phase-locked conditions, and their harmonics are usable in the 1-2 THz band. Unfortunately the sub-microwatt power levels available from harmonic sources above 2 THz are not adequate for realistic LO applications. Even with HEB mixers, > 5 μW of LO power (measured at the source) is needed to insure a low receiver noise and high dynamic range for the mixer. A recent invention, the terahertz quantum cascade laser (QCL), potentially solves the problem of a space-qualifiable THz LO. Recent 3 THz devices, no bigger than a transistor, need only LN_2 cooling and yet produce > 500 μW of CW power while dissipating 2-4 W with 10 V bias.

THz emission from a QCL was first demonstrated about 2 years ago, and already a large amount of progress has been made by several groups [1,2,3]. Although QCLs work best at higher THz frequencies (because the energy levels are more separated), they have been demonstrated in CW operation down to 2.1 THz so far [4]. QCLs are heterostructures made from materials of the III-V semiconductor group. A heterostructure is a multiple-quantum well (MQW) structure of alternating high and low gap materials. THz photons are emitted by these devices as electrons make transitions between sub-band states in the conduction band. A large number of repeating MQW subsections are cascaded during MBE layer deposition to enhance the gain path. A single electron traveling through this composite structure under DC bias emits hundreds of identical THz photons without any recombination (in contrast to conventional diode laser operation). Add optical feedback from facet reflectivity and you have a laser.

QCL Parameters

The QCL frequency is determined by the gain profile and the mode spacings of the basic FP cavity. The gain peaks at the design frequency determined by the quantum well structure and has an overall 3 dB bandwidth of ~1 THz. Within this bandwidth, the oscillating frequency is set by the FP longitudinal resonances. Higher order off axis modes may have sufficient gain to oscillate under some circumstances, but they can usually be suppressed by selecting the DC operating point. Frequency tuning is accomplished by changing the QCL channel temperature either via the cold plate temperature (slow tuning) or through the bias current (fast tuning). The emitted radiation is TM mode - the electric vector is parallel to the growth direction of the MQW stack,

which is nominally 10 μm thick. These QCLs are edge emitters with typical facet dimensions of 10 μm x 40 μm. Because the material index is relatively high (n = 3.8), the emitting face has minimum dimensions of about λ/2, and optical coupling is not a serious problem.

Two distinguishing features of the MIT QCL lead to CW operation at higher temperatures and longer wavelengths. The first is that the lower laser level is depopulated by resonant optical phonon scattering, and the second is that mode confinement is achieved by a metal-semiconductor-metal waveguide. Figure 1 shows the power output and I/V curves for the device used here. This laser is 1.22 mm long, 40 μm wide, and 10 μm thick, and has 177 cascaded sections. This device was the first THz QCL to operate CW above the temperature of liquid nitrogen, and in fact oscillates CW at 3.1 THz up to 93 K [5]. The QCL was made at the MIT Research Laboratory of Electronics with MBE material grown at Sandia. We measured the THz polarization to be 88 ± 3 % parallel to the growth direction (as expected), and 12% cross polarized. (As a check we measured the polarization of the FIR gas laser used here with the same wire grid, and found it to be 98 ± 2% linearly polarized.)

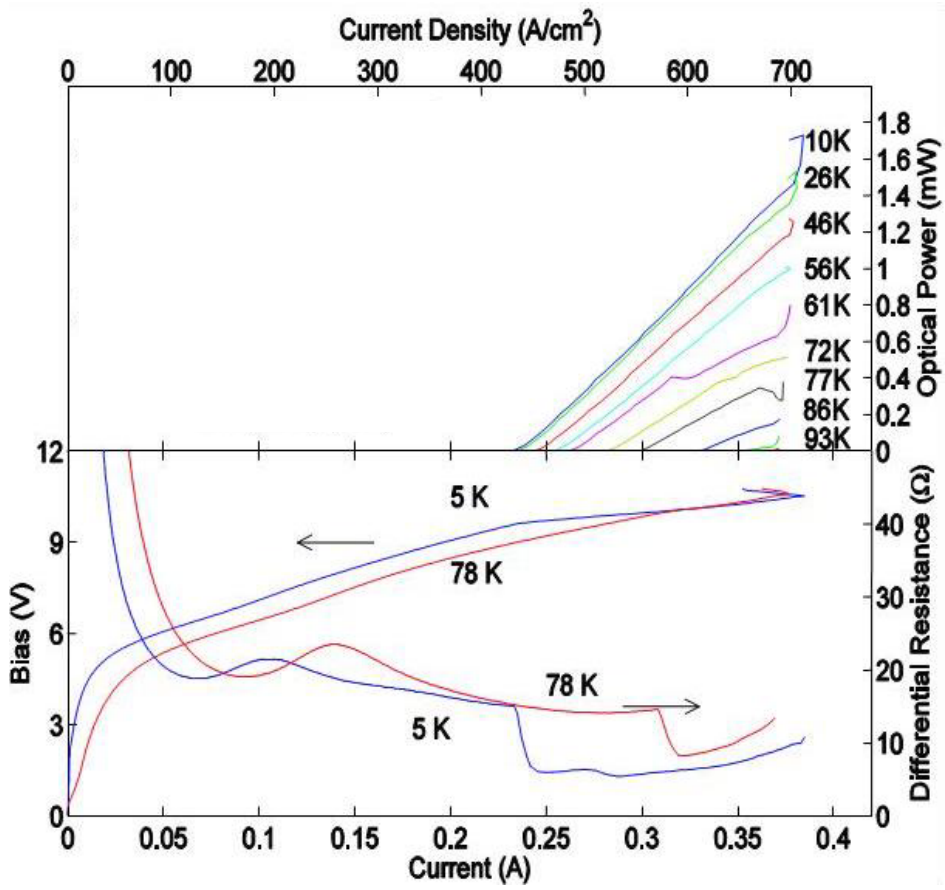

Figure 1 – Output Power and I/V Curve of 3.1 THz QCL labeled FL177C-M5

Optical Coupling

The 10 μm × 40 μm end faces of the QCL are uncoated. The reflections from the facets are governed by the impedance discontinuity between the QCL waveguide and free space. A 2-dimensional EM simulation shows that the reflection is greater than 80%, which is much larger than the 34% expected from simple Fresnel reflection. The front, back, and sides of the QCL are defined by a mesa structure. The top and bottom planes are defined by copper metallizations that provide waveguide confinement. Emission from one output face is coupled through a hemispherical silicon lens (4 mm diam. - transmission 60%) in near contact. The diverging beam proceeds through a crystal quartz window on the dewar (transmission 65%), and is refocused by a 90-degree off-axis ellipsoidal mirror. Fig. 2 shows a simplified schematic of the experimental hardware. The beam propagates in air for 1.25 m and is reflected from a wire grid polarizer used as a variable beam-combiner. A signal from an optically-pumped FIR gas laser passes through the same beam-combiner. A second off-axis ellipsoid focuses the combined QCL and FIR laser signals onto a room-temperature GaAs Schottky-diode-mixer (UVa type 1T15) in a corner reflector mixer mount [6].

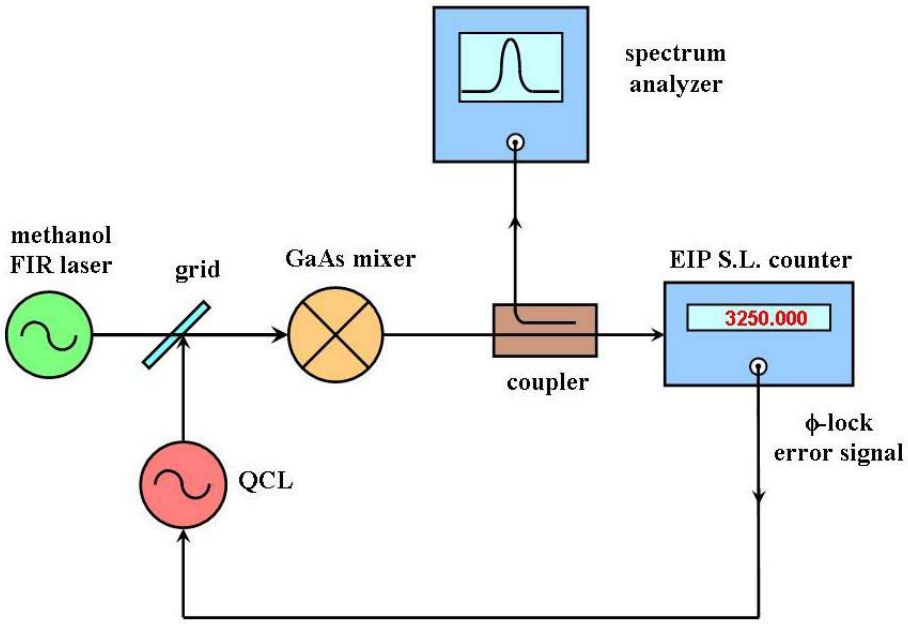

Figure 2

Only 40% the laser signal is transmitted over this open-air path because of absorption by atmospheric water vapor. Fig. 3 shows 1-m path transmissions calculated from the HITRAN data base. The maximum QCL power measured in the focal plane of the mixer was about 25 μW (± 30 %). This power and the measured absorptions imply that the QCL power at the output face was about 160 μW (± 30 %), which is comparable to that expected for the operating temperature of 81 K used in this experiment (see Fig. 1). The FIR laser runs on the 3105.9368 GHz line of methanol. IF signals over a bandwidth of

0.1-4.0 GHz are amplified by 65 dB and directed to a source locking counter (EIP Model 575). A –13 dB directional coupler diverts part of the IF signal to the spectrum analyzer. The phase-lock output signal from the counter is added as an error voltage to the negative sense lead of the QCL bias supply (HP 6632B). For protection purposes, the error voltage is limited to 1 volt by a resistive divider network. This divider also effectively cuts the overall laser oscillator gain down to 270 MHz/volt, which is within the operating range of the source locking counter.

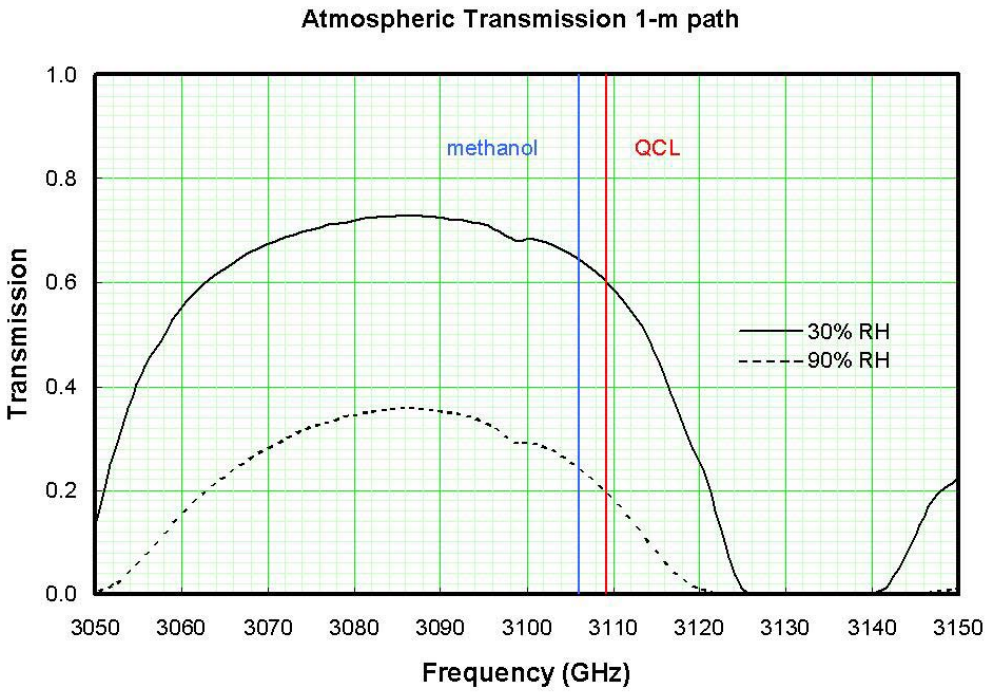

Figure 3

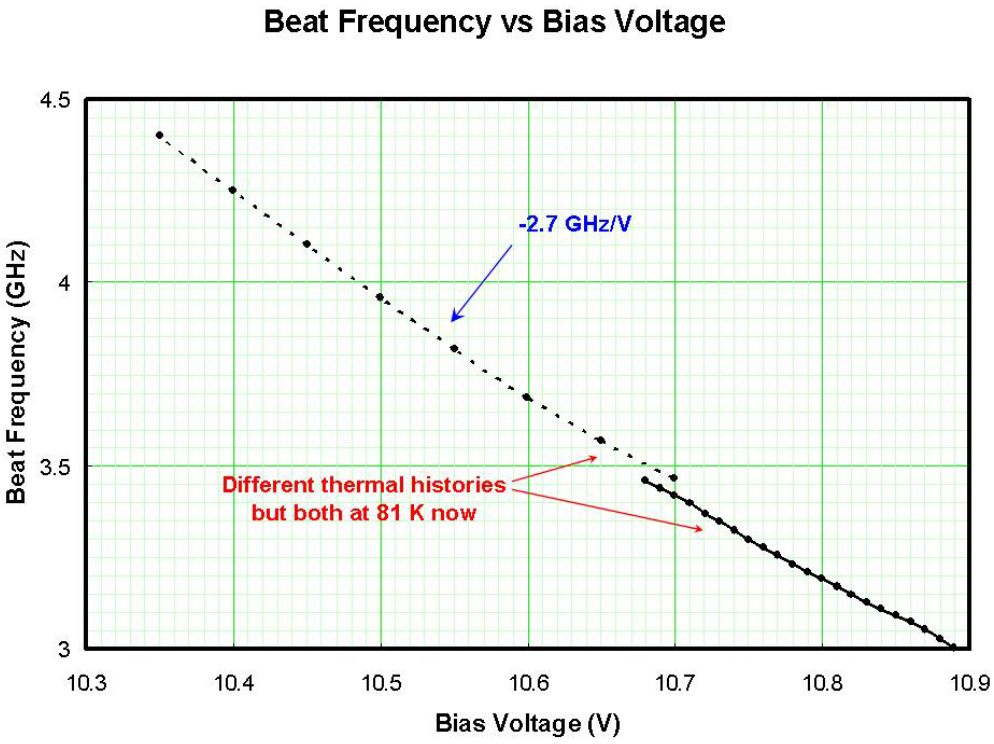

Figure 4

Mixing Results

A plot of the beat note frequency as a function of QCL bias voltage is given in Fig. 4. The open-loop tuning sensitivity is about -2.7 GHz/V. With a differential resistance of 13 ohm at the operating point, the tuning sensitivity is equivalently -35 MHz/mA. Examples of QCL spectra under offset-locked conditions are provided in Figure 5(a-d). The lock-offset frequency is arbitrarily set to 3250.000 MHz, and the QCL runs in the upper sideband at 3109.1868 GHz. The circuit locked on first try and remained locked for 1 hour, after which the test was intentionally terminated. During lock, the DC component of the error voltage at the QCL bias terminal gradually increased by +20 mV. This bias change corrects for thermal effects that otherwise would have produced a total drift of 54 MHz.

The QCL linewidth when locked is about 350 kHz (FWHM). This is similar to the unlocked linewidth, which is to be expected since the loop bandwidth of 10 kHz is insufficient to correct the obviously wider sidebands. The overall lineshape is Lorentzian but has considerable fine structure, which suggests that current fluctuations are broadening an intrinsically narrower line. The "noise" apparent in the linear-scale plots of Fig. 5(a-c) is all due to laser fluctuations. Given the -2.7 GHz/V tuning sensitivity of the QCL, and the specified 1.5 mV ppk AC noise of the power supply, we would roughly expect bias noise to broaden the line by 4 MHz. The source of the sideband peaks at multiples of 700 kHz is under investigation but probably is due to the power supply. Future experiments will

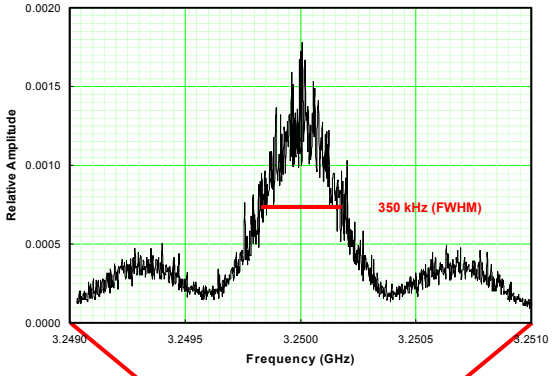

Figure 5(a)

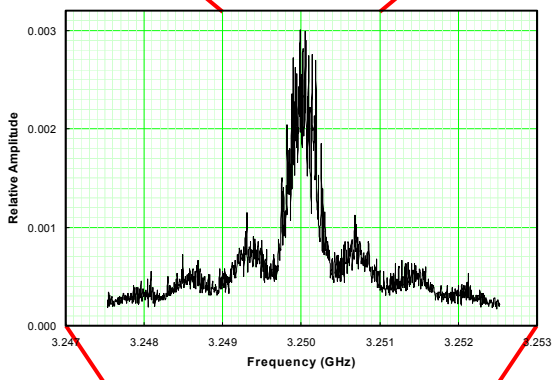

Figure 5(b)

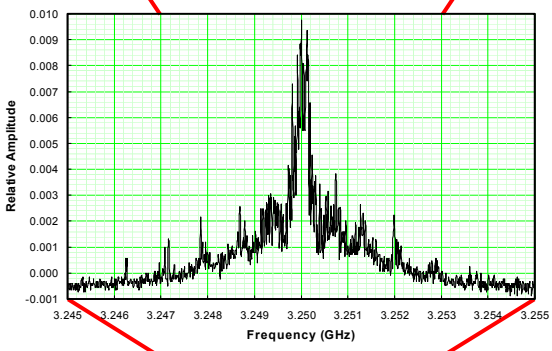

Figure 5 (c)

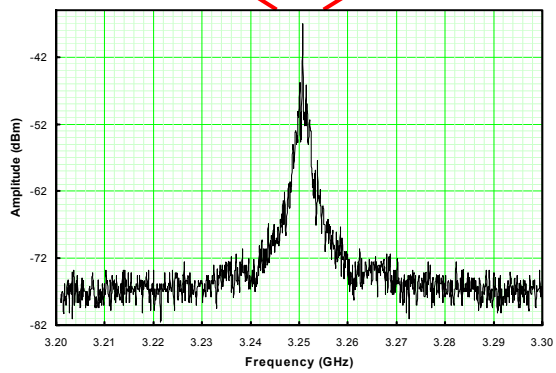

Figure 5 (d)

use a low noise constant current source (perhaps a battery) and increase the loop bandwidth to at least 10 MHz. Although line widths of 0.4-4 MHz are tolerable for astronomical spectroscopy at 3.1 THz, we must be certain that phase noise is low within the expected IF band (*e.g.*, 4-8 GHz away from the LO).

Conclusions

The deleterious effects of temperature drift and optical feedback can be corrected by phase-locking the QCL frequency to an external reference. A phase-locked QCL can be stable in both frequency and amplitude. Although both the laser power and frequency are functions of bias current, we can use the low-frequency component of the phase-error signal to control the block temperature (and thereby the laser frequency) such that the bias current remains constant long term. In this experiment we used a FIR laser as the reference (the FIR laser linewidth is <10 kHz). Next we will try locking to a high harmonic of a 120 GHz source. At that point the QCL frequency can be set by computer control, as astronomers expect (and demand). Further refinements on loop electronics and bias noise control should lead to linewidths of 30 kHz at 3 THz, or 1 part in 10^8.

This work was supported in part by NASA grant NAG5-9474 at the Univ. of Colorado. Work at MIT is supported by AFOSR, NASA, and NSF. Sandia is a multi-program laboratory operated by Sandia Corporation, a Lockheed Martin Company, for the US Dept. of Energy under Contract DE-AC04-94AL85000.

References

1. R. Koehler, A. Tredicucci, F. Beltram, H. E. Beere, E. H. Linfield, A. G. Davies, D. A. Ritchie, R. C. Iotti, and F. Rossi, Nature, **417**, 156 (2002)

2. M. Rochat, L. Ajili, H. Willenberg, J. Faist, H. Beere, G. Davies, E. Linfield, and D. Ritchie, Appl. Phys. Lett., **81**, 1381 (2002)

3. B. S. Williams, H. Callebaut, S. Kumar, Q. Hu, and J. L. Reno, Appl. Phys. Lett., **82**, 1015 (2003)

4. B.S. Williams, S. Kumar, Q. Hu, and J.L. Reno, "Resonant-phonon terahertz quantum-cascade laser operating at 2.1 THz ($\lambda \approx 141$ μm)," Elect. Lett. **40**, 431 (2004)

5. S. Kumar, B.S. Williams, S. Kohen, Q. Hu, and J.L. Reno, "Continuous-wave operation of terahertz quantum-cascade lasers above liquid-nitrogen temperature", Appl. Phys. Lett. **84**, 2494 (2004)

6. A. Betz and R.T. Boreiko, "A Practical Schottky Mixer for 5 THz (Part I)", in Proc. Sixth Int. Symp. on Space Terahertz Tech., Pasadena, CA, 21-23 March 1995, pp. 28-33 (1995); *ibid*, (Part II), in Proc. Seventh Int. Symp. on Space Terahertz Tech., Charlottesville, VA, 12-14 March 1996, pp.503-510

THz Quantum Cascade Laser as Local Oscillator in a Heterodyne Receiver

H.-W. Hübers, S. G. Pavlov, and A. D. Semenov
German Aerospace Center (DLR)
Rutherfordstr. 2, 12489 Berlin, Germany

A. Tredicucci and R. Köhler
NEST-INFM and Scuola Normale Superiore
Piazza dei Cavalieri 7, 56126 Pisa, Italy

Harvey E. Beere, Edmund H. Linfield, David A. Ritchie
Cavendish Laboratory, University of Cambridge, Madingley Road, Cambridge CB3 0HE, United Kingdom

Heterodyne spectroscopy of molecular rotational lines and fine structure lines of atoms or ions is a powerful tool for the investigation of the interstellar medium as well as planetary atmospheres. The Terahertz (THz) part of the electromagnetic spectrum is especially rich in these lines. Some examples are the CII fine structure line at 1.6 THz, the 1-0 transition of HD at 2.7 THz, and the OI fine structure line at 4.7 THz. Several THz heterodyne receivers are currently under development. One example is GREAT, the German Receiver for Astronomy at THz Frequencies, on board of SOFIA. GREAT is a modular receiver with three frequency bands operating at 1.6-1.9 THz, 2.5-2.7 THz and particular frequencies between 3 THz and 5 THz. A key component of any heterodyne receiver is the local oscillator. It should be a continuous wave, narrow linewidth, and frequency tunable source with at least several µW output power. However, above about 2 THz there is a lack of sources of this kind.

Recently a new type of THz laser, the THz quantum cascade laser (QCL), has been developed. The lasing mechanism is based on interminiband transitions in the conduction band of GaAs/AlGaAs heterostructures. Laser operation between 2.1 THz and 4.4 THz, operation temperatures up to 93 K, and high output power up to 50 mW have been achieved. Although for record performance in terms of output power and temperature the laser is typically not single moded the THz QCL a very promising source for application in a heterodyne receiver. We will report on the characterization of a THz QCL with respect to relevant performance parameters when used as local oscillator. This includes operation in a closed cycle cryocooler, beam profile measurements and pumping of a HEB mixer at 4.4 THz. The prospects for this particular application of a QCL will be discussed.

The Study of Harmonic-Mode Operation of GaAs TUNNETT Diodes and InP Gunn Devices Using a Versatile Terahertz Interferometer

H. Eisele, M. Naftaly, J. R. Fletcher, D. P. Steenson, M. R. Stone

Institute of Microwaves and Photonics, School of Electronic and Electrical Engineering
University of Leeds, Leeds, LS2 9JT, United Kingdom

Abstract

A simple Fourier transform terahertz spectrometer was constructed to evaluate the transmission and reflection spectra of materials as well as the emission spectra of pulsed broadband and continuous-wave narrowband sources. It works as a Michelson interferometer without a beam splitter and operates at room temperature with a Golay cell as the detector. This interferometer was employed to study the extraction of power from GaAs TUNNETT diodes and InP Gunn devices at the second or higher harmonic frequency above 325 GHz. As initial results, output power levels of more than 80 μW were generated with a GaAs TUNNETT diode at 355 GHz in a third-harmonic mode, more than 0.6 mW at 328 GHz, with an InP Gunn device in a second-harmonic mode, and more than 5 μW at 415 GHz, with an InP Gunn device in a third-harmonic mode.

1. Introduction

Compact fundamental solid-state sources of coherent continuous-wave (CW) radiation are instrumental in many systems applications at submillimeter-wave frequencies [1]. Tunneling as a fast and "quiet" carrier injection mechanism makes the tunnel-injection transit-time (TUNNETT) diode one of the prime candidates for such sources and its CW operation has been demonstrated already up to 400 GHz [2], [3]. The InP Gunn device is another prime candidate for such sources since it is the most powerful fundamental solid-state source above 290 GHz. Predictions also indicate that substantial amounts of power can be generated up to at least 450 GHz [4]. Both types of two-terminal devices are mounted on diamond heatsinks and were operated in an efficient second-harmonic mode when they yielded radio-frequency (RF) output power levels comparable to those from frequency multipliers in the frequency range of 190–325 GHz [4], [5]. The strongly nonlinear nature of most two-terminal devices also causes higher harmonic frequencies to be present, but the extraction of higher harmonic frequencies has not been studied in greater detail. Some initial experimental results at submillimeter-wave frequencies are known only from Si impact avalanche transit-time (IMPATT) diodes [6], whereas some output power at third-harmonic frequencies of 135 GHz and 270 GHz was reported from GaAs [7] and InP Gunn devices [8], respectively.

A spectrum analyzer with a harmonic mixer is used routinely to determine the output frequency and spectral purity of, for example, GaAs TUNNETT diodes [5] and InP Gunn devices [4], [5]. However, its limitations, a high noise floor and long scan times, become more and more evident at higher submillimeter-wave frequencies and, in particular, when one tries to scan a large frequency range for different harmonics in the output signal from an oscillator. In addition, many commercially available spectrum analyzers are limited to displaying results with an external mixer only up to center frequencies of 325 GHz.

2. System Description

The Fourier-Transform terahertz interferometer was developed originally to study the emission spectra of broadband THz sources such as, for example, photoconductive switches [9], and the transmission (or reflection) spectra of materials [10]. Its configuration is shown schematically in Figure 1. The THz radiation is collected and collimated by a 2" gold-coated off-axis parabolic mirror (90°, numerical aperture = 1). The collimated beam is directed onto a movable split mirror (shown in the insert), which divides the beam into two halves and introduces a variable phase shift between the two reflected beams of nearly equal power. This phase shift is proportional to the differential delay. The reflected beams are then directed onto the second identical off-axis parabolic mirror, which focuses and combines them to form an interference pattern at the location of the THz detector. For material transmission measurements, a horizontal slit can be placed at the focal plane of the second mirror to increase the sensitivity at higher frequencies. A calibrated Golay cell (QMC Instruments Ltd., UK) with an aperture of 6 mm and a virtually flat responsivity curve in the frequency range 0.1–2 THz is placed directly at the focal plane (and directly behind the slit) and used as the THz detector. It is

connected to a computer-controlled lock-in amplifier, which receives the synchronization signal from the mechanical beam chopper with a crystal-controlled chopper frequency of 8–16 Hz. A motorized and computer-controlled translations stage with a total travel distance of 25 mm moves the top half of the split mirror back and forth with respect to the other half. This motion causes a precise and variable time delay between the two halves of the THz beam and thus produces the interferogram.

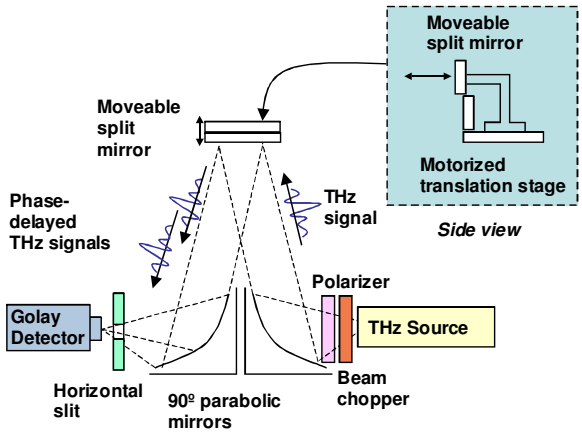

Figure 1: Schematic diagram of the Fourier transform THz interferometer.

This type of interferometer was originally proposed in the 1960s for wavelengths in the infrared (IR), but has never been employed at submillimeter-wave frequencies. The prime advantage of this design is that it does not require a 45°-beam splitter and therefore avoids the loss and frequency dependence introduced by such a beam splitter. Figure 2 compares the transmission spectra of two different fabric materials, whereas Fig. 3 compares two transmission spectra of a 0.75-mm thick cellulose sample, one from the Fourier transform THz spectrometer of Fig. 1, the other from a THz time-domain spectroscopy system with a femtosecond-pulse IR laser [11], [12]. Both figures show the versatility of this type of interferometer and illustrate a very useful application in the area of material characterization [10].

3. Harmonic power extraction from active two-terminal devices

Initial work in the area of CW electronic sources focused on identifying favorable conditions particularly for the extraction of the third and fourth harmonic frequencies from GaAs TUNNETT diodes and InP Gunn devices above 300 GHz.

Figure 4 shows the example of a GaAs TUNNETT diode with an output power of more than 50 µW at 356 GHz, where both signals at the fundamental and second-harmonic frequencies were blocked by the output waveguide with a cut-off frequency of approximately 285 GHz. A power level of more than 80 µW was generated by the same diode at a slightly lower oscillation frequency of 345.5 GHz, which was confirmed with a spectrum analyzer and a harmonic mixer as shown in Fig. 5. To increase the sensitivity, an active frequency multiplier that doubles the original local-oscillator (LO) frequency of approximately 3–6 GHz had been inserted between the spectrum analyzer and the harmonic mixer. The output power levels were determined with a Thomas Keating quasi-optical absolute power meter and represent a significant improvement in the performance of GaAs TUNNETT diodes when compared with other results from GaAs TUNNETT diodes above 240 GHz [2], [3]. They are the highest output power levels reported to date from TUNNETT diodes.

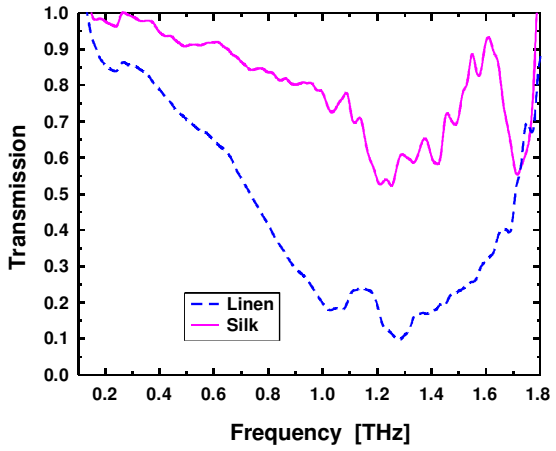

Figure 2: Transmission spectra of linen and silk fabrics.

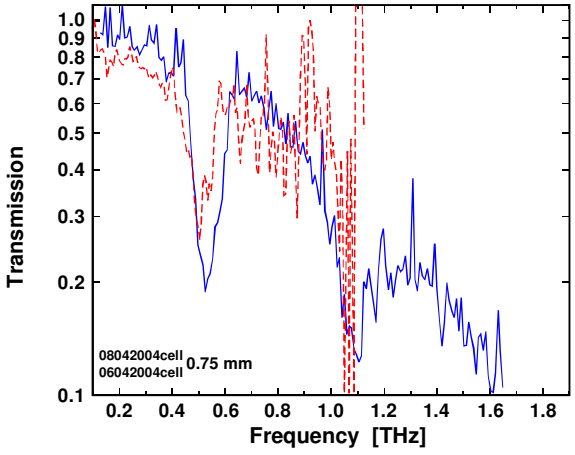

Figure 3: Comparison of the transmission spectra of a 0.75-mm thick cellulose sample measured with the THz interferometer of Fig. 1 (- -) and a THz time-domain spectroscopy system (—)[11], [12].

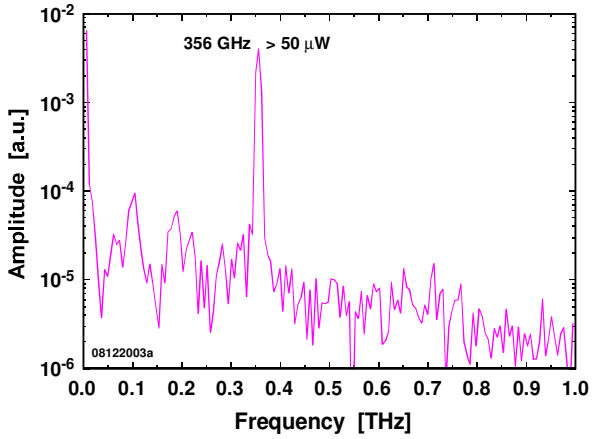

Figure 4: Spectrum of a 354-GHz oscillator with a GaAs TUNNETT diode operating in a third-harmonic mode.

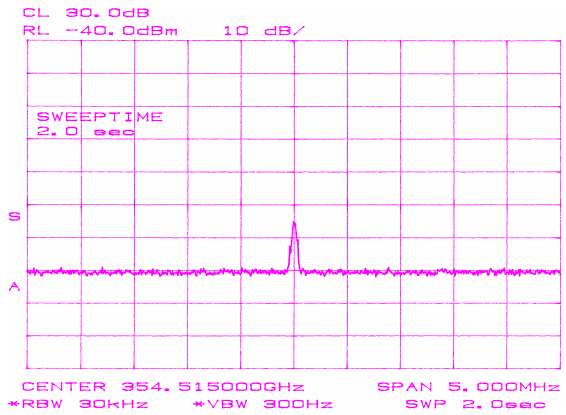

Figure 5: Spectrum of an oscillator with a GaAs TUNNETT diode in a third-harmonic mode recorded with a spectrum analyzer and a harmonic mixer (center frequency: 354.5 GHz, vertical scale: 10 dB/div., vertical scale: 500 kHz/div., resolution bandwidth: 30 kHz, video bandwidth: 300 Hz).

The operation at second-harmonic frequencies above 325 GHz as well as the extraction of higher harmonic frequencies was investigated with InP Gunn devices of two different doping profiles, one originally optimized for fundamental-mode operation [5], [13] and the other one optimized for second-harmonic power extraction [4]. Untested devices as well as those that had already yielded state-of-the-art results in a second-harmonic mode at *J*-band (220–325 GHz) frequencies [4], [5], [13] were employed in the experiments. Figure 6 illustrates an example of second-harmonic power extraction at 328 GHz as measured with the THz spectrometer of Fig. 1, whereas Fig. 7 shows the corresponding result from the spectrum analyzer with the harmonic mixer and the active frequency multiplier that doubles the original LO frequency of approximately 3–6 GHz. The output power level of more than 0.6 mW was determined with a Thomas Keating quasi-optical absolute power meter.

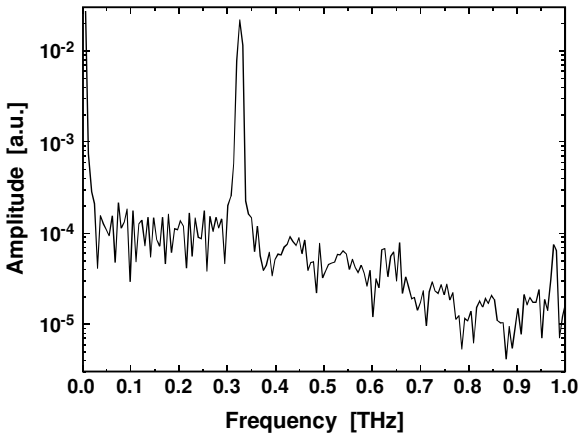

Figure 6: Spectrum of a 328-GHz oscillator with an InP Gunn device operating in a second-harmonic mode.

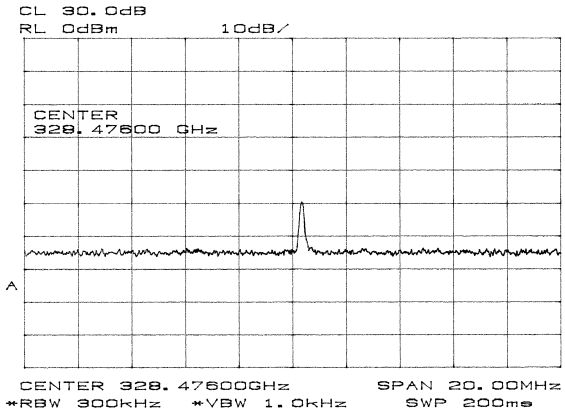

Figure 7: Spectrum of an oscillator with an InP Gunn device in a second-harmonic mode, recorded with a spectrum analyzer and a harmonic mixer (center frequency: 328.5 GHz, vertical scale: 10 dB/div., vertical scale: 2 MHz/div., resolution bandwidth: 300 kHz, video bandwidth: 1 kHz).

The device of Figs. 8 and 9 has the same doping profile as that of Figs. 6 and 7, but operates in a third-harmonic mode at 416 GHz. Its output power of more than 5 μW was estimated from a measurement with a *W*-band (75–110 GHz) thermocouple-based power meter. As can be seen from Fig. 9, power extraction at the third-harmonic frequency of 414.3 GHz with a similar output power was also confirmed with a different spectrum analyzer and a different harmonic mixer in a measurement setup that is much more sensitive than that of Figs. 5 and 7.

The THz spectrometer becomes the most suitable tool in a situation where several harmonic frequencies are

present. This situation is illustrated with Fig. 10 where the second-harmonic frequency of 283 GHz is slightly below the cut-off frequency of the waveguide, and, therefore, the signal from the InP Gunn device [5] at the second-harmonic frequency is suppressed only partially and the second-, third-, and fourth-harmonic frequencies are present. The total output power is too low to be ascertained correctly with the Thomas Keating quasi-optical power meter, but it was estimated from the output voltage of the Golay cell that more than 1 μW is available at the third-harmonic frequency of 425 GHz. In a very similar experiment with a different InP Gunn device that had the same doping profile as those of Figs. 6–9, the interferogram indicated approximately three times higher output power levels at 436 GHz.

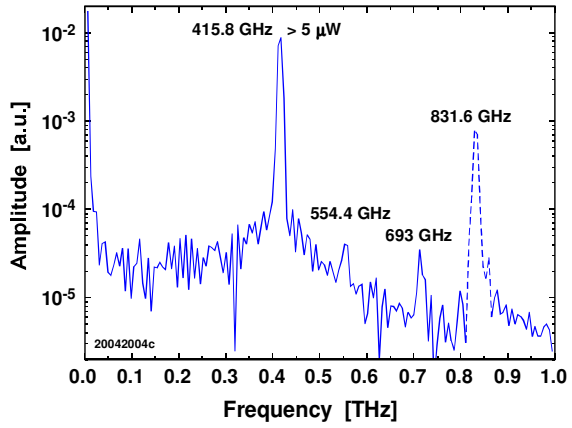

Figure 8: Spectrum of a 416-GHz oscillator with an InP Gunn device operating in a third-harmonic mode.

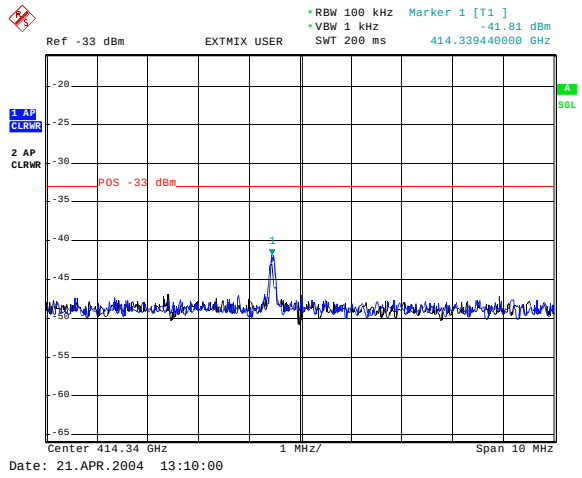

Figure 9: Spectrum of an oscillator with an InP Gunn device in a third-harmonic mode, recorded with a spectrum analyzer and a harmonic mixer (center frequency: 414.34 GHz, vertical scale: 5 dB/div., vertical scale: 1 MHz/div., resolution bandwidth: 100 kHz, video bandwidth: 1 kHz).

All output power levels from InP Gunn devices are not only the highest reported to date from any Gunn device, but also the highest reported from any fundamental source operated at room temperature. Further work is required to ascertain the output power levels at the fourth-, fifth-, and sixth-harmonic frequency.

4. Conclusion

The harmonic content in the output of GaAs TUNNETT diodes and InP Gunn devices was evaluated for the first time using a simple Fourier transform spectrometer without a beam splitter. The initial measurement of output power levels in the frequency range 325–475 GHz from GaAs TUNNETT diodes and InP Gunn devices indicate that the method of extracting higher harmonic frequencies from active two-terminal devices is promising and has a strong potential of reaching 1 THz. The bias conditions of the GaAs TUNNETT diodes and InP Gunn devices in these experiments were similar to those in a second-harmonic mode, which ensured low active-layer temperatures for long-term reliability.

Higher RF output power levels are expected from an optimization of the impedances seen by the device at the fundamental and harmonic frequencies, the coupling of the device into the output waveguide, and the device structures.

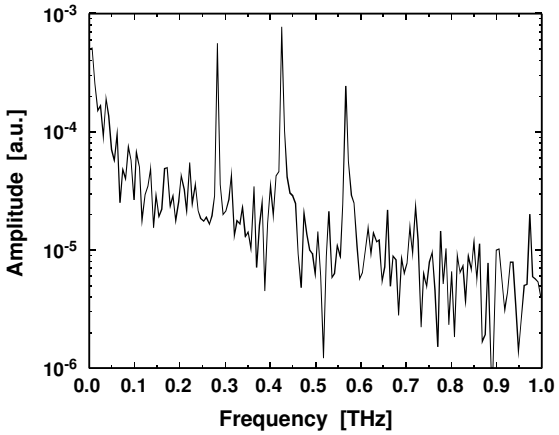

Figure 10: Spectrum of an InP Gunn oscillator with fourth-harmonic, third-harmonic, and partially suppressed second-harmonic frequencies of 566 GHz, 425 GHz, and 283 GHz.

Acknowledgment

This project was supported in part by UK Research Councils' Basic Technology Research Grant GR/R88106/01, Engineering and Physical Science Research Council's Joint Infrastructure Fund GR/M87535/01, Paul Instrument Fund PIF/GECL,

Teravision, and an EPSRC studentship. The authors would like to thank Peter Busch and Herbert Schmitt, Rohde & Schwarz, for their timely help with spectrum analyzer measurements as well as Andrew Foulds and Bob Miles for helpful discussions.

References

[1] P. Siegel, "Terahertz technology," *IEEE Trans. Microwave Theory Tech.*, vol. 50, no. 3, pp. 910–928, March 2002.

[2] P. Płotka, J-i. Nishizawa, T. Kurabayashi, and H. Makabe, "240–325-GHz GaAs CW fundamental-mode TUNNETT diodes fabricated with molecular layer epitaxy," *IEEE Trans. Electron Devices*, vol. 50, no. 4, pp. 867–873, April 2003.

[3] P. Płotka, J-i. Nishizawa, T. Kurabayashi, and H. Makabe, "GaAs fundamental-mode CW TUNNETT oscillators for THz-band applications," *11th Int. Conf. Terahertz Electronics*, Sendai, Japan, Sept. 24–26, 2003, p. 38.

[4] H. Eisele and R. Kamoua, "Gunn Devices as Compact Low-Noise High-Performance Submillimeter-Wave Sources: Current Status and Future Potential," *3rd ESA Workshop on Millimetre Wave Technology and Applications*, Espoo, Finland, May 21–23, 2003, pp. 149–154.

[5] H. Eisele, A. Rydberg, and G. I. Haddad, "Recent advances in the performance of InP Gunn devices and GaAs TUNNETT diodes for the 100–300-GHz frequency range and above," *IEEE Trans. Microwave Theory Techniques*, vol. 48, no. 4, pp. 626–631, April 2000.

[6] M. Ohmori, T. Ishibashi, and S. Ono, "Dependency of the highest harmonic oscillation frequency on junction diameter of IMPATT diodes", *IEEE Trans. Electron Devices*, vol. 24, no. 12, 1977, pp. 1323–1329, Dec. 1977.

[7] H. Barth and W. Menzel, "GaAs Gunn oscillators reach the 140-GHz range," *1985 IEEE MTT-S Digest*, pp. 367–369, June 1985.

[8] A. Rydberg, "High efficiency and output power from second- and third-harmonic millimeter-wave InP-TED oscillators at frequencies above 170 GHz," *IEEE Electron Device Lett.*, vol. 11, no. 10, pp. 439–441, Oct. 1990.

[9] M. R. Stone, M. Naftaly, R. E. Miles, J. R. Fletcher, and D. P. Steenson, "Electrical and radiation characteristics of semi-large photoconductive terahertz emitters," *Terahertz Discussion Meeting*, Royal Society, London, UK, June 4–5, 2003.

[10] M. R. Stone, M. Naftaly, R. E. Miles, J. R. Fletcher, and D. P. Steenson, "Terahertz Fourier transform spectrometer based on a lamellar grating interferometer for pulsed and CW applications," *11th Int. Conf. Terahertz Electronics*, Sendai, Japan, Sept. 24–26, 2003, pp.49–50.

[11] M. Naftaly, R.E. Miles, M.R. Stringer, "THz transmission spectroscopy of nonpolar materials and relationship with composition and properties," to be presented at the *Joint 29th Int. Conf. Infrared and Millimeter Waves and 12th Int. Conf. Terahertz Electronics*, Sept. 27 – Oct. 1, 2004, Karlsruhe, Germany.

[12] A. J. Fitzgerald, E. Berry, N. N. Zinov'ev, G. C. Walker, M. A. Smith, J. M. Chamberlain, "An introduction to medical imaging with coherent terahertz frequency radiation," *Physics in Medicine and Biology*, vol. 47, no. 7, pp. R67–R84, April 2002.

[13] H. Eisele and G. I. Haddad, "*D*-band InP Gunn devices with second-harmonic power extraction up to 290 GHz," *Electronics Lett.*, vol. 30, no. 23, pp. 1950–1951, 1994.

THz Spectrometer Based on a Josephson Oscillator and a Cold-Electron Bolometer

M.Tarasov[1,2], L.Kuzmin[1], E.Stepantsov[1,3], I.Agulo[1], A.Kalabukhov[1,4], T.Claeson[1]

[1]*MC2, Chalmers University of Technology, SE-41296 Gothenburg, Sweden*
[2] *Institute of Radio Engineering and Electronics, RAS, Moscow, Russia*
[3]*Institute of Crystallography,Russian Academy of Sciences, Moscow, Russia*
[4] *Moscow State University, Moscow, Russia*
E-mail: mikhail.tarasov@mc2.chalmers.se

We have demonstrated a low temperature spectrometer operating in a wide range of frequencies from 100 GHz to 1.8 THz. The spectrometer has utilized unique properties of high-T_c superconducting Josephson junctions and wideband response of sensitive Cold-Electron Bolometers (CEB). The voltage response of the CEB integrated with log-periodic and double-dipole antennas, has been measured using an oscillator consisting of high-T_c Josephson junction integrated on separate substrate with a log-periodic antenna. The response of the bolometer with a double dipole antenna has resonance shape with maximum corresponding to the designed central frequency of 300 GHz. A voltage response of the bolometer up to $4 \cdot 10^8$ V/W corresponds to a technical noise equivalent power of the bolometer of $1.2 \cdot 10^{-17}$ W/Hz$^{1/2}$ including bolometer and amplifier sources of noise. A high-T_c Josephson junction operated at temperatures below 2 K shows advantages of high I_cR_n product that enhances the oscillation frequency to over 1.8 THz. The resolution of the spectrometer is determined by the linewidth of Josephson oscillations and for this temperature is of the order of 1 GHz.

Introduction: samples, layout and fabrication

For sensitive spectroscopy studies at THz frequencies one needs a simple, cheap, light, tunable, narrow linewidth THz source and a sensitive detector. The detector may need to be cooled to sub-Kelvin temperature in order to obtain a low enough noise level. It is an advantage if the generator can be at a substantially higher temperature if samples are placed at low temperature.
A cold electron bolometer with capacitive coupling (CCNHEB) was proposed in [1] and experimentally demonstrated in [2]. Responsivity and noise equivalent power (NEP) of the bolometer are mainly determined by its electron temperature. To improve CCNHEB performance we suggest using direct electron cooling of the absorber by a superconductor-insulator-normal metal (SIN) tunnel junction [3]. The effect of electron cooling was demonstrated in [4] and further developed in [5]. General view on NHEB chip is presented in Fig. 1. The first step of sample fabrication was thermal evaporation of 60 nm Au for fabrication of the normal metal traps and contact pads. The pattern for the traps and the pads were formed using photolithography. The next step was the fabrication of the tunnel junctions and the absorber. The structures were patterned by e-beam lithography and the metals were thermally evaporated using the shadow evaporation technique. The Al (superconductor) was evaporated at an angle of about 60° up to a thickness of 65 nm and oxidized at a pressure of 10^{-1} mbar for 2 minutes. A Cr/Cu (1:1) absorber of a total thickness of 75 nm was then evaporated directly perpendicular to the substrate. The cooling junctions have a normal state resistance R_N equal to 0.86 kΩ, while the two inner junctions have R_N equal to 5.3 kΩ. The inner junctions have a simple cross geometry, where a section of the normal metal absorber overlaps the thin Al electrodes. The area of overlap, which makes to the area of each of the tunnel junction, is equal to 0.2 x 0.3 μm^2. The structure of the outer junctions is such that the ends of the normal metal absorber overlap with a corner of each of the Al electrodes, which have a much larger area, compared to the middle Al electrode. The area of each of these junctions is 0.55 x 0.82 μm^2. The purpose of the larger area Al electrode is to give more space for quasiparticle diffusion compared to the middle Al electrode with simple cross geometry. In the described structure, the two outer and inner junctions have the R_N equal to 0.85 kΩ and 5.4 kΩ, respectively. The volume of the absorber was 0.18 μm^3.

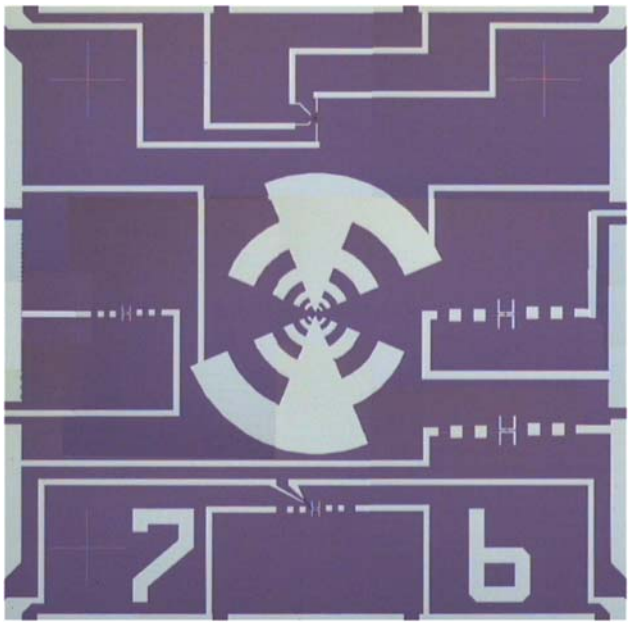

Figure 1. A bolometer chip layout. A wideband log-periodic antenna at the center, a 600 GHz double-dipole antenna to the left and two 300 GHz double-dipole antennas to the right.

A bias cooling current is applied through the outer junctions and the absorber. These tunnel junctions act as the cooling junctions, and therefore serve to decrease the electron temperature of the absorber. To determine the electron temperature, the voltage across the inner junctions is measured. A small current bias is applied to these junctions. The bias has to be optimal to obtain the maximum linear voltage response on temperature, and yet not too large so as to disturb the cooling process in the absorber.

High critical temperature Josephson junctions on tilted bicrystal sapphire substrates were fabricated in YBaCuO epitaxial films with c-axis inclined in <100> direction by angle 14^o+14^o. Films 250 nm thick were deposited by pulsed laser ablation on tilted sapphire bicrystal substrates covered by a CeO_2 buffer layer. The critical temperature of the film was T_c=89 K and ΔT_c=1.5 K. Bicrystal Josephson junctions of width from 1.5 to 6 μm demonstrated a characteristic voltage I_cR_n of over 4 mV at a temperature of 4.2 K. Junctions were integrated with log-periodic antennas designed for frequency range 200-2000 GHz (see Fig. 2).

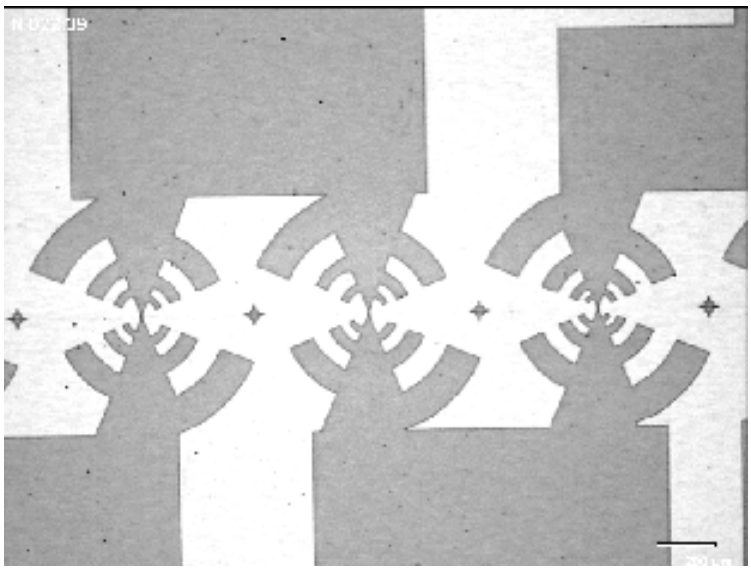

Figure 2. Central part of a Josephson oscillator chip

Power and temperature responses of the bolometer.

We measured the temperature response of the bolometers at the lowest temperature of about 260 mK that is available in our He3 sorption cooler cryostat. The dc response was measured at upper and lower structures with four SIN junctions. Two external junctions were used as thermometers and two internal as heaters. The highest value of voltage response to temperature variations is over 1.6 mV/K and the largest current response about 37 nA/K for a 10 kΩ junction and 55 nA/K for a 6 kΩ junction.

It was possible to apply a dc power to the central pair of junctions and measure the response of the outer pair of SIN junctions for these samples with four SIN junctions. Results of current and voltage responses on dc power are presented in Fig. 3. We observed the largest voltage response of 400 V/μW for a 70 kΩ junction and 550 A/W for a 10 kΩ junction. The obtained values of current and voltage responses can be converted to the natural figure of merit for the sensitivity of the bolometer in terms of a Noise Equivalent Power (NEP).

$NEP=I_n/S_i$ or $NEP=V_n/S_v$ (1)

in which I_n is the current noise, V_n is the voltage noise, $S_i=dI/dP$ is the current response, $S_v=dV/dP$ is the voltage response of the bolometer. Taking the voltage noise of a room-temperature preamplifier about 3 $nV/Hz^{1/2}$ one can obtain the amplifier-limited technical noise equivalent power TNEP value

$TNEP=0.75\cdot10^{-17}$ $W/Hz^{1/2}$

Using measured values of the temperature response and the power response one can also obtain the thermal conductivity of the bolometer.

$$G_V = \frac{\partial P}{\partial T} = \frac{\partial V / \partial T}{\partial V / \partial P} = 0.8 \cdot 10^{-11} W / K$$

Now we can calculate the thermodynamic NEP arising from the electron-phonon interaction $NEP_{ep}^2=4kT^2G$ in which thermal conductivity $G=5\Sigma\nu T^4=10^{-11}$ W/K, ν is the absorber volume. This brings a thermodynamical noise equivalent power $NEP_{TD}=6\cdot10^{-18}$ $W/Hz^{1/2}$, and if we compare with the thermal conductivity in the voltage bias mode it corresponds to a $NEP_V=1.3\cdot10^{-18}$ $W/Hz^{1/2}$.

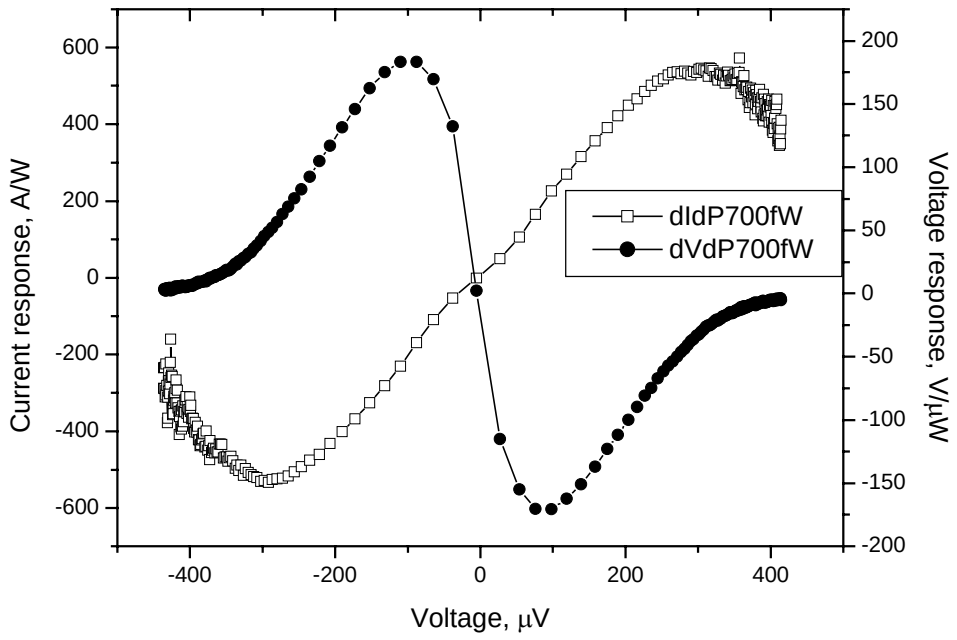

Fig. 3. Current and voltage responses for a 10 kΩ SIN junctions on the applied power at 260 mK.

Measurements of the response with a Josephson junction as a radiation source at 260 mK

In the experiment we use a direct connection of the substrate with the Josephson oscillator to the substrate with the receiver (see Fig 4). When a planar antenna is placed on a dielectric substrate with a high refraction index, the main lobe of the beam-pattern is directed into the substrate. In this case most of the radiation from the Josephson oscillator is directed to the antenna with the bolometer. The log-periodic antennas used in both oscillator and receiver chips (see Fig. 1,2 central part) are designed for frequencies 100-2000 GHz.

The measured dependencies of the bolometer voltage response are presented in Fig. 5. We choose a Josephson junction with rather low critical current about 20 μA to avoid overheating of both Josephson oscillator and attached bolometer. Applying a magnetic field one can suppress the critical current of Josephson junction, which leads to a decrease of the output power of Josephson oscillations and the frequency range according to the Josephson equations. When the critical current is suppressed below 2 μA the response voltage is clear proportional to the square of the JJ bias current and is no more affected by magnetic field. It means that we completely suppressed Josephson radiation and the residual radiation is just a thermal radiation by overheated normal resistance of the Josephson junction matched to the broadband antenna. This brings clear evidence that we can separate the Josephson radiation at frequencies below 1 THz and the thermal radiation of overheated matched load for bias voltages over 1 mV.

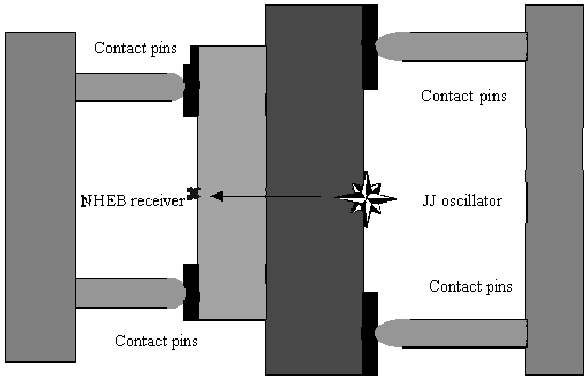

Figure 4. Schematic view for experimental setup at 260 mK in back-to-back configuration

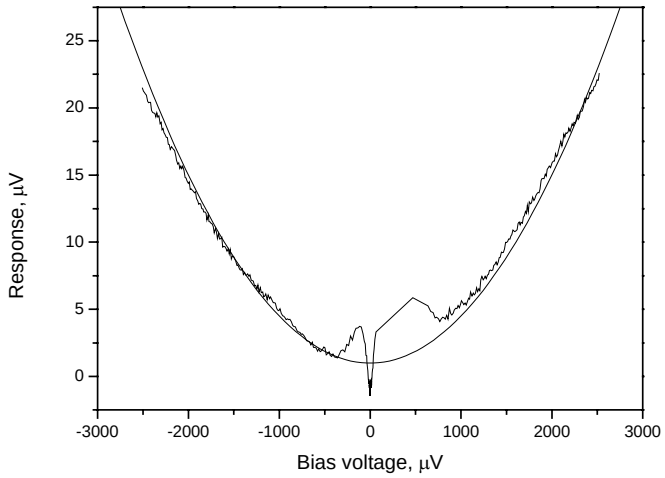

Figure 5. Bolometer response measured with a Josephson junction radiation source at 260 mK. The solid parabola is a fit for Joule heating.

For Josephson oscillators we can estimate the maximum available power as $P_{osc}=0.1 \cdot I_c V_c=2 \cdot 10^{-9}$ W. Misalignment of antennas, mismatch of beam-patterns, material losses, mismatch of impedances can bring the total attenuation of the maximum power up to 30 dB that corresponds to an available power at the bolometer of about 10^{-12} W. The estimated above bolometer responsivity is $S=1.1 \cdot 10^{8}$ V/W that brings the maximum voltage response to this power about $1.1 \cdot 10^{-4}$ V. In our experiments we measured the voltage response up to 10 μV. The order of magnitude difference in response can be explained due to a non-ideal IV characteristic of the Josephson junction (excess current) and overheating that reduces the output power.
If we take as an approximation a model of overheating in a Josephson junction by [6] for a variable thickness microbridge

$$T_m = \sqrt{T_b^2 + 3\left(\frac{eV}{2\pi k}\right)^2} \qquad (6)$$

in which T_b is bath temperature, V is a dc voltage bias; it brings the equivalent electron temperature at 1 mV bias of about 3 K. Taking into account that IR radiation is spread in a 4π solid angle and the bolometer is at a distance of over 1 mm, the dielectric can absorb a small part of this radiation, the measured increase in received temperature of 5 mK looks reasonable. Now we should take into account that this power is radiated and then received. It means that Plank's radiation law should be applied

$$P_r = \frac{hf}{e^{\frac{hf}{kT}} - 1} 0.3 f \qquad (7)$$

for which the maximum of radiation is obtained at hf≈kT. If we apply the Plank's formula to equation (1) neglecting the phonon temperature

$$P_{rad} = \frac{0.6}{4\pi^2} \cdot \frac{e^2 V^2}{h} \qquad (8)$$

it brings the square-law voltage dependence, as observed in the experiment.

Irradiation of the bolometer by a distant Josephson junction at 1.8 K.

To increase the output microwave power from the Josephson junction, the characteristic voltage I_cR_n , and oscillation frequency, it is necessary to increase the critical current of the Josephson junction from 20 μa as above, to over 500 μA. Placing the Josephson junction separately on the He4 stage prevents the bolometer from overheating by the relatively high power absorbed by the Josephson junction. Schematic view on experimental quasioptical setup is presented in Fig. 6. As the example if we take a junction with 10 Ωnormal resistances and oscillation frequency 300 GHz, it brings the absorbed power over 0.2 μW. At 1 THz it is already 2.5 μW. Such power is acceptable for He4 stage, but is rather high for millikelvin stage.
The layout of the Josephson sample was the same as in the 260 mK experiments with similar log-periodic antennas, but the critical current was over 500 μA at 2 K. As a result the I_cR_n product exceeds 5 mV for non-hysteretic junctions and such oscillators can in principle operate at frequencies over 2.5 THz. Experimental curve in Fig.7 measured by bolometers integrated with log-periodic antennas, reveals that there is a smooth spectrum for LPA. Smooth reduction of signal received by log-periodic antenna can be easy explained by the increase of the beampattern width. In the simplest case of Gaussian telescope the output beam waist that is located at the focal distance L_f from the lens can be estimated as

$$w_{out} = \frac{\lambda L_f}{\pi w_{in}}$$

It is proportional to frequency, and corresponding losses

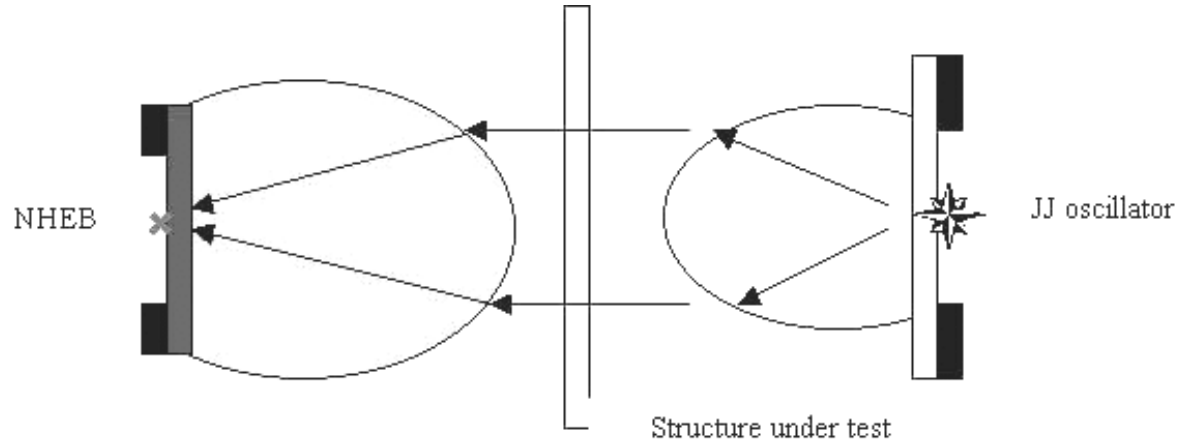

Fig. 7. Schematic view for quasioptical setup with NHEB lens-antenna unit at 260 mK and Josephson junction oscillator lens-antenna unit at 1.8 K.

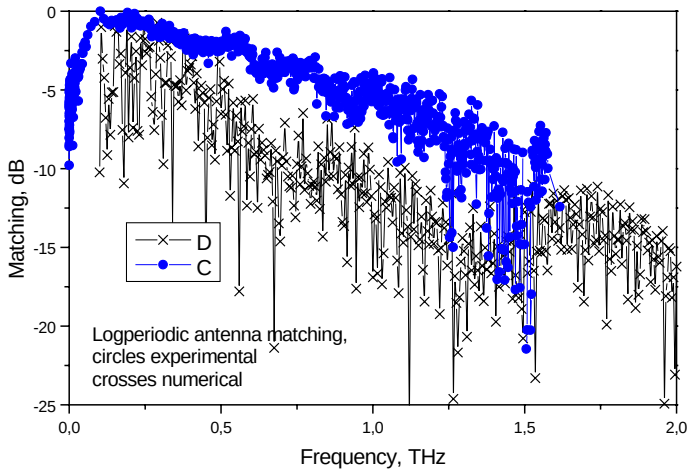

Figure 8. Experimental and calculated response by LPA.

In Fig. 8 signal is measured with a double-dipole antenna and demonstrate a clear maximum at the design frequency 300 GHz. We observed that suppressing the critical current by a magnetic field reduces the output power of the Josephson oscillator. The highest maximum corresponds to an oscillation frequency of 1.75 THz.

Discussion

A simple analytic analysis of the voltage response gives a rough relation for the practically achievable power response for single SIN junction:

$$S_V^{\max} = \frac{2k_b}{e\Sigma\upsilon T_e^4} = 100 \text{ V/}\mu\text{W}$$

We can roughly estimate the characteristics for voltage bias mode with electron cooling. The main power stream from phonons to electrons is

$$P_{Ph-e} = \Sigma\nu T_{Ph}^5 = 0.5pW$$

To remove such a power from the electron system it is necessary to apply a cooling current

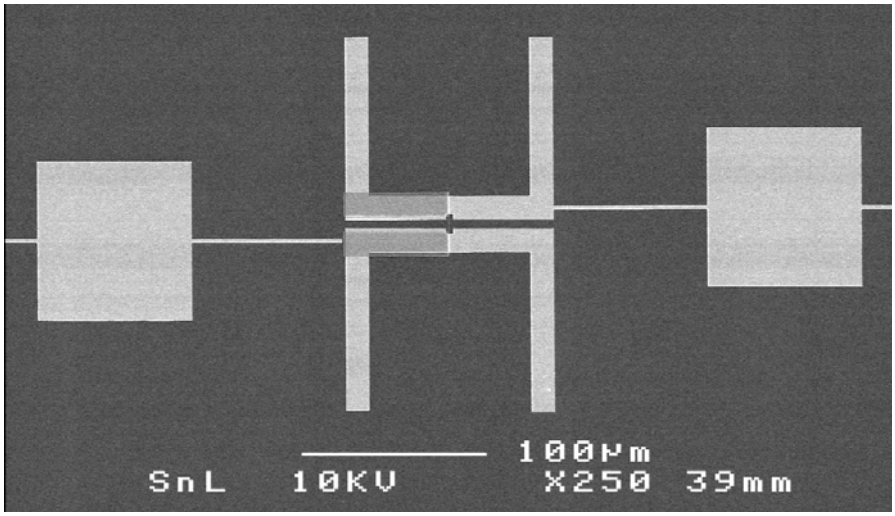

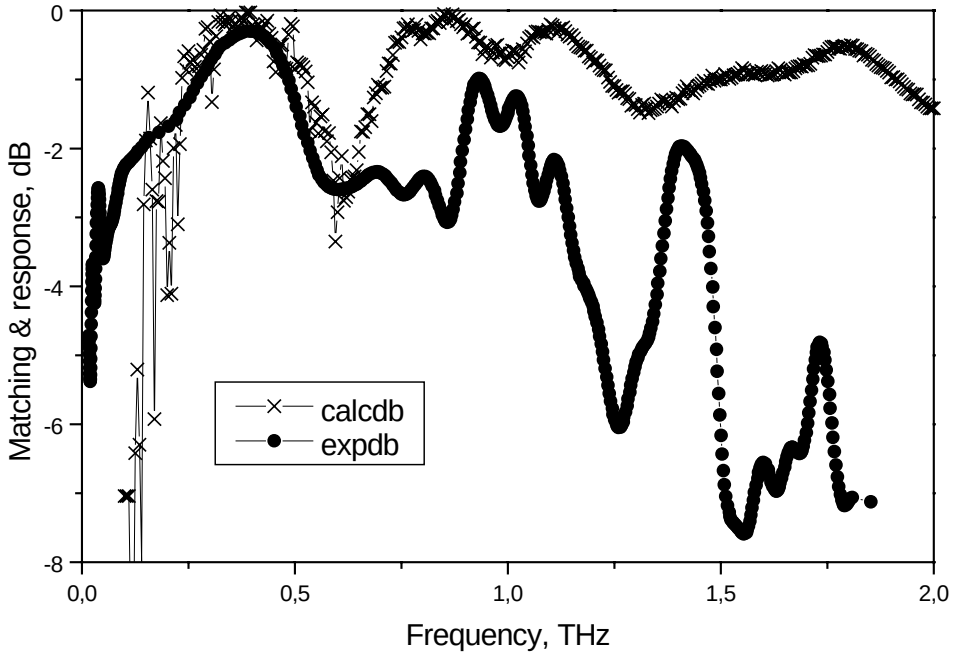

Figure 9. SEM view of the bolometer integrated with a double-dipole antenna in top panel and its experimental response (circles) and numerical modeling (crosses) in bottom panel.

$$I_c = \frac{eP_{Ph-e}}{k_b T} = 2.2 \cdot 10^{-8}\, A$$

This cooling current is associated with a shot noise. If we take the theoretical value for the current response $S_I = e/2k_bT = 6 \cdot 10^4$ A/W for electron temperature 100 mK it brings the shot noise impact $NEP_{sh} = 1.2 \cdot 10^{-18}$ W/Hz$^{1/2}$.

For phonon impact

$$NEP_I = \sqrt{4k_b T_e \Sigma \nu T_{Ph}^5} = 1.6 \cdot 10^{-18} \text{ W/Hz}^{1/2}$$

From the two dependencies above one can also obtain the required noise equivalent power for a voltage bias mode of operation. It is determined by the thermal conductivity of the SIN junction. For comparison below is presented a table with main characteristics of two cryogenic spectrometers: with cyclotron emission from 2DEG composite bolometer (see [7]) and our Josephson-CEB spectrometer

Main Characteristics	Cyclotron emission from 2DEG - composite bolometer*)	Josephson - CEB
Spectral range	0.1 – 2 THz	0.1 – 1.7 THz, Josephson - up to 4 THz CEB – up to 50 THz
Spectral resolution	200 GHz	1 GHz
Emitted power Received power Bolometer sensitivity	1 mW 50 pW 0.5 pW/Hz$^{1/2}$	1 nW 1 pW 10^{-17} W/Hz$^{1/2}$
Sweep	Magnetic feild	Voltage
Modulation frequency	Few Hz	up to several GHz for Josephson oscillator

Conclusion

We demonstrated the first experimental response of a normal metal cold electron bolometer at frequencies up to 1.8 THz. A voltage response of the bolometer is $4 \cdot 10^{8}$ V/W and experimental noise equivalent power of the bolometer is $1.3 \cdot 10^{-17}$ W/Hz$^{1/2}$. We were first to use electrically tunable high critical temperature Josephson quasioptical oscillator as a source of radiation in the range 0.2-2 THz. A high critical temperature Josephson junction operated at temperature about 2 K shows a I_cR_n product over 4.5 mV that enables an oscillation frequency over 2 THz. Combination of a Terahertz-band Josephson junction and a high-sensitive hot electron bolometer brings a possibility to develop a quasioptical cryogenic compact spectrometer with a resolution of about 1 GHz. Such cryogenic spectrometer can be used for low-temperature spectral evaluation of any cryogenic detector, quasioptical submm wave grid filter, neutral density filter, absorber, etc. Cold electron bolometer detected that a Josephson junction is overheated by a transport current even when it is placed on millikelvin stage.

Acknowledgements

Authors appreciate help by S.Shitov for numerical modeling of antennas spectral response and acknowledge support from VR, STINT, INTAS-01-686.

References

[1] Kuzmin L 2000 Physica B 284-288 2129-2130
[2] Tarasov M Fominsky M Kalabukhov A and Kuzmin L 2002 JETP Lett. 76 507-510
[3] Kuzmin L Devyatov I and Golubev D 1998 Proc. Of SPIE 3465 193-199
[4] Nahum M Eiles T M Martinis J M 1994 Appl. Phys. Lett. 65 3123-3125
[5] Leivo M Pecola J and Averin D 1996 Appl. Phys. Lett. 68 1996-1998
[6] Tinkham M Octavio M Scocpol W J, JAP 48 3 (1977) 1311-1320
[7] Burke et al., Rev. Sci. Instr. (2002) 130-135.

Submillimeter SIS Receiver Gain Stabilization

James Battat, Raymond Blundell, Todd R. Hunter, Robert Kimberk, Patrick S. Leiker, Cheuk-yu Edward Tong
Harvard-Smithsonian Center for Astrophysics, Cambridge, MA USA

ABSTRACT

We have designed a system to stabilize the gain of a submillimeter heterodyne receiver against thermal fluctuations of the mixing element. In the most sensitive heterodyne receivers, the mixer is usually cooled to 4 K using a closed-cycle cryocooler, which can introduce ∼1% fluctuations in the physical temperature of the receiver components. We compensate for the resulting mixer conversion gain fluctuations by monitoring the physical temperature of the mixer and adjusting the gain of the intermediate frequency (IF) amplifier that immediately follows the mixer.

This IF power stabilization scheme, developed for use at the Submillimeter Array (SMA), a submillimeter interferometer telescope on Mauna Kea in Hawaii, routinely achieves a receiver gain stability of 1 part in 6,000 (rms to mean). This is an order of magnitude improvement over the typical uncorrected stability of 1 part in a few hundred. Our gain stabilization scheme is a useful addition to SIS heterodyne receivers that are cooled using closed-cycle cryocoolers in which the 4 K temperature fluctuations tend to be the leading cause of IF power fluctuations.

1. Introduction

Superconductor insulator superconductor (SIS) receivers are in use on many millimeter and submillimeter telescopes because of their good spectral line sensitivity. Their continuum sensitivity, however, does not usually reach the theoretical limit because of receiver gain fluctuations. These arise predominantly from changes in mixer conversion gain, which result from physical temperature changes and local oscillator (LO) power changes. Here we describe a technique to reduce the impact of physical temperature changes on mixer conversion gain variations by changing the intermediate frequency (IF) gain of the receiver in proportion to fluctuations of the physical temperature of the SIS junction used as a mixing element.

A number of radio observatories make use of liquid Helium filled cryostats so that temperature induced receiver gain fluctuations are minimized. However, due to their lower degree of maintenance and upkeep, closed-cycle Helium cryocooler systems may be preferred. For example multi-receiver systems with high heat loads, such as those in use at the 8-element Submillimeter Array (SMA) (Moran 1998) or the upcoming 64-element Atacama Large Millimeter Array (ALMA) (Wootten 2003), are dependent on the use of cryocoolers. For these applications it is necessary to develop techniques to reconcile the need for highly stable receivers with the practical benefits of cryocoolers. An obvious approach is to design more stable cryocoolers, another is to compensate for the fluctuations in the mixer's conversion gain.

In some systems it is possible to stabilize the physical temperature of the mixer in a cryocooler system to 1-2 mK by using a heating resistor or a pot of liqid helium (Plambeck 1998; Sekimoto *et al.* 2001; Orlowska 2004). At the SMA these options are not feasible, so we take a different approach to receiver stabilization. While monitoring the physical temperature of the mixer we actively vary the gain of the third stage of the low noise HEMT amplifier to compensate for mixer conversion gain variations. We achieve nearly an order of magnitude improvement in receiver gain stability from 1 part in ∼800 to 1 part in 6,000 (rms to mean ratio) using a 33 ms integration time over 10 minutes. This corresponds to an effective temperature stability of < 2 mK. Such a scheme is straightforward to implement and can be applied to existing systems without redesigning the cryocooler.

2. Theoretical Considerations

The conversion gain of an SIS mixer has a negative temperature coefficient (Baryshev *et al.* 2003; Kooi *et al.* 2000). In simple terms, as the physical temperature, T_{phy}, of the mixer increases, the leakage current increases and the current-voltage relationship near the gap voltage becomes less sharp causing the mixer conversion gain, G, to decrease. For small temperature changes we may write

$$\frac{\Delta G}{G} \propto -\frac{\Delta T}{T_{phy}} \tag{1}$$

where ΔG and ΔT represent small fluctuations in the conversion gain and physical temperature of the mixer, respectively, and the minus sign reflects the anti-correlation between physical temperature and conversion gain.

At the SMA a two stage Gifford-McMahon (G-M) and a single Joule-Thomson (J-T) stage closed-cycle cryocooler maintain the SIS mixer at a nominal operating temperature of 4.2 K. In our system, cryocooler-induced temperature swings of about 1% (10-60 mK) result in mixer gain fluctuations of about 0.5%. Under the assumption that the $1/\sqrt{B\tau}$ fundamental gaussian radiometer noise and the instrumental gain fluctuations are statistically independent, (Tiuri and Räisänen 1986) show that they contribute to the fractional error in the system temperature by adding in quadrature to give:

$$\frac{\Delta T}{T_{sys}} = \sqrt{\left(\frac{1}{\sqrt{B\tau}}\right)^2 + \left(\frac{\Delta A}{A}\right)^2} \tag{2}$$

where $\Delta T/T_{sys}$ is the fractional error in the measured system noise temperature, B and τ are the IF bandwidth and integration time, respectively, and $\Delta A/A$ is the fractional gain fluctuation in the entire receiver chain.

The SMA receivers have a 2.5 GHz IF bandwidth and the digital correlator has a minimum integration time of 1 second, so the fundamental radiometer noise is $\lesssim$ 2 x 10^{-5}. Therefore fractional instrumental gain fluctuations, typically of order 10^{-2}-10^{-3}, dominate the system temperature fluctuations. In order to approach the fundamental noise limit of the receiver, the instrumental gain stability must be significantly improved.

Ignoring losses at the receiver input, the power output of an SIS receiver, shown schematically in Figure 1, can be written in the Rayleigh-Jeans limit ($h\nu << kT$) as

$$P_{IF} = k_B BGH\left(T_S + T_M + \frac{T_H}{G}\right) \tag{3}$$

where k_B is Boltzmann's constant, B is the IF bandwidth, G is the conversion gain of the mixer, H is the total HEMT amplification, T_S is the noise temperature of the source, T_M is the mixer noise temperature and T_H is the HEMT amplifier noise temperature.

If we assume that mixer conversion gain fluctuations are the dominant source of receiver gain fluctuations, and that T_M and T_H are independent of the physical temperature of the mixer and IF amplifier, then we can compute the necessary change in IF gain required to maintain a constant IF power from the following condition

$$\Delta P_{IF} = \frac{\partial P_{IF}}{\partial G}\Delta G + \frac{\partial P_{IF}}{\partial H}\Delta H = 0. \tag{4}$$

Using Equations 3 and 4, we find that the necessary fractional change in IF amplification is related to the fractional change in mixer conversion gain by

$$\frac{\Delta H}{H} = -\left(1 - \frac{P_H}{P_{IF}}\right)\frac{\Delta G}{G}. \tag{5}$$

where we have introduced $P_H \equiv k_B BHT_H$, the output noise power of the HEMT amplifier.

The observed physical temperature fluctuations, ΔT, are small compared to the nominal operating temperature, T_0 (generally $\Delta T/T_0 \lesssim 5\%$). Thus for linear perturbations, and under the assumption that the conversion gain of the mixer is only a function of its physical temperature, T_{phy}, we can write

$$\Delta G \equiv G\left(T_{phy}\right) - G\left(T_0\right) \approx g_T \Delta T. \tag{6}$$

where g_T is equal to the first derivative of the curve of mixer conversion gain versus physical temperature, evaluated at T_0. Over a broad temperature range, g_T is well approximated by the derivative of the Fermi function (Kooi *et al.* 2000).

Over temperatures relevant to this work, $G(T_{phy})$ is approximately quadratic so g_T varies linearly with physical temperature as confirmed by our measurements described in Section 4.1.

In our system, we alter the IF gain by changing the bias current of the final stage of the low noise 3 stage HEMT amplifier immediately following the mixer. The HEMT gain, H, is a linear function of its bias current, I_B, as shown in Section 4.2. With the assumption that the HEMT gain depends only on its bias current, in other words, by ignoring its dependence on physical temperature (in practice, temperature induced HEMT amplifier gain fluctuations are much smaller than mixer gain variations, as shown in Figure 2), we have

$$\Delta H \equiv H(I_B) - H(I_0) \approx h_I \Delta I \tag{7}$$

where h_I is the slope of the HEMT gain versus bias current curve evaluated at current I_0 and ΔI is a small change in the HEMT bias current.

Thus, from Equations 5, 6 and 7, we see that the necessary change in HEMT bias current for a given change in the physical temperature of the mixer is given by

$$\Delta I = -\frac{g_T}{h_I}\frac{H}{G}\left(1 - \frac{P_H}{P_{IF}}\right)\Delta T \tag{8}$$

In order to change the HEMT third stage bias current, we generate a voltage with a digital to analog converter, V_{DAC}, and feed it through a series resistor, R. Therefore the required DAC voltage is

$$V_{DAC} = -R\left[\frac{g_T}{h_I}\frac{H}{G}\left(1 - \frac{P_H}{P_{IF}}\right)\right]\Delta T \tag{9}$$

$$= -f\Delta T \tag{10}$$

where f is the proportional gain of the open-loop servo system, an experimentally determined value, with units of V K^{-1}, that relates changes in the physical temperature of the mixer to the DAC voltage necessary to stabilize the receiver. By changing the third stage of HEMT gain, we introduce negligible receiver noise temperature changes.

Because f is not known ahead of time and it changes with operating conditions, we have a training period of 5-10 minutes during which we place a fixed temperature load in the receiver beam and select a value of f to minimize dP_{IF}/dT_{phy}. Then the calibration load is removed from the beam and the value of f is maintained during the astronomical observation. We routinely achieve a stability of a part in 6,000 during the training period, and the derived value of f is typically valid over many hours.

3. Experimental Setup

We have made stability measurements using a 230 GHz SIS heterodyne receiver designed for the SMA (Blundell *et al.* 1995). A schematic of the receiver and the open-loop gain stabilization system is shown in Figure 1. The horn, mixer, isolator and 3 stage low noise HEMT IF amplifier with ∼30 dB gain are maintained at a nominal temperature of 4.2 K, and an additional gain of 20 dB is provided by an amplifier maintained at 20 K (not shown in Figure 1). The receiver output, 2.5 GHz wide centered at 5 GHz, is measured with a Herotek DT-4080 tunnel diode that is temperature stabilized near room temperature to 1 part in 10^5 (rms to mean ratio). The rms stability of this continuum detector was measured at 1 part in 8,000 over 600 seconds with a 33 ms integration time. This value is ∼15% larger than the $1/\sqrt{B\tau}$ fundamental radiometer noise and sets a noise floor for our gain stabilization system. The detected signal is digitized by an Analog Devices AD7716 22-bit, 4 channel sigma-delta analog to digital converter (ADC) at 230 Hz and averaged down to a ∼30 Hz sampling rate (33 millisecond integration time) in software. The physical temperature of the mixer is measured with a Lakeshore DT-470 silicon diode and recorded simultaneously by the same ADC. Temperature fluctuations, ΔT, are computed by differencing each temperature measurement with the first temperature measurement of the time series. The microprocessor then instructs the digital to analog converter (DAC) to output a voltage proportional to ΔT, as described in Equation 10. The analog voltage from the DAC, V_{DAC}, is fed through the resistor, R, to generate an excess bias current for the third stage of the HEMT IF amplifier. This excess current is used to change the HEMT gain (see Section 4.2) to compensate for the physical temperature induced conversion gain fluctuations in the mixer.

During a servo system training period, the receiver observes a constant temperature source, for which we used a microwave absorber immersed in liquid nitrogen. The proportional loop gain factor, f, is selected to minimize the correlation between the physical temperature of the mixer and the detected IF power.

4. Measurements and Discussions

4.1. Mixer Conversion Gain

By adjusting the J-T valve on the cryocooler, we varied the physical temperature of the mixer from 4 K to 6 K. From this data, we then determined the conversion gain of the mixer and the gain of the IF chain as functions of the physical temperature, using the technique described in (1). We sampled this temperature range in steps of $\sim$0.2 K. Figure 2 shows that over the entire 2 K temperature range, the data are well fit by a quadratic and that the gain of the mixing element is more sensitive to physical temperature fluctuations than is the IF gain. At the SMA, the amplitude of cryocooler-induced temperature fluctuations is typically 50-200 mK. Over such a small fractional temperature range (1-5% of 4.2 K), the temperature dependence of the mixer conversion gain is well modeled by a straight line and the linear approximation to the Taylor series expansion of $G\left(T_{phy}\right)$ (Equation 6) is sufficient. From the quadratic fit to $G(T_{phy})$, we compute that g_T, the derivative of the gain curve, increases in magnitude with temperature from -0.322 K^{-1} at 4 K to -0.504 K^{-1} at 6 K.

4.2. HEMT Amplifier Gain

The majority of the SMA receivers incorporate three stage HEMT amplifiers fabricated by the National Radio Astronomy Observatory (NRAO) with a total gain of $\sim$30 dB. Using an 8510 HP network analyzer, the total HEMT gain at 4 GHz, 5 GHz and 6 GHz (IF band center and edges) was measured at room temperature while we varied the bias current of the third stage from 9.0 mA to 10.5 mA. As shown in Figure 3, the gain is well fit by a straight line over the entire range of bias currents for all measured frequencies, so h_I is nearly constant over the entire range of bias currents at a given frequency. When the gain stabilization scheme is active, the bias current changes by $\lesssim$ 0.1 mA and over this range, h_I is sufficiently constant. We note that h_I has a frequency dependence that may ultimately limit the usefulness of this gain stabilization technique.

4.3. IF Phase

At the same time that we measured the effect of bias current on the gain of the HEMT amplifier (see previous section), we also measured the effect of the bias current on the signal phase. Figure 3 shows that the phase changes linearly with the bias current and that the slope of the phase error versus bias current increases with frequency. The maximal phase gradient ($d\phi/dI_B$) is -1.3 degree mA^{-1}. During normal servo operation, the bias current is changed by $\lesssim$ 0.1 mA, and therefore the servo system will introduce $<<$ 1 degree of phase error in the IF signal. Using data from (Masson 1994), we find that under median weather conditions on Mauna Kea on a 100 meter baseline, one expects 0.12 degrees of atmosphere induced phase fluctuations per GHz of observing frequency (27 degrees at 230 GHz).

4.4. The Gain Stabilization System Performance

Figure 4(a) shows the response of a 230 GHz receiver observing an absorber immersed in liquid nitrogen. The cryocooler in use during these tests had a very stable 4 K stage temperature compared to a typical SMA cryocooler. To simulate temperature instabilities more typical of SMA cryocoolers, we manually adjusted the J-T valve of the cryocooler to induce periodic $\sim$50 mK peak to peak fluctuations in the physical temperature of the mixer. Figure 4(a) shows the time variation of V_{DAC}, which generates the bias current correction for the third stage of the HEMT amplifier, T_{phy}, the physical temperature of the mixer and P_{IF}, the detected IF power. P_{IF} is normalized to its mean during the time when the gain stabilization system is inactive.

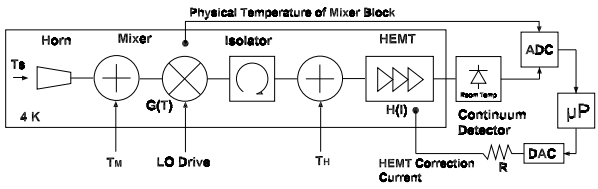

Fig. 1.— A schematic of the SIS receiver and gain stabilization servo system. The horn, mixer, isolator and HEMT amplifier are maintained at cryogenic temperatures by a cryocooler. The physical temperature of the mixer, T_{phy}, is monitored by a diode thermometer. The continuum detector measures the IF power. An ADC records the mixer temperature and the detected continuum power simultaneously. The microprocessor (μP) directs the DAC to generate a voltage, V_{DAC}, in direct proportion to measured mixer temperature fluctuations (see Equation 9). This voltage is converted to a correction bias current for the third stage of the HEMT IF amplifier by the resistor, R. The symbols, G, H, T_S, T_M and T_H are described in the text after Equation 3.

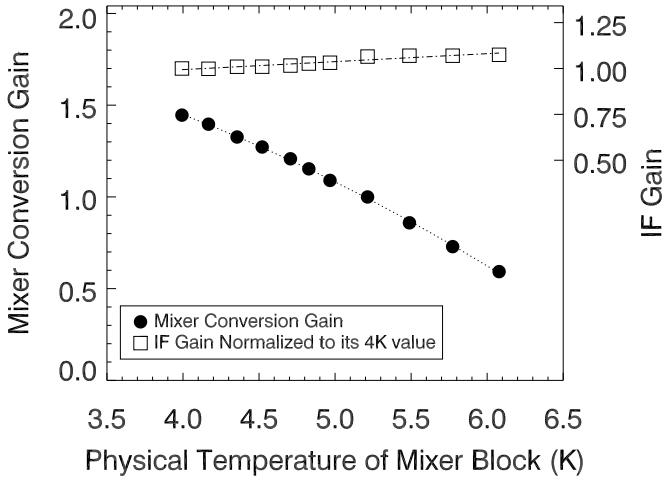

Fig. 2.— The conversion gain of the 230 GHz SIS mixer and the normalized IF gain as a function of the mixer physical temperature. The mixer data are well fit by the displayed quadratic $2.006 + 0.042 * T_{phy} - 0.045 * T_{phy}^2$ over entire temperature range. The slope of this curve, g_T, increases in magnitude from -0.322 K^{-1} at 4 K to -0.504 K^{-1} at 6 K. The IF gain is a weaker function of temperature, with less than an 8% change over the full temperature range. It is well fit by the linear function $0.820 + 0.0435 * T_{phy}$. Over a typical operating temperature swing of 50-100 mK, the IF gain would vary by 0.22-0.44%.

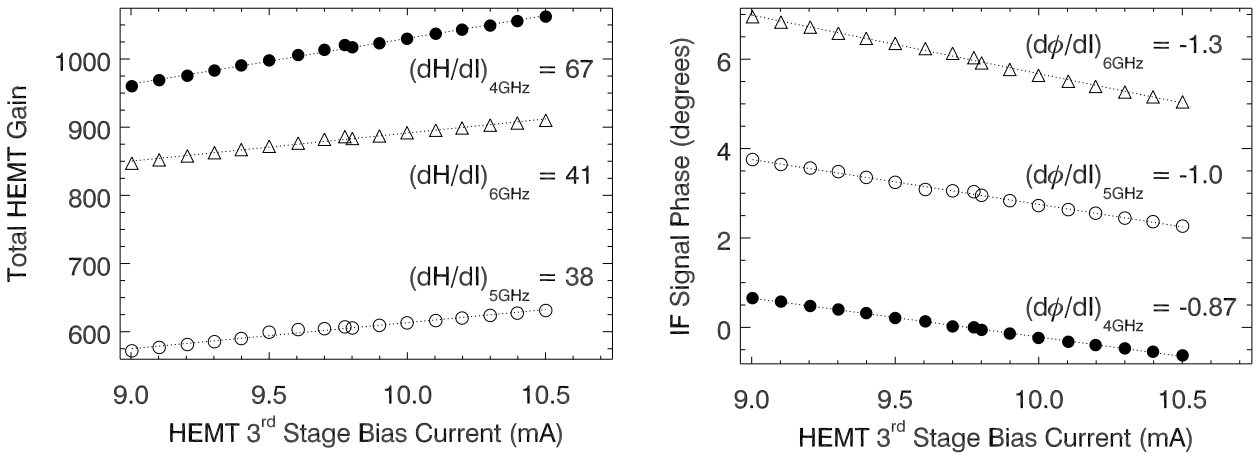

Fig. 3.— **Left** - The gain of the HEMT IF amplifier at room temperature as a function of its the third stage bias current at 4, 5 and 6 GHz, and corresponding linear fits. The slope of the gain curve, h_I, is frequency dependent. Nevertheless, we can achieve a receiver gain stability of 1 part in 6,000 using this technique. **Right** - The phase, ϕ, of the IF signal out of the HEMT amplifier as a function of its the third stage bias current at 4, 5 and 6 GHz, and corresponding linear fits. The phase data has been mean subtracted and offset for clarity.

During the first 311 seconds of the data set, V_{DAC} is held constant so that the servo system is inactive. The direct correlation (with negative proportional factor) between the physical temperature of the mixer and the receiver output is observed. When the physical temperature of the mixer increases, its conversion gain decreases and the receiver output decreases. As seen in the bottom plot of Figure 4(a), the resulting instrumental gain fluctuations limit the receiver stability to 1 part in 780 (rms to mean ratio).

From 318 seconds onward, when the gain stabilization system is activated, V_{DAC} is set in proportion to fluctuations in the physical temperature of the mixer. The resulting gain change in the third stage of the HEMT amplifier reduces the fluctuations in IF power caused by mixer conversion gain fluctuations, and the IF power stability improves by a factor of ~ 7.3 from 1 part in 780 to 1 part in 5,700.

Figure 4(b) demonstrates that the IF power depends linearly on the physical temperature of the mixer without the servo loop. A linear fit to the correlation between the IF power and physical temperature of the mixer is shown and it has a slope of -10^{-4} mK^{-1} with a negative sign indicating that an increase in the physical temperature of the mixer corresponds to a decrease in receiver output.

Figure 4(b) also demonstrates that the gain stabilization servo system decreases the slope of the correlation between the IF power and the physical temperature of the mixer. The data for 318 seconds onward are plotted along with the best-fit line with slope 5.8 x 10^{-6} mK^{-1}. The positive slope indicates that the servo system has slightly overcorrected for the mixer conversion gain fluctuations. Nevertheless, the receiver output power has been significantly decorrelated from the temperature of the mixer.

In Figure 5 we present the results of the same tests performed with a freely running cryocooler (i.e. with no J-T adjustment). The order of the plots are the same as in Figure 4. Fluctuations in the physical temperature of the mixer are largely due to the G-M cycle of the cryocooler on about a one second time scale, and a larger amplitude, ∼60 second semi-periodic fluctuation of unknown origin. In addition, there is a low frequency drift (∼5 minute period) in the physical temperature of the mixer. Here, the intrinsic temperature stability of the cryostat and thus the IF power is very good even before activating the servo system. Still, the gain stabilization servo loop improves the receiver stability from 1 part in 2,600 to 1 part in 6,000. Figure 5(b) shows that the proportional coefficient between IF power and mixer temperature has been reduced to 1.7 x 10^{-5} mK^{-1}.

The effective temperature fluctuations, $\Delta\tilde{T}$, that would generate the observed residual IF power fluctuations in the absence of any receiver stabilization can be written $\Delta\tilde{T} = |\,(dP/dT)^{-1}\,\Delta P|$ where dP/dT is the slope of the IF power versus mixer temperature plot and ΔP is the residual fluctuation in continuum power when the servo is active.

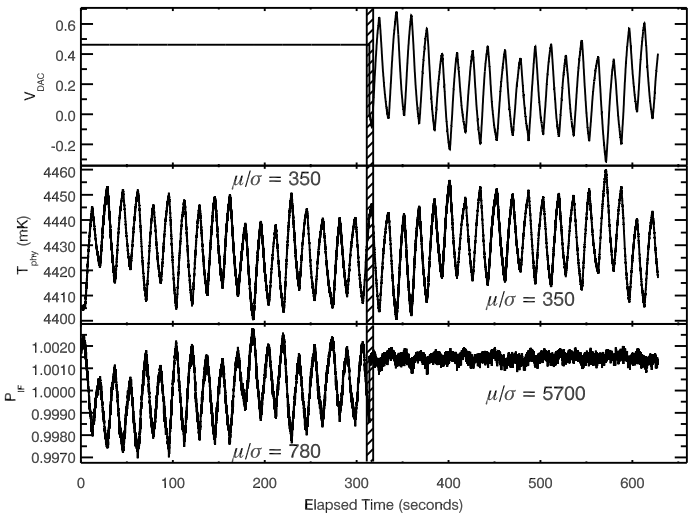

(a) Time Series Data

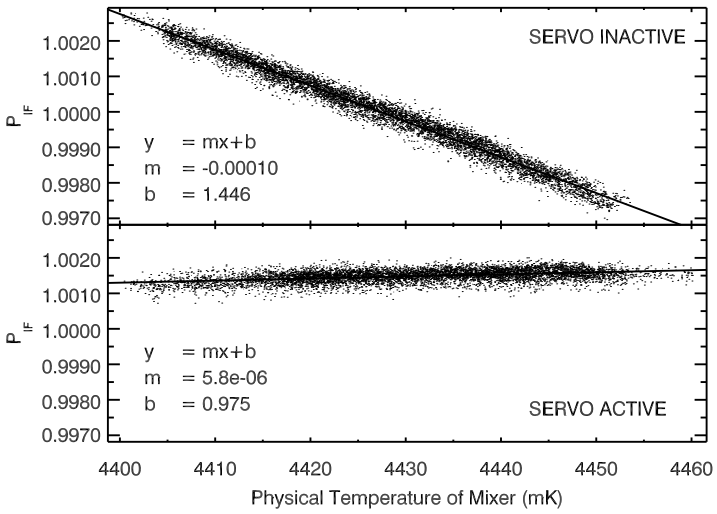

(b) Correlation Between Continuum Power and Mixer Temperature

Fig. 4.— **At left:** The middle and bottom plots are the physical temperature of the mixer and the detected continuum power. In the top plot, V_{DAC} is proportional to the correction current applied to the third stage of the HEMT amplifier. Here the J-T valve is continuously manually adjusted. The gain stabilization servo system improves the receiver stability by a factor of ∼7.3 from 1 part in 780 to 1 part in 5,700 (rms to mean ratio).
At right: The correlation plots show that the activation of the gain stabilization servo system reduces the slope of the correlation between the IF power and the temperature of the mixer.

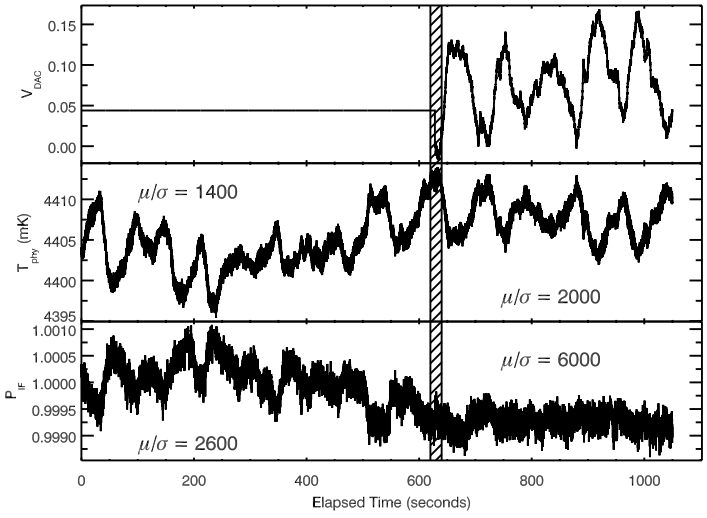

(a) Time Series Data

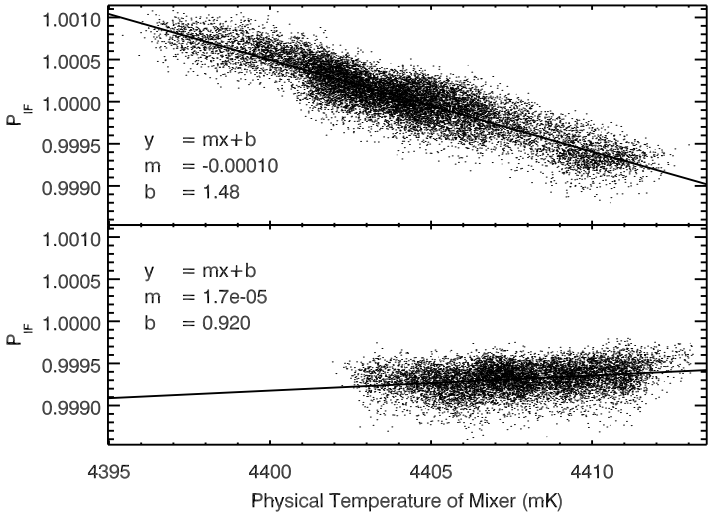

(b) Correlation Between Continuum Power and Mixer Temperature

Fig. 5.— Same as Figure 4, but this time with a freely running cryocooler (i.e. the J-T Valve was not adjusted). The temperature stability of the 4 K stage of this cryocooler is significantly better than a typical SMA cryocooler, with 4 K temperature fluctuations of only 3-5 mK rms. Even with such a stable operating temperature, we improve the receiver stability by a factor of ∼2.4 with our gain stabilization servo system.

From the top part of Figure 4(b) we find that $dP/dT = -10^{-4}$ mK^{-1}. The bottom part of Figure 4(b) shows that ΔP = 0.0013 peak to peak or ΔP = 1.7 x 10^{-4} rms (in normalized units). Therefore the gain stabilization servo system achieves an effective peak to peak temperature stability of $\Delta\tilde{T} = 13$ mK or an effective rms temperature stability of $\sigma_{\tilde{T}} = 1.7$ mK.

5. Conclusion

We have developed a system that stabilizes the gain of a 230 GHz SIS heterodyne receiver to 1 part in 6,000 (rms to mean). With the use of an open-loop proportional servo system, we monitor the physical temperature of the mixer block and adjust the gain of the third and final stage of a low noise HEMT IF amplifier in order to compensate for the subsequent variations in the conversion gain of the mixer. We have shown that the conversion gain of the mixer varies linearly over the range of typical cryocooler-induced physical temperature fluctuations, and that the gain of the HEMT amplifier varies linearly with its third stage bias current. Using our gain stabilization system, we routinely achieve a total receiver gain stability of 1 part in 6,000 (rms to mean ratio) for a 0.033 second integration time over 10 minutes, which corresponds to an effective rms temperature fluctuation of 1.7 mK. In comparison, the typical fluctuations in the physical temperature of the mixer at the SMA are on the order of 50-100 mK, and the corresponding power fluctuations are 1 part in several hundred. Therefore, our gain stabilization servo system can provide more than an order of magnitude improvement over a typical unstabilized system. Our technique introduces a negligible level of instrumental phase error into the source signal. This gain stability system can be implemented on any heterodyne receiver system in which the physical temperature of the mixer can be monitored and the IF amplification can be adjusted in real time.

REFERENCES

Baryshev, A., Hesper, R., Gerlofsma, G., Kroug, M., and Wild, W. 2003. Influence of Temperature Variations on the Stability of a Submm Wave Receiver. unpublished.

Blundell, R. *et al.* 1995, IEEE Trans. Microwave Theory Tech., **43**, 933–7.

Kooi, J. W., Chattopadhyay, G., Thielman, M., and Phillips, T. G. 2000, Int. J. IR and MM Waves, **21**, 689–718.

Masson, C. R. 1994. Atmospheric Effects and Calibrations. In Ishiguro, M. and Wm. J. Welch, editors, *Astronomy with Millimeter and Submillimeter Wave Interferometry*, volume 59, pages 87–95.

Moran, J. M. 1998. The Submillimeter Array. In Phillips, T. G., editor, *Advanced Technology MMW, Radio and Terahertz Telescopes. Proc SPIE*, volume 3357, pages 208–19.

Orlowska, A. 2004. private communication - courtesy of the European Southern Observatory and CCLRC Rutherford Appleton Laboratory.

Plambeck, R. L. 1998. Long-Term Performance of 4 K Gifford-McMahon Refrigerators on the BIMA Array. In Kittel, P., editor, *Advances in Cryogenic Engineering*, volume 43, pages 1815–21, New York. Plenum.

Sekimoto, Y. *et al.* 2001, PASJ., **53**, 951–8.

Tiuri, M. E. and Räisänen, A. V. 1986. Radio-Telescope Receivers. In *Radio Astronomy*, chapter 7. Cygnus-Quasar Books, Powell, OH. by John D. Kraus.

Woody, D. P., Miller, R. E., and Wengler, M. J. 1985, IEEE Trans. Microwave Theory Tech., **33**, 90–5.

Wootten, A. 2003. Atacama Large Millimeter Array (ALMA). In Oschmann, J. M. and Stepp, L. M., editors, *Large Ground-based Telescopes*, volume 4837, pages 110–8.

This preprint was prepared with the AAS LaTeX macros v5.2.

SPIFI
The South Pole Imaging Fabry-Perot Interferometer on AST/RO

Nikola, T. [1], Stacey, G.J. [1], Oberst, T.E. [1], Parshley, S.C. [1],Stark, A.A. [2], Tothill, N. [2], Harnett, J. [2]

Introduction

The **S**outh **P**ole **I**maging **F**abry-Perot **I**nterferometer, SPIFI, is a direct detection imaging spectrometer for submillimeter astronomy in the telluric windows at 200 μm, 350 μm, and 450 μm that are available at the South Pole (B1, B2). The main components of SPIFI are the cryogenic Fabry-Perot interferometers (FPI's) which can be tuned to any wavelength within the atmospheric windows and the detector array which provides a two dimensional field of view.

Two of the three FPIs in SPIFI are equipped with cryogenic stepper motors to provide scanning capability and piezoelectrical elements to ensure the parallelism of the FPI plates. Using stepper motors to change the FPI plate separation enables spectral scans with very large bandwidth only limited by the mechanical design of the FPI. The spectral resolution can be set between R~500 – 10,000. The fixed FPI is used as a band pass filter to select the desired telluric observing window. An additional scatter filter and an edge filter are used to ensure spectral purity.

The detector array consists of 25 monolithic silicon bolometers, arranged in a 5×5 grid providing the imaging capability. Winston cones direct the radiation to the pixels, which are placed in integrating cavities to increase the quantum efficiency. In order to reach high sensitivity, the detector is cooled to 60 mK using an adiabatic demagnetization refrigerator. To ensure a long hold time an additional ^{3}He closed cycle refrigerator is used as a thermal guard between a pumped ^{4}He system and the 60 mK stage. Each pixel has its own signal and ground wire, but all pixels share a common bias wire. The high impedance signal from the bolometers is converted to low impedance using JFETs which are mounted inside the detector dewar and thermaly shorted to 77 K. The signal then passes a preamplifier before it gets registered by a data acquisition board and processed in a PC.

SPIFI has been successfully used on the James Clerk Maxwell Telescope (JCMT) several times over the past few years. Now we have deployed SPIFI to the Antarctic Submillimeter Telescope and Remote Observatory (AST/RO) at the South Pole, where SPIFI will operate during the 2004 Austral winter. For this observing run SPIFI is optimized for the 200 μm telluric window, which is accessible during the Austral winter. We plan to observe the Galactic Center (GC), the Small Magellanic Cloud (SMC), the Large Magellanic Clouds (LMC), and the galaxies NGC 4945, CenA, and M83 in the 205 μm [N II] fine structure line and in the CO (J=13→12) rotational transition at 200 μm during the observing run. These observations are part of a larger program investigating the physical properties of the ionized and molecular gas in the GC and extragalactic objects.

Submillimeter Spectroscopy with SPIFI

Atmospheric Transmission

Observations in the submillimeter wavelength regime are strongly affected by water vapor in the earth's atmosphere, which lowers the atmospheric transmission very significantly. Figure 1 shows a model plot of the atmospheric transmission with a precipitable water vapor of 0.2 mm. This model was calculated using the "CSO Atmospheric Transmission Interactive Plotter" (www.submm.caltech.edu/cso/weather/atplot.html). Only at these conditions is it possible to observe in the 200 μm telluric window from the ground. While it is possible to observe at 370 μm from Mauna Kea, Hawaii, the 200 μm telluric window is only accessible during the winter at the South Pole and at some sites at Atacama, Chile. SPIFI is currently mounted on AST/RO at the South Pole.

[1] Department of Astronomy, Cornell University, Ithaca, NY 14853
[2] Harvard-Smithsonian Center for Astrophysics, Cambridge, MA 02138

SPIFI Science

SPIFIs main objective is to measure the physical conditions, dynamics, and gas cooling of the interstellar medium (ISM) near star forming regions. The physical properties of the spectral probes that can be observed with SPIFI are summarized in Table 1. These tracers are important diagnostics to determine the physical conditions in the ISM, especially of photodissociation regions (PDR), molecular coulds, and warm ionized medium (WIM). They have two major advantages over other ISM tracers. First, they are completely unaffected by interstellar extinction, allowing to study the dusty environment associated with star formation regions and galactic nuclei. Second, the line emitting levels are easily excited by low energy collisions at modest densities. Therefore they are very important coolants for the most important phases of the ISM.

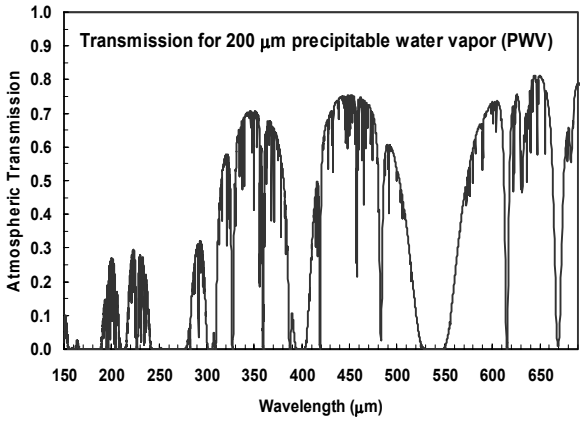

Fig 1. Atmospheric Transmission Model

Table 1. SPIFI Spectral Probes

Species	Transition	E.P.[1]	λ (μm)	A (s^{-1})	n_{crit} (cm^{-3}) [2]
N^+	**$^3P_1 \rightarrow {}^3P_0$**	**70**	**205.178**	**2.1×10^{-4}**	**4.8×10^1**
C^0	$^3P_2 \rightarrow {}^3P_1$	63	370.415	2.7×10^{-7}	1.2×10^3
	$^3P_1 \rightarrow {}^3P_0$	24	609.135	7.9×10^{-8}	4.7×10^2
^{12}CO	**J =13→12**	**503**	**200.273**	**2.4×10^{-4}**	**5.6×10^6**
	J = 7 → 6	155	371.651	3.6×10^{-5}	3.9×10^5
	J = 6 → 5	116	433.338	2.2×10^{-5}	2.6×10^5
^{13}CO	J = 6 → 5	111	453.497	2.0×10^{-5}	2.3×10^5

[1]Excitation potential, energy (K) of upper level above ground.
[2]Molecules: Collision partner H_2 (100 K). Atoms: [CI] (H atoms), [NII] (electrons).

Key Science of SPIFI on AST/RO

Ultimately, we plan to map the Galactic Central Molecular Zone (CMZ) and nearby galaxies in the [NII], CO, and [CI] lines listed in Table 1. The [NII] line intensity is directly proportional to the ionizing flux from stars for low density HII regions, so that it traces star formation in most galaxies. It is also an important coolant for low density HII regions. The mid-J CO rotational lines constrain the molecular gas pressure near regions of recent star formation and dominate the cooling of such gas. Molecular clouds must cool to form the next generation of stars, so that by observing these CO lines, we address the life cycle of the molecular ISM. The [CI] lines also are important coolants of neutral gas clouds, and can be used to determine molecular cloud temperatures. Finally, the CO (J=13→12) line traces the very highly excited molecular gas associated with molecular shocks from the birth of high mass stars, or the highly excited molecular ISM associated with galactic tori, such as the circumnuclear ring rotating at about 1.5 pc from the central black hole in the Milky Way galaxy.

Galactic Center. Ultimately, we plan to image the inner 1.5° × 5.0° regions of the Galaxy (84,000 spectra/map) in the [CI] 370 μm, CO(7→6) 372 μm, and [NII] 205 μm lines, and smaller regions in the high J CO lines**,** thereby characterizing star formation and its effects on the ISM in the CMZ, and tracing the gas dynamics. Is neutral gas flowing through the CMZ to the inner few pc of the Galaxy? Are there shocks from cloud-cloud collisions in this flow? What is the connection between the CMZ molecular clouds and the circumnuclear ring? Figure 2 shows the

extend of the CMZ and the region we plan to map with SPIFI. For the [NII] line, the observing time will be about 30 minutes per footprint, and the total time to complete the map should be about 6 days.

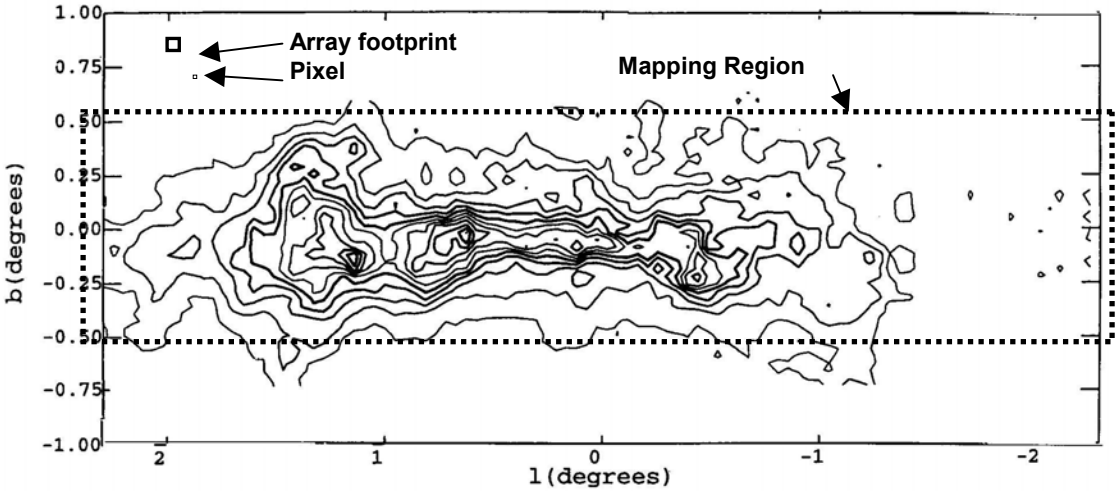

Fig 2. CO (J=1→0) contour map of the inner region of the Milky Way (U1)

Dwarf Galaxies. During the Austral winter 2004 we will map the two closest by dwarf galaxies, the large Magellanic cloud (LMC) and the small Magellanic cloud (SMC) in the CO(13→12) 200 μm, and [NII] 205 μm lines. These dwarf galaxies are low metalicity galaxies and thus may mimic the environment of protogalaxies, which were formed in the early Universe. Therefore investigating star formation in these dwarf galaxies is key to understanding star formation in the early Universe. These observations can reveal the reservoir of neutral gas in dwarf galaxies that is "hidden" to CO (J=1→0) observers because of the effects of the low metallicity. This gas reservoir is the source out of which stars are born. Another important question targeted by the SPIFI observations is, what is the density of the ionized gas? And how much of the bright [CII] emission observed in these galaxies arises from low density HII regions?

Nearby Galaxies. SPIFI will map a selection of nearby galaxies in the [NII] line at 205 μm. Combining the results of these observations with results obtained by the ISO mission and other millimeter/submillimeter molecular tracers will fully characterize the physical conditions in the ISM. The main objective of the SPIFI observations is to determine the relationship between spiral density waves, bar potentials, interactions, and star formation in nearby galaxies. SPIFIs prime targets are M83, CenA, and NGC4945.

Instrument Design

SPIFI Optical Path. The optical path of SPIFI is shown in figure 3. Before the f/8.4 beam from the AST/RO telescope enters SPIFI it passes through the calibration unit which is mounted in front of SPIFI. This calibration unit consists of a blackbody, a gas cell, and a chopper blade and is used for the wavelength calibration of the Fabry-Perot interferometers (FPIs) in SPIFI. For this purpose the blackbody and the gas cell which are mounted on a linear translation stage can be moved into the beam. The beam reaches its focus just outside SPIFI and then enters the main dewar via a polyethylene window. The off-axis parabola mirror M1 creates a collimated beam with a diameter of 9 cm. Then the beam travels via flat mirror M2 through the high order Fabry-Perot Interferometer (HOFPI), is reflected by the flat mirror M3 and then passes the scatter filter which is placed at the Lyot stop. After that the beam is decollimated by the off-axis parabola mirror M4, which sends it through the low order FPI (LOFPI) via flat mirror M5. Then the f/12.6 beam enters the detector dewar. Inside the detector dewar the beam passes through a series of filters before it is imaged on the Winston cones which couple the beam to the bolometer array. The Winston cones accept a beam corresponding to $1.4 \cdot \lambda/D$, where λ is the wavelength and D is the diameter of the telescope. This results in beam sizes of 34" at 205 μm and 62" at 370 μm at AST/RO and 7" at 370 μm at JCMT.

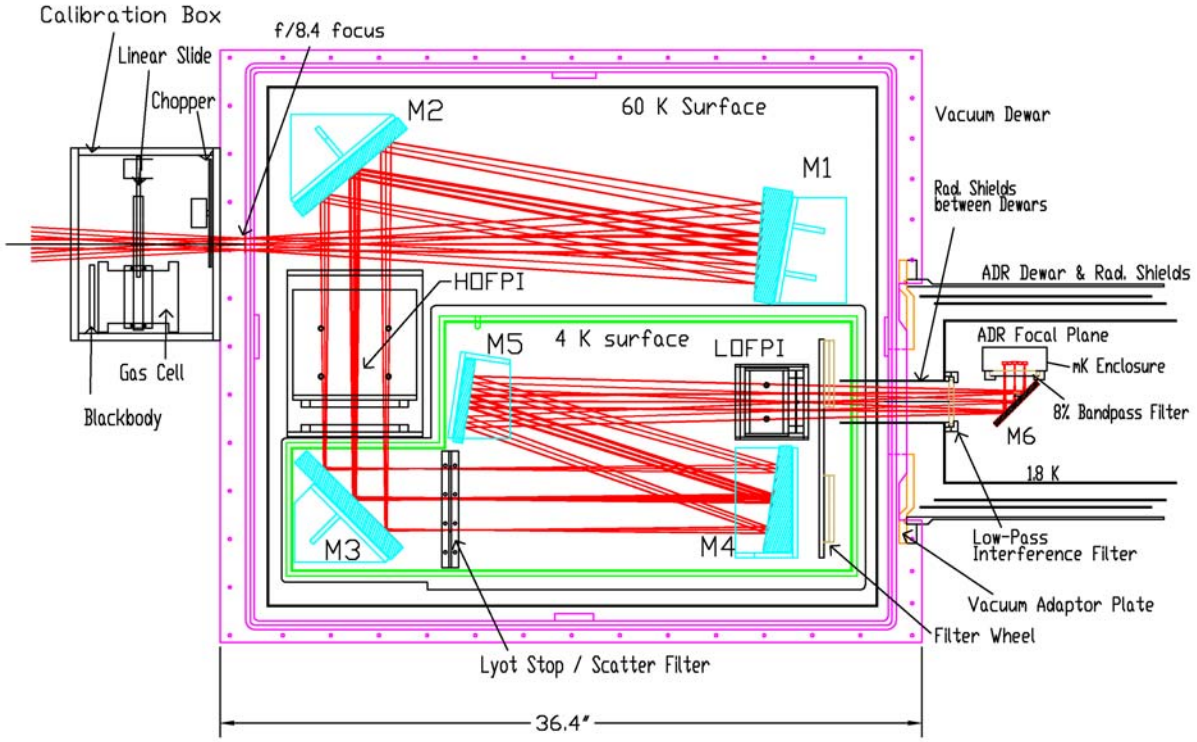

Fig 3. Optical Layout of SPIFI

Fabry-Perot Interferometer (FPI). SPIFI employs two scanning FPIs. Each consists of two highly reflective parallel plates. In the submillimeter regime these plates are made of free-standing metal meshes. A FPI transmits wavelengths according to the simplified relationship $n \cdot \lambda = 2 \cdot d$, where n is the order of the FPI, λ is the wavelength, and d is the physical plate separation. The transmission wavelength and the spectral resolution are selected by adjusting the plate separation of the FPI. An example is shown in figure 4. The resolution is determined by the HOFPI. Since the HOFPI also transmits several unwanted additional wavelengths a second FPI (LOFPI) operating in a lower order is used to sort out the desired transmission peak. A band pass filter is used to eliminate the unwanted transmission peaks of the LOFPI. The size of the HOFPI is determined by the size of the collimated beam that is required to ensure spectral similarity between the spectra in the off-axis pixel and the spectrum in the on-axis pixel.

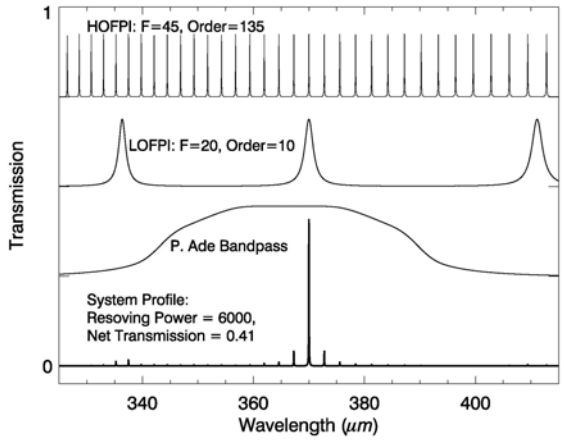

Fig 4. Transmission of HOFPI, LOFPI, band pass filter and combined transmission.

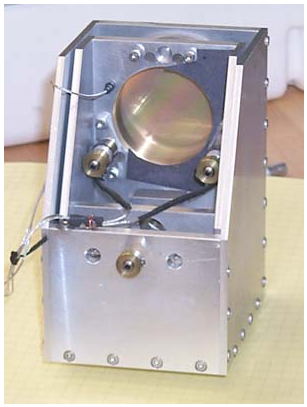

Fig 5. LOFPI

Both FPIs have a similar design. One of the plates is fixed to the main structure while the other plate is mounted on a flex-stage resembling a parallelogram. This design allows changing the plate separation (scanning) without loosing

the parallelism of the plates. The parallelism of the meshes is adjusted with three piezoelectrical elements (PZTs). A picture of the LOFPI revealing the free-standing metal meshes and micro-screws pushing on the PZTs is shown in figure 5. The scanning of the FPIs is accomplished with cryogenic stepper motors which then turn a micro-screw, allowing for arbitrarily long scans limited only by the length of the micro-screw and the mechanical design of the FPIs. The design of the SPIFI FPIs allows selecting spectral resolutions between $R=\lambda/\Delta\lambda$ ~500 to 10,000, which corresponds to a velocity resolution of Δv ~ 600 to 30 km/s.

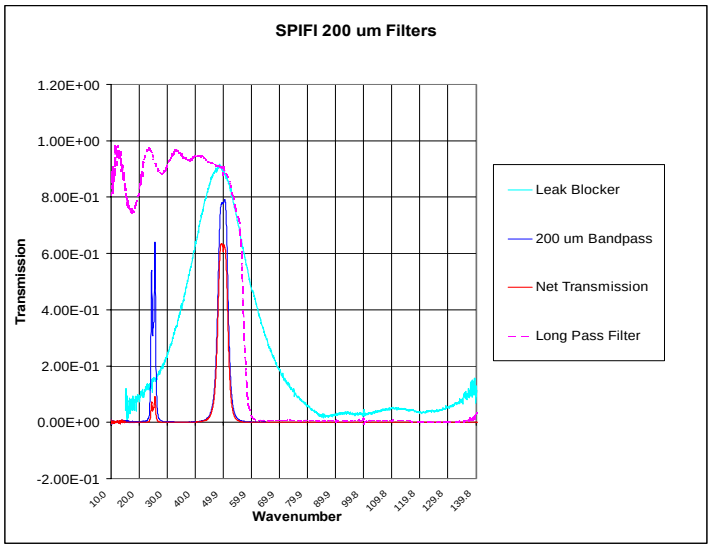

Fig 6. Transmission curves of SPIFIs fixed filters.

Fixed Filters. To ensure spectral purity and to minimize background radiation (and thus heating by radiation) several fixed filters are mounted in SPIFI. The scatter filter at the Lyot stop is a 100 μm long pass filter, which scatters radiation with wavelengths shorter than 100 μm into a 4π volume. The scatter filter and all optics afterwards are at a temperature of 4.2 K or lower. An additional 150 μm long pass interference filter is placed just inside the detector cryostat. The main part of the detector cryostat is cooled to about 2 K, further reducing the thermal background radiation. Finally a narrow (10%) and a broad (50%) 200 μm band pass interference filter is mounted at the entrance of the 60 mK enclosure delivering the final limiting band pass for background radiation. The reason for the broad band pass filter is to eliminate a leakage of the narrow band pass filter at about 25 cm^{-1}. Good filtration and baffling is essential for reaching background limiting performance in direct detection instruments. All fixed filter were provided by P.A.R. Ade at Cardiff Univeristy. The transmission curves of the fixed filters are shown in figure 6.

Detector Array. The detector array is a 5×5 array of monolithic silicon bolometers provided by S.H. Moseley at NASA Goddard Space Flight Center. Each bolometer consists of a frame, four support legs, and the detector pixel itself, which is a 1mm diameter × 12 μm thick disk. The support legs provide the thermal conductance from the pixel to the detector block. Two of the legs are boron doped also providing the electrical connection to the thermistor, which is a small phosphorus-doped, 50% boron compensated region implanted on the circular detector. To increase the submillimeter absorption, a 120 Å thick layer of bismuth is applied to the detector surface. Each detector is mounted in an Invar structure that forms the closed end of a 2 mm diameter integrating cavity. This Invar cap is mounted to the base of a copper Winston cone. Figure 7 shows a picture of the front of the detector block exhibiting the Winston cones and the connectors for the signal, ground, and bias wires. The detector is cooled to 60 mK using an adiabatic demagnetization refrigerator (ADR). A closed cycle ^{3}He system is used in addition as a thermal guard to ensure a long enough hold time of the ADR.

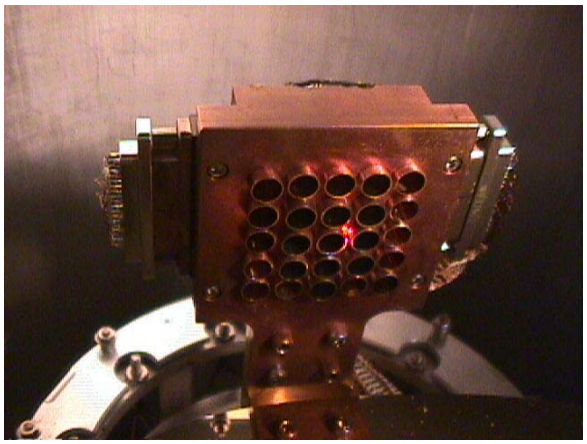

Fig 7. Detector block with Winston cones.

Figure 8 shows a sketch of the electrical diagram for each pixel as well as the control electronics of the stepper motors and the telescope interface. The impedances of the bolometers reach between 0.1 and 5 MΩ when cooled to 60 mK and exposed to background radiation. Each of the bolometers is biased in series with a 29 MΩ load resistor. This large impedance of the load resistor together with a fixed bias voltage ensures that the bolometers are current

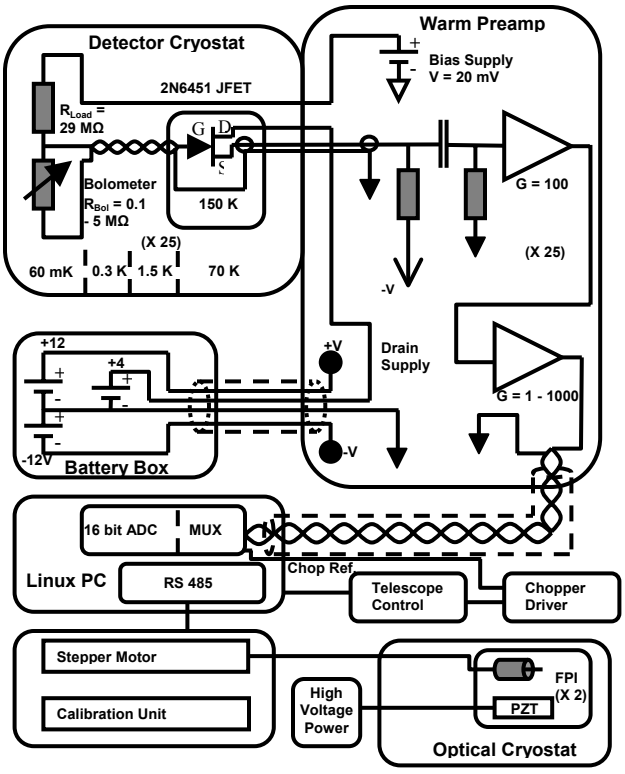

Fig 8. Electrical Block Diagram of the readout electronics and the control electronics.

biased. The voltage signal from the bolometers is then buffered with cooled (150 K) junction field-effect transistors (JFETs), which convert the high impedance signal to a low impedance signal. The JFETs are connected to the detector via twisted pairs of thin constantan wires. They are mounted to the l-N_2 tank in the detector cryostat (77 K) and heat themselves to a temperature of about 150 K. The low impedance signal then enters the warm preamplifier, which is firmly attached to a connector at the outside of detector cryostat. This preamplifier consists of a low noise G = 100 amplifier and a programmable gain amplifier (G = 1 – 1000) for each pixel. After the preamplifier the resulting amplified low impedance signal is fed via shielded twisted pair cables to two 16 channel, 16 bit data acquisition boards inside a Linux operated PC. To ensure low noise operation of the detector and preamplifier the voltage power is provided by batteries.

SPIFI Operation. The electronic block diagram in figure 8 also shows the interface with the telescope and with the stepper motor and calibration unit control electronics. During an observation the secondary of the telescope is chopping with a selected frequency (1 to 2 Hz at AST/RO, about 8.5 Hz at JCMT) between two defined celestial positions. The sync-signal of the telescope chopper is fed to the data acquisition board in the Linux PC and provides the reference signal for the lockin-detection of the bolometer signal. This final signal is integrated for a few seconds and then stored as a data point on the harddisk. During this integration time the FPIs stay at a fixed position. Then the plate separation of the FPIs is changed with stepper motors by a distance corresponding to a fraction of a resolution element and then a new data point is taken. After a predefined number of data points each pixel acquired a full spectral scan at a different spatial position of the sky. This observation method thus provides a data cube with 2 spatial dimensions and a spectral dimension at the same time.

Before the observation the spectral setup of the FPIs is checked using the calibration unit that is mounted in front of SPIFI. The resulting spectrum of a blackbody whose radiation passes through a gas cell with a known gas shows an absorption line at a known wavelength and thus provides an absolute wavelength calibration of the FPIs. In addition, since the step sizes of the stepper motors are known the full wavelength coverage of a spectrum is known absolutely.

Sensitivity. The preferred detection method (heterodyne versus direct detection) depends on the scientific goals. The key science projects SPIFI was built for require moderately high spectral resolution (up to R ~ 10,000), a broad wavelength coverage (to observe the [CI] 370 μm and CO (7→6) 371 μm line in a single scan), and imaging capabilities (to observe extended emission regions simultaneously), highest possible sensitivity in the wavelength regime between 200 μm and 500 μm. To meet all these objectives a direct detection FPI imaging spectrometer is an excellent choice. For a background limited spectrometer with warm optical elements of temperature T the noise equivalent flux (in units W m^{-2} $Hz^{-1/2}$) above the atmosphere is given by

$$NEF = \frac{h \cdot \nu}{A \cdot \eta \cdot t_c \cdot t_w} \sqrt{\frac{2A\Omega}{\lambda^2} \cdot \Delta\nu \cdot \varepsilon \cdot \eta \cdot t_c \cdot \tilde{n} \cdot \left(1 + \varepsilon \cdot \eta \cdot t_c \cdot \tilde{n}\right) \cdot 2 \cdot 2 \cdot 2}$$

where h is the Planck constant, ν is the frequency, $A\Omega/\lambda^2 = 1.4$ is the number of photon modes, A is the area of the telescope (diameter of the AST/RO telescope is 1.7 m), $\tilde{n} = 1/(\exp(h\nu/kT)-1)$ is the mode occupation number, η is the quantum efficiency (80%), t_c is transmission of the cold optical elements (25%), t_w is the transmission of the warm optical elements, ε is the emissivity of the warm optical elements, and $\Delta\nu=\pi/2\cdot\nu/R$ ($R\equiv\lambda/\Delta\lambda$) is the resolution bandwidth. The various factors of 2 are from detecting both polarizations of light, expressing NEF in $Hz^{-1/2}$, and

chopping (2·2). Since the NEF is given above the atmosphere the transmission of the warm optics consists of $t_w = \eta_{sky} \cdot \eta_{MB} \cdot \eta_{tel} \cdot \eta_{window}$, where η_{sky} is the telluric transmission, η_{MB} is the main beam efficiency, η_{tel} is the telescope efficiency, and η_{window} is the transmission through the polyethylene entrance window into SPIFI (96%). Table 2 summarizes the relevant parameters for the 370 μm and 205 μm windows on AST/RO.

To compare the sensitivity of SPIFI with a heterodyne instrument we follow the calculations presented in the Users Guide of the JCMT (www.jach.hawaii.edu/JACpublic/JCMT/User_documentation/Users_guide/guide/node29.html). This is a subtle comparison because the NEF includes the shot noise contribution of the background T_{back}, while T_{rec} does not. So at the telescope, the relevant noise for heterodyne receivers is $T_{rec} + T_{bac}$, while for a background limited direct detection system $T_{rec} \rightarrow 0$, so that the relevant noise is T_{bac}. Also, SPIFI "sees" only one sideband of thermal noise, whereas a double sideband receiver sees two sidebands of noise. A straightforward way is to convert SPIFIs NEF to a system noise temperature at the telescope by comparing the detected power to a main beam rms noise, T_{MB}(rms), then converting T_{MB}(rms) back to T_{sys}. According to the JCMT web page

$$NEF = \frac{2 \cdot k \cdot T_{MB}(rms)}{\lambda^2} \Delta\nu \cdot \Omega \quad \text{and} \quad T_{MB}(rms) = \frac{2 \cdot T_{sys} \cdot \kappa}{\eta_{MB} \cdot \sqrt{\Delta\nu \cdot t}},$$

where κ is the backend degradation factor (=1.15 for a 2-bit digital correlator) and the total integration time, *t*, is 1 second (but only about ½ of this time is spend on source). This results in a system noise temperature of T_{sys}=222 K for one resolution element for SPIFI on AST/RO if SPIFI is background limited. Note that the system noise temperature is independent of the resolution.

The best reported heterodyne receiver temperature to date is T_{rec}(DSB) = 275 K at 810 GHz (K1). The T_{rec}(DSB) is related to the system noise temperature by

$$T_{sys} = 2 \cdot \frac{T_{rec} + \eta_{tel} \cdot \left(1 - \eta_{sky}\right) \cdot T_{sky} + \left(1 - \eta_{tel}\right) \cdot T_{tel}}{\eta_{tel} \cdot \eta_{sky}}$$

where T_{sky} and T_{tel} are the sky and telescope temperatures, respectively. For the AST/RO we assume that T_{sky} and T_{tel} are the same as the background temperature T_{bac} given in Table 2. This then results in a system temperature of T_{sys}(heterodyne) = 1570 K, which is a factor of 7 worse than SPIFI at 370 μm. At 200 mm we anticipate T_{sys} = 1065 K.

Table 1. SPIFI-AST/RO Sensitivity

Parameter	**370 μm**	**205 μm**
Sky Trans., η_{sky}	0.65	0.30
MB Efficiency, η_{MB}	1.0	1.0
Telescope Eff., η_{tel}	0.71	0.50
Warm emissivity, ε	0.50	0.78
Background T_{bac}	210	210
T_{sys} (K)	222	1064
R=2000 NEF(W m^{-2} Hz$^{-1/2}$)	2.73×10^{-16}	1.76×10^{-15}
T_{MB}(rms), 1σ, 1 hour	0.35 mK	1.55 mK
R=10,000 NEF(W m^{-2}Hz$^{-1/2}$)	1.22×10^{-16}	7.87×10^{-16}
T_{MB}(rms), 1σ, 1 hour	0.79 mK	3.47 mK

Fig 9. Left: AST/RO, Right: SPIFI mounted on AST/RO

SPIFI on AST/RO

We have deployed SPIFI on AST/RO at the South Pole during the Austral summer season 2003/2004. Figure 9 shows the AST/RO telescope mounted on top of the AST/RO building and also SPIFI mounted on AST/RO. SPIFI is inside a heated enclosure (shown partially assembled in figure 9) to protect the instrument, the control PC and the control electronics form the cold and harsh environment. The best weather conditions at the South Pole for observations in the 200 μm window are expected between July and September. Thus SPIFI will be cooled down in July of 2004 and will operate carry out observations of the CO (13→12) transition at 200 μm and of the [NII] line at 205 μm.

Acknowlegdment: We are indebted to S.H. Moseley and C.H. Allen at NASA Goddard Space Flight Center for providing SPIFIs bolometers and to P.A.R. Ade at Cardiff University for providing the fixed filters. This research was made possible with NASA grants NAGW-4503 and NAGW-3925 and National Science Foundation grants OPP-8920223 and OPP-0085812.

References:

(B1)Bradford, C.M. 2001, PhD Thesis, Cornell University
(B2) Bradford, C.M., Stacey, G.J., Swain, M.R., Nikola, T., Bolatto, A.D., Jackson, J.M., Savage, M.L., Davidson, J.A., & Ade, P.A.R. 2002, Applied Optics 41, 2561
(K1) Kawamura, J., Chen, J., Miller, D., Kooi, J.W., Zmuidzinas, J., Bumble, B., LeDuc, H.G., & Stern, J.A. 1999, Applied Physics Letters
(U1) Uchida, K.I., Morris, M., & Bally, J. in prep

Upgrade to the *TREND* Laser LO at the South Pole Station

Sigfrid Yngvesson[a], Eyal Gerecht[a], John Nicholson[a], Fernando Rodriguez-Morales[a], Xin Zhao[a], Richard Zannoni[a], Jason Dickinson[b], Thomas Goyette[b], William Gorveatt[b], Jerry Waldman[b], Dathon Gholish[c], Jacob Kooi[d], Christopher Martin[e], and Eric Mueller[f]

[a]University of Massachusetts at Amherst
[b]Submillimeter Wave Technology Laboratory, University of Massachusetts at Lowell
[c]Department of Astronomy and Steward Observatory, University of Arizona
[d]California Institute of Technology
[e]Smithsonian Astrophysical Observatory
[f]Coherent-Deos, Inc.

ABSTRACT

The *TREND* (*Terahertz REceiver with NbN HEB Device*) system was deployed during the austral summer 2002-2003 on the 1.7 meter AST/RO submillimeter telescope. *TREND* is a 1.25 THz to 1.5 THz low noise heterodyne receiver user instrument based on HEB technology [1]. The AST/RO telescope is located at the Amundsen/Scott South Pole Station, which is the best of the presently available sites for ground-based terahertz observations due to the very cold and dry atmosphere over this site. The *TREND* system was operating stably on the CO J = 11→10 line at 1.27 THz after the installation was completed in February, 2003. The DSB receiver noise temperature was typically measured on the telescope to be 1,000K. The local oscillator is a CO_2 laser pumped, CD_3OH gas laser, which allowed many hours of continuous operation without adjustments. During the winter season of 2003 a tentative detection was obtained of the J= 11 → 10 line of CO in NGC6334a, but the laser LO became less stable. The laser did not stabilize sufficiently well at the higher frequency of 1.46 THz, required for the NII line.

During the austral summer of 2003-2004, the entire local oscillator (LO) optical system was redesigned and re-aligned. With the addition of an acousto-optic modulator (AOM) to the CO_2 pump laser system beam path, the CO_2 laser output was frequency shifted by 40 MHz, allowing optimal absorption in the CD_3OH far-infrared (FIR) laser. The improved gas absorption in the FIR laser produces several milliwatts of stable power, more than adequate for use as an HEB LO. The system is now ready for detection of the NII transition. This paper describes this upgrade to the *TREND* laser LO in detail.

1. INTRODUCTION

A number of significant technological research efforts aimed at the development of terahertz low-noise heterodyne instruments are underway in laboratories around the world. Instruments that will be operational in a few years include the far infrared space telescope (HERSCHEL) and other platforms in the upper atmosphere (SOFIA, balloons). Low-noise receivers based on HEB devices deployed on ground-based telescopes at the best available sites are becoming operational now, however. It has only recently been realized that observations above 1 THz are feasible at such sites. Ground-based telescopes can be dedicated to specific tasks for longer periods of time compared with facilities in space or in the upper atmosphere. Furthermore, larger diameter telescopes, such as the 8 meter one under construction at the South Pole, and APEX (12 meters) at the ALMA site, will be superior to air and spaceborne dishes in terms of angular resolution. Several other telescopes are also in various stages of planning.

Presently, the 1.7 meter diameter AST/RO submillimeter wave telescope is operated at the South Pole by the Smithsonian Astrophysical Observatory, and has successfully performed observations up to the 800 GHz (350 μm) window for several years. The Antarctic Plateau, with an altitude of 2847 meters, is unique among observatory sites for unusually low wind speeds, absence of rain, and an extremely cold and dry atmosphere. The *median* Precipitable Water Vapor (PWV) value is less than 0.3 mm during the austral winter season. Expected *median* transparency at frequencies corresponding to important spectral lines is from 5% to 11%, and on unusually good days may reach values 2 or 3 times higher. Atmospheric transmission measurements with an FTS instrument from the South Pole site [2] confirm the above model predictions (see Figure 1). It is clear that installing a low noise terahertz receiver at the South Pole site is thus well justified.

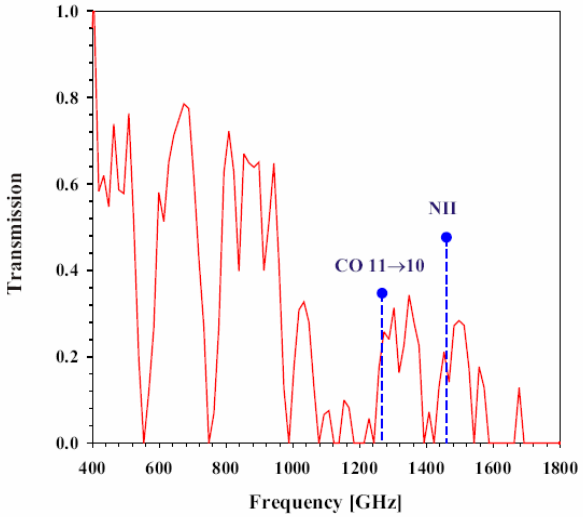

Figure 1. Atmospheric transmission at the South Pole measured with an FTS [2].

NbN HEB THz receivers have been under development at the University of Massachusetts for a few years [3] and are now ready to be used for astronomical observations. *TREND* ("*Terahertz Receiver with NbN Device*") is a low-noise heterodyne receiver system for the 1.25 THz to 1.5 THz frequency range, which was deployed on AST/RO during the austral summer season of 2002-2003. We identified two spectral lines, located in the above atmospheric windows, which are of special interest (marked in Figure 1). The first is the NII (singly ionized nitrogen) line, at 1461.3 GHz (205.4 μm), which is the second strongest spectral line in a typical galaxy (only CII at 156 μm is stronger). The other line is the J=11→10 line of CO at 1267.014 GHz. It is important to observe higher order CO lines and compare these with the well studied millimeter lines of CO in warmer, denser sources.

The *TREND* system was operating stably on the CO J = 11→10 line at 1.267 THz after the installation was completed in February, 2003. The DSB receiver noise temperature was measured on the telescope to be 1,000K. The local oscillator is a CO_2 laser pumped, CD_3OH gas laser. During the winter season of 2003 a tentative detection was obtained of the J= 11 → 10 line of CO in NGC6334a, shown in Figure 2. The laser LO did not stabilize as well at the higher frequency of 1.46 THz, required for the NII line.

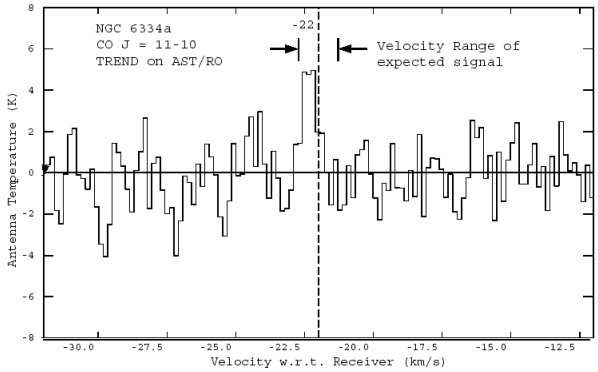

Figure 2. Tentative detection with *TREND* of the J=11→10 line of CO in NGC6334a.

During the austral summer of 2003-2004, we have re-aligned the entire system and re-established stable operation. In addition, we tested a new addition to the CO_2 laser system that allows the laser line required for observing the NII line to be operated stably. In doing this we rely on an innovative solution of shifting the CO_2 laser line to the required frequency for optimum pumping of the CD_3OH molecules in the FIR cell. As a result, the laser line required for NII is now very stable, with a power output of a few mW. This paper describes the upgrade to the *TREND* laser LO in detail.

2. THE *TREND* LASER

The LO source for *TREND* is a model # SIFIR-50 FPL gaseous terahertz laser system that was designed and manufactured by the Coherent/DEOS company [4]. Similar to other terahertz gas lasers, it is pumped by a CO_2 laser. In the case of the *TREND* laser, the pump laser is sealed, and is expected to be able to operate at least 10,000 hours before it needs to be filled with gas, a feature which facilitates operation at a remote site. The pump laser is RF excited and thus does not require a high-voltage power supply. Its maximum power output is 50 W. The CO_2 laser is grating tuned, and utilizes a PZT translator, to actively frequency lock the laser frequency to one of the resonance frequencies of a high-Q temperature-stabilized Fabry-Perot resonator. The terahertz laser uses a thermally compensated design for amplitude and frequency stability. Its cavity length can be adjusted either by a micrometer or a PZT translator. All of the laser components are integrated into a rugged, transportable package, with dimensions of about 185 cm by 50 cm by 25 cm. The laser system requires liquid cooling. Figure. 3 shows a photograph of the *TREND* system after installation at AST/RO. The laser was installed on an optical breadboard, which was bolted to the steel-beam structure which supports the telescope as well as the pallets on which all receivers are mounted.

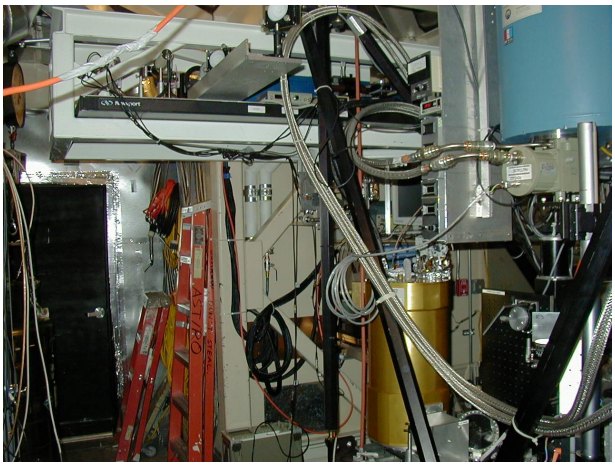

Figure 3. The TREND system as installed at AST/RO in the austral summer 2002-2003.

At the present time, the best known laser line sufficiently close to the required frequency of 1461.31 GHz for NII is a line produced by CD_3OH at 1459.3913 GHz (205.423 μm wave length), which yields a convenient IF of 1.7 GHz. The output power on this line in stable operation is a few milliwatts, which is sufficient since we found that less than 10 μW of laser power at the dewar window was needed to pump the mixer to its optimum point. We use a 6 μm thick beam splitter, which reflects about 1 % of the power. The CD_3OH laser line demonstrates some of the constraints on obtaining a laser local oscillator at a specific terahertz frequency: The problem is that the center of the CD_3OH line to be pumped is offset from the tunable range of the CO_2 pump laser line (10P36). Available laser line tables did not list a value for the offset, but on initial experimentation with this line, it became clear that there was a rather large offset. Specifically, we found that the offset is larger than the free spectral range of the particular pump laser used, and that the CO_2 laser therefore can not be operated at the optimum pump frequency for CD_3OH. This results in lower than typical laser gain and thus less output power, as well as greater sensitivity to small variations of any parameters effecting the stable operation of the sub-millimeter wave laser. During the first operational season, we therefore concentrated on observing the J=11→10 CO line.

3. MODIFICATIONS TO THE *TREND* LASER

3.1. Re-alignment of the Fabry-Perot Cavity

Stability problems had also developed during the austral winter for laser line used with the J=11→10 CO line. As members of the *TREND* team revisited the site beginning in November, 2003, the stability problems were diagnosed as being caused by misalignment of the portion of the CO_2 beam which was being fed to the Fabry-Perot used for frequency stabilization. The misalignment caused a decreased signal to noise for the lock-signal and the excitation of additional modes in the FP cavity The overall effect of this was that frequency locking of the CO_2 laser became erratic, and could only be maintained for very short periods. Optical components in the CO_2 beam path were also found to have been damaged, and were cleaned and re-aligned. A new Eltec detector and a revised lock-circuit for the feedback loop were installed. The new lock-circuit was designed to allow more user-friendly and robust operation, which is especially important during the winter season at POLE The modified feedback loop installed in the TREND system consisted of a simple lock-in amplifier arrangement with a variable gain. A 100 Hz sine wave was used to modulate one of the two reflectors of the FP resonator cavity. This modulation traces out the line width of the CO2 radiation passing through the FP cavity. The signal generated by the Eltec detector, accessed through a signal junction and bias circuit installed outside the laser housing, was fed into a lock-in amplifier, using the 100 Hz sine wave as a reference. The signal was also fed into an oscilloscope to provide the visual reference needed for monitoring and locking the laser system. The output of the lock-in amplifier, which represented the derivative of the line shape, was fed into a bias circuit designed to drive the PZT which tunes the cavity length of the CO_2 laser. This circuit consisted of a 0-10 volt bias circuit with a summing amplifier section. The summing amplifier added the output of the lock-in onto the variable bias of the circuit. This circuit also had a variable amplification section, allowing the signal generated in the lock-in to be either removed completely or amplified up to a factor of 100 times. These modifications allowed a more robust feedback loop with a wider frequency band which led to a more stable long term performance out of the CO_2 laser. After these modifications the signal-to-noise from the Fabry-Perot was substantially improved and the frequency-locking of the CO_2 laser was working well.

3.2. Modifications to allow stable operation of the 1.46 THz laser line

We described above that there was a substantial offset between the CO_2 pump laser operating on the 10P36 line, and the optimum pump frequency required to produce the 205.4 μm submillimeter laser line. In order to circumvent this problem we have used an innovative solution, which as far as we are aware has never been employed before. The CO_2 laser was shifted with the help of a commercially available [5] Acousto-Optical Modulator (AOM). This AOM functions as a Bragg diffraction device. The active component is a bar of germanium with anti-reflection coatings for CO_2 laser frequencies. The germanium bar also has an acoustic transducer attached to one end. Application of 40 MHz RF modulation to this transducer sets up an ultrasonic wave in the crystal, which scatters most of the incident laser radiation into the first order diffraction, with approximately 80-90 percent efficiency. The diffraction process sets up conditions that require frequency matching of the incoming radiation, the outgoing radiation and the acoustic wave [6]. As a result, the diffracted CO_2 laser beam experiences a frequency shift equal to the frequency of the RF modulation. The frequency shift can be either positive or negative, depending on the relative orientation of the wave-vectors of the three waves. We used this 40 MHz frequency shift to compensate for the frequency offset between the CO_2 laser pump transition and the center frequency of the CD_3OH absorption envelope. Since the Bragg diffraction process also requires wave vector matching, the diffracted beam will exit a different angle than the incident beam (typically a few degrees). The non-diffracted beam is absorbed by a beam dump. Initial tests of the AOM were performed in the THz Laboratory (UMass/Amherst), using a laser configuration for our laboratory laser very similar to that of the TREND. These experiments confirmed that we could now obtain very stable operation on the 205.4 μm line.

The installation of the AOM in the *TREND* system at the South Pole required substantial modification of the beam path coupling the CO_2 laser into the FIR cell. It was not feasible to accommodate the new optical components within the original laser package, so the CO_2 laser was directed out of the laser housing through an existing sample port, via a new primary mirror. Beam diagnostics were performed on the CO_2 laser consisting of a power measurement, and an inspection of the mode shape of the CO_2 beam. The CO_2 laser required a slight adjustment to the alignment of the diffraction grating. Adjusting the grating for maximum power also decreased a vertical ellipticity of the mode. With power adjustments completed, the CO_2 laser produced approximately 32 Watts and a slightly elliptical mode.

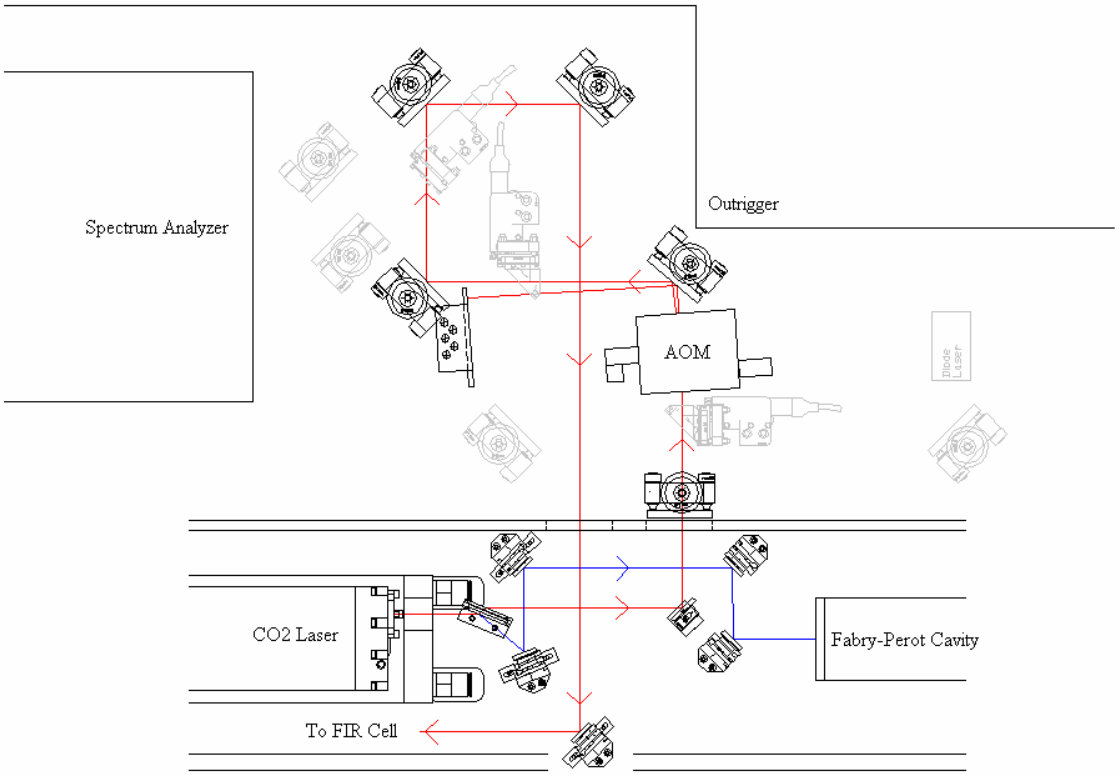

Figure 4. The new beam path and the placement of the AOM.

With the beam directed through the sample port of the laser housing, the remainder of the optics path was established as shown in Figure 4. The original laser housing is in the lower part of the figure. The components outside the housing were placed on the original optical breadboard which supported the laser. The 19.68 inch focal length lens, located just outside the TREND laser enclosure, produced a collimated beam with a waist of 1.6mm, which could then be passed through the AOM. It was essential to collimate the beam at this point to minimize divergence over the total path length, ensure the proper beam waist for the next focusing optic, and to ensure maximum efficiency through the AOM. After the installation of the AOM was completed, we measured a coupling efficiency of 80 percent of the incident power into the first order diffraction. Note the beam dump for the un-shifted CO_2 beam, both beams are indicated after the AOM in Figure 4. The 40 MHz upshift of the CO_2 frequency produced by the AOM causes a skew in the CO_2 laser beam path that is a function of the CO_2 frequency passing through the device. Since future research utilizing the TREND LO might involve pumping FIR laser lines at other frequencies, a bypass path was created around the AOM using two motorized flip mirrors, not shown in figure 4. For both beam paths, the AOM shifted and bypassed, the return beam re-enters the laser housing through a hole drilled in the laser enclosure. This beam was aligned to coincide with the original beam path, and an appropriate new lens was used to focus the CO_2 beam at the input hole of the FIR laser, as shown in the lower part of Figure 4.

In addition to the installation of the AOM, a third motorized flip mirror was integrated into the design for the purpose of directing the full power CO_2 beam into the spectrum analyzer. Previously, the spectrum analyzer could only be activated by directing the FP beam out of the sample port; however, due to the low power of this beam, about 5 mW, the process of changing CO_2 laser lines had been difficult. With access to the full power beam this process has greatly improved. The position of the spectrum analyzer on the optical breadboard can also be seen in Figure 4. The blue beam path indicates how a small portion of the CO_2 beam is reflected from an (intentionally) slightly misaligned Brewster window, and directed to the FP cavity, as described.

To aid in the overall alignment, and possible future modifications to the beam path, a red diode laser was aligned onto the beam path of the CO_2 laser following the AOM. This laser was left as a permanent addition to the system to aid in the realignment of the CO_2 spectrum analyzer should this be necessary. Coupling of this diode laser

into the CO_2 beam path required sending the diode laser over the top of the flip mirror closest to the AOM input. Because of the orientation of the diode laser and the nature of the AOM device, it was not possible to follow the beam path of the CO_2 through the AOM, only the path around the AOM could be illuminated. At the third mirror both paths were axially aligned and remain so for the rest of the optics path.

Two photographs in Figure 5 show the completed installation of the AOM and nearby components.

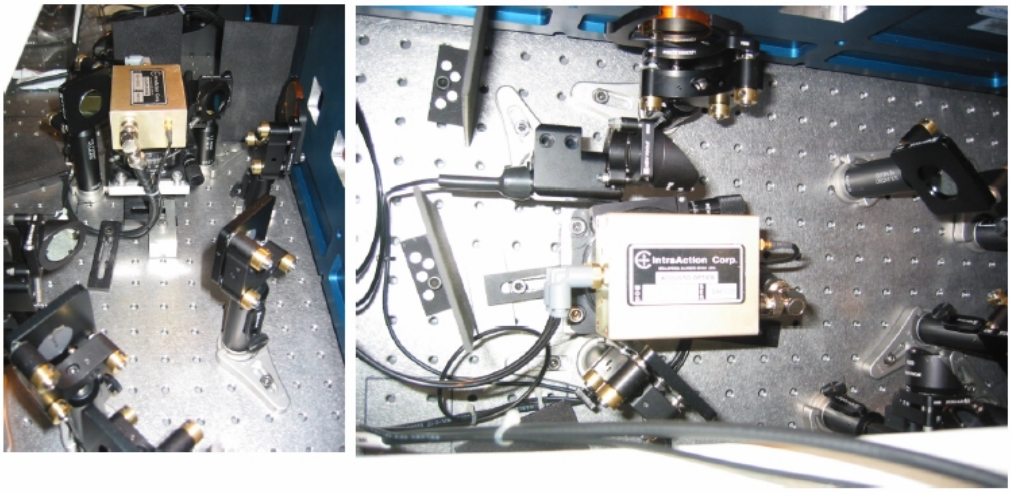

Figure 5. The acousto-optical modulator (AOM) installed into a new optical path of the CO_2 laser.

3.3. Alignment of the CO_2 Beam with the FIR Cell

An alignment telescope was used to project a diode laser along the axis of the FIR laser bore. This procedure allowed for proper orientation of the mirrors in the FIR laser perpendicular to the axis of the cell. In order to align the FIR laser with the CO_2 path, the diode pointer was also oriented to pass out the input coupling hole of the FIR cell. The beam was brought into alignment with the diode laser established along the CO_2 beam path requiring adjustment of the location of the secondary lens and the remaining mirrors.

The FIR laser cell was opened and inspections were made to the input and output resonator coupling mirrors. Minor damage, caused by the CO_2 radiation, was found on the surface of both coupling mirrors. This damage had little effect on the performance of the submillimeter laser lines, however. The damaged 1.5mm hole coupler at the output of the laser was replaced with a new 2mm hole coupler.

The CO_2 laser was tuned to the proper pump line for the 205.4 μm CD_3OH laser line. Bright glowing on the input coupling hole is a typical first point of reference for evaluating the quality of the alignment between the CO_2 and FIR lasers. No glowing of the input coupling hole was observed with the CO_2 traveling down either the AOM shifted or the AOM bypassed beam path. This observation demonstrates that the alignment procedure had been successful. Using a small bolometer, a significant amount of power was measured at the output of the FIR cell. Estimates of the power, based upon the amount of attenuation required by the bolometer, were made. Conservative estimates place the power output at a minimum of 3 mW, more than adequate power for the TREND experiment.

3.4. Other modifications to the TREND system

We installed a modified feedback system for stabilizing the FIR laser output power. This system diverts a small amount of the FIR power via a mylar beam splitter, chops it at a low frequency, and detects it in a liquid helium cooled semiconductor bolometer. The signal from the bolometer is amplified in a lock-in amplifier, compared to a reference level, and fed back to the PZT cavity tuning element of the FIR laser after further amplification and low-pass filtering. In tests on the TREND system before shipment to the South Pole we showed

that this type of system can keep the laser power stable within a fraction of a percent. This is important for performing long astronomical observations since the IF output power level from the HEB depends quite strongly on the LO power.

Stabilizing the laser power over even longer times requires maintaining the FIR laser gas at a stable pressure. Since the FIR laser tube inevitably has small vacuum leaks, we designed a system to trickle flow gas into the FIR tube (see Figure 6). The CD_3OH gas is quite expensive, so a system which produces only a small flow is required. The system uses solenoid operated valves and a capillary glass tube to solve this problem.

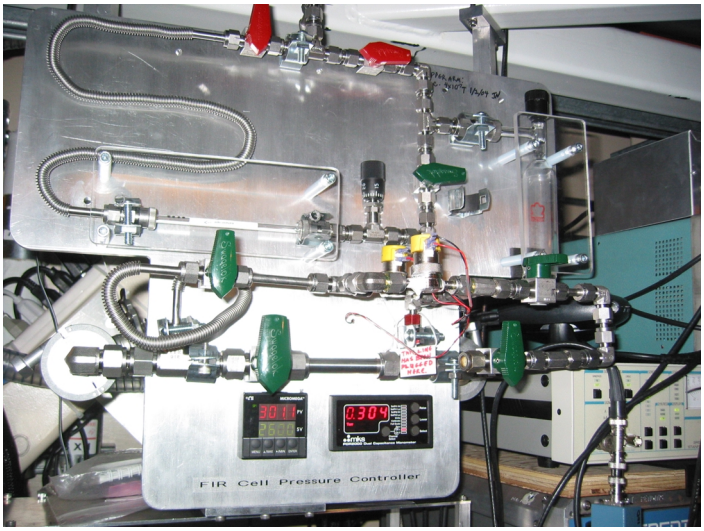

Figure 6. The manifold for creating a trickle flow of CD_3OH gas to the FIR laser tube.

4. CONCLUSIONS

As a result of this year's modifications, the TREND laser

- *was very stable on the 205.4 μm (NII) line; the laser amplitude can be stabilized to a fraction of 1 %*
- *had output power ~ 3 mW*
- *an alternative beam path allows by-passing the AOM for lines which do not require it*
- *system was completely re-aligned. The re-alignment fixed problems which had occurred during the first winter*
- *had a total DSB receiver noise temperature measured through the telescope Acousto-Optic Spectrometer of 1,000 K at 1.46 THz (the NII line)*

We have demonstrated a general method for substantially extending the number of laser lines which can be used for THz LOs. This method should be useful in the future, for example for array receivers for the NII line, and for HEB receivers at higher frequencies. We expect to be able to perform extensive high-resolution observations of NII for the first time from a ground site using the upgraded *TREND* system.

5. ACKNOWLEDGEMENTS

We gratefully acknowledge support for this project from the National Science Foundation, NSF Award Numbers: 0126090; 0350871.

6. REFERENCES

1. E. Gerecht et al., "Deployment of *TREND* - A Low-Noise Receiver User Instrument at 1.25 THz to 1.5 THz for AST/RO at the South Pole", Proc. 14th Intern. Symp. Space THz Technology, Tuscon, Arizona, April, 2003, p. 179-188.

2. Chamberlin R A, Martin B, Martin C, Stark A A, "South Pole Submillimeter Fourier Transform Spectrometer [4855-83]", in Millimeter and Submillimeter Detectors, Proceedings of SPIE (Volume 4855), Kona, Hawaii, 2002),

3. E. Gerecht, C.F. Musante, Y. Zhuang, K.S. Yngvesson, T. Goyette, J. Dickinson, J. Waldman, P.A. Yagoubov, G.N. Gol'tsman, B.M. Voronov, and E.M. Gershenzon, "NbN Hot Electron Bolometric Mixers - A New Technology for Low Noise THz Receivers," *IEEE Trans. Microwave Theory Tech.*, vol. 47, pp. 2519-2527, Dec. 1999.

4. Coherent/DEOS, 1280 Blue Hills Ave, Bloomfield, CT 06002.

5. IntraAction Corporation, 3719 Warren Avenue, Bellwood, IL 60104, Model AGM-406B21; power amplifier model PA-4030-8.

6. See for example A. Yariv, "*Quantum Electronics*", Third Edition, John Wiley and Sons (1989), p 329 ff.

High Resolution Imaging using 325 GHz and 1.5 THz Transceivers

Jason C. Dickinson, Thomas M. Goyette, and Jerry Waldman

Submillimeter-Wave Technology Laboratory
University of Massachusetts Lowell
175 Cabot St.
Lowell, MA 01854

ABSTRACT

The Submillimeter-Wave Technology Laboratory (STL) at the University of Massachusetts Lowell has designed and constructed two high resolution terahertz imaging systems based on 325 GHz and 1.5 THz transceivers. While the systems were originally designed to acquire radar signatures of high fidelity scale models, their high sensitivity and high stability at 325 GHz and 1.5 THz make them novel systems for demonstrating the imagery capabilities of terahertz rays. Unlike many terahertz detection systems, the imaging system described here uses ultra stable CO_2 pumped far-infrared (FIR) lasers to produce nominally 100 milliwatt continuous wave (CW) terahertz beams. Custom CO_2 and FIR laser designs have produced systems with extremely stable power output and low phase drift. The imagery generated by these systems is formed by full beam illumination of the target of interest, followed by coherent processing of the backscattered signal. Several terahertz images will be presented, including high resolution imagery of a concealed weapon, detected through clothing from a distance of 25 meters for each system. An image collection time of less than three minutes produced 512 x 512 pixel image with 1 to 2 mm resolution. The overall systems, including the generation of the 325 GHz and 1.5 THz beams, heterodyne detection systems, target positioning apparatus, and image formation algorithms will be discussed.

Keywords: Terahertz, THz, Imagery, Security, Concealed weapon.

1. INTRODUCTION

For the past twenty years the Submillimeter Wave Technology Laboratory (STL) at the University of Massachusetts Lowell has performed radar signature measurements of physical scale models of tactical vehicles. Currently STL and the Expert Radar Signature Solutions (ERADS) consortium have six compact radar ranges spanning frequencies from several gigahertz up to 1.6 terahertz. Two of the laser based systems located at STL will be discussed.

The earliest work in simulating full-scale radar measurements involved the use of a carbon dioxide laser, optically pumping a far-infrared (FIR) laser cell, to produce frequencies in the terahertz[1]. Bolometric detectors were used to measure the amplitude of the scatter from complex targets.

Over a decade ago, bolometric detectors were replaced with corner-cube mounted, Schottky diode heterodyne mixers in a new 1.56THz system[2]. The prototype system was replaced with an all new ultra-stable, fully polarimetric 1.56 THz transceiver system a few years later[3]. Very recently, newly designed waveguide mounted heterodyne mixers were installed into a new ultra-stable, laser based, 325GHz transceiver system at STL[4]. The use of these heterodyne detectors increases the available dynamic range of sensitivity to around 170dB. The heterodyne detection systems in use also allow the complex scatterer back-reflection components (R, θ) or (I, Q) to be collected. Recently, terahertz laser systems have been used as local oscillator (LO) sources in remote areas for radio astronomy[5]. While the attainable frequency and power output of solid-state multiplier-chain devices is improving, they are presently too weak to be utilized as a local oscillator for a heterodyne detector. For now, the best source of milliwatt class terahertz radiation is a CO_2 laser pumped, far-infrared laser.

A typical measurement sequence conducted inside an STL Compact Radar Range would involve the use of a swept frequency source, usually a Schottky diode or waveguide mounted sideband generator. This sideband generator takes an RF signal and mixes it with the terahertz laser frequency to produce a new frequency at the base laser frequency plus the RF frequency. Positioning the target and collecting the backscattered data at a number of discreet frequency steps in a chirp of the outgoing laser allows post-collection generation of an Inverse Synthetic Aperture Radar (ISAR) image.

For the imagery and data collection described here, no frequency chirp was applied. The measurements collected for this work were a bit unusual to the typical ISAR measurement, in that these measurements consist of a single frequency measurement taken at numerous angular poses. Since the compact ranges were originally designed to accurately position the target object, rather than scan the actual far infrared beam, the measurements described produce imagery via controlled motion of the scan object. While this approach has little use in scanning live or moving objects, it is presented as an exercise for studying the terahertz phenomenology of complex scattering objects.

Following data collection, Fourier Transform (FT) or Fast Fourier Transform (FFT) processing of a series of the back-scattered values collected across a two dimensional angular aperture effectively convert the data into an angular Doppler Shifted image. This Doppler Shift image looks to the eye like the physical object being measured. Scattering centers reflected from the target of interest are represented via a false color Z-axis.

2. TERAHERTZ TRANSCEIVER SYSTEM

2.1. The Transmitter Source and Receivers

Many of the radar measurements at STL utilize the CO_2/FIR laser combination as the preferred source of terahertz radiation. While the output from the FIR laser is fairly narrowband for a chosen operating wavelength, it is currently the best source for high power (nominal 100mW) requirements requiring high stability.

Following many years of minor in-house improvements to commercial CO_2 and FIR laser designs, STL scientists and engineers set out to design an entirely new FIR laser, using information gleaned from years of operating commercially available CO_2 paired FIR lasers. The new FIR laser design included a balance of ease of use, nimbleness in controls, neutral cavity thermal expansion, and extremely low vacuum leak rate. The new FIR lasers were designed with thermal stability as a primary goal, with water jacketed tube bores and water cooled optics mounts. Because the FIR lasers used would potentially operate at frequencies anywhere from 50μm to 5000μm, the laser design allows the use of dielectric waveguide resonator tube bores over a wide range of diameters, as dictated by Eigenmode resonator design. Performance figures of these lasers show that after only a few hours of warm up time, the output power is very stable, and the phase stability is better than 10° in absolute phase in a 24 hour period.

With the great success of a more stable FIR laser, STL set out to improve on the CO_2 laser design, to produce a pump laser with more frequency stability. Pacific Research (Topanga, CA) delivered a custom CO_2 laser that proved to be extremely stable in power and frequency drift. With a typical output power of close to 200 watts continuous wave (CW) in the CO_2 laser, the resulting power levels produced by the far-infrared lasers are impressive, usually around 100 milliwatts. Our five Pacific Research CO_2 lasers have now become the standard optical pump laser for six operating STL FIR lasers.

The rotational/vibrational transition of the CO_2 molecule in the carbon dioxide laser provides a robust source of mid-infrared input power for the rotational transitions needed in the FIR laser. For a discreet CO_2 laser pump line, in a particular molecular gas, at a particular pressure, and in an optimally designed resonator, FIR power can be achieved with modest efficiencies of around 0.10%.

The measurements were performed on two entirely separate compact radar ranges at STL, each system consists of two CO_2/FIR laser pairs whose outputs are zero order transverse Gaussian modes. One CO_2/FIR is used to generate the transmit beam, and another is used to produce a local oscillator (LO) beam. The two beams produced are approximately 2 GHz apart, which requires each FIR laser to be pumped by it's own CO_2 laser, often requiring an entirely different molecular gas in the FIR laser. The 1.56 THz system uses the 1.5645 THz line in methanol (CH_3OH) gas for the transmitter, and the 1.5626 THz line in difluoromethane (CH_2F_2) for the LO. The 325 GHz

system uses the 325.9 GHz line for the transmit beam, and the 323.6 GHz line for the LO, both in O-deutero-formic acid (HCOOD) vapor.

The receivers in use on the two terahertz systems use both old and new technologies. The 1.56 THz receiver is a corner-cube mounted, whisker contacted Schottky diode, made originally by University of Virginia in the 1990's. The 1.56 THz system noise temperature is about 9000°K, with a conversion loss of 14 dB. The receivers for the 325 GHz system are relatively new technology, and use a freestanding waveguide mounted detector made by Virginia Diode (Charlottesville, VA). In the current 325 GHz system, they have a 1500°K system noise temperature and a system conversion loss of around 8.5 dB. Both heterodyne detectors enable the measurement systems to have a dynamic range of around 170 dB.

2.2. Anechoic Chamber and Data Collection System

Compact radar ranges in use at STL consist of a climate controlled room with materials specifically designed to absorb terahertz radiation (anechoic materials)[6] attached to all the walls in the room. The transceiver system sits just outside the anechoic chamber, and a small opening in the chamber allows the passage of the transmitted and back-reflected radiation. The outgoing beam, the transmit or illumination beam, is close to 24 inches in diameter at the full-width-half-maximum (FWHM), which fully illuminates the target object with a planar phase front. An overview of a typical laser based transceiver may be found in Figure 2.

To produce the aforementioned Angular Doppler imagery, commonly referred to as azimuth/elevation or "Az/El" imagery, a very accurate control over the motion of the scanned object is required. The positioning apparatus is located in the anechoic chamber, and the mechanical components are shielded from the illuminating beam. The target object sits atop the stepper motor positioning staging, which allows positioning accuracy on the order of 0.005 degrees in both the azimuth and elevation axis of motion. The azimuth axis stage allows full rotation of the object through 360 degrees. The elevation axis allows motion from 0 degrees, fully upright, to 90 degrees, where the scan object would be tilted full forward. The combination allows an entire hemisphere to be measured.

For each azimuth/elevation pose of the object, complex scatterer data is collected by way of a lock-in amplifier, which provides in-phase and quadrature (I,Q) values. The signals from the lock-in amplifier are acquired using National Instruments analog-to-digital hardware, controlled by custom designed LabVIEW® software.

3. DATA COLLECTION AND PROCESSING

3.1 Angular Doppler Data Collection Theory and Practice

The Angular Doppler imagery techniques are described in detail by Mensa,[7] the slight difference in implementation for this work involves use of a stationary transceiver, and a strictly two dimensional holographic recording of data. The target object to be measured is placed in the center of the terahertz laser transmitter beam. The resultant imagery produces pixel values in a coordinate system of vertical and horizontal cross-range, corresponding to a two dimensional matrix of amplitude values.

For the azimuth axis, it is convenient to place the object centered about the axis of rotation. The object is revolved around the azimuth axis, and complex (I, Q) pairs are collected at evenly spaced intervals. To add a second dimension to the image, a similar collection is performed in the elevation axis. A two-dimensional scan would consist of an azimuth sweep, followed by an elevational increment, and the process would repeat until a two dimensional "window" is swept out in angle. A complex Fourier Transform can then performed on this data, to generate coordinate values as a function of phase change between angular increments as shown in Figure 3, a scatterer that is some radius from the center of azimuth rotation will change the received phase value as the object is moved in azimuth. The phase change corresponds only to motion perpendicular to the illuminating beam's phase front. A positive change in phase between two successive azimuth positions would correspond to a motion moving towards the receiver, while a negative phase change would correspond to motion away from the receiver. By Fourier Transforming a number of these positions, the phase change trend can be extracted in the conversion from spatial frequency to distance. The displayed plot in Figure 4 shows the Fourier transform of 512 points collected in a single azimuth scan. Values to right of center are objects moving towards the receiver, objects to the left of center are

moving away from the receiver, and the center of the plot shows zero phase change, no movement with respect to the receiver. The X-axis of the plot in Figure 4 shows the spatial frequency Doppler shift transformed into horizontal distance from the center of rotation. With a few simple conversion calculations, the x-axis may be assigned convenient units of distance.

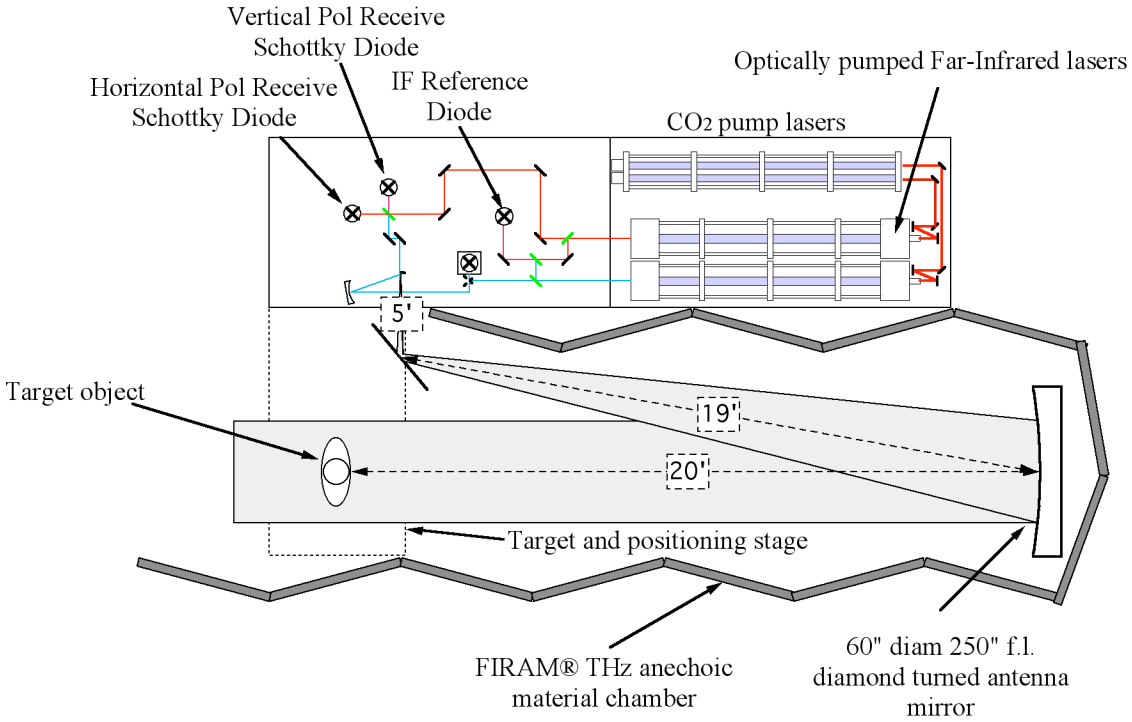

Figure 2. Schematic of a laser based terahertz transceiver at STL.

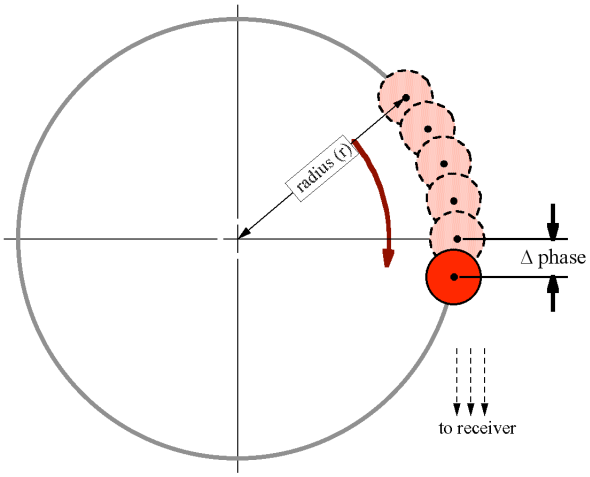

Figure 3. A phase change on a scatterer occurs between two azimuth positions.

To ensure proper sampling of the azimuth points and to prevent under-sampling, Equation 1 must be used to determine the unambiguous cross-range and the maximum diameter of the object to be scanned. For the

calculated diameter, the change in phase at the edges corresponds to 90 degrees. A phase change greater than 90 degrees between points becomes ambiguous, that is, it is not possible to determine which direction in which the Doppler shift occurred. The result would produce a corrupt "folded" image, where anything outside the unambiguous cross range would look folded in at the edges. Larger scan objects would require a finer scan resolution, smaller objects can afford a more coarse scan resolution.

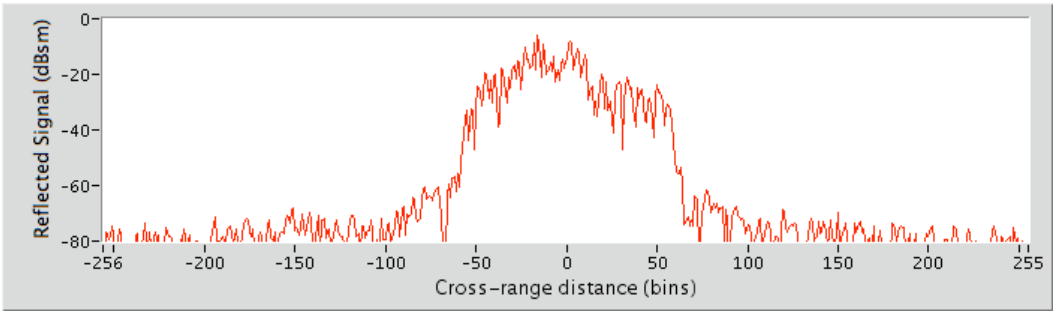

Figure 4. A sample Fourier Transform of an azimuth scan showing Angular Doppler shift as horizontal cross-range.

The elevation axis calculations are similar in unambiguous cross-range, but for generating the following images, the object was above the axis of rotation in the elevation direction. An unfortunate artifact of the data collection and processing exists at the zero azimuth, zero elevation location, corresponding to all signals that did not change in the duration of the scan. This small grouping for pixels in the 2D image shows the amplitude for all noise and background signals in the system. In order to prevent these pixels from appearing in the center of the terahertz image, the object is mounted such that the elevation axis is below the scan object. In the final imagery the lower part of the image, that which corresponds to objects moving away from the receiver, is removed by cropping the image.

(1) $$R_u = \lambda / 2\theta_{inc}$$

To calculate the pixel size as a function of the angular extent of the FT processing, Equation 2 may be used. Through a simple equation manipulation, a desired pixel size could also be used to determine the required angular extent to process.

(2) $$\Delta R_c = \lambda / 2\Delta\theta_{integrated}$$

For the imagery formed at 325 GHz and 1.56 THz, the integrated angle was kept fairly small, under 10 degrees, to prevent blurring or smearing of the imagery. As the integrated angle becomes large, phase focusing algorithms are needed to compensate for horizontal motion as the object traces out the curvature of the azimuth pivot. Because the data presented here is processed over relatively small angles, the phase focusing need not be applied.

4. RESULTS

Results of the two-dimensional data collection and data processing are shown below. The amplitude (Z-axis) values are shown in a false color "rainbow". Values in red are the most intense, moving down in amplitude of back-scatter to orange, yellow, green, blue, and purple. As the amplitude drops below a threshold value, the color goes to black, allowing the background to threshold all the very low level residual noise. Preliminary measurements were performed on $1/16^{th}$ scale models of vehicles, readily available in-house at STL. It is interesting to also note that because all dielectric materials on the models are modeled to simulate W-Band radar at 94 GHz, the terahertz images taken at 1.56 THz simulate true 94 GHz imagery of the full scale target. Figure 5 shows a 1.56 THz Az/El image of a $1/16^{th}$ scale model of a truck. The upper display is the false color imagery, and the lower display shows a photograph of the model. The apple in the photograph is to show the relative size of the model. The pixel resolution in the image is around 1.1mm square, corresponding to an FT integrated angle of 5.12 degrees in both azimuth and elevation.

The image on the left of Figure 6 shows the 1.56 THz imagery of a 4" square aluminum plate with raised letters "STL" and the words "University of Massachusetts" and "Submillimeter-Wave Technology Laboratory" wrapped along a circle above and below the center. On the right of Figure 6 is a photograph of the metal plate.

With the recent concerns of Homeland Security, and the recent scientific interest in manipulating terahertz waves, an attempt was made to image a concealed weapon through several layers of clothing. A mannequin was dressed in a cotton Tee shirt and a cotton jacket. The mannequin serves only to support the clothing material. The mannequin torso is a commercially available model, and no effort was made to replicate human skin. The mannequin is composed of a painted fiberglass form that is hollow, and has metal reinforcing material distributed throughout the torso for structural strength.

The image in Figure 7 shows a 1.56 THz image of a mannequin torso wearing a cotton jacket, with a gun object placed in an inside breast pocket of the jacket. The outline of the mannequin torso is a bit difficult to see, but the mannequin is facing directly towards the receiver (and the viewer) the head is not visible, but the shoulders and sides of the torso can be seen, down to about the elbows. The gun is clearly visible through the jacket, with good contrast against the mannequin.

The imagery in Figure 8 is the same mannequin with the same concealed weapon, in the same pose, but at 325 GHz. Here the contrast of the weapon seems to be reduced. The mannequin is constructed of a fiberglass and metal mesh, and since the wavelength of a 325 GHz beam is on the order of 920μm, it is believed that there is actually too much penetration through the clothing material. The 325 GHz beam is believed to be penetrating the fiberglass shell and reflecting around inside the hollow torso cavity. The measurement can therefore not be used as a true representation of measuring a human with a concealed weapon. Additional studies must be performed to assess the properties of a live object with skin and flesh.

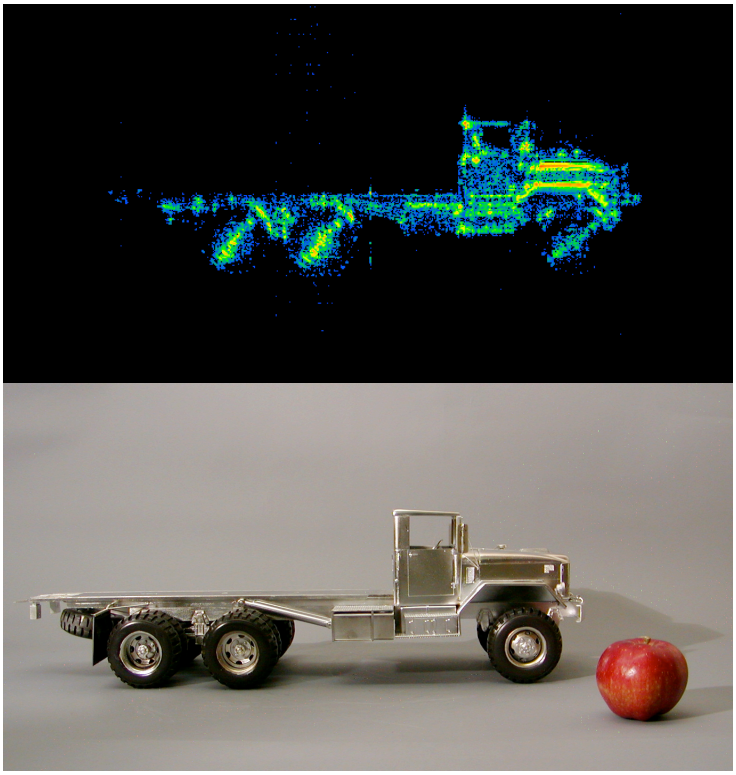

Figure 5. 1.56 THz Azimuth/Elevation imagery of a scale model truck with pixel resolution of about 1.1mm x 1.1mm.

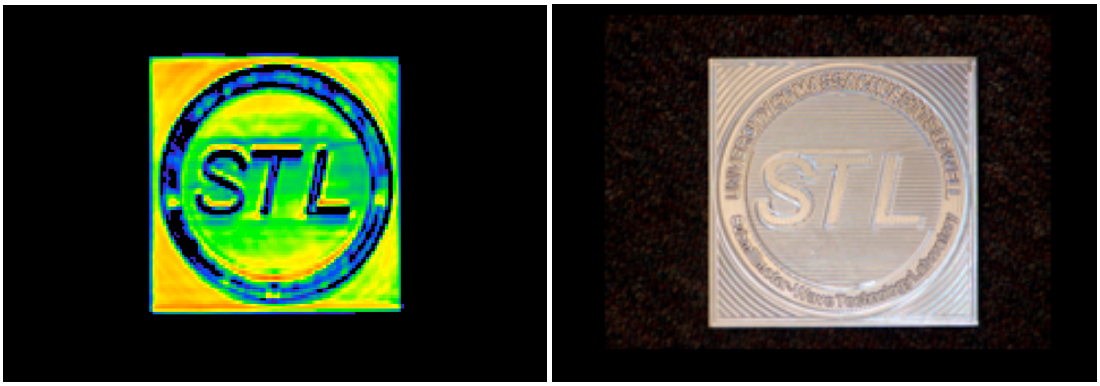

Figure 6. 1.56 THz image of a metal plate with raised lettering.

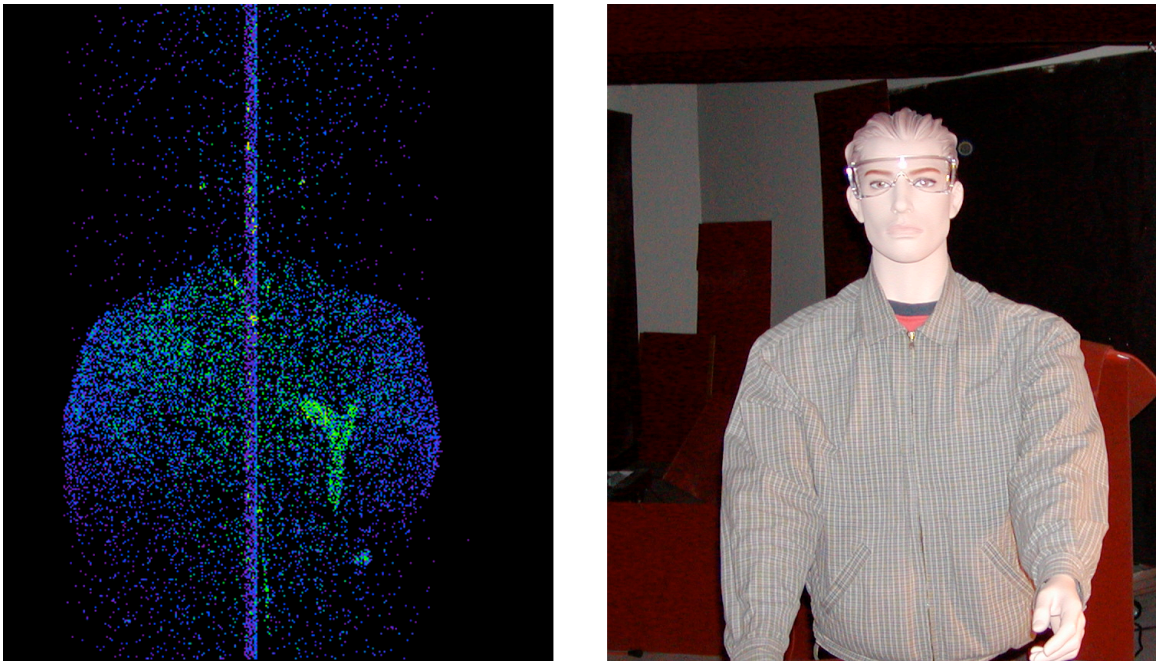

Figure 7. 1.56 THz image of dressed mannequin with concealed weapon (left), photograph of the mannequin as measured (right).

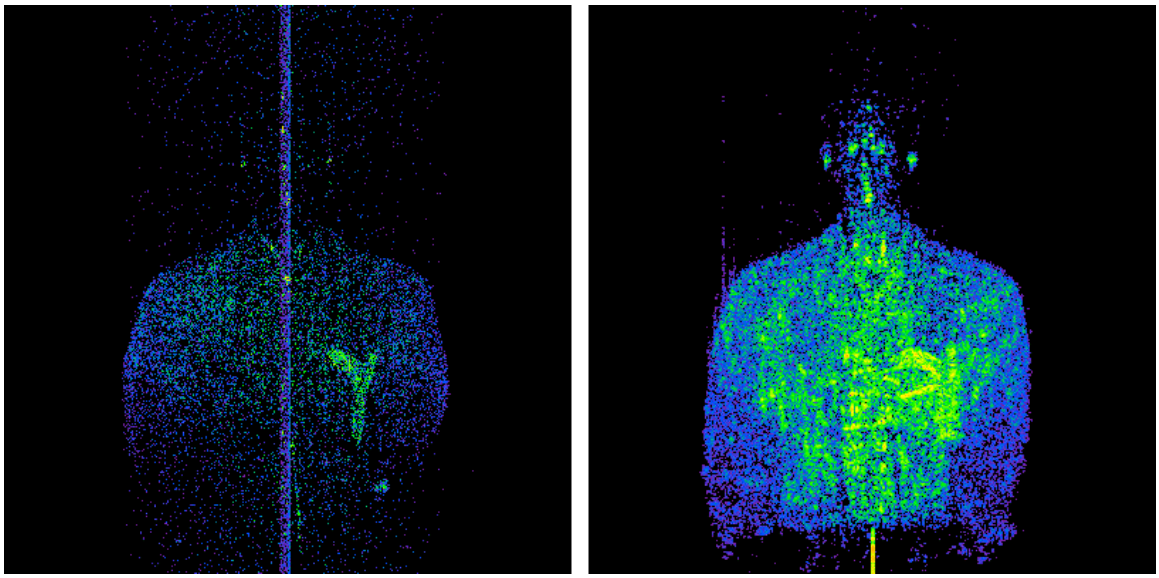

Figure 8. 1.56 THz image of mannequin with concealed weapon (left), same configuration at 325GHz (right)

5. SUMMARY

Terahertz images of several objects were produced, using a technique borrowed from the radar community. The images shown were collected at 1.56 THz and 325 GHz (0.325 THz). Both terahertz transceiver systems used a fixed position transmitter and receiver, and the scan object was moved in a precise motion through a series of angles. By two dimensional Fourier Transform post-processing, the data collected over an angular window in the azimuth axis and the elevation axis, forms a two dimensional image of variable resolution and very high sensitivity.

6. REFERENCES

1. J. Waldman, H. R. Fetterman, W. D. Goodhue, T. G. Bryant, D. H. Temme,"**Submillimeter Modeling of Millimeter Radar Systems**", SPIE Proceedings on Millimeter Optics , Vol. 259, p. 152 (1980).

2. E.R. Mueller, and J. Waldman,"**Power and Spatial Mode Measurements of a Sideband Generator Submillimeter-Wave Source**", Proceedings of the Eighth International Symposium on Space Terahertz Technology, Cambridge, MA, March 1997

3. Thomas M. Goyette, Jason C. Dickinson, William J. Gorveatt, Jerry Waldman, William E. Nixon,"**X-Band ISAR Imagery of Scale Model Tactical Targets Using a Wide Bandwidth 350GHz Compact Range**", SPIE AeroSense Conference. 12 - 16 April 2004, Orlando, Florida

4. Thomas M. Goyette, Jason C. Dickinson, Jerry Waldman, William E. Nixon,"**Three Dimensional Fully Polarimetric W-band ISAR Imagery of Scale-Model Tactical Targets Using a 1.56 THz Compact Range**", SPIE AeroSense Conference. 21 - 25 April 2003, Orlando, Florida

5. K.S. Yngvesson, C.F. Musante, M. Ji, F. Rodriguez, Y. Zhuang, E. Gerecht, M. Coulombe, J. Dickinson, T. Goyette, J. Waldman, C.R. Walker, A. Stark, and A. Lane,"**Terahertz Receiver With NB/N Device (TREND) - A Low-Noise Receiver User Instrument For AST/RO at the South Pole**", Proceedings of the 12th International Symposium on Space Terahertz Technology, California Institute of Technology, Pasadena CA, March 2001.

6. R.H. Giles, T.M. Horgan, and J. Waldman,"**Silicon-Based Anechoics at Terahertz Frequencies**", Proc. of the 17th Int. Conf. on Infrared and Millimeter Wave , Dec. 1992, Los Angeles, CA.

7. D.L. Mensa, *High Resolution Radar Cross-Section Imaging*, Artech House, Boston, MA 1991.

Increased bandwidth of NbN phonon cooled hot electron bolometer mixers

M. Hajenius[1,2], J.J.A. Baselmans[2], J.R. Gao[1,2], T.M. Klapwijk[1], P.A.J. de Korte[2], B. Voronov[3] and G. Gol'tsman[3]

[1]*Kavli institute of Nanoscience, Delft University of Technology, Lorentzweg 1, 2628 CJ Delft, The Netherlands.*
[2]*SRON National Institute for Space Research, Sorbonnelaan 2, 3584 CA Utrecht, The Netherlands*
[3]*Moscow State Pedagogical University, Moscow 119435, Russia.*

Abstract

We study experimentally the IF gain bandwidth of NbN phonon-cooled hot-electron-bolometer (HEB) mixers for a set of devices with different contact structures but an identical NbN film. We observe that the IF bandwidth depends strongly on the exact contact structure and find an IF gain bandwidth of 6 GHz for a device with an additional superconducting layer (NbTiN) in between the active NbN film and the gold contact to the antenna. These results contradict the common opinion that the IF bandwidth is determined by the phonon-escape time between the NbN film and the substrate. Hence we calculate the IF gain bandwidth of a superconducting film using a two-temperature model. We find that the bandwidth increases strongly with operating temperature and is not limited by the phonon escape time. This is because of strong temperature dependence of the phonon specific heat in the NbN film.

1. Introduction

Phonon cooled Superconducting Hot Electron Bolometer (HEB) mixers are the most sensitive heterodyne receivers for frequencies above 1 THz and are therefore expected to play a key role in future atmospheric and space borne missions. However, the IF Gain Bandwidth at the bias point that gives the maximum sensitivity is of the order of ~ 3 GHz, which is disappointingly low for many applications [1].

The maximum bandwidth, set by thermal relaxation processes in the bolometer, is believed to be limited by the phonon escape time and not by the electron-phonon interaction time. The phonon escape time is determined by the NbN film thickness and the film-substrate interface. For that reason higher bandwidths were mainly achieved by NbN thin film development [2, 3].

In contrast we investigate the bandwidth for devices with different types of contacts between the Au antenna and the active NbN film. We find that the IF bandwidth at the optimum operating point increases to 6 GHz if we modify the conventional contact structure by sputter cleaning of the NbN surface and adding a superconducting layer (NbTiN) in between the antenna and NbN film. For a HEB, in which the NbN film is not cleaned and no superconducting interlayer is used, we find a bandwidth of 2 GHz. The processing of the latter contacts is similar to that reported by others [4-6].

We will first introduce the devices with different contacts and then describe the IF bandwidth measurement setup and results. Subsequently we use the Perrin and Vanneste two-temperature model [7, 8] to understand the observed high bandwidth.

2. Devices with different contacts.

The device geometry and contacts are illustrated in Fig. 1. Table 1 summarizes the parameters of the contact types. Devices of type "I" have a conventional contact structure similar to the ones reported in Refs. [4-6]. No cleaning of the contact is performed except for the 6 seconds O_2 plasma etch to remove resist remnants prior to the contact deposition. For type "II" and "III" additional physical etch using Ar^+ is performed to clean the NbN surface prior to the *in-situ* deposition of the contact pads. The rest of the device fabrication is identical for all devices and similar to the HEB mixer fabrication process used by others. All devices are identical in dimensions with a bridge width of 4 μm and length of ~ 0.4 μm and all are using parts of the same 3.5 nm thick NbN film with a T_c of ~ 10 K on a (single) Si substrate. The details of device characteristics and processing can be found elsewhere [9].

The typical uncorrected DSB noise temperatures at 2.5 THz for the different device types are: $T_{N,DSB,I}$ = 2200 K, $T_{N,DSB,II}$ = 1300 K and $T_{N,DSB,III}$ = 950 K [10].

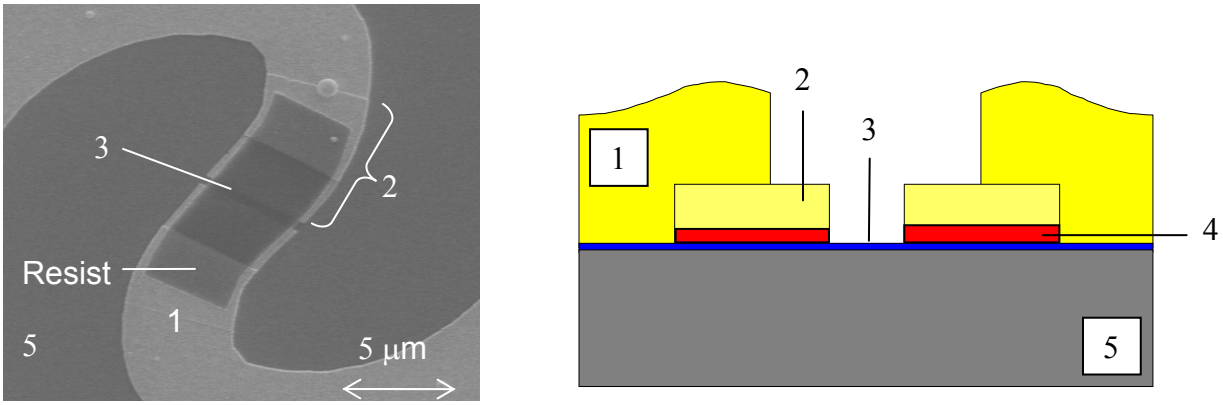

Figure 1. Spiral antenna coupled NbN HEB devices. On the left a SEM picture of the top view of a device and on the right a cross section of the device. "1" indicates the Au spiral antenna structure which is ~ 150 nm thick; "2" the Au layer on the contact pads; "3" the superconducting NbN film, which extends underneath the contact layer/antenna; "4" the intermediate layer between the Au and the NbN film; "5" the Si substrate.

Table 1: Device contact parameters. In all cases a 6 seconds ex-situ O_2 plasma etch is included prior to the contact deposition.

Contact Type	Contact-NbN interface	Contact material
I	No additional cleaning	5 nm Ti + 65 nm Au (Conventional process)
II	15 sec Argon etch	5 nm Nb +45 nm Au (in situ)
III	15 sec Argon etch	10 nm NbTiN + 40 nm Au (in situ)

3. IF gain bandwidth measurement setup.

The IF gain bandwidth is measured using the setup described in Fig. 2. As a signal source we use a carcinotron with a doubler at a fixed frequency of 600 GHz. The signal is combined with that of a BWO as variable LO source by means of a 60 μm Mylar beam splitter. The cryostat has a 0.9 mm HDPE window and 2 Zyteg G104 heat filters. The beam is focused on the device by a hyperhemispherical Si lens. The device is DC biased using a bias T. The IF signal goes through an attenuator before it is fed to a Miteq 0.1 - 8 GHz cryogenic amplifier at 4.2 K with a noise temperature of about 100 K and 30 dB Gain. At room temperature the signal is further amplified and

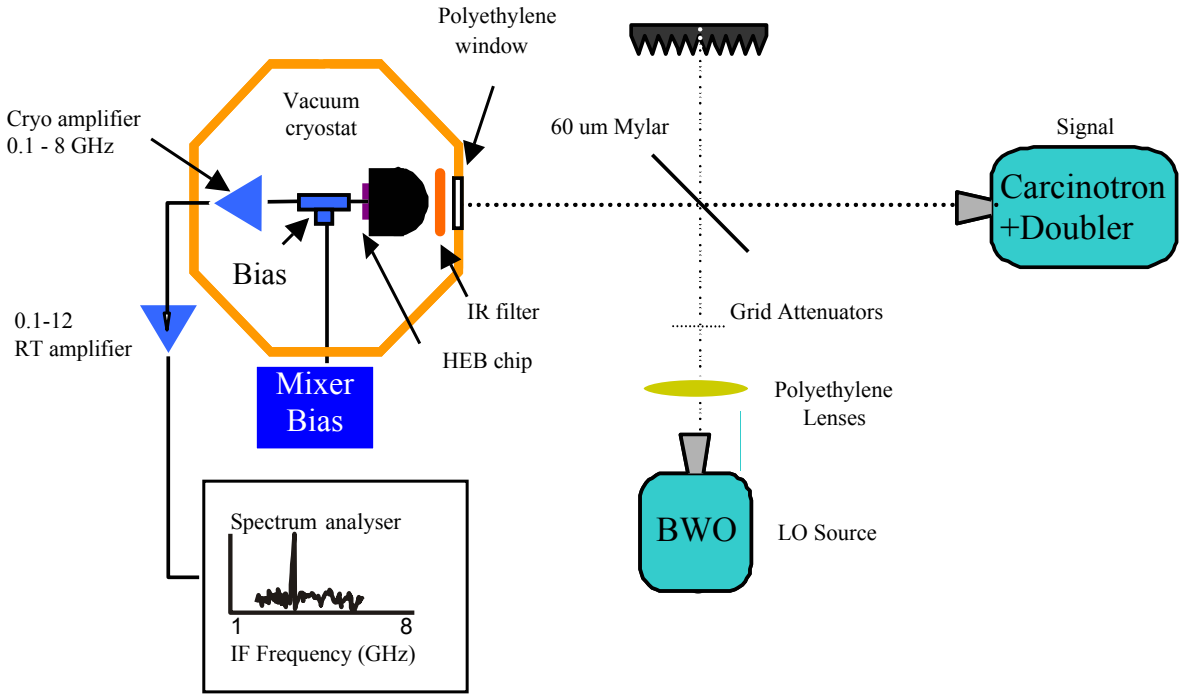

Fig. 2: Measurement setup used to determine the IF gain bandwidth. Essential elements consist of the Signal and LO, which are combined in the beam splitter. This signal is then fed through the cryostat window and heat filter to a lens and focused on the device. The device is biased with a DC voltage bias via the bias T. The resulting signal is subsequently amplified and read out using a spectrum analyzer.

measured using a spectrum analyzer. The amplitude of the IF signal is recorded for different LO frequencies at a fixed signal frequency and care is taken to maintain a constant pumping level of the mixer by monitoring the bias current. The bandwidth is defined as the frequency at which the gain has dropped -3 dB.

The upper frequency limit of our IF chain is measured to be 6 GHz using a SIS junction as a calibrated (shot) noise source. We measure the bandwidth at two bias points: low bias and high bias. The optimum bias point that yields the lowest $T_{N,DSB}$ is called "low bias". We note that the noise temperature is bias dependent and increases at higher bias voltages. The DC voltage for "high bias" (also listed in table 2) is chosen such that $T_{N,DSB}$ is twice the value at optimum bias. The "low bias" point is close to 0.8 mV for all devices. The measurements are given in Fig. 3 and are summarized in table 2.

4. IF gain bandwidth results for different contacts.

Focusing on the bandwidth at optimal bias point, we find for type I an IF gain bandwidth of 2 GHz, shown in Fig. 3 to the left. This is in line with values reported earlier for similar HEB devices [3-5]. Type II shows a higher bandwidth of 3 GHz (not shown in the figure). The highest bandwidth of 6 GHz is measured for the type III contact, shown in Fig. 3 to the right. Table 2 summarizes the measured bandwidths for all device types.

These results show a clear dependence of the bandwidth on the exact contact structure. The largest difference is found between type I and type III devices. It cannot be explained by a difference in film properties such as phonon escape time since all devices are made from a single wafer. It also cannot be attributed to the out-

diffusion of hot electrons due to the improved contact structure since the latter can not contribute more than 0.5 GHz in IF bandwidth. It is worthwhile to mention that the higher IF bandwidth in type III device is consistent with the estimated LO power. The type III device needs 67 % more LO power than the type I device. This indicates stronger phonon cooling for type III devices. Moreover, the measured value of 6 GHz is higher than the maximum bandwidth of 4.5 GHz for a 3.5 nm NbN film on a Si substrate anticipated by Ref. [3].

We now turn to the bandwidth at high bias. For type I devices we observe that the bandwidth increases to 5 GHz for high bias. This is similar to the previously observed bias dependence of the IF bandwidth for similar devices [2, 5]. Note that for device type III hardly any bias dependence is present.

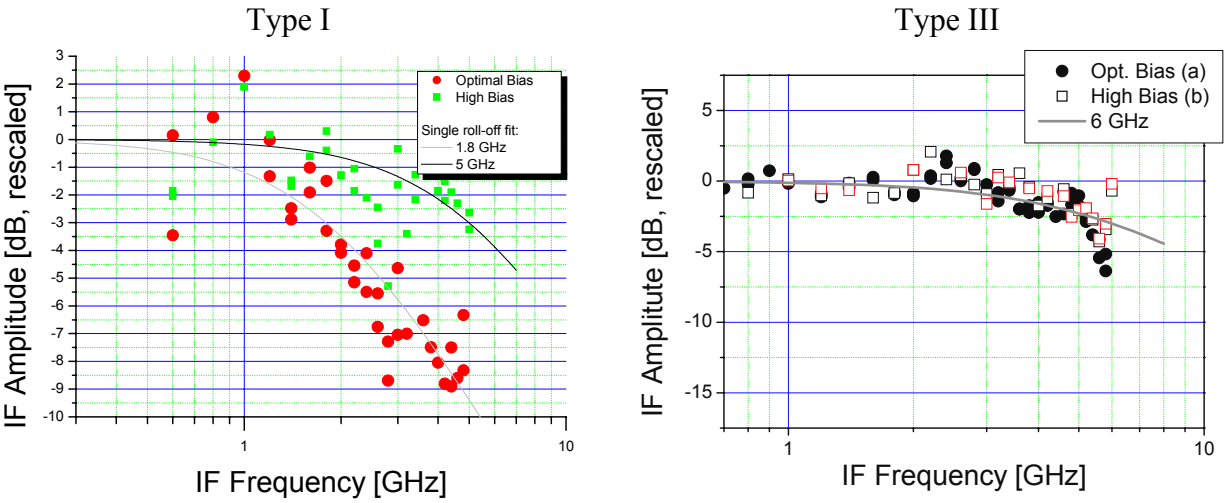

Fig 3: Measured IF amplitude (Relative IF gain). To the left the results for device type I are shown. To the right the results for type III. In both figures the low bias (dots) and high bias (squares) are plotted. The spreading in the data leads to an estimated uncertainty of 1 GHz. The IF bandwidth is defined as the frequency at which the relative IF amplitude is decreased by 3 dB.

Table 2 .Measured IF gain bandwidths at 600 GHz of all device types as described in table 1. The IF gain bandwidth is given for both low and high bias points.

Contact Type	IF Gain Bandwidth at low bias	IF Gain Bandwidth at high bias
I	2 GHz	5 GHz
II	3 GHz	5 GHz
III	6 GHz	6 GHz

5. Calculated IF gain bandwidth by Perrin and Vanneste model

Motivated by these experimental results, we have calculated the thermal time constant and thus the IF bandwidth of an irradiated superconducting film by using the two-temperature model proposed by Perrin and Vanneste [7, 8]. Such calculations, also used previously, are believed to provide a guideline for explaining the observed gain bandwidth and to suggest possible further improvement of the bandwidth.

The modeling closely follows the original derivation by Perrin and Vanneste. The results of the model calculations are shown in Fig. 4. Details will be published elsewhere [11].

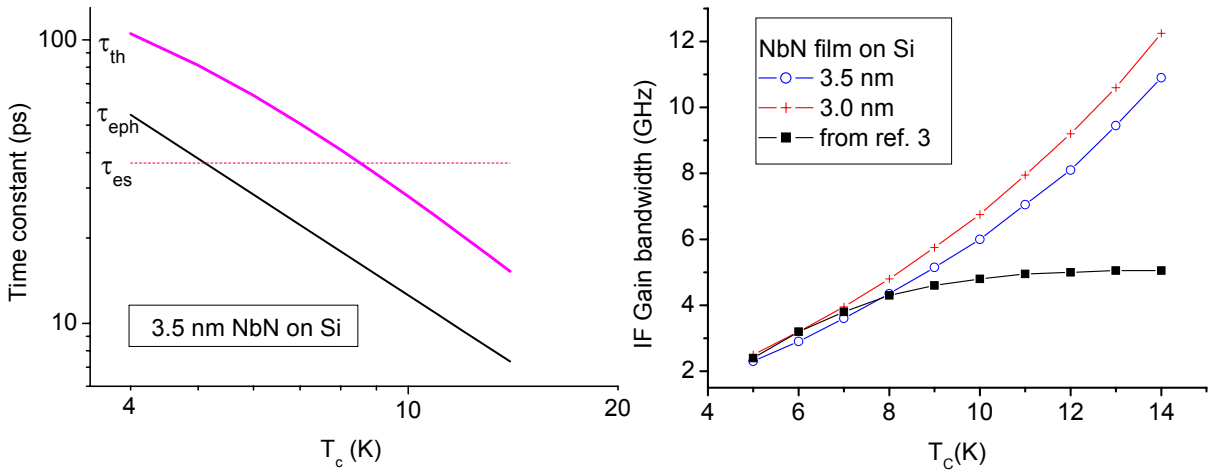

Fig. 4. To the left the dependence of the τ_{es}, the phonon escape time, the τ_{eph} electron phonon relaxation time and the total effective time constant as a function of critical temperature. To the right the IF gain bandwidth as a function of the critical temperature of the film are shown. The black line indicates result of the calculation in Ref. [3]. The crosses give the calculation for a 3 nm NbN film on Si and the connected open circles the calculation for a 3.5 nm NbN film.

In the left graph of Fig. 4 we see the thermal time constant as a function of T_c, the effective temperature for both electrons and phonons, of the devices. Although the phonon escape time is independent of temperature, the thermal time constant still decreases strongly with increasing temperature and becomes significantly shorter than the escape time. Similarly, in the right plot of Fig. 4, we see that the bandwidth increases strongly with temperature, in contrast to the result reported in Ref. [3] in which the bandwidth saturates due to the phonon escape time. Our calculation predicts an IF gain bandwidth of 6 GHz for a 3.5 nm thick NbN film and a T_c of 10 K.

For clarity we like to point out the difference with the modeling in Ref. [3]. Although largely identical, our calculation includes the temperature dependence of the specific heats of both electrons and phonons. Assuming a normal metal, the ratio of the electron heat capacity [12] over the phonon heat capacity [13, 14] rapidly decreases with increasing electron temperature as shown in Fig. 5. Although the escape time for phonons remains constant with increasing temperature, they carry more heat due to their increase of heat capacity, thereby reducing the effective thermal time constant. In the extreme limit where $C_e/C_p \rightarrow 0$, the phonons act as an ideal thermal bath despite of a finite phonon escape time.

To show that the phonon escape time still plays an important role we compare the calculations for a 3.0 with a 3.5 nm NbN film in Fig. 4. The reduction in escape time due to the decrease in thickness corresponds to a significant increase in bandwidth of up to 1 GHz.

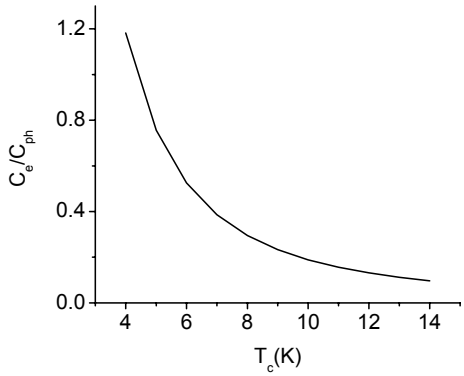

Fig. 5. The ratio of electron heat capacity C_e over the phonon heat capacity C_{ph} as a function of critical temperature. The metal is assumed to be in the normal state and we assume $T_e = T_{ph}=T_c$.

6. Conclusions

In conclusion we have found that the IF bandwidth strongly depends on the HEB contact structure. The improved contacts result not only in improved noise temperatures but also in an enhanced bandwidth. Revisiting the two temperature model of Perrin and Vanneste leads to the result that the calculated gain bandwidth increases strongly with the T_c of superconducting NbN film. The model predicts that a higher electron temperature leads to larger IF bandwidths. The calculation using 3.5 nm and a T_c of 10 K yields the maximum IF bandwidth of 6 GHz, which is consistent with the measured data. However, how the contact structures influence the IF bandwidth remains to be explained. Likely, the contact structures impose a different temperature profile on the NbN bridge, which changes the thermal time. As a by-product of our analysis based on the two temperature model we found the attractive approach to further enlarge the IF bandwidth by increasing the T_c.

Acknowledgments

We wish to thank Willem Jan Vreeling for his skillful assistance during the bandwidth measurements. This work is supported partly by the European Space Agency (ESA) under Contract No. 11653/95/NL/PB.

References

1. Herschel home Page at ESA:http://astro.estec.esa.nl/SA-general/Projects/First/first.html.
2. Yuri B. Vachtomin et al. 13th Int. Symp. on Space THz. Techn., Harvard University, Cambridge, MA, May 26-28, 259 (2002)
3. S. Cherednichenko, P. Khosropanah, E. Kollberg, M. Kroug, H. Merkel, Physica C 372-376, 407 (2002)
4. S. Miki, Y. Uzawa, A. Kawakami, Z. Wang, IEEE Trans. On Appl. Supercon. 11 (1), 175 (2001)
5. Matthias Kroug, "NbN Hot Electron Bolometric Mixers for a Quasi-Optical THz Receiver". Ph.D Thesis, Chalmers University of Technology, Goteborg, Sweden (2001).
6. A.D. Semenov, H.-W. Huebers, J. Schubert, G.N. Gol'tsman, A.I. Elantiev, B.M. Voronov, E.M. Gershenzon, J. Appl. Phys. 88, 6758 (2000).
7. N. Perrin and C. Vanneste, "Response of superconducting films to a periodic optical irradiation", Phys. Rev. B 28, 5150, 1983.
8. N. Perrin and C. Vanneste, "Dynamic behavior of a superconductor under time dependent external excitation", J. Physique. 48, 1311 (1987);
9. M. Hajenius, J. J. A. Baselmans, J. R. Gao, T. M. Klapwijk, P. A. J. de Korte, B. Voronov and G. Gol'tsman "Low Noise NbN superconducting Hot Electron Bolometer mixers at 1.9 and 2.5 THz." Supercond. Sci. Technol. 17 (2004) S224–S228
10. J.J.A. Baselmans, M. Hajenius, J.R. Gao, T.M. Klapwijk, P.A.J. de Korte, B. Voronov and G. Gol'tsman, "Doubling of sensitivity and bandwidth in phonon cooled hot electron bolometer mixers", Applied. Phys. Letters, 84, 1958 (2004).
11. J.R. Gao, J.J.A. Baselmans, M. Hajenius, T.M. Klapwijk, and P.A.J. de Korte, Increased Gain Bandwidth of NbN Hot Electron Bolometer Mixers by Raising the Critical Temperature, (in preparation).
12. Ashcroft and Mermin, Solid State Physics, 1979.
13. A.D. Semenov, R. S. Nebosis, Yu. P. Gousev, M. A. Heusinger, and K. F. Renk, "Analysis of the nonequilibrium photoresponse of superconducting films to pulsed radiation by use of a two-temperature model", Phys. Rev. B 52, 581 (1995).
14. S. Cherednichenko, P. Yagoubov, K. Il'in, G. Gol'tsman and E. Gershenzon, "Large bandwidth of NbN phonon cooled hot-electron bolometer mixers on sapphire substrates", Proc. 8th Int. Symp. on Space Terahertz Technology, Cambridge, MA, 245, 1997.

Characterization of NbTiN Hot Electron Bolometer Mixers at 0.8 THz

Denis Loudkov*, Edward Tong and Raymond Blundell
Harvard-Smithsonian Center for Astrophysics, Cambridge, MA 02138
Krikor Megerian and Jeffrey Stern
Jet Propulsion Lab., California Institute of Technology, Pasadena, CA 91109.

Abstract

We present recent measurements of receiver noise temperature and intermediate frequency bandwidth performed at a local oscillator frequency of 0.8 THz for waveguide NbTiN Hot Electron Bolometer mixers of various dimensions. These devices are fabricated from an NbTiN film deposited on crystalline quartz substrates with an intermediate AlN buffer layer. The lengths of the mixer elements vary from 0.3 to 0.5 μm and their widths vary from 3 to 10 μm. Critical temperatures are typically 8.5 K, and critical current densities are about 13 mA/μm^2. A double side band receiver noise temperature as low as 550 K has been measured at an IF frequency of 1.8 GHz, with a conversion loss of around 14 dB. At the optimum bias point for low noise operation, these mixers have an instantaneous bandwidth of only 1.1 GHz. This may be increased by either overpumping the mixer or increasing the bias voltage. However, such conditions result in increased mixer conversion loss and poorer overall performance.

Introduction

At the present time, there are only two ground-based telescopes equipped with heterodyne receivers designed to operate at frequencies in excess of 1 THz, one in Northern Chile [1] and another at the South Pole [2]. In both cases, NbN thin film phonon-cooled Hot Electron Bolometer (HEB) mixers are employed as the mixing element as they have been proven to offer low noise performance. Furthermore, mixers of this type are currently being developed for receivers to be used in future air- and space- borne missions, such as Hershel and SOFIA, for which the deployment of similar receivers is envisioned [3, 4].

Mixers incorporating thin film NbTiN HEBs have previously demonstrated low-noise performance [5] and could be a good alternative to the NbN devices currently in use for low-noise heterodyne applications. In this paper, we report on the performance of waveguide HEB mixers at between 0.75 and 1.05 THz fabricated from superconducting NbTiN thin film deposited on an AlN buffer layer over crystalline quartz. This study is a continuation of work previously made at lower frequencies 0.6-0.8 THz [5].

Device preparation

The mixers used in this study were all fabricated from a 4 nm thick superconducting NbTiN film. This film was deposited over a 20 nm AlN buffer layer on a Z-cut crystalline quartz substrate by reactive DC sputtering. The buffer layer is used to improve the quality of superconducting film and to provide a better phonon match to the supporting substrate. Crystalline quartz was chosen as the substrate material due to its relatively small dielectric constant and reasonably good thermal properties. The details of device processing are described in [5]. After fabrication, the wafer is lapped to a thickness of 30 μm before dicing into chips, 2 mm long and 0.12 mm wide.

In this investigation, we have made a series of DC and heterodyne measurements using a number of different sized NbTiN micro-bridges with dimensions outlined in Table 1. In essence, the lengths of the mixer elements vary from 0.3 to 0.5 μm and their widths vary from 3 to 10 μm, which results in a device volume variation of a factor of 5.5.

* dloudkov@cfa.harvard.edu

DC characteristics

In Figure 1 we plot the resistance versus temperature curve of a representative NbTiN mixer. The critical temperature is estimated at 8.5 K, and the transition width is about 1 K. This mixer has a critical current of 150 μA at a bath temperature of 4.2 K, which translates to a critical current density of 12.5 mA/μm^2. This is close to the average of 12.7 mA/μm^2 for all of the measured devices from the same wafer.

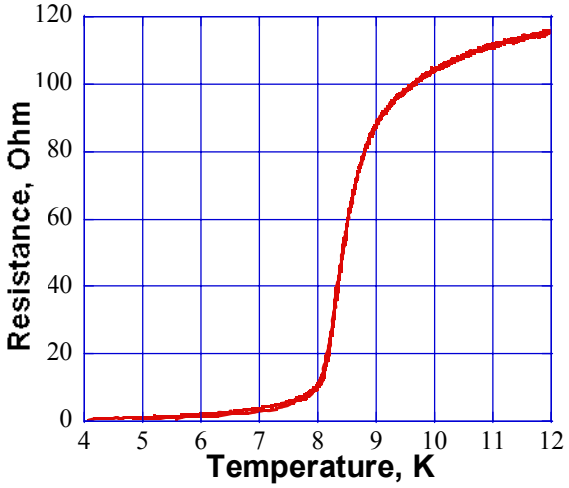

Figure 1: Resistance – Temperature curve of an NbTiN device, 0.3 μm long by 3 μm wide.

In Figure 2 we plot the normal state resistance versus the bridge size, length divided by width, for the set of devices studied. From the figure we obtain a sheet resistance of 1000 Ohms/square. Furthermore, the data is well-fit by a straight line which demonstrates the fact that the NbTiN film is highly uniform.

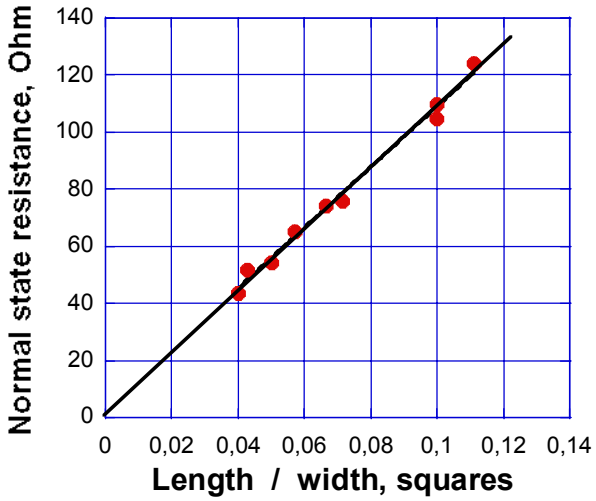

Figure 2: The normal state resistance vs. bolometer size.

Receiver noise measurements

Double side band (DSB) noise temperature measurements have been performed using the standard Y-factor technique with the mixer, a fixed-tuned waveguide structure, mounted in a liquid helium filled cryostat. A Martin-Puplett interferometer was used to combine signal and local oscillator. The signal passes through a vacuum window, made from 0.5 mm Teflon sheet, and two Zitex G-108 infrared blocking filters, mounted on the 77 K shield and on the 4.2 K cold plate, before entering the mixer. This measurement set up is discussed in more detail in [6]. Output from the mixer passes to a low noise intermediate frequency (IF) amplifier, and 1 GHz wide filters are used to select either a 1.8 or 3 GHz center frequency.

Current - Voltage characteristics and IF output power in response to hot and cold loads are presented in Figure 3 for mixer b54n4 (size 0.3 x 7 μm^2). At an IF of 1.8 GHz, the best measured Y-factor is 1.3, which corresponds to a receiver noise of 650 K, and the conversion loss is estimated at 14 dB.

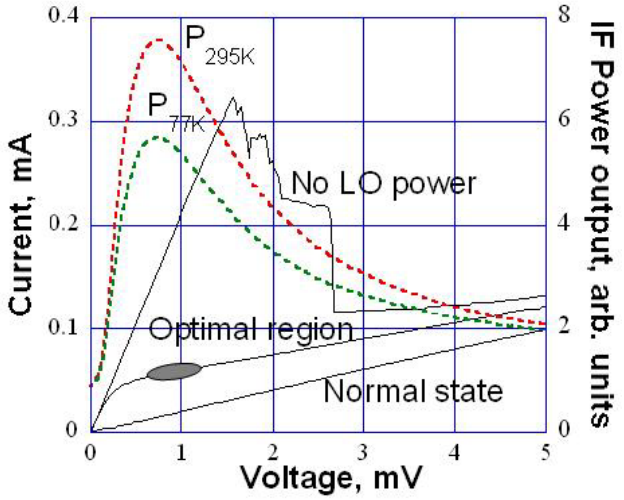

Figure 3: Current – Voltage (I-V) characteristics of an NbTiN HEB mixer b54n4 (see Table 1) with and without LO power at 800 GHz, and in the normal state. The I-V curves were measured using a 2-point measurement set-up in which the series resistance is a few ohms. The shaded region shows optimal bias region for low noise. The dotted lines represent the IF output power as a function of bias voltage in response to hot and cold loads.

Device	Length, μm	Width, μm	Resistance at 295 K, Ohm	Critical Current at 4.2 K, mA	DSB Noise Temperature, (K)*	3 dB roll-off freq., GHz
b54n2	0.3	3	99	0.15	620	1.2
b54n3	0.3	4.5	75	0.23	690	0.9
b54n4	0.3	7	52	0.32	570	0.9
b54n8	0.4	4	88	0.21	790	1
b54n9	0.4	7	62	0.43	680	1.2
b54n10	0.4	10	45	0.53	550	1.2
b54n13	0.5	4.5	110	0.21	700	1.4
b54n14	0.5	7	78	0.31	590	1.3
b53n15	0.5	10	50	0.51	690	1

*Measured at the IF central frequency 1.8 GHz and the bandwidth 1 GHz.

Table 1 DC characteristics and RF performance, measured at LO frequency of 0.8 THz, for the different NbTiN HEB mixers. In all cases, thickness of NbTiN superconducting film is 4 nm.

Also in Table 1 we list the measured DSB receiver noise temperature for all nine devices at an LO frequency of 0.8 THz and an IF center frequency 1.8 GHz. Clearly, the noise performance of these mixers has only weak dependence on the bolometer dimensions. This is not surprising since the bolometer resistance only varies by a factor of two for the devices tested so far. It would be instructive to extend the range of mixer dimensions to include a larger resistance variation.

We have also measured DSB receiver noise temperature across the frequency range: 0.75 to 1.05 THz, and in Figure 4 we plot the noise performance for the 3 GHz IF. Also shown for comparison is the measured noise performance for the 1.8 GHz IF at an LO frequency 0.8 THz. The higher noise temperature at 3 GHz IF is due to the small IF gain bandwidth of these NbTiN mixers (see below). However, the increase in noise temperature (~20 %) is relatively small. From the figure we note that the noise temperature is below 1000 K up to 0.87 THz even with the 3 GHz IF.

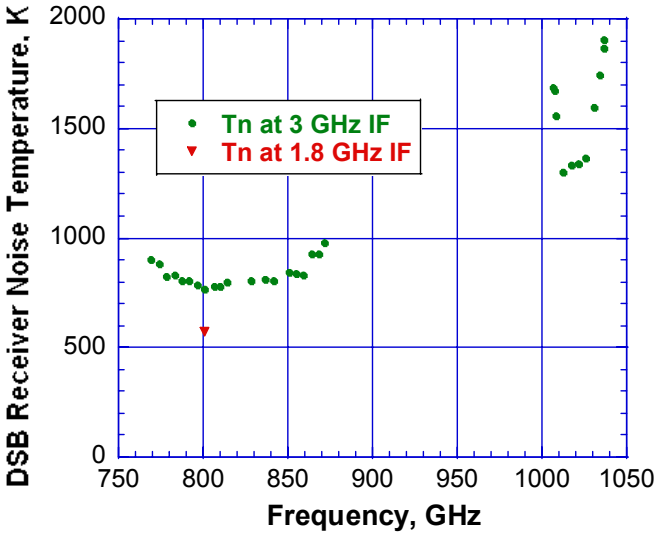

Figure 4: The Double side band receiver noise temperature measured around 0.8 THz and 1.026 THz for the NbTiN mixer with microbridge dimensions 0.3 x 7 μm^2. The circles represent measurements at an IF centered on 3 GHz, and the triangle is for the 1.8 GHz IF. In both cases, the measured bandwidth is 1 GHz.

Bandwidth at high bias

We have also measured the IF gain dependence at the optimal bias point for each of the mixers using a thermal noise source: a ceramic infrared radiating element focused by an off-axis parabolic mirror. This technique has been described previously in [7]. In each case, the experimental data has been fitted to the curve $1/(1+(f/f_{3dB})^2)$, where f_{3dB} is the characteristic 3 dB roll-off frequency. Referring to Table 1, all of the measured devices demonstrate a 3 dB roll-off frequency of about 1.1 GHz at optimal bias point. Since there appears to be no dependence on device length, we conclude that the cooling mechanism for these NbTiN mixers is predominantly via phonons rather than diffusion.

We have also measured the mixer gain dependence at high bias, and in Figure 5 we plot the measured IF output signal as a function of IF at three bias voltages under optimum LO drive. The curves have not been shifted relative to one another. Rather, there is a significant loss in conversion at higher bias voltages, even though the 3 dB roll-off frequency increases from 1 GHz at 1.1 mV bias to 3.7 GHz at 7 mV bias.

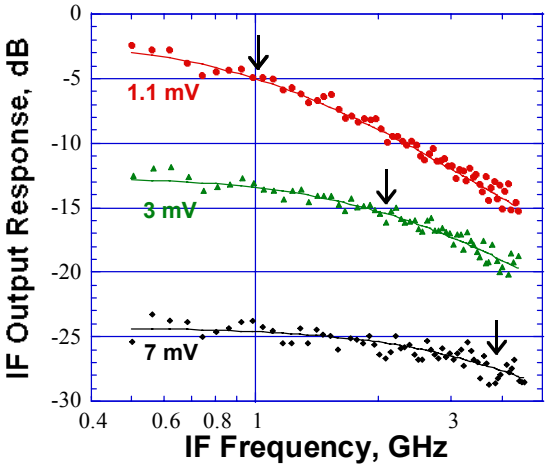

Figure 5: IF gain bandwidth measurements for mixer b54n4 at three bias voltages: 1.1, 3 and 7 mV. The experimental data points are shown and the solid lines give the best fit single pole roll-off of $1/(1+(f/f_{3dB})^2)$ to each data set. The arrows show the fitted 3 dB roll-off frequencies (f_{3dB}).

Conclusion

We have investigated the performance of NbTiN HEB waveguide mixers deposited on AlN buffer layer over quartz have at 0.8 THz. These devices demonstrated good uniformity DC characteristics. A double side band receiver noise temperature of 550 K has been measured at 0.8 THz for a 1 GHz-wide IF centered at 1.8 GHz. Finally, the measured 3-dB IF roll-off frequency is about 1.1 GHz at the optimal bias point, and operation at higher bias a yields higher roll-off frequency but at the expense of increased conversion loss.

Acknowledgment

We would like to thank Matvey Finkel for the useful discussions and assistance in the measurements.

References

[1] D. Marrone, R. Blundell, H. Gibson, S. Paine, D. C. Papa, C.-Y. E. Tong, "Characterization and Status of a Terahertz Telescope." *Proc. of the 15th International Symposium on Space Terahertz Technology*, Northampton, Massachusetts, USA, April 27-29, 2004

[2] K. Yngvesson, C. Musante, M. Rodriguez, Y. Zhuang, E. Gerecht, M. Coulombe, J. Dickinson, T. Goyette, J. Waldmann, C. Walker, A. Stark, A. Lane, "Terahertz receiver with NbN HEB device (TREND) – a low noise receiver user instrument for AST/RO at the south pole." *Proc. of the 12th Intern. Symposium on Space THz Technology*, p.26, San Diego, CA, 2001

[3] S. Cherednichenko, P. Khosropanah, T.Berg, H. Merkel, E. Kollberg, V.Drakinskiy, B. Voronov, G. Gol'tsman, "Optimization of HEB mixer for the Herschel Space Observatory." *Proc. of the 15th International Symposium on Space Terahertz Technology*, Northampton, Massachusetts, USA, April 27-29, 2004

[4] A.Semenov, H.-W. Hubers, H. Richter, M. Birk, M. Krocka, U. Mair, K. Smirnov, B. Voronov, G. Gol'tsman, "Performance of Terahertz Heterodyne Receiver with a superconducting hot-electron mixer." *Proc. of 13th Int. Symp. on Space Terahertz Technology*, p. 229, Cambridge, MA, March 2002,.

[5] C.-Y. E.Tong, J. Stern, K. Megerian, H. LeDuc, T.K. Sridharan, H. Gibson, R. Blundell, "A Low-noise NbTiN Hot Electron Bolometer Mixer." *Proc. of the 12th International Symposium on Space Terahertz Technology*, pp. 253-261, San Diego, CA, 2001.

[6] C.-Y. E. Tong, D. Meledin, D. Loudkov, R. Blundell, N. Erickson, J. Kawamura, I. Mehdi, and G. Gol'tsman, "A 1.5 THz Hot-Electron Bolometer Mixer Operated by a Planar Diode Based Local Oscillator." *2003 IEEE MTT-S Digest*, pp.751-754, vol.2, 2003.

[7] D. Meledin, C.-Y. E. Tong, R. Blundell, G. Gol'tsman, "Measurements of Intermediate Frequency Bandwidth of Hot Electron Bolometer mixers at Terahertz Frequency Range." *IEEE Microwave and Wireless Components Letters*, vol.13, n.11, p.493, November, 2003.

Ultra-Thin Silicon Chips for Submillimeter-Wave Applications

R.B. Bass,[1] J.C. Schultz,[1] A.W. Lichtenberger,[1] R.M. Weikle[1]
S.-K. Pan,[2] E. Bryerton,[2] C.K. Walker,[3] Jacob Kooi[4]

1 - University of Virginia, Charlottesville, Virginia
2 - National Radio Astronomy Observatory Charlottesville, Virginia
3 - University of Arizona, Tucson, Arizona
4 - California Institute of Technology, Pasadena, California

We present a process for fabricating ultra-thin silicon chips for submillimeter-wave mixing applications using SOI (Silicon On Insulator) wafers. Such chips allow the profile of the mixer substrate to be minimized within the microstrip channel, thereby simplifying RF design considerations and minimizing machining constraints. The chips feature gold beam leads, RF filter structures, and hot-electron bolometers as the non-linear element.

We designed a prototype receiver to demonstrate the feasibility of the ultra-thin silicon chip technology. The receiver has a center frequency of 585GHz and accommodates both diffusion-cooled and phonon-cooled hot-electron bolometer mixers fabricated atop an ultra-thin silicon chip. The chip fits within the microstrip channel of a split-block horn antenna. Protruding from the sides and ends of the silicon chip are thick gold beam leads, which provide electrical and thermal contact between the chip and the waveguide block. In addition, the beam leads provide mechanical support to the chip, allowing the chip to be suspended within the middle of the microstrip channel between the two block halves.

Ultra-thin silicon chips with beam leads will facilitate the construction of large format spectroscopic imaging arrays. Such arrays would contain an assembly of individual chips, each featuring a single nonlinear mixing element. The chips could be added, removed of replaced without disturbing the rest of the elements within the array. There are myriad potentials for such systems; examples include atmospheric research, astrophysics, and security systems.

1 Introduction

The bulk of our work at the University of Virginia has centered on the development of niobium-based SIS mixers fabricated atop quartz substrates. These are single-element receivers, which rely on waveguides to couple RF radiation from a feedhorn antenna to a mixer chip [1,2]. Single-element waveguide receivers are standard for SIS- and HEB-based receivers, with the exception of a few arrayed waveguide receivers consisting of SIS mixers [3,4].

Our research group, in cooperation with researchers at the University of Arizona and the California Institute of Technology, has made progress towards integrating HEB mixers atop silicon nitride membranes as another approach for assembling receiver arrays [5]. Integrated arrays offer the benefits of rapid assembly and dense receiver integration since all of the mixers are fabricated atop a single chip. However, all of the devices on the array chip must have similar characteristics. In addition, the silicon nitride membranes must be extremely thin, around 1μm, at which point the membranes are extremely brittle and difficult to handle. Failure of any one of the mixing devices or membranes on a chip would lead to a loss in pixel density, jeopardizing receiver performance and possibly requiring the replacement of the entire mixer array chip.

These problems can be circumvented if each mixing element of an array is fabricated atop a single, smaller chip that could be placed within an array frame. By contacting these ultra-thin chips to the array frame via beam leads, the array can be quickly assembled with pre-tested devices, and later individually removed without disturbing other elements within the array frame [6]. In addition, ultra-thin silicon chips can be used in single-element metal waveguide receivers, greatly reducing the amount of dielectric in the waveguide channel while facilitating rapid prototyping and device replacement.

Ultra-thin chips with beam leads are a potentially powerful technology for THz mixers if several considerations can be met. First, the technology has to be compatible with SIS and HEB fabrication processes. Second, the chips need

to be 1μm to 10μm thick, and must be robust enough to survive receiver assembly and repeated thermal cycling down to cryogenic temperatures. And finally, because these chips are incredibly thin, they will have to be integrated with beam leads in order to mount them in THz mixer blocks or array frames.

Our fabrication process utilizes silicon-on-insulator (SOI) substrates integrated with gold beam leads to achieve ultra-thin silicon chips, and is a unique idea that we first implemented and published in 2003 [7]. Given our earlier work on beam leads for quartz-based millimeter-wave mixers, we realized that the solution to the requirements mentioned above lay in the integration of beam lead technology with SOI substrates [8,9]. Ultra-thin chips can be defined from the device layer of an SOI substrate while the handle layer of silicon provides mechanical rigidity during preceding processing steps.

2 Limitations of THz Receiver Assembly

THz circuits are extremely small and usually fabricated on very thin and fragile substrate materials such as silicon or quartz. As the operating frequency of circuits increases, the size of the circuit housing decreases. In addition, the dimensional tolerances of the circuit housing decreases, making the placement of the circuit both more difficult and more critical. All of these problems make replicating state-of-the-art submillimeter-wave devices extremely difficult. To overcome these difficulties, the circuit mount should be designed so that it is as simple as possible to assemble and non-critical to the function of the circuit. Also, the assembly procedures must be as clear and reliable as possible.

There are several critical design issues that need to be considered when developing both the circuit housing and the assembly procedures for THz receivers. First, improper mounting techniques may mechanically damage chips and circuits. A small displacement of the chip in the receiver block may result in excessive loss, degradation of device sensitivity, or unwanted resonance. A good receiver block design should provide a robust mechanical interface for the fragile circuit. The housing must be simple to fabricate and non-critical to the circuit placement. It should also be easy to assemble, disassemble and reproduce. Second, while mounting submillimeter-wave circuits, any wiring lead or contact becomes a circuit element. An incorrectly sized or misplaced lead may de-tune the circuit or excite unwanted resonance. A small extra length of ground lead may result in decibels of loss. Improper electrical contacts increase circuit loss, degrade device sensitivity and reduce reliability. Third, with HEB's device failure is typically a result of electro-static discharge (ESD). ESD most likely happens during the assembly process when the circuit is exposed to other objects that are on a different electrical potential. To avoid ESD, a suitable assembly environment and a proper mounting procedure need to be established and strictly followed.

This work attempts to address these issues by integrating hot-electron bolometer mixer circuits with new beam lead and ultra-thin chip technologies. Implementing these circuits on ultra-thin chips greatly simplifies the RF design process by limiting the amount of dielectric material within the microstrip channel of the waveguide. The beam leads provide electrical, thermal and mechanical contact between the circuit and the waveguide. Furthermore, a beam lead design reduces the complexity of the microstrip channel structure, and eases the process for making contact between the chip and the mixer block.

3 Submillimeter-wave Circuit Mounting Techniques

There are several ways to mount millimeter and submillimeter-wave circuits into receiver blocks. Conductive adhesive provides electrical contact and thermal heat sinking to some power device packages. After the adhesive is set, however, it is difficult to remove the circuit from the package without incurring damage. Also, applying the appropriate amount of adhesive at the intended places is not a simple task. Other microwave products commonly employ wire bonding and soldering. However, as the operating frequency of circuits increases, the electrical traces of the circuit shrink. Some of the circuit traces of millimeter and submillimeter-wave circuits are so small (less than 25μm) that it is very difficult to make a reliable bond to the circuit. Also, as the frequency increases, the required bond wire length becomes shorter and more critical. This makes attaching the leads to the circuit very difficult. In general, wire bonding and soldering are used to assemble millimeter and submillimeter-wave circuits, but they are not without their share of difficulties.

Conductive adhesive, wire bonding, and soldering all attach leads permanently to the circuit. None are ideal for prototyping tasks where frequent changing of circuits is needed. Several other mounting techniques offer easy

circuit replacement. SIS mixer chips often incorporate micro-spring contacts, which are formed by pressing a narrow (0.125mm in diameter) gold-plated beryllium-copper wire against the circuit contact pad [10,11]. However, micro-spring contacts are usually not as robust as those formed by wire bonding and soldering. Also, the initial fine adjustment of the micro-spring wire is very time-consuming. But since it is very easy to replace a circuit chip in a micro-spring contact package, this method is particularly useful in prototyping low-power dissipation devices.

Another popular mounting technique makes contact between the block and the circuit through conductive wire gasket contacts. This technique offers easy chip replacement capability and provides excellent mechanical, electric and thermal contact to the circuit. For example, our SIS mixer circuits are clamped between the left and right halves of a receiver block in a suspended-substrate stripline configuration. The RF and DC ground leads connect between the substrate and block through gold crush wires (the conductive gaskets). The wires sit atop shoulders that are milled along the lengths of the microstrip channel. The substrate sits atop these wires, with the wires contacting metal pads on the substrate. The wires compress between the block and the metal pads when the two halves of the block are brought into contact. Since the connections are made solely by compressing gold wires, the depth from the top surface of the lower half-block to the shoulder of the substrate channel becomes very critical. This technique has been applied successfully in packaging SIS mixers for many years at NRAO [12,13]. However, due to the difficulties in machining the shoulders along the microstrip channel with the precision required for high frequency applications, it may not be practical to use this technique in submillimeter-wave circuits.

A preferable method for packaging submillimeter-wave circuits is the beam lead technique. The beam lead technique was developed in the 1960's by Marty Lepselter at Bell Labs as a simple and reliable way for connecting integrated circuits to printed circuit boards [14]. In this approach, thick (1μm to 10μm) metal beam leads are formed directly on the circuit during the circuit fabrication process, becoming an integral part of the circuit. The metal lead patterns extend beyond the perimeter of the circuit. The beam lead circuits are usually packaged in a split-block housing. Using the beam lead as a handle, the circuit is picked up and placed into the substrate channel with the extended beam beads positioned along the perimeter of the channel. As a result, the chip is suspended within the middle of the substrate channel. When the two halves of the block are brought together, the beam leads are clamped between the two block-halves. The beam leads provide good thermal and electrical connection to the device, and a rigid physical support for the chip. The beam leads are crushed between the block halves, securing the chip in place within the microstrip channel. The contact force is between the beam leads and the block halves, and not on the chip as other contacting methods require. As a result, beam leads allow for the use of thinner, more fragile substrates that might otherwise break when clamped between two block halves.

4 Design of the 585GHz Test Receiver

The original basis of our design for the 585GHz HEB waveguide mixer block derives from a family of receivers designed by researchers at the Harvard-Smithsonian Center for Astrophysics for the Submillimeter Array (SMA). The basic SMA mixer block design consists of two halves; a feed horn half and a back short half. A quartz substrate containing an SIS junction and low pass filter structures is suspended in a microstrip channel between the two halves, parallel to the block split plane. The feed horn, located in the upper block half, is perpendicular to the split plane. A reduced height waveguide couples the RF and LO radiation from the feed horn to a bowtie antenna structure on the quartz chip. A backshort, located behind the bowtie antenna in the lower block half, terminates the reduced-height waveguide behind the antenna.

The first SMA receiver operates around a center frequency of 200GHz [15,16]. Additional SMA receivers, operating at 300GHz, 450GHz and 600GHz, are scaled versions of the 200GHz receiver [17-19]. Kawamura, et al., designed a similar receiver that operates around 800GHz. This receiver features a phonon-cooled hot-electron bolometer as the non-linear mixing element, and was used in the Heinrich Hertz Telescope atop Mt. Graham in Arizona [20]. Researchers at the Space Research Organization of the Netherlands and Delft University adopted this design as well, and now plan to use their design for bands 3 and 4 of the Heterodyne Instrument for the Far-Infrared (HIFI) on the Herschel Space Observatory [21].

We made several major structural changes when adopting the 585GHz design from the SMA design. First, we replaced the 50μm quartz substrate in the SMA design with an ultra-thin silicon substrate. Second, the quartz substrate in the SMA design sits atop shoulders milled along the sides of the microstrip channel. Since gold beam leads suspend the ultra-thin silicon substrate within the channel, the shoulders are unwarranted. As a result, the

microstrip channel of the 585GHz receiver has a truly rectangular cross-section. We also scaled the dimension of the SMA design by a ratio of 600/585 in order to accommodate the change in operating frequency. And finally, we rotated the orientation of the feed horn so that the length of the feedhorn runs parallel to the mating faces of the block halves. In the SMA designs, the long axis of the feed horn is perpendicular to the mating faces, which requires electroforming and a mandrel in order to define the feed horn. With the feed horn oriented parallel to the block mating faces, the feedhorn antennae becomes easier, and therefore less expensive, to machine.

5 Advantages of Ultra-thin Silicon Chips

Silicon offers several material advantages over quartz for THz substrate applications. First, the rupture modulus of silicon is greater than that of quartz; 135MPa versus 50MPa. As a result, silicon may be thinned more so than quartz before it becomes too brittle to handle. Another advantage of silicon is its higher thermal conductivity, 150W/mK versus 2W/mK for quartz. On the other hand, silicon has a dielectric loss tangent that is nearly 40 times larger. However, due to the much larger thermal conductivity of silicon over quartz, the heat generated within a silicon substrate due to RF propagation dissipates rapidly.

A second disadvantage that silicon has over quartz is its larger dielectric constant, 11.9 versus 3.8 for quartz at 10GHz. As a result, a beam of silicon looks electrically thicker to an RF signal than a quartz beam of equal physical thickness. The square root of the ratio of the two dielectric constants determines the difference in electrical thickness, which for silicon over quartz is a factor of 1.77.

Most importantly for ultra-thin silicon chips, silicon is far more resilient than quartz. Resilience is the ability of a material to absorb energy when deformed elastically. This energy does not contribute to deformation of the material. Rather, the energy is release upon unloading. While silicon and quartz both have similar Young's moduli (179GPa for silicon, 75GPA for quartz), the yield strength for silicon is significantly larger than that of quartz (7GPa versus 50MPa), resulting in a modulus of elasticity for silicon that is far greater than that of quartz, 450MPa versus 17kPa for quartz at room temperature [22]. Virwani et al have shown that Young's modulus for silicon remains unchanged between bulk measurements and measurements made from deflecting nano-scale beams [23].

The modulus of resilience represents the amount of energy a sample can absorb per unit volume before yielding. A 3μm thick silicon chip contains 16 times less volume than a 50μm quartz chip of equal width and length, but can absorb far more energy per unit volume. Ultra-thin silicon chips are therefore far less likely to rupture under applied loads during handling and receiver assembly .

We conducted numerous analytical RF studies on the feasibility of using our ultra-thin silicon chips in THz receiver applications for both single-chip receivers and array antenna structures [24]. The use of an ultra-thin silicon chip as the substrate for THz circuitry greatly simplifies the RF design process. In addition, since shoulders need not be milled within the microstrip channel to accommodate the chip, machining of the receiver block becomes much more straightforward.

6 Fabrication of Ultra-thin Silicon Chips with Beam Leads

The process for fabricating ultra-thin silicon chips with beam leads is discussed in three subsections: (i) beam lead fabrication, (ii) silicon thinning, and (iii) chip definition. In Figure 1, a process diagram outlines the fabrication steps. A batch of ultra-thin silicon chips is defined from a square piece SOI (silicon on insulator) wafer measuring 2cm on a side. A dozen such SOI squares are diced from a larger three-inch SOI wafer, which is supplied by Soitec, Inc. An SOI wafer consists of three layers: the thick handle silicon, followed by a buried oxide layer (BOX), and then the thin device silicon. The ultra-thin chips are ultimately defined from the device silicon layer.

Beam Lead Definition Gold beam leads are electroplated atop the device silicon layer. The beam lead thickness can be varied from wafer to wafer; we have fabricated beam leads ranging in thickness from 1.0μm to 10μm thick. The beam lead structures are defined using AZ4330 positive photoresist and an i-line contact mask aligner. The resist is 4μm thick, allowing for at least several a few hundred nanometers of spacing between the top of the beam leads and the top of the resist. Following resist patterning, the beam leads are plated using Techniq 25E plating solution.

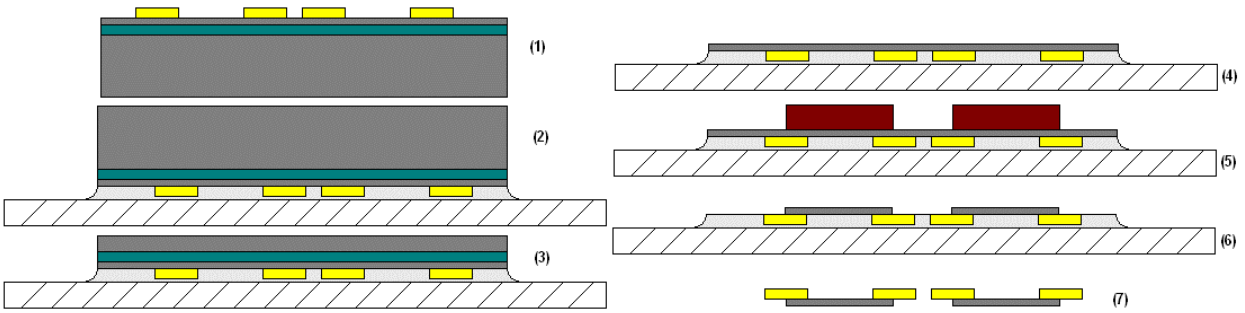

Figure 1 The fabrication of ultra-thin silicon chips with gold beam leads is summarized in seven steps. In (1), beam leads are fabricated atop the device silicon layer of an SOI wafer. The wafer is then mounted, beam lead side down, on to a quartz carrier (2). The handle silicon and BOX layer are then removed using a combination of mechanical lapping (3) and wet etching (4). The exposed device silicon is then patterned with thick photo resist (5), which serves as an etch mask during a reactive ion etching (RIE) process. After the RIE defines the chip extents (6), the individual chips are separated from the quartz carrier (7).

Silicon Thinning After fabricating the beam leads, we remove the handle silicon from the backside of the wafer in a two-step process. First, we thin the bulk of the handle to 30μm by mechanical lapping. Second, we use a silicon wet etch process to remove the remaining 30μm of handle silicon.

Prior to thinning, we mount the silicon wafer, beam lead side down, atop a 250μm thick quartz carrier. The quartz carrier serves as a rigid support for the wafer, which loses most of its mechanical rigidity after the handle silicon has been removed. A clear mounting wax (Stronghold 7036) adheres the wafer to the carrier. The quartz carrier and clear mounting wax allow for a subsequent backside alignment process, which is necessary for aligning the chip extents with respect to the beam leads.

Next, the wafer/carrier pair is mounted atop a thick metal lapping block using the same clear wax. A mechanical pressure jig then planarizes the wafer and carrier with respect to the lapping block [25]. With the wafer, carrier and lapping block inside, the jig is heated to an internal temperature of 120C, which causes the wax to melt. Pressure is uniformly applied to the wafer via a silicon membrane within the jig for 20 minutes. The jig is then cooled to solidify the planarized wafer and carrier atop the lapping block. After cooling, the pressure is released and the wafer is ready for the first step of the thinning process.

A mechanical lapping process removes the majority of the handle silicon. Our lapping system consists of a Techprep Polishing Machine and a Multriprep Positioning Device, both made by Allied High Tech Products, Inc. A 30μm grit diamond lapping film reduces the handle silicon to within 30μm +/- 5μm of the BOX layer.

A wet etch solution removes the remaining handle silicon. The etchant consists of TMAH (tetramethyl ammonium hydroxide, $(CH_3)_4NOH$), diluted to 8% by weight in de-ionized water, and heated to 60C +/- 3C [26]. The BOX layer serves as an etch stop; the high selectivity of the TMAH etchant between silicon and silicon dioxide ensures that the BOX layer protects the underlying device silicon from the heated etchant.

The etch rate depends significantly upon temperature, and increases considerably with increasing etchant temperature [27,28]. However, the etchant is maintained at a temperature no higher than 60C because the clear mounting wax will soften and re-flow at temperatures beyond 70C. When the handle silicon is etched to within a few microns of the BOX layer, the membrane becomes extremely delicate. At this stage, the thin film may crack and peel if perturbed by flowing wax. At 60C, the wax does not free-flow, yet the etchant is heated sufficiently to maintain a reasonable etch rate.

Silicon Etching After removing the handle silicon, an etch mask is patterned on the backside of the wafer in preparation for reactive ion etching of the device silicon. The etch mask defines the individual chip extents, so it must withstand the high energy ion bombardment and chemical attack associated with the reactive ion etch of the device silicon. Etching of silicon with this chemistry is discussed in detail by Rangelow, et al [29].

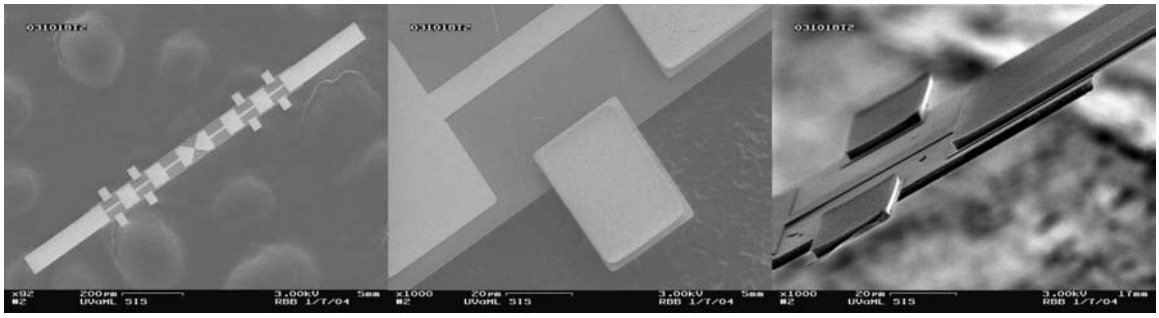

Figure 2 The left-most micrograph shows a top-down view of an ultra-thin silicon chip with beam leads and integrated RF circuitry. The middle micrograph shows a close-up of a structural beam lead, while the right-most micrograph shows a 3µm thick silicon chip with 2µm thick gold beam leads of various lengths protruding from the perimeters. The longest beam lead extends 250nm beyond the edge of the silicon.

The BOX layer is removed by an HF-based wet etchant prior to photoresist patterning. In order to withstand the RIE conditions, a photoresist mask several microns thick is patterned on the exposed device silicon. For this work, we use 4µm AZ4330 photoresist, which can withstand the extended etch periods and energetic etch conditions associated with the Rangelow etch. These resists etch at a rate of around 80nm/min.

After etching, the individual chips are removed from the quartz carrier by rinsing in acetone, which dissolves the mounting wax. The chips separate from the carrier and collect on a piece of filter paper. Three SEM micrographs of completed chips with beam leads and RF circuitry are shown in Figure 2.

7 Conclusion

In order to determine the feasibility of using ultra-thin silicon chips in the microstrip channel of a THz receiver, we mounted several of these chips within our 585GHz mixer blocks, then cooled the blocks to 4.2K in a cryostat. All of the chips featured NbN p-HEBs as the non-linear mixing element, which allowed for current-voltage (I-V) and resistance-temperature (R-T) curves to be measured. These measurements established the presence of electrical continuity through the chips, as well as the non-linear response of the p-HEBs with respect to temperature and current, implying that the chips remain whole and in electrical contact with the block after assembly and cool-down. At the time of writing this paper, RF noise measurements were just beginning to e set up.

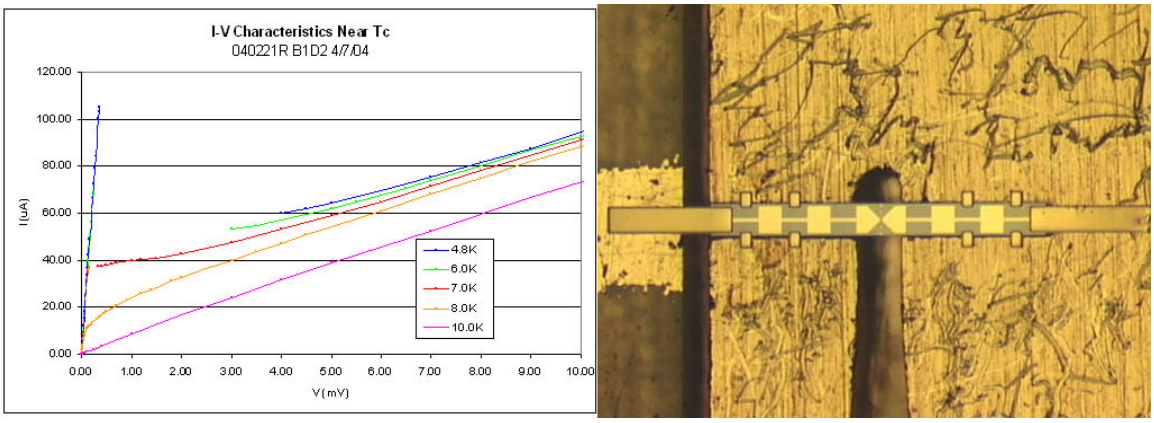

Figure 3 (Left) Current-Voltage curves from a device mounted within the 585GHz HEB receiver block resemble the curves presented in Figure 1. The batch from which this device was drawn has average dimensions of 164nm long, 4.05µm wide and 4nm thick. The critical current at 4.8K is 105µA, giving a critical current density of $0.66 \times 10^6 A/cm^2$. A 3Ω series resistance is introduced through the measurement connections and the IF filter structures on the ultra-thin silicon chip, as indicated by the steep I-V response observed while the bolometer is superconducting. (Right) An ultra-thin silicon chip rests atop the microstrip channel of our 585GHz test receiver. The beam leads contact the mounting face of the split-block receiver, suspending the chip within the middle of the waveguide channel.

Current-voltage curves from cryogenic testing of a NbN device mounted within a mixer block are shown in Figure 3. We measured I-V curves at several temperatures around the transition region of the R-T curve. The I-V curves presented in Figure 3 demonstrate a self-heating affect within the bolometer that causes a non-linear response for temperatures below T_c. In particular, the curves plotted at 4.8K, 6K and 7K all show that the device superconducts until the current within the device exceeds the critical current density. These three curves also demonstrate the self-heating affect where current flow, less than the value of the critical current, dissipates enough heat within the normal-state microbridge to maintain a local temperature above the critical temperature. These I-V measurements demonstrate our ability to fabricate hot-electron bolometers on ultra-thin silicon chips with beam leads, mount those chips within the microstrip channel of a metal waveguide block, and cool the entire assembly down to liquid helium temperatures.

We developed a process for fabricating ultra-thin silicon chips based on SOI substrates that has yielded robust detector chips as thin as 1.6μm. This process also permits the definition of non-rectangular chip geometries with control of final chip dimensions to better than +/-2um. The chips feature RF circuitry, including filter choke segments and bowtie antennae. We have demonstrated ultra-thin silicon chips as long as 2mm (1.6μm thick) and gold beam leads as long as 250μm (1μm thick).

Importantly, the beam leads allow ultra-thin silicon chips to be incorporated into the design of terahertz receivers. There exist no circuit contacting methods capable of providing robust electrical continuity to an ultra-thin silicon chip that would not damage the chip or secure it permanently to the receiver housing except beam leads. By using beam leads to secure ultra-thin silicon chips within a microstrip channel, the complexity of the microstrip channel is reduced from an RF design standpoint because most of the microstrip channel volume may be assumed to be vacuum. Current terahertz mixer designs must consider the effects of a thick dielectric substrate inside the microstrip channel when analyzing the propagation and mixing of signals within the receiver. When using ultra-thin silicon chips to position the submillimeter-wave circuitry within the microstrip channel, only 3μm or less of silicon need be considered instead of tens of microns or more of quartz. The machining of waveguide components is also greatly simplified when using ultra-thin silicon chips since complex structures need not be machined within the waveguide channel in order to support thick quartz chips, conductive wire gaskets, or other non-ideal structures that would require the microstrip channel shape to deviate from rectangular. Our ultra-thin silicon beam lead technology is also an excellent match with our existing laser micromachining capabilities at the University of Arizona. We are presently working on non-rectangular SOI chip array designs with asymmetric IF/ground mounts scalable to several THz.

8 References

[1] A. R. Kerr, S.-K. Pan, E. F. Lauria, A. W. Lichtenberger, J. Zhang, M. W. Pospieszalski, N. Horner, G. A. Ediss, J. E. Effland, R. L. Groves, *15th Inter. Symp. Space THz Tech.*, Northampton, MA, April 2004

[2] S.-K. Pan, A. R. Kerr, M. W. Pospieszalski, E. F. Lauria, W. K. Crady, N. Horner, Jr., S. Srikanth, E. Bryerton, K. Saini, S. M. X. Claude, C. C. Chin, P. Dindo, G. Rodrigues, D. Derdall, J. Z. Zhang, A. W. Lichtenberger, *15th Int. Symp. Space THz Tech.*, Northampton, MA, April 2004

[3] C.E. Groppi, C.K. Walker, D. Golish, A. Hedden, G. Narayanan, A.W. Lichtenberger, *Astronomical Telescopes and Instrumentation 2002: Topics in Astronomy: Information Technologies, MMW and Sub-MMW Detectors, Solar Astrophysics, Non-EM Astronomy, Exo-Planet Detection, and Astrobiology*, Waikoloa Village, HI, Aug. 2002

[4] C.K. Walker, C.E. Groppi, C.Y. Drouet d'Aubigny, C. Kulesa, A. Hedden, D. Golish, D.E. Prober, S. Yngvesson, J. W. Kooi, A. W. Lichtenberger, *Astronomical Telescopes and Instrumentation 2002: Topics in Astronomy: Information Technologies, MMW and Sub-MMW Detectors, Solar Astrophysics, Non-EM Astronomy, Exo-Planet Detection, and Astrobiology*, Waikoloa Village, HI, Aug. 2002

[5] A. Hedden, C. K. Walker, D. Golish, C. Drouet d'Aubigny, C. Groppi, C. Kulesa, D. Prober, J. W. Kooi, G. Narayanan, A. Lichtenberger, A. Datesman, *15th Inter. Symp. on Space THz Tech.*, Northampton, MA, April 2004

[6] A. Hedden, C. K. Walker, D. Golish, C. Drouet d'Aubigny, C. Groppi, C. Kulesa, D. Prober, J. W. Kooi, G. Narayanan, A. Lichtenberger, A. Datesman, *15th Inter. Symp. on Space THz Technology*, Northampton, MA, April 2004

[7] J.W. Kooi , C.D. d'Aubigny , R.B. Bass, C. Walker, A.W. Lichtenberger, "Broad Bandwidth Suspended Membrane Waveguide Transition for use in Silicon Micromachined Mixer blocks at THz Frequencies," *14th Inter. Symp. on Space THz Tech.*, Tucson, AZ, April 2003
[8] R.B. Bass, A.W. Lichtenberger, R. Weikle, J.W. Kooi, C.K. Walker, S.-K. Pan, *6th Euro. Conf. on App. Supercond.*, Sorrento, Italy, Sept. 14, 2003
[9] R.B. Bass, J.C. Schultz, A.W. Lichtenberger, C. Walker, J. Kooi, *14th International Symposium on Space THz Technology*, Tucson, AZ, April 2003
[10] Y. Taur and A. R. Kerr, *App. Phys. Lett.*, 32 **11**, 775-777, 1978
[11] C. E. Tong, R. Blundell, S. Paine, D. C. Papa, J. Kawamura, X. Zhang, J. Stern and H. G. LeDuc, *IEEE Trans. Micro. Theory and Tech.*, 44, 1548-1556, 1996
[12] A. R. Kerr, S.-K. Pan, S. Whiteley, M. Radparvar and S. Faris, *IEEE Inter. Micro. Symp. Digest*, 851-854, 1990
[13] A. R. Kerr, S.-K. Pan and A. W. Lichtenberger and D. M. Lea, *IEEE Micro. Guided Wave Lett.*, 2 **11**, 454-456, 1992
[14] M.P. Lepselter, *Bell Laboratories Record*, 299-304, Oct., 1966
[15] R. Blundell, C.-Y.E. Tong, D.C. Papa, R.L. Leombruno, X. Zhang, S. Paine, J.A. Stern, H.G. LeDuc, B. Bumble, *5th Inter. Symp. on Space Terahertz Tech.*, Ann Arbor, MI, 27-37, 1994
[16] R. Blundell, C.-Y.E. Tong, D.C. Papa, R.L. Leombruno, X. Zhang, S. Paine, J.A. Stern, H.G. LeDuc, B. Bumble, *IEEE Trans. Micro. Theory and Tech.*, 43 **4**, April 1995
[17] C.E. Tong, R. Blundell, S. Paine, D.C. Papa, J. Kawamura, X. Zhang, J.A. Stern, H.G. LeDuc, *IEEE Trans. on Micro. Theory and Techn.*, 44 **9**, Sept. 1996
[18] R. Blundell, C.-Y.E. Tong, J.W. Barrett, J. Kawamura, R.L. Leombruno, S. Paine, D.C. Papa, X. Zhang, J.A. Stern, H.G. LeDuc, B. Bumble, *6th Inter. Symp. on Space Terahertz Tech.*, Pasadena, CA, 123-133, March 1995
[19] C.-Y.E. Tong, R. Blundell, D.C. Papa, J.W. Barrett, S. Paine, X. Zhang, J.A. Stern, H.G. LeDuc, *6th Inter. Symp. on Space Terahertz Tech,* 295-304, Pasadena, CA, March 1995
[20] J. Kawamura, R. Blundell, C.-Y.E. Tong, D.C. Papa, T.R. Hunter, S. Paine, F. Patt, G. Gol'tsman, S.Cherednichenko, B. Voronov, E. Gershenzon, *IEEE Trans. Micro. Theory and Tech.*, 48 **4**, April 2000
[21] G. de Lange, B.D. Jackson, M. Eggens, H. Golstein., W.M. Laauwen, L. de Jong, S. Kikken, C. Pieters, H.. Smit, D. Van Nguyen, M. Kroug, T. Zijlstra, T.M. Klapwijk, *14th Inter. Symp. on Space Terahertz Tech.*, Tucson, AZ, April 2003
[22] K.E. Peterson, "Silicon as a Mechanical Material," *Proceedings of the IEE*E, pp. 420-457, 70 (5), 1982
[23] K.R. Virwani, A.P. Malshe, W.F. Schmidt, D.K. Sood, "Young's modulus measurements of silicon nanostructures using a scanning probe system: a non-destructive evaluation approach," *Smart Materials and Structures*, 12, pp. 1028-1032, December 2003
[24] J.W. Kooi**,** C.K. Walker, and J. Hesler, "A Broad Bandwidth Suspended Membrane Waveguide to Thinfilm Microstrip Transition", *9th Inter. Conf. on Terahertz Electronics*, Oct. 2001
[25] W.L. Bishop, D.M. Summers and A.W. Lichtenberger, "Precision Techniques for Whole Wafer Dicing and Thinning of Superconducting Mixer Circuits," *IEEE Transactions on Applied Superconductivity*, 11 (1), pp. 171-174, March 2001
[26] O. Tabata, R. Asahi, H. Funabashi, K. Shimaoka, S. Sugiyama, "Anisotropic Etching of Silicon in TMAH Solutions," *Sensors and Actuators A*, 34, pp. 51-57, 1992
[27] P.-H. Chen, H.-Y. Peng, C.-M. Hsieh, M.K. Chyu, "The Characteristic Behavior of TMAH Water Solution for Anisotropic Etching of Both Silicon Substrate and SiO_2 Layer," *Sensors and Actuators A*, 93, pp. 132-137, 2001
[28] I. Zubel, M. Kramkowska, "The Effect of Isopropyl Alcohol on Etching Rate and Roughness of (1 0 0) Si Surface Etched in KOH and TMAH Solutions," *Sensors and Actuators A*, 93, pp. 138-147, 2001
[29] I.W. Rangelow, P. Hudek, F. Shi, "Bulk Micromachining of Si by Lithography and Reactive Ion Etching (LIRIE)," *Vacuum*, 46, pp. 1361-1369, 1995

A Gaussian Beam Measurement Range for MM and Sub-MM Receivers

M. Pantaleev, V. Belitsky, K. Ermisch, M. Fredrixon, M. Svensson
Group for Advanced Receiver Development
Chalmers University of technology
SE41296, Gothenburg, Sweden

Introduction

The European Space Agency Far Infra Red and Sub-millimeter Telescope, "Herschel Space Observatory" [1] - the mission formerly known as FIRST - is a corner-stone mission with the planned launch date in the year 2007. The Heterodyne Instrument for the Far-Infrared (HIFI) [2] of FIRST covers 470 to 1200 GHz frequency band with two additional bands around 1.6 and 1.9 THz. The Instrument that uses Gaussian beam optics (quasioptics), combines the beams from the receiver channel frontends and matches this multi-frequency, multi-element receiver to the main telescope mirror. The importance of the quasioptical system for the overall instrument performance is clearly understandable from the fact that it is placed between the receiver and the antenna, and therefore any (extra) loss will directly increase the system noise temperature and be detrimental to the entire instrument performance. In order to build this instrument the HIFI team needs a testing facility to characterize the beams of the mixer assemblies / subassemblies of the Heterodyne Instrument. The Instrumentation Group of the Onsala Space Observatory has committed and built such a testing setup for measuring the mixer sub-assemblies' beams. Besides the measurement of the input beam of the mixer subassembly (MSA), a basic unit of the HIFI receiver, the measurements should produce accurate data on the beam waist position and its size in absolute coordinate system referred to the MSA reference point. In order to achieve the required performance and obtain data on the waist position we use scalar method of measurement, which includes several scans across the axis of the receiver beam and further data processing to extract the waist size and position. The measurement procedure includes triangulation in order to couple the scanner-referenced coordinate system of the probing source to the reference installed on the mixer subassembly bracket situating at 4 K ambient temperature. To avoid interference of the measurements with vacuum cryostat window the entire measurements are done under vacuum. The system realization is described in details in [3, 4, 5].

Measuring Technique and Hardware

The general idea of the measurements is to move a probe source radiating within the band of the receiver under test (MSA) across its input beam, as it is shown schematically in Figure 1. The quantity that is then measured is the power-coupling coefficient [6]

$$|C_{21}|^2 = \iint dy\,dx\, E_{\mathrm{MSA}}(r)\, E^{*}{}_{\mathrm{Source}}(r)$$

where E_{MSA} and E_{Source} are the electric field amplitudes of the MSA and the Source.

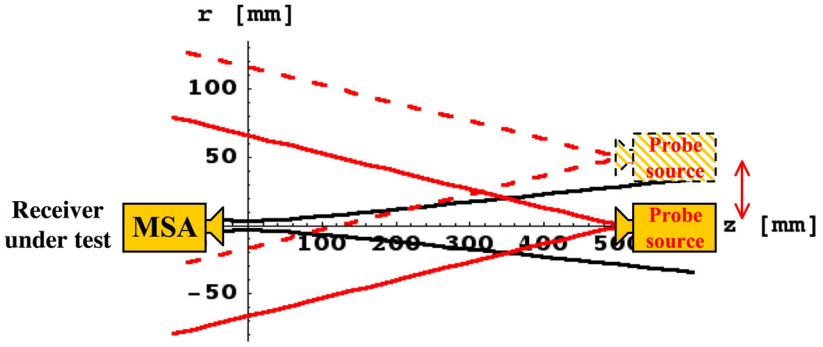

Figure 1. Illustration of the beam-profile measurement.

In order to provide all-in-vacuum measurements to avoid interference of the measuring with the vacuum windows and absorption of the probe signal in the air the entire measurement setup is placed into two vacuum vessels connected via a gate-valve of about 30 cm of diameter and having separate pumping facilities, Figure 2. The larger chamber contains a precision scanner employing hexapod mechanism, which is mounted on a linear stage with position accuracy of <40 μm in *x*-,*y*- and z-direction. On the centre of the hexapod platform, a probing source has been mounted. Using the hexapod, it can be moved in the *x*-*y* plane in few μm steps up to +/- 150 mm. Further rotational stages enable rotations of the source around the *x*- and *y*-axis up to angles of 20°. Movements along the *z*-axis, which coincides almost with the beam-axis, can be performed using the linear stage with high precision. Measurements of the beam can be done at distances between approximately 600 mm and 1050 mm from the beam waist. The source used for the first measurements was a Gunn-chain [7] operating at 480 GHz. The source was phase locked to external commercial synthesizer. The corrugated horn of the source was constructed to simulate a point-source [8]. To avoid overheating of the source, when operated in vacuum, cold nitrogen gas flashed through the pipe system and the source bracket providing the temperature controlled within 0.3° C. To diminish effects due to reflections, the larger vacuum-chamber walls are protected with plates covered by a combination of silicon-carbide grains and Stycast [9].

The second, smaller, vacuum-chamber contains a cryostat, which accommodates the MSA to be measured and, for the HIFI MSAs, the second stage cryogenic amplifier. The cryostat consists of a liquid nitrogen (LN_2) cooling stage at 77 K and a liquid helium (LHe) cooling stage at 4 K. The MSA itself is mounted on the bottom of the LHe cooling plate. Further, we used a grid to inject the LO signal into the MSA beam with LO-power transmitted through the grid dumped by an absorbing plate made also from Stycast and silicon carbide. During the measurements, when the cryostat is cooled down to 4K, the cryostat itself acts as a cryo-pump and the turbo-molecular pump can be turned off to avoid vibrations. Typical operational pressures are about 10^{-7} mbar.

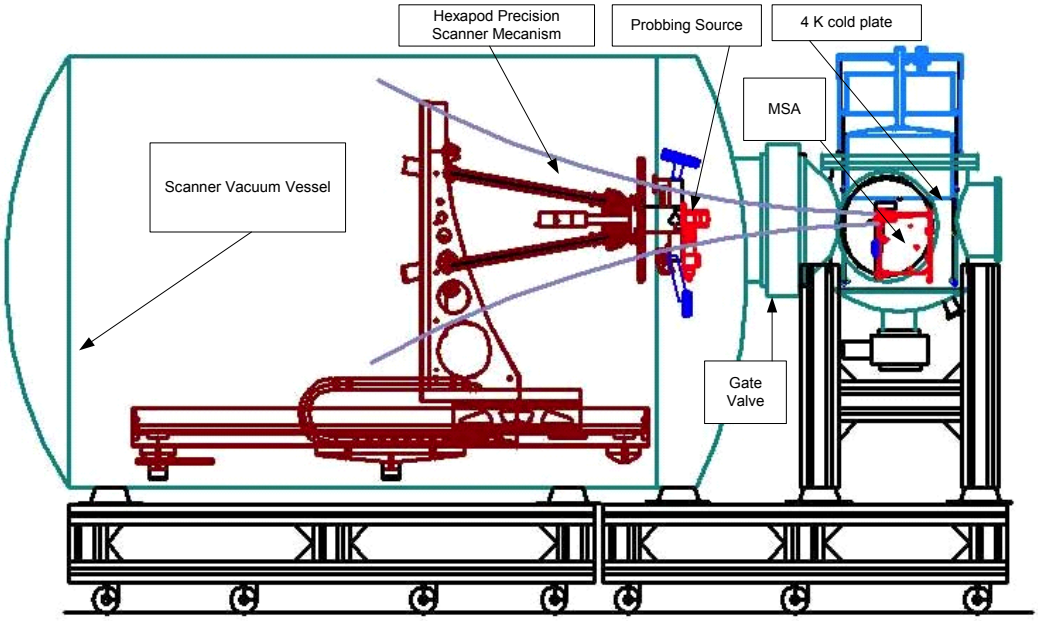

Figure 1. Setup of the measurement range for quasi-optical beam characterization at GARD.

The local oscillator itself is mounted outside the small vacuum chamber containing the MSA and coupled into the vacuum-chamber via a Teflon-window. For the measurements with DM of MSA band 1, a Carcinotron was used. The Carcinotron was operated at a frequency of 484 GHz, leading to an intermediate frequency (IF) of ~ 4 GHz. For the measurements of DM of MSA band 2, a backward-wave oscillator was used operated at a frequency of 644 GHz, leading also to an IF of ~4 GHz.

For absolute position determination, an in-house developed laser-triangulation system is used [3]. It consists of two diode-lasers and two PSDs mounted on the hexapod platform next to the source. A reference mirror is mounted on

the bracket of the MSA,. The position of one corner of this rectangular mirror has been measured within μm accuracy with respect to the centre of the aperture for the input beam in the bracket holding the MSA. Using the triangulation system, the position of the hexapod with respect to the aperture in the MSA-bracket can be determined. A second mirror for calibration purposes is mounted on the linear stage of the hexapod. The positions of the second mirror and of the bracket holding the source were measured by the Swedish Metrological Institute using a laser-tracking system. During each cool-down of the MSA, the triangulation system is used to calibrate the hexapod against the position of the MSA. The level of overall accuracies reached with this laser-triangulation system are presently about 400 μm. However, accuracies of <300 μm in the direction transversal to the axis of beam-propagation should be feasible.

Measurement Results and Discussion

Several measurements were done testing the general response of the system and the repeatability. Furthermore, tests for standing waves and the stability of the system were performed. An example of the data for the test of standing waves is shown in Figure 3. Here, a scan along the *z*-direction (i.e., the axis of beam-propagation) was performed along 20 mm at an initial distance of about 780 mm from the beam-waist. The scan was performed at fixed *x*- and *y*-positions of *x*=-12 mm and *y*=8 mm, the approximate centre of the beam at this distance from the beam-waist. Several more scans were performed at different *x*- and *y*-positions and at different distances from the beam-waist. The results shown in Figure 3 show standing wave patterns due to the source or the LO which are of the order of 0.1 dB (at this *x, y* - position). The Fourier-transform of the signal, also shown in Figure 3, shows a peak at 32 cm^{-1}, which corresponds to 960 = 2x 480 GHz. This indicates that the origin for the standing waves are reflections in the signal-path of the source or the LO. To account for the standing waves, the measurements of planar scans, starting with the DM of MSA2 was done at two adjacent planes, which are shifted by a quarter of the corresponding wavelength, thus eliminating in the average the effect of standing waves.

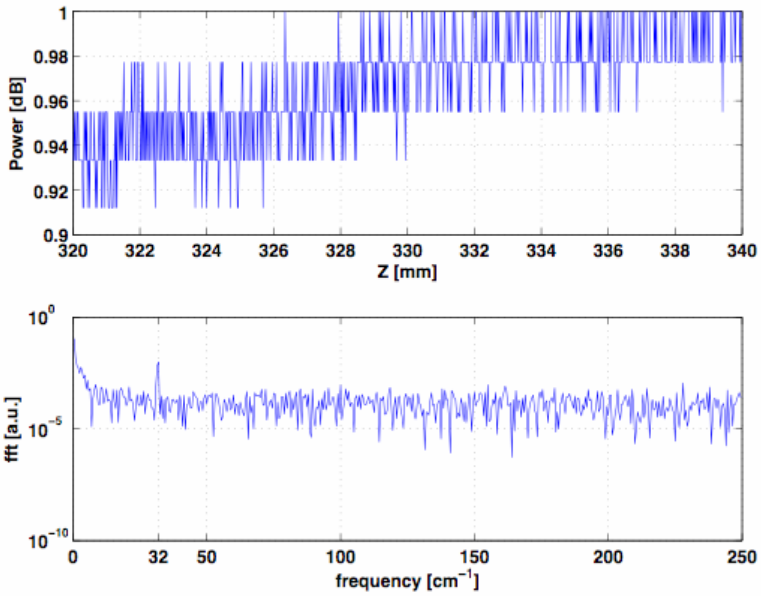

Figure 3. Standing wave test. The measurement for constant *x* and *y* along the *z*-axis, showing a standing wave ripples. In the upper plot, the measured data are shown, in the lower plot, the spectra (FFT) of those data.

Further tests were done of the overall signal stability, shown in Figure 4. This measurement was performed at a fixed position of the hexapod near the centre of the beam, while the power was monitored for about 30 minutes. The standard deviation here is about 0.1 dB, which is probably due to the free-running source of the LO signal. The Fourier-transform of the signal shows only white noise at a very low level.

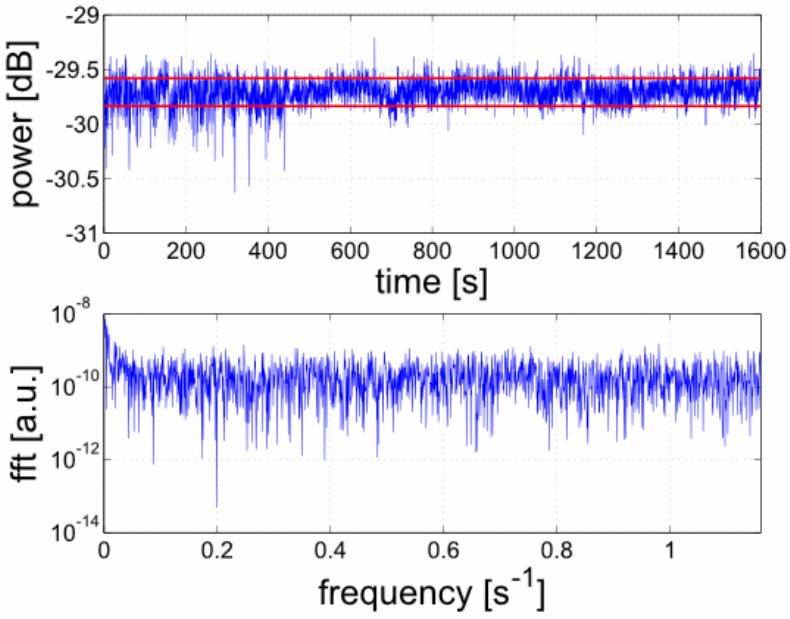

Figure 4. Stability test of the power at a fixed hexapod-position as a function of time (the upper plot). The lower plot shows the spectra (FFT) of the power stability data of the above plot.

In Figures 5 and 6, the contour plots of the raw measurements are shown for MSAs Band 1 and Band 2 respectively. For both bands, the maximum power of the beam profile was measured about 25-30 dB above the noise-floor. The contour plots show a Gaussian peak with a slight asymmetry in the *y*-direction. The measurement for MSA Band 1 shown in Figure 5 was performed at a distance of ~700 mm from the beam-waist. The measurements for MSA Band 2 shown in Figure 6 were performed at 622, 722 and 902 mm from the MSA-aperture.

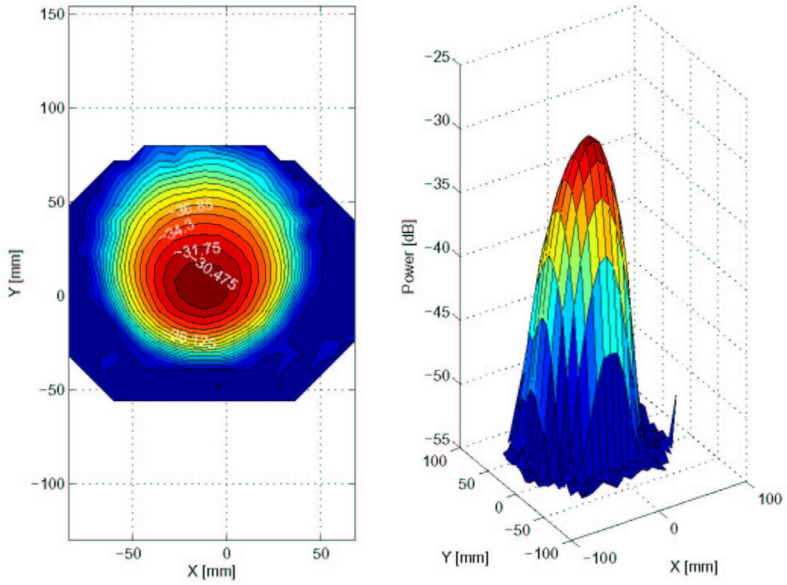

Figure 5. Beam-profile measured for the demonstration model of MSA band 1 about 700 mm from the position of the beam-waist.

For DM of MSA band 1, the direction of the beam-axis and the point of intersection of the beam-axis with the aperture-plane of the MSA bracket were determined from the data [4]. The calibration of the triangulation of those measurements was done using an external calibration mirror, which involved removing the bracket holding the

source from the vacuum-chamber. The results apparently contain a systematic uncertainty due to the triangulation system, as has been observed by comparison to the measurements done at SRON [10]. For DM of MSA band 2, preliminary results for the beam axis and the intersection in the aperture plane were obtained. However, the internal calibration mirror is still being commissioned.

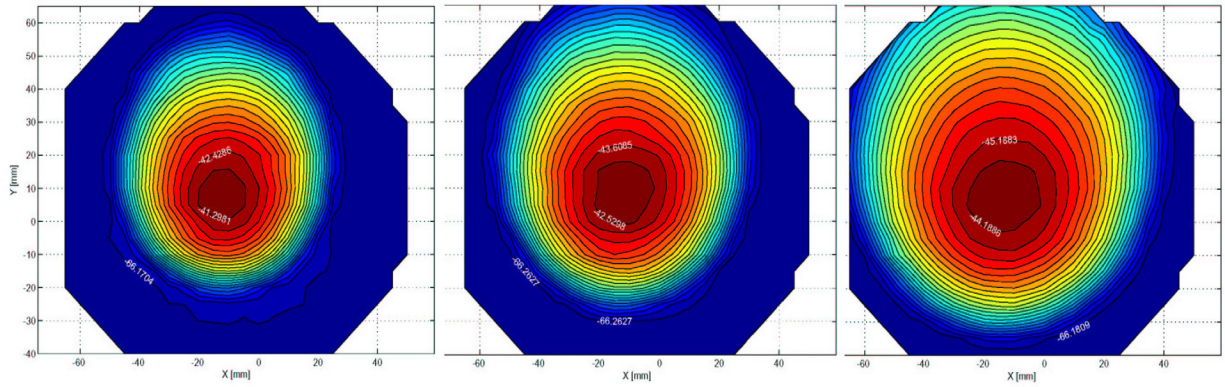

Figure 6. Beam-profiles measured for the demonstration model of MSA band 2 at distances (from left to right) of 620 mm, 720 mm and 900 mm from the beam-waist.

A general method for the measured data analysis is to fit fundamental Gaussian beam of the form

$$G(x,y) = a\exp\left\{-\frac{(x-x_c)^2}{\Delta x^2} - \frac{(y-y_c)^2}{\Delta y^2}\right\}$$

to the data, where the amplitude a, the central positions x_c, y_c and the widths Δx, Δy are the fitting parameters. An example of this fit is shown in Figure 7 .The central positions of the measured beam-profile at several distances from the beam-waist can be used for a three-dimensional line-fit of the axis of beam propagation. From the direction of the beam axis, the point of intersection at the MSA aperture can be determined. Furthermore, the angular deviations of the axis of propagation from the MSA mechanical axis can be determined. Unfortunately, this method is not sufficient to obtain the position or the size of the beam waist.

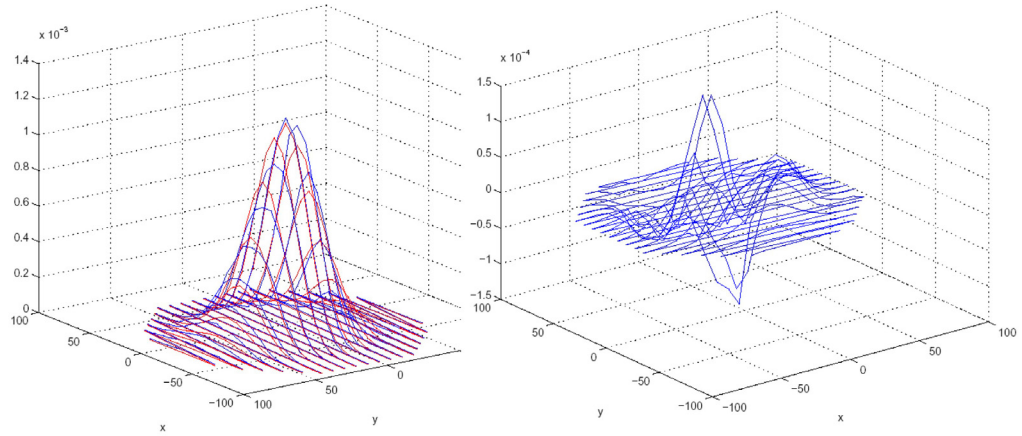

Figure 7. Gaussian fit to a planar scan about 720 mm from the beam-waist (left picture). Residuals of the fit at the right.

Conclusion

Gaussian beam measurement range has been built to provide possibilities to characterize the input beam of the mixer subassemblies for HIFI of Herschel Project. The beam measurement range is operational and has produced the first data. So far, measurements of the design-models of MSAs band 1 and 2 have been performed, using planar scans for a fixed z-coordinate of the probe-source from the MSA. Possible sources of errors, e.g., the standing waves and the measured power stability were calibrated allowing us 25-30 dB of the dynamic range. In order to achieve accurate reference in the MSA referred coordinate system the in-house developed laser-triangulation system was used. This triangulation system is still being commissioned to achieve ultimate accuracy.

Acknowledgements

The authors would like to acknowledge contribution of Dr. P. Dieleman and W.Jellema, SRON Groningen, through discussions and collaboration via AIV team of the HIFI Project. This work was supported by Swedish National Space Board under contract Dnr. 73/02.2.

References:

[1] European Space Agency, "Official web-page of the Herschel Project", http://sci.esa.int/home/herschel/

[2] T. de Graauw and F.P. Helmich, "Herschel-HIFI: The heterodyne instrument for the far-infrared", in *Symposium "The Promise of the Herschel Space Observatory",* pp. 45-51, ESA SP-460, 2001.

[3] M. Pantaleev, M. Fredrixon, K. Ermisch and V. Belitsky, "Source-receiver triangulation system for a gaussian beam measurement setup", in *Nordic Matlab Conference,* Copenhagen, 2003.

[4] K. Ermisch, M. Pantaleev, M. Fredrixon, M. Svensson and V. Belitsky, "Measurement report DM MSA1 at GARD/CTH", 2004.

[5] M. Pantaleev, "Gaussian Beam Measurement Range for HIFI Insrument of Herschel Space Observatory", Licentiate Thesis, Chalmers University of Technology, 2004.

[6] P.F. Goldsmith, "Quasioptical Systems", IEEE Press, ISBN 0-7803-3439-6, 1998.

[7] W. Jellema, A. Murphy, T. Peacocke, C. O'Sullivan, S. Withington, P. Wesselius and G. Yassin, "Performance, characterisation and measurement of the submillimetre-wave near-field facility for HIFI", in *3rd ESA Workshop on Millimetre Wave Technology and Applications,* 2003.

[8] W. Jellema, private communication, 2003.

[9] M.C. Diez, T.O. Klaasseen, C. Smorenburg and K.J. Wildeman, "Reflectance measurements on sub-millimetre absorbing coatings for sub-millimetre radiation", in *Proc. of the 4th Annual Symposium IEEE/LEOS,* pp. 107-110.

[10] W. Jellema, private communication, 2004.

Gaussian Beam Analysis of Relay Optics for the SEQUOIA Focal Plane Array

Gopal Narayanan[1]

Department of Astronomy, University of Massachusetts, Amherst, MA 01002

Abstract

The Large Millimeter Telescope (LMT) is a 50 m diameter millimeter-wavelength telescope being built in Mexico as a joint project between UMass and Instituto Nacional de Astrofisica, Óptica, y Electrónica (INAOE) in Mexico. The scientific goals of the LMT require high efficiency imaging over wide fields at wavelengths from 4 to 1 mm (75 to 300 GHz). Large-format focal plane arrays are being planned for the LMT. Of these, SEQUOIA (Second Quabbin Optical Imaging Array), a dual-polarization 16-pixel 3 mm wavelength focal plane array [1] has already been constructed, and has been operating at the FCRAO 14 m telescope. SEQUOIA will be installed on the LMT once the telescope has been commissioned. System-level optical and mechanical constraints results in a large focal ratio of 10.5 at the Cassegrain focus of the LMT. However, smaller focal ratios are usually more suitable for illuminating the individual detector elements of focal-plane arrays. Indeed SEQUOIA has an input focal ratio of ~ 4. A reimaging or relay optics (RO) system is required in the LMT receiver cabin to convert between these focal ratios.

A first-cut design of the RO system for SEQUOIA on the LMT was done using geometric optics principles using ray-tracing procedures available in the commercial optics package CODE V. In this paper, we present a new design for the SEQUOIA RO system based on full gaussian beam propagation considerations. The design utilizes gaussian beam modules in a software package called ASAP (Advanced Systems Analysis Package). Gaussian beam analysis in ASAP uses the principle of Gaussian Beam Decomposition (an ensemble of Gaussian beams is used to simulate coherent beam propagation). We present various test cases that verify the gaussian beam analysis in ASAP against analytical formulations. We present the final optimized RO design and various efficiency parameters.

1 Introduction

Heterodyne receivers at millimeter and submillimeter wavelengths are starting to approach the quantum limit in noise temperature. High efficiency widefield spectroscopic imaging is still a very important goal of radio astronomy. Given that we are approaching the limits in single-pixel receivers, further gains in mapping can be derived by building large format focal-plane arrays. Indeed, in the last fifteen years, rapid development has been achieved in the area of sensitive focal-plane arrays [2].

The Large Millimeter Telescope (LMT) is a 50m diameter millimeter-wavelength telescope being built atop Sierra Negra, a volcanic peak near Mexico City [3]. The LMT will have a wavelength coverage of 4 mm to 1 mm (75 - 300 GHz). The scientific goals of the LMT require high efficiency imaging over wide fields at wavelengths from 4 to 1 mm (75 to 300 GHz). Large-format focal plane arrays are being planned for the LMT. For the 3 mm wavelength band, SEQUOIA (Second Quabbin Optical Imaging Array), a dual-polarization 16-pixel focal plane array [1] has already been constructed, and has been operating at the FCRAO 14 m telescope. SEQUOIA will be installed on the LMT once the telescope has been commissioned.

Optical and mechanical considerations (like keeping the size of the secondary manageable) dictated that the final designed Cassegrain focal-ratio, $\mathrm{F_{CAS}} = 10.5$. However, for illumination of detectors in a focal-plane array, a much smaller focal-ratio is desirable. In fact, as designed, SEQUOIA has an f-ratio $\mathrm{F_{SEQ}} \approx 4.1$. Thus, a "reimaging" or "relay" optics (RO) system is needed to convert the focal ratio from the Cassegrain focus to that required by SEQUOIA. The scientific goals for SEQUOIA on the LMT require high efficiency imaging over the entire field-of-view (FOV). The RO package is required to contribute minimally to the system temperature, and hence large off-axis mirrors (rather than lenses) will be required to maintain high image performance over large fields.

[1]e-mail: gopal@astro.umass.edu

A first-cut design of the RO system for SEQUOIA on the LMT was done using geometric optics principles using ray-tracing procedures available in the commercial optics package CODE V [4]. In this paper, we present a new optimized design for the SEQUOIA RO system based on full gaussian beam propagation considerations. The design utilizes gaussian beam modules in the commercial optics package called ASAP (Advanced Systems Analysis Package) from Breault [5].

2 Requirements and Design Concept of RO

The operational band for SEQUOIA is 85–115 GHz. On the LMT, at 100 GHz, the Gaussian beam-waist at the Cassegrain focal plane is $\omega_{0,CAS} = 0.22[T_e(dB)]^{1/2} F_{CAS}\lambda = 22.43$ mm, where we assume that the antenna edge taper, T_e (dB)$= 10.5$. Figure 1 shows a view of the gaussian beams launched from the throats of the SEQUOIA feed-horns. The far-field beam pattern of the SEQUOIA square feedhorns have been measured, and they were found to be gaussian in nature to 98% accuracy. The fitted $\omega_{0,SEQ}$ of this beam pattern $= 8.7$ mm. So, we will need a RO system with magnification of $M = \frac{22.43}{8.7} = 2.6$ to transform the SEQUOIA focal-plane gaussian beam-waist to the Cassegrain focal-plane beam-waist requirement.

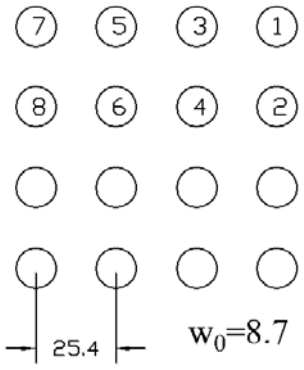

Figure 1: (a) SEQUOIA focal-plane array layout. The size and location of the gaussian beams launched by the 16 SEQUOIA feedhorns is depicted. The numbers correspond to the beams that were simulated.

Other requirements of the RO system are: (a) the FOV must be wide enough to cover the entire 4×4 array of SEQUOIA beams, (b) the antenna performance over the FOV must have minimal gain variation, (c) off-axis reflecting surfaces should be used to minimize any noise temperature penalties that could be incurred by refracting RO systems (d) the Gaussian beam coupling coefficients to the desired Cassegrain focal-plane illumination pattern should be uniform and as high as possible across the entire FOV across the entire receiver bandwidth of SEQUOIA.

One elegant solution for the design of a RO for a broadband receiver system is the so-called "Gaussian beam telescope" (GBT) as outlined in [6]. In a GBT, the pair of focusing elements are separated by a distance equal to the sum of their focal lengths, ($f_1 + f_2$). Figure 2 shows a schematic representation of a GBT. The magnification factor of the GBT is $M = w_{o,out2}/w_{o,in1}$, where $w_{o,out2}$ is the output beam-waist of the second mirror, and $w_{o,in1}$ is the input beam-waist of the first mirror. The output beam-waist location after the second mirror is given by,

$$d_{o2} = \frac{f_2}{f_1}\left(f_1 + f_2 - \frac{f_2}{f_1} d_{i1}\right) \tag{1}$$

where d_{i1} is the distance to the input beam-waist at the first mirror. It can be seen that if $d_{i1} = f_1$, then the location of the output beam-waist is wavelength independent, and is given by, $d_{o2} = f_2$. The size of the output and input beam-waists are proportional to wavelength as desired.

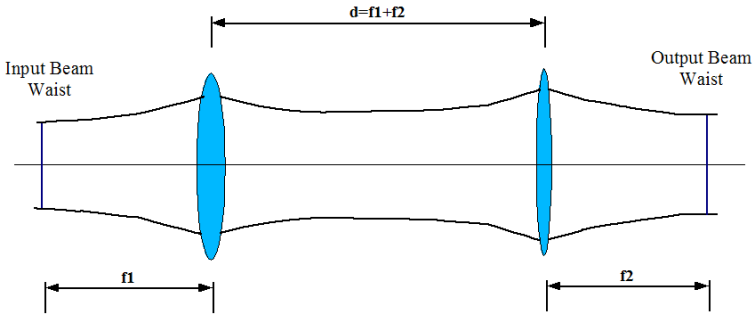

Figure 2: (a) A Gaussian Beam Telescope, consisting of two focusing elements, with focal lengths, f_1 and f_2, separated by the sum of their focal lengths.

While, these desirable features of the GBT make it suitable for this RO application, it must be noted that the derivation is strictly valid only for the beam propagating on-axis. For the case of a focal-plane array of feedhorns, the GBT conditions cannot be simultaneously met by the central beam *and* off-axis beams. The resulting efficiencies will have to be calculated using non-analytic techniques.

As has been demonstrated in the geometric optics modeling [4] of a proposed RO package for the LMT, if we use the GBT system for the RO, and postulate a few more conditions, then the only free parameters in the design of the SEQUOIA RO system are the focal-length f_1, and the incident angle γ_1 at the first mirror. The conditions that reduce the number of free parameters in the design are: (1) the input SEQUOIA beam-waist and the output Cassegrain beam-waist at the output of the GBT are exactly one focal-length away from the respective mirror, (2) the phase centers of the incident and reflected Gaussian beams are the geometrical foci of the generating ellipse of each elliptical mirror of the off-axis mirrors used in the GBT, and (3) the two incident angles at each mirror, $\gamma_1 = \gamma_2 = \gamma$. Given the required magnification, $M = 2.6$, it is possible to optimize for the best f_1 and γ that will improve the efficiency of the RO system. Such an exercise was done purely using geometrical ray-tracing in [4]. In this paper, we will carry out a similar exercise using a commercial software package that has the ability to treat gaussian-beam propagation.

3 Comparison of Commercial Optics Packages

Many commercial optics software packages are available for the design and analysis of optical designs. Most of them, however, are not well-suited for application to the far-infrared to millimeter-wavelength regime. Of these software packages, the following have show varying levels of success for modeling millimeter-wave optical systems: ASAP, GLAD, CODE V, ZEMAX and GRASP. Table 1 shows a comparison of the various packages.

While GRASP appears to be the best commercially available package, it is quite expensive. GLAD is a good compromise but it is not cheap either. We decided to use ASAP as it has a free academic license program. We ran a suite of tests to determine the applicability of ASAP for gaussian beam propagation calculations. The resulting tests are summarized in the next section, and the final ASAP analysis of the SEQUOIA RO system is provided in § 5.

4 Overview of ASAP and Gaussian Beam Propagation Tests

Advanced Systems Analysis Program (ASAP) from Breault Research Inc. is a ray tracing program with surface/structure modeling for incoherent or coherent beam propagation. The Gaussian beam is a solution to the

Table 1: **Comparison of Optics Design Packages**

Package	ASAP	GLAD	ZEMAX/CODE V	GRASP
Underlying Theory	Gaussian Beam Decomposition & Complex Ray Tracing	Angular Spectrum Techniques	Ray Tracing & Diffraction calculation only at exit pupil	Physical Optics & Geometric Theory of Diffraction
Ability to Model Sources	Using Gaussian beamlets	Arbitrary Source Fields	Only Point Sources / Single Gaussian Beams	Standard horns & arbitrary fields
Available Fields	Through Synthesis & Decomposition	At all planes (both polarizations)	Only at output plane	At all planes (both polarizations)
Speed	Complex Ray Tracing – Fast	Diffraction Calculations – slower	Fast	Slow for aberration Calculations
Optimization	No - but Perl-scripting possible	Yes	Yes	No
Cost	Free academic license	\$5k	$<$\$2k	\$20k

paraxial wave equation. The propagation of a Gaussian beam is well understood, and easily characterized by a few simple parameters. In ASAP, each gaussian beam is represented in turn by five rays – one base ray and four "parabasal" rays (see Figure 3a). In performing Gaussian beam propagation, ASAP performs complex ray tracing of all five of these parabasal rays. The next important principle in ASAP's gaussian beam analysis is its Gaussian Beam Decomposition. Here any complex field is represented as a superposition of individual Gaussian beams (called beamlets). Figure 3b shows the principle of ASAP's Gaussian beam decomposition (GBD) as applied to an example optical system. Complex source fields can be well-modeled using GBD. In general, Gaussian beams have a form that comes close to the spatially localized, non-diverging ideal. The angular divergence of their wavefront normals is the minimum permitted by the wave equation for a given beam width. The energy of the beam is concentrated primarily along the propagation axis, and falls off rapidly with radial position. This in turn allows Gaussian beams to perform localized sampling of optical surfaces. This is important especially for surfaces with higher-order structure, such as off-axis mirrors. Usually, GBD is done for the input fields before being incident on off-axis mirrors, thereby increasing the accuracy of the treatment. The accuracy in calculation of the resulting fields is always a tradeoff between accurate sampling of fields and optical surfaces versus violating the paraxial approximation (as can happen when the beam-waists of the individual beamlets approach the wavelength). When using ASAP to analyze millimeter and submillimeter wavelength quasi-optical systems, the user has to have a rather careful understanding of the underlying theory and assumptions in ASAP. One of the main limitations of ASAP's treatment is that when aperture dimensions (or object spatial frequencies) are near to, or below the operating wavelength, the method tends to break down, and may produce spurious results.

4.1 Tests of Gaussian Beam Propagation in ASAP

4.1.1 Free Space Propagation

In a suite of tests to determine the propagation behavior of single gaussian beams (without any decomposition), single gaussian beams of varying beam waist radii at the same wavelength ($\lambda = 3$mm) were launched, and the beam is propagated to different test positions, and the resultant waist radii as predicted by ASAP is compared to the theoretical expectation. ASAP does a very good job with free-space propagation of Gaussian beams and there is less than 0.2% error up to 20 m of distance from the beam waist even for beams with $\omega_0 = 8$mm. At larger beam waist radii, the errors are even smaller.

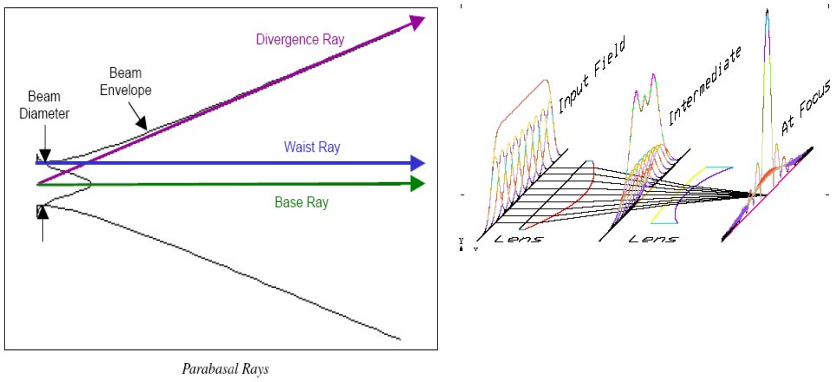

Figure 3: (a) ASAP Representation of Gaussian Beam. Parabasal rays are paraxial with respect to the base ray. Only one each of the 4 paraxial rays (2 waist rays and 2 divergence rays) are shown in the figure, the other 2 are out of the plane of the paper. If the divergence of the Gaussian beam is too rapid, the beam does not stay gaussian as it propagates, and ASAP keeps track of this violation, and duly reports it. (a) ASAP Propagation using Gaussian Beam Decomposition. The arbitrary input field is represented using a superposition of individual Gaussian beamlets. Complex ray tracing of the parabasal rays of the individual beamlets is performed, followed by reconstituting the field at the output detector plane.

4.1.2 Reflection off of Flat Mirror

In the next test, we probed the effect of reflection of a gaussian beam as it reflects off a flat mirror. Figure 4a shows a plot of the variation of coupling efficiency of the ASAP predicted beam to the theoretically expected perfect gaussian beam at varying distances from the flat mirror. Gaussian beams with 25, 12, and 8 mm beam waist radii are launched 300 mm away from the flat mirror. The incident angle of the beam is 45 degree. Coupling efficiency variation as a function of the propagation distance from the flat mirror is shown. It is seen that beyond a distance of 10 m from the flat, with gaussian beams that approach the wavelength (here $\lambda = 3$mm), ASAP starts to become inaccurate. However, with beam widths which are several times the wavelength, the errors are tolerable.

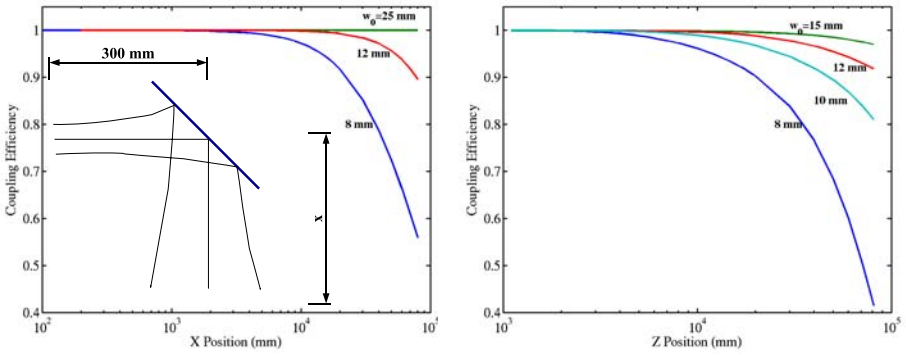

Figure 4: (a) Variation of Coupling efficiency with propagation distance after reflection from a flat mirror. A single gaussian beam of beam width 25, 12 or 12mm is launched 300 mm from a flat mirror oriented at $45°$ with respect to the incident beam. The X-axis represents the distance x from the mirror.

4.1.3 Tests of Decomposition

In ASAP, decomposition allows us to define a new set of individual beams to represent the same field as the original beams. While more beamlets will accurately sample the original field, each beamlet becomes smaller and smaller in waist size. When the beam waist size of the individual beamlets approach the wavelength of operation, the principle of gaussian beam propagation breaks down. In general, as the beam waist radius gets smaller than a few times λ, the accuracy suffers. This can be seen in Figure 4b, where a single gaussian beam is allowed to propagate in free-space, then decomposed at 1000 mm. The subsequent field is allowed to propagate and coupling efficiency to a fundamental Gaussian beam mode at various distances are plotted. When the original gaussian beam is several times λ, decomposition and subsequent propagation is accurate. At $\omega_0 = 8$ mm, the individual beamlets become small enough at decomposition, that the decomposed field does not do a good job of representing the field, as seen by the decreasing coupling efficiency with distance.

4.1.4 Gaussian Beam Coupling Tests

In the SEQUOIA RO system, we launch approximately gaussian beams from the 32 SEQUOIA feedhorns to the Cassegrain focal-plane. At the CFP these beams should meet the requirements of the field that is necessary to properly illuminate the secondary mirror. This involves optimizing the coupling efficiencies at each location at the CFP, where the SEQUOIA beam that propagates through the RO system is coupled with an ideal gaussian beam at the CFP for each pixel. In an effort to determine how well ASAP calculates coupling efficiencies between gaussian beams, we ran three tests. These tests have analytical formulations [6]. Imperfect coupling can occur between two aligned beams, if they have mismatched beam radii and/or radii of curvature. Figure 5a shows the result for two beams which are axially aligned, but with differing beam waist radii. It is seen that the ASAP prediction of coupling efficiency agrees with the analytical result.

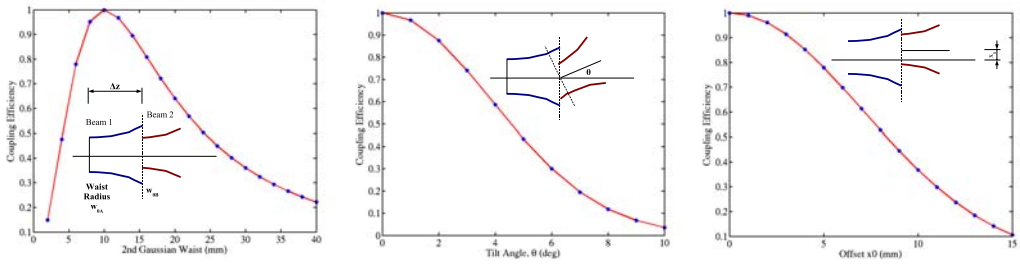

Figure 5: Gaussian Beam Coupling Tests. In all three plots, the solid line shows the analytical expectation from [6], and the starred-symbols show the ASAP analysis. (a) Coupling efficiency variation for axially aligned beams with offset beam waist radii. Beam 1 coming from the left is a $\omega_0 = 10$mm gaussian beam. Coupling efficiency variation with beam waist radii of the second beam is plotted. (b) Identical waists, tilted beams. Here, both beam 1 and 2 have the same waist radii (10 mm), but beam2 is tilted with respect to beam 2 with an angle of θ degrees. The variation of coupling efficiency with θ is plotted. (c) Identical beams, offset waist locations. Here both beam 1 and 2 have the same waist radii (10 mm), but the center of beam2 is offset by a distance x_0 with respect to that of beam 1.

Figure 5b shows the result for *tilted beams*, and Figure 5c shows the result for *offset beams*. Again, it is seen that ASAP prediction is inline with the analytical formalism, showing the ASAP's coupling integral calculations are accurate.

5 Gaussian Beam Analysis of SEQUOIA RO

Having tested ASAP for a variety of test cases, we concluded that ASAP works well except when the beam waist approaches the wavelength of operation. In the SEQUOIA RO system, we need to expand the size

of the Gaussian beam waists from 8.7 mm at the SEQUOIA focal plane to 22.43 mm at the CFP (see §2). The errors in decomposing the input gaussian beam field will be more than at the CFP, as the beam keeps expanding through the RO system. It is expected that errors can be minimized by careful decomposition in front of the first mirror, after the initial beam from the feed horn has expanded in size.

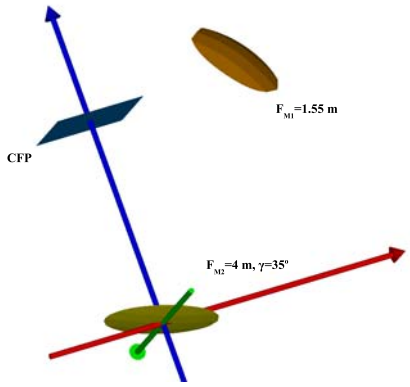

Figure 6: SEQUOIA RO System. M1 and M2 are the two elliptical mirrors that form the Gaussian Beam Telescope. SEQUOIA is located in front of M1. The incident angle of the beams at both mirrors are equal, and is given by $\gamma = 35°$.

Figure 6 shows the final optimized layout of the final adopted SEQUOIA RO system. As has been outlined in § 2, the final design of the RO system can be expressed in terms of two free parameters – the focal length of one of the mirrors of the Gaussian Beam Telescope (GBT) and the incident angle in each of the mirrors, γ.

ASAP does not have a built-in optimizer module. However, the latest version of ASAP comes equipped with the ability to use Perlscript [7], a perl-based programming language, which permits the use of ASAP commands from within the perlscript, whilst maintaining the power of an interpreted programming language with powerful procedural and object-oriented programming techniques.

In the optimization procedure, we followed the following recipe. A large perlscript macro was written and called from within ASAP. The second mirror, M_2 is always located at the origin (see Figure 6). For each focal length f_1 and incident angle, γ, we determine the rest of the parameters of the RO system as described in § 2. We then perform a geometric ray trace of the top 8 beams from the SEQUOIA feed horns to determine the approximate phase center positions and direction cosines after the first reflection from M_1. After this procedure, full coherent optics calculations are performed on all 8 beams with two decompositions, first before M_1, and then before M_2 (with careful checks along the way to ensure appropriate sampling of the fields and non-violation of the paraxial approximation). The beams are propagated to the CFP, and the coupling integrals are computed for all 8 beams. A global error figure is determined with all 8 beams to the ideal condition of unity gain of the system, and this error figure is minimized by successive iterations. The whole procedure takes a whole day of iterating on a modern computer, but eventually an optimized solution is reached. The design presented in Figure 6 is close to this optimal design, and the resulting coupling integrals from this design are presented in Figure 7. The design was optimized at 3 mm wavelength, but verified for the whole SEQUOIA band.

In the final optimized design, the focal lengths of M_1 and M_2 are 1.55 m and 4 m respectively, with an angle of incidence at each mirror given by $\gamma = 35°$. The SEQUOIA focal plane is thus located 1.55 m from M_1, and the 8.7mm beam waists from the feedhorns have expanded already to $\sim$ 170mm by the time they reach M_1. Reasonably acurate decomposition was possible for such a beam. The resulting beam efficiencies

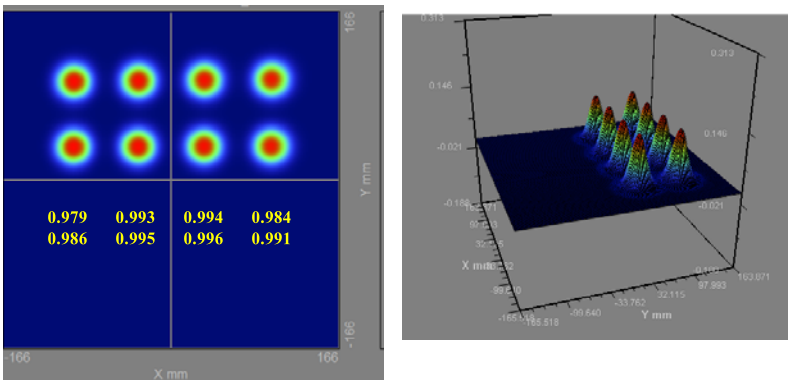

Figure 7: Output Field of 8 pixels at the CFP. The top 8 beams of SEQUOIA are launched from the SEQUOIA focal plane through the RO System, and plotted at the CFP. The coupling efficiencies to the required gaussian beams at the CFP for the 8 pixels are noted in the lower half of the figure. The figure on the right shows the isometric surface plot of the SEQUOIA beams at the CFP.

show less than 3% degradation in efficiency even for the edge pixels (see Figure 7).

6 Conclusions and Future Work

A large relay optics system has been designed for the 3mm SEQUOIA focal plane array on the LMT. Full gaussian beam analysis has been used to design the system using Breault Research Inc.'s ASAP software. In the future, we intend to perform a complete tolerance analysis of the location and orientation of the mirrors that form the RO system, and also determine cross-polarization losses in the system.

Acknowledgements: This work was supported by NSF grant AST 02-28993 to the Five College Radio Astronomy Observatory. Wenhao Zhang, a former graduate student working with GN helped with some of the initial ASAP programming.

References

[1] N. R. Erickson, R. M. Grosslein, R. B. Erickson, and S. Weinreb, "A cryogenic focal plane array for 85-115 GHz using MMIC preamplifiers," *IEEE Trans. Microwave Theory and Tech.*, vol. 47, no. 12, pp. 2212–2219, 1999.

[2] D. T. Emerson and J. M. Payne, "Multi-feed Systems for Radio Telescopes," in *ASP Conference Series, vol. 75*, (Tucson, AZ), 1994.

[3] F. P. Schloerb and L. Carrasco, "The Large Millimeter Telescope," in *Proc. of the 15th Int'l Symp. on Space Terahertz Technology*, (Northampton, MA), April 2004.

[4] L. Olmi, "The Optical Design of Relay Optics for Heterodyne Millimeter Focal Plane Arrays," *International Journal of IR and MM Waves*, vol. 21, no. 3, pp. 365–393, 2000.

[5] ASAP, Breault Research Organization, Tucson, Arizona.

[6] P. F. Goldsmith, *Quasioptical Systems*. IEEE Press, New York, 1998.

[7] `http://www.xav.com/perl/Components/Windows/PerlScript.html`.

Satellite antenna measurement at 322 GHz using a computer-generated hologram as the focusing element

J. Ala-Laurinaho[1], J. Häkli[1], T. Koskinen[1], A. Lönnqvist[1], J. Mallat[1], A.V. Räisänen[1], S. Ranvier[1], J. Säily[1], J. Tuovinen[2], V. Viikari[1]
[1]MilliLab, Radio Laboratory/SMARAD, Helsinki University of Technology,
P.O Box 3000, FIN-02015 HUT, Finland
[2]MilliLab, VTT Information Technology, P.O. Box 1202, FIN-02044 VTT, Finland
Antti.Raisanen@hut.fi

Summary

Computer-generated holograms [1] can be applied in space terahertz technology; they are particularly suitable as focusing elements in compact test ranges, for example, in testing of high-gain antennas [2,3,4] and measuring radar cross section (RCS) of scaled models [5]. Radio holograms have also been demonstrated in other millimeter- and submillimeter-wave beam-shaping applications, such as the creation of non-diffracting mm-wave Bessel beams, mm-wave vortices, and custom-designed beam patterns [6,7,8].

During summer 2003 we built a temporary measuring facility, Figures 1 and 2, at the High Voltage Institute of the Helsinki University of Technology to test the ADMIRALS antenna, shown in Figure 3, built by EADS Astrium. Astrium manufactured the ADMIRALS representative test object (RTO) for demonstrating the current satellite antenna technology and for comparing the potential antenna testing methods at mm- and sub-mm wavelengths. The diameter of the offset-fed reflector of the ADMIRALS RTO is 1.5 m and the total weight of the RTO is about 400 kg. The feed and related quasioptics are placed 3 m away from the center of the main reflector. Astrium has tested the ADMIRALS RTO in a compact antenna test range (CATR) based on reflectors at the frequencies 203, 322, and 503 GHz [9].

Because the diameter of the quiet-zone of the compact antenna test range (CATR) must be larger than the diameter of the antenna under study, a quiet zone of the required size was produced with a 3-m-size circular amplitude-hologram pattern. The pattern was exposed with a laser on the photosensitive resist on top of the copper layer of the hologram material (17-μm copper on 50-μm Mylar film). Chemical wet etching was used for processing the slots to the copper layer. The hologram was made from three 1m × 3m pieces, which were joined by soldering the metal stripes of the hologram together to form the final 3m × 3m hologram structure.

A dedicated transmit module constructed for the ADMIRALS antenna tests was used as the transmitter both in the quiet-zone probing and in the antenna measurements. In the quiet-zone measurements, the ABmillimètre MVNA-8-350 millimeter-wave network analyzer with its receiver extension ESA-2 was used. This configuration gave a sufficient dynamic range of about 50 dB and also allowed a phase measurement of the quiet-zone field. Phase errors due to the cable flexing during the probe movement were corrected with a phase-correction system based on the use of a pilot signal [10]. In the measurements of the high-gain antenna the dynamic range was about 80 dB when the dedicated receiver module of the ADMIRALS antenna was used.

The measurement results obtained at 322 GHz (Figure 4) are so promising that we are currently proposing a hologram CATR test for the Planck telescope at 500 GHz.

Discussion

Computer-generated holograms (diffractive elements) can be used for shaping mm-wave beams, e.g. for producing a plane wave in a compact space. So far, the most useful application found for the mm- and submm-wave holograms is testing of antennas at these short wavelengths where traditional test methods are useless. A computer-generated

amplitude hologram has been successfully used as a focusing element in a compact antenna test range (CATR) in 1998 at 119 GHz for the Odin satellite antenna tests, and more recently at 322 GHz for the ADMIRALS RTO tests.

The need to find a good solution for submm-wave antenna testing is urgent, as the aim of several ongoing space research projects is to launch satellites equipped with scientific or remote sensing instruments to probe space or the atmosphere at sub-mm wavelengths. These satellites will have on board electrically large reflector antennas, which should be tested before the launch.

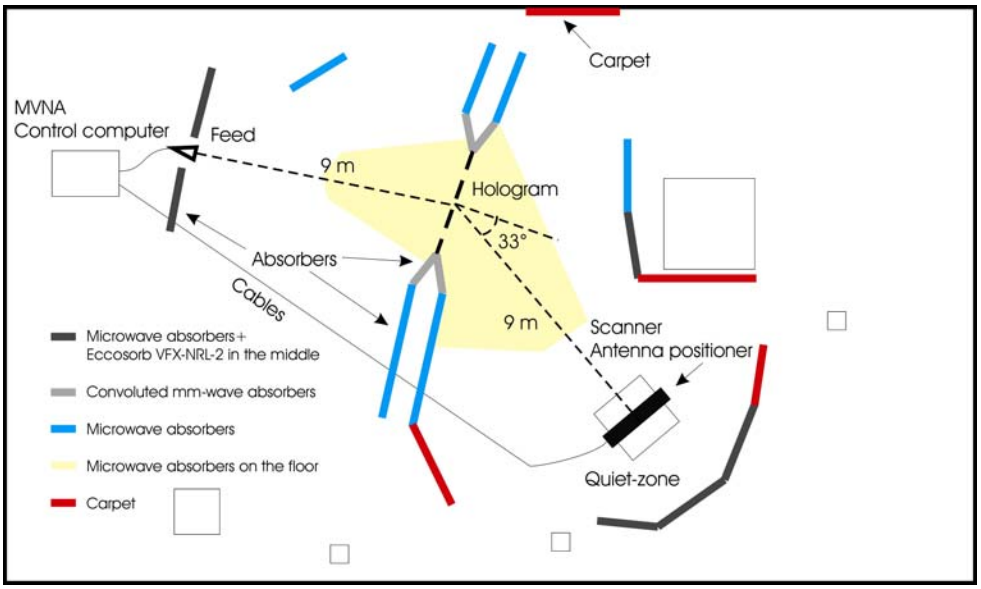

Figure 1 Schematic top view of the hologram CATR set-up for the ADMIRALS RTO tests at 322 GHz.

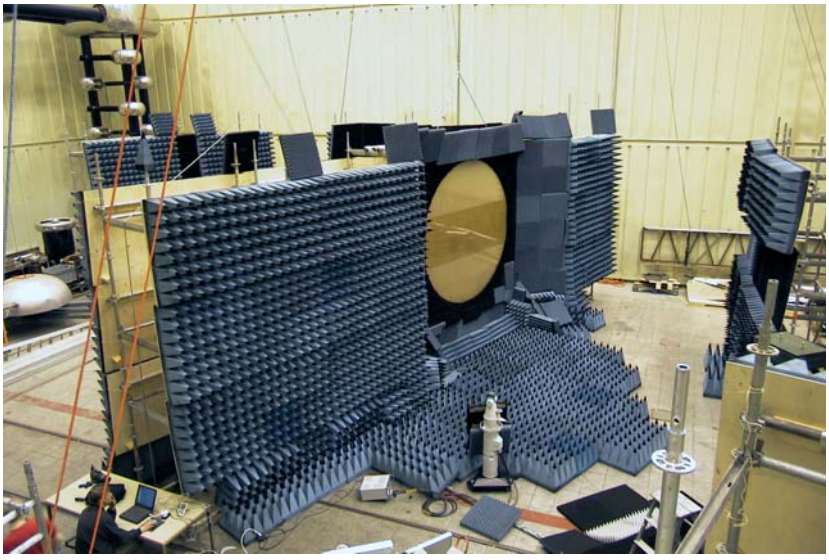

Figure 2 Hologram-based CATR under construction in the high-voltage test hall of HUT.

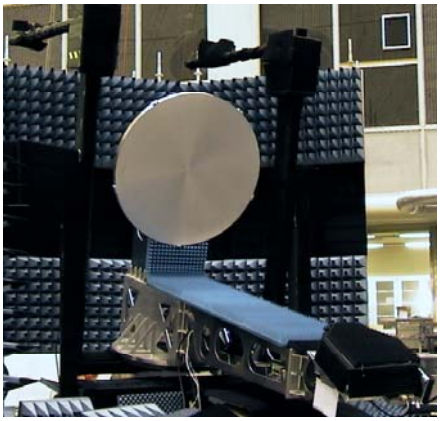

Figure 3 ADMIRALS RTO under test.

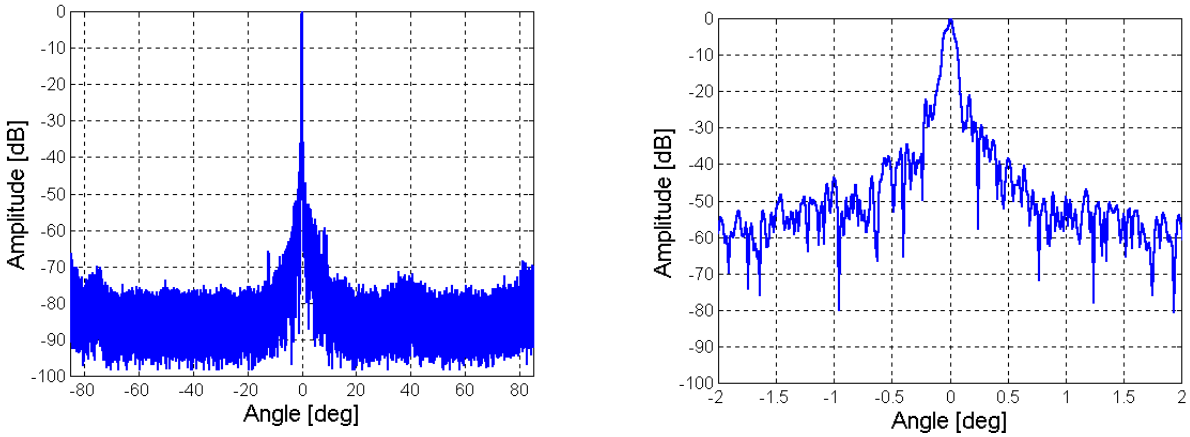

Figure 4 Azimuth pattern of the ADMIRALS RTO at 322 GHz.

Acknowledgements

This work has been partially funded by ESA/ESTEC, the Academy of Finland and Tekes (National Technology Agency of Finland) through the Center-of-Excellence program, and the Graduate School in Electronics, Telecommunication and Automation, GETA. The authors would like to thank CSC – the Finnish IT Center for Science for providing computer resources. The authors would also like to thank Mr. Eino Kahra, Mr. Lauri Laakso, and Mr. Lorenz Schmuckli for valuable help in these studies.

References

[1] W.-H. Lee, "Computer-generated holograms: Techniques and applications," pp. 121-231 in *Progress in Optics XVI*, E. Wolf (ed.), Elsevier, Amsterdam, 1978.

[2] T. Hirvonen, J. Ala-Laurinaho, J. Tuovinen, and A.V. Räisänen, "A compact antenna test range based on a hologram," *IEEE Trans. Antennas Propagat.*,. vol. 45, no. 8, pp. 1270-1276, 1997.

[3] J. Ala-Laurinaho, T. Hirvonen, P. Piironen, A. Lehto, J. Tuovinen, A. V. Räisänen, and U. Frisk, "Measurement of the Odin telescope at 119 GHz with a hologram-type CATR," *IEEE Trans. Antennas Propagat.*, vol. 49, no. 9, pp. 1264-1270, 2001.

[4] A.V. Räisänen, J. Ala-Laurinaho, T. Koskinen, A. Lönnqvist, J. Säily, J. Häkli, J. Mallat, V. Viikari, S. Ranvier, J. Tuovinen, "Computer-generated hologram and its use for submm-wave antenna measurement" (invited keynote), *Proc. of the 2004 IEEE Aerospace Conference*, Big Sky, MO, USA, March 7-13, 2004, CD-ROM.

[5] A. Lönnqvist, J. Mallat, A.V. Räisänen, "A phase hologram based compact RCS range for scale models", *Proc. of the 25th Annual Meeting & Symposium of the Antenna Measurement Techniques Association (AMTA)*, Irvine, CA, October 19-24, 2003, pp. 118-123.
[6] J. Meltaus, J. Salo, E. Noponen, M.M. Salomaa, V. Viikari, A. Lönnqvist, T. Koskinen, J. Säily, J. Häkli, J. Ala-Laurinaho, J. Mallat, and A.V. Räisänen, "Millimeter-wave beam shaping using holograms," *IEEE Trans. Microwave Theory Techniques*, vol. 51, no. 4, pp. 1274-1280, 2003.
[7] J. Salo, J. Meltaus, E. Noponen, M.M. Salomaa, A. Lönnqvist, T. Koskinen, V. Viikari, J. Säily, J. Häkli, J. Ala-Laurinaho, J. Mallat, and A.V. Räisänen, "Holograms for shaping radio-wave fields," *J. Opt. A*, vol. 4, no. 5, pp. S161-S167, September 2002.
[8] J. Salo, J. Meltaus, E. Noponen, J. Westerholm, M. M. Salomaa, A. Lönnqvist, J. Säily, J. Häkli, J. Ala-Laurinaho, and A. V. Räisänen, "Millimetre-wave Bessel beams using computer holograms," *Electr. Lett.* vol. 37, no. 13, pp. 834-835, 2001.
[9] J. Hartmann, J. Habersack, H.-J. Steiner, J. Lemanczyk, and P. de Maagt, "Calibration and verification measurements in compensated compact ranges up to 500 GHz", *Proceedings of 23rd AMTA*, Denver, USA, October 2001, pp. 377-382.
[10] J. Säily, P. Eskelinen, A.V. Räisänen, "Pilot signal based real-time measurement and correction of phase errors caused by microwave cable flexing in planar near-field tests," *IEEE Transactions on Antennas and Propagation*, vol. 51, no. 2, pp. 195-200, 2003.

The Terahertz Atmosphere

Scott Paine, Raymond Blundell
Smithsonian Astrophysical Observatory
Harvard-Smithsonian Center for Astrophysics
60 Garden Street, Cambridge, MA 02138 USA

Abstract

The recent development of sites in unusually high and dry locations, notably the Atacama desert of northern Chile and the South Pole, has extended the range of ground-based radio astronomy to frequencies beyond 1 THz. Instruments for observations at these frequencies are being planned, or are under development, for several telescopes. One experimental telescope, the SAO Submillimeter Receiver Laboratory's RLT, has operated routinely above 1 THz since late 2002.

Observations at these frequencies, where atmospheric attenuation is always high, require a good understanding of the propagation path to be successful. We have spent several years investigating terahertz atmospheric propagation from two sites in northern Chile—the Atacama Large Millimeter Array (ALMA) site near Cerro Chajnantor, and the site of the RLT on Cerro Sairecabur. Using an automated Fourier transform spectrometer (FTS), a large volume of atmospheric emission spectra, covering 300 GHz – 3.5 THz, has been obtained from these sites under a full range of meteorological conditions. As part of this effort, we have developed a general-purpose atmospheric model for terahertz frequencies which is well-validated by these data. We continue to operate the FTS in conjunction with the RLT, and have found that the combined measurement and modeling capability is invaluable for calibrating the astronomical observations.

In this paper, we discuss the observed characteristics of these sites, modeling methods and results, and the use of the FTS as a calibration tool for radio astronomy.

1. Introduction

Ground-based radio astronomy at terahertz frequencies is developing rapidly. Instruments already in operation include the RLT (Blundell et al. 2003), a 0.8 metre terahertz telescope operating on Cerro Sairecabur in northern Chile since 2002, and the TREND receiver (Yngvesson et al. 2004) recently tested on the 1.7 metre AST/RO telescope (Stark, et al. 2001) at the South Pole. THz receivers are planned for the 12 metre APEX telescope near the Atacama Large Millimeter Array (ALMA) site near Cerro Chajnantor in Chile. Meanwhile, Submillimeter interferometry has been extended to 690 GHz by the Submillimeter Array (SMA) on Mauna Kea, Hawaii.

At these frequencies, the observer has to contend with significant atmospheric attenuation. For example, the RLT typically observes in the 1030 GHz atmospheric window with a zenith atmospheric transmittance of 20%, and a system temperature of order 20,000 K. Under these conditions, calibration of the atmospheric attenuation by the usual sky dip method is not feasible, both because of the poor signal to noise ratio (Marrone 2004), and because the approximation of the atmosphere as a single isothermal, isobaric slab may not be valid.

At the RLT, the solution to these difficulties has been to operate a zenith-looking Fourier transform spectrometer (FTS) in conjunction with the astronomical observations. This instrument was originally developed for the SAO Submillimeter Receiver Lab's terahertz site testing program (Paine et al. 2000). The broadband (300 GHz – 3.5 THz) emission spectra produced by the FTS enable accurate calibration of the atmospheric transmission. This capability is enhanced by fitting the emission spectrum using an atmospheric model, which can in turn be used to calculate the atmospheric transmission at full resolution.

This paper presents an overview of the characteristics of the atmosphere over terahertz observatory sites. Examples are presented of emission spectra and model fits for two sites: Sairecabur and Chajnantor. Finally, the use of FTS spectra in conjunction with model fits for calibration of the atmosphere is discussed.

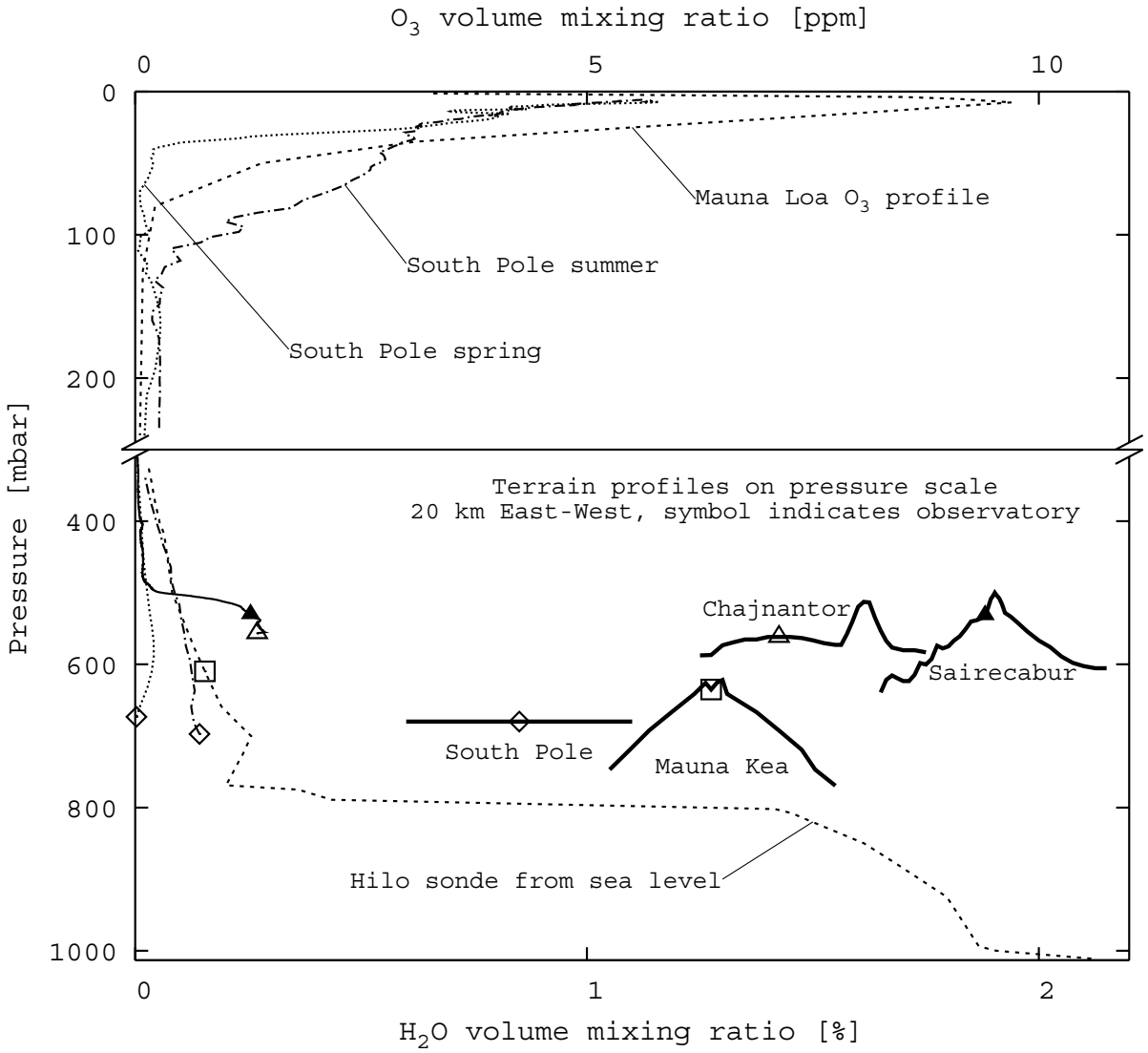

Fig. 2.1 – Vertical profiles of water vapor and ozone above terahertz observatory sites. Symbols indicate the observatory pressure altitudes on the terrain profiles and on the H_2O mixing ratio profiles. Mixing ratio data are from particular soundings which are representative of typical conditions. South Pole data are courtesy of the National Oceanic and Atmospheric Administration (NOAA) Climate Monitoring and Diagnostics Laboratory, Boulder, Colorado, and are from launches on 7 Oct 2003, just before the spring equinox, and in the summer on 29 Dec 2003. The Mauna Loa ozone profile is derived from data in MacDermid (1999). Hilo sonde data are courtesy of the Department of Atmospheric Science, University of Wyoming, for a sonde launched 15 Jan 2003. Chajnantor sonde data here and in Fig. 3.3 are from a series of launches on 10 Nov 1999 as part of collaboration between Cornell University, the European Southern Observatory (ESO), the National Radio Astronomy Observatory (NRAO), and SAO.

2. Characteristics of Observing Sites

The greatest contribution to the atmospheric opacity at terahertz frequencies is from rotation lines of water vapor. These are pressure broadened in the lower troposphere to linewidths of order 3 GHz, and, even at the low column densities encountered above a good terahertz site (0.2 mm – 1 mm precipitable water vapor, or pwv), the strongest

lines are further saturation broadened to many tens of GHz. The weak spin-rotation lines of O_2 contribute significant opacity within a few GHz of these lines. Rotation lines of stratospheric ozone, which have much narrower pressure-broadened linewidths of order 10 MHz, can be a significant factor when these fall close to the observing frequency, or its image in a DSB receiver. In addition to line absorption, short-range collisions among N_2, O_2, and H_2O, produce broad, unresolved continua peaking near 3 THz. A thorough discussion of the roles of these and other atmospheric constituents may be found in Goody & Yung (1989), and references therein.

2.1 Vertical profiles of water vapor and ozone

Fig. 2.1 illustrates typical vertical profiles of water vapor and ozone above four principal sites for terahertz astronomy. The profiles shown are from particular radiosonde flights, but represent typical conditions at each of these sites. By plotting mixing ratio against pressure, the area to the left of each profile is directly proportional to the column density of the plotted species. For comparison, the geographic relief of the sites is plotted on the same vertical pressure scale.

Besides being at high altitude, each of these sites achieves typically low precipitable water vapor (pwv) by different means. At the South Pole, despite the fact that humidity is close to saturation in the lower atmosphere, the water vapor mixing ratio is nevertheless very low by virtue of the extreme cold (Chamberlin 2001). The water vapor profiles presented Fig. 2.1 for the South Pole are the saturated H_2O mixing profiles based on temperature data. Mauna Kea, on the island of Hawaii, presents an entirely different scenario. During good observing weather, humid air at lower levels is trapped under an inversion below summit level. Above the inversion, the air is dry, and the water vapor density typically falls off gradually with altitude. Chajnantor and Sairecabur are located in the dry Atacama climate of northern Chile. During good conditions at Chajnantor, a typical situation is for moderately low humidity at ground level to persist up to an inversion 0.5 – 2 km above ground level, above which the relative humidity level drops to extremely dry levels of a few percent or less. This characteristic was the basis for locating the RLT on Sairecabur, 0.5 km above the ALMA site at Chajnantor.

Representative ozone profiles for the South Pole and Hawaii are shown in the upper part of Fig. 2.1. For northern Chile, local ozone profile measurements have not been made, but the profile is expected to be similar to Hawaii (Andrews 2000). The difference between the spring and summer South Pole ozone profiles is the Antarctic spring ozone hole phenomenon.

As Fig. 2.1 illustrates, these two variable atmospheric constituents, water vapor and ozone, are well-separated vertically. Moreover, while the water vapor distribution varies rapidly on the length and time scales associated with turbulent air movement in the troposphere, ozone varies more slowly over the synoptic length scales associated with the stratosphere. These observations have motivated a recent proposal to use stratospheric ozone line emission as a calibration source to correct for tropospheric phase fluctuations, associated with water vapor, over radio interferometers (Paine 2004b).

2.2 Boundary layer phenomena

Boundary layer phenomena include the effects of heat exchange with the ground, evaporation from soil, snow, or ice, and slope winds. These effects can result in a thin layer near the ground, from several metres to tens of metres thick, having temperature and humidity significantly different from the air just above. Readings from a weather station immersed in the boundary layer may give a poor indication of conditions just above. Because the boundary layer is thin, its effect on the radiometric temperature of the sky will generally be small in atmospheric windows where astronomical observations can be made. Nevertheless, in some cases even small fluctuations can be important, as when using water vapor radiometry to estimate tropospheric delay (Sutton & Hueckstaedt 1996).

The radiometric signature of a warm, humid boundary layer is frequently observed in daytime FTS spectra obtained on Mauna Kea, Chajnantor, or Sairecabur. On clear days, the sun heats the soil, driving evaporation and convection. Under these conditions, the strongest water lines can be saturated at the line centers within the warm, humid layer of air at ground level, resulting to the appearance of warm features in the spectrum. An example of this effect is shown in Fig. 3.2, below. In contrast, on clear nights, when a surface inversion develops due to radiative cooling of the ground, no analogous cold features are seen, since there is no strong enhancement of the ground level humidity when the soil is cool.

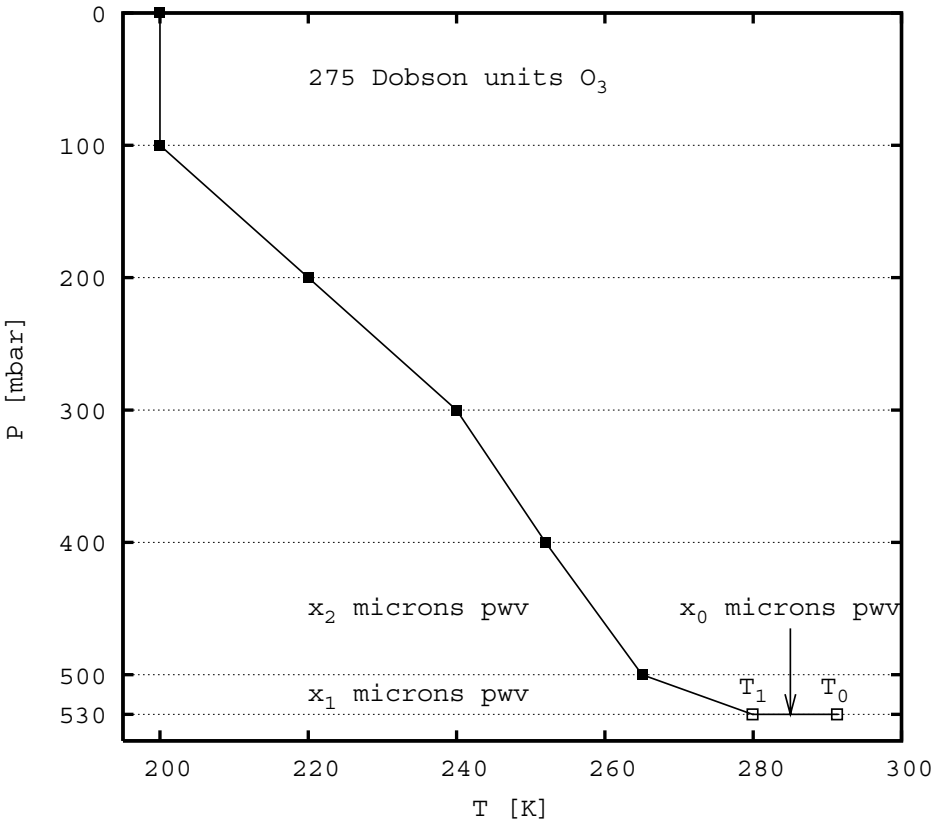

Fig. 3.1 – Schematic of an *am* model layer configuration for fitting FTS spectra at Sairecabur. The atmosphere is divided into 6 layers at the pressure boundaries shown, plus an additional thin, humid, layer at ground level. Fit variables are the three H_2O column densities and two temperatures shown. In addition to H_2O and O_3 indicated, each model layer contains N_2 and O_2 at hydrostatic column density.

3. FTS spectra and modeling

We have developed a general-purpose atmospheric model, *am* (Paine 2004a), for calculating synthetic atmospheric spectra at terahertz frequencies, and for making model fits to measured spectra. A schematic of a simple layer specification for *am*, a representation of the spring daytime atmosphere over Sairecabur, is shown in Fig. 3.1. The layers are defined on a pressure grid, with specified temperatures, derived from Chajnantor radiosonde data, at the layer boundaries. Here, a simple two-step approximation is used to represent the water vapor profile, with an additional thin layer added at ground level to represent the humid daytime surface boundary layer. For the model fit presented here, the three water vapor column densities, as well as the base temperatures of the 500-530 mbar layer and of the surface layer, are designated as fit variables, with all other parameters held fixed.

An example of a fitting run on an FTS spectrum obtained at Sairecabur is shown in Fig. 3.2. The fit clearly demonstrates the validity of the simple layer model described. For the fit, the model spectrum was convolved with the 3 GHz wide resolution function of the FTS. The rms residual is 4.4 K, with much of this coming from the poor signal-to-noise of the FTS spectrum towards low frequencies. The FTS has constant noise per frequency channel, but the thermal radiance from the sky falls of rapidly towards low frequencies, with consequent degradation of the signal-to-noise ratio. Much of the noise is fluctuation noise proportional to the total power admitted to the

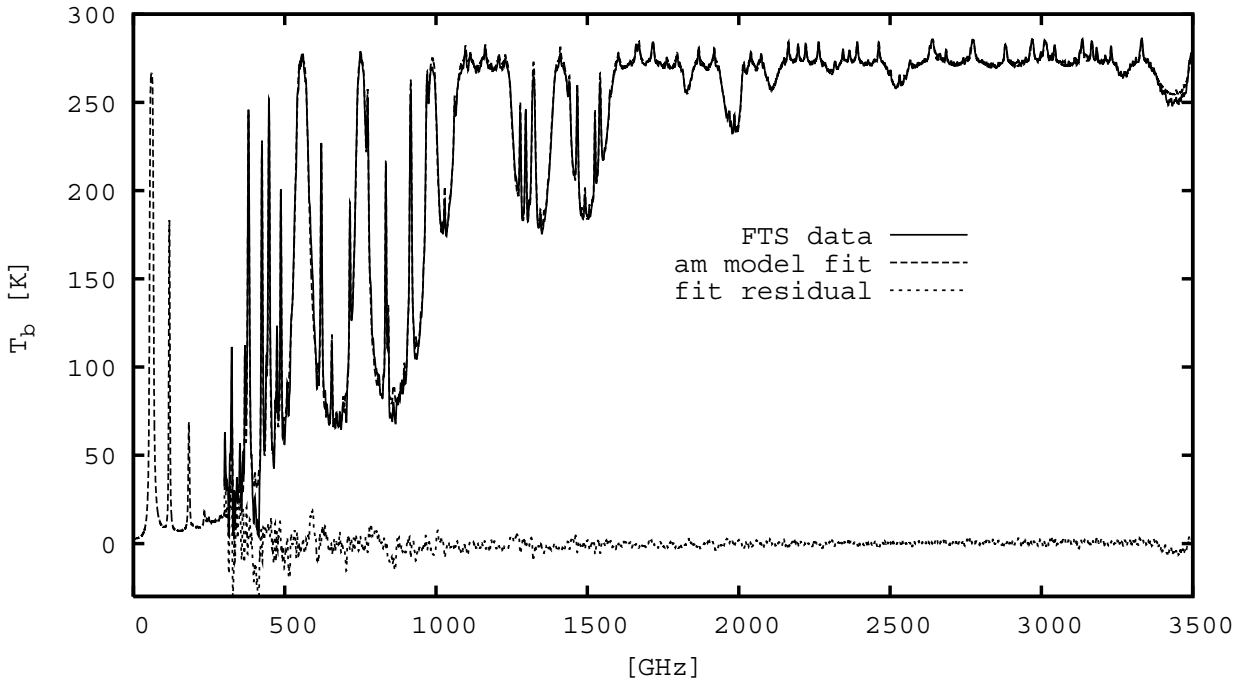

Fig. 3.2 – Sky brightness temperature spectrum measured at Cerro Sairecabur on 2000 Nov 25 at 13:40 UT, and *am* atmospheric model fit using the model layer structure illustrated in Fig. 3.1. The converged parameter values are T_0 = 291 K, T_1 = 280 K, x_0 = 0.5 μm pwv, x_1 = 47 μm pwv, x_2 = 132 μm pwv (total H_2O column 180 μm pwv).

spectrometer, controlled by filters defining the total spectrometer bandwidth. The low-frequency signal-to-noise ratio could be improved at the expense of high-frequency sensitivity.

3.1 Case Study—10 Nov 1999 FTS and radiosonde measurements at Chajnantor

Beginning in 1998, a collaborative effort was undertaken by Cornell University, ESO, NRAO, and SAO, later joined by the Large Millimeter-Submillimeter Array (LMSA) project, to characterize the atmosphere above the ALMA site at Chajnantor through a series of radiosonde launches. A set of five launches made in the course of a single day on 10 Nov 1999, during which the SAO FTS was simultaneously recording sky brightness spectra at 10-minute intervals, provided an opportunity to make a direct comparison between these two measurements.

Fig. 3.3 shows the water vapor mixing ratio profiles and temperature profiles derived from the radiosonde data for these five radiosonde flights. The water vapor profiles show the characteristic ceilings dividing humid air below and drier air above, associated with relatively weak thermal inversions. During the night, the water vapor ceiling subsides, and the soil cools by radiation in the clear, high altitude conditions, with the associated formation of a surface thermal inversion. The same clear conditions, and tropical latitude, result in substantial solar heating of the soil during the day, with the development of a warm, humid surface layer in the afternoon at 19 UT. The solar heating also drives convection, and the water vapor ceiling rises.

FTS spectra taken over the same period were fitted using a layer configuration and fit parameters similar to Fig. 3.1, with the exception that the ground pressure level was 560 mbar. Also, the surface layer was omitted from the fit for spectra taken at night. In Fig. 3.4, time series of the H_2O column density from ground level to 500 mbar, and the total H_2O column density, are plotted both from the model fits to the FTS spectra, and from the integrated radiosonde H_2O profiles. Both show the same trend associated with the descent of the water vapor ceiling, however the night time radiosondes appear to overestimate the column density somewhat. This overestimate, and the shape of the corners in the H_2O profiles as they approach zero, are indicative of a lag in the humidity sensor response time.

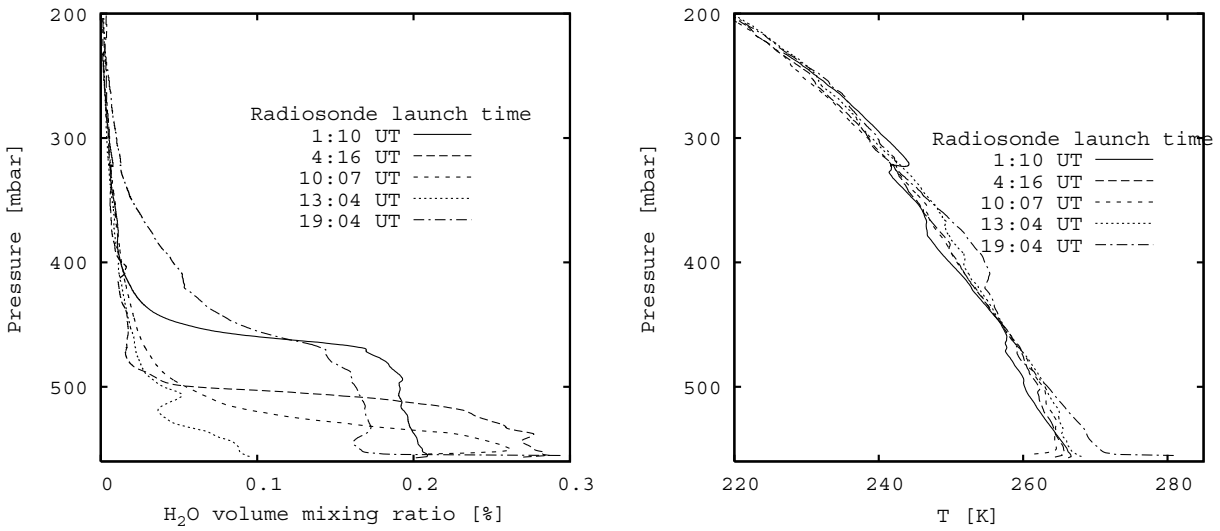

Fig. 3.3 – H_2O volume mixing ratio (left) and temperature profiles (right) from a series of five radiosonde launches at Chajnantor, on 1999 Nov 10. Sun rise, transit, and set times were 9:42 UT, 16:16 UT, and 22:49 UT, respectively.

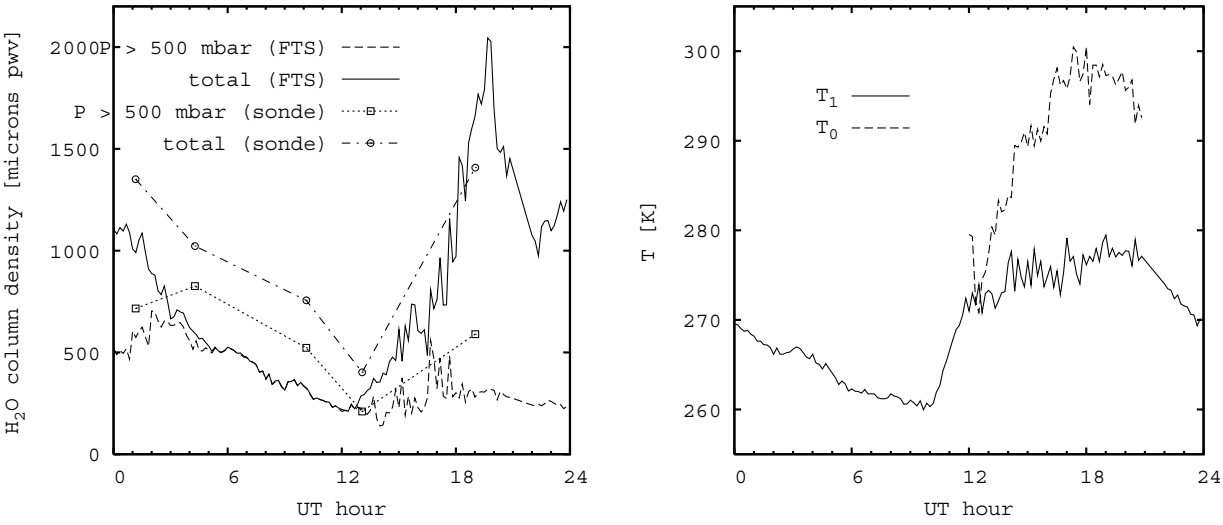

Fig. 3.4 – Time series of model fit parameters for FTS spectra acquired at 10-minute intervals at Chajnantor on 1999 Nov 10. Left: the fitted total pwv, and pwv column from ground level to the 500 mbar level, are displayed. Also shown are the same pwv columns derived from integrating the radiosonde H_2O mixing profiles in Fig 3.3. Right: the fitted base temperatures T_1 and T_0 (daytime only) defined in Fig. 3.1.

To the right in Fig. 3.4, time series are plotted for the fitted layer base temperatures T_0 (daytime only) and T_1 defined in Fig. 3.1. These may be compared with the radiosonde temperature profiles in Fig 3.3 at ground level. Towards sunrise, the fitted T_1 approaches the temperature at the base of the surface inversion measured by the radiosonde at 10 UT, as the water vapor profile descends towards ground level. After sunrise, the steep temperature

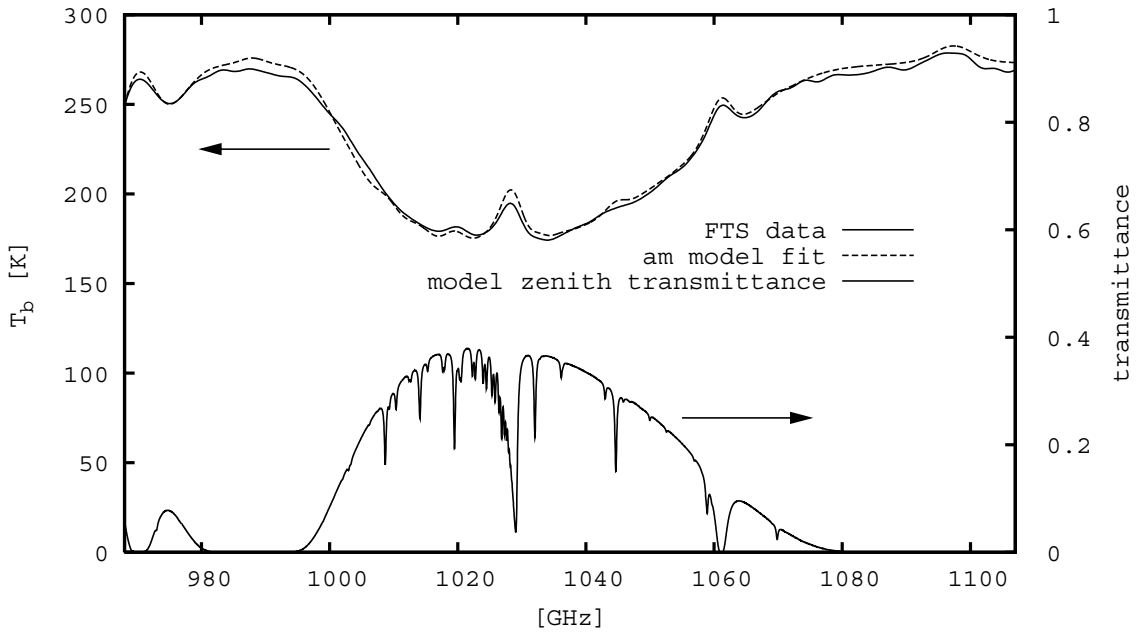

Fig. 4.1 – Model fit, at spectrometer resolution, to FTS sky brightness spectrum, and zenith transmittance spectrum, at full resolution, calculated from the fitted model.

gradient at the surface is well modeled by T_1, which follows the air temperature just above ground level, and T_0, which follows the actual surface temperature. Note that T_0 is higher than the first recorded temperature in the daytime radiosonde temperature profiles, as this point is logged a metre or more above the surface. Between T_1 and T_0, the fitted H_2O column density never exceeds 0.35 μm pwv.

4. Atmospheric calibration for astronomical observations.

The FTS records sky brightness temperature at the zenith. For calibrating astronomical observations, what is needed is the transmittance through the atmosphere at the elevation of the astronomical source. With the model fit in hand, it is a simple matter to recalculate this from the model. Moreover, the recalculation can be done at full resolution, rather than at the broader resolution of the FTS, in this case 3 GHz. This procedure is particularly useful in the neighborhood of unresolved ozone lines. Fig. 4.1 shows an example using the same spectrum from Sairecabur presented in Fig. 3.2, focusing on the 1030 GHz atmospheric window. Several O_3 rotation lines which are unresolved in the FTS spectrum, are resolved in the model calculation.

5. Conclusion

This paper has demonstrated the use of a Fourier transform spectrometer for obtaining a clear picture of the atmospheric conditions above an observatory. This information is invaluable for observations at terahertz frequencies, where the optical depth of the atmosphere is generally high, and where boundary layer phenomena can play a significant role in the radiometric properties of the sky. At the RLT, we have found the FTS to be an essential tool for calibrating the atmospheric transmittance during astronomical observations. It is our belief that operation of a similar instrument at present and future submillimeter and terahertz observatories can offer a significant enhancement to the quality of the observations, and provide useful auxiliary data for use with other site characterization instruments such as atmsopheric phase monitors.

References

Andrews, D. G. 2000, An Introduction to Atmospheric Physics (Cambridge, Cambridge University Press)

Blundell, R. et al. 2003, Proc. Thirteenth Int. Symp. Space Terahertz Tech., p. 159-166

Chamberlin, R. A. 2001, Journal of Geophysical Research (Atmospheres), 106 20,101

Goody, R. M., & Yung Y. L. 1989, Atmospheric Radiation, Theoretical Basis, 2nd ed. (New York, Oxford University Press)

MacDermid, et al. NOAA CMDL Summary Report #25 (1999). Data in Fig. 2.1 have been scaled by 1.25, so that the integrated column matches the typical integrated Dobson column measured from Mauna Loa.

Marrone, D., et al., these proceedings

Paine, S. 2004a, "The *am* Atmospheric Model" SMA Technical Memo #152 rev. 2.0, available at http://sma-www.cfa.harvard.edu/private/memos.

Paine, S. 2004b, "Tropospheric Phase Calibration Using Stratospheric Ozone Line Emission" SMA technical memo, in preparation.

Stark, A. A. et al. 2001, Publications of the Astronomical Society of the Pacific 113, 567

Sutton, E. C., and Hueckstaedt, R. M. 1996, Astron. Astrophys. Suppl. Ser. 119, 559

Yngvesson, S. et al. 2004, these proceedings

Characterization and Status of a Terahertz Telescope

Daniel P. Marrone, Raymond Blundell, Hugh Gibson*, Scott Paine, D. Cosmo Papa, C.-Y. Edward Tong
Harvard-Smithsonian Center for Astrophysics
60 Garden Street, Cambridge, MA 02138 USA
dmarrone@cfa.harvard.edu

Abstract

The Receiver Lab Telescope (RLT) is a ground-based terahertz observatory, located at an altitude of 5525 m on Cerro Sairecabur, Chile. The RLT has been in operation since late 2002, producing the first well-calibrated astronomical data from the ground at frequencies above 1 THz. We discuss the status of this telescope after 18 months of operation and plans for the upcoming observing season.

There are many practical challenges to operating a telescope at these frequencies, including difficulties in determining the pointing, measuring the telescope beam and efficiency, and calibrating data, resulting from high receiver noise, receiver gain instabilities, and low atmospheric transmission. We present some of the techniques we have employed for the RLT, including the use of atmospheric absorption lines in the place of continuum measurements for efficiency and beam measurements, and the utility of a Fourier-transform spectrometer for producing reliable data calibration.

1 Introduction

Astronomy at frequencies above 1 THz has long been considered impossible from ground-based observatories because of strong atmospheric absorption. As a result, there is a great deal of effort currently directed toward developing airborne and space observatories for this portion of the electromagnetic spectrum. Development of the HIFI instrument of the Herschel satellite is discussed extensively in these proceedings. Recently it has been shown that terahertz astronomy is possible from extremely dry ground sites, such as the South Pole and high in the Atacama Desert of Chile, where transmission is routinely observed in several windows between 1 and 3 THz (Paine et al. 2000, Matsushita et al. 2000). Many groups are now attempting to use the windows offering the highest transmission, centered at 1.03, 1.35, and 1.5 THz (see Figure 1), for astronomical observations. The Antarctic Submillimeter Telescope and Remote Observatory (AST/RO) (Stark et al. 2001) now has two instruments in place for such observations: SPIFFI (Nikola, et al. 2004), and TREND (Gerecht et al. 2003). The 12-meter APEX telescope, located at the ALMA site, will also have receivers for these terahertz windows in the next year.

The first (and currently only) telescope to make routine ground-based observations in these terahertz windows is the Receiver Lab Telescope, built by the Smithsonian Astrophysical Observatory (SAO) in collaboration with the Universidad de Chile. The development of this telescope has been reported on in previous editions of these proceedings, beginning with its introduction by Blundell et al. (2002), and followed by the presentation of early data (Radford et al. 2003). In this paper we provide a summary of the status of the RLT and planned upgrades (§2). The unique challenges of ground-based terahertz observations are discussed in §3. In order to properly calibrate our data we have explored new techniques (§3.1, 3.2) which may be of interest at other observatories facing similar conditions.

*Present address: RPG Radiometer Physics GmBH

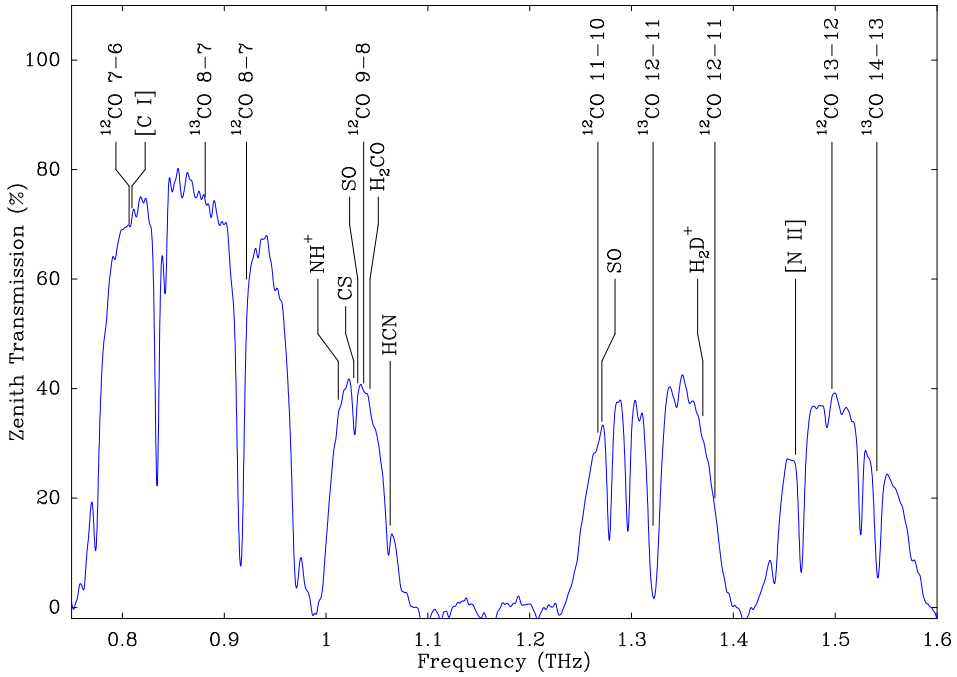

Figure 1: An example of the terahertz windows available from Cerro Sairecabur. This atmospheric transmission spectrum is actual data from the Receiver Lab Fourier-transform spectrometer (discussed briefly in §3.1, see also Paine et al. 2000), obtained on a very good day at the RLT site. The frequencies of several astronomically interesting lines are also plotted.

2 The Receiver Lab Telescope

The RLT is located on Cerro Sairecabur in northern Chile, 40 km north of the future ALMA site. This site, at a latitude of 22.5° S, is well suited for studies of the inner galaxy and nearby spiral arms as most objects in these regions pass almost directly overhead. The telescope sits at an elevation of 5525 meters, 500 meters higher than ALMA, making it the highest telescope in the world. During the SAO site testing program that preceded the construction of the RLT, the Receiver Lab Fourier-transform spectrometer (FTS) was used at the ALMA site (Paine et al. 2000) and on Sairecabur. It was found that the Sairecabur site shows better peak transmission and a higher fraction of time available for terahertz observations because it is more often above the atmospheric inversion layer responsible for trapping moisture. An example of the transmission at Sairecabur is shown in Figure 1.

The RLT (Figure 2) is an 80 cm alt-az telescope sitting atop a 20-foot shipping container. The container houses the telescope tower, receivers, correlator, control computer, and equipment associated with the solar power system. The telescope is outfitted with two receivers for frequencies between 800 GHz and 1.6 THz. Frequency coverage is currently limited by the availability of solid state local oscillators, so the 1.5 THz window is not accessible. The mixers are waveguide-mounted phonon-cooled HEBs. All of those used on the telescope have been NbN devices, with and without MgO buffer layers. Typical noise temperatures are 950-2000 K in our frequency range. The 1 GHz wide IF is centered on 3 GHz. Spectra are obtained from a 330 channel digital autocorrelation spectrometer with 3 MHz resolution (1 km/s at 1 THz).

The RLT routinely observes spectral lines that are rarely, if ever, observed anywhere else. The most commonly used lines are ^{12}CO $J = 7 \rightarrow 6$ (806.65 GHz), ^{13}CO $J = 8 \rightarrow 7$ (881.27 GHz), and ^{12}CO $J = 9 \rightarrow 8$ (1.03691 THz). With an $85''$ beam at 1 THz, the RLT is well suited to mapping of extended emission, such as that arising in large H II regions. The first RLT terahertz spectrum was obtained on November 11, 2002. First scientific results can be seen in Marrone et al. (2004).

In the near future there are many upgrades planned for the telescope. In May we will begin observations of the CO $J = 11 \rightarrow 10$ line at 1.2670 THz, the first ground-based observations of this line. Expansion to the 1.5 THz window awaits a local oscillator, which should arrive this year. The correlator is due to be

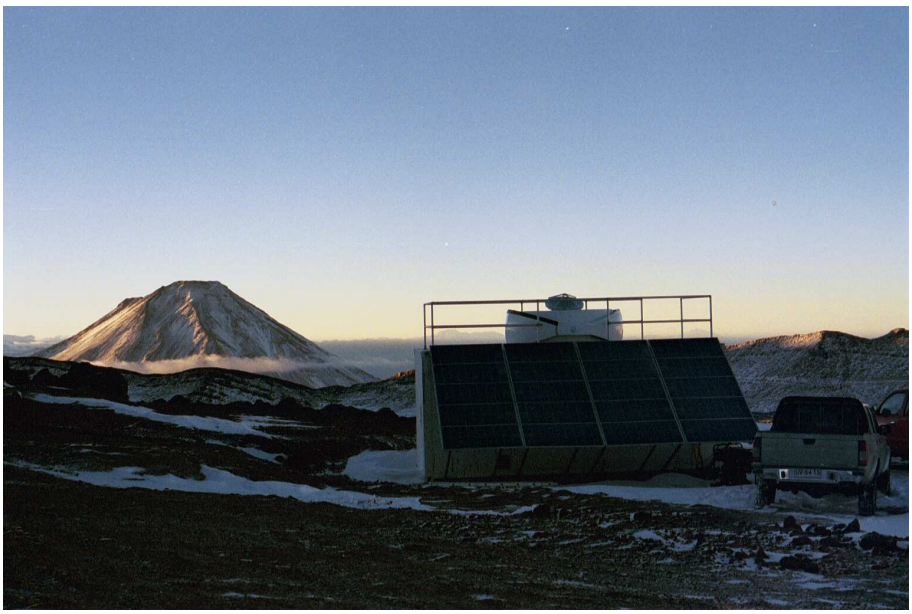

Figure 2: The Receiver Lab Telescope, on Cerro Sairecabur, Chile.

replaced with a new 512-channel correlator with 1 and 2 MHz resolution, providing greater detail in the narrow galactic emission lines we normally observe.

3 Challenges of Ground-based Terahertz Astronomy

Ground-based terahertz telescopes have some advantages over airborne or spaceborne instruments. Ground telescopes can be made larger than is feasible in the air or in space, are considerably cheaper, are easier to service than satellites, and may provide more observing time than can be obtained from an aircraft. Of course, observations from the ground are strongly limited by the properties of the atmosphere. Most importantly, observations are only possible in a few windows, but even within these windows the high atmospheric opacity, lack of strong calibrators, and the instabilities of terahertz receivers conspire to make common pointing, calibration, and telescope characterization tasks difficult. In the following sections we discuss solutions to these problems derived from 18 months of RLT operations.

3.1 Atmospheric Calibration

In order for spectra obtained from a terahertz telescope to be scientifically useful they must be properly calibrated. A common convention is to correct measured spectra for receiver gain, inefficiencies in the telescope, and atmospheric absorption, placing the observed line on a temperature scale that would be observed by a perfect telescope above the atmosphere (this is the T_A^* scale of Ulich & Haas 1976). The atmospheric correction, and typically the efficiency correction, requires a reliable method of determining the opacity.

At the best well-characterized observing sites the atmospheric transmission in the windows above 1 THz is no better than $\sim 40\%$, and is generally much lower. In addition, our experience at Cerro Sairecabur shows that large variations in transmission are common: in a single night the zenith transmission can vary by as much as 50% of its peak value. Changes in transmission between and within observing nights, whether due to changing source elevation or atmospheric fluctuations, can have a significant effect on the apparent strength of a spectral line. Without reproducible atmospheric correction, data taken on different nights, or even at different times in the same night, cannot be usefully compared.

There are several techniques for properly accounting for the atmospheric attenuation. Most radio astronomy calibration techniques have been developed at lower frequencies where the atmospheric effects are smaller and receivers are more sensitive and stable, making it difficult to apply them directly to observations

with the RLT. One such example is the skydip, in which the sky temperature is measured as a function of elevation and the resulting curve is used to determine the mean atmospheric temperature and zenith opacity. Although the variation in sky temperature with elevation is small when the atmospheric transmission is low, it is still easily measurable with RLT receivers. The most significant problem we have encountered with this technique is that instabilities in the power output of the receiver are greatly magnified in skydips when atmospheric transmission is low.

The magnification of power instabilities by skydips can be understood from the equation for the antenna temperature (T_A) on blank sky. At elevation ϵ, with receiver noise T_{rx}, mean atmospheric temperature T_{atm}, and zenith transmission t, the measured T_A is:

$$\begin{aligned} T_A &= T_{rx} + T_{sky} + T_{cmb} \\ &\simeq T_{rx} + T_{atm}\,(1 - t^x) \end{aligned} \tag{1}$$

where $x = csc(\epsilon)$. The cosmic background term (T_{cmb}) has been dropped in the second line because the Rayleigh-Jeans brightness temperature of the CMB is vanishingly small at 1 THz. The transmission inferred from T_A measured at one elevation (as a function of the usually unknown T_{atm}) can be found by rearranging equation 1:

$$t = \left(1 - \frac{T_A - T_{rx}}{T_{atm}}\right)^{1/x} \tag{2}$$

Instabilities in the IF output power (P_A), whether they originate in the receiver or the atmosphere, correspond to changes in the measured T_A because $T_A = KP_A$, where K is a conversion factor between power and antenna temperature determined using hot and cold loads. Differentiating equation 2 with respect to P_A and substituting for T_{sky} (as in equation 1), we obtain:

$$\frac{\partial t}{\partial P_A} = \frac{-t}{xP_A}\left[\left(1 + \frac{T_{rx}}{T_{atm}}\right)t^{-x} - 1\right] \tag{3}$$

Ignoring all other error contributions, we can translate this equation into a relationship between the rms power fluctuations and the rms error on t. By noting that T_A^* is proportional to t^{-x}, we can go directly to the fractional error ($\sigma_{T_A^*}/T_A^*$) in spectra calibrated using a single skydip transmission measurement for power fluctuations σ_{P_A}/P_A:

$$\frac{\sigma_{T_A^*}}{T_A^*} = \left[\left(1 + \frac{T_{rx}}{T_{atm}}\right)t^{-x} - 1\right]\frac{\sigma_{P_A}}{P_A} \tag{4}$$

In reality, one does not use a single measurement to determine both t and T_{atm}. For a more typical 10 point skydip, using RLT values for T_{rx} (1000 K), T_{atm} (250 K), and t for frequencies above 1 THz (20%), the random calibration error contributed by transmission measurement error is of the order of 15-20 times the power instabilities. A typical rms noise on the continuum power output of an RLT receiver is 0.5%, making this a significant cause of error in calibration.

Rather than the skydip method described here, we directly measure the zenith transmission using our FTS during all RLT observations. This instrument generates an atmospheric transmission spectrum from 300 to 3500 GHz at 3 GHz resolution every 10 minutes, and does not require any of the telescope observing time (as skydips would). An example of the reproducibility of the FTS calibration is shown in Figure 3. Despite an interval of an hour between two observations of the same object, during which time the transmission was observed to decrease from 22.5% to 19% (or 19% to 12.5% at the source elevation), the two calibrated spectra show very similar amplitude. More details about the use of an FTS in calibrating astronomical data, including refinements that can be made using atmospheric models, can be found in Paine & Blundell 2004.

3.2 Telescope Characterization

The RLT has also faced difficulties in determining the telescope efficiency, beamshape, and radio pointing. Typically, these properties would all be measured by mapping the continuum emission of a planet, but we have found that drifts in the power output of our HEB receivers make continuum maps unreliable.

An alternative approach is to use a more narrowband signal as a calibration source, since other noise sources should be less important relative to radiometric noise in a smaller bandwidth (e.g. Schieder & Kramer

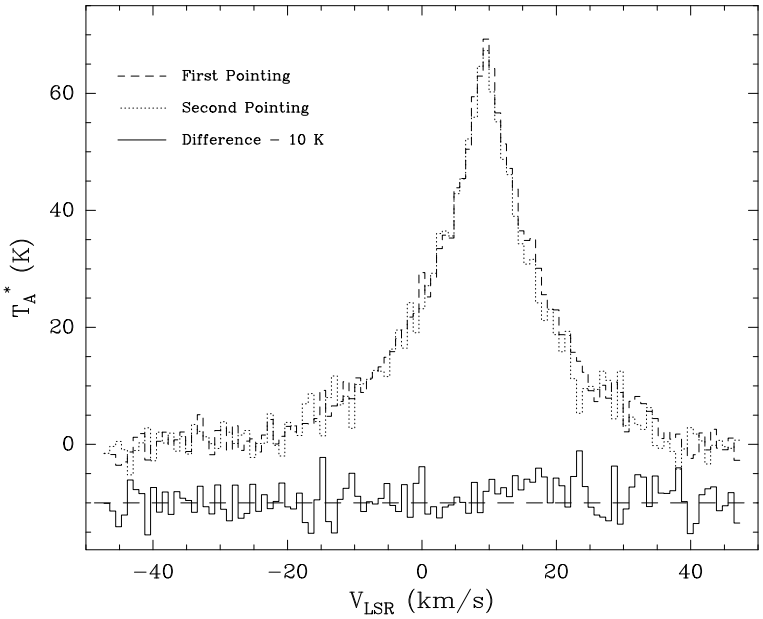

Figure 3: An example of the results of our FTS calibration technique. Shown are two spectra of Orion KL in CO $J = 9 \rightarrow 8$ (1.037 THz), each required 1 minute of on-source integration time and the two observations were made one hour apart. The system temperature increased by 56% between the observations, but the difference between the two calibrated spectra is almost consistent with the rms noise seen in the baseline channels.

2001). Narrow, unsaturated atmospheric lines, such as O_3 lines, provide exactly such a signal when observed against the disk of a planet. Moreover, by using planets as a backlight we retain the source geometry that is normally used for these purposes.

Our procedure for obtaining a beam map, pointing offsets, and a beam efficiency is as follows. We make a map of a planet using an ozone line near to the observing frequency of interest. Once calibrated, we fit each spectrum in the map with a model ozone line profile to determine a best-fit line depth. The line depths form the basis for a beam map because the variations in line depth reflect changes in the coupling of the telescope beam to the planet (rather than an atmospheric effect), just as continuum measurements would. By fitting the derived map we obtain a beamshape and an offset from the nominal source position. The fit also yields the line depth that would be observed if there were no pointing error, which, after accounting for the coupling of the beam to the planet, can be used to determine the efficiency.

Our method and the standard continuum method are similar in many respects. We require good calibration to ensure that the individual map spectra can be reliably compared to each other, but this is no different than what is required for a continuum map taken over a long enough interval that the atmospheric transmission and source elevation change. Once the calibrated line depths are obtained, the procedures for determining the pointing and beam shape are the same as one would use with a continuum map. The only additional requirement of this portion of our method is a model ozone lineshape, which we obtain from the *am* atmospheric model[1] (Paine 2004) and a vertical ozone profile from ozonesonde and lidar observations made from Hawaii (Oltmans et al. 1996, Leblanc & McDermid 2000). The line depths we determine are only weakly dependent on the assumed vertical ozone profile for reasonable profiles. For the efficiency determination we need a good estimate of the true strength of the ozone absorption. The absorption represents the known signal to which we compare our observed signal and obtain an efficiency, analogous to comparing a measured continuum brightness temperature to an expected planetary brightness temperature. Fortunately, the total O_3 column is measured daily at many sites worldwide, including the nearby Marcapomacocha, Peru, and is made available by the NOAA Climate Monitoring and Diagnostics Laboratory[2].

Figure 4 is an example of a beam map made with the technique just described. The map was made using

[1] *am* is available at: http://cfarx6.harvard.edu/am

[2] Ozone column measurements are available on-line at: http://www.cmdl.noaa.gov/ozwv/dobson

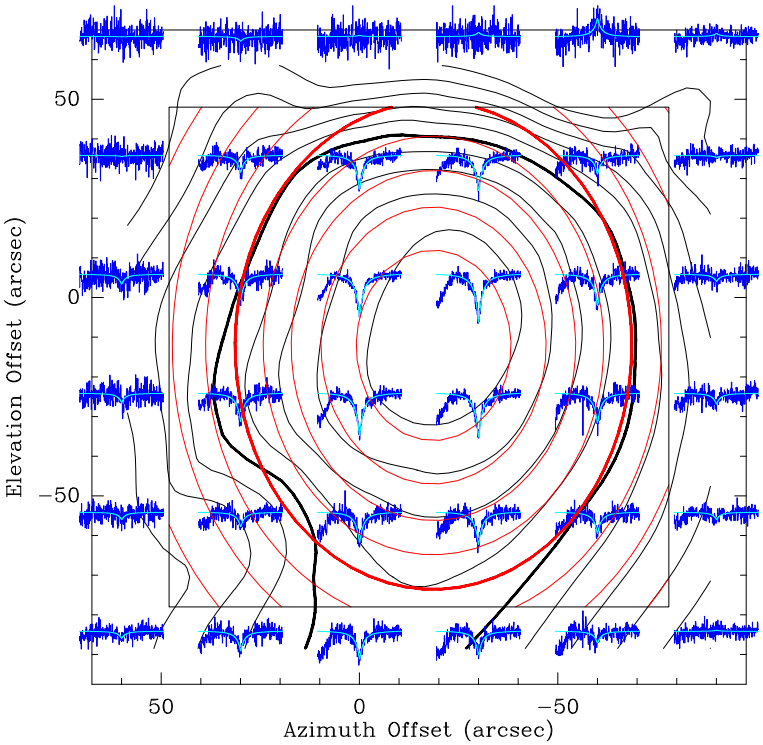

Figure 4: An O_3 beam map made with the RLT against Jupiter. Spectra were taken on a 30″ grid in an irregular order to reduce the biasing effects of calibration errors. The individual spectra (——) and best fit line profiles (——) are shown at each map point. The absorption at the left edge of each spectrum is a correlator artifact. The beam is fit to the central 16 spectra (enclosed in a box). The measured (——) and best fit (——) beams are contoured in 10% steps with the 50% contour reinforced. The two contour sets are seen to agree well over most of the map, except toward the north where noisy spectra that have been excluded from the fit cause the measured contours to deviate from the best fit contours.

the 883.057 GHz line of ozone, with Jupiter (41.7″ diameter) as the continuum source. From this map we find pointing offsets of -19.0±1.6″ and -12.4±2.1″ and FWHM beamsizes of 96±5″ and 117±9″ in azimuth and elevation, respectively, along with a line depth of 5.3±0.3 K[3], which corresponds to an efficiency of 44%. The measured pointing offsets are small compared to the beamsize and are comparable to those suggested by previous terahertz observations. The beamsize is similar to what is expected from the optics design, while the efficiency suggests that at the time that this map was made the receiver was shifted slightly from the designed position so that its beam was clipped before reaching the telescope.

We believe that the use of ozone lines as a calibration tool can also be extended to other telescopes. To determine whether this is a useful technique at a given telescope one must compare the fluctuations in the receiver output power, scaled by the system temperature, to the signal strength from available planets. For the RLT and Jupiter, the expected signal is around 10 K at 1 THz, but the receiver instabilities (of the order of 0.5% rms in 1 second integrations on the RLT) applied to a T_{sys} of 20000 K correspond to 100 K fluctuations. Larger telescopes see a larger planetary signal, so they may be able to tolerate small instabilities. On the other hand, if beam maps are made in poorer transmission or at lower source elevation T_{sys} can be significantly larger than the 20000 K used here. The use of ozone as a calibrator is not something that restricts this technique to Chile; daily ozone measurements are also made from Mauna Loa, Hawaii, and the South Pole, so this information is available for all major submillimeter sites. This technique can be used near to any frequency of interest because suitable ozone lines are available throughout all of the terahertz windows. As a final consideration, the measurement technique employed in making the beam map may affect the expected depth of the ozone line. For position- or beam-switched observations, where the map

[3]These errors are obtained from simulations of the effects of reasonable random errors in the zenith transmission and receiver noise, and will be larger when systematic effects are included.

spectra are obtained by combining on- and off-source spectra as (ON-OFF)/OFF, the expected line depth is not simply proportional to the planet signal times the fractional absorption due to ozone. As T_{rx} decreases, a term in the expansion of the line depth that is insignificant for the RLT (<5% for $T_{rx} + T_{sky} = 1200$ K) grows like $1/(T_{rx} + T_{sky})$ and could be relevant for lower noise terahertz receivers.

4 Conclusions

We have discussed the status of the SAO Receiver Lab Telescope, presently the only telescope making ground-based astronomical observations at frequencies above 1 THz. We are currently beginning observations in the 1.3 THz atmospheric window, while observations in the 1.5 THz window await a local oscillator. Neither of these windows has previously been used for astronomical observations.

We have also presented techniques for making ground-based terahertz observations. In particular, we have discussed the difficulty of using skydips for data calibration and the power of a Fourier-transform spectrometer as a calibration tool. We have also presented a new technique for characterizing a telescope in the presence of high system temperatures and receiver instabilities.

References

Blundell, R. et al. 2002, in Proc. Thirteenth International Symposium on Space Terahertz Technology

Gerecht, E. et al. 2003, in Proc. Fourteenth International Symposium on Space Terahertz Technology

Leblanc, T. & McDermid, I. S. 2000, Journal of Geophysical Research, 105, 14613

Marrone, D. P., et al. 2004, Astrophysical Journal, submitted

Matsushita, S., et al. 2000, in Proc. SPIE Vol. 4015, Radio Telescopes, ed. H. R. Butcher, 378-389

Nikola, T, et al. 2004, these proceedings

Oltmans, S. J. et al. 1996, Journal of Geophysical Research, 101, 14569

Paine, S. et al. 2000, Publications of the Astronomical Society of the Pacific, 112, 108

Paine, S. 2004, "The am Atmospheric Model" SMA Technical Memo #152, available at http://sma-www.cfa.harvard.edu/private/memos

Paine, S. & Blundell, R. 2004, these proceedings

Radford, S. J. E., et al. 2003, in Proc. Fourteenth International Symposium on Space Terahertz Technology

Schieder, R. & Kramer, C. 2001, Astronomy & Astrophysics, 373, 746

Stark, A. A. et al. 2001, Publications of the Astronomical Society of the Pacific, 113, 567

Ulich, B. L. & Haas, R. W. 1976, Astrophysical Journal Supplement Series, 30, 247

Design and Verification of ALMA Band 9 Receiver Optics

A. Baryshev[1], R. Hesper[1], K. Wielinga[2], G. Gerlofsma[1], M. Carter[3]

[1]SRON, Landleven 12, P.O.Box 800, 9700 AV, The Netherlands.
[2]Mecon Engineering BV, Koopmanslaan 25, Postbus 679, 7000 BK Doetinchem, The Netherlands.
[3]IRAM, 300 Rue de la Piscine, Domaine de Universitaire de Grenoble, 38406, St. Martin d'Heres, France.

ABSTRACT

The Atacama Large Millimeter Array (ALMA) is an interferometer consisting of 64 antennae of 12 m diameter. It will be placed in Chile at a high altitude plateau (5000 m) with exceptionally good atmospheric conditions for astronomical observations at sub-mm wavelengths. The ALMA frequency coverage (30 GHz – 950 GHz) is divided into ten bands corresponding to the atmospheric transparency windows. The receiver for each band is mounted as a separate module in the ALMA front-end cryostat, which provides 4K, 12K, and 90K temperature levels.

We would like to report on the design of the ALMA band 9 (602-720 GHz) receiver module. A detailed optics layout for coupling between the telescope secondary and the SIS mixer feed horns will be presented. The local oscillator insertion optics will be described allowing for mounting a local oscillator module inside the receiver module at the 90K level.

To verify our intended production technique (CNC machining without any need for adjustment), a two-mirror prototype, representative of the signal path, has been produced. The output beam of this prototype was measured in phase-and-amplitude sensitive set-up. A superlattice device, used as a subharmonically pumped mixer, was mounted instead of the SIS device into the mixer housing. This allowed the evaluation of the optics (including the influence of machining tolerances) to be performed at room temperature. The receiver beam was measured in the near field at several signal frequencies using a Gunn-multiplier chain to generate the probe signal. A homodyne detection technique was used to retrieve both phase and amplitude, achieving a 60 dB signal-to-noise ratio. The measured patterns are then compared with theoretical predictions. Far-field beam patterns are computed from the measured near-field data allowing to predict the illumination of the telescope secondary mirror. Finally, the data was also used to verify if our CNC production method is suitable for production of mirrors with high enough quality for sub-mm wavelengths

INTRODUCTION

1.1 ALMA instrument

The Atacama Large Millimeter Array (ALMA) is an interferometric array of 64 heterodyne receivers. It will be located at an altitude of 5000 meters in northern Chile. This array is being built in collaboration between North America and Europe with Japan in the process of joining the project.

Each antenna consists of a 12 m diameter parabolic main reflector, a 0.75 m diameter secondary mirror. The receiver frequency coverage is 30-950 GHz. It is subdivided into ten bands, corresponding to the regions of high atmospheric transparency. For the first scientific operations four frequency bands were chosen: 3 (85–116 GHz), 6 (211-275 GHz), 7 (275-375 GHz) and 9 (600-702 GHz). All of these receivers are dual polarization and have either sideband separation or double sideband SIS tunnel junction mixers. A wide Intermediate Frequency (IF) bandwidth of 8 GHz was chosen as a baseline requirement.

The chosen mixer technology requires cryogenic temperatures of liquid Helium level (4K) and high vacuum. Due to the high number of systems to be produced, special attention should be paid to product/quality assurance [1,2,3].

1.2 ALMA front-end design

An artist impression of the ALMA front-end cryostat is shown in fig. 1. Each front-end holds 10 receivers housed in so-called cartridges and provides four temperature levels: 4K, 12K, 90K and ambient temperature.

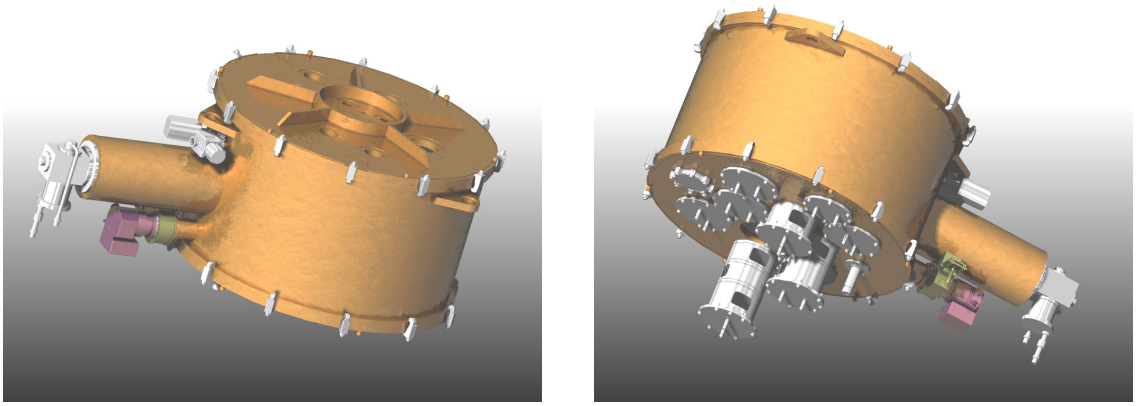

Fig. 1 Artist impression of the ALMA front-end cryostat holding 10 receiver cartridges. The design is done by the Rutherford Appleton Laboratory (UK).

Fig. 2 Photograph of an ALMA cartridge structure.

The heat contact between the cryostat and the cartridge is provided by flexible links, allowing the insertion of the cartridges from the bottom of the front-end cryostat without accessing any internal structure [5]. The internal cryogenic connections are made automatically during cool down.

The telescope beam is entering the cryostat at the top, with the beam waist located near the cryostat window. Lower frequency bands have active optical elements (lenses and elliptical mirrors) mounted outside the cryostat vacuum space. However, for bands 5 – 10 all optics are contained within the cartridge at 4K.

The cartridge structure, on which all receiver elements will be mounted, is presented in fig. 2. A Sumimoto cryocooler provides four temperature levels (4K, 12K, 90K and ambient). The mechanical reference for the 4 K plate is provided through the cartridge support structure from the bottom of the cryostat. A finite element analysis was performed by RAL to ensure that the cartridge structure is rigid enough to perform within tolerance for all telescope elevation angles (from 0º to 90º).

BAND 9 OPTICS DESIGN

2.1 Design requirements and concept

The band 9 receiver optics has the following main design goals: a) all optics is mounted in the cartridge structure shown in fig. 2; b) the LO power source is located on the 90 K stage of the cartridge; c) most of the optics is located at the 4 K level; d) two orthogonal linear polarizations should be received from the sky; e) the secondary mirror illumination edge taper should be -12 dB and should not depend on frequency within the observing band; f) the design should be based on reflective optical elements; g) five waists beam clearance should be observed; and h) the cross polarization signal level should be less than –20 dB.

The ALMA antenna is a classical Cassegrain system, with an f-ratio of 8 for the beam entering the receiver. The receiver position is 0.1 m offset from main symmetry axis of the antenna.

Additional attention should be paid to the series production of the optics. The ALMA project requires 64 receivers to be built. Because of this requirement it was decided to build all the optics using conventional CNC machining and make machining tolerances sufficiently tight to avoid additional alignment procedure.

The frequency of band 9 requires a 7 micron RMS mirror roughness, and tolerances for the mirror surfaces of the order of 40 microns. These parameters are well within reach of up-to-date CNC machining techniques. Note that 7 micron RMS will not allow optical verification of the mirror alignment, and therefore use of a sub-mm wave antenna beam pattern measurement system is essential to asses the quality of the optical system. In order to verify the design concept and the applicability of direct CNC machining for these frequencies, a simple model of the signal

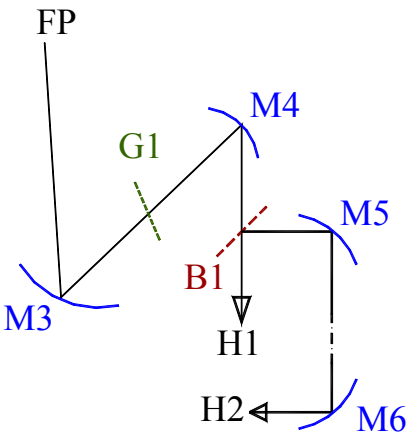

Fig. 3 Layout of optics. Beam dumps and one of the signal polarizations are not shown.

chain – a two-mirror block - has been built, together with a mixer horn, the details of it will be presented later in the section about measurement results.

2.2 Signal path

Drawing of signal path is presented in fig. 3. Telescope focus is located in the point FP. Two elliptical mirrors (M3, M4) are used to reimage the secondary mirror of telescope (M2) into the mouth of a mixer horn with the size, which is appropriate for -12 dB edge taper. The quarterly focal point (the second focal point of mirror M4) coincides with an apex of the corrugated horn H1. This construction allows for frequency independent coupling of the telescope beam to a corrugated horn feed. Mirror diameters are chosen to put through a 5 w size beam.

The second polarization beam is split off from the main beam at 90 degrees angle by means of a grid G1. The grid is located between mirrors M3 and M4 at the narrowest point of the beam (near tertiary focus). M3 is used for both polarizations and an additional mirrors M4', M5', and M6' are used for forming an orthogonal polarization beam arriving at second mixer horn H2. The cross polarization signals are absorbed by a special absorber plate mounted behind the grid G1 at 4K level.

2.3 LO insertion

Local oscillator signal is inserted quasioptically using a beamsplitter B1 in fig. 3. It is mounted between signal horn and mirror M4. A 12 micron Mylar film is used as beamsplitter material that corresponds to approximately 7% of LO signal insertion. The LO signal is then reflected towards 90 K plate of the cartridge where additional mirror M6 and final local oscillator multiplier (quintupler) is located. The quintupler beam is formed by a horn H2. The system is designed to put through a four waists size beam. Additional infrared heat filters are mounted on 12 K stage to decouple 4K and 90 K levels thermally.

The second polarization has its LO inserted in exactly the same way using mirrors M5' and M6' that are identical to M5 and M6 respectively. It has its own multiplier and horn H2'. This polarization is not shown in fig. 3.

An absorber plate is mounted behind each of the beamsplitters for both polarizations to dump LO power that is not coupled into the beam.

2.4 Opto-mechanical design

The layout that is briefly described below has to be realized in practice, i.e. mirrors, beamsplitters, grids and mixer horns have to be mounted within a certain tolerances with respect to each other and optics should be aligned. A tolerance budget was made for current optics layout indicating that 40 micron displacement is the highest requirement for displacement to produce 1% of efficiency loss [3,4].

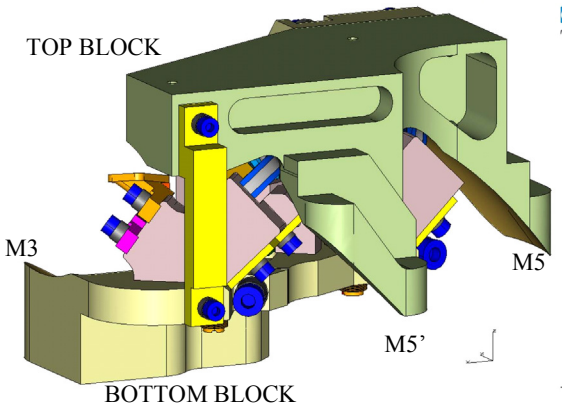

Fig. 4. Main signal optics design concept.

The main idea of the design is to make all the parts using CNC machining techniques observing tolerances. In this way all optics will be aligned upon assembly. Additional effort, like shimming or alignment using a lazer beam is not required. This allows for significant ease of requirements on mirror accuracy, grid foil flatness and beamsplitter foil flatness.

As it can be seen from the layout, mirrors M4, M5 and M4', M5' are pointing downwards. It is the most natural to make them out of one block during one CNC machining run. All beamsplitters and grids can be mounted in the block, also containing a mirror M3, which is directly machined in it. This concept is presented in fig. 4. The two blocks, bottom and top are

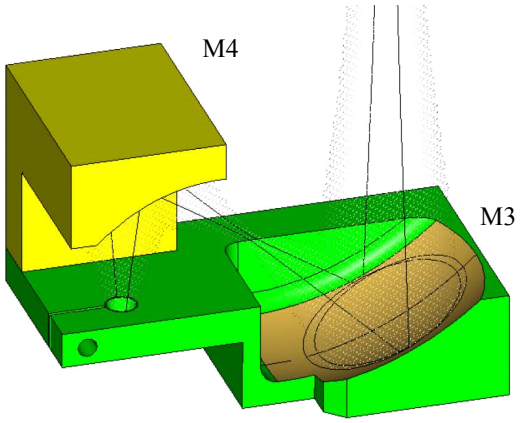

Fig. 5 A prototype two-mirror block for evaluating production techniques.

bolted to each other and interface is designed to keep these blocks within required tolerances.

2.5 Prototype mirror block

In order to verify if a selected machining techniques or design approach works a simplified model of a signal path consisting of two mirrors M3, M4 and mixer horn mount has been built as shown in fig. 5

MEASUREMENT SYSTEM

3.1 Scanning system and detection technique

A Measurement System: The measurements were made in the near field of the optics under test and similar to that described in [6]. A scheme of this system is shown in fig. 6. A small flared waveguide probe formed a transmitter beam in front of the receiver. Movements of the probe in the X, Y and Z planes were made in small discrete steps and at each point values of amplitude and phase were taken. The transmitter was a phase locked Gunn oscillator working between 100-120 GHz, which fed a X6 multiplication chain to have a transmitted signal between 600 and 720 GHz. A microwave synthesizer was used to drive a harmonic mixer within the phase lock loop. Signal of the same synthesizer was used as a LO for a detector. The intermediate frequency of 75 MHz was used the Gunn diode PLL circuit. An intermediate frequency of 75 MHz X 6 = 450 MHz can be detected by a subharmonically pumped mixer. A 450 MHz reference, coherent with IF signal, was created by multiplying the signal from 75 MHz PLL reference oscillator six times.

For most of the measurements a network analyzer with an access to internal reference and signal ports were used. This allows for using detection bandwidths up to 10 Hz (30 Hz was used in the measurements).

3.2 Standing waves compensation method

A standing wave in the setup was suppressed by using the following technique. Two data points were taken with lambda over four separation in z-axis. These two points were added up with correction of the phase of Pi over two. The forward signal is than added constructively, unlike the first order reflections, which has a phase difference of Pi. These reflections are added destructively. This method allows to effectively suppress parasitic effects due to first order reflections for beams, close to a parallel. Band 9 receiver f#8 beam is slow enough to achieve good standing wave suppression without degrading the quality of measurement itself. Additionally, an absorber plate around the

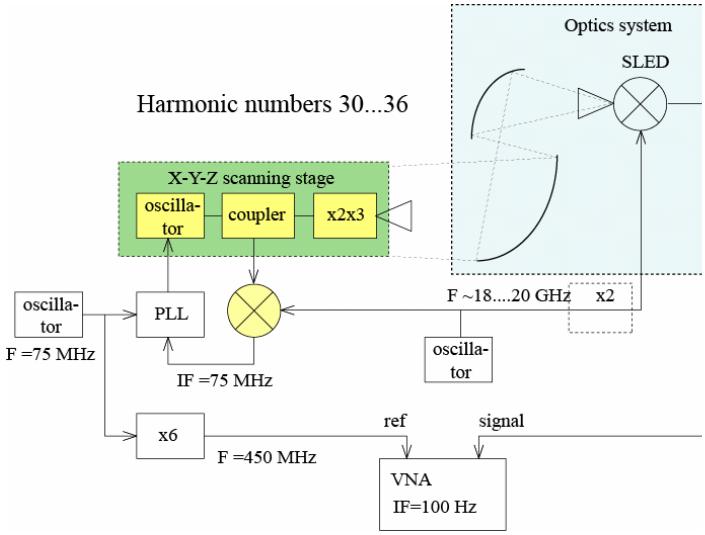

Fig. 6 Signal connections in the measurement setup

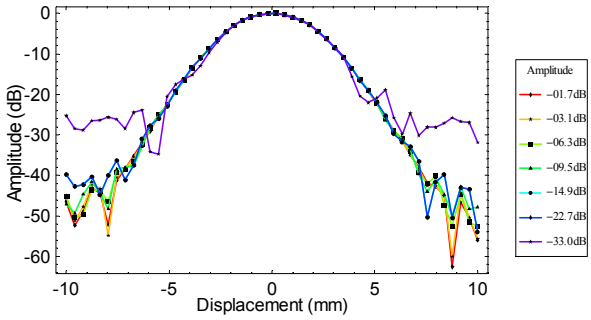

Fig. 7 Normalized amplitude field distribution measured at different signal source levels to check for a detector saturation effects.

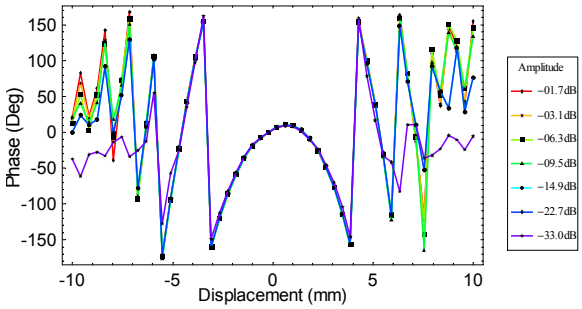

Fig. 8 Normalized phase field distribution measured at different signal source levels to check for detector saturation effects.

source was used to damp reflections.

3.3 Room Temperature detector and saturation

An SLED (super lattice electronic device) [7] was mounted instead of an SIS junction in one of our mixer holder to ensure that system under test fully represents mechanically the final receiver. This detector potentially has better conversion efficiency as conventional diode. Although, no specific matching circuit was designed to couple the SLED to an RF environment, signal to noise ratio of 72-80 dB has been obtained for all frequencies in ALMA band 9, using about 50-70 microwatt as an input signal. All measurements were done at room temperature. The SLED was pumped subharmonically. 36th harmonics of LO was typically used.

Since SLED is relatively new detector device for this type of measurements, special attention was paid for detector saturation by the input signal. To check this effect, subsequent measurements were done for a corrugated horn while only changing a source output power. Results of this measurement are presented in fig. 7 and 8 for amplitude and phase respectively. No significant compression was found in the data as well as phase appears to be stable even for very significant drop (-33 dB) of input signal power.

MEASUREMENT RESULTS

4.1 Laser beam propogation

The two-mirror block, presented in fig. 5 was produced by a CNC machining technique. Mirror surfaces were machined by a boll mill in the 5-axis CNC machine. After light polishing, the surface quality was good enough to put through a laser beam. The beam itself can be visualized by applying a water vapour fog during long time exposure of digital camera. The result is shown in fig. 9.

Intermediate (tertiary focus) and final (quarterly focus) are clearly visible. Some beam splitting can be observed at lower right corner of the picture. This is due to approximation errors that occur during milling of the mirror surface. Note that frequency, at which the effect is observed, is 1000 times higher than the required frequency.

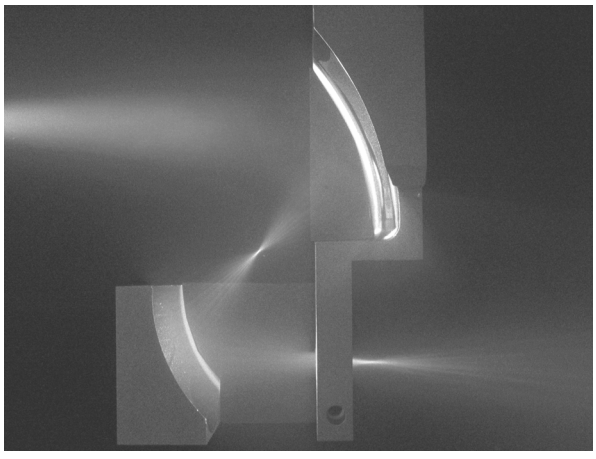

Fig. 9 Laser beam sent through machined two-mirror block.

4.2 RF beam pattern measurement and analysis

A 2-D plot of amplitude and phase beam distributions are shown in fig. 10 and 11 respectively. The mirror symmetrical axis coincide with Y-axis of scanner. One can see that a central maximum has a symmetrical shape both in phase and amplitude. A low levels of sidelobes are observed. A round ring structure at lower levels can be explained by periodical deviations of mirror shape from nominal curve due to machining strokes of the mill tool.

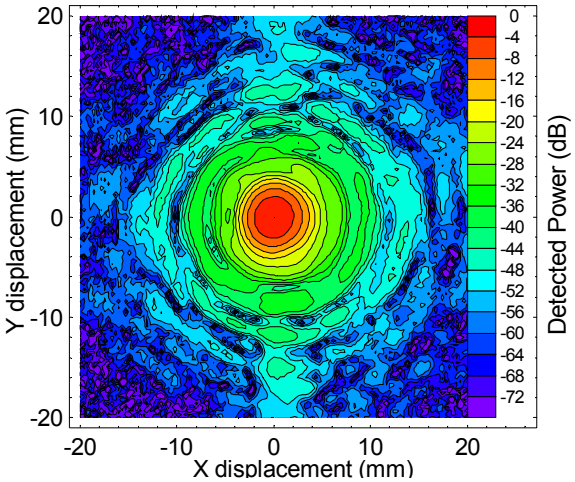

Fig. 10 Measured near field beam amplitude distribution of the two-mirror block at -50 mm from the waist plain. Frequency is 672 GHz.

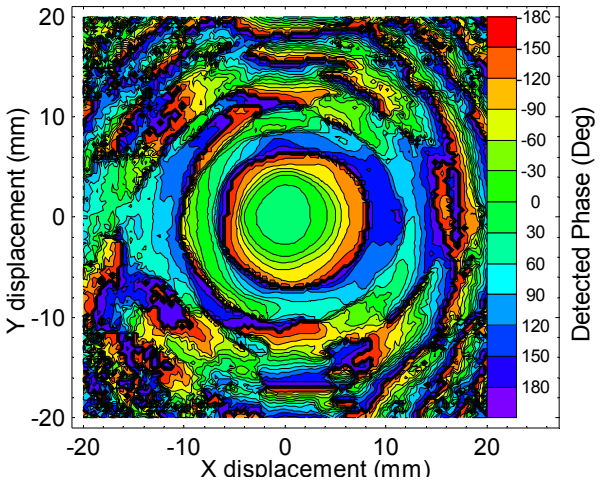

Fig. 11 Measured near field beam phase distribution of the two-mirror block at -50 mm from the waist plain. Frequency is 672 GHz.

Amplitude and phase information allows to calculate an overlap integral of the measured data with fundamental mode Gaussian beam. Ideally, this beam has six parameters, which can be determined from the data by maximizing Gaussian beam coupling. These parameters are: beam waist size, waist position (X,Y,Z), and two beam tilt angles. If the scanning plane is referenced to a mirror surface by a calibration device, obtained parameters allow to conclude about the production and mounting errors

frequencies. and the efficiency loss. The Gaussisian beam efficiency of the beam shown in fig. 10-11 is about 98%, which is very close to a theoretical predictions. The waist size, offsets and tilt angle are within the required

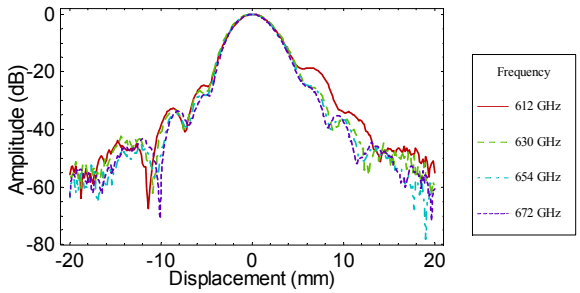

Fig. 12 Normalized amplitude field distribution measured along mirror asymmetrical axis at different signal frequencies.

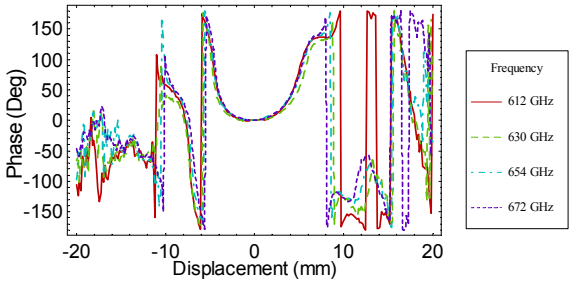

Fig. 13 Normalized phase field distribution measured along mirror asymmetrical axis at different signal frequencies.

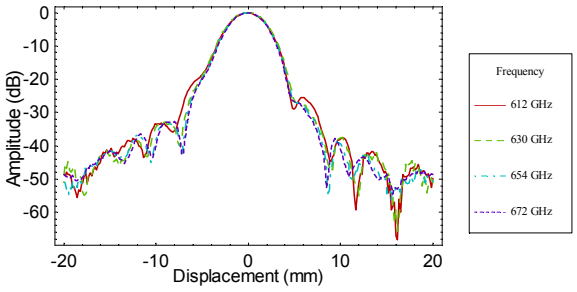

Fig. 14 Normalized amplitude field distribution measured along mirror symmetrical axis at different signal

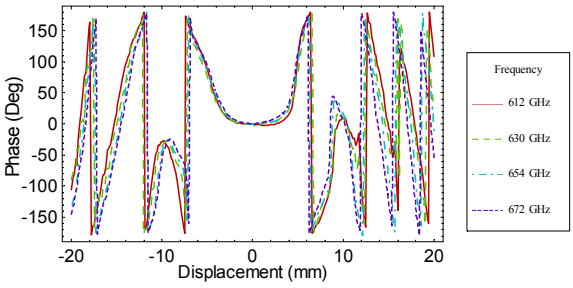

Fig. 15 Normalized phase field distribution measured along mirror asymmetrical axis at different signal frequencies.

tolerances. The efficiency loss is less than 1%.

Measured beam cross-sections both for symmetrical (Y) and asymmetrical (X) mirror axes are shown in fig. 12-15. These measurements were done for several frequencies in ALMA band 9. Note that beam quality maintains over whole frequency range except the lowest frequency. At the lowest frequency, some deviation can be explained by a corrugated horn beam pattern change. A new horn design is underway.

As expected, the beam is largely symmetrical for symmetrical mirror axes. Visible aberrations effects are present in the cuts along the asymmetrical mirror axes. These effects, give rise to a beam tilt with respect to a nominal beam direction. Beam tilt, determined from measurements, is still within the required boundaries.

Finally, a far field antenna beam pattern can be determined from the 2-D data of fig. 10-11 by means of 2D Fourier transform. The resulting amplitude angular distribution is shown in fig. 16 and central part of the distribution is shown in fig. 17 compared with the angular size of ALMA antenna secondary mirror. Since mirror is in the far field zone of the waist, this gives a good indication of the illumination edge taper. From fig. 17 one can conclude that the edge taper is very close to the required 12 dB and illumination pattern of the secondary is well centered. A semi-round fringes are visible at the beam pattern at very low signal levels. These fringes are again due to approximation error of the CNC machine (and due to tool stroke direction). However, still visible, these effects do not degrade significantly the illumination pattern at the secondary mirror.

Periodical mirror surface deviations produce a various peaks at far field pattern, see fig. 16. The angle of these peaks allows to determine the period of these deviations. Random deviations with white spectrum result in increase of a spill over from the main beam towards all directions uniformly. Good signal to noise level obtained in the figure and low level of peaks due to periodical deviations suggests that the selected production technique is sufficient for application in ALMA band 9 receiver.

CONCLUSION

An opto-mechanical layout of ALMA band 9 receiver is proposed. A production method of direct CNC machining of mirror surfaces and alignment of optics by assembly was demonstrated by building a prototype optics system and developing a near field beam pattern measurement system. The proposed technique proves

to be successful and can be applied for not only for ALMA band 9 but also for any ground based or space instrument requiring to build many copies of optics, for instance a free flying interferometer.

A super lattice electronic device (SLED) detector was successfully used as a replacement of an SIS junction for room temperature evaluation of optics layout. A signal to noise level as high as 80 dB has been achieved for 30 Hz

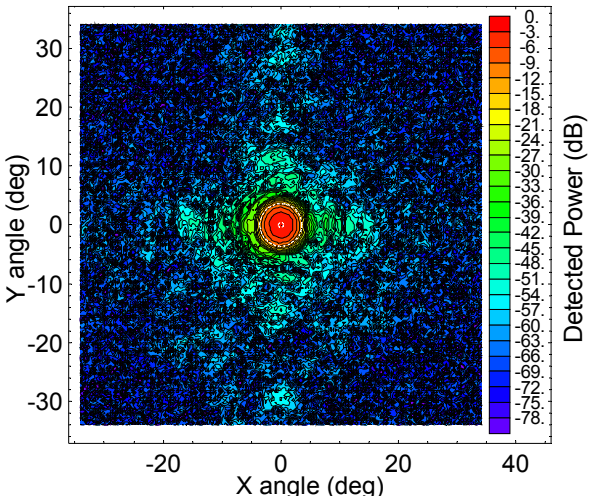

Fig. 16 Calculated far field amplitude angular distribution of the two-mirror block. Frequency is 672 GHz. The boundary of secondary mirror and central blockage of antenna are presented by a dashed line.

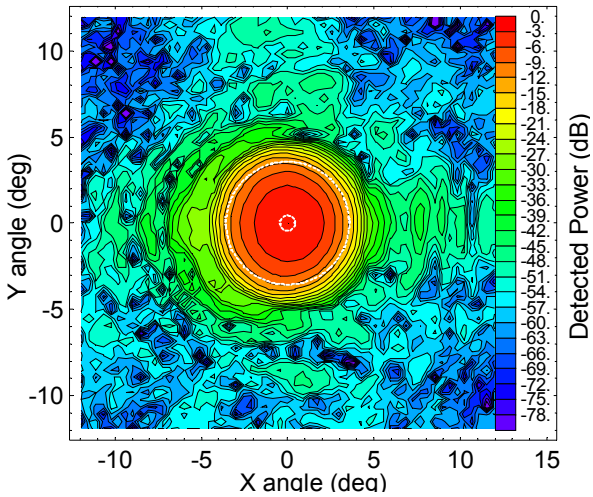

Fig. 17 Calculated far field amplitude angular distribution of the two-mirror block. Frequency is 672 GHz. The boundary of secondary mirror and central blockage of antenna are presented by a dashed line.

detection bandwidth at 672 GHz signal frequency for room temperature detector.

ACKNOWLEDGEMENT

The authors would like to thank Mark Harman of RAL for the overall design of the cartridges and cryostat that were given in section 1.2 We would also like to thank Fabrice Coq for the help in making the measurements. We would like to thank Willem Jellema for help in developing beam pattern measurement system. Authors also would like to thank Paveliev D.G. for providing SLED devices and Th. De Graauw for stimulating discussions. This work was supported by European Southern Observatory as a part ALMA band 9 contract.

REFERENCES

[1] ALMA Receiver Optics Design, J.Lamb et al, ALMA memo 362

[2] ALMA Project Book chapter 5, W.Wild et al.

[3] ALMA Front-end Optics, M.Carter et al, to be published

[4] ALMA Receiver Optics 2nd report, C-Y.Tham, S.Withington ALMA EDM

[5] ALMA project Book, chapter 6 Cryogenics, A.Orlowska et al

[6] Phase and Amplitude Measurements on an SIS Mixer fitted with a double slot Antenna for ALMA Band 9, M.Carter et al, Proceedings of The 13th International Symposium on Space Terahertz Technology

[7] Schomburg et al, Electronics Letters, vol 35, No 17 (1999)

List of Attendees and Authors for the 15th International Symposium on Space Terahertz Technology

Lastname	Firstname	Affiliation	Address	Telephone	Email
Asayama	Shin'ishiro	National Astronomical Observatory of Japan	2-21-1 Osawa, Mitaka Tokyo 181-8588 Japan	+81-422-34-3816	asayama@nro.nao.ac.jp
Austermann	Jason	University of Massachusetts, Amherst	619 LGRT; 710 North Pleasant Street, Amherst MA 01003 USA	413-545-1879	austermann@astro.umass.edu
Baryshev	Andrey	SRON/RuG	Landleven 12, P.O. Box 800, Groningen 9700 AV The Netherlands	+31 50 3638287	andrey@sron.rug.nl
Baselmans	Jochem	Space research Organistaion of the Netherlands, SRON	Landleven 12, , Groningen 9747 AD the Netherlands	+31503636648	j.baselmans@sron.nl
Battat	James	Harvard University	60 Garden Street MS-10, Cambridge MA 02138 USA	617-496-7667	jbattat@cfa.harvard.edu
Benford	Dominic	NASA / GSFC	Code 685, Greenbelt MD 20771 USA	301-286-8771	Dominic.J.Benford@nasa.gov
Berg	Therese	Chalmers University of Technology	Microtechnology and Nanoscience, MC2, Gothenburg 412 96 Sweden	+46 (0)31 772 5035	therese.berg@mc2.chalmers.se

Lastname	Firstname	Affiliation	Address	Telephone	Email
Betz	Albert	University of Colorado	593 UCB, 1255 38th St., Boulder CO 80309-0593 USA	303-492-4880	betz@colorado.edu
Blundell	Raymond	Harvard Smithsonian Center for Astrophysics	60 Garden Street, Cambridge MA 02138 USA	617-495-7367	rblundell@cfa.harvard.edu
Chattopadhyay	Goutam	Caltech/JPL	320-47 Caltech, Pasadena CA 91125 USA	626-395-3741	goutam@caltech.edu
Chen	Ming-Tang	ASIAA	645 N. Aohoku Plane, Hilo HI 96720 USA	808-933-8133	mchen@asiaa.sinica.edu.tw
Chuss	David	NASA Goddard Space Flight Center	Code 685, Building 21, Room C129D, Greenbelt MD 20771 United States	301-286-1858	chuss@stars.gsfc.nasa.gov
Coulombe	Michael	University of Massachusetts, Lowell	175 Cabot St., Suite 130, Lowell MA 01854 USA	978-458-3807	michael_coulombe@uml.edu
de lange	gerhard	SRON (Space Research Organization of the Netherlands)	landleven 12, Groningen 9747 AD the Netherlands	050-3634051	gert@sron.rug.nl
Deshpande	Prachi	University of Massachusetts, Amherst	Brandywine Drive, Apt # 6-D, Amherst MA 01002 USA	413-627-0853	pdeshpan@ecs.umass.edu

Lastname	Firstname	Affiliation	Address	Telephone	Email
Dickinson	Jason	University of Massachusetts, Lowell	175 Cabot St, Lowell MA 01854 USA	978-458-3807	Jason_Dickinson@uml.edu
East	Jack	The University of Michigan	2301 EECS Building, Ann Arbor Michigan 48109 USA	734-763-0212	jeast@eecs.umich.edu
Ediss	Geoffrey	National Radio Astronomy Observatory	2551 Ivy Road, Bldg. 4, Charlottesville VA 22903 USA	434-296-0245	gediss@nrao.edu
Eisele	Heribert	University of Leeds	School of Electrical Engineering, Woodhouse Lane, Leeds West Yorkshire LS2 9JT UK	0044113 343 7074	h.eisele@leeds.ac.uk
Emrich	Anders	Omnisys	Grougatan 8, Vastra Frolinda 42130 SWEDEN	46317343401	ae@omnisys.se
Erickson	Neal	University of Massachusetts, Amherst	Astronomy Dept, Lederle 619, Amherst MA 01003 USA	1-413-545-1873	neal@astro.umass.edu
Erickson	Ronna	University of Massachusetts, Amherst	619 Lederle GRC, Amherst MA 01003 USA	413-545-2764	erickson@astro.umass.edu
Ermisch	Karsten	Chalmers University of Technology/Onsala Observatory	Kemivägen 9, Gothenburg 41296 Sweden	+46-31-7721831	ermisch@oso.chalmers.se

Lastname	Firstname	Affiliation	Address	Telephone	Email
Fung	Andy	Jet Propulsion Laboratory	4800 Oak Grove Drive Mail Stop 302-306, Pasadena CA 91109 USA	818-354-1832	andy.k.fung@jpl.nasa.gov
Gao	Jianrong	SRON/TU Delft	Lorentzweg 1, Delft 2628 CJ The Netherlands	31-15-2781370	j.r.gao@tnw.tudelft.nl
Gerecht	Eyal	NIST	325 Broadway, Boulder CO 80305	303-497-4199	gerecht@boulder.nist.gov
Goeller	Robert	University of. Massachusetts, Amherst	619A LGRT, University of Massachusetts, Amherst MA 01003 USA	413-545-0789	rgoeller@nova.astro.umass.edu
Gorveatt	William	University of Massachusetts, Lowell-Research Foundation	600 Suffolk St., Lowell Massachusetts 01854 U.S.A.	978-458-3807	bill_gorveatt@yahoo.com
Goyette	Thomas	University of Massachusetts, Lowell	Suite 130, 175 Cabot St , Lowell MA 01854 USA	978-458-3807	Thomas_Goyette@uml.edu
Gradziel	Marcin Lukasz	Dep. Exp. Physics, NUI Maynooth, Ireland	Dep. Exp. Physics, NUI Maynooth, Maynooth Ireland	+353 1 708 4770	Marcin.Gradziel@may.ie
Graf	Urs	KOSMA, University of Cologne	I. Phys. Inst., Zuelpicher Str. 77, Cologne NRW 50937 Germany	+49-221-470 4092	graf@ph1.uni-koeln.de

Lastname	Firstname	Affiliation	Address	Telephone	Email
Groppi	Christopher	National Radio Astronomy Observatory	949 N. Cherry Ave., Tucson AZ 85721 USA	520-882-8250 x145	cgroppi@nrao.edu
Grosslein	Ron	University of Massachusetts, Amherst	LGRT 619, Amherst MA 01003 USA	413-545-2923	rmg@fcrao1.astro.umass.edu
Gu	Dazhen	University of Massachusetts, Amherst	University of Massachusetts, Amherst	303-497-3939	dazhen_gu@hotmail.com
Hajenius	Merlijn	SRON			m.hajenius@tnw.tudelft.nl
Hesler	Jeffrey	VDI/UVA	321 W. Main Street, Charlottesville VA 22903 US	434-297-3257	hesler@vadiodes.com
Hesper	Ronald	Kapteyn Astronomical Institute / SRON	Landleven 12, Groningen 9747 AD The Netherlands	+31-50-3638287	hesper@sron.rug.nl
Huebers	Heinz-Wilhelm	German Aerospace Center	Rutherfordstr. 2, Berlin 12489 Germany	+49-30-67055596	heinz-wilhelm.huebers@dlr.de
Hunter	Todd	Harvard-Smithsonian Center for Astrophysics	60 Garden St MS-78, Cambridge MA 02138 USA	617-384-8011	thunter@cfa.harvard.edu
Hurm	Volker	Fraunhofer IAF	Tullastr. 72, Freiburg D-79108 Germany	+49-761-5159555	volker.hurm@iaf.fraunhofer.de

Lastname	Firstname	Affiliation	Address	Telephone	Email
Irimajiri	Yoshihisa	Communications Reserach Laboratory (CRL) (National Institute of Information and Communications Technology (NICT) from April 1, 2004)	4-2-1 Nukui-kita, Koganei Tokyo 184-8795 Japan	+81-42-327-6089	irimaji@crl.go.jp
Ito	Hiroshi	NTT Photonics Laboratories	3-1 Morinosato Wakamiya, Atsugi Kanagawa 243-0198 Japan	+81-46-240-2885	hiro@aecl.ntt.co.jp
Jellema	Willem	SRON / Kapteyn Astronomical Institute	P.O. Box 800, Groningen NL-9700 AV The Netherlands	+31-(0)50-363-4058	W.Jellema@sron.nl
Karpov	Alexandre	California Institute of Technology	Caltech MC 320-47, Pasadena CA 91125 USA	626-395 8588	karpov@submm.caltech.edu
Kerr	Anthony	National Radio Astronomy Observatory	2551 Ivy Road, Bldg. 4, Charlottesville VA 22903 USA	434-296-0363	akerr@nrao.edu
Kimberk	Robert	Smithsonian Astrophysical Observatory	60 Garden st., Cambridge Massachusetts 02138 USA	617-496-7667	rkimberk@cfa.harvard.edu
Kimura	Kimihiro	Osaka Prefecture University		81-72-254-9727	kkimura@deal.cias.osakafu-u.ac.jp
Kodipelli	Vikram	Department of Astronomy, UMASS Amherst		413-545-4261	vkodipel@ecs.umass.edu

Lastname	Firstname	Affiliation	Address	Telephone	Email
Kollberg	Erik	Chalmers University of Technology	Dpt of Microtechnology and Nanoscience, Gothenburg SE-412 96 Sweden	+46-31-7721841	erik.kollberg@mc2.chalmers.se
Kooi	Jacob	Caltech	Downs Lab 320-47, Pasadena CA 91125 USA	626-395-4286	kooi@submm.caltech.edu
Kroug	Matthias	Delft University of Technology	Feldmannweg 17, Delft NL - 2628 CT Netherlands		kroug@tnw.tudelft.nl
Kuzmin	Leonid	Department of Microtechnology and Nanoscience	CXhalmers University, Gothenburg 412 96 Sweden	+46 31 772 3608	leonid.kuzmin@mc2.chalmers.se
Lauria	Eugene	National Radio Astronomy Observatory	2551 Ivy Road, Bldg. 4, Charlottesville VA 22903 USA	434-296-0270	glauria@nrao.edu
Lee	Mark	Sandia National Laboratories	PO Box 5800, MS 1415, Albuquerque NM 87185-1415 USA	505-844-5462	mlee1@sandia.gov
Lichtenberger	Arthur	University of Virginia	ECE Dept, 351 McCormick Rd., P O Box 400743, Charlottesville VA 22904-4743 USA	434-924-7545	lichtenberger@virginia.edu

Lastname	Firstname	Affiliation	Address	Telephone	Email
Logan	Daniel	University of Massachusetts, Amherst	Dept. of Astronomy, 619 LGRT-B, University of Massachusetts - Amherst, Amherst MA 01003 USA	413-545-3797	logan@nova.astro.umass.edu
Loudkov	Denis	Harvard Smithsonian Center for Astrophysics			dloudkov@cfa.harvard.edu
Maiwald	Frank	JPL/Caltech	4800 Oak Grove Drive, Pasadena CA 91109 USA	818-354-0214	Frank.Maiwald@jpl.nasa.gov
Marrone	Daniel	Harvard-Smithsonian Center for Astrophysics	60 Garden Street, MS 10, Cambridge MA 02138		dmarrone@cfa.harvard.edu
Mather	John	NASA Goddard Space Flight Center	Code 685, Greenbelt MD 20771 USA	301-286-8720	john.c.mather@nasa.gov
Mehdi	Imran	JPL	M/S 168-314, 4800 oak Grove Drive, pasadena ca 91030		imran.mehdi@jpl.nasa.gov
Merkel	Harald	Chalmers University of Technology	Kemigården 9, Göteborg Sweden SE41296 European Union	+46-31-772 1848	harald.merkel@mc2.chalmers.se
Moseley	Samuel	NASA Goddard Space Flight Center	Code 685, Bldg. 21, Rm. 066, Greenbelt MD 20771 USA	301-286-2347	Samuel.H.Moseley@nasa.gov

Lastname	Firstname	Affiliation	Address	Telephone	Email
Mueller	Eric	Coherent-DEOS	1280 Blue Hills Ave., Bloomfield CT 06002 USA	860-769-3325	eric.mueller@coherentinc.com
Muñoz	Pedro	KOSMA (Uni Köln, I. Phys. Inst.)	Zülpicher Str. 77, Köln 50937 Germany		espacio@ph1.uni-koeln.de
Narayanan	Gopal	University of Massachusetts, Amherst	Lederle GRC B628, Department , Amherst MA 01003 USA	413-549-0665	gopal@astro.umass.edu
Newman	Tom	Millitech, Inc.	29 Industrial Dr. E., Northampton MA 01060 USA	413-582-9620	TNewman@Millitech.com
Nicholson	John	University of Massachusetts, Amherst	UMASS/Amherst, Marcus Hall, Rm. 8C, Amherst MA 01003 USA	413-545-1395	nicholso@ecs.umass.edu
Nikola	Thomas	Cornell University	224 Space Sciences Building, Ithaca NY 14853 USA	607-255-3140	tn46@cornell.edu
Paine	Scott	Harvard Smithsonian Center for Astrophysics	60, Garden Street, Cambridge MA 02138 USA	617-495-7077	spaine@cfa.harvard.edu
Pan	Shing-Kuo	National Radio Astronomy Observatory	2551 Ivy Road, Bldg. 4, Charlottesville VA 22903 USA	434-296-0262	span2@nrao.edu

Lastname	Firstname	Affiliation	Address	Telephone	Email
Pearson	John	Jet Propulsion Laboratory	4800 Oak Grove Dr., Mail stop 301-429, Pasadena CA 91109 USA	818-354-6822	John.C.Pearson@jpl.nasa.gov
Philipp	Martin	KOSMA (Uni Cologne, I Phys. Inst.)	Zuelpicher Strasse 77, Koeln (Cologne) 50937 Germany	0049-221-470-2626	philipp@ph1.uni-koeln.de
Predmore	Read	Predmore Associates	120 Pulpit Hill Road, Suite 22, Amherst MA 01002 USA	413-549-8554	predmore@PredmoreAssociates.com
Prober	Daniel	Yale Univ.	15 Prospect St. POB 208284, New Haven CT 06520-8284 US	203-432-4280	daniel.prober@yale.edu
Raisanen	Antti	Helsinki University of Technology	Radio Laboratory, P.O. Box 3000, Espoo FI-02015 Finland		antti.raisanen@hut.fi
Reese	Matthew	Yale University	15 Prospect St, New Haven CT 06511	203-432-4270	matthew.reese@yale.edu
Rodriguez-Morales	Fernando	University of Massachusetts, Amherst	Marcus Hall 201 University of Massachusetts, Amherst MA 01003 USA	413-577-0695	frodrigu@ecs.umass.edu
Santavicca	Daniel	Yale University	15 Prospect St. - Becton Center Room 405, New Haven CT 06511	203-432-4270	daniel.santavicca@yale.edu

Lastname	Firstname	Affiliation	Address	Telephone	Email
Schlecht	Erich	Jet Propulsion Laboratory/Caltech	MS 168-314 4800 Oak Grove Dr., Pasadena CA 91106 USA	818-354-4887	erichs@merlin.jpl.nasa.gov
Schloerb	F. Peter	University of Massachusetts, Amherst	Astronomy Lederle GTWR B Univ. of Massachusetts, Amherst MA 01003 USA	413-545-4303	schloerb@astro.umass.edu
Schoelkopf	Robert	Yale University	15 Prospect St., 423 Becton Center, New Haven CT 06511 USA	203-432-4289	rob.schoelkopf@yale.edu
Schultz	Jonathan	University of Virginia	122 Washington Avenue, Charlottesville VA 22903 United States	434-982-2262	schultz@virginia.edu
Serapiglia	Brendan	University of California, Santa Barbara	IQuest Building 981, Santa Barbara California 93117 United States	805-893-7023	brendan@iquest.ucsb.edu
Shen	Minghao	Yale University			minghao.shen@yale.edu
Skalare	Anders	Jet Propulsion Laboratory	4800 Oak Grove Drive, Mail Stop 168-314, Pasadena California 91109 United States	818-354-9383	anders.skalare@jpl.nasa.gov
Staguhn	Johannes	NASA/GSFC			staguhn@stars.gsfc.nasa.gov

Lastname	Firstname	Affiliation	Address	Telephone	Email
Takeda	Masanori	Kansai Advanced Research Center, CRL	588-2, Iwaoka, Iwaoka-cho, Nishi-ku, Kobe Hyogo 651-2492 Japan	+81-78-969-2173	takeda@po.crl.go.jp
Teufel	John	Yale University	Dept of Applied Physics, PO Box 208284, New Haven CT 06520-8284 USA	203-436-0453	john.teufel@yale.edu
Tils	Thomas	KOSMA	Zuelpischer Strasse 77, Cologne NRW 50937 Cologne	+49 221 470 3489	tils@ph1.uni-koeln.de
Tong	Edward	Harvard-Smithsonian Center for Astrophysics	60 Garden Street, MS 42, Cambridge MA 02138 USA	617-496-7641	etong@cfa.harvard.edu
Uzawa	Yoshinori	Kansai Advanced Research Center, CRL			uzawa@crl.go.jp
Ward	John	JPL	4800 Oak Grove Drive - Mail Stop 168-314, Pasadena CA 91109-8099		john.ward@jpl.nasa.gov
Werner	Karen	University of Massachusetts, Amherst			kbwerner@astro.umass.edu
Wielgus	John	University of Massachusetts, Amherst	619 Lederle Tower (Radio Astronomy), Amherst MA 01003 USA	413-545-3076	jwielgus@fcrao1.astro.umass.edu

Lastname	Firstname	Affiliation	Address	Telephone	Email
Wilson	Grant	University of Massachusetts, Amherst	710 N. Pleasant St., Amherst, MA MA 01003 US	413-545-0460	wilson@astro.umass.edu
Wollack	Edward	NASA Goddard Space Flight Center	Code 685, Bldg. 21, Rm. 064, Greenbelt MD 20771 USA	301-286-1379	Edward.J.Wollack@nasa.gov
Yassin	Ghassan	University of Cambridge	Cavendish Laboratory, Madingley Road , Cambridge CB3 0HE UK	+4412235337309	ghassan@mrao.cam.ac.uk
Yngvesson	Sigfrid	University of Massachusetts, Amherst	ECE Dept., University of Massachusetts, Amherst MA 01003 USA		yngvesson@ecs.umass.edu
Zannoni	Ric	University of Massachusetts, Amherst			thezs@att.net
Zhao	Xin	THz lab, Umass	990 N. Pleasant St., Apt. F10, Amherst MA 01002 U.S.A.	413-545-2170	xinzhao@ecs.umass.edu